Size Control in Pelletisation
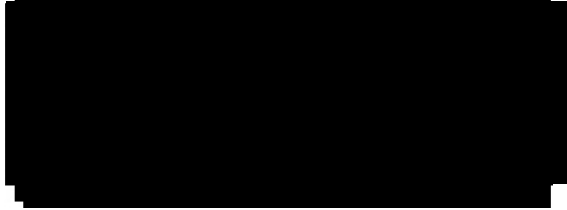
William Kennedy Walls

May, 2022

**Prifysgol Abertawe
Swansea University**

Department of Engineering

Swansea University

This thesis is submitted in fulfillment of the requirements for the degree of

Doctor of Engineering

I

Declaration

This work has not previously been accepted in substance for any degree and is not being concurrently submitted in candidature for any degree.
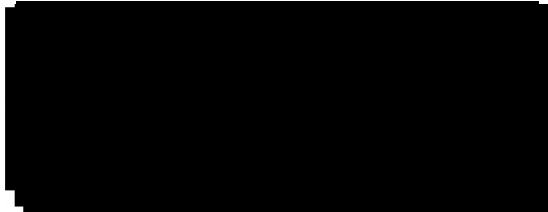
May 24, 2022

_____   _____

Candidate Signature   *Date*

This thesis is the result of my own investigations, except where otherwise stated. Other sources are acknowledged by footnotes giving explicit references. A bibliography is appended.
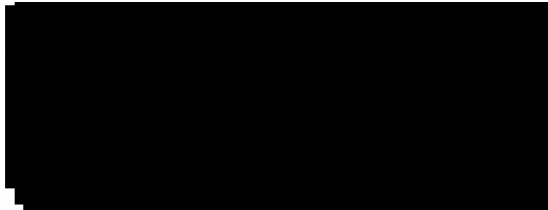
May 24, 2022

_____   _____

Candidate Signature   *Date*

I hereby give consent for my thesis, if accepted, to be available for photocopying and for inter-library loan, and for the title and summary to be made available to outside organisations.

May 24, 2022

_____   _____

Candidate Signature   *Date*

The University's ethical procedures have been followed and, where appropriate, that ethical approval has been granted.

May 24, 2022

_____

_____

Candidate Signature

Date

Acknowledgements

Thanks are given to technical knowledge and support provided by the staff at TATA, DLS and Swansea university over the years.

I would like to thank my friends for all the support provided over the years, who always were there to help keep me grounded and provide companionship through the difficult periods. Their advice was invaluable in providing an outside perspective which allowed the re-examination that was vital to the completion of this work.

I would like to acknowledge my dads support through the project, who was always willing to lend an ear to my explanation of the work in great detail.

I would like to thank Alejandra Garcia Cabanillas, who provided support during the first half of this project but more importantly set off a series of events that lead to my starting my doctorate.

I would like to thank Jack David Green, for listening to my relentless nonsense about granulation and generally putting up with me for the latter half of my doctorate.

I give thanks to Mark Holmes for his excellent DEM program, without which the verification and validation of the modelling would have never succeeded.

Thanks are given to my industrial supervisor Martin Allen, for providing support regarding the material usage and production at Tata and supplying me with sludge to analyse.

And of course, I thank my academic supervisor Steve Brown for his tireless support through the madness that was carving through this project, and allowing me to plow through endless dead ends that all came together to produce gold.

Abstract

This thesis covers an investigation into the topic of size control in pelletisation, with a focus on how it relates to the pelletisation of ferrous by products. The ferrous by product of focus is oily mill sludge, which has had its properties examined. The kinetic behaviour is also examined using Discrete Element Methods. Over the course of the investigation the growth behaviour of granules has been clarified as being able to be explained entirely through external saturation sources such as spray and consolidation behaviours. These contribute to the cohesion of individual pellets, and adhesion of pellets together, which constitute a completely new model of agglomeration. This Adhesion-Cohesion model is physically in line with agglomeration research and granular mechanics as a whole, and was subsequently integrated into a Discrete Element Method simulation of agglomeration which provided validation for the growth behaviour predicted.

VI

Contents

List of Figures

XVI

XVII

XVIII

XIX

XXI

XXII

XXIII

XXIV

XXV

XXVII

XXVIII

XXX

XXXI

XXXII

XXXIII

XXXV

XXXVI

XXXVII

XXXVIII

List of Tables

XLI

Chapter 1

Introduction

1.1 Synopsis

Tata steel perform pelletisation of ferrous-by products such as mill sludge as a matter of practicality, though the output often has wide variations in the size and strength.

Pelletising can provide a cheap and effective alternative to the sintering process. The general process of pelletising is understood, however the specifics are still very difficult to understand, due to the multi-faceted and multi-scale nature of the process. The properties and behaviour change continuously during the process, and it is difficult to make measurements as the most important components of the process happen in very short time scales in very chaotic environments that do not scale well.

The pelletisation of waste materials is also not as well understood as ideal pelletisation, such as for finely prepared natural ores. These ferrous wastes, such as mill sludge, have larger particle sizes and size ranges, and higher water contents or other contaminants that also affect the behaviours.

The original aim of the project was to test various material inputs, however the direction changed so that the project became more about understanding the

1

fundamental mechanisms of granulation, which then in turn would allow better understanding of why different inputs could alter the behaviour and product properties as they do.

To gain insight into the process the material was investigated, however the majority of the work went into developing better analytical models which could be implemented into discrete element method models, which in turn allowed the process to be analysed in great detail, revealing never before shown behaviours.

This understanding of the process revealed a number of mechanisms relating to the consolidation and coalescence requirements which explain why the variation in the output size is to some extent intrinsic and even somewhat necessary if a stable average output size is desired.

1.2   Project overview

The original title for this work was "Pelletisation of ferrous by-products", The by-products in question were an unpleasant product referred to as "Oily mill sludge". Pelletisation is the process by which this sludge, which is a mixture of oils and fine particulate iron, is formed into balls around 1-2cm diameter, ready for introduction into the blast furnace.

Tata steel requested and partially funded this topic for research because the pellets that were being formed were inconsistently produced, with variation in both the strength and size distribution. Ordinarily, plant would sinter waste or by-product iron scraps for return to the furnace, but because of the oily nature of the sludge, this was not practical.

To give some context, mill scale is one of a variety of iron oxide wastes formed during the steelmaking process. The reason why it is abnormal is because it is removed from steel during the rolling process using high pressure water jets, along with lubrication oils. When this occurs, the scale washes into settling tanks, where two main grades of waste develop. The largest coarse particles settle in

the early tanks, while the oil and fine particles collect in secondary tanks.

The high iron content makes it well suited to be recycled and the oils would provide additional carbon for the furnace. To be reintroduced to the blast furnace, it needs to be agglomerated in some fashion to maintain the blast furnace efficiency [1].

At Tata steel, the current primary solution to recycle waste is through sintering, and the larger scale product is easy enough to sinter. However, the oil content in the sludge renders it unsuitable for sintering as it damages the processing equipment at a high rate. Instead, it is pelletised.

Pelletisation (in this context) is the process of agglomerating small particles together using a binder to form the feed into larger products, i.e. Pellets. Pelletising is commonly performed on iron ores, especially ores such as taconite that need beneficiating from low grade ores. Once formed, pellets of the desired size are then usually sintered in preparation for the blast furnace. Though it requires more work, this process is more efficient than typical sintering.

As mentioned, mill sludge cannot be sintered, so the sintering step cannot be performed. The current methodology used on site by Coarse Mill Scale at Tata steels production site to resolve this problem is to allow the sludge to drain as much as possible simply under gravity. Once as much as possible has drained, a chemical conditioner is added which combines with the water and oil content, which again takes some time to complete depending on the surrounding conditions. Once this step is finished, then the material is pelletised using a cement binder, which provides the structural strength required that sintering usually provides.

The process is imperfect, and generates a large quantity of outsize material and the strength is a little low for the blast furnace to use as a consistent feedstock. Because cement is added to the mixture, returning the outsize also slightly reduces the total iron content of the feed when it is cycled, so minimising the amount needed to be returned is beneficial for multiple reasons.

Because the material choice is unusual, the emphasis was placed on the material being the primary reason that the production was inconsistent. From this, the solution therefore was presented as being solved through materials, by adjusting the feed content, additives, or binder content.

1.2.1 Subsequent Understanding

This proved to be a serious oversimplification of the problem. Certainly, the material was unusual, but there is no "standard" particle material for pelletisation to compare against. The material is also treated with conditioner which, while this does not make it able to be sintered, it does significantly alter the properties through ab/adsorption of the oil and water in the sludge. Further, discussion with contacts at Tata Port Talbot suggested that a variety of materials had been added or tested in the production of the pellets, further muddying the water.

As the project matured, technicians from Darlow Lloyd & sons who produce the pellets on site at Tata Port Talbot were consulted on their experience in the production, and their view on what causes the variability in the process. Here it was determined that, in fact, the product is made much more consistently with the same inputs, and despite this there remained variability within and between batches. Additionally, a phrase was casually mentioned, which had been noticed within the literature:

"Pelletisation is more of an art than a science"

This phrase has been applied to other fields, particularly in materials science, to describe how relating the inputs to the outputs is hard to quantify but those with experience generally understand how they connect. The irony that comes from the initial description of the project being that "pelletisation is well understood" notwithstanding, the phrase is relevant to pelletisation since even among the more well developed models, the actual demonstrated performance was underwhelming. The phrase has even been quoted in a couple of papers to suggest

that those days are long past [2], however the lack of application of the models they provide suggested otherwise [3].

The research was itself hampered by the fact that the literature was very inconsistent. Definitions were used which apply to many extraneous fields, and multiple terms were used for the same final product. Often only the most basic information is reported, and often when testing either the size or the strength the other is not reported at all, leaving no way to really relate the two. Finally, often models are not compared against previous results or models, and the assumptions not evaluated or carried forwards to ensure that the extensions remain valid. For example, a model which assumes perfect elasticity of the pellets [4] ignoring the coefficient of restutution being less than 0.1 [5], is nonetheless carried forwards by subsequent authors [6].

On top of this, actually measuring the apparently important parameters is difficult at the best of times, and impossible at the worst. The process occurs at multiple scales, which makes scaling a challenge, which is unfortunate as scaling is a practical means to develop a better understanding of the process.

With this said, some of the elements of the process are understood, but the implications of what these behaviours mean for the actual size is lacking, instead more focus is placed on growth rates. To be tasked with improving the size distribution without knowing what influences the size is challenging. This lead to the heavy focus on understanding what dictates the size, then how the behaviours influence this size. Only then could efforts be made to improve the distribution. The strength properties were less heavily investigated because of the focus required for the investigation of the size, as the literature had better directions on how to increase the strength.

The process was modelled using a Discrete Element Method model, which allowed every pellet to be modelled as they interact with the environment and one another. This was because the effect of different pellet drums could be modelled simply by creating a model and putting it into the simulation. It also, as it turns

out, had the very important effect of testing agglomeration model validity. Any model which had assumptions in the mechanics had to actually experience the full range of interactions explicitly, instead of assuming global behaviours.

Over the course of this research assumptions about the primary location of collisions are overturned, and the location where the most frequent collisions and the location of the strongest collisions are determined are in separate places. The location of the strongest consolidation is described which explains the induction type behaviour in finer detail which fits the collision behaviour. Most importantly, the first major new model for agglomeration in 20 years is presented, which ties both the saturation and the dynamic behaviour to the ability of the granules to grow, and provides the first steps to really allowing scaling to be implemented.

The topics that this thesis will cover are the material itself, the use of DEM as a means to model the granular behaviour, the kinetics of the pellets, granule mechanisms such as yield strength and consolidation, how to simulate agglomeration both from the mechanism and the program sides, and the results of implementing agglomeration methods into DEM.

1.3   Aims

Based on the literature review, and the overall task required of the problem at hand, the aims of this thesis are as follows:

1. Understand the composition of the Mill Sludge

2. Model the granular flow process using discrete element methods

3. Understand the kinematics of pelletisation

4. Simulate granule agglomeration

5. Evaluate the existing models of agglomeration and their effectiveness in the context of DEM

6. Determine how to improve the granule size distribution using passive methods

1.4 Overview

This document is split up into the following sections:

- **Chapter 1** Current section; Introduction.

- **Chapter 2** Background research and commentary on the literature.

- **Chapter 3** Material Analysis; of both the particles and the oils.

- **Chapter 4** DEM implementation; The details of the method and program, and the results of simulating the kinematic behaviour of pellets.

- **Chapter 5** DEM Kinetics; and the results of simulating the kinematic behaviour of pellets.

- **Chapter 6** Granule Mechanisms; Effect of saturation, The yield strength, and consolidation behaviours, and assumptions in current models regarding them all.

- **Chapter 7** Agglomeration Theory; Analysis of theories of agglomeration, invalidating a major model both conceptually and mathematically, and introduction of a new model and theory for the agglomeration process

- **Chapter 8** Agglomeration implementation; briefly covers the implementation of agglomeration models into the DEM program.

- **Chapter 9** Agglomeration Modelling; Covers the actual results found from the agglomeration, for previously tested partially functional models and the newly developed model.

- **Chapter 10** Reflection; Reflects on the work as a whole, discussing the important conclusions from an industrial point of view as well as the scientific perspective.

Glossary

agglomerate all entities which are formed of multiple particles bound together in a fashion which allows the individual components to still be identified discretely. For clarity, this excludes composites of materials where strands allow indefinite boundaries. 9

Binder the binder in granulation research refers to the material which holds the granules together. However it is sometimes referring to an additive to water which provides viscosity or other useful properties on its own, and sometimes refers to the totality of the liquid. Here refers to the additive, and the liquid content referred to as simply "Liquid". 9

coalescence the action of granules coming into contact and merging into a single granule. 9

Cold Strength The strength of a granule when set, only for cold bonded pellets. 9

consolidation the action of the particles coming closer together, reducing the porosity. 9

Crumb Poorly defined in the literature, other than "small, weak" granules. High aspect ratios associated with them. . 9

Discrete Element Method A method of simulating the behaviours of discrete elements. No grid is used, the elements instead determining interactions

through collision detection mechanisms and respond according to the rules defined. 9, 13, 44

Dry Strength The strength of a granule formed without a chemically setting binder, when the moisture has been removed, hence, "dry". 9

element individual modelled objects in a DEM simulation. Distinguished here for clarity from Particles, though in the literature DEM elements often are referred to as "particles" as well. 9, 71, 83

Granule Used interchangeably in the literature with agglomerate as well as pellet and even for non agglomerates (eg, granulated sugar). Here defined as an agglomerate of particles bound together by liquid though a non-compressive process. 9

Green Strength The strength of a granule when freshly formed (and thus "green") and thus wet. 9

Induction Growth Growth regime where the granules remain small for a long time before suddenly growing very rapidly. 9

Nuclei Very small granules, formed from the direct interaction of the liquid or liquid and binder, and the particles. 9

particle used variously by different authors. Here will be used exclusively in reference to individual solid sub-components of the feed. Point-like, not long strands. 9, 223

Pellet Used interchangably with granule in some parts of the literature. Here defined as a granule in the later stages of growth, more finished and spherical. 9

Pellet Bed the total pile at the bottom of the granulation drum, with shape defined by the morphology of the drum as well as the pellet properties. 9

Population Balance Model A model which applies an operation to a distribution which alters the resultant shape of the distribution, to model the effect the "population" distribution has on itself, the balance being that without additional sources or sinks the sum of the population remains static. 9, 13, 33, 43, 45, 48, 49

Porosity the amount of bulk volume of the agglomerate that is not filled with solid. 9

process units Production elements of a plant, such as the blast furnace or the rolling mill. 9, 13, 15

production control equipment Equipment used to reduce contamination of the environment. 9, 13, 15

Rapid Growth Growth regime where the granules grow very quickly, and typically grow excessively. 9

saturation the amount of pore volume in the agglomerate that is filled with liquid rather than gas. 9

Steady Growth Growth Regime where the granules grow steadily. 9

Voidage the volume of the agglomerate which is neither filled with solid or liquid. 9

Acronyms

BOF Basic Oxygen Furnace. 9, 19

BTM Blank Trimodal Model. 9, 183

CMS Coarse Mill Scale. 3, 9, 16, 18, 21, 147, 153

DEM Discrete Element Method. 9, 43, 44, 49, 71, 100, 157, 158

DLS Darlow lloyds Sons. 9

DRI direct reduced iron. 9

HTM Helically ridged Trimodal Model. 9, 183

OMS Oily Mill Sludge. 9, 16–21

PBM Population Balance Model. 9, 43, 44, 47, 49

PCE production control equipment. 9, 15

PU process units. 9, 15

RTM Ridged Trimodel Model. 9, 183

List of Symbols

The symbols demonstrated below show the symbol used in this work, the meaning of that symbol, (and alternatives sometimes used in previous literature, listed after a colon :), for the readers benefit. $\star$ is also used as a wildcard for the prefixes.

Prefixes

$\overline{\star}$	Arithmetic Mean
$\widehat{\star}$	Geometric Mean
$\widetilde{\star}$	Harmonic Mean
$\star_{50}$	Median Value
$\Delta\star$	Difference between two boundary Values
$\star_0$	Value at $t = 0$
$\star_\infty$	Value at $t = \infty$
$\star_{max}$	Maximum Value
$\star_{min}$	Minimum Value
$\star_g$	Physical parameter related to the granules, in contrast to the particles
$\star_l$	Physical parameter related to the granule Liquids
$\star_p$	Physical parameter related to the particles
$\star_s$	Physical parameter related to the granule Solids
$\star_T$	Physical parameter related to the Totality of the granule, to distinguish from the other properties $\star_T = \star_s + \star_\epsilon$
$\star_v$	Physical parameter related to the granule Voids
$\star_{ch}$	Characteristic
$\star^*$	Critical
$\star^*$	Difference between two boundary Values
$\dot{\star}$	Derivative
$\star_\epsilon$	Physical parameter related to the granule pores - $\star_\epsilon = \star_l + \star_v$

Granule properties

AR	Particle Aspect Ratio, $\mathit{AR} = a/c$: α
Z	Coordination Number
ρ_g	Granule Density, $\rho_g = m_T/V_T$
ρ_l	Liquid Density, $m_l = m_l/V_l$
ρ_s	Solid Density, $\rho_s = m_s/V_s$: ρ_t , ρ_p
$d_{3,2}$	Particle saunter mean diameter
a	Particle longest half-axis

b	Particle intermediate half-axis		$V_l/(V_T \epsilon)$
c	Particle shortest half-axis	S_∞	Saturation at end of consolidation, $S_\infty = V_l/(V_T \epsilon_{min})$
q	Intermediate-Long fraction, $q = b/a$	$S_{f,c}$	Saturation at start of capillary state
m_l	Liquid mass		
m_{lmax}	Maximum Liquid Mass for a given granule before oversaturation occurs	$S_{p,f}$	Saturation at limit of pendular state
m_s	Solid mass	K_{Smax}	Saturation at complete pore filling, when it starts to appear on the surface and slurry forms
m_T	Total Granule Mass		
$m_{l/s}$	Liquid to solid Mass ratio, m_l/m_s	F	Shape Factor, $F = p/q$
		p	Short-Intermediate fraction, $p = c/b$
m_{l/s_∞}	Liquid to solid Mass ratio when oversaturation occurs, m_{lmax}/m_s	S_{sa}	Specific Surface Area of the particles
ϕ	Packing fraction : Φ		
$\phi(\infty)$	Packing at end of consolidation, $\phi(\infty) = 1 - \epsilon_{min}$	Ψ	Particle Sphericity, $\Psi = \frac{12.8 \sqrt[3]{p^2 q}}{(1+p)(1+p)6\sqrt{(1+p^2)(1+p^2)}}$
$\phi(n)$	Packing at point n	V_l	Liquid Volume
$\phi(0)$	Packing at start of consolidation, $\phi(0) = 1 - \epsilon_0$	V_ϵ	Granule Pore Volume
		V_s	Solid Volume
d_p	Particle diameter	V_T	Total Granule Volume
$d_{p_{max}}$	Particle maximum diameter	V_v	Granule Void Volume
d_m	Particle fines components	$V_{l/s}$	Liquid to solid Volume ratio, m_l/m_s
r_p	Particle radius		
ϵ	Granule Porosity, $\epsilon = V_\epsilon/V_T$	F_{adh}	Adhesion Force
$\epsilon_{p=0}$	Pre-compression Porosity	α_{wet}	function describing relation of radial surface strain to adhesion
ϵ_0	Porosity at start of consolidation		
ϵ_{min}	Minimum Granule Porosity	$A_s p$	Area Sprayed
S	Granule Saturation, $S =$	h_a	asperity height

$\dot{z}$	Axial rate of speed through the drum	d_d	Droplet Diameter
F_{bond}	Bond strength in N	ε_a	Dielectric Constant
σ_{bond}	Bond Strength	d_g	Granule diameter
Σ_{bond}	Bond force	$d_{g/p}$	Ratio of granules to particles
V	Bridge Volume	τ_p	Dimensionless penetration time, $\tau_p = \frac{t_p}{t_c irc}$
F_c	Capillary Force	Ψ_a	Dimensionless spray flux $\Psi_a = \frac{3\dot{V_s}p}{2\dot{A_s}pd_d}$
Ca	Capillary number $Ca = \frac{\mu\dot{\varepsilon}d_p}{\gamma cos\theta}$		
Ca^*	Modified Capillary Number $Ca^* = \frac{\mu V_c}{\gamma(1+cos\theta)}$	Ψ_{alt}	Modified Dimensionless spray flux $\Psi_{alt} = \frac{\dot{V_s}p}{v\dot{A_s}p}$
m	Constant exponential for relating capillary number to σ_y^* : n	τ_A	Dimensionless Time, $\tau_A = t \times k_{\epsilon A}$
		R_{Dr}	Drum radius
$A_c irc$	Circulating Area	ω	Drum Rotation Rate
$t_c irc$	Dimensionless penetration time, $\tau_p = \frac{t_p}{t_c irc}$	$\mu_{f_d}^*$	Dry interparticle Friction
		F_E	Electrostatic Force
Δx	Distance closed between particles	a	Flaw Size
		μ_f	Friction
σ_c	Cohesive Stress	φ	half fill angle
θ	Contact Angle	A_{ham}	Hamaker Constant
θ_c	Critical angle of collapse	H	Hardness
St_v^*	Critical Stokes Viscous number	I	Impact rate function
H	Liquid surface curvature	I	Inertial Number $I = \frac{\dot{\gamma}d_p}{\sqrt{\sigma_n\rho_s}}$
κ	Debye length	J_{IC}	J-integral, from crack propagation analysis
Δ_{lim}	Limiting Granule Diameter		
Δ_{limAdh}	Limiting diameter from Adhesion criterion	β_{Adh}	Size fraction term in population balance kernel Form
Δp	Capillary induced pressure difference	β_{eke}	Equipartition of kinetic energy Kernel
D_{pile}	Pile Depth	β_{OK}	Orthokinetic Kernel

β_0	Time dependence part of Population Balance Kernel	r_g	Granule Radius
l_{cr}	Cohesive Stress	r_d	Ratio diameter, $d = r_d D$
Δ_{limCoh}	Limiting Diameter due to cohesion	δ''	Final deformation depth
		P^*	Reduced Pressure, $P^* = \frac{\sigma_n d_p^2}{\pi \gamma}$
Δ_{limCoh}	Limiting Diameter due to saturation	h	Height of liquid drawn up by capillary force
λ_{ch}	Characteristic mean free path	R	Sample original Radius : r_0
V^*Bo	Modified Bond number	α	Constant relating Diameter ratios, A_M and M
g_M	Function relating the diameters to the Separating Moment	F_{sep}	Separating Collision Force
N_g	Current number of granules	S_d	Separation distance between sphere surfaces
N_g	Impact rate function	B	Separation Force Function, $B = (3A)/(4\pi^{3/2})$
N	Number of rotations		
Ω_{def}	Simplified agitation values collected	S_{drup}	Separation Rupture Distance
n	Number of impacts	σ_{sep}	Separation stress
d_k	Particle coarse components	τ_f	Shear strength due to friction
P	Particle	k_1	$\sigma_y{}^*$ correlation Value
X	Particle fines to coarse ratio, d_m/d_k	k_2	$\sigma_y{}^*$ correlation Value
		$\sigma_{t,c}$	Tensile Strength, Capillary contribution
S_p	Particle Diameter Span	$\sigma_{t,f}$	Tensile Strength, Pendular contribution
t_p	Time taken for droplet to penetrate	$\sigma_{t,p}$	Tensile Strength, Funicular state
ν	Poisson's Ratio	$\sigma_{t,v}$	Tensile Strength, Viscous Contribution
C_s	Prior Compressive Stress applied		
p_{ref}	Reference Pressure	$\sigma_y{}^*$	Dimensionless Yield Strength σ_y
ρ	principal Radius of curvature	$V_s p$	Volume of liquid sprayed
R_e	External radius from liquid	St_{def}	Stokes Deformation Number,

$St_{def} = \frac{\rho_g V_c^2}{\sigma_y}$: De

St_v Stokes Viscous Number, $St_v = \frac{8\rho_g \widetilde{d_g} V_{cN}}{9\mu}$

Δp Capillary Suction

φ Surface electric potential

h_0 Liquid Surface height

ε_r Surface radial Strain

γ Surface tension

v velocity of feed bed

σ_t Granule Tensile Strength

$\mu_{fw,theor}{}^{*}$ theoretical wet interparticle Friction

V_{ch} Characteristic Velocity

F_{vw} Van der Waals Force

V_f Fluidisation Velocity

V_I Impeller tip Velocity

$\overline{V_R}$ relative velocity

F_v Viscous Force

μ Viscosity

v_p Particle Velocity

σ_y Granule Yield Strength : Y_d

Y Y(x) of liquid bridge curvature

Proportionality Constants

C Proportionality constant relating inverse porosity to coordination

A_5 Proportionality constant related to a limiting size prediction.

C_m Math constants collected for convinience in Adhesion Criterion

   Value

a Proportionality constant related to a limiting size prediction and plasticity.

α_0 Intrinsic Interaction Parameter related to a limiting size prediction.

b Saturation gradient component of α_0

f Constant accounting for additional effective voume due to inclusion of air pockets

K_g Proportionality constant relating the the liquid penetration to the surface

c Proportionality constant related to a limiting size prediction and x .

$k_{F_{bond}}$ Bond strengthening rate constant

k Consolidation Rate

k_ϵ Proportionality constant related to consolidation

$k_{\epsilon A}$ Consolidation rate constant, General

$k_{\epsilon B}$ Consolidation rate constant, St_{def} proportionality

K_α Agitation constant derived from K_A and α

K_A	Constant of proportionality describing A_M relation to V_{ch} L_{ch} and ρ_g	**General Mechanical Response**	
		ρ	Density
		V	Volume
K_φ	Constraint, $\varphi = H/\sigma_y$: φ,K	ε_z	Axial Strain
K	Hertzian contact constant, $K = \frac{3\pi}{8E}$	σ_z	Axial Stress
		ζ_r	Bending damping
λ	Scaled difference between the maximum and minimum compressive strengths in the granulator, $\lambda = \frac{Q_{max}}{Q_{max}-Q_{min}}$	δ_r	Bending extent of interpenetration
		μ_r	Bending spring constant
		$\omega_{r,sum}$	Rotation vector of bending
A_M	Dimensioned Constant relating the Separating Moment to a function of the diameters	k_r	Bending spring constant
		D	Distance between centres of spheres i and j
K_γ	Proportionality constant that varies between 5 different methods to scale between the granule diameters and the moments applied in the system.	Q	Compression Force
		Q_{max}	Maximum Compressive Force
		Q_{min}	Maximum Compressive Force
		T_c	Critical time step
		F	Cumulative probability
β	Proportionality constant related to consolidation	ζ	Damping Factor
		δ	Deformation
C	Proportionality constant related to consolidation, $\frac{(\phi(\infty)-\phi(0))}{\phi(\infty)}$	D_s	upper limit of all particles in fuller/power law equation
A	Constant relating size to separation force	d_s	upper limit of passing particles in fuller/power law equation
K_s	Bond strength constant related to viscosity and surface liquid availability.	R	Sphere Radius
		e_{rest}	Coefficient of Restitution
		$F_{r,i}$	Bending Force
$K_{\frac{t}{c}}$	Constant relating the tensile to compressive strengths	F_{dn}	Damping force
		F_g	Force due to Gravity

F_n Normal Force

F_s Shear force

F_{kn} Spring Force

m parameter to define the shape of the curve of the fuller/power law equation

g Gravitational acceleration

$\hat{g}$ Direction of gravity

E_g Gravitational potential energy

h drop height

I_i Inertia

E_k Kinetic energy

ε_{max} maximum compressive strain

M Moment

V_n Normal Velocity

δ distance of overlapping between spheres r_i and r_j

p proportion passing through as a function of d_s

η Shear Rate

E_p Plastic Deformation Energy

ζ Shear Rate

p Power law exponential

p Pressure

P Probability

P_n Probability of surviving n impacts

r_{eff} Effective Radius

R Sphere Radius

$r_{c,i}$,$r_{c,j}$ Rotation vector for torque values for sphere 1 and 2

S_d Separation of surfaces of approaching Spheres

B Separating Force

ζ_s Shear damping

δ_s Change in distance across the surfaces of two spheres

$\dot{\gamma}$ Shear Rate

k_s Shear spring constant

μ Sliding driction

$\dot{s}$ Slide dotion

$\hat{s}$ Slide directional vector

D Diameter of sphere

d Diameter of sphere smaller than D in calculations

R Radius of sphere

k Spring Constant

p_0 pressure applied to sphere

A Sphere contacting area

a Radius for sphere contacting area

E Stiffness

ε Strain

ε_{ij} Strain in (i,j) directions

ε_{ii} isostatic Strain

ε_{11} Tensile Strain

$\dot{\varepsilon}$ Strain Rate

σ Stress

σ_n Normal stress

ε_r Surface Radial Strain

C Constant relating the critical time step to the DEM system properties

Δt Time step

t time

$T_{r,i}$, $T_{r,j}$ Torque applied due to Twisting on sphere 1 and 2

$T_{r,i}$, $T_{r,j}$ Torque applied due to bending on sphere 1 and 2

$T_{s,i}$ Torque due to shear

$T_{t,i}$,$T_{t,j}$ Torque due to twist applied to sphere 1 and 2

ζ_t Twisting damping

δ_t Twisting extent of interpenetration

μ_t Twisting spring constant

$\omega_{t,sum}$ Twisting vector of bending

k_t Twisting spring constant

V_{cN} Normal Collision Velocity

V_c Collision Velocity

V Velocity

$r_{4,3}$ Volume Mean Radius

Other symbols

E_t Averaged cumulative collision energy over time

I Pan pelletiser inclination

L Litres

Chapter 2

Background Research

This section reviews the current literature published on pelletisation including industrial practice, numerical modelling of pelletisation and how they relate to the specific task.

Across the literature, symbols vary considerably for the same parameters, so these will be changed to the same symbol for consistency where possible, and modifications specified.

2.1 Mill scale overview

First, some context into how this problem fits into the general overview of the field of iron waste and iron waste recycling is discussed.

Iron waste, specifically iron waste generated in manufacturing (as opposed to material disposed of after use) is a significant source of inefficiency at a plant. These values may vary but provide a useful reference point. Up to 5% of the iron is lost in dust during the sintering, smelting and steelmaking processes, which is mostly re-captured [7]. The process of smelting meanwhile results in losses of 1-4% of the iron is lost in the slag [8]. The loss of steel in the mill scale varies

between authors, with some reporting 3-7% of the total steel milled [9, 10] while others report lower values, of around 1.9% losses [11].

Combined these make up a worst case scenario for losses of approximately 16% losses of the iron from the ore to the milling stage, though it is more likely less than this. Fortunately, these high iron wastes are naturally well suited to being re-introduced to the iron-making process at the site they were formed at.

Not all waste is formed equally, and the specific composition of the waste in question depends significantly on the internal source, and Makkonen et al [12] highlight how contamination can harm the primary processes of ironmaking. Pei et al [8] analysed the solid wastes formed at a iron and steelmaking site for their use in sintering, and find that it can range from nearly pure iron oxide to waste material having more contaminant alkali metal oxides than iron. Dalal et al [13] divides the sources of waste into process units (PU) and production control equipment (PCE) . These categories tend to share general trends. The PU solid waste is usually larger and has less contamination because they tend to be formed as a consistent by-product in the processing, while PCE waste is more variable, though it will generally have more chemical contaminants, such as chlorine or alkali metals, and the form will tend to be a sludge or a fine dust which requires more processing. Comparing this division to the waste analysed by [8] finds that these divisions are present, with scale and slag having relatively low contaminants, while the assorted ashes having comparatively higher harmful contaminants.

The contamination and division of the forms of waste is a useful means to understand the differences in the needs of handling and managing the wastes formed on the plant. The method of reprocessing needs to account for the contamination, and not all methods are suitable for all forms of waste.

The particular form of waste for which this project was initiated to manage is mill scale. Mentioned previously, mill scale, is produced during the milling process as the scale is removed from the surface of steel being rolled using high

pressure water to keep the surface clear of oxides as the bars and plates are pressed. The scale, along with lubrication oils for the machinery and the steel washes into settling tanks below [10]. The amount of scale lost reported may vary due to the different ways it can be classified. Shatokha, Gogenko and Kripak [10] and Liu et al [14] tackle the issue of managing the scale in different ways but both note the presence of a larger, Coarse Mill Scale (CMS), and a finer, Oily Mill Sludge (OMS). The CMS is collected in the primary settling tanks, and the particles are large and have very low oil contents. The OMS, on the other hand, is collected from secondary settling tanks and has high moisture and oil contents and is generally finer, usually below 2mm.

The OMS, with its high initial moisture and oil content is more difficult to process. A high oil content is a major impediment to sintering, as it can evaporate during the process, and then cause numerous problems further down the line [10]. The exact composition of the oil is indeterminate, but it is mostly composed of lubricants and coolants used in the process, with the lubrication oil is formed of 5-20% (w/v) additives for specific functions to a base fluid, itself a complex mix of linear, branched, cyclic and aromatic hydrocarbons [15, 16].Meanwhile even the high moisture content can cause problems to recycling processes, and draining fine powders can be difficult [17]. This is not as much of an issue for the coarse mill scale, being comprised as it is of larger scale.

The division between the CMS and the OMS fits into the division of more pollution control waste having more contamination and thus requiring more processing.

This processing is still worthwhile, as the product is beneficial to re-introduce into the furnace because it tends to have a higher iron content [8,11]. Additionally, as it is in a low oxidation state, mainly magnetite, it has a higher calorific content.

The need for reprocessing is particularly important for the blast furnace iron-making process, where the amount of fines must be minimised [1]. An excess of fines reduces the permeability of the blast furnace charge, lowering the overall

efficiency of the furnace. Thus, converting the fines into larger product through agglomeration is an important step.

Since the reprocessing is tricky, but it is a valuable source of iron, the best method of re-processing should be used.

Not all re-processing methods necessarily involve processing the material for suitability for the blast furnace. In practise, there are five generally used means of re-cycling of dust and sludge generated in integrated steel plants. These are: sintering, cold bonded agglomeration, injection, direct reduction and smelting reduction [8, 18].However, of these, injection, direct reduction and smelting reduction all require separate reducing furnaces, which in turn requires additional investment. Meanwhile sintering and cold bonded agglomeration can and typically are integrated into more typical BF-BOF plants [18].

Between pelletisation and sintering, Hooey et al [19] shows that pellets, while more energy intensive to initially produce make up the losses during the smelting process. These savings are between 5-8%, which makes it worthwhile.

As the material does require agglomeration for the blast furnace, of the methods listed cold bonded pelletisation is the best choice that does not require excessive additional infrastructure, even before considering that doing so prevents damage to the pollution control systems in the sinter plant.

2.1.1 Pelletising Mill Sludge

Mill sludge pelletising has not been significantly covered in the literature, so most of the literature will need to be essentially inferential.

Mill sludge is quite good at forming pellets, and of all the ferrous particulate feeds tested by Przemysław and Mróz [20] it had the highest "total ability for self-pelletising" index. This methods compares the inclination of the feeds to stick together while dry sieving, which is disrupted with wet sieving, and the amounts that are sieved are compared. Since the work mentions that the oils in the rolling scale likely strengthened the interparticle bonds, they are working with OMS.

Oils have some binding capability by themselves, and hydrocarbon based binders in pelletising have been tested with some success, such as bitumen and heavy fuel oils [21]. These would have longer chains than the lubricating oils found in mill sludge, but some of the findings are still relevant. The highly viscous nature of the oils helps induce the binding of the particles, but the hydrophobicity of the oils interferes with water, which causes problems when attempting to add water to grow the pellets. Using just organic binders is currently only suitable in contexts such as DRI, where the process was less intense since the heat required for reduction will invariably burn away the binder, causing very weakly bound pellets.

The fact that the oil is hydrophobic would explain why mill sludge was reported to have a high self-pelletising index. The wet sieving procedure is intended to disrupt any pre-existing moisture bonds, however the oils would remain as they are hydrophobic, continuing to bind the particles and giving a possibly false reading of the index. However, the presence of the oils itself still nonetheless results in intrinsic binding of the OMS.

Regarding the strength of pellets formed of mill scale, the literature is similarly sparse. OMS has been found to increase the reduction potential of cold bonded pellets, though at the same time it reduced the cold strength of the pellets the most, and had the highest variability in the results when compared to other forms of ferrous waste [22].

On the other hand mill scale has also been found by other authors to reduce the reduction potential of pellets when added to a blend, at least for fired pellets, though the strength was also found to decrease similarly with the addition of mill scale [11]. It is not clear whether the mill scale used here is OMS or CMS however, and this is for fired pellets, so the oils will have burnt away.

The variation in reducibility may be a result of secondary effects, as if the magnetite is not reduced to hematite completely then shrinkage occurs which impedes reducibility due to the closing of pores [23].

26

So, it seems that the mill scale does weaken the produced pellets, whether cold bonded or fired, but the reducibility is less clear and may be a property of the mill scale itself, or because they are formed of magnetite and need to be treated accordingly.

A very interesting solution is suggested by Tang et al [24] who have developed an explosive pellet suitable for Basic Oxygen Furnace (BOF) steelmaking. The pellets are made with three layers, an inner core of assorted iron wastes including sludge along with a binding additive, an intermediate layer of iron and steelmaking dusts combined with gas ash that contains free carbon, which defines the explosive capability, and an external layer of calcium oxide which provides strength and stability. This prepared pellet form entrains the carbon and other volatiles long enough for the pellet to be immersed in the liquid metal before it explodes, dispersing the iron completely throughout the mixture for immediate dissolution. Their conclusion was that this was cheaper than the other solutions available, and though it was not suitable for low sulphur steel this was because of their specific feedstock, not the general properties of the solution.

Partially because this is another potential source of contamination to the BOF, and partially because it explicitly involves exploding pellets, this solution was turned down when suggested to be investigated further.

2.1.2   Mill sludge General Management

Managing the mill sludge in other ways comes down to whether or not the oil is left in or not.

It has been demonstrated to be possible to prepare OMS in a way that makes it suitable for sintering. By blending the OMS with peat and allowing it to age the primary issues can be worked around [10]. The oils and water are absorbed, and the humic acids degrade the oil component into more volatile components which burn in the sinter process rather than simply vaporise. This is not perfect, but it is sufficient for the plant to close the cycle.

Alternatively, as mentioned previously oils tend to work best in DRI production, which has a lower strength requirement. This has been shown in practise to work and in fact be the most cost effective option when compared against cleaning to sinter and cold bonding, though the oils are not enough to reduce the pellets completely and so require additional coke dust or other reducing materials [25]. These pellets were prepared using a press, so are in practise closer to briquettes.

So, pelletising the OMS is not the only solution, and removal of the oils is not even strictly required for processing through other means. However, the reason for the lack of production using pellets is more to do with the difficulties of manufacture rather than intrinsic flaws in the properties of pellets.

Alternatively, if cleaning is to be considered, then there has been research on the production of materials specifically as part of the cleaning process. A variety of alternative processes for cleaning the product and use as a raw feedstock has been developed by Liu et al [14,26,27]. The first of which is a method of processing the OMS with vacuum distillation, the vaporised oils can be separated and used as fuel, while the high purity iron powders can be used to produce pigments or similar products. The other methods use a multi-step chemical process to similarly produce high quality iron powders, and the oily component can be filtered off as needed.

If a high temperature cleaning process is used, then it is possible to use the fact that the scale is formed of iron oxides to an advantage. The Iron oxides can be used as a catalyst in cracking pyrolytic oils and water into carbon monoxide and hydrogen [28], both valuable blast furnace gasses by using iron oxide pellets, and the pre-existing oil content will cause no issues.

However, in the end, the issue with these is that they require investment required for this process, and the investment is likely significantly higher than the current costs involved in the Cold bonded pellet production.

2.1.3   Mill Sludge Research Summary

As an initial summary, generally speaking pelletisation is more efficient than other methods in general, and cold bonded pellets do not cause direct problems for pollution control equipment. The OMS seems to pelletise well enough, though the produced strength seems to be lower than comparative materials, and the reduction behaviour varies. There is unfortunately no research on the effects that the unique properties have on the size or growth behaviour of the pellets.

Mill sludge is a low priority topic, and is inherently tricky to work with, leading to generally low levels of interest in the research community. On top of that, when searching through literature, the term mill scale is used for both OMS and CMS. As such, the topic of mill sludge management will be left for the time being, and re-examined in the light of literature on the pelletisation process.

2.2   Pelletisation

To better understand what could lead to the variation in pellet size and strength, the process of pelletisation will be examined now, and in particular, what factors affect the size and strength of pellets.

Pelletisation describes a number of processes that come under the umbrella of "Wet Agglomeration", which also includes some granulation processes. Both pelletisation and granulation are used to refer to other processes which are unrelated in any theoretical sense, and linked only in the size or type of product generated. This has been an issue since 1958 [29] and continues today [3]. All of the designs in Figure 2.1 have been described as producing granules, though they all share similar principles of wet agglomeration the mechanics are quite distinct, and they can all have variations on the basic designs shown from the shape of the vessel to introduction of additional or shaped impellers or tools.

One of the key features necessary to recognise when understanding pelletisation, is that is intrinsically a multi-scale process. The different scales interact
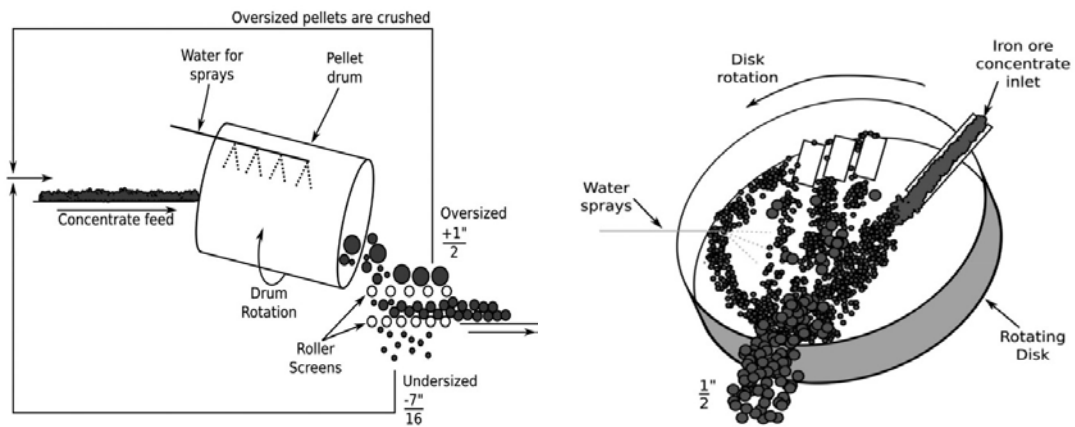
(a) Drum Pelletiser Diagram [30]

(b) Disk Pelletiser Diagram [30]
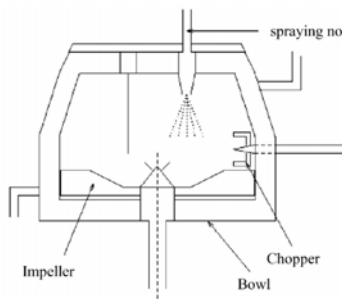
(c) Vertical High Shear Granulator [31]
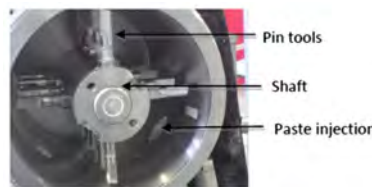
(d) Horizontal High Shear Granulator Design [32]
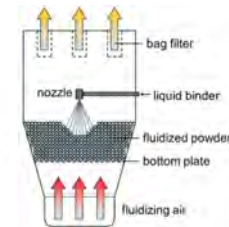
(e) Fluidised Bed Granulator [33]

Figure 2.1: Assorted granulator and pelletiser designs.

making it difficult to separate the parameters [34]. The wide range of scales of interactions means that it is not always possible to improve all product qualities simultaneously, because the way that agglomerates are formed determines their properties but is also itself controlled by their properties [35]. Further, the processes occur in a very chaotic environment that is difficult to observe directly, and the relevant properties are unclear, vary a lot, and are generally very difficult to measure reliably [36].

So, scaling, controlling and measuring the process are all difficult, and as a result these impede understanding what influences the key parameters of size and strength. To reduce the variability of the size and strength requires first under-

standing of what influences these, and this understanding needs to be able to account for the different scales that are intrinsic to the process, through mechanisms that can be validated.
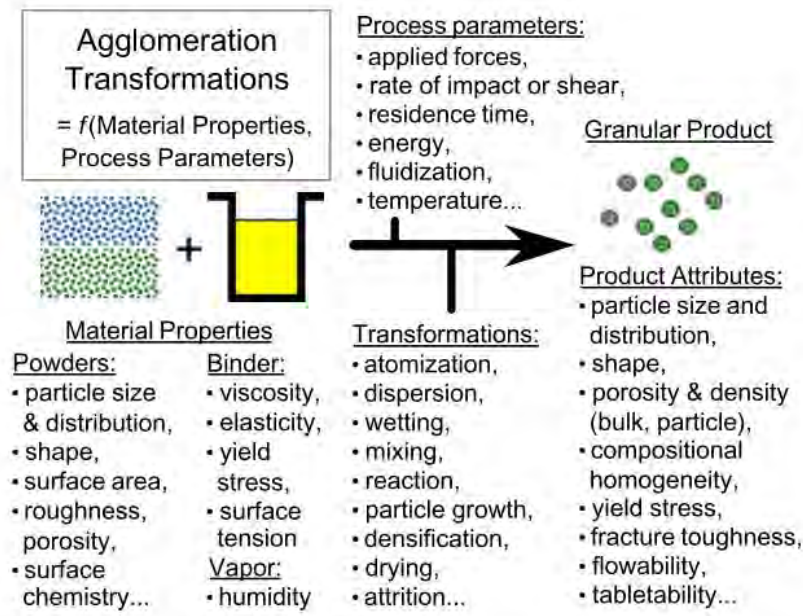
Figure 2.2: A wide variety of the relevant parameters and transformations relevant to the pelletisation process. Figure 1 from [34]

Mort shows how the processes can be considered in terms of transformation in Figure 2.2 [34].

Not all of these transformations are equally important. Iveson, Litster, Hapgood and Ennis divide the most important processes in agglomeration into "Nucleation, Growth and Breakage" [37].

Beyond the act of pelletising, the feed preparation and the pellet post-processing are also important when considering the quality of the pellet in practical application. If overlooked it can result in negative overall quality even if the granulation is working very well [34, 37, 38].

This literature review will therefore not put as much emphasis on the process, rather the focus will be on the end results, and then tracing back what trans-

formations or controlling parameters were involved. Important processes will be reviewed as needed.

The research here will be distinguishing between theoretical solutions, and connected results, and those which simply report their findings, or provide simply empirical relations, with no explicit theoretical backing. Additionally, growth behaviours were separated, as they simply describe the rate of change of size, but are also well researched.

This division allows a practical comparison between which theories match their results more strongly, and the empirical research can also be considered in the light of the theories.

Finally, in order to keep things clear, granule will be used consistently for wet agglomerates in the literature review as it is used more commonly in the field, and it allows for clarity regarding subscripts as the particle and granule properties are often both used in single equations.

2.2.1   Size

Size Theories

As a starting point, it is reasonably well established in the literature that the saturation is a significant driver of growth [3,37,39,40]. It is fortunate then, that a relatively early paper by Butensky and Hyman developed a theoretical model which relates the diameter of the pellet to the saturation, along with a few other properties [41]. This relation is reproduced below in Equation 2.1

$$\frac{1}{\overline{d_{g/p}}} = \frac{1}{K_g} - \frac{1}{K_g f^{\frac{1}{3}}} \frac{m_{l/s}^{\frac{1}{3}}}{\left(m_{l/s_\infty}^{\frac{1}{3}}\right)} \tag{2.1}$$

$\overline{d_{g/p}}$ is the mean granule diameter relative to the particle size, K_g describes the liquid penetration to the surface, f is the fraction of the pore space filled with liquid), and m_{l/s_∞} is the limit of $m_{l/s}$ as $\overline{d_{g/p}}$ approaches infinity, i.e forms

a granule of infinite size, or more practically, a slurry.

Equation 2.1 is relating the saturation to the diameter, as is shown, and in general is discussed in much greater detail later in section 7.4. For now though it is in good agreement with Figure 2.3, which describes granules of 8mm diameter and feed-granule ratios over 50.
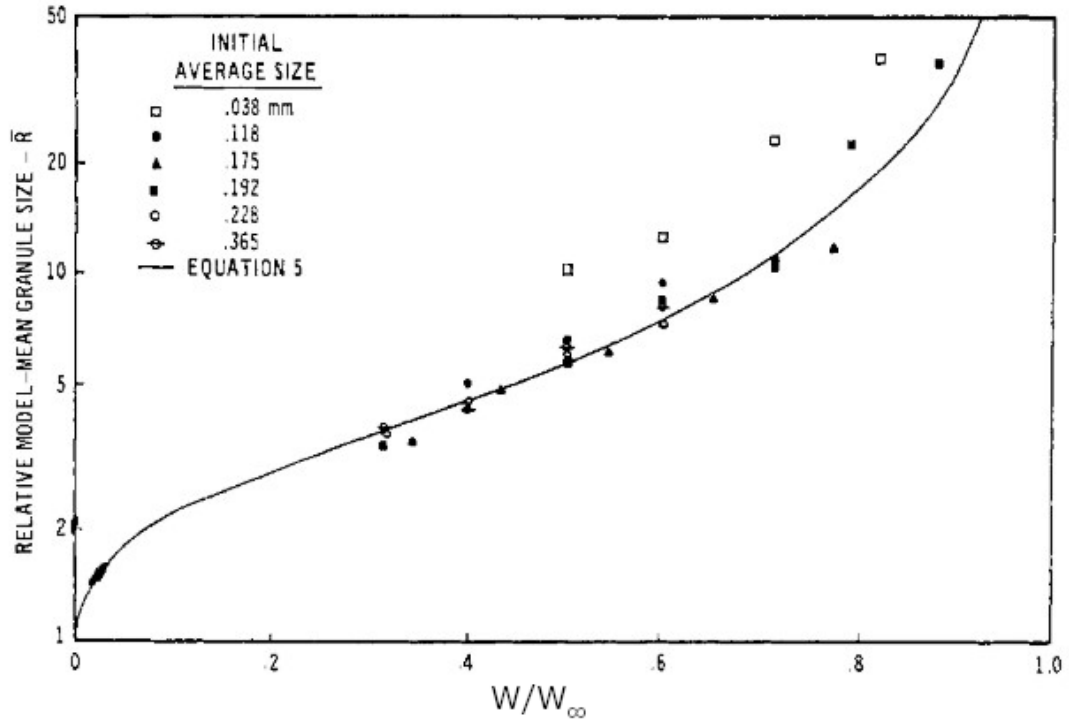
Figure 2.3: Growth of $\overline{d_{g/p}}$ as the parameter W/W_∞ increases. This parameter describes how close the moisture to solid ratio is to the maximum before a slurry forms, as a fraction and is described here as $m_{l/s}/m_{l/s_\infty}$ for clarity. This plot compares between Equation 2.1 and results of experiments. Note the logarithmic scale of the Y axis, which reports the dimensionless granule size ($\overline{d_{g/p}}$). $f = 0.89$, and $K_g = 1.15$. The values for the case described by □ fit the curve for a value of $f = 0.74$. Figure 7 from [41].

This experiment involved pelletising glass beads of various diameters in a small drum of 25cm diameter (10 inches as reported originally), and the binder was a mixture of various chemicals which would produce a time delayed setting action. This allowed the pelletisation process to be performed as normal, before the

gelling fixed the values in place. The next step then makes use of the fact that the only source of nitrogen is in the binder, and the composition of the binder being completely known, allowed the nitrogen content to be used as a means to measure the saturation content of each granule size group separately. This is different from most saturation measurements, which either involve assuming a porosity similar to the wet tapped porosity measured externally or drying the formed granules, allowing it to measure the saturation without altering the composition. The distribution in the granule sizes reportedly varied in each run, but in every case the distribution of saturation matched the relation described, with larger granules containing more liquid. Finally, ungranulated feed was removed, as this was found to distort the results unreasonably.

Another solution which accounts for the liquid content is the Stokes Criterion, as developed initially by Ennis, Tardos and Pfeffer, in [4]. This solution predicts growth based on whether the kinetic energy is dissipated by the viscous damping of liquid on the surface of two colliding spheres, and is an extension of previous work [42] which was developed for a sphere colliding with a flat surface. It is named for the repeated use of Stokes dimensionless numbers in evaluating the behaviour. The solution is examined in greater detail in section 7.2, but for now the explicit size prediction that is made for tumbling agglomeration is described in Equation 2.2

$$\Delta_{lim} = d_{g_{N \to C}} = \left[\frac{9\mu}{4\rho_g\omega} \left(1 + \frac{1}{e_{rest}} \right) ln \left(\frac{h_0}{h_a} \right) \right]^{\frac{1}{2}} \qquad (2.2)$$

Here Δ_{lim} is first presented, as a consistent term which describes the limiting diameter to differentiate it from simply the granule diameter. $d_{g_{N \to C}}$ is the diameter where the nucleation phase ends and the coating phase begins, where growth can only occur through the coalescence of smaller to larger granules. h_0 is the surface liquid thickness and is defined via Equation 2.13 and h_a is the surface asperity thickness and is defined via Equation 2.14. μ is the viscosity of the binder, ρ_g is the granule density, ω is the rotation rate of the drum and e_{rest}

is the coefficient of restitution of the granules.

This is derived from consideration regarding when the growth behaviour that the Stokes Criterion predicts ends. The growth behaviour described by the authors are listed in section 2.2.2.

The actual validation for the final size value predicted by Equation 2.2 is limited to comparing against another authors findings, with the equation predicting Δ_{lim} of 2.8mm and the observed value being 6mm, and no other validation of this size predictor is performed.

The intensity of the collisions are also recognised as having some impact on the final size [34, 37, 43, 44] which is recognised in Equation 2.2 though not Equation 2.1.

A theoretical limiting diameter which only considers the intensity of these collisions is that found in Ouchiyama and Tanaka's work [45]. This considers the growth from the other direction as in [4], and assumes that each collision initiates some sort of bond, and then determines if the intensity of the process is enough to disrupt that bond. This solution as developed leads to a probabilistic determination regarding whether the granules bond, but as part of it a limiting diameter is still determined, calculated using Equation 7.3

$$\Delta_{lim} = \left(\frac{2^{\alpha - \frac{3\eta}{2}}}{B} Q_{max}^{\frac{3\zeta}{2}} K^{\frac{3}{2}} \sigma_{bond} \right)^{\frac{1}{4 - \frac{3\eta}{2}}}$$
(2.3)

B and α are constants which relate the granule masses to the separation forces while Q_{max} describes the maximum compression force in the system, and K describes the relation between compressive force to the area of contact, over which σ_{bond} applies.

This theoretical limit is not validated in [45], though the authors are more focussed on the growth mechanisms that are occurring, and the predictions of the probabilistic solution are in agreement with previous empirical models [46]. Further considerations of this solution can be found in section 7.3.

These solutions are the only ones that could be found for a final predicted size, and even these are not definitively fixed limits but rather the mean values that the system is bound to. The dynamic behaviour has some impact, as does the saturation. Of the above limits shown, only Equation 2.1 has strong evidential backing, though it appears to be missing any dynamic relation. Equation 2.2 makes some attempt, though the validation was not compelling, but this may be due to an incorrect choice of value for e_{rest} or other values which were not reported in the original source. Equation 7.3 meanwhile makes no direct attempt at validation, as the focus was primarily on the mechanism of growth found by other authors.

All of these solutions will be compared against the following empirical findings in chapter 7, as they all provide consistent predictions to relate the size to the variables, though to show this benefits from some additional analysis. For now, the different limits will be mentioned if they are related to a given empirical finding, and note whether they find the dynamics or the saturation a limiting factor.

Size Empirical Findings

The review by Iveson et al [37] has had a significant effect on the field, and this is very clear from the shift in research towards understanding granulation as the three stages previously mentioned. It covers a wide range of parameters that influence the granule size and growth rate. The growth rate parameters will be considered in that section, for now, here is a summary of their findings:

- Increasing binder content, and in particular higher saturations result in larger sizes.

- Smaller particles tend to reach a smaller maximum size, and may not form granules without large amounts of liquid addition.

- If the strength is too low, then the feed can be too weak to form granules of any size

  – Large particles meanwhile can be too weak to form granules at all.

  – Some critical surface tension is required, otherwise only weak crumb material is formed.

  – Some critical viscosity is required to form granules of any size.

Saturation and Moisture content need to be clarified at this point. Saturation describes the proportion of the total porosity which is filled with liquid, $V_{l/p}$ while moisture content simply is the ratio of the solids to liquids $V_{l/s}$, and does not account for the porosity. As such, the moisture content does not neccesarily act as a proxy for the saturation, as seen in Figure 2.4 [47].
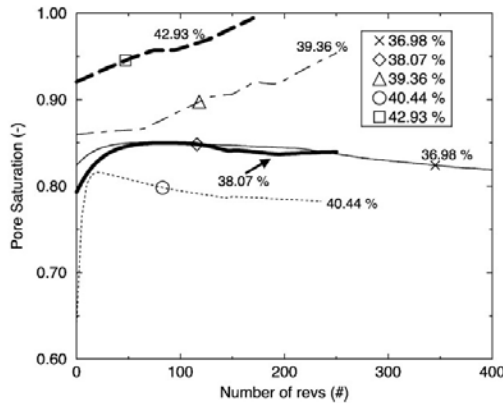
Figure 2.4: Saturation S over time (in drum revolutions) for all experiments. the different lines correspond to different liquid addition quantities, specified in the figure. The points in the figure correspond to the time when rapid growth began. Figure 8 from [47]

The experimental research agrees with the importance of the binder content, and the specific curve of the relationship between the saturation and the diameter is found by multiple authors. When testing a variety of binders on a single particle type then, measuring the saturation rather than the proportional liquid volume added, then the mean granule size forms a consistent curve as seen in Figure 2.5, in research by Ritala et al [48].

The various binders tested in Figure 2.5 have viscosities which range from 1 to 119 mPas. Following from this, some of the authors test melt granulation, which
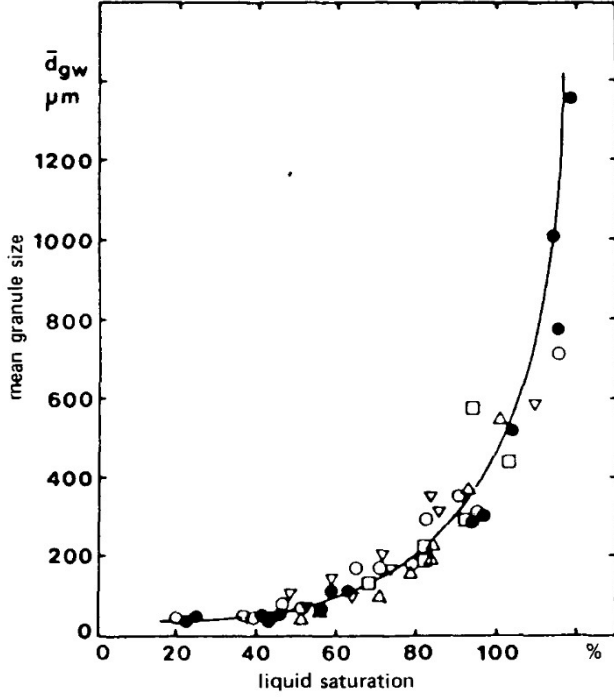
Figure 2.5: The effect of S on d_g, for various types of binder, and concentrations of those binders. In all cases, $\overline{d_p}$ was 21μm. ● : Kollidon 90 3%, 5%, 8%, ○ : Kollidon VA 64 10%, 20%, 30%, △ : Methocel E5 3%, 6%, and 8% , □ : methocel E15 2%, 3.5%, and 4.5%, ▽: Kollidon 25 3% and 20%). Figure 2 from [48].

produces similar results Figure 2.6 but with a lower consistency [49].

This variability may be because of the difficulty in measuring porosity with a solid binder, or could be because of the different run conditions that were applied. Each of the separate cases do seem to have the overall shape, though the curve would need to be adjusted for all of these.

Equation 7.3 is further developed by Kristensen, Holm and Schaefer, who include further mechanisms to define some of the parameters in that equation [50]. The results of their solution is presented here in Equation 2.4 , which relates the critical strain and other parameters related to the tensile strength to the limiting diameter

$$\Delta_{lim} = \left(A_5 l_{cr}^3 \frac{\epsilon^{1+c}}{1-\epsilon} \frac{1}{\alpha_0 - bS} \right)^{\frac{a}{2}} \tag{2.4}$$

Here ϵ is the porosity, and will be used regularly throughout this thesis. Most of these parameters are empirical fitting values from the derivation, A_5 c a b , though the source of these are not well explained. However, these do fit the

38
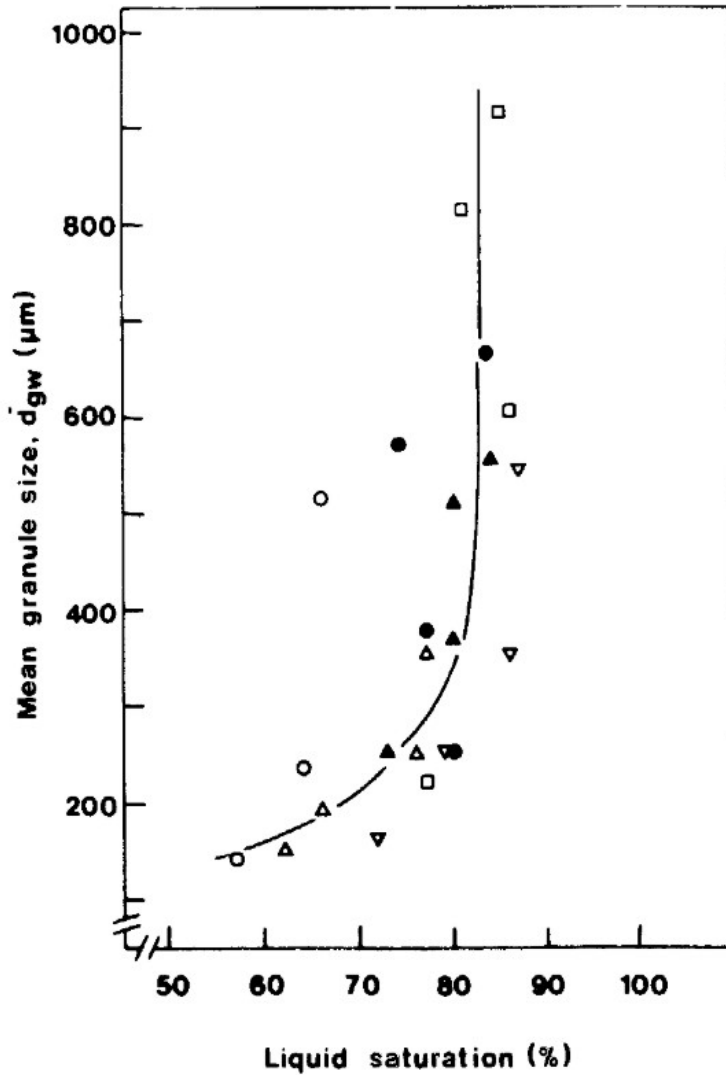
Figure 2.6: The effect of a range of saturations on the growth of granules. For all, the binder used was finely powdered PEG 6000, and the impeller speed during the first 20 mins of processing was 1400rpm. Binder mass:∘:360 g; △: 360 g; ∇: 380 g; □, •, ▲ : 400 g. Impeller speed after 20 mins: ▲: 500rpm;•: 800rpm; ∘, △, ∇, □: 1400rpm. Figure 5 from [49].

results obtained. In particular, ϵ^c and $\alpha_0 - bS$ are both experimentally obtained. $\alpha_0 - bS$ describes the intrinsic interaction parameter α which describes the work required to separate the particles in the granule, and ϵ^c comes from $x = x_\infty \epsilon^c$ is the distance parameter of particles as they become separated. The saturation component of $\frac{1}{\alpha_0 - bS}$ is found to match the behaviours found in their experimental results [50]. The feed particle size is also seen to have an impact on the granule size.

It is possible to add the powder to the liquid, though this is not typically
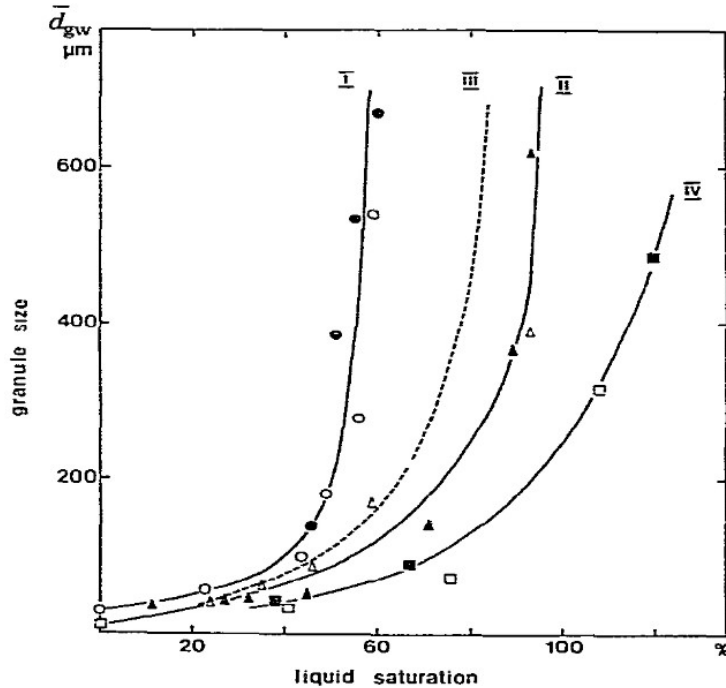
Figure 2.7: Comparison of the effect of saturation on mean granule diameter on a range of particle sizes. I: $\overline{d_p} = 28\mu m$, II: $\overline{d_p} = 8.8\mu m$, III: $\overline{d_p} = 21\mu m$, IV: $\overline{d_p} = 14\mu m$ $\circ, \triangle, \square$: Impeller rotational speed 250 RPM; $\bullet, \blacktriangle, \blacksquare$: Impeller rotational speed 500 RPM Figure 4 from [50]

performed. Where it has been performed the granules formed seem to be larger on average for the liquid first, see Figure 2.8, and again the viscosity produces no variation in the granule size produced [51].

The distributions were also reported in [51], and show that this reverse phase graunlation resulted in widely varying diameter of outputs. The conventional method meanwhile produced granules of a more consistent diameter.

The methodology had a not insignificant flaw, which is that the granulation time was dependent on the quantity of solid or liquid that needed to be added, which would have resulted in the low liquid volume conventional tests being run for less than a minute, while the reverse phase cases would all have run for more than two minutes. This is not commented on by the authors.

Another process which is similar to wet agglomeration is spherical agglomeration. This process involves re-shaping crystals in solution through the use of a second immiscible liquid which bridges the gaps between crystals, aggregating them in situ into spheres [52]. This re-formation of the crystals into a more spher-

40
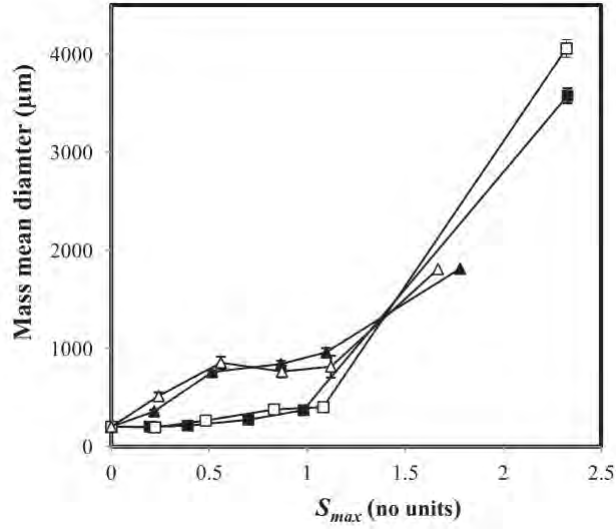
Figure 2.8: Mass median diameter of graunles produced by both conventional and reverse phase granulation as a function of saturation, using Hydroxyapatite with a d_{50} of $275\mu m$. ■ represents the granulation using 10% w/w PVP binder conventional granulation,□ represents the granulation using 20% w/w PVP binder conventional granulation, ▲ represents the granulation using 10% w/w PVP binder reverse-phase granulation and △ represents the granulation using 20% w/w PVP binder reverse-phase granulation. Fig. 12a from [51].

ical shape improves their handling, and in this process the diameter is related to the relative bridging liquid to solid ratio, as seen in Figure 2.9.

When comparing their Population Balance Model to experimental results, Le et al found that consistently the smaller granules contained a smaller binder fraction compared to larger granules [53].

The relation of the moisture content to the pellet diameter is also present in disk pelletisers, even though in disk pelletisers self-selection causes the largest pellets formed to rise to the top and tip out [54]. Thella and Venugopal develop Equation 2.5, to predict the produced output pellet size.

$$d_{g50} = 4.226 + (3.106 * m_{l/s}) - (0.544 * m_{l/s}^2) + (2.044 * I) - (0.644 * I^2) \quad (2.5)$$

Where d_{g50} is the median pellet diameter and I is the angle of inclination of the
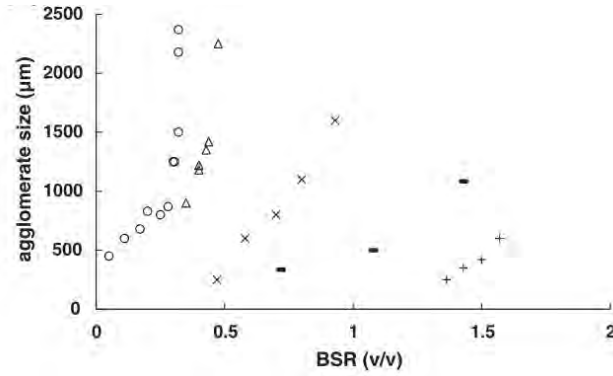
Figure 2.9: Agglomerate size in spherical agglomeration as a function of bridging liquid to solid ratio (V_l/V_s) from a variety of sources as described in [52]. ○: CaCO3 particles, kerosene bridging liquid; △: Salicylic acid particles, Chloroform bridging liquid; ×: benzoic acid particles, toluene bridging liquid; −: lobenzarit disodium particles, hexane bridging liquid, +: atorvastatin calcium particles, dichloromethane bridging liquid

disc pelletiser.

This was experimentally tested for their pelletiser and for the range of values tested of $m_{l/s}$ (11% to 13%) and I (30° to 40°). The factorial design limited the equation to this form ultimately, and the nature of disk pelletisers explains why the authors found that time had little impact on the final diameter.

Clearly, all the above agree that the addition of liquid results in a greater extent of growth. Further, there is a general trend that is shared between them all, a hyperbolic curve, with low variability at one end and a sudden increase at the other. These will be compared against Equation 2.1 and Equation 2.2 in chapter 7, but they do appear to be in general agreement with the form shown by Figure 2.3 so far.

The intensity of the agglomeration also affects the limiting size. Watano et al performed a thorough series of experiments on the scaling behaviours of a fluidisation bed granulator [44,55–58]. The most relevant results are those shown in Figure 2.10, which show that how the diameter of the granules is proportional to $d_{g50} \propto 1/\left(\frac{V_I{}^2}{V_f{}^2}\right)^{0.25}$, or simply $d_{g50} \propto \left(\frac{V_f{}^{0.5}}{V_I{}^{0.5}}\right)$.
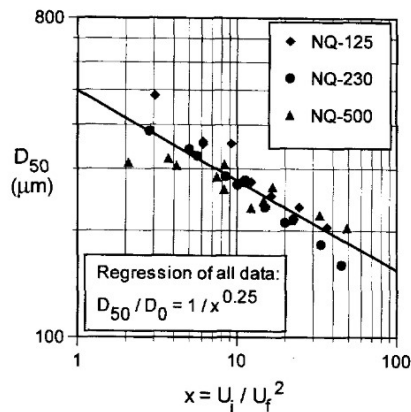
Figure 2.10: $d_{g_{50}}$ proportional to the impeller speed V_I and the inverse fluidisation velocity V_f squared. Data from [44], figure from [59] due to ease of reading the results

Another direct comparison of impeller speeds shows that there seems to be a high and low speed linear region, Figure 2.11, though it may simply be the case that there is a single curve which would describe this functionally. This small scale test shows similar patterns of break-up and re-growth when plotted against a dimensionless diameter of the granules thus produced [60].
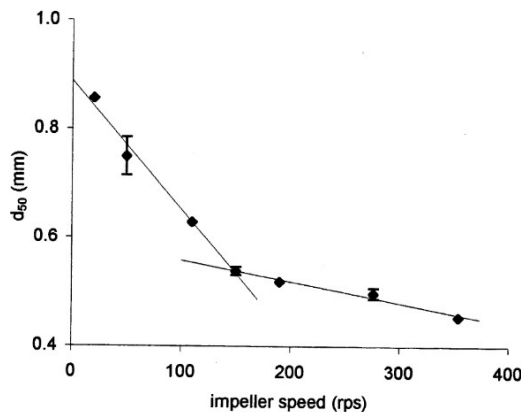
Figure 2.11: Median pellet diameter $d_{g_{50}}$ as a function of impeller speed V_I . Fig 2 from [60]

Nakamura, Fujii and Watano increase the length of time to account for the variation in collisions, which is proportional to the impeller speed, giving Figure 2.13 [43]. This scaling was with respect to the amount of kinetic energy experienced as the granules impacted divided over time, E_t , and was found to be proportional to $E_t = 1.036L^{-0.259}$, where L is the granulator volume in litres.

An increased impeller speed can result in more rapid growth [61], which means

43
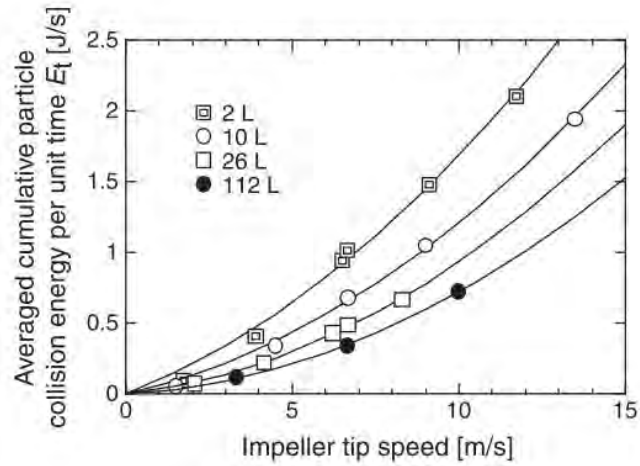
Figure 2.12: The Averaged Cumulative energy of collisions per unit time E_t for different vessel volumes in L . Fig 10 from [43].
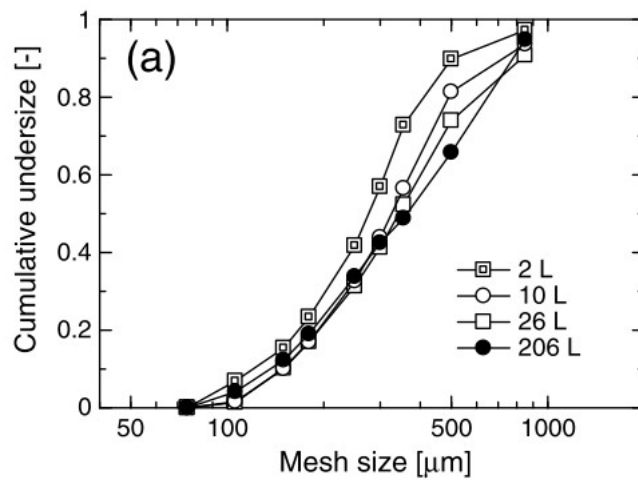
Figure 2.13: Size distribution of produced granules for different vessel volumes, when the length of time of granulation is scaled to ensure similar collision energy over time. The impeller tip speed was kept constant between vessels of different diameters. Figure 12a from [43].

that the diameter may seem to be larger for higher impeller speeds if the time of granulation is not accounted for between samples. This can be seen clearly in Figure 2.7.

44

The tip speed does not necessarily result in smaller granules, as shown in Figure 2.15,

The intensity of the process appears to generally have a negative correlation with the final diameter, which agrees with both Equation 2.2 and Equation 7.3, though derivations for why is different for both, which will be considered later on in chapter 7. The fact that it does not always needs to be considered during the modelling process, and understanding of why this is.

The strength of the granules can also result in a change in the diameter, though this may be due to the effect of viscosity or surface tension, other methods which
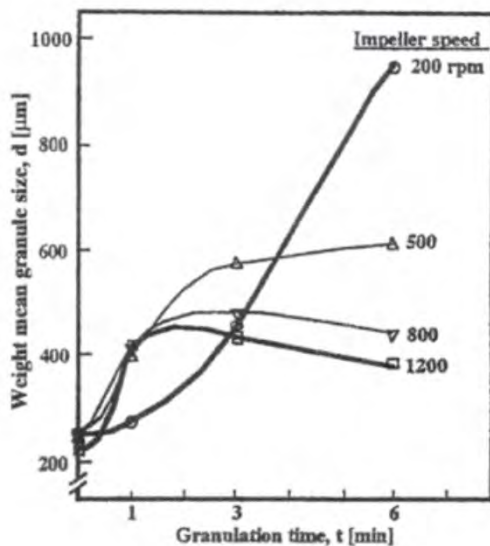
Figure 2.14: Mass mean granule diameter $\overline{d_g}$ as a function of time, for various impeller speeds. The binder used in a 15 wt% solution of PVP/PVA Kollidon®VA64. Impeller rotational speeds are ○: 200 rpm, △: 500 rpm,□: 800 rpm, ▽: 1200 rpm. Figure originally from [61], though taken from [4] as original unavailable.
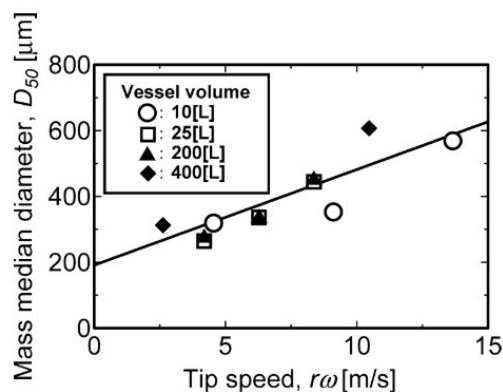
Figure 2.15: Median granule diameter d_{g50} as a function of tip speed. Figure 10 from [62]

45
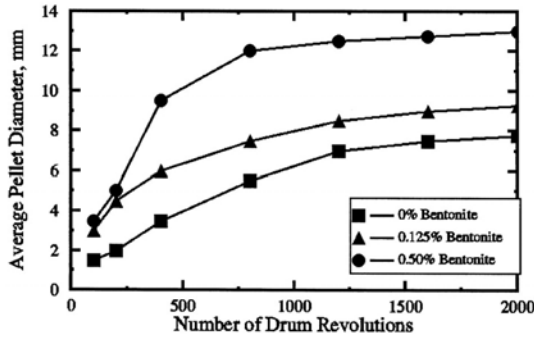
(a) $\overline{d_g}$ as a function of drum revolutions, which is effectively a measure of time, for various proportions of bentonite added. The amount of liquid added is not specified. Figure 9 taken from [63], original source unavailable.
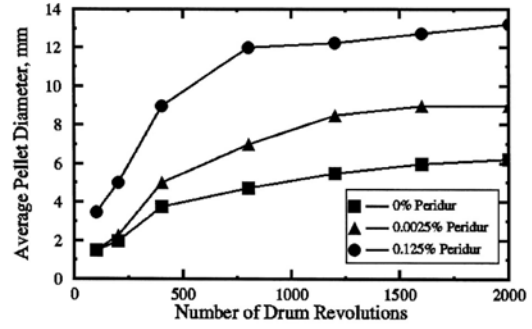
(b) $\overline{d_g}$ as a function of drum revolutions, which is effectively a measure of time, for various proportions of Peridur added. The amount of liquid added is not specified. Figure 12 taken from [63], original source unavailable.

Figure 2.16: Granule diameter as a function of drum revolutions for two different binders

increase practical strength also result in larger diameters. For example, bentonite is a commonly used binder which is known to increase the strength of the granules but the mechanism does not neatly fit into the frameworks established later in subsection 2.2.3. Bentonite is also shown to be able to increase the diameter proportional to the quantity added, Figure 2.16a, and similar observations can be made regarding Peridur, an organic binder, Figure 2.16b

In both cases, the addition of the binder is also shown to increase the wet drop number and the wet crush strength [63].

The reason for mentioning this is that though the increase in the diameter due to strength may be due to the increases from parameters which affect both, it may also be that the strength directly is correlated to the diameter of the granules produced.

Other parameters which will be noted to alter the strength, for example, include the viscosity. A critical viscosity has been found to be required for granulation [64]. This critical viscosity can be mapped in relation to the particle size, see Figure 2.17
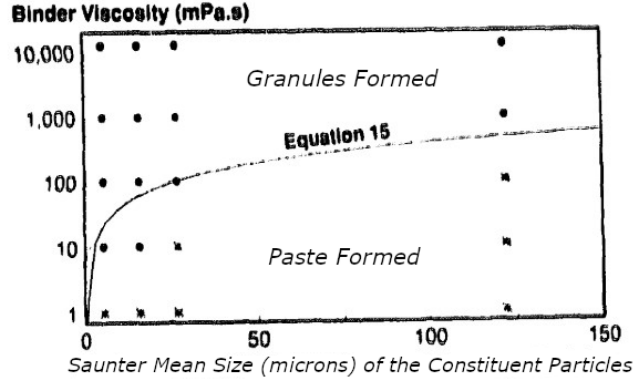
Figure 2.17: Data showing whether granulation occurred or not for various viscosity and particle diameters. ● points indicate that granules were formed, while × indicates that no granules formed, the mixture shifted directly into a paste. The quantity of liquid added varied for different particle sizes. Equation 15 referenced in the image is given here as Equation 2.6 Fig. 4 from [64].

It is theorised that this boundary is defined by the maximum strain ε_{max} that the particular feed mixture can sustain, Equation 2.6, similar to the critical strain specified in Equation 2.4.

$$\varepsilon_{max}{}^2 = \frac{1}{540} \frac{\epsilon^3}{1 - \epsilon^2} \frac{\rho_g V_c d_{3,2}}{\mu} \tag{2.6}$$

The study which produced Figure 2.17 has some flaws, such as inconsistent granulation time and liquid added. The experiments were merely to test whether granules of, it seems, 500µm diameter could be formed in the specified device.

The surface tension effects are not reported on significantly, though it appears to be slightly correlated with the diameter of the granules produced [65]. The hydrophobicity of the feed also affects the final granule diameters formed [66]

When compared to other effects, this is relatively minor. It does also seem to result in a narrower distribution, which may be useful [65].

47
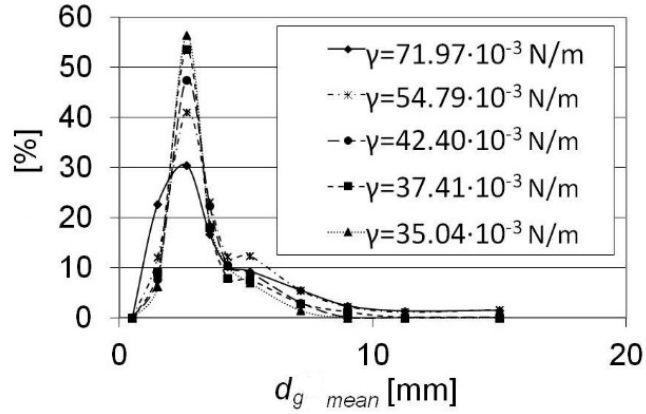
Figure 2.18: Distribution of the diameters produced for various binders differing in the surface tension γ . The droplet size of the spray was 20µm and the total liquid added was $m_{l/s}$ = 0.19 Fig. 10 from [65].

Final Size Distribution

In drum granulation, the size distribution of the granules has been found to be proportional to the mean diameter of the granules [67]. This property, referred to as "Self-similarity" can be seen in Figure 2.19 [68]. This is not always the case for other forms of granulation, as others have found increasing the moisture content reduces the standard deviation in fluidized bed granulation [58], though this is reported to be due to removal of the ungranulated fine powder.
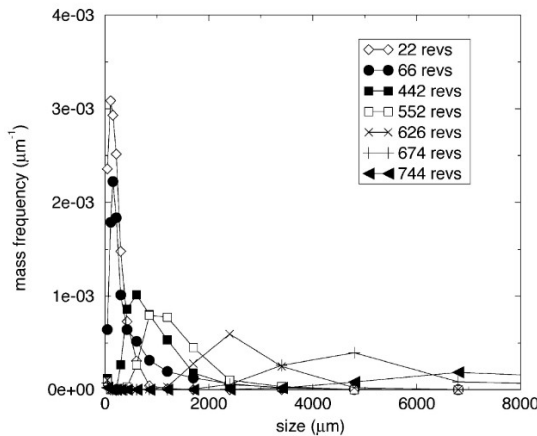
Figure 2.19: Mass mean diameter $\overline{d_g}$ and binder content versus number of revolutions. The smaller ($d_g \leq 710\mu m$) granules were removed after 200 revolutions during experiments 1 and 2. During experiment 3, the smaller granules were not removed. Figure 17 from [68]

The nuclei size distribution is reported to affect the final size distribution

48

[38, 69–71]. Therefore, controlling the nuclei size distribution would allow an improvement in distribution control.

When modelling the process, if the properties of the nuclei are measured, these can be used to significantly improve the results of the model compared to using properties measured later on in the process [53].

One way to measure the consistency of the nuclei is through the dimensionless spray flux Ψ_a as calculated using Equation 2.7 [72]. This, combined with the dimensionless drop penetration time τ_p as calculated via Equation 2.8 is used to create the nucleation regime map shown in Figure 2.20.

$$\Psi_a = \frac{3\dot{V_s}p}{2\dot{A_s}pd_d} \tag{2.7}$$

$$\tau_p = \frac{t_p}{t_circ} \tag{2.8}$$

Where $\dot{V_s}p$ is the liquid added as a spray over time, $\dot{A_s}p$ is the area that passes under the spray over time, and d_d is the droplet diameter. Meanwhile, t_p is the time taken for the liquid to penetrate into the feed bed, and t_circ is the circulation time of the feed between spray periods.

When both Ψ_a and τ_p are low, the droplets are more distinct and therefore, theoretically, the more consistent the nuclei size distribution.

The above value of Ψ_a has been criticised as not accounting for the effect of larger drops due to the construction of the dimensionless number [73]. An alternative Ψ_a value which may be more useful when the density of the spray is important, or when $\Psi_a > 0.5$, is suggested to be Equation 2.9.

$$\Psi_{alt} = \frac{\dot{V_s}p}{vA_sp} \tag{2.9}$$

where v is the velocity of the surface of the feed, and A_circ is the area circulating. However, as the goal is to keep Ψ_a as low as possible to begin to begin with, if this is being applied then the process already has other issues to manage.
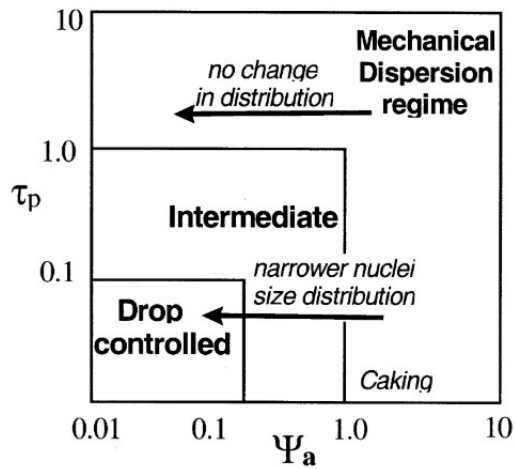
Figure 2.20: Nucleation Regime map. Ψ_a is the dimensionless spray flux found using Equation 2.7, τ_p is the dimensionless drop penetration time found using Equation 2.8. Figure from [70]

The drop penetration time is dependent on the pore size and whether the material is pre-wetted, though whether the pre-wetting increases or decreases the penetration time is dependent on the particle size as the mechanism becomes more complicated [74].

This effect of the nuclei size distribution may also explain the high variability found in the reverse phase granulation process [51]. Figure 2.21 and Figure 2.21 show the significantly higher variability that occurs when the powder is added to the liquid rather than the other way around, though the difference in saturation may also play a part.
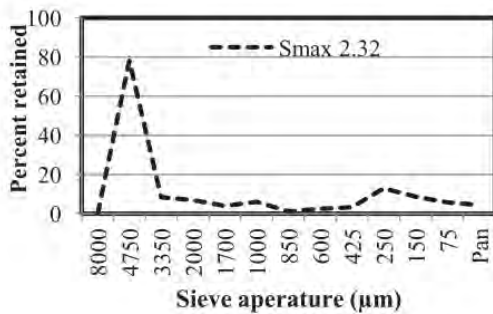
Figure 2.21: Size distribution for Hydroxyapatite granules prepared using conventional granulation processes, for a Saturation of 2.32. Figure from [51]

50
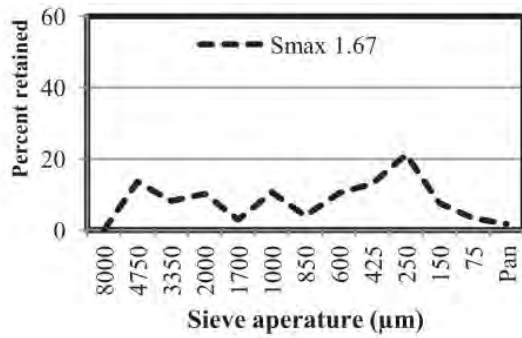
Figure 2.22: Size distribution for Hydroxya-patite granules prepared using reverse phase granulation processes, for a Saturation of 1.67. figure from [51]

The definition of "Nuclei" varies among authors. For some authors, [38,69–71], the nuclei are the granules that are formed in the instantaneous moment where moisture or the binder induces coalescence between dry particles. However older authors [41, 67] uses this term to refer to the phase where the coalescence is rapid, before slowing down into a slower balling region, a behaviour which is also observed by some authors in the intermediate period but do not explicitly refer to as nuclei period [4, 50].

Other efforts to manage the size distribution have included work involving Population Balance Model (PBM)s, which inherently track and use the size distribution in their calculations. It was suggested that controlling the liquid binder distribution would allow control of the granule size distribution [69]. When testing, this was not found to be feasible if the liquid is added to the particles as a whole, with the self-similarity of the deviation returning [75]. It was then suggested that adding the liquid to separate points in the granulator may in turn resolve this [75]. This was tested using a compartmentalised population balance model, to some success [76], though this is not directly compared to experimental results. To account for the collision dynamics and the location of the liquid addition more accurately, a DEM model can be linked to the Population Balance Model to give a model which better accounts for the kinetics, and doing so accounts for the presence of the un-agglomerated fines that can occur while also having a few larger, moistened granules [77].

The mean granule size can reach a peak before falling again, as seen in Fig-

ure 2.14. This can occur through breakage of whole granules, or through attrition [34]. This can alter the final mean size, but also importantly the final distribution, as the smaller granules take up the losses, which makes accepting the reported findings on the final size distribution tricky if the distributions are not pelletised for the same length of time.

A final point worth mentioning in this section is that [38] state that "Where the feed has a broad size distribution which overlaps the product size distribution, arbitrary division between the "powder" (continuous phase) and granules is neither sensible nor logical." This can be relevant in cases where feed is returned, resulting in a feed particle distribution which has sizes reaching to the final product already, as is typical for drum granulation. This does however mean that controlling the particle size to control the final granule size will have some interference.

Overall this looks relatively unpromising for the case of controlling the size distribution. In particular, the self-similarity of the pellet mean size and the pellet standard deviation will make things much harder. The use of an appropriate Ψ_a seems to be a matter of damage control, rather than a solution which will actively improve the distribution. Perhaps with a better understanding of what leads to the self-similarity can this be resolved, though there may be kinetic effects not accounted for here, as suggested by the Discrete Element Method (DEM) models results.

2.2.2 Growth Rate

The growth rate behaviour has attracted significant research itself, likely because it is well suited to PBMs, and because knowing the growth rate allows finishing the process once the size desired has been created.

There are many types of growth behaviour reported [3, 37, 39], which have been summarised in Figure 2.23, which describes the conditions of the saturation and the value of St_{def} under which they occur, and how other parameters shift

the growth regime.

The stokes deformation number St_{def} is a common dimensionless number in the field of granulation, and measures the extent of deformation from kinetic energy that is resisted by the granules yield strength during impacting. It is calculated using $St_{def} = \frac{\rho_g V_c^2}{\sigma_y}$
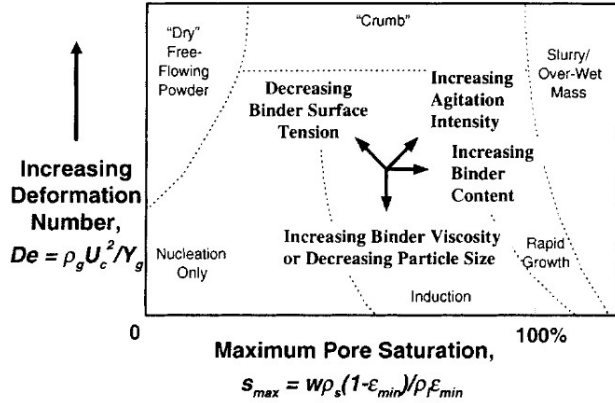
Figure 2.23: Regime map describing the growth behaviours of granules according to the saturation S and Stokes Deformation number St_{def} Fig. 4 from [39].

Regime maps are relatively common within granulation as they provide a method of relating how to adjust parameters as needed in a practical way, while also providing a slightly deeper understanding of the effect of the parameters. However, they are often restricted as they cannot predict the extent of the granulation process by themselves, [3] and are generally confined to being merely descriptive rather than predictive [37]

Another growth mechanism not shown in Figure 2.23 but which is present in the field is layering. Layering is the process where larger seed particles are introduced with smaller feed particles to produce granules of a consistent size [38, 78, 79]. Layering can also occur when the process is under-moisturised, as less of the feed is nucleated and instead clings to the surface of the larger already nucleated particles [78].

Also, part of the growth process has typically involved considering the break-

age, as this provides one of the components of a Population Balance Model, as well as because the strength behaviour is significant [80], so this will be accounted for as relevant.

Growth Rate Theory

A well established theory for the growth in agglomeration is that which will be referred to from here on as the Stokes Criterion. This is because it makes significant use of both the St_v and St_{def} to determine whether or not coalescence occurs between two colliding granules. St_v is the stokes viscous number, and measures the relative effect of inertia and viscous damping. It is calculated using $St_v = \frac{8\rho_g \widetilde{d_g} V_{cN}}{9\mu}$

The first of these was mentioned previously and is where Equation 2.2 is derived from. Equation 2.10 calculates whether the relative normal velocity between two granules that are approaching will dissipate due to a liquid surface layer present [4].

$$\frac{8\rho_g \widetilde{d_g} V_{cN}}{9\mu} \leq \left(1 + \frac{1}{e_{rest}}\right) ln \left(\frac{h_0}{h_a}\right) \tag{2.10}$$

This inequality can also be summarised as $St_v \leq St_v{}^*$. Equation 2.10 is limited to elastic particles, though it does accommodate plastic losses to some extent, as it includes e_{rest}. If the granules deform plastically during collision this deformation will alter the nature of the viscous interaction [6]. Equation 2.11 accounts for the effect of this deformation on the viscous behaviour and the restitution.

$$\left(\frac{\sigma_y}{E}\right)^{\frac{1}{2}}(St_{def})^{-\frac{9}{8}} < \frac{0.172}{St_v}\left(\frac{\widetilde{d_g}}{h_0}\right)^2\left[1 - \frac{1}{St_v}ln\left(\frac{h_0}{h_a}\right)\right]^{\frac{5}{4}} \times$$

$$\left[\left(\frac{h_0^2}{h_a^2} - 1\right) + \frac{2h_0}{\delta''}\left(\frac{h_0}{h_a} - 1\right) + \frac{2h_0^2}{\delta''^2}ln\left(\frac{h_0}{h_a}\right)\right] \times$$

$$\left[1 - 7.36\left(\frac{\sigma_y}{E}\right)(St_{def})^{-\frac{1}{4}}\left(1 - \frac{1}{St_v}ln\left(\frac{h_0}{h_a}\right)\right)^{-\frac{1}{2}}\right]^2 \quad (2.11)$$

If the surface of the granules are dry, then the viscous dissipation effects can be calculated for that underneath the surface of the granule to provide a similar solution, Equation 2.12 [6].

$$\left(\frac{\sigma_y}{E}\right)^{\frac{1}{2}}(St_{def})^{-\frac{9}{8}} < \frac{0.172}{St_v}\left(\frac{\widetilde{d_g}}{h_0}\right)^2\left[1 - 7.36\left(\frac{\sigma_y}{E}\right)(St_{def})^{-\frac{1}{4}}\right]^2 \quad (2.12)$$

The final depth of deformation including elastic reformation δ'' depends on whether or not the surface is wet or not. This topic will be discussed later on in section 7.2, so will be left for now.

These equations are stated as not providing predictions unless suitable values for h_0, the liquid surface layer and h_a, the asperity height, can be determined [4,6,81]. A method for determining these from the pellet properties are given, as Equation 2.13 for the saturation in the surface wet cases, and Equation 2.14 is the asperity height as a function of the particle diameters.

$$h_0 \begin{cases} (d_g\epsilon\,(S - K_{Smax}))\,/6 & \text{if } S > K_{Smax} \\ 0 & \text{if } S \leq K_{Smax} \end{cases} \quad (2.13)$$

$$h_a = k_{asp}d_p \quad (2.14)$$

Combining all of these together, a variation on the regime map can be developed, Figure 2.24 [82]. The function $f(St_v)$ is not specified by the original source,

other than being generally recognised as being related to assumptions relating to Equation 2.12.
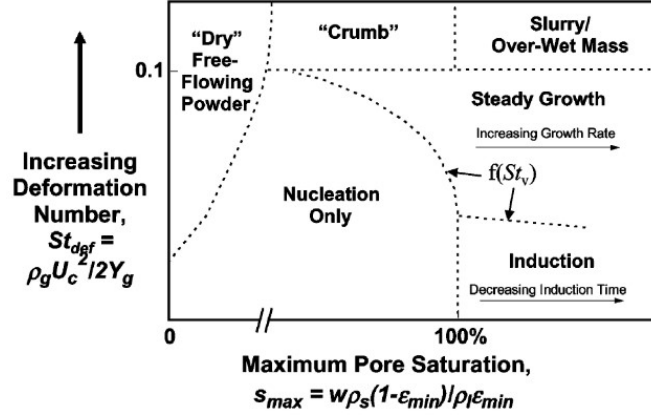
Figure 2.24: Modified Regime map based on work in [6] and accounting for breakage and the lack of clear boundaries describing where rapid growth begins. The growth behaviours of granules according to S_∞ , the newly defined value describing the final saturation possible in the system for a given $m_{l/s}$ and ϵ_{min} and Stokes Deformation number St_{def} Fig. 5 from [82].

The validation of this map, and these equations are somewhat questionable. The equations ultimately merely predict whether coalescence will occur, assuming the premise is correct. No evidence is given for the values involved as being those assumed, nor how the findings relate to the values given. Again, this will be examined in greater detail later on in section 7.2.

Layering is the easiest process to model in a PBM, as it is a consistent process of addition which can be distributed among the population [38]. This is in contrast to the other mechanisms described, including nucleation, agglomeration of granules and breakage, since the discrete nature of the interactions in removing and adding particles to the population complicates matters. Rather than allowing any size, the practical solution is to discretise the diameters the granules can have, which ensures consistency as the losses in one population are balanced out exactly between those populations it contributes to [83].

The agglomeration kernels are the most important ones to mention here.

Nearly all Population Balance Models use a single variable to which the granules can be assigned. In the case of granulation, this variable is the diameter of the granules. This variable then is used when considering the interaction behaviours between the different populations of granules. The relationship which connects the two potentially interacting populations is referred to as the "kernel". This kernel can be experimentally deduced or theoretically based, and the latter will be discussed here.

Hounslow, Pearson and Instone compare three aggregation kernels in [84], a control kernel which is size independent, the equipartition of kinetic energy kernel (EKE), Equation 2.15, and the orthokinetic (OK) kernel [80], also described as Smoluchowski's shear kernel, Equation 2.16

$$\beta_{eke}\left(D, d, t\right) = \beta_0\left(t\right)\left(D + d\right)^2 \sqrt{\frac{1}{D^3} + \frac{1}{d^3}} \tag{2.15}$$

$$\beta_{OK}\left(D, d, t\right) = \beta_0\left(t\right)\left(D + d\right)^3 \tag{2.16}$$

The primary difference is that Equation 2.15 favours large-small agglomeration and Equation 2.16 favours large-large agglomeration. When compared to previous results, the equipartition of kinetic energy kernel was more successful for the general granule size distribution while the orthokinetic kernel was slightly better at describing the way that tracer granules were re-distributed. However, none of the kernels provided an especially strong resemblance to the data.

PBMs also often include time as a correlating variable, however this is not very realistic, and is merely used as evidence that a physical property is also varying with time [84].

Including multiple variables in a Population Balance Model increases the complexity [53]. However, if the moisture distribution is included as well as the granule size distribution, then the predictive capabilities can be significantly improved [53]. A way to reduce the complexity of calculations can be to implement

a Monte Carlo method to work around the worst of the implementation requirements [85].

Combining Population Balance Model with DEM is possible, though the nature of the two models do not naturally fit, as Population Balance Models act on the entire distribution while DEM considers the individual interactions. Working around these can produce some practical results, depending on how the two models are used. DEM can be used to model the particle motion in a compartmentalised system, which can improve the quality of the Population Balance Model [86]. Alternatively, DEM can be used to account for the moisture distribution and the collision interactions, again, similarly improving the quality of the results [77].

Overall though, Population Balance Models are useful in that they can be easily modified and tested, but this also makes them very easy to fit to the data without a conceptual explanation needed. Further, provided that a critical cutoff or limiting granule diamater where coalescence is not possible is included, a wide range of kernels can approximate similar results, [87]. This allows many different kernels to come close, especially once further fitting constants variables are included. Finally, the difficulty in introducing additional variables make it much harder to account for multiple interactions that can vary within a population.

Growth Rate Empirical Findings

Some of the other general findings which describe the growth rate but not in a specific way are as follows [37]:

- Smaller particles tend to grow slower and reach a smaller maximum size, and eventually do not coalesce unless there are large amounts of liquid.

- Granulation time is a key factor in determining the granulation size if not agglomerated to a constant value.

- Equipment speed and type affect the frequency and energy of collisions, which affects the other properties.

- In some cases, the equipment speed and time collapsed onto a single curve if they are combined to give the effective pellet distance. in other cases, higher speed resulted in faster growth even when this is accounted for.

- There is an upper limit to the effect of the equipment effect, as the higher speed eventually contributes to the formation of crumbs.

Induction is the most complicated growth phenomena, but it has been researched by various authors to try and establish patterns [68, 82, 88]. The moisture content added to the initial feed is strongly related to how soon the rapid growth period begins as can be seen in Figure 2.25 and Figure 2.26.
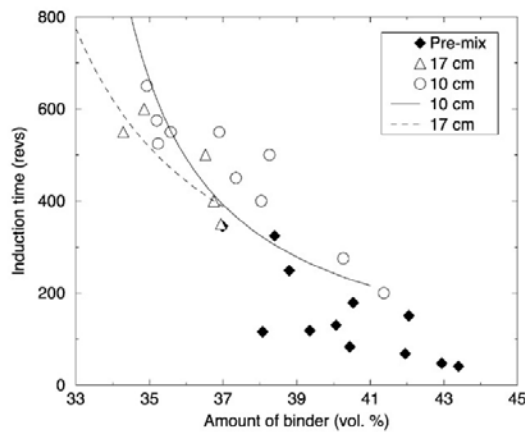
Figure 2.25: Induction time as a function of volumetric binder content $V_{l/s}$ % for all experiments. The numbers indicate the height of the nozzle from the surface of the granule bed. "pre mix" indicates some previous experiments, where the liquid was added beforehand and then passed through a coarse sieve to produce a homogenous consistency. Figure 11 from [68]

Figure 2.27 also shows definitively how the amount of moisture added at the start is a poor indicator for the amount of moisture over time. Figure 2.27 also shows that the rapid growth is tied to the larger granules, because when the smaller granules are not removed they delay the rapid growth. Any theoretical solution would need to account for this phenomena.

The regime map in Figure 2.23 is based partially on the industrial experience of the original authors, though work has been performed to validate it [39, 82, 89].
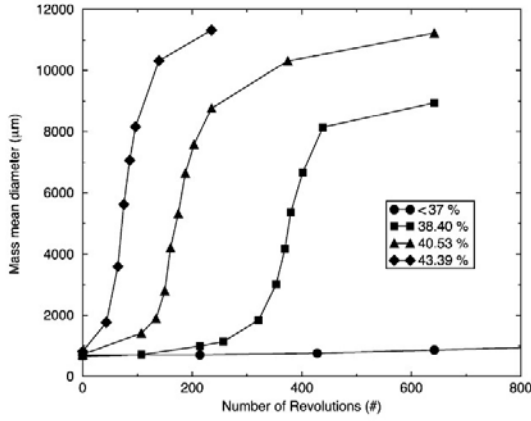
Figure 2.26: $\overline{d_g}$ over time for four different liquid addition quantities. Figure 3 from [47]
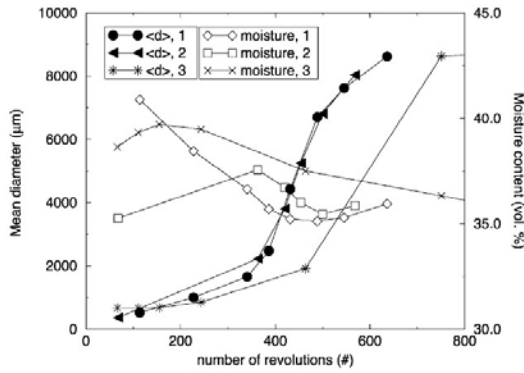
Figure 2.27: Mass mean diameter and binder content versus number of revolutions. The smaller ($d_g \leq 710$ µm) granules were removed after 200 revolutions during experiments 1 and 2. During experiment 3, the smaller granules were not removed. Figure 17 from [68]

Figure 2.28 shows a few examples of experimental findings showing the type of growth as St_{def} is plotted against S_∞ .

The results in Figure 2.28 do generally agree with Figure 2.23, though the boundaries are not very clear. This could be due to the difficulty in clearly establishing the values of S_∞ and St_{def} . Given that growth clearly occurs below S_∞ of 1, the agreement with Figure 2.24 is much less firm. In all cases though, the boundary between each growth type is not strictly quantitative but rather subjective, and there is no strict requirement for the length of time, which is important for whether a material is simply nucleating or will experience induction growth.

Another regime map option is to compare St_{def} to Ca^* , the modified capillary number calculated using $Ca^* = \frac{\mu V_c}{\gamma(1+cos\theta)}$ [90]. Doing so creates Figure 2.29, which

60
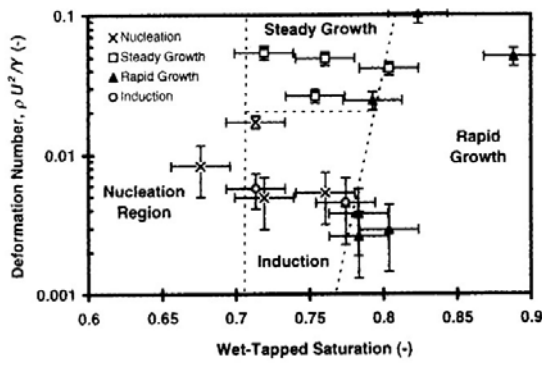
(a) Drum granulation data assembled from various sources [39]. Figure 7 from [39]
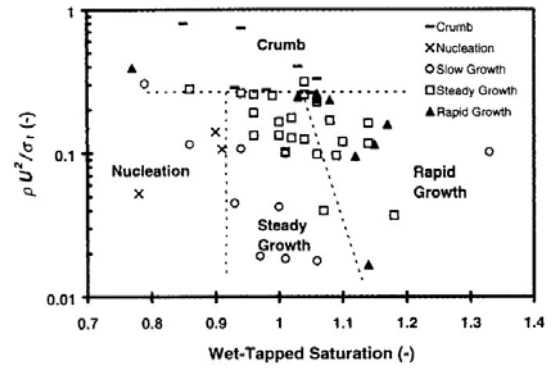
(b) Drum granulation data for tests of various particle sizes and two different viscosities [39]. Figure 8 from [39]
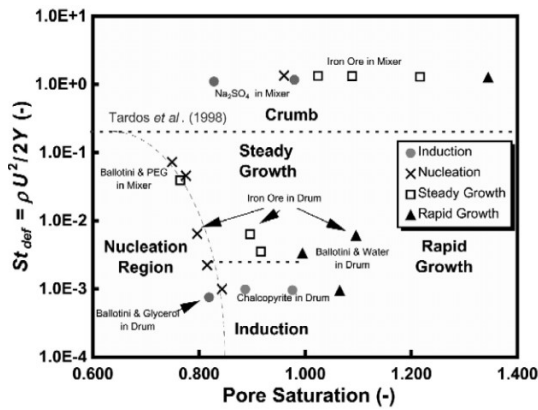
(c) Growth behaviours observed in a variety of Drum and Mixer experiments using various particles and liquids and binders, listed. Figure 14 from [82]
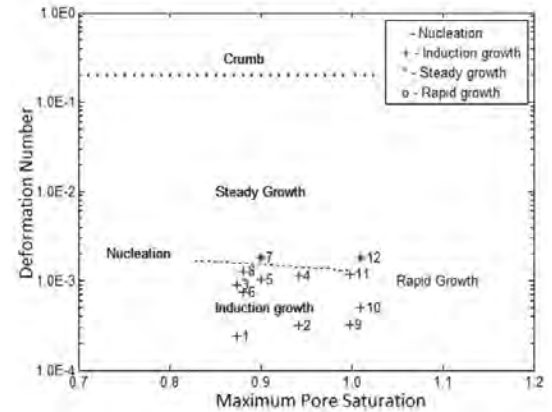
(d) Growth behaviours of zirconium hydroxide granulated with yttrium nitrate solutions. Figure 6 from [89]

Figure 2.28: Growth behaviours described with respect to deformation number St_{def} and saturation S_{∞}

61
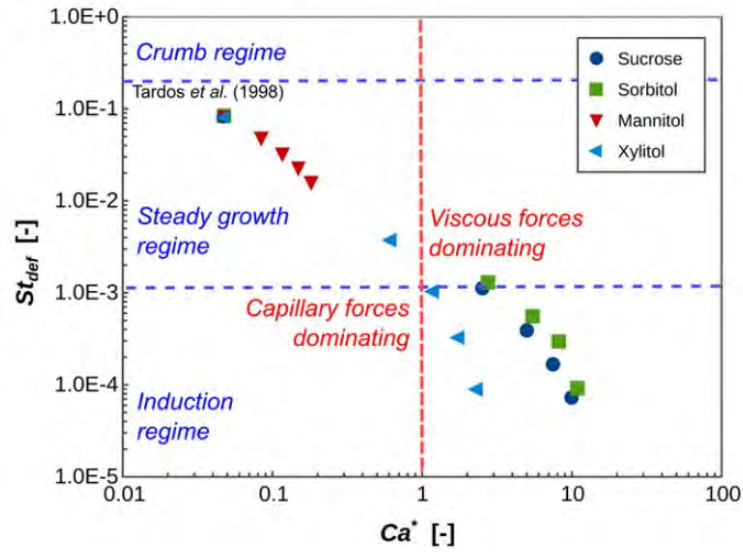
Figure 2.29: Granulation of various sugars with different quantities of Micro-crystalline cellulose binder to produce different values of St_{def} and Ca^* . Figure 13 from [90]

shows how induction growth is highly correlated with a Ca^* greater than 1 and steady growth is correlated with a Ca^* less than 1. This validation is fairly strong, and Ca^* is easier to measure than St_{def} . The capillary number Ca is a dimensional measure which describes the relative strength of the viscous to capillary forces in a given system, and is calculated as $Ca = \frac{\mu \dot{\varepsilon} d_p}{\gamma cos\theta}$

One exception can be found in a series of experiments performed by Hoornaert et al [88]. Unexpectedly, in the results shown in Figure 2.30 show that the lower viscosity binders result in longer induction times, while the more viscous ones bind immediately. It also shows the importance of granulating for a consistent time, as the size varies significantly, as is noted in Figure 2.7.

This may be due to other variables, which are rarely considered in granulation. For example, the granulation process in high shear granulation can generate a lot of heat [88]. Granulation equipment may be cooled, but this cooling is not perfect, the result of the cooling on the growth rate is shown in Figure 2.31

The mechanical heating may be causing the viscosity to lower, however a
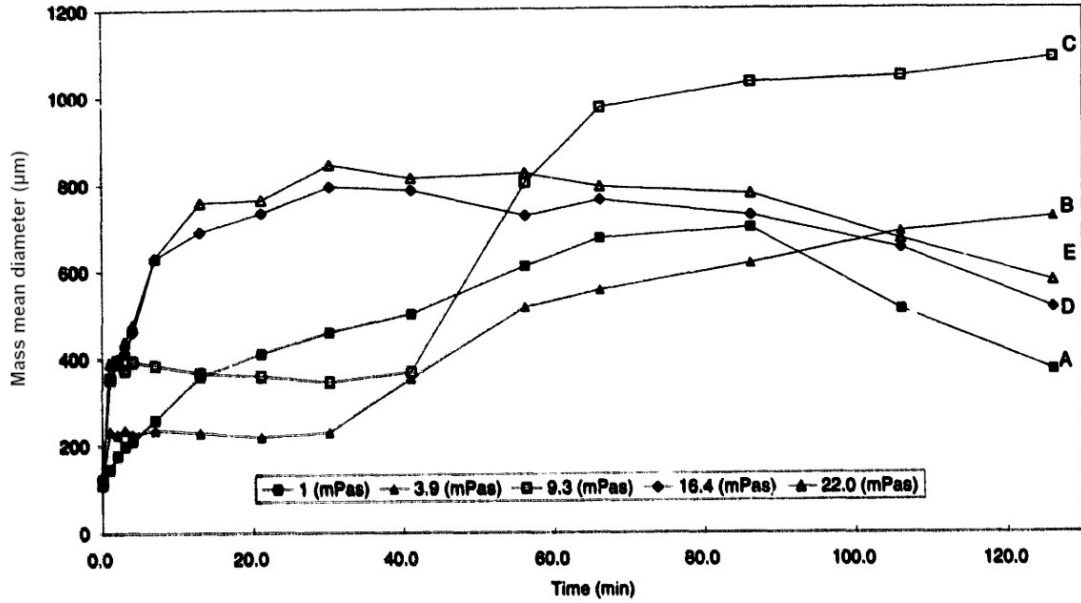
Figure 2.30: $\overline{d_g}$ of sodium sulphate granules in a Lödige mixer granulator with varying liquid viscosities, and a constant 19.1% $m_{l/s}$ % liquid content. ∎: 1 mPas, ▴: 3.9 mPas, ∎: 9.3 mPas, ◇: 16.4 mPas, ▲: 22.0 mPas. Figure 9 from [88]

more complex explanation would be that noted by the authors. They recognise that the sodium sulphate particles being granulated has a decahydrate that it can form which decomposes at 32.4°C. This decomposition temperature lines up with the temperatures observed in Figure 2.31 where the temperature levels out, since decomposition is an endothermic process that releases moisture. To test this theory, they compare the results of high temperature, but less liquid content and high liquid content with cooling in Figure 2.32.

Though this looks promising, this is not the only explanation. The higher temperature may result in easier compaction, which would in turn increase the saturation, and this is the explanation given for why turning on the chopper results in growth Figure 2.33.

The shape of the chopper may be important. The chopper used here was shaped more like a "christmas tree" with hammers rather than blades. Knife shaped blades tend to result in a reduction in the quantity of larger granules,

63
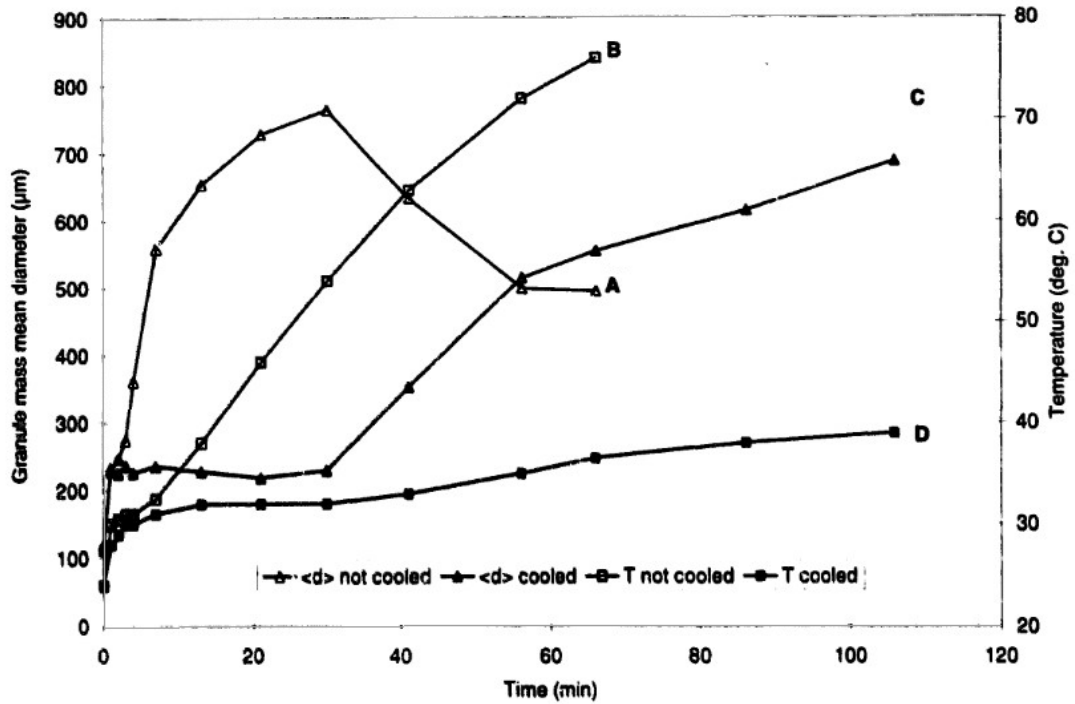
Figure 2.31: $\overline{d_g}$ and temperature developed in sodium sulphate granules in a Lödige mixer granulator over time. Viscosity = 3.9 mPas, and a constant 19.1% $m_{l/s}$ % liquid content. (A $\triangle$): $\overline{d_g}$ not cooled, (B ▲): $\overline{d_g}$ cooled , (C □): T not Cooled, (D ■): T Cooled. Figure 12 from [88]

and when not turned on do not affect the growth rate [88]. On the other hand, though not tested by the authors, it may be that the chopper also increases the temperature sufficiently due to its shape causing impacting and deformation rather than cutting, so this is still unclear.

These experiments are very useful in highlighting the need to note the assumptions in the experiments, and that the chemistry of the process is important even if the goal is a simple physical transformation. The clear and strong evidence for induction reported by other authors [82, 87] as occuring within this setup may be occuring through chemical processes rather than mechanical processes that is ascribed to it.
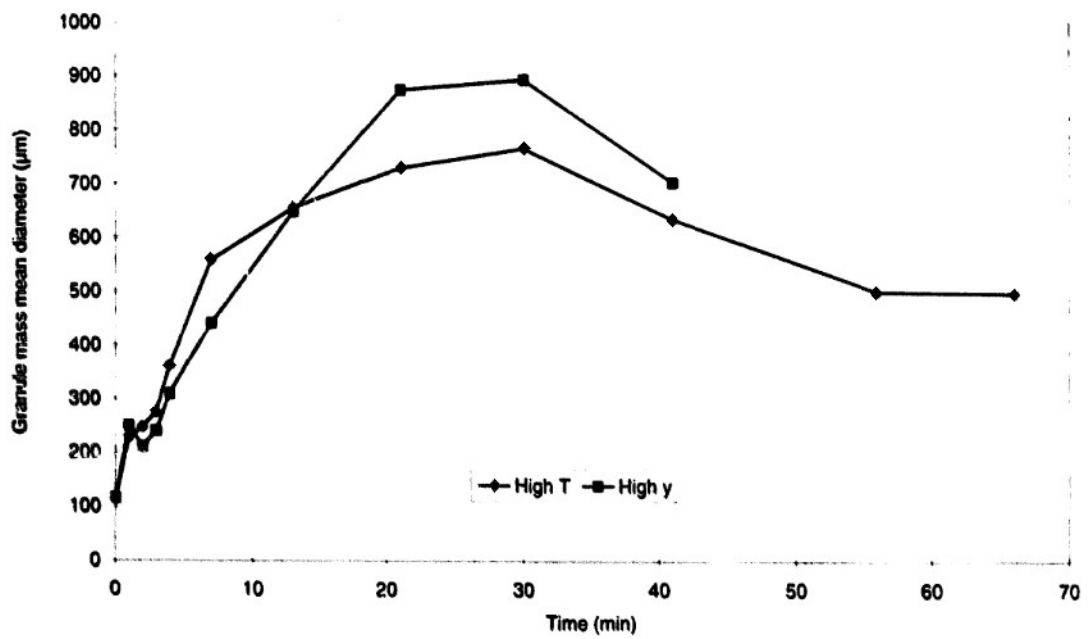
Figure 2.32: $\overline{d_g}$ developed in sodium sulphate granules in a Lödige mixer granulator over time, for two cases: high temperature (no cooling) and low liquid content 19.1% $m_{l/s}$ % and low temperature (cooling applied) and higher liquid content (20.4% $m_{l/s}$ %) for both tests, viscosity = 3.9 mPas. Figure 13 from [88]
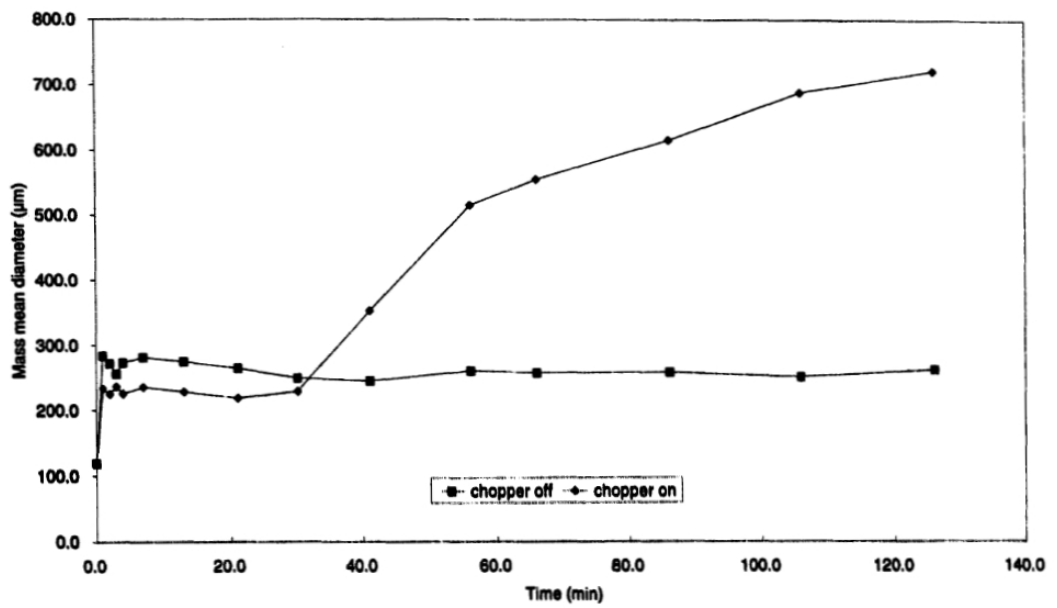
Figure 2.33: $\overline{d_g}$ of sodium sulphate granules in a Lödige mixer granulator , comparing the effect of what occurs with and without the chopper active. Viscosity $= 3.0$ mPas, and a constant 19.1% $m_{l/s}$ % liquid content. Figure 11 from [88]

2.2.3 Strength

The size and the strength of the pellets are not independent. As shown previously, greater strength appears to result in larger granules. The strength is also involved in the calculation of the value of St_{def} , which describes the amount of applied kinetic energy of collisions to the plastic deformation energy [37].

Interestingly, the size also in turn impacts the strength. larger granules will be experiencing a greater moment when shear force is applied, and larger agglomerates will contain larger flaws, both of which will result in increased crack propagation, and overall lower strength [34, 91].

Strength theory

A key component of the granules is the particles. The liquid serves to bind them together, however there are additional features which can alter the strength. There are many possible properties that may be present and thus could alter the behaviours [38, 80, 92]. Figure 2.34 shows a number of these that may be considered.

However, not all of these are relevant, present or necessary to measure. Appropriate characterisation will describe the properties in as few features as possible. In the literature this is sometimes taken too far, with too few characteristics accounted for or assumptions made, or inappropriate characterisation is used which does not accurately represent the importance of the particles in the granular behaviours [80].

With this in mind, the basic building block of the granule is simply two bound particles. This binding is provided in the form of a liquid under normal granulation, which provides capillary and viscous forces [93–95]. Other forces can be calculated for particles, such as Van der Wals forces and electrostatic forces [96].

All of these can be calculated, but in practise the liquid binder and proximity
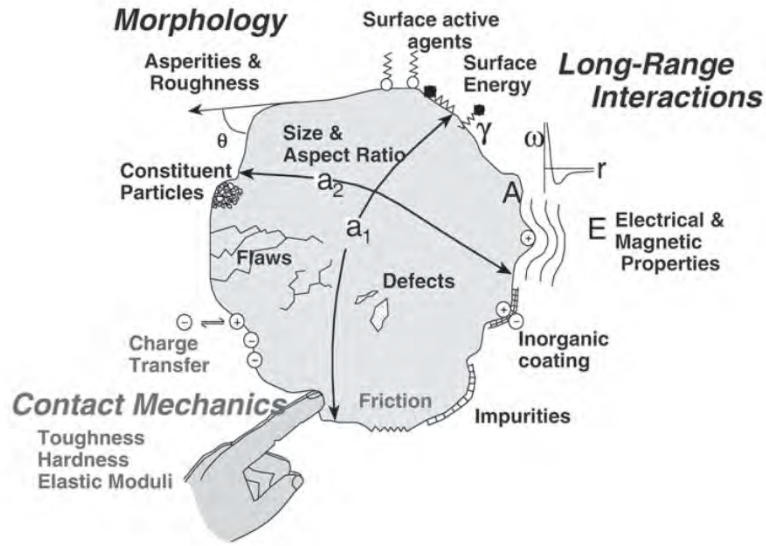
Figure 2.34: Particle properties which may or may not be relevant during the pelletisation process. Figure 2.1 from [38]

Force	Symbol	Equation	Relation to x or ϵ
Capillary force	$F_c(h)$	$h = \frac{(1-\epsilon)}{\epsilon} \frac{\gamma S_{sa} \rho_s \cos(\theta)}{\rho_g}$	$\frac{(1-\epsilon)}{\epsilon}$
Viscous Force	F_v	$F_v = \frac{3\pi\mu D}{x} \cdot \frac{dx}{dt}$	$1/x$
Van der Wals Force	F_{vw}	$F_{vw} = \frac{A_{ham}}{6x^2}\widetilde{D}$	$1/x^2$
Electrostatic Force	F_E	$F_E = 4\kappa\pi\varepsilon_a\varphi_1\varphi_2\widetilde{D}e^{-\kappa x}$	$e^{-\kappa x}$

Table 2.1: Interparticle cohesive forces, Table 2 from [96]. The symbols are as follows: x is the distance between particles, h is the pressure induced increase of height due to capillary forces, S_{sa} is the specific surface area, ρ_s is the solid density,θ is the contact angle, ρ_g is the granule density, D is the diameter of the spheres interacting in the simplified cases presented where particles are assumed to be spherical, A_{ham} is the Hamaker Constant, κ is the Debye length, ε_a is the absolute dielectric constant of dispersion medium, φ is the surface electric potential of the numbered particles.

of the particles will neutralise the particles, resulting in no electrostatic force. The Van der Wals forces meanwhile will be significantly weaker than the capillary and viscous forces [80]. A comparison of the effect of distance on the strength is shown in Figure 2.35
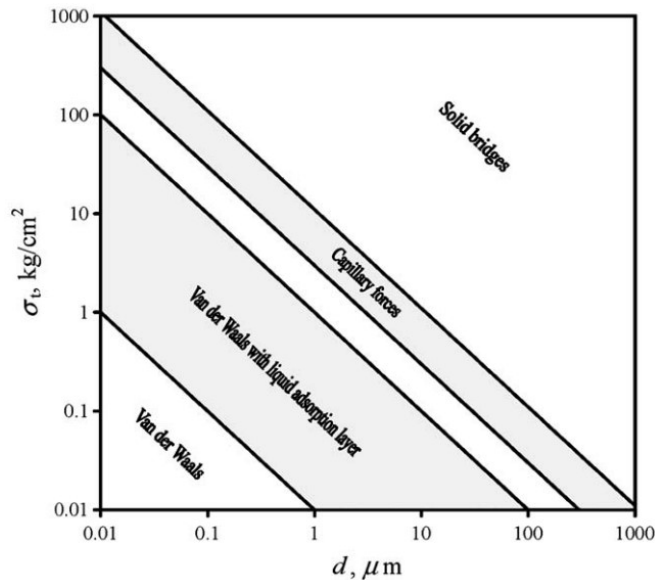
Figure 2.35: Theoretical tensile strength σ_t as a function of size d according to the bond mechanism. Figure 4 from [80].

Comparing the viscosity to the capillary strength is trickier however, since the viscosity is a function of the movement of the liquid and is a dissipative force, while the capillary pressure is a cohesive force. Under industrially relevant conditions, it can be shown that theoretically for two-sphere interactions the strength of the dynamic bridge exceeds that of the static bridge by at least an order of magnitude [4]. However this depends strongly on the intensity of the process, as for low shear and low viscosity processes, the viscous forces are negligible [97].

Together, these conflicting findings establish that identifying the dominant mechanisms in any interaction is important,as it will be regime dependent. None of the cohesive forces in Table 2.1 account for interparticle locking or friction, which will be highly relevant for the compressive strength of the granules [98]. Depending on the specific context, whether the compressive or the tensile strength needs to be applied is important. The two values are related, but they can differ

significantly depending on the context. At higher saturations they appear to be closer to one another [99].

This is made more complex in that there are multiple different states of saturation that have different strength characteristics [17,100,101]. Diagrams of these states can be seen in Figure 2.36.
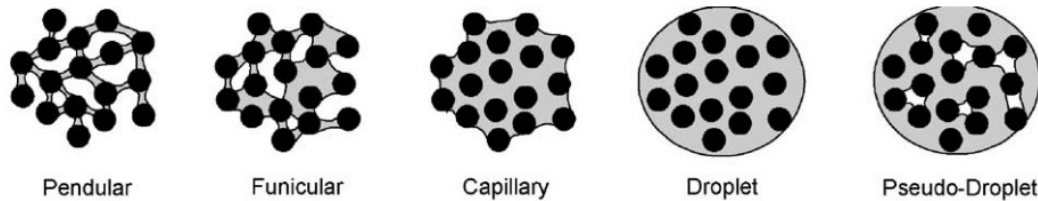
Figure 2.36: General Depictions of the different states of saturation of liquid bound granules. Figure 2 from [100].

The Pendular, Funicular and Capillary states are the three stable states. In a pendular system, all the bonds are direct bridges and no webbing occurs between multiple particles. In a capillary system, all the particles are connected through the liquid, but the liquid does not exceed the circumscribed surface boundary, indicating that it has a inward pressure. The funicular state is everything between these two, where there is some webbing, but not every particle is bound. Saturating beyond these can result in the droplet state, when the liquid exceed the surface boundary, and liquid appears on the surface of the granule and there is no inward pressure. The pseudo-droplet state may also exist, as there is some evidence that often the liquid content does not fill the entirety of the inside of the granule.

The tensile strength was studied earlier, and analytical solutions were developed based on the interactions of the bonds across the granule [93, 94]. The behaviour of the liquid bond can be separated into pendular and the capillary states. In the pendular state, the liquid bonds between particles are distinct, while in the capillary state they bridge multiple particles. Pendular bonds are

70

easier to calculate, as they only need to consider the many interactions which can be combined linearly.

For equal sized spheres randomly packed, with the moisture in a pendular state, the tensile strength can be calculated as [93]

$$\sigma_t = \frac{(1-\epsilon)}{\epsilon}\frac{F_c}{d_p^2} \tag{2.17}$$

where F_c is the capillary suction force. The capillary force between spheres has been calculated to a high degree of complexity, because it is mathematically practical to do so [102, 103].

Calculating the adhesive force involves solving Equation 2.18 [102, 103].

$$2H = \frac{\ddot{Y}}{(1+\dot{Y}^2)^{\frac{3}{2}}} - \frac{1}{Y(1+\dot{Y}^2)^{\frac{1}{2}}} = -2\frac{\Delta p}{2\gamma} \tag{2.18}$$

This is the Laplace-Young equation, and allows the calculation of valid curvature profiles of two interacting fluids. The value Y is a geometric point is space, and the equation needs to be equal at all points to provide a valid curvature when being calculated, which naturally forms in the real case. This is the solution for a rotationally symmetric case, such as interacting spheres or plates, and as such allows a calculation of the pressure difference between the two liquids for the simplified assumption of particles as spheres. This equation usually requires numerical solving, though an analytical solution which is valid for any interacting pairs of spheres has been developed, although it requires knowing three points on the curve to fully define [103].

The capillary force between two equal sized particles is surprisingly similar for a range of bridge liquid volumes and contact angles, the primary parameter which alters the behaviour being the separation distance [102]. Different size particles significantly alters the interactions however.

The bulk tensile strength of the pendular state will differ from the strength of a single bridge. A way to model this is to model the behaviour of the granule as

a chain of spherical particles connected vertically, and the weakest bridge being strained alone. The alternative would be every bridge vertically being pulled equally. Comparing these two is Figure 2.37. The results do not agree with either of the models alone, which is suggested to be due to the non-spherical nature of the particles being tested.
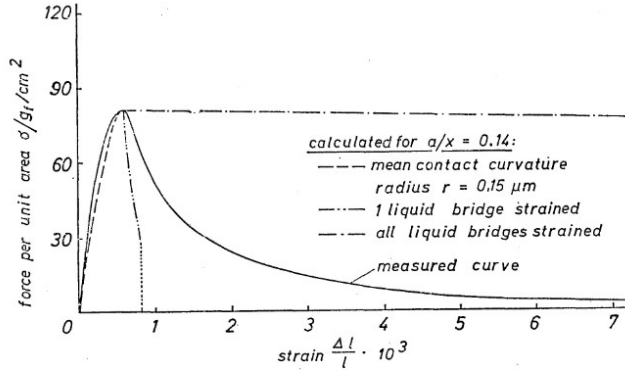
Figure 2.37: Strain behaviour of a limestone pellet, particle diameter $d_p = 12.5m$ and $S = 0.13$. In this figure, a represents the distance between spheres and x represents the sphere diameter under analysis . Figure 7 from [93]

The bulk tensile strength of a pendular system is non-linear with respect to the amount of liquid. It rises extremely quickly, before it then plateaus to a relatively constant value [93, 94]. The reason for this is that simply increasing the volume of the bridges does not significantly alter the capillary force, as mentioned. This is supported by the fact that the bond coordination number is a better predictor for the tensile strength of the granule in a pendular state [104].

In subsection 6.2.1, the nature of the pendular state and its use in granular materials has been examined in more detail.

The capillary state, meanwhile, must be described by necessity through bulk behaviours, as it describes the case when the whole agglomerate is held together [93, 94]. This can be calculated using Equation 2.19.

$$\sigma_{t,c} = SC \frac{(1-\epsilon)}{\epsilon} \frac{\gamma cos\theta}{d_p} \qquad (2.19)$$

When tested, the porosity function $\frac{(1-\epsilon)}{\epsilon}$ was found to be valid for a range of porosities ϵ and the constant $C = 6$ [93, 94].

The pendular strength being unrelated to the saturation while the capillary force is linearly related is well supported by the results shown in Figure 2.38 [93, 94].
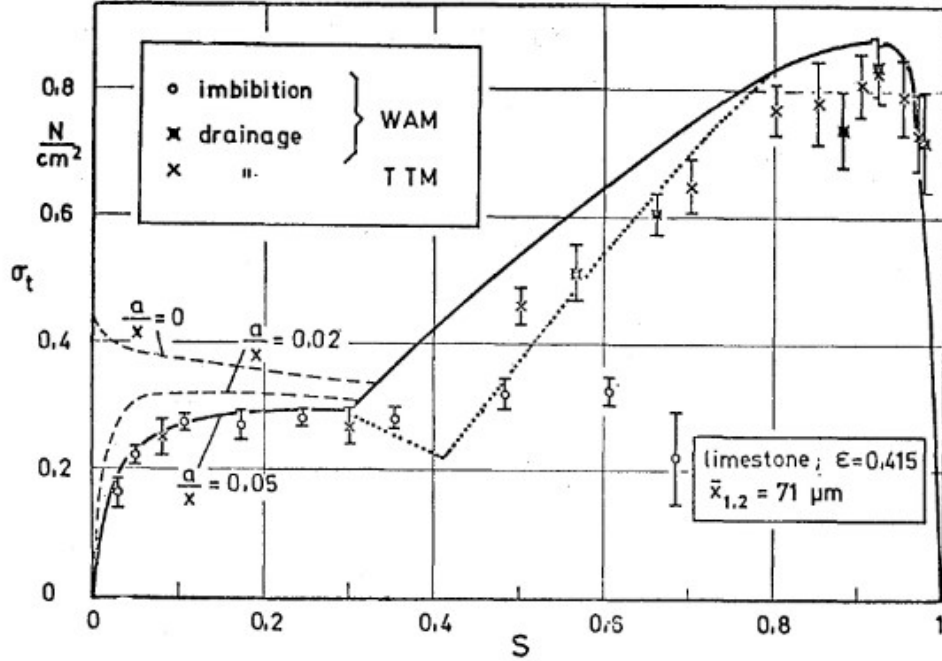
Figure 2.38: Tensile strength relation to saturation for wet limestone powders. Figure 1 from [93].

The dynamic strength due to viscous effects has also been derived Equation 2.20 based on the principles of Equation 2.19 [93, 95].

$$\sigma_{t,v} = \frac{9}{8} \left(\frac{(1 - \epsilon)}{\epsilon} \right)^2 \frac{9\pi \mu v_p}{16 d_{3,2}} \tag{2.20}$$

This however has not been explicitly validated as far as could be determined by the author beyond the features already validated for Equation 2.19. v_p is the velocity of the particles, and this raises questions regarding this validity, since the velocity of the particles internally cannot be assumed to be equal to the velocity of the colliding granules.

Equation 2.19 and Equation 2.20 have been combined to form Equation 2.21, which accounts for both the capillary features and the viscous features [105].

$$\sigma_t = S \left[C \frac{(1-\epsilon)}{\epsilon} \frac{\gamma cos\theta}{d_p} + \frac{9}{8} \left(\frac{(1-\epsilon)}{\epsilon} \right)^2 \frac{9\pi\mu v_p}{16d_{3,2}} \right] \quad (2.21)$$

The theory behind this, and the previous strength equations are considered later in this document. However, for now note that this extension is a combination of strength theoretical equations which appear to be overextending beyond the original scope of the theories.

As for the funicular case, the tensile strength can be formulated as a weighted combination of the pendular and capillary strengths $\sigma_{t,p}$, $\sigma_{t,c}$, which represent different states of moisture filling shown in Figure 2.36. This gives Equation 2.22 [106, 107].

$$\sigma_{t,f} = \sigma_{t,p} \frac{S_{f,c} - S}{S_{f,c} - S_{p,f}} + \sigma_{t,c} \frac{S - S_{p,f}}{S_{f,c} - S_{p,f}} \quad (2.22)$$

The weightings $S_{f,c}$ and $S_{f,c}$ are the limit saturation of the pendular state and the saturation at the start of the capillary state respectively. This linear combination has been found to be in good agreement with the experimental results [106, 107].

Pierrat and Caram in calculating the tensile strength of granular materials to try and improve Rumpf's equation [106] and Louati et al's work to determine the shear behaviour of wet granular material both describe the way that funicular can be described as a weighted combination of the pendular and capillary strengths. This combination fits the form described by [105], suggesting the validity of the linear combination.

The compressive strength is most easily specified as the peak compressive yield strength, the maximum stress required to deform the granule. This value has been nondimensionalised to form Equation 2.23 [100].

$$\sigma_y{}^* = \frac{\sigma_y d_p}{\gamma cos\theta} = f\left(\frac{\mu\dot{\varepsilon}d_p}{\gamma cos\theta}, \mu_f, S, \phi\right) \tag{2.23}$$

the value $\frac{\mu\dot{\varepsilon}d_p}{\gamma cos\theta} = Ca$ is the capillary number,,and μ_f, S, ϕ are the interparticle friction, the saturation and the granule packing fraction respectively. Of these, only Ca has a clearly established direct relation with σ_y , and the strain rate dependence is quite important [108].

When analysing the shear behaviour, the granular nature of the material allows a calculation to relate how multiple shear planes failing at once affect the strength [109]. This results in a relation between σ_y and Ca in the form of Equation 2.24

$$\sigma_y{}^* \propto \overline{Ca}^m \tag{2.24}$$

with m being equal to 0.5 to 1 depending on the strain rate. The higher the strain rate, the closer m is to 0.5. $\overline{Ca}$ is the mean Ca for all the shear planes, and is equivalent to the practical Ca in a granule. This is validated quite well, with experimental results finding m values of 0.58, 0.47, and 0.401 [100, 110, 111].

This leaves μ_f, S, ϕ, which have not been researched nearly as much. There is one solution to calculate the value of μ_f for wet granular materials which is limited to the pendular state Equation 2.25 [112]. This is developed for moistened particles in a shear cell, rather than unconfined pellets.

$$\sigma_{t,f} = \sigma_{t,p}\frac{S_{f,c} - S}{S_{f,c} - S_{p,f}} + \sigma_{t,c}\frac{S - S_{p,f}}{S_{f,c} - S_{p,f}} \tag{2.25}$$

where I is the inertial number defined as $I = \frac{\dot{\gamma}d_p}{\sqrt{\sigma_n \rho_s}}$, σ_n being the stress applied, and P^* is the reduced pressure, $P^* = \frac{\sigma_n d_p^2}{\pi\gamma}$. P^* is the inverse of the cohesion number η_c which characterises the intrinsic cohesion. Z is the coordination number which is also relevant for pendular tensile strength [104], and $\mu_{f_d}{}^*$ is the dry particle friction coefficient. Equation 2.25 matched the data quite well, and showed that the frictional component in granular materials is also rate dependent.

The compressive strength of granular materials is more dependent on the packing and the particle properties than the tensile strength. The interparticle friction and interparticle locking has to be overcome [113], on top of the liquid interactions, though the liquids can also act to lubricate the interparticle interactions [100].

The yield strength of the pellets is quite important, and as such will be discussed further in section 6.3

The plasticity of the pellets matters, as the contact behaviour between elastic spheres and plastic spheres differs [114]. Further, some growth models depend on whether the pellets are elastic or plastic to determine the mechanism [4,6]. For pellets yielding quickly, the theoretical deformation behaviour is plastic as the granule shears [109], and this is in agreement with various findings, which will be discussed later.

Because wet agglomerated materials experience some flow under stress, and are ultimately formed of weakly bound particles, their behaviour differs from a bulk solid [36].
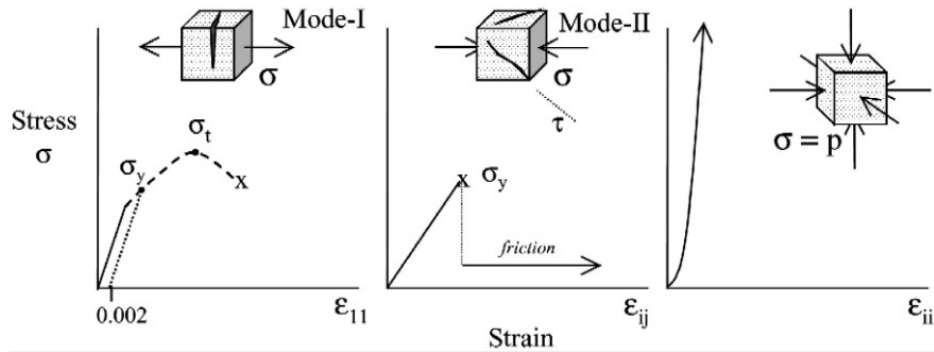
Figure 2.39: Characteristic stress-strain behaviour for a pseudo-elastic, compressible agglomerate. Figure 1 from [36].

This can be seen in their stress strain behaviours in Figure 2.39, in particular the compressive behaviour. The peak stress occurs, at which point the material begins to flow requiring much less force to deform. Despite this, they also have

76

a pseudo-elastic region, where the stress-strain is roughly linear. This is referred to as pseudo-elastic as wet agglomerates nonetheless deform in a fully plastic manner, with no recovery after the deformation has occurred (unlike with bulk solids) as the particles lack long range coordination [36].

The plastic spherical deformation is related to force applied through the hardness of the material [114]. This hardness can be related to the σ_y though the constraint, variously reported using φ [36] described in Equation 2.26 .

$$\frac{H}{\sigma_y} \equiv \varphi = 0.28 + 0.6 \ln \left(\frac{3E}{\sigma_y \left(4 + \nu \right)} \right) \tag{2.26}$$

Equation 2.26 was developed as a theory to determine the indentation of test materials by a hemispherical indentor. This value is greater than unity as the surrounding material constrains the test section, which leads to values around 3 [36].

Strength Empirical Findings

Beyond the previous theoretical relations, there are other important factors and empirical relations some of which are described by the previous theories [36, 37, 80, 110]:

- Smaller particle sizes result in greater yield strength, and conversely larger particles result in weaker granules.

- Higher viscosities and surface tension both result in stronger granules

- Higher porosities result in weaker granules

- Saturation increases the strength up to a point before the granules lose all cohesion.

- Particles with irregular shapes and rough surfaces tend to be stronger

For the empirical findings, and in fact the results which validated the theories, the tests are not all on spherical granules. This is important, as the specimen shape significantly affects the determined strength even when nondimensionalised, as the shape particularly alters the failure behaviour in granular materials due to the lack of long range order [36]. Further, because the strength is related to the strain rate, [110,112], the behaviour has to not only be measured with appropriate specimen shapes but also at appropriate speeds [36,115].

Increasing the saturation also leads to increased plasticity, which in turn alters the stress response, the behaviour under compression and the coefficient of restitution [111, 116]. The crushing strength actually reduces as the saturation increases [111,116].

Empirical support for the relation of the particle size being inversely related to the strength can be found in addition to those mentioned previously [5,98,106]. This yield strength increase also extends to industrially measured strengths. After high pressure roller grinding of magnetite ores Chen et al reduced the median diameter by 40% [96]. This resulted in a doubling of the crushing strength, and an increase in the drop number from 3.2 to 5.1, which also shows that the crushing strength, which is directly related to the peak strength, is only partially related to the drop number.

Viewing the bonds themselves is not usually possible within the bulk, however it has been done through x-ray microtomography [112, 117]. This allows direct observations of the pendular bonds formed between 1% to 15%. The stiffness of the material being constant for this range is in agreement with the previous findings regarding the bond coordination being more important than the liquid content. The morphology of the bonds did change as the liquid increased, and rather than the total liquid content of every bond increasing, a few specific clusters absorbed most of the liquid, leaving the rest of the bonds unchanged.

The manner in which the saturation is added seems to be quite important. The difference in the stress-strain curves for saturations reached through imbibition

(addition) and drainage (subtraction) is shown in Figure 2.40 and Figure 2.41 [94, 118].
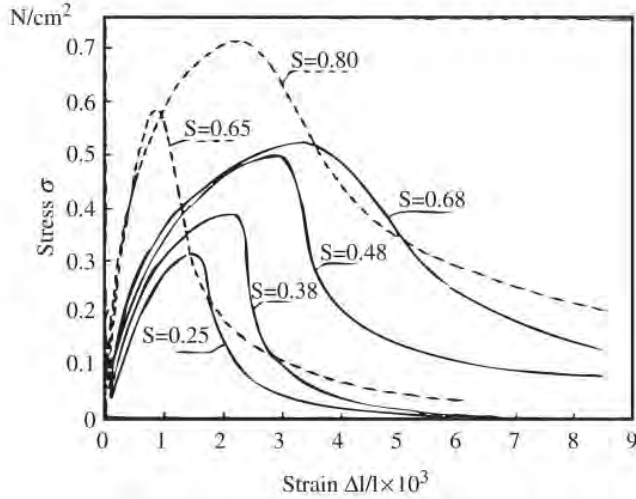
Figure 2.40: Tensile Stress-Strain relation of wet limestone, with a porosity $\epsilon = 0.33$ and $d_p = 65m$. Solid lines indicate samples prepared through wetting processes (Imbibition) and dashed lines indicate samples prepared through a drying process (Drainage). Figure 14 from [118], original data from [94]
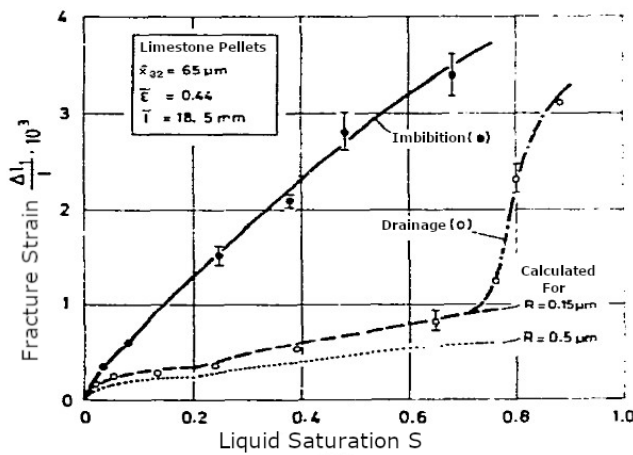
Figure 2.41: Critical tensile strain - Saturation relation of wet limestone, with a porosity $\epsilon = 0.44$ and $d_p = 65m$. Solid line indicate samples prepared through wetting processes (Imbibition) and dashed lines indicate samples prepared through a drying process (Drainage). Figure 10 from [94]

The relationship between the saturation and the strength of the material is therefore path dependent. This is shown in Figure 2.42, and particularly leads to difficulties in specifying the strength of the funicular state. The details of the funicular state as a whole are considered in subsection 6.2.3.

Figure 2.40 shows that whether through addition or subtraction, greater saturations lead to greater tensile strength. This is not necessarily the case with compressive strength [111, 116, 119], as shown in Figure 2.43.

79
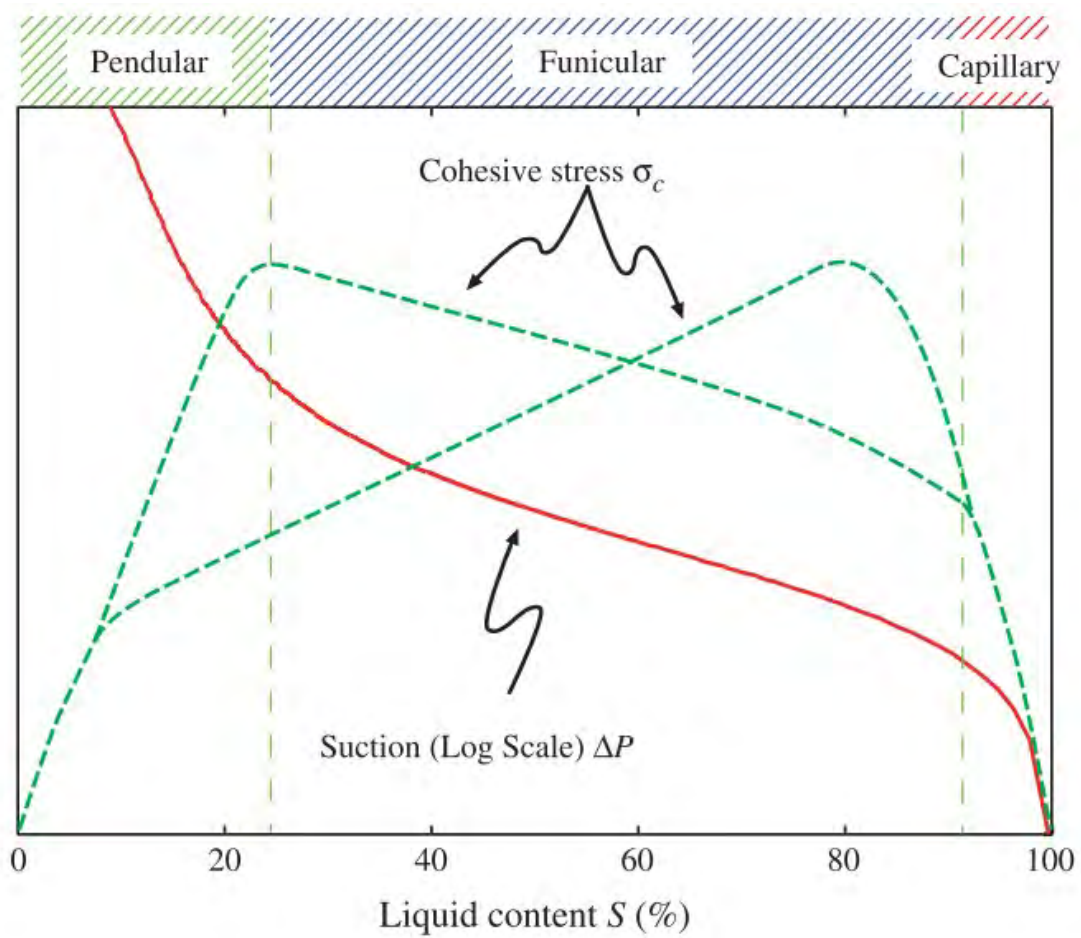
Figure 2.42: Schematic Diagram summarising the variations of the suction Δp and cohesive strength σ_c wet granular materials with changing saturation contents. Figure 24 from [118].

This may be because the increased saturation allows the liquid to lubricate the particles better, and the interparticle friction is significantly more relevant for compressive strength [118].

Increasing the saturation has also been found to increase plasticity, which in turn alters the stress response, the behaviour under compression and the coefficient of restitution [111, 116].

Modelling granular materials using DEM provides a useful method to visualise the cohesive behaviour and thus the strength [120–124]. It allows a finer details
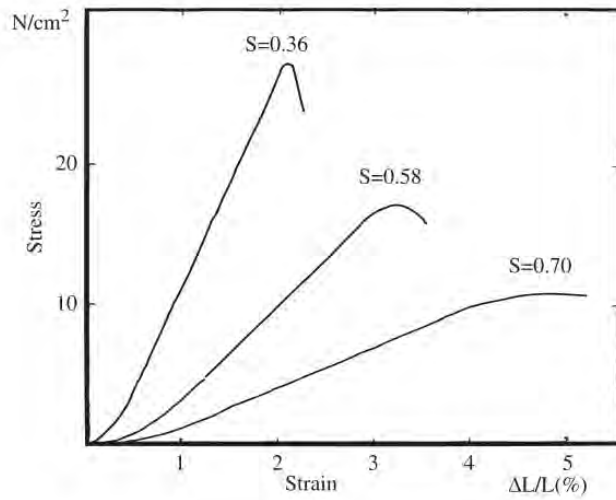
Figure 2.43: Compressive Stress-Strain relation of three different samples of dicalcium phosphate, with a porosity $\epsilon = 0.5$ and $d_p = 21\mu m$. S refers to the Saturation of the samples. Figure 14 from [118], original data from [119]

to be noted, such as the heterogeneity of the stress response of the component particles, as can be seen in Figure 2.44.
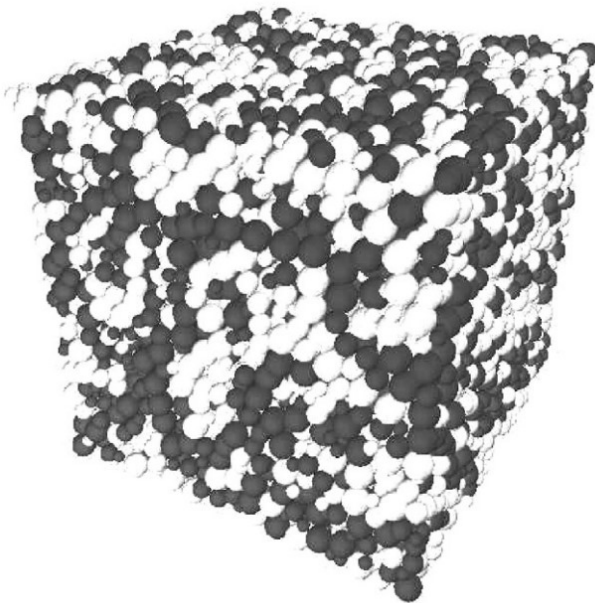
Figure 2.44: Image of DEM model, modelling unconfined packing in a wet granular material. The black elements are experiencing positive (compressive) pressure, the white elements are experiencing negative (tensile) pressures. Figure 9 from [121]

When the quantities of the pressures the elements apply to one another are counted, the pressure distribution can be plotted, as in Figure 2.45, which shows that a few key elements sustain the strongest forces.
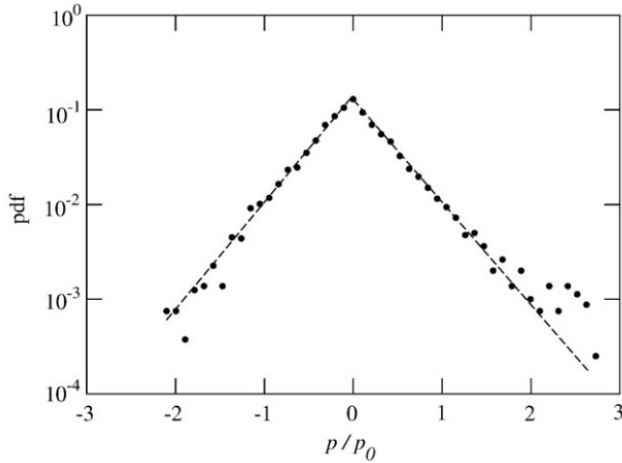
Figure 2.45: Probability density function of particle pressures normalised by a reference pressure p_{ref} in unconfined packing. Figure 8 from [121]

The heterogeneity in the internal stress structure may also contribute to the wide variation observed in the strength of individual granules tested [124]. This variability is present primarily for lower saturation experiments [99, 125], while higher saturation studies tend to have more consistent values of strength [100, 111]. This can be seen in Figure 2.46a

Figure 2.46a provides a line of best fit, though the data is not well suited to this type of fitting.

The saturation has a strong linear relationship with the fracture toughness, as shown in Figure 2.46b [125]. The primary mechanism which dissipates the energy of the fracture is plastic dissipation, which is responsible for 99% of the energy dissipation, which also increases with higher saturation values [125].

One of the more useful methods of analysing the yield strength is through the dimensionless yield strength, the function of which is shown in Equation 2.23. This then allows a more generalised formula to be theoretically be determined, though this requires appropriate treatment of the variables in question. One of the earlier attempts to find a solution for this is Equation 2.19, which is reasonably accurate, and the relations observed are relatively well validated for the specific case tested. Equation 2.27 is one such equation, and fits the pendular regime for a range of porosities better than Equation 2.19 [106].
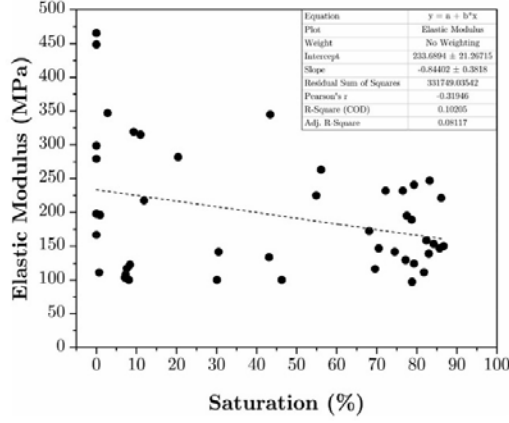
(a) Elastic Modulus E relation with saturation experiments. The dashed line is a linear fit to the data, of the form $[E = -0.844(\%S) + 233.7]$ with E in MPa, or equivalently in base units $[E = (-84.4 * S) + 233.7) * 10^6]$. However, a fit of this nature is unsuited to the data as presented, as demonstrated by the R^2 value of 0.1, though two distinct lines do appear to be present.

Figure 3 from [125]

(b) J-integral J_{IC} ,(a measure of fracture toughness) relation to Saturation. a/R is the ratio of flaw size a to sample radius R . Figure 7 from [125]

Figure 2.46: Behaviour of wet agglomerated materials from [125]

$$\sigma_y{}^* = 7.80 \left(1 - \epsilon\right)^{3.03} \tag{2.27}$$

Equation 2.24 was developed after a series of tests, during which an empirical relation between σ_y , Ca and d_p was observed [5, 100]. The nondimensional empirical relation given in Equation 2.28 was found to produce a reasonable fit for the initial series of experiments, though as higher aspect ratio particles were introduced the accuracy began to drop.

$$\sigma_y{}^* = k_1 + k_2 Ca^m \tag{2.28}$$

The values of k_1, k_2 and m have been developed for a few different cases. These include glass ballotinis and various oils ($k_1 = 5.3 \pm 0.4, k_2 = 280 \pm 40, m =$

0.58±0.4) [100], irregular copper powder ($k_1 = 30 \pm 0.4, k_2 = 740, m = 0.47$) [110], and lactose ($k_1 = 7.0, k_2 = 221, m = 0.58$) [111]. Further developments have also accounted for the aspect ratio [111] and the formation compression stress [126]. The saturations for which these were tested range from 0.39 to 0.73.

The aspect ratio corresponds to a greater degree of interlocking and interparticle friction [113, 127], which would support the findings that it improves the yield strength [111]. Though the frictional component of the response can be modelled by increasing the value of μ_f of the particles, the strain response actually differs depending on the aspect ratio, with more angular particles demonstrating contractive response while spherical particles show a dilatory response [113] which in turn affects the porosity.

Another empirical relation was developed for high Ca values through regression analysis of variables measured and the results is Equation 2.29 [111].

$$\sigma_y{}^* = 4346(Ca^{0.401} S^{1.577} \epsilon^{2.059} \mathcal{R}^{-2.25} S_p^{0.799}) \tag{2.29}$$

Here $\mathcal{R}$ is the aspect ratio of the particles, and S_p is the range of the particle diameters in the agglomerate. This equation fits the data well, as would be expected given how it was developed. The positive correlation it predicts between porosity and the strength however contradicts other findings, which universally find that a higher porosity reduces the strength [36, 128] and is physically implausible.

The pre-compressive force, i.e. the force applied in the formation of the granule, increases the strength of the formed granule [126, 129]. This pre-compression is known to reduce the porosity [129], which may explain the relation between pre-compression and the yield strength observed by [126, 129].

The dosage of special binders into water being used as the liquid component is unsurprisingly important, but it can be hard to quantify the relationship. Empirical relations have been determined for some binders, Figure 2.47 but unless the mechanism is described, these results are not especially useful for understanding
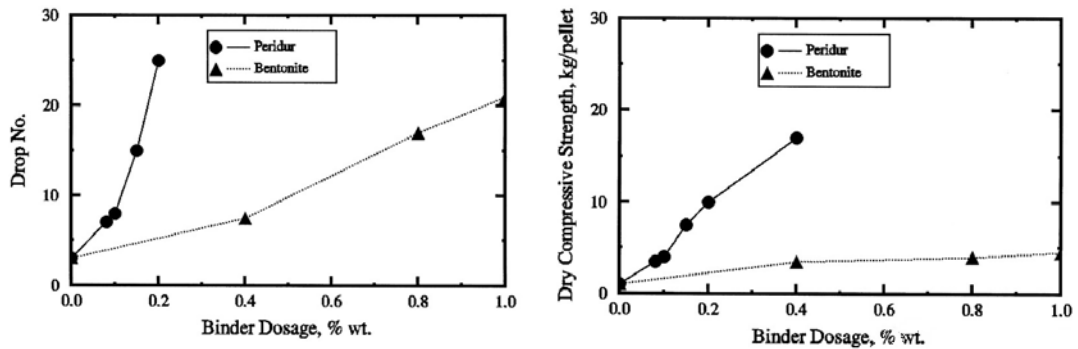
(a) Comparison between Peridur and Bentonite drop strengths, for given binder dosages. Figure 11 A from [63]

(b) Comparison between Peridur and Bentonite dry compressive strengths, for given binder dosages. Figure 11 B from [63]

Figure 2.47: Effect of binder dosages in water on the drop strengths, Figures from [63]

how to model the strength and improve it. The drop strength is an comparative measure of the granule strength, as it measures how well it can sustain drops from a given height from the ground, usually a proxy for the drop height between belts in industry.

Finally, the nuclei formed from the direct addition of liquid droplets to the dry feed have a different morphology to those formed from the agglomeration and reformation of multiple granules combined. The misalignment of the particles which occurs as the granules are agglomerated together results in the subsequent granules being weaker and having a higher porosity [91].

2.3 Additional Literature

The previous section was focussed on the features of the material, and what directly impacts the size and strength. There are other extraneous features inherent to cold-bonding pelletisation that need to be considered which indirectly impact and are impacted by the mill scale in pelletising, and the other extraneous behaviours which impact the pelletisation process indirectly.

These include:

85

1. Mill Scale Pelletising

   (a) Scale

   (b) Oils

   (c) Cement

2. Pelletisation Mechanisms

   (a) Binder Mechanisms

   (b) Pellet Bonding

   (c) Segregation and Kinetics

   (d) Coefficient of restitution

   (e) Saturation

   (f) Liquid State

   (g) Porosity and Packing

   (h) Consolidation

2.3.1 Mill Scale Pelletising

Scale

The chemical composition of the scale may be relevant to the granulation properties, specifically the surface chemistry as this can affect the contact angle which in turn affects the capillary strength [130]. The literature suggests that hematite has quite high contact angles, around 75° [131], while goethite ores can be significantly lower, being somewhere between 29° to 56° [131, 132]. This reduction in contact angle may be linked to the fact that hematite is an oxide while goethite is a hydroxide, and so will have hydrogen bonds available [133]

The size of the scale particles has been found to be larger than typical ores and with a longer distribution tail of larger particles [20, 134], which may be relevant since the particle size is important for the strength of the pellets.

Oil

The oil is managed through the use of a conditioner. The effects it has are therefore mitigated, but may still be important

The oil is not alone, but rather in a mixture with water and particles. When granular assemblies are wetted with two immiscible liquids, unusual phases can be generated as the liquids maintain a separation from one another and the particles are bound together through the surface tension [135]. This surface tension between two liquids means that, if the saturation simply is a measure of the liquid content, then it does not capture the effect of the surface boundaries between the three present fluids, since usually the surface boundary is between the liquid and the air.

Ignoring the particles briefly, the viscosity of an emulsion formed of a mixture can be orders of magnitude higher than either of the liquids alone [136] and the behaviour non-Newtonian [137]. The surface tension on the other hand can be significantly reduced, though this is dependent on the specific liquid combination [138].

Since the sludge is stored for relatively long periods of time as it drains, the oil may weather due to exposure to UV, oxygen, varying temperatures and so on. This is a relatively complicated process, but there is some research as it is highly relevant to crude oil spills. Observed effects include the evaporation of lighter oils to form a more uniform mixture of thicker oils, formation of a crust composed of resins and waxes, and photo-oxidation to alter the composition to form more of these [139]. Biodegradation can occur, however this is highly dependent on the oxygen availability and is significantly impaired even a few centimetres below the surface. Trends associated with weathering include a linear increase in density with evaporative mass loss, an unspecified relationship for the viscosity increase as weathering occurs, and a slight increase in surface and interfacial tensions as weathering progresses [140].

Cement

Cement and concrete strength have been well researched, and since cold-bonded pellets are formed using cement, these should have some application. For reference, concrete is formed of two components, the cement paste which is the fluid part which sets, and the aggregate which is the filler rocky material, and together form a slurry. Workability in the context of concrete is the flowability of the slurry, since the slurry needs to fill the desired shape completely. A lower workability will thus correspond to a higher yield strength of the wet pellets. The cement used on site is Portland cement.

With concrete, the aggregate is stronger than the cement, so the less cement paste used the stronger the resulting concrete, though a minimum amount of paste is necessary for an acceptable workability [141]. Because of this, more of the aggregate should consist of larger particles, as these are more efficient overall in the subsequent packing behaviours (discussed further section 2.3.2) [142].

Increasing the aggregate size by recycling concrete has also been found to be an effective way to improve the compressive strength of the set concrete. even though the total cement quantity should be the same, it seems in practise to reduce the amount of mortar used as well [143].

The shape of the particles also affects the workability, with more rounded particles requiring lower water content for a given workability, meaning the more angular the aggregate the lower the lower workability (and thus higher yield strength) [142].

Additives can alter the workability as well, for example addition of excess lime to Portland cement reduces the workability [144]. In an intersection with the oil research above, the addition of a very small amount (0.15%) of used engine oil to the mixture has been shown to increase the workability similar to superplasticisers (which are additives specifically designed for this purpose). This is suggested to be because of the SO_3 content of the oil used, but the development of surface micelles on the particles (which reduce the strength if a concentration thresholdis

reached) is possible [145].

The rheology of cement pastes is affected by the specific surface area of the fines, which have a linear correlation with the flow resistance, the gradient depending on included plasticisers [146]. The viscosity is also strain rate dependent, and dependent on the cement and superplasticiser concentration [147]. The viscosity is also exponentially related to the volume fraction of the cement in the paste, and starting around a volume fraction of around 0.5 the viscosity begins to increase quickly.

The effect of hydration is also important, especially the immediate effects, as the liquid is added during the process. If the chemistry is altering the behaviour in the first minute or so then this could have an impact on the other elements of the dynamic process. The hydration process does crystallise some of the water, so not all the moisture in the material is free liquid, and this occurs almost immediately upon contact with the water [148].

Lime has been shown to decrease the rate of setting [144] and potentially relatedly, reduce the rate of heat generation in the first few minutes of the hydration reaction [149]. Gypsum is included in cement to suppress "flash setting" [148], which is very important in keeping the concrete fluid. An excess of gypsum meanwhile delays the setting process further [150], which means that if the setting timing during the process was important this could be adjusted.

2.3.2 Pelletisation Mechanisms

Other pelletisation mechanisms are important to the process but are only indirectly associated with either the size or the strength. Because these will be explored later in this work, the literature covering them will also be discussed.

Binder mechanisms

Not all bond strengthening mechanisms can be described simply as capillary or viscous. Bentonite, a very common binder, produces fibrous plates that connect the particles together, which can be seen directly in Figure 2.48 and Figure 2.49 [63, 151].
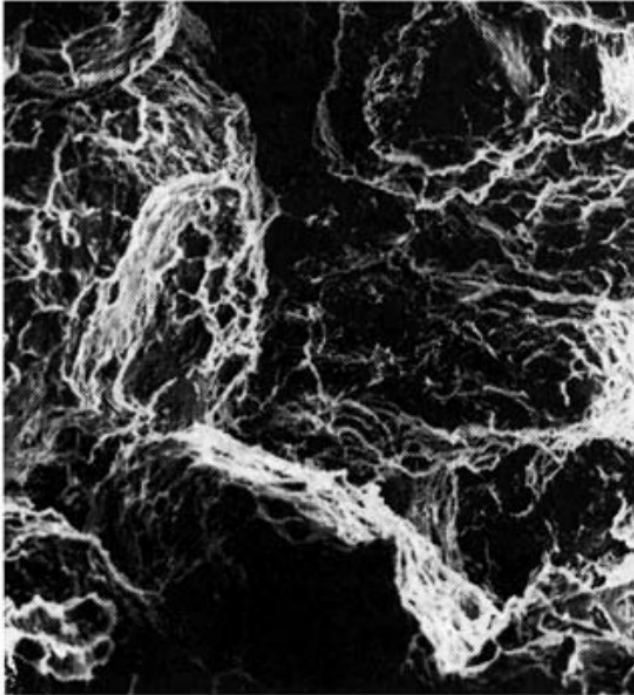
Figure 2.48: SEM images of silica sand bonded with bentonite. Figure 4 from [63].
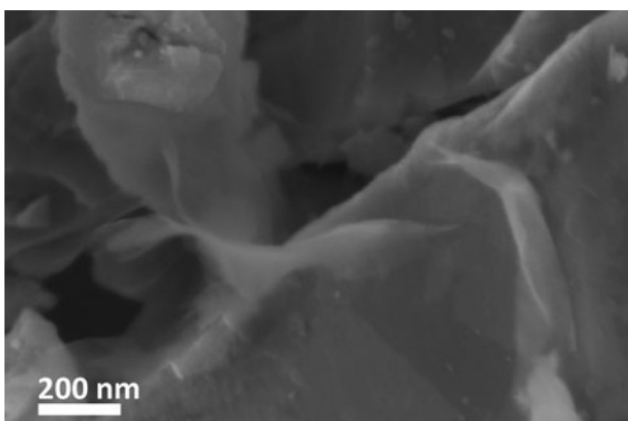
Figure 2.49: SEM images of dry iron ore pellet surface bonded with bentonite. Figure 6 from [151].

The mechanism appears to be the bentonite, upon hydration, expands into the separate clay layers, and then shear forces spread it into a fibrous form, akin to spreading of a deck of cards. These fibres then provide strength between the granules when wet, and when they dry they form solid bridges between the particles. This does not require the previously assumed behaviour of electrostatic bonds between the platelets to work. Bentonites have been shown to be effective at improving the strength and being mineral they are effective at high temperatures. Despite being commonly used and providing consistent strength increases one major issue is that they are difficult to quantify due to their unusual mechanism compared to typical binders, leaving the findings often simply comparative.

Pellet Bonding

The growth variation may come from adhesion after the production, with pellets bonding to one another as the cement cures. Additives could be sprayed on after the tumbling to prevent this if this is a significant problem [152].

The strength of the initial bond is very important in determining Equation 7.3, and there is a solution which calculates this, derived from analogy to cold welding [153]. In this case, rather than exposing fresh metal between oxides, instead wetter material is exposed which induces bonding. This mechanism requires material with relatively high saturation values, of 70% or more [153]. The strength of the bond can be found using Equation 2.30

$$\Sigma_{bond} = \ 0.65\sigma_y\pi r_0{}^2 \left[\left(\varepsilon_r^2 + 2\varepsilon_r\right) + 1 - e^{(-K_s\varepsilon_r)}\right] \tag{2.30}$$

Equation 2.30 showed good correspondence to the results, and will be analysed further in subsection 7.3.2

Segregation and Kinetics

The kinetic behaviour of granular materials is unique in that upon agitation they appear to become more ordered, rather than less. This phenomena is sometimes referred to as "granular de-mixing", "the Brazil nut effect " and more generally covered by "Segregation" which will be used here, this describes the propensity of larger granules/nuts/objects of equal density to rise to the top of the pile [154–156].

Given that the principle of agglomeration intrinsically involves merging smaller granules to one another, and that this distribution changes over time [53,84], the segregation may be important in understanding the results.

One method to maintain kinematic similarity is suggested to be the froude number, which describes the relative ratio of the gravitational acceleration to the centripetal acceleration, and is determined through Equation 2.31

$$Fr = \frac{\omega^2 R_{Dr}}{g}/ \tag{2.31}$$

By measuring the ratio of centrifugal to gravitational forces, the Froude number potentially provides a means of scaling between drums of different radii.

This however does not account for granules of different size, and there is an interesting interaction that occurs when these are introduced. This can be seen in DEM models of tumbling mills Figure 2.51 [158] demonstrates how it is more complex than simply the largest rise to the top. The elements rather show that the largest granules move in the direction opposite to the greatest acceleration experienced by the mass.

The mechanism by which this segregation occurs may be important if this is to be modelled abstractly. There are four primary suggested mechanisms of segregation, which are not mutually exclusive [155, 159].

1. Percolation, in which the particles move and interact with the spaces between one another, which tends to lead smaller particles to move downwards
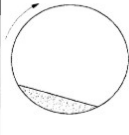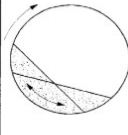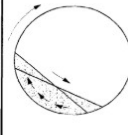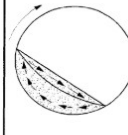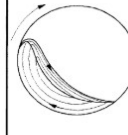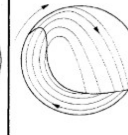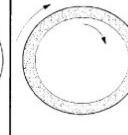
92

Basic form	Slipping motion		Cascading ("tumbling") motion			Cataracting motion	
Subtype	Sliding	Surging	Slumping	Rolling	Cascading	Cataracting	Centrifuging
Schematic							
Physical process	Slipping		Mixing			Crushing	Centrifuging
Froude number Fr [-]	$0 < Fr < 10^{-4}$		$10^{-5}< Fr < 10^{-3}$	$10^{-4}< Fr < 10^{-2}$	$10^{-3}< Fr < 10^{-1}$	$0.1 < Fr < 1$	$Fr \geq 1$
Filling degree f [-]	f < 0.1	f > 0.1	f < 0.1	f > 0.1		f > 0.2	
Wall friction coeff. μ_w [-]	$\mu_w < \mu_{w,c}$	$\mu_w \geq \mu_{w,c}$	$\mu_w > \mu_{w,c}$			$\mu_w > \mu_{w,c}$	
Application	no use		Rotary kilns and reactors; rotary dryers and coolers; mixing drums			Ball mills	no use

Figure 2.50: Forms of transverse motions of solids in rotating cylinders. Table 1 from [157]
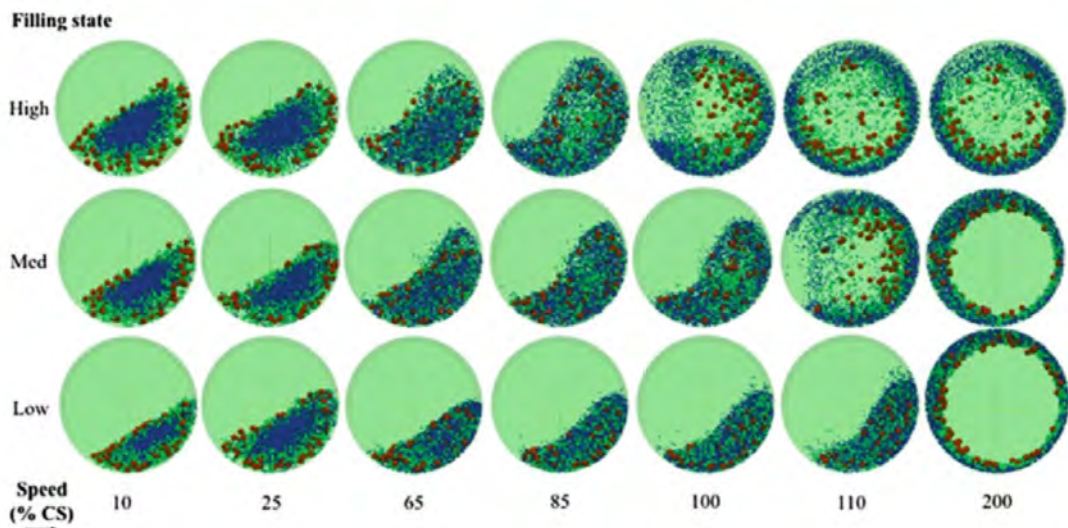
Figure 2.51: Snapshots of granular arrangements for different conditions, demonstrating the segregation behaviour as both the fill increases and the rotation rate increases as a function of the critical speed, $Cs = Fr \times 100\%$. Figure 1 from [158].

and larger particles moving upwards. The percolation velocity is the rate of this segregation, and the ratio of the diameters is the most important

parameter in this.

2. Diffusion. The motion of the granules is partially random, similar to gas kinetics, and is not related to the direction of agitation. This behaviour is connected to the shear rate in chute flows, and is important in faster flows as in faster flows particle collisions are more common.

3. Settling rate variation. In highly viscous and low solids fractions flows, or flows with different densities of granules, larger granules can settle to the bottom through gravitational settling, as the denser particles have higher settling velocities.

4. Squeeze expulsion and Kinetic sieving is the final explanation. This mechanism depends on the probability that a small particle is more likely to find openings than larger ones, and that particles always attempt to move towards the impermeable bed of the flow, with the net result being the small particles move towards the bed and the largest move towards the top.

Kinetic sieving and squeeze expulsion are the dominant mechanisms for dense gravity flows which are free to flow, however this does not adequately describe flow in rotating drums such as Figure 2.52, which are suggested to better described through erosion and deposition mechanisms only partially covered by the above [155].

Mixing of monodisperse particles is difficult as well, as they experience little diffusion, though a rocking motion can be applied to the drum mixer to significantly improve this [160].

The polydisperse nature of agglomerating pellets might work against this, as it has been found that granule mixtures experience less segregation the more polydisperse they are in vibrated beds at least, though whether this applies to drums is a different matter [156]. Another way to prevent segregation is with sufficient interparticle binder [161].
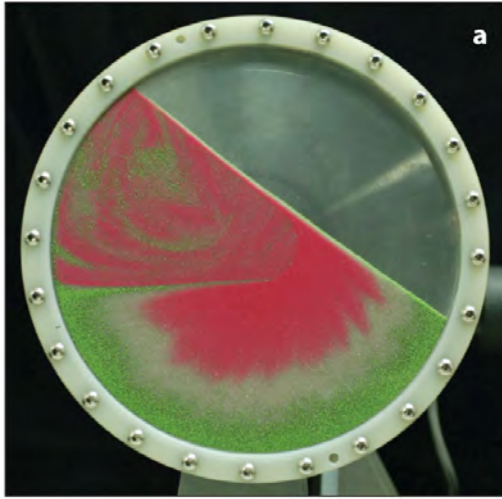
Figure 2.52: Image of partially rotated random mixture of sizes, showing that the larger particles (green) segregate over the medium (White) and small (red) particles immediately upon moving. Figure 5 from [155].

The angle of repose of the material in a rotating drum is an important feature in granular kinetics as well. Slumping occurs when the drum is moving slowly enough that the granule bed can transition from the upper angle of repose (when the motion begins) to the lower angle of repose and rest at that state, with the motion in between permitted as the flow has acquired some momentum [157, 162]. The transition from this state to the rolling state is quite sudden, and is dependent on the particle size and interparticle friction [162].

The rate and strength of the collisions are relevant to determining theories for the granule size and the growth behaviours described previously. One estimate for drum granulation is Equation 2.32 [163], which is based on the velocity gradient between layers of tumbling pellets.

$$V_c = 2R_{Dr}\omega \qquad (2.32)$$

Here, V_c is the velocity of the collisions, R_{Dr} is the drum radius, and ω is the drum rotation rate. This is not in agreement with experimental findings in ball mills, where larger mills with a lower angular velocity have collisions with greater kinetic energies [164]. In addition, in practise the granule will experience a wide range of velocities [37, 164].

95

The measurement of the speed of particles in a tumbling mill is difficult, but has been successfully achieved using positron emission particle tracking [165], which shows that the behaviour mostly fits into that modelled by DEM studies.

The distribution of the granules also significantly varies with the collision frequency, though the largest granules tend to be the most frequently collided with [33, 77].

Coefficient of restitution

The coefficient of restitution is also used in the limiting size solutions. This value is assumed by those solutions to be equal to 1 for simplicity [4]. When the coefficient of restitution was actually tested though, $e_{rest} \leq 0.1$ [5].

It has been shown to be possible to calculate the coefficient of restitution for elastic-plastic spheres based on material properties, though so far this is limited to low strain values [166]. The coefficient of tangential restitution also matters, as the granules will be colliding obliquely. This can also be calculated, though the response is fairly complex for the low stiffness case [167].

Saturation

During a study of binding mechanisms, Formso et al create wet iron ore pellets and record the various properties of these pellets [116]. As they are primarily focussed on the binding mechanisms, they screen the pellets to limit to only those between 10 and 12.5 mm. The saturation of these pellets is found to be high, with the lowest being 85%.

The saturation begins to level out at a moisture content of $\approx 8.5\%$, which is odd since saturation and moisture content are directly related. However, the porosity can be seen to begin to rise at this precise value linearly, see Figure 2.54 which may account for this.

If the saturation defines the final size of the granules, as the pellets were selected based on their size, then this would be the results that would be expected.
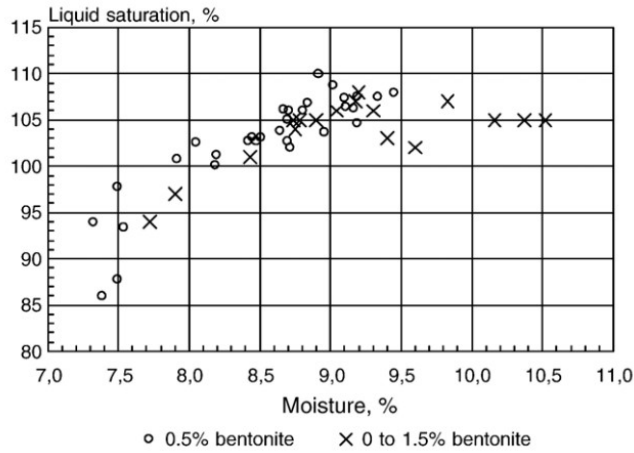
Figure 2.53: S as a function of moisture content $m_{l/s}$. Figure 4 from [116].
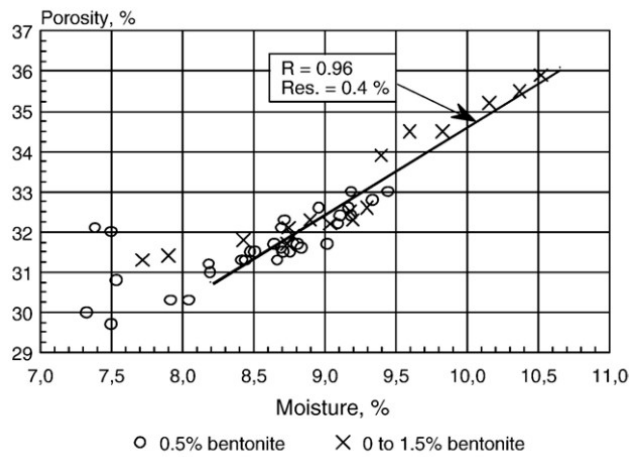
Figure 2.54: ϵ as a function of moisture content $m_{l/s}$. Figure 5 from [116].

The final saturation is not the same as that saturation where the pores are completely filled, rather it is a function of the minimum porosity and the moisture content. Similarly, the saturation where liquid begins to emerge onto the surface is lower than the saturation that would correspond to all the pores being filled with liquid, as there appears to be hidden void factor which accounts for small hidden pockets of air, leading to a practical maximum saturation of around 80% to 90% [41, 82].

Liquid State

The liquid state is not just dependent on the saturation but, as mentioned, it is also path dependent, so examining what leads to the various states is relevant.

In 2D, it can be proven that there are energetically favourable states for the liquid to be in [168]. For three circles, the most energetically favoured states are three separate, evenly distributed pendular bonds, or a single capillary bridge between all three. This is significantly harder to prove in 3 dimensions, due to the lens shape distortion, but the empirical evidence supports the same conclusion. In microtomography scans of slightly moistened granular materials nearly all the 3 particle contacts are trimers, where all three particles are bridged similar to the capillary bridge mentioned [112, 169]. Two particle pendular bridges are also observed but dimers, where two particles are bridged but the third is not connected as well are extremely rare. For a given volume, the pressure difference is lower for a capillary bond between 3 spheres than 3 separate pendular bonds [101] which supports this, as this would result in a more energetically favourable state overall.

The precise regime boundary where the moisture content liquid bridges start having to come into contact depends on the morphology, however for perfectly wetting equisized spheres the pendular state has to end at a moisture content of 13.6%, or a saturation of 34.1% assuming no internal bubbles.

Porosity and Packing

A lower porosity generally has been found to result in an improved strength [36], and also means that for a given moisture content the saturation will be greater [170, 171]. In turn though, some moisture results in greater packing densities [172]

Calculating the porosity requires knowing at the very least not just the particle size but the particle size range, as the mechanism for this shown in Figure 2.55. For bi-disperse particles, an approximation can be determined for the porosity,
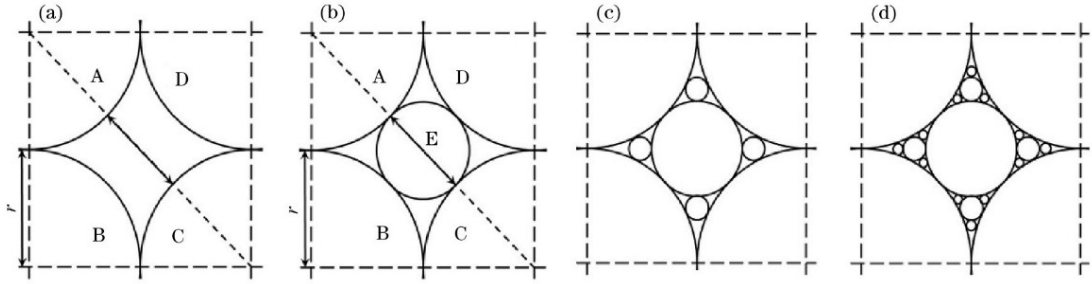
Figure 2.55: Ideal arrangement of particles of different diameters to produce decreasing porosity. Figure 3 from [96].

which is dependent on the proportion of each, as seen in Figure 2.56.
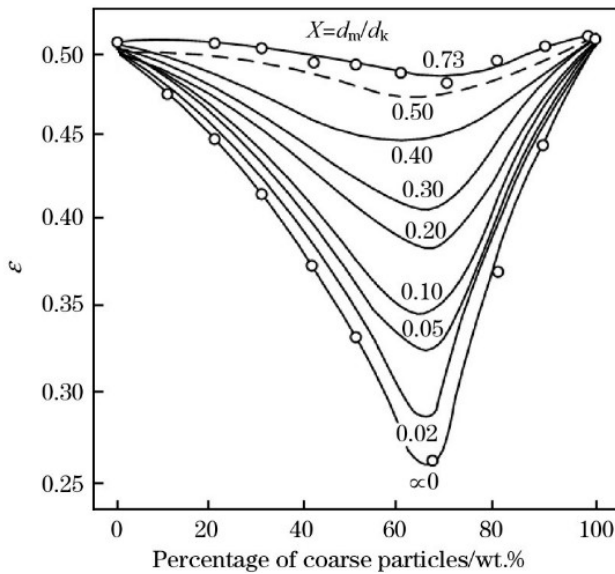
Figure 2.56: Porosity relation with ratio X of fine-coarse particles d_m $/d_k$ for different relative particle sizes. As the ratio X decreases, the minimum possible porosity also decreases as the gaps can be more efficiently filled. Figure 4 from [96].

The two parameter mechanism for bi-disperse particles has been extended to slightly polydisperse, non-spherical particles [173, 174] though this requires some empirical values by necessity to account for the compaction behaviour and still assumes dominant coarse and dominant fine particles. Full polydisperse models have been developed which are more complex but are effective, to the point that they begin to be limited by the limitations of real feed materials to be infinitely divided as would be needed [175].

Genetic algorithms have been applied to develop the best packing states for

99

random polydisperse packings and three key size groups were determined to contribute to the packing behaviour, for which the largest size group needed to be 50% for the most efficient packings [176]. These are :

1. the pre-packed particles which correspond to the largest particles, $d_{p_{max}}$

2. the structure forming range which corresponded to particles sized $d_{p_{max}}$ to $(0.5 \sim 0.7)d_{p_{max}}$

3. void filling range corresponding to the particles less than $(0.5 \sim 0.7)d_{p_{max}}$

This appears to fit into the model of the dominant coarse and dominant fines, while also better accounting for polydispersity by including the structure forming range. This also fits into a hierarchical model for particle packing, as the structure forming range and void filling range efficiently fill in the voids which allow a more efficient method of modelling highly polydisperse media [177, 178].

Empirically, a larger proportion of larger particle have been found to improve the compressibility of ceramic powders [179], and powders with an abnormally low "true" density for the material they are formed from also are easier to compress, likely due to internal voidage which breaks during compression [179] which is a phenomena not discussed much.

The shape of the particles will also affect this, as it has been demonstrated that the effect of altering the aspect ratio can rapidly alter the packing fraction [180]. Perfectly spherical assumptions and calculations will thus overestimate the porosity, and this occurs regardless of how the particles diverge from sphericity, as shown in Figure 2.57 which shows the effect of monodisperse sized particles packing. The peak packing occurs at an aspect ratio of $\alpha = 1.6$, which is very close to the golden ratio, though this may be a coincidence.

The downward trend continues indefinitely, at least for oblate objects, as coins in a jar demonstrate a lower packing fraction than even spheres [180].
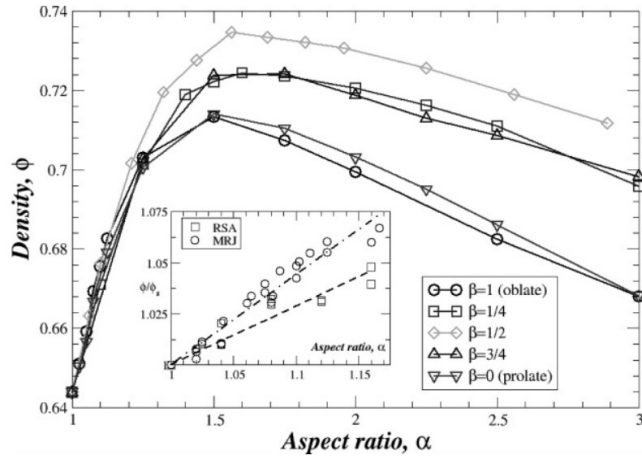
Figure 2.57: Packing fraction $\phi = 1 - \epsilon$ vs aspect ratio for 10000 particles. The semi-axes for the particles are $1/\alpha^{\beta}/\alpha$. Figure 1 from [180].

The aspect ratio shown above is suitable for spheroids, though for arbitrary particles other measures such as shape factor and sphericity are also useful for descriptions [181], which are all related in Figure 2.58.

Unfortunately, the packing density cannot be calculated from particle size distribution alone [182]. The presence of "jammed" states accounts for varying coordination numbers (Z) which are nonetheless stable which would fit into this finding [183]. The particle shape also affects this in a similar way as it affects the packing density, as shown in Figure 2.59, as does particle size [184]. One method to approximate the coordination number is the "isostatic conjecture" which states that the coordination number has twice the quantity of degrees of freedom [180], which does seem to be partially supported by Figure 2.59.

The coordination number Z for jammed particles may be related to a form of granular entropy. Edwards theory of powders [185] develops a means to use thermodynamic principles to instead predict the behaviour of static powders. By using volume in place of energy, a number of behaviours can be extrapolated. For instance, entropy is inversely related to the coordination number of the system, because the greater number of contacts, the fewer ways the system can be re-arranged to produce the same volume [159, 186]. This then leads to why segregation occurs, as it corresponds to the highest entropy. This has an upper limit, in that the system will shift towards the state with the fewest contacts that

101
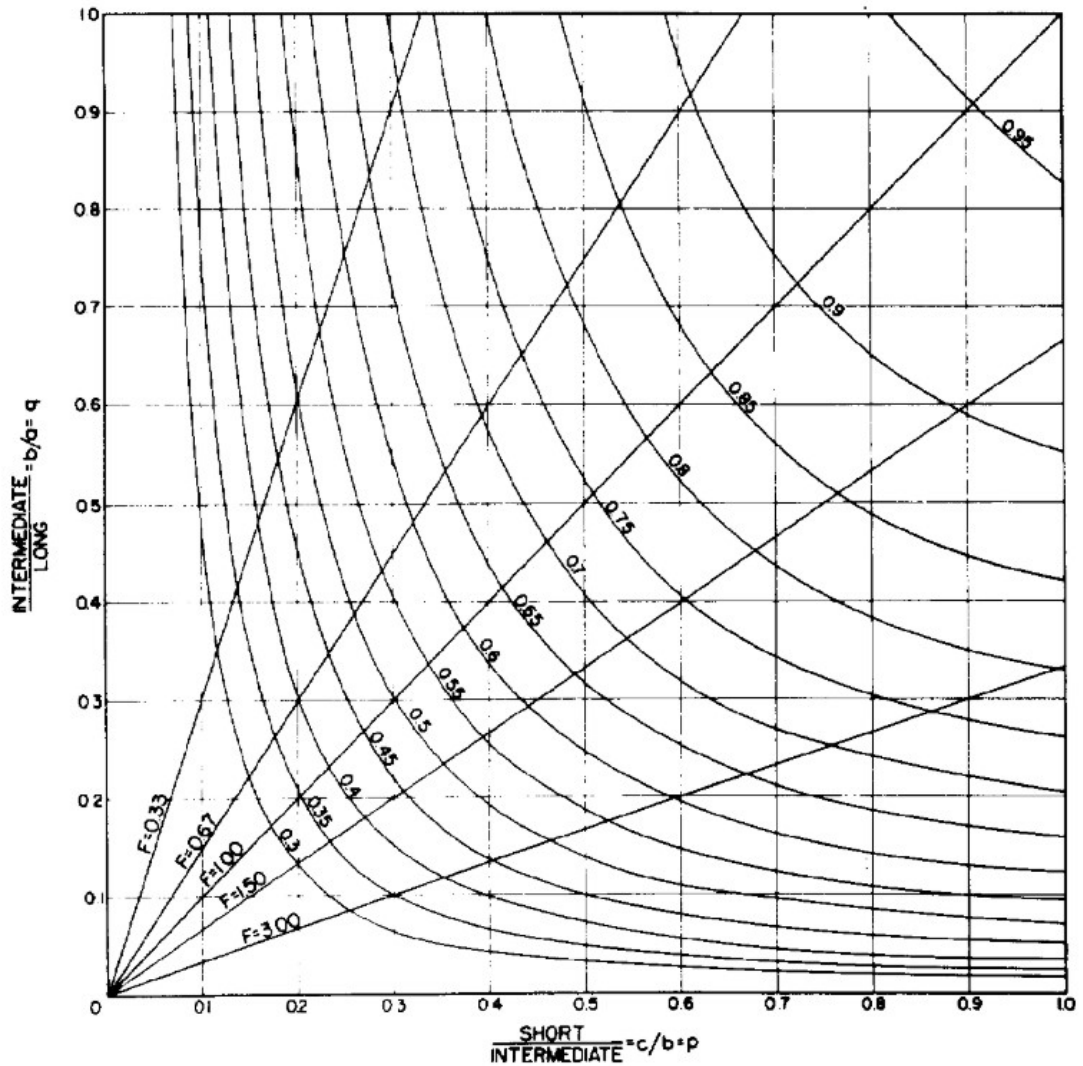
Figure 2.58: Chart for converting between particle dimensions ratios $q = b/a$ and $p = c/b$, shape factor $F = p/q$ and Sphericity $\Psi = \frac{12.8\sqrt[3]{p^2 q}}{(1+p)(1+p)6\sqrt{(1+p^2)(1+p^2)}}$ (curved lines). Figure 4 from [181].

remains stable. Even the nature of the need for agitation for diffusion and thus segregation can be derived from this thermodynamic framework [185]. Because of the success of this solution, this has even been explored for understanding the kinetics of mixing in liquids [187].

Another way to describe this behaviour is that in a monodisperse system,

102
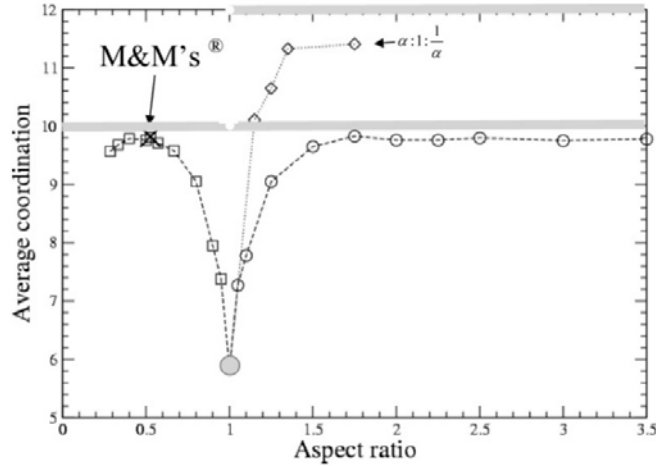
Figure 2.59: Mean contact number as a function of aspect ratio for the light grey lines are the expected coordinations for the "isostatic conjecture". Figure 1 from [180].

the entropy per particle is independent of the diameter of the particles. At the boundary between two different particle size regions the entropy reduces, as the number of stable configurations decrease due to wall effects. This in turn allows different granule sizes to be considered different fluids, with a surface tension between them [188].

A different method of using thermodynamic principles, where the average granular kinetic energy is converted to a temperature using the same methods as used in statistical methods for kinetic theory of gasses, can be used to evaluate the behaviour of agitated granules [161]. As the granules will have weights on the order of grams, rather than atomic masses, the temperatures will be in the range of TeraKelvins, which may then result in interactions with their room temperature component atoms, which act as a thermal sink.

Consolidation

Consolidation is the behaviour of the granules reducing their porosity over time. Similar to the growth rate, empirical models have been developed. One example is Equation 2.33 which provides a very strong fit to the results [189].

$$\frac{\epsilon - \epsilon_{min}}{\epsilon_0 - \epsilon_{min}} = e^{-kN} \tag{2.33}$$

N is the number of drum revolutions, and thus is a measure of time, and for the results tested $k \propto d_p/\mu^{0.25}$. A theoretical mechanism for this suggests that the value k is a function of St_v [4], which leads to Equation 2.34

$$\Delta x = h_0(1 - e^{-St_v}) \tag{2.34}$$

The porosity can also be reduced through compression, and Equation 2.35 gives a relation between the pressure and porosity developed [129].

$$\epsilon = \epsilon_0 + \frac{(\log_{10} p)}{-4.5} \tag{2.35}$$

The consolidation behaviour as well depends on the morphology of the particles, as found by Parafiniuk et al [190] where similar behaviour regarding the aspect ratios for the packing state also applies to the consolidation rate. The authors also provide a fully generalised form of the consolidation behaviour Equation 2.36, which is essentially the same as Equation 2.33

$$\phi(n) = \phi(\infty) - [\phi(\infty) - \phi(0)]e^{-(Cn)^\beta} \tag{2.36}$$

$\phi(\infty)$ is the maximum packing value, or the packing after an infinite amount of impacts have been applied. $\phi(0)$ is the initial packing, and C and β are packing parameters which alter the packing rate dependent on the system properties, $C = \frac{(\phi(\infty) - \phi(0))}{\phi(\infty)}$, though β isn't known.

All of these require a maximum packing value, or equivalently minimum porosity, which can range from 0.49 [191] to 0.05 [97,192] though for iron pellets 30-35% seems to be suitable [116, 193].

Other fields find consolidation to be relevant, such as soil science [194]. The behaviour of soils under high shear strain, seen in Figure 2.60a is quite different to the behaviour under low amplitude cyclic deformation Figure 2.60b.

The porosity under a single shear strain does not reach that of the cyclical strain, which suggests that many small rearrangements are necessary to reach the highest porosities in a specific system.
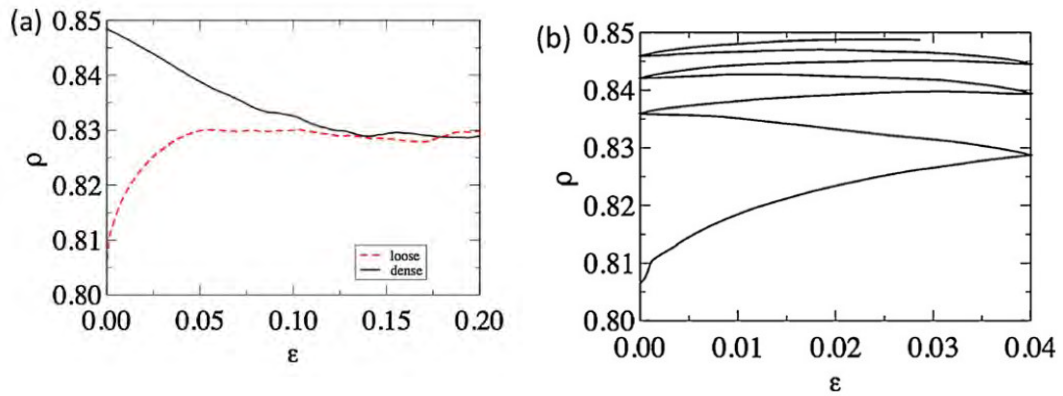
(a) Change in density ρ for initially loose and denser samples as a function of total shear strain ε. Figure 5a from [194].

(b) Increase in density ρ as a function of cyclical shear strain ε. Figure 5b from [194].

Figure 2.60: Increase in density due to consolidation under different conditions

Finally, an effect unique to wet agglomeration is that the density increase and then decreases multiple times as the material homogenises. The initial wetting results in very moist cores surrounded by very dry particles, and then as the material homogenises this weakens and crumbles before consolidation strengthens it again, allowing full growth similar to induction type behaviour [195]. If the material is crumbling and this is assumed to be the result of insufficient moisture then this can lead to oversaturation of the material.

2.4 Background Discussion

The field tends to have very disparate research efforts, and is spread over many disciplines which makes forming a cohesive narrative tricky, so below is a collection of the conclusions regarding various components of the literature.

2.4.1 Mill sludge Discussion

Mill sludge is relatively poorly researched and it is comprised of two major components, weathered oils and particulate iron, that do not usually occur together. Be-

cause it is a relatively rare material, but also a waste product made out of common components and is mixed with pollution control components, it is unglamourous, and the interest in researching it tends towards minimising its disadvantages with as little involvement as possible.

The two main constituents, the oil and the scale work together and make managing the material particularly difficult. Both halves tend to make managing the other half difficult. The oil prevents sintering, or landfilling. The iron prevents the oil from simply being burnt or processed as a liquid. They even interfere with some of the methods to make it easier to manage, as the oil would inhibit the ability to grind the scale down. This is very unfortunate, as independently the oil would provide energy for the reduction process, while the scale itself seems to be comprised of high proportion of iron, which would make it a prized source of ore for steel. A good direction for the scale would, in theory, to go to direct reduction. In such a case the oil would be able to act as the binder itself, as the only places where hydrocarbon based binders seem to have worked consistently is in the lower intensity environments of direct reduction furnaces, and the oil would also be contributing to the reducing environment there.

However, such an option is not being considered here since ultimately the purpose is to send it to a blast furnace. The cold bonded pelletisation method does appear to be the best option, cost wise, even if sintering was feasible. The use of a conditioner to manage the oils in different ways does seem to be a good choice as well, as it is used elsewhere. The oil does require managing, and other methods would require separate infrastructure to be implemented.

The application of the cement to provide the cold bonding seems to be reasonable. There are other methods, but they would require infrastructure as well. The presence of the oil may affect the setting process of the cement, or the binding to the scale, though again it is conditioned.

2.4.2   Pelletisation literature

The pelletisation literature has two clear distinguishing control factors, these being the saturation of the material and the dynamics of the system. Most of the research tends to suggest though that there is not really a true "limiting size", only a point where the growth slows down, which would explain why most of the research is instead on the growth rate.

The saturation is unfortunately tricky to measure, as it requires a firm value for the porosity at any point which is dependent on the minimum porosity, and the moisture content, which will be similar to that added but can vary due to chemistry, evaporation and simple sprays being applied to the surface only and mixing not being perfect.

The three primary limiting size theories are very distinct, and of these only the Stokes criterion appears to account for both the saturation and the dynamic behaviour. As such, this was the initial focus of the research. However, as will be established later, a number of issues arose in attempting to implement it, culminating in the finding that it was simply an unrealistic and implausible model to begin with. As a result, the other two theories were explored more heavily which resulted in the development of a new model.

Particularly for iron ore pelletisation, a lot of the properties are measured in only comparative ways, such as the effect of bentonite dosage on drop strength on a given material. This makes it impossible to compare against other binders as the mechanisms are not discussed or investigated as to how they interact with the yield strength in an analytical way. This is likely due to the heavy industrial focus on improvement of current processes.

Other issues are that some results are presented and the accompanying report acts as if they are very strong, though they do not directly support the theories themselves. This can be due to inappropriate test specimens or procedures, flawed saturation choice, or even simply that the theory is extremely malleable to the needs of the result.

Comparing against previous models and checking their assumptions and adjusting for these is also not as well accounted for, which has lead to the scenario where there are four separate empirical equations for the yield strength that do not account for properties or assumptions in previous models that they build on.

The nomenclature of the field is difficult to navigate, because of the high rate of re-use of nomenclature from other fields as the field grew organically. "Pelletisation" is less commonly used, and describes processes where feed material such as wood or animal feed is pressed through circular holes as well as forming spherical pellets through tumbling. "Granulation" describes more wet agglomeration processes, but also describes sugar crystallisation and the grinding up of hard materials into smaller particles though not powder sized. "High-Shear Granulation" is used a lot, but low shear granulation is rarely used to describe behaviours.

A useful distinction, and the one that will be used in this thesis, is that high-shear granulation relies on breakage, or the dynamics, as a primary means of size control, while low shear does not. Drum granulation, and tumbling agglomeration in general then can be considered a low shear form of granulation. This is not perfect, as it is possible for the saturation to still lead to a over-wetted mass even in high shear granulation if too much moisture is added.

This makes collecting suitable literature a challenge and ultimately slowed down the research, as determining which research was relevant and which was not required a lot more investigation. One example is that disk pelletisers do generally produce particles of consistent size and behave mechanically quite similar to drum pelletisers, yet the research for them ended up being less useful than high shear granulators which behave quite differently. The reason being that disk pelletisers actively classify the granules by size and pour out the largest fraction continuously, which makes the research for these focus a lot more heavily on what affects the final strength of the pellets, and this in turn was often the more industrially focussed comparative data results which is less useful when attempting

108

to understand such systems from a theoretical standpoint.

Collecting data on what affects the granule size distribution is even more difficult, as often just the mean granule size is reported, sometimes over time, but not the distribution. And when discussing the strength, even the mean size is not reported, and the pellets are screened for those that are to be tested. This is likely because these are mirroring industrial practise to revert the output if outsize occurs and assuming the size will trend towards the mean. This obviously is not ideal when the reverting process is not desirable.

Population balance models are a popular method for evaluating the growth behaviour, but they have two significant flaws. The first is that including multiple "coordinates" (i.e. size, moisture, location, velocities) is very difficult and only a couple of models explicitly included the moisture. More significant than this is that because of their nature they allow many fitting parameters which in turn makes it easy to fit the data strongly to particular results but extrapolating from this is less reliable.

Whether the breakage and nucleation are important for the drum granulation being examined is uncertain. The large initial size distribution makes the nucleation process not particularly matter in terms of generating initial nuclei, while breakage seems to be dependent on large impact forces which do not seem to occur for drum granulation. This may on the other hand not apply to the adhesion bond formed from the initial impact of the granules, where they form a two-granule dumbell and seems to be weaker, and this bond is used in some models.

2.4.3 Challenges

The modelling of pelletisation is difficult because of the particulate and discontinuous nature of the process, along with its multi-scale nature which will inevitably require some approximation.

Measuring the properties in the real experiments are difficult as well because

109

of what they require to be measured. Porosity requires some form of volumetric measurement, such as pnycometry, or other roundabout methods of measurement. This leads to problems of measuring the saturation in turn, as this is dependent on the moisture fraction and the porosity.

Measuring the specific surface area or the surface mean diameter is required for many of the yield strength measurements as well. This is possible to do using various particle measurement devices available, but will require cleaning of the sludge at the very least.

Finally, measuring the dynamic properties is also extremely tricky, as the behaviour of the bulk flow does not lend itself to measurement being opaque and comprised of rapidly shifting particles. Positron emission particle tracking has been used, but even this would be unable to directly measure the strength of collisions.

Modelling resolves most of these issues, so long as the model is valid. DEM solves most of the issues and satisfies the needs of the system. The behaviours observed in the literature can be implemented into this model and tested and improved. Therefore, the aims will be twofold, first providing useful non-dimensional values that go beyond simply fitting variables that can ultimately be measured, and secondly developing a way to passively control the pellet size for drums in a similar fashion as can be found in disks.

Chapter 3

Material Examination

3.1 Introduction

Given that the material properties are important to the process, characteris-
ing the sludge is a suitable first step. Some work had previously been done by
Tata, primarily comprising ratio determinations of the pellet/moisture content
and oil/water ratio in the sludge. To build on this, finding out the particle char-
acteristics, especially the surface characteristics is useful, as well as verifying the
oil composition.

3.1.1 Appearence and Previous Work

Figure 3.1 Shows the raw sludge itself, just prior to conditioning. The material,
on handling, stains anything it touches, and is a coarse, dense material. At this
stage, it does not behave like a liquid, as can be observed from the fact that it
collects in small pellets.

Based on the consumption of oil on site, it is assumed that the oils that are
bound within the sludge are comprised of three specific types, these being 46,
570 and 680 oil. 46 oil is a light lubrication oil, while 570 and 680 are heavier

Figure 3.1: Photograph of a sample of the raw sludge, batch 4.

lubrication and machine oils. These oils are a mixture of mostly relatively simple chains, with some additives to adjust the properties which are proprietary.
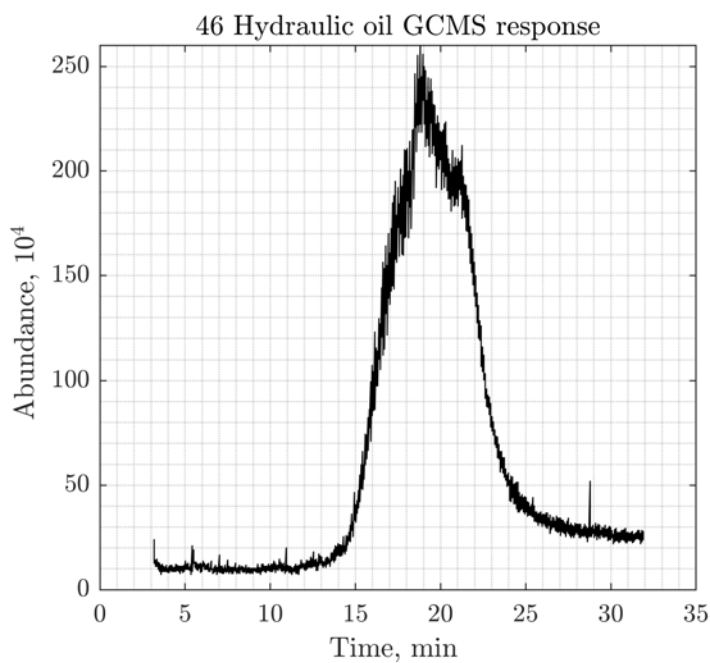
Figure 3.2: 46 light hydraulic oil Gas Chromatograph response. This is a Hydraulic oil used at the plant, this data acquired at a prior date by TATA.

Tata steel has previously examined the gas chromatography responses of these oils, see Figure 3.2, Figure 3.2 and Figure 3.2. The large unresolved mixtures representing the broad plateaus are expected for hydrocarbons [196]. They represent
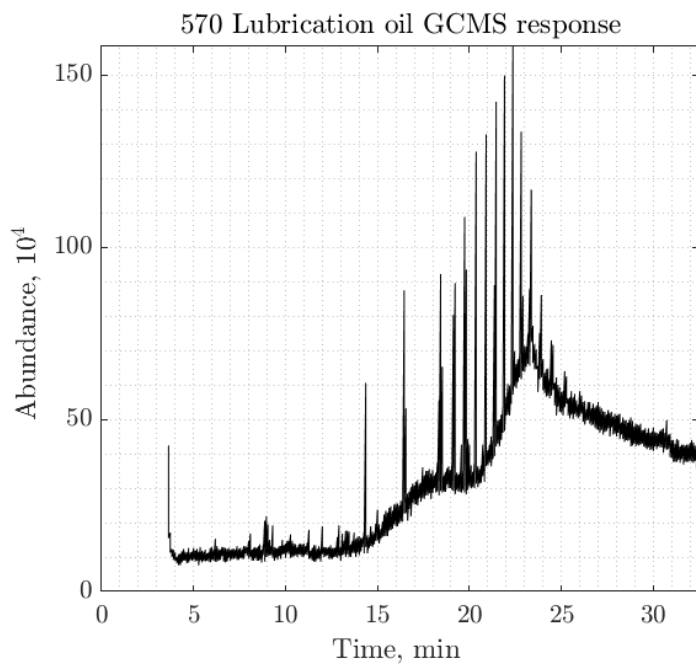
Figure 3.3: 570 heavy oil Gas Chromatograph response. This is a Lubricating oil used at the plant, this data acquired at a prior date by TATA.
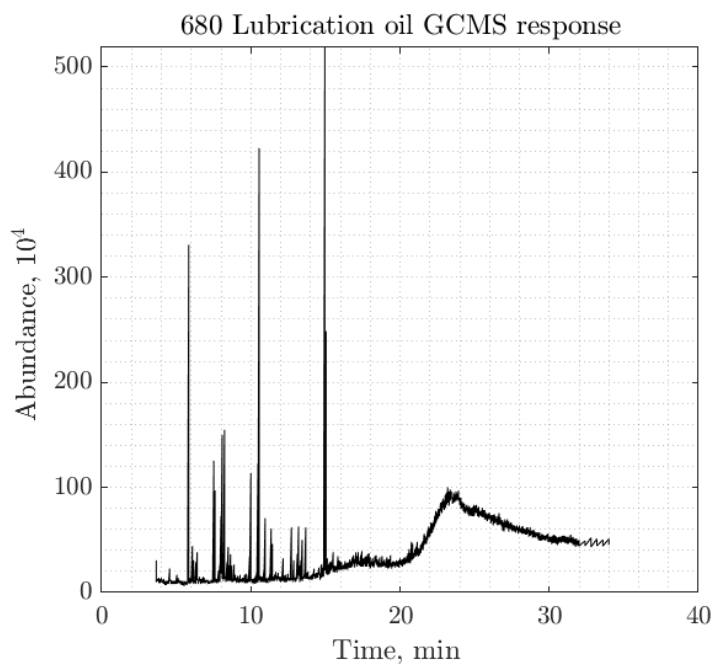
Figure 3.4: 680 heavy oil Gas Chromatograph response. This is a Lubricating oil used at the plant, this data acquired at a prior date by TATA.

the assorted branched and aliphatic compounds that occur at these ranges for petroleum oil products that have slight variations in their responses, but evaporate within the same distillation bounds as a product. As a general rule then, the

longer the retention time, the heavier the hydrocarbon. Though these unresolved mixtures do mean that the specific compounds cannot be identified, at least they permit some form of comparison to be made between the compounds.

As such, these will be the primary focus of the subsequent analysis of the oil compositions.

There had been some previous work evaluating the effect of the quantity of liquid per tonne added.
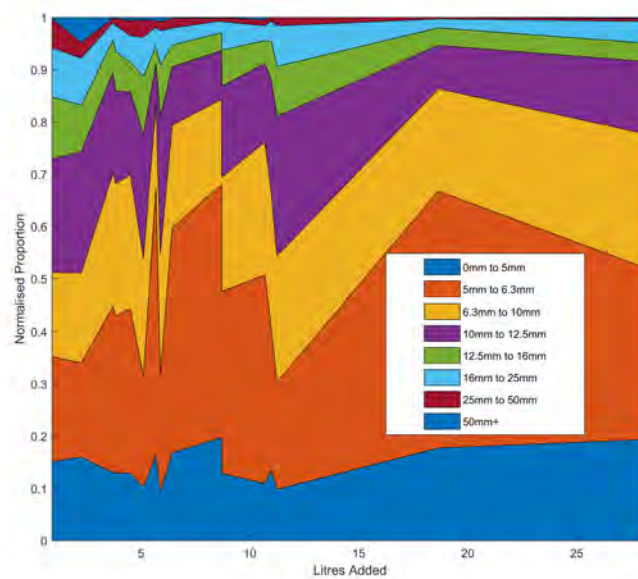
Figure 3.5: Area chart showing the effect of liquid added, in Litres, to the size distribution of the pellets, normalised according to the span of the bins. These results are from a previous set of tests performed by Tata Steel. The lack of smoothness to the data is a consequence of the poor relation of the liquid added alone to the moisture content.

Figure 3.5 shows that there is not a very strong relation that can be immediately seen regarding the proportion of the target diameter and the liquid added. For reference, the target diameter is between 10 to 12.5 mm, but 6.3 to 16 mm can be used but is not ideal. The liquid added was easier to measure than the moisture content, though this too was measured, the results of which are shown

in Figure 3.6.
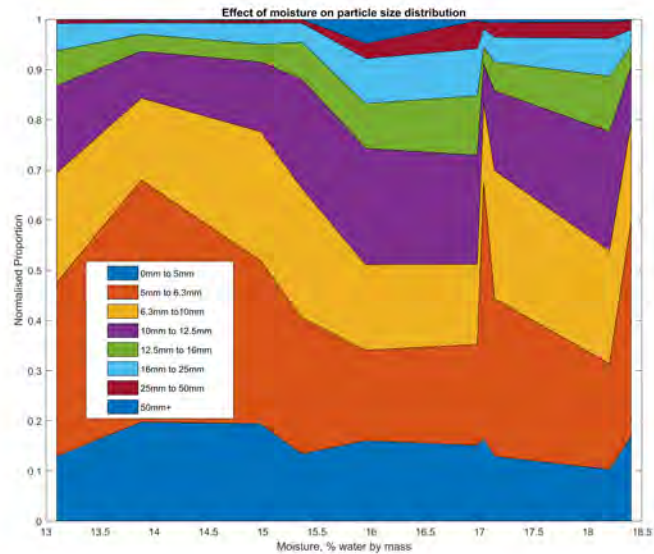
Figure 3.6: Area chart showing the effect of $m_{l/s}$ to the size distribution of the pellets, normalised according to the span of the bins. These results are from a previous set of tests performed by Tata Steel. The data is much smoother, however some outlier data remains present at 17% and 18.4%, which may be a consequence of the fact that there are differing environmental effects during each test which may alter the results.

The results in Figure 3.6 are smoother, with a stronger trend towards higher moisture contents giving larger quantities of target (purple) diameter pellets. There are still significant outliers, and the trend is not particularly smooth or consistent.

Further, the proportion of the fines is very consistent at around 10% of the total regardless of the moisture, which is not what would be expected if the moisture was directly driving the growth behaviour. The total number of the largest pellets also varies significantly, with the largest quantity of oversize being present at the same moisture content as the highest quantity of target pellets, 16-17% moisture.

The relation between the iron and oil/water quantities are shown in Figure 3.7.
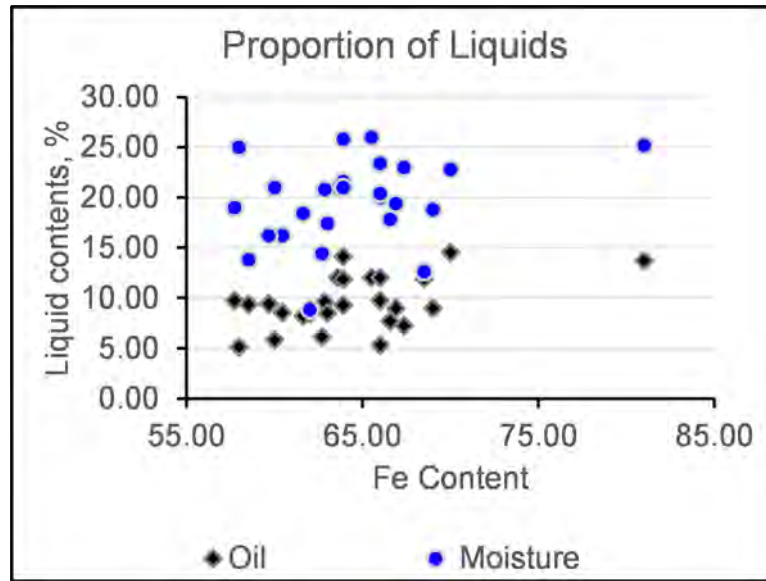
Figure 3.7: No correlation appears to be present between the quantity of oil and water with the amount of iron in each given sample. These results are from a previous set of tests performed by Tata Steel.

The mill sludge also contains other elements, such as carbon and slag which collect in the tanks from dust on site. This data shows that there is not any particular relationship between the iron contents (which exclusively comes from the descaling in the mill, and hence ignores contamination after the fact), and the constituent liquids. The source data does not however indicate at which point during the drainage operation this was collected, or if it was collected directly from the settling tanks.

The previous results shown are simply re-analysed work from Tata Steel, as an initial starting point. The following is where new work is performed on the sludge to determine possible correlations which would allow more targetted pre-treatment of the sludge.

3.1.2 Sludge Preparation

The composition of whole pellets was to be evaluated through microscopy, while the feed was to be cleaned and the oils, water and particles separated to see if there was anything of importance. The particles would be examined through electron microscopy, while the liquids examined through chromatography.

One advantage of the material is that because of the moisture in the sludge, the particle size distribution will be significantly more evenly distributed and mixed than if it were dry because the liquid inhibits segregation [118].

The following preparation methods are the final ones used, with initial preparation methods being iterated to improve the techniques. The material had some flaws which caused unresolvable problems.

To examine pre-formed and cured pellets under the microscope, they were prepared through the following steps:

1. Saw pellet in half

2. Set pellet in a resin

3. Grind pellet until smooth, using incrementally finer grit.

In practise, this could not be implemented fully, for reasons that will be explained.

To examine the particles and oil content, the sample was cleaned and dried. The following method was developed after some iterations to minimise the disruption of the intrinsic distribution and retained oils. The best process for this was found to be:

1. Prepare sample to be cleaned, weighing it out.

2. Add to flask and add enough hexane to cover the sludge, in a fume hood.

3. Break any clumps with a glass rod until dispersed into the hexane, then swirl. Do not use a magnetic stir bar as this collects the fines preferentially.

117

4. Allow to settle, then carefully decant the hexane and dissolved oils into a prepared bottle.

5. Add hexane again, and warm the mixture until the hexane is boiling to provide agitation.

6. Allow to cool. Then, without removing the hexane, add water so that the hexane and dissolved oils floats over the particles

7. Stir mixture with a glass rod.

8. Allow to settle, and then decant the hexane into the oil bottle.

9. Add more water, stir, and boil for agitation.

10. Allow to cool and settle, before decanting water into a different prepared bottle

11. Then dry the scale in a vacuum oven at 0.1MPa and 50°C until completely dry.

12. Weigh the dried scale, to determine the liquid weight.

13. Weigh each pan of the sieves used.

14. Then sieve the material according to ISO 4701 [197]

15. Then weigh the sieves with the sieved material in to determine the weight in each sieve class.

This technique minimises any possibility of changes to the particle distribution due to the cleaning process, while also ensuring that the distributions are consistently prepared and measured perfectly clean. Hexane boils at 69°C, and the boiling was found to be necessary for complete cleaning and dissolution of the oils as the mixture could not be stirred using a stir-bar. This temperature was

maintained for a relatively short time and is assumed to not alter the measured responses of the non-polar fraction.

The sieve hole sizes used in this were 2000 µm, 900 µm, 600 µm, 400 µm, 250 µm, 200 µm, 140 µm, 125 µm, 63 µm, and pan (fines). These hole sizes were used as they were available in a single set, and a separate set of sieves were needed to prevent contamination from other users, and were estimated based on the literature to be suitably sized for the material. This turned out to be an underestimation, as the largest particles were over 2mm.

3.2 Results

3.2.1 Microscopy

Though examining the pellet cross section was planned, the cold-bonded pellets wound up being too soft. More specifically, the fact that it was a composite with imperfect bonding. The cement would grind away easily, leaving iron particles exposed, which would in turn experience more force than the surrounding matrix, tearing them out, or at least leaving them at a different level than the surrounding matrix. None of the pellets resulted in a perfectly flat surface, and only one provided a suitably flat face to provide acceptable images.

Figure 3.8 and Figure 3.9 are the two best images that show useful features. The black, geometric shapes are probably the scale itself, with a low oxidation state surface, and the large metallic grey shape is definitely scale, given the rust around it. The white particles though clearly have different morphology, and initial suspicion is that they are lime due to the colour and shape. The remaining light grey matrix is then naturally the cement and conditioner.

The scale seems to all be long and thin, but since the particles were relatively loosely bound, these orientations would be the only ones that would be held in place during the preparation work. The general morphology of the scale is

119
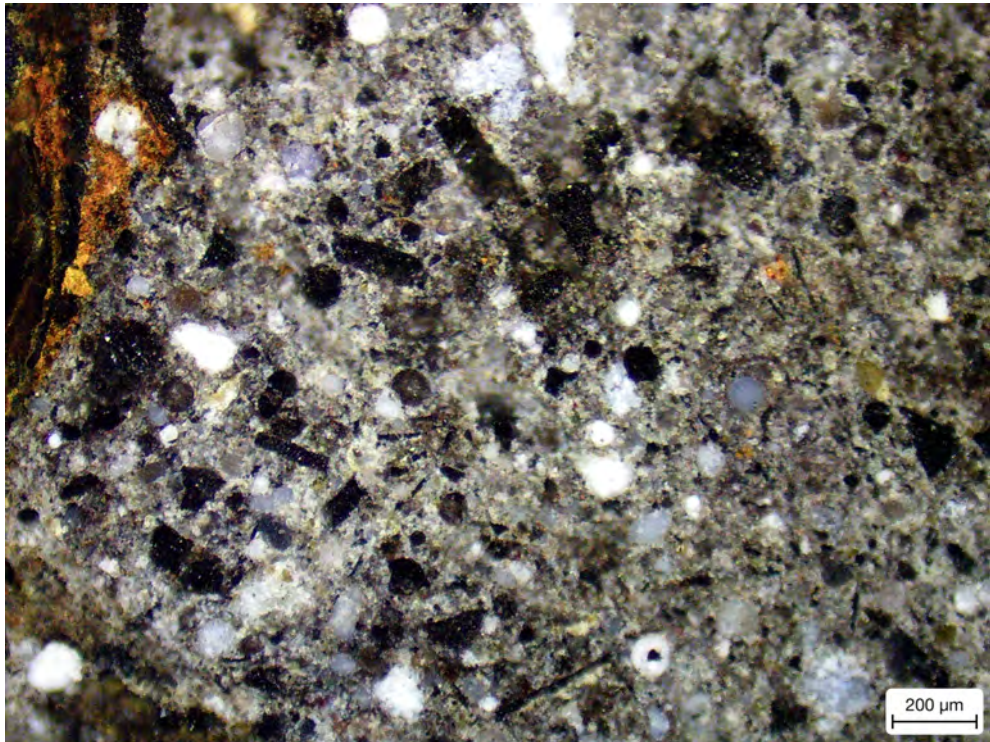
Figure 3.8: Micro-photograph showing the morphology of a pellet cut in half.

unsurprisingly plate-like.

The rust around the large scale piece in Figure 3.9 shows both the reddish rust of iron oxides, as well as clearly demonstrating yellowish rusts corresponding to hydroxides, and if these are present, then there may also be more exotic hydroxides which can form white particles, though these $Fe(OH)_2$ compounds oxidise rapidly. [133, 198].

The centre meanwhile appears to be un-oxidised steel, which in turn suggests that the oxidation period is relatively short as the oxides do not penetrate through the particles.
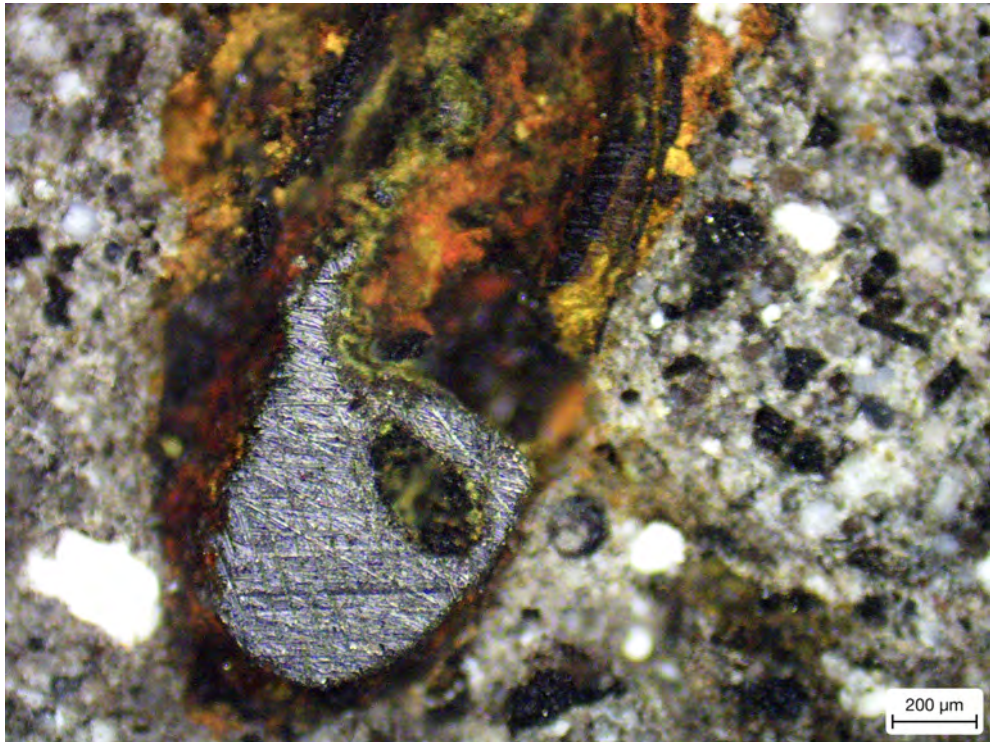
Figure 3.9: Micro-photograph showing the morphology of a pellet cut in half, with a large chunk of scale as the focus.

3.2.2 Sieving

The term batch is referring to bulk samples provided by Tata steel from the stockyards, specifically Yard Zero. Samples were then taken from these, and the batch from which they are taken is noted.

The first samples washed resulted in significant losses of the fines, and was not even dried, simply disposed of. The second and third samples had reasonable amounts of fines, and so drying and sieving was performed, but a sharp drop in the fines contents suggested that further improvements were required, which can be seen in Figure 3.10. This was a quantifiable confirmation of the visual observations where an unreasonable amount of fines were left in the flask, and the general cleanliness of the process did not seem to be satisfactory.

At this point, it was clear that significant losses were occurring when attempt-
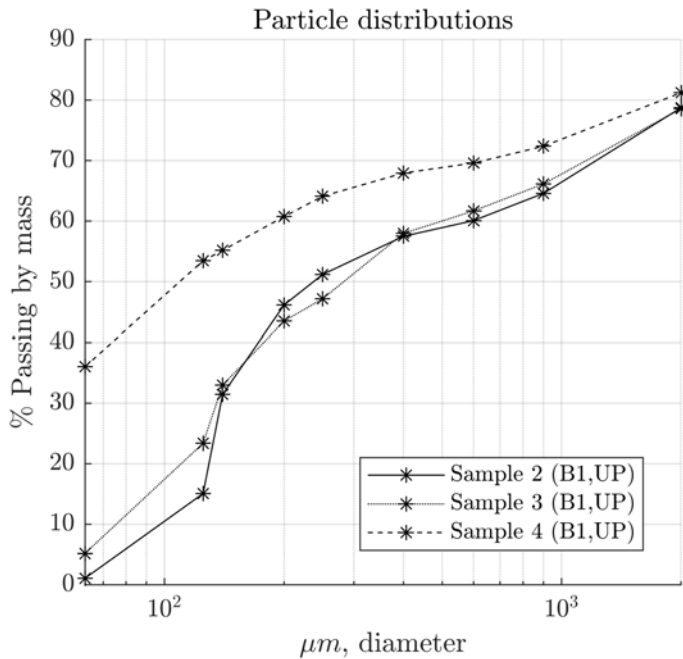
Figure 3.10: Sieve results of samples 2,3 and 4. These samples were taken from Batch 1, the first bulk sample acquired from Yard Zero, on site at Tata Port Talbot.

ing to filter out the hexane wash was occurring.

This type of problem was characteristic of analysing the sludge. Finding the size distribution requires cleaning, but cleaning can alter the "true" distribution in uneven ways, i.e. fines stick to the glassware more than the larger particles. Nonetheless, starting from sample 4 the method described in subsection 3.1.2 was used. This clearly improved the retention of fines as there was less transfer between flasks, and this can also be seen in Figure 3.10 where sample 4 has a much larger proportion of fines. The shape of the distribution, once the losses of samples 2 and 3 are accounted for, is roughly the same.

The weight of the samples were tracked throughout the process to determine the liquid content, and the difference in the weight of the initial sample and the weight of the dry feed also corroborates this. Sample 2 and 3 had significantly higher differences between the wet and dry weight than sample 4, despite all the samples being sieved only when dry.

Batch 4 was a bulk sample that was taken from the pile that was just short of having conditioner added, to get material as close to the pre-modified product as

possible. This resulted in relatively dry sludge that in fact was naturally forming pellets with suitable agitation. This can be seen from the image in Figure 3.1 which is a photograph of this batch.

As such, to see whether pellets were formed of distinct distributions, an experiment was performed. A small amount was placed in a small lab scale pelletiser, (a cement mixer with the paddles removed), until the granule size distribution seemed to be stable, and then it was poured out. This was only performed as a quick test to determine whether the oils could pelletise the solids. The sludge demonstrated that it could easily, however as the variables were uncontrolled this was followed up with ballotini experiments which would have allowed finer control, the results of which are discussed in subsection 3.2.7
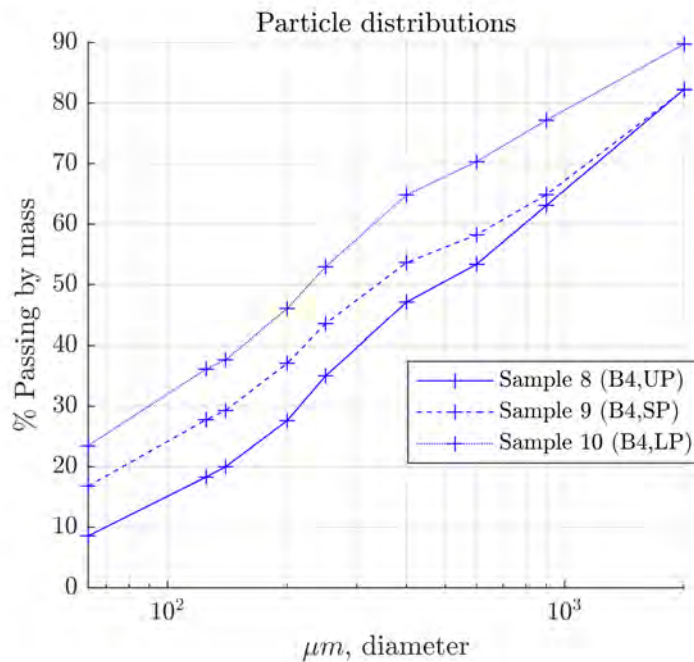
Figure 3.11: Sieve results of samples 8,9 and 10. These samples were taken from Batch 4, and represent unpelletised, small pellets and large pellets.

Then 3 samples were cleaned and compared, large pellets (2 large pellets, both around 25 mm diameter) and a number of small pellets ($<$5 mm) of equal weight, along with a sample from the storage bin of the same weight. These produced the results found in Figure 3.11. Among these samples, the large pellets had a larger proportion of small particles, compared to the small pellets and the unpelletised

123

bulk.

Other batches were tested, and the results are shown in Figure 3.12 removing the samples that were considered to be unrepresentative of the bulk. (the first two samples due to loss of fines, and the pelletised samples due to their implicit selection bias).
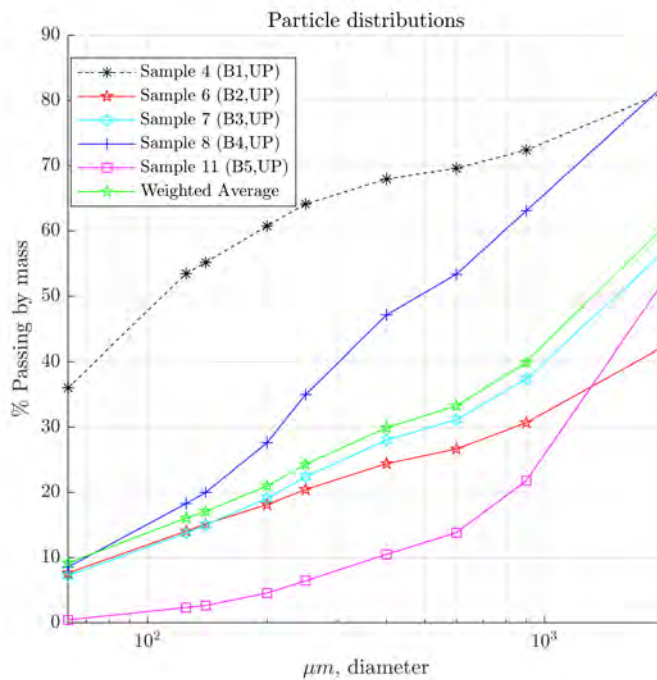
Figure 3.12: Cumulative passing size distribution sieve results of representative samples.

Somewhat surprisingly, sample 7 matches the distribution of the averaged distributions (weighted by sample size) of all the samples impressively well. Because of this, it was the first to be scanned in the electron microscope. However, by now it became obvious just how much variation there is in the batches. Batch 5 was a batch which comprised of nearly dry scales that came from earlier settling tanks but was left in the yard zero settling pits.

Out of curiosity, the weighted average is plotted with the standard deviation recorded, and is also compared to various Fuller curves, see Figure 3.13. The variability between the batches is considerable, as can be seen here.The values stop after 2mm, as anything above that did not pass through. This is not dis-

124
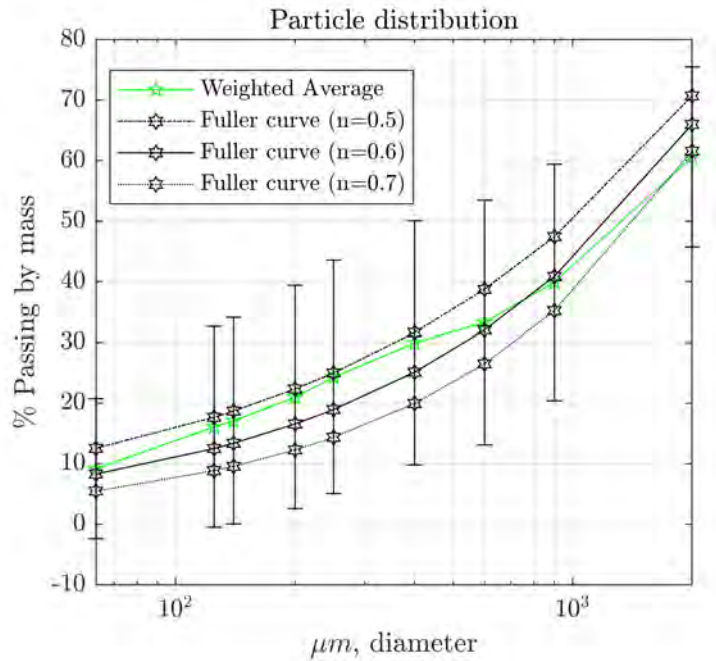
Figure 3.13: The weighted average compared to fuller curves with n of different values. The vertical bars indicate the standard deviation.

played as a true breakdown could not be displayed above this point due to the limitations of the sieves.

The Fuller curve is also plotted as it is used in concrete proportioning and is often considered an ideal distribution for packing, at least as a starting point. With a higher packing value, there is less cement per unit volume, and more aggregate. The benefit of this is that greater volume of the aggregate results in a stronger concrete overall. In addition, less cement also results in a cheaper concrete, though this all requires a strong cement-aggregate bond.

The values stop after 2mm, as anything above that did not pass through. This is not displayed as a true breakdown could not be displayed but it is worth noting that above 2mm the particle size and the nuclei start approaching the same order of magnitude.

3.2.3 Electron Microscopy

The goal of this examination was to simultaneously evaluate the morphology of the particles as well as the composition of their surfaces. The microscopy had already established that some of the particles would have rust on their surface, so the elemental composition would be able to be determined from the iron-oxygen ratio of the particles.

By sampling from each separate size group the material composition could also be evaluated to determine if it changed with size group, such as smaller scale particles corresponding to higher oxygen contents.

A random sub-sample of powder from each pan of sample 7 was prepared for the electron microscope. Sample 7 was chosen as it had a distribution closest to the average, with further examinations planned if this proved beneficial.

The size groups were listed as size group 1 through 10 depending on the pan in which they fit, with size group 1 being the largest. The size groups from 2 (2mm to 900µm) to 10 (>63µm) were examined under the electron microscope. Certain groups proved difficult to fully examine due to the large size and the shadowing effects, as the particles did not stick well to the substrate, and embedding them in a resin proved unhelpful for similar reasons as found with the pellet microscopy. The most significant of these being size group 1 (>2mm) were not examined as they could not be mounted suitably.

For all the sizes, a texture electron microscope image is shown, as well as a composite layered image of the elemental spectra scans, along with individual elemental spectral scans and the elemental composition counts by mass and by quantity, when enough of the particles are in the image to give a reasonable estimate.

3.2.3.1   Size group 2: 2000 µm to 900 µm
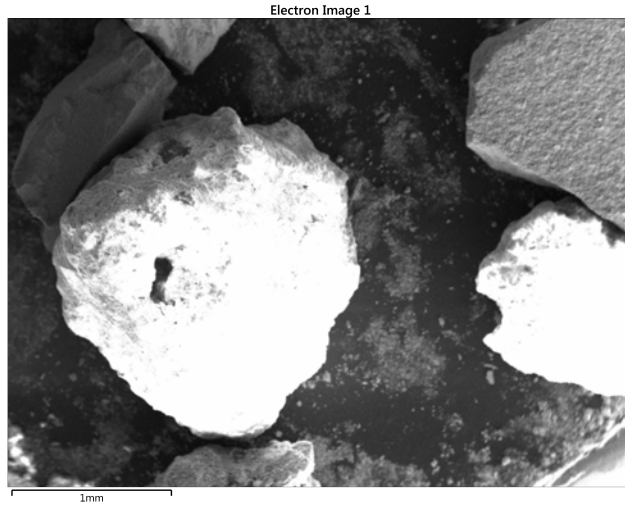
Figure 3.14: Electron microscope photograph of the particles between 2000 µm to 900 µm

The shadows occlude many of the details from the particles in Figure 3.14 and Figure 3.15. These particles were imaged simply as examples.

Figure 3.15 shows a composite scan, as well as individual scans of the Fe, O and Ca distributions for the particles. These three elements were chosen as they highlighted the three primary elements that occurred in the solids. The surface features are very distinct between the scale and the high calcium particles.

(a) EDS composite

(b) Iron Distribution

(c) Oxygen Distribution

(d) Calcium Distribution
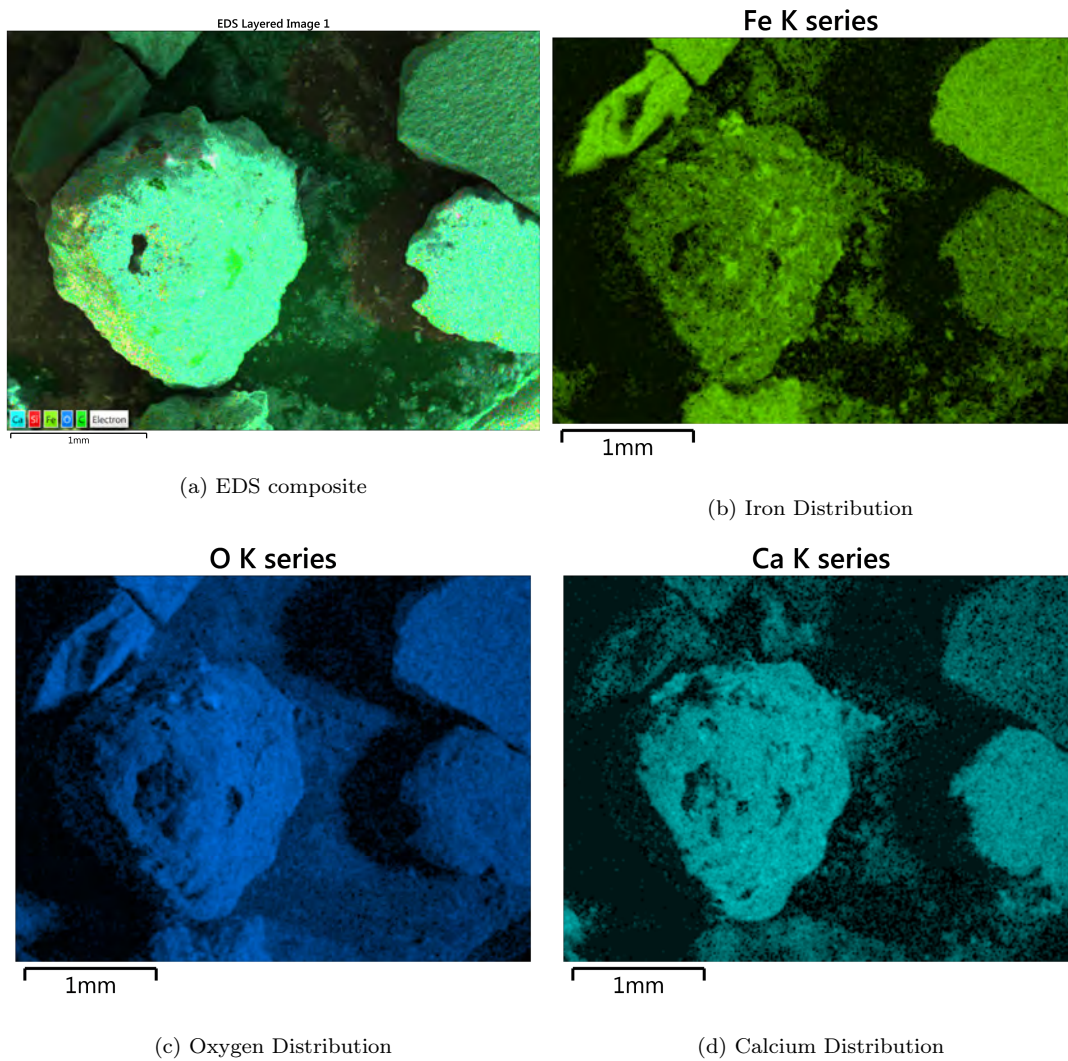
Figure 3.15: EDS elemental spectra for particle surfaces for some particles in Size group 2

3.2.3.2   Size group 3: 900 µm to 600 µm
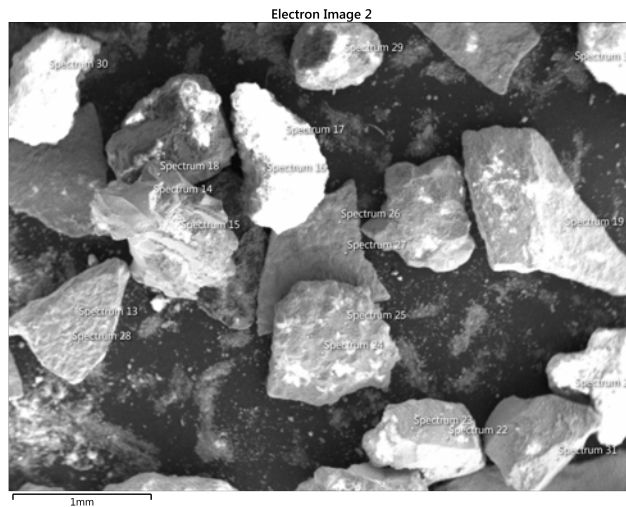
Figure 3.16: Electron microscope photograph of the particles between 900 µm to 600 µm

Between 900 µm to 600 µm, the particles can now be more clearly seen, with less shadowing appearing in Figure 3.16. The EDS scans in Figure 3.18 still show some shadowing due to the nature of how the EDS scans are performed.
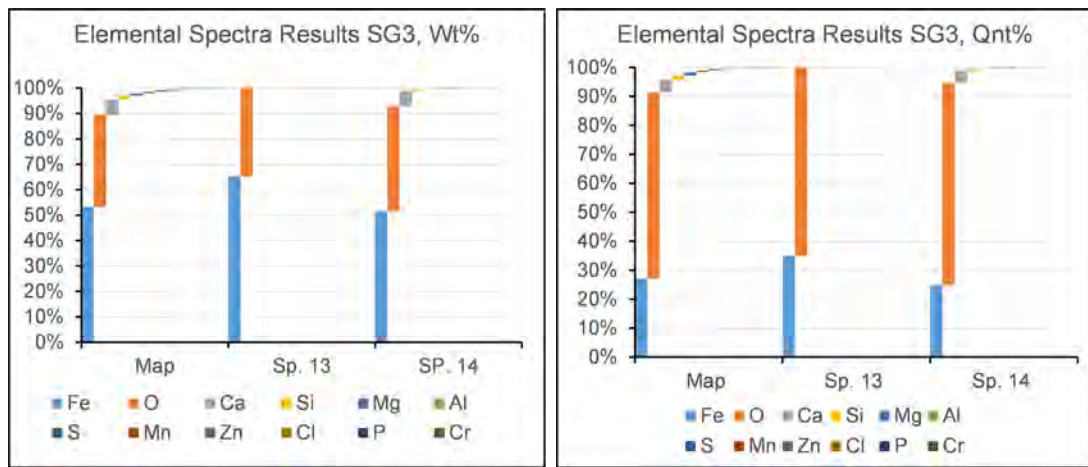
(a) Proportion of particle compositions by weight

(b) Proportion of particle compositions by quantity

Figure 3.17: Elemental quantitative proportions in Size group 3

The mass of carbon counts are not tracked as the tape securing the particles to the sample pegs are formed from carbon and this would give a false high reading

for the map spectra. However, C is tracked at the individual spectrum levels, and so can be displayed if needed to show variations in the surface carbon level. This is used as there is an unusually high carbon reading of one of the particles in the scan, visible in Figure 3.18d just left of centre. What this particle is cannot be determined from this scan, but subsequent scans do show similar particles in greater detail.

(a) EDS composite

(b) Iron Distribution

(c) Calcium Distribution

(d) Carbon Distribution
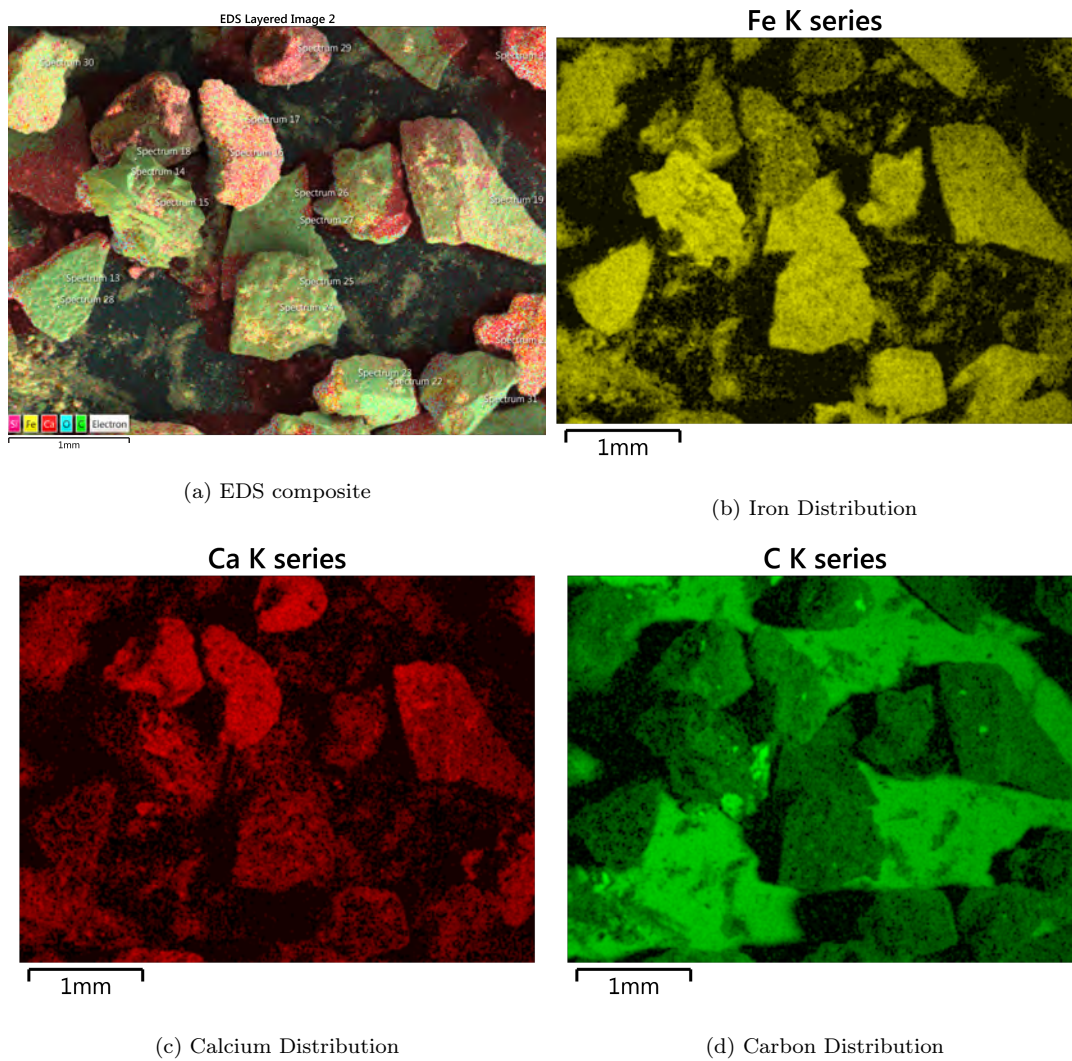
Figure 3.18: EDS elemental spectra for particle surfaces for some particles in Size group 3

The proportional counts are shown in Figure 3.17. At this size range, the iron

130

oxide is the most common surface compound, but more than that, the surface has an extremely high oxygen content proportionally compared to the iron. The calcium content is significantly higher than any of the other extraneous materials as well.

3.2.3.3   <u>Size group 4: 600 µm to 400 µm</u>
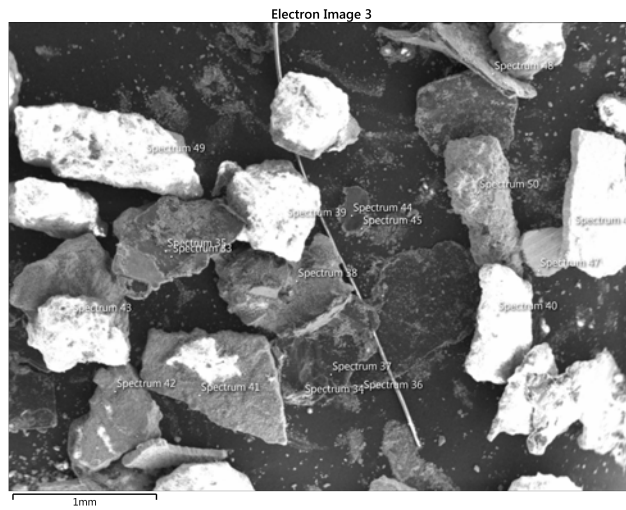
Figure 3.19: Electron microscope photograph of the particles between 600 µm to 400 µm

Figure 3.19 shows the particles in the 600 µm to 400 µmrange start to exhibit more consistently flake like shapes than the larger particles.
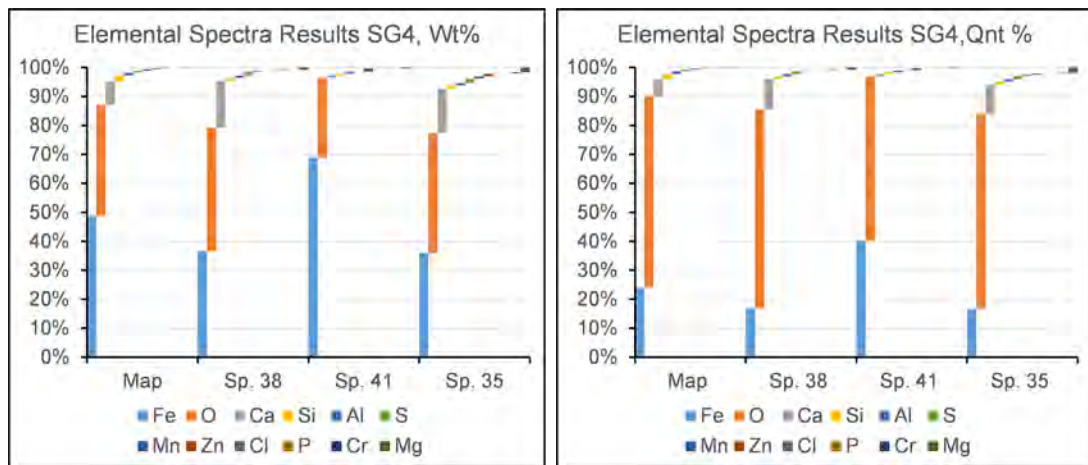
(a) Proportion of particle compositions by weight

(b) Proportion of particle compositions by quantity

Figure 3.20: Elemental quantitative proportions in Size group 4

In terms of composition, Figure 3.20 show a significantly higher oxygen content than for typical hematite or magnetite as seen in the larger size group.

At this size range, the difference in morphology between the high calcium and

scale particles can be clearly seen in Figure 3.21. The silicon distribution is also shown, to determine the source, and if it correlates to any of the other materils.

The high carbon particles are more clearly visible here, which allows their more crystalline shape to also be observed. The single strand running along the centre is likely just a strand of hair, based on the sulphur content.

(a) Iron Distribution

(b) Carbon Distribution

(c) Calcium Distribution

(d) Silicon Distribution
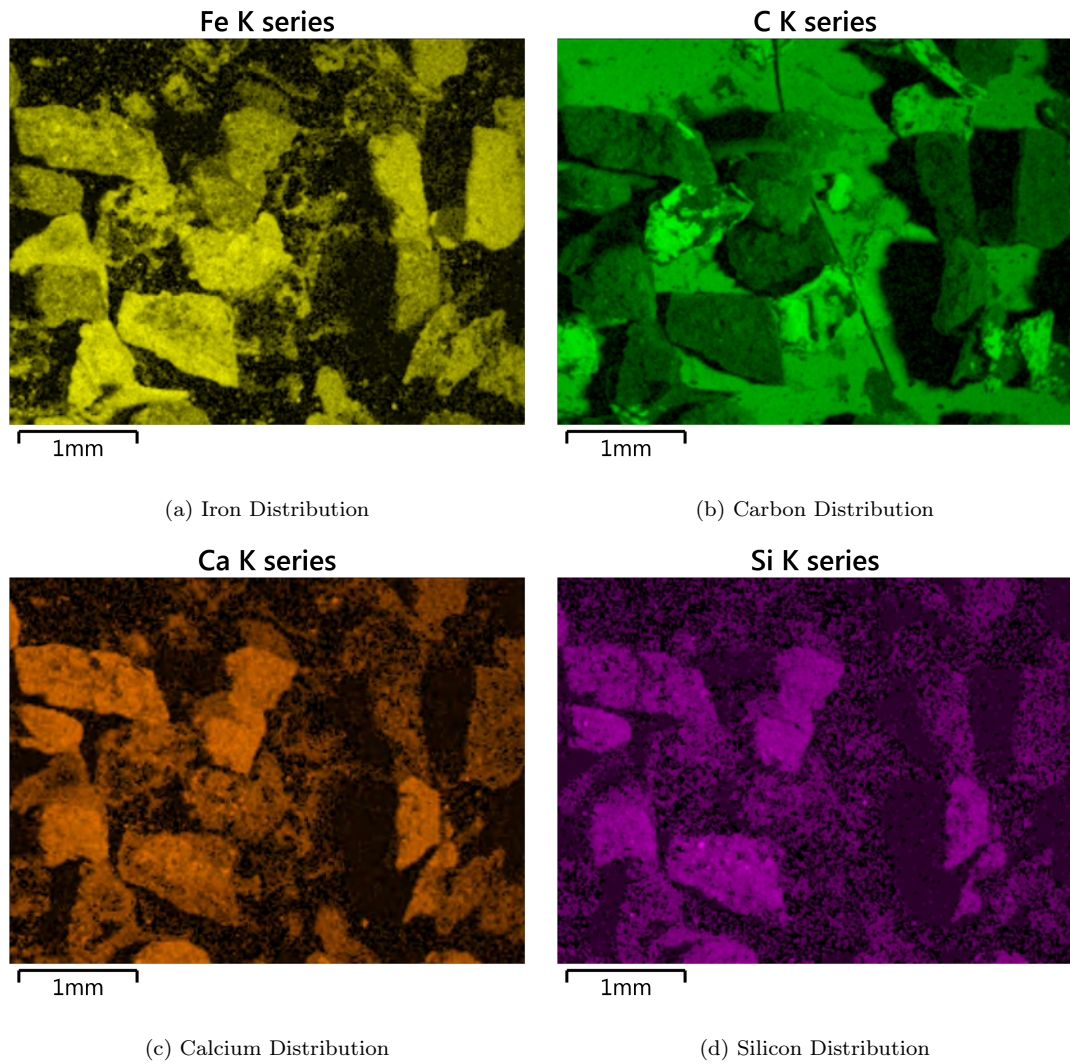
Figure 3.21: EDS elemental spectra for particle surfaces for some particles in Size group 4

3.2.3.4 Size group 5: 400 μm to 250 μm
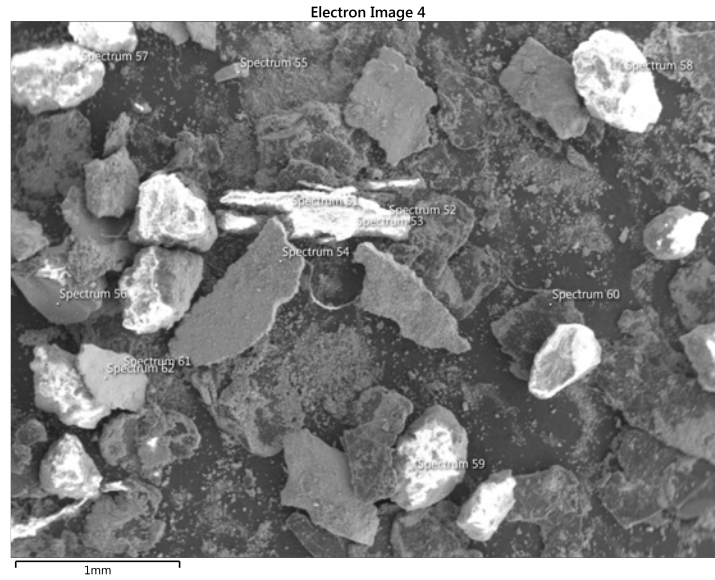
(a) Electron microscope photograph of the particles between 400 μm to 250 μm
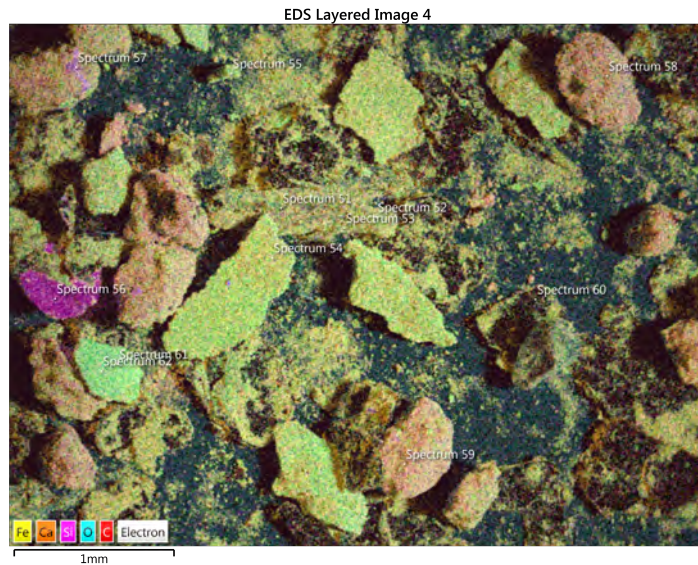
(b) EDS composite scan showing the elemental distributions. The black flakes are
nearly pure carbon, which is not coloured in the composite

Figure 3.22: Electron microscopy overview

Becuase Figure 3.22 shows a large number of unusual features, the EDS scan

was shown in greater detail. These include the long rough bright feature in the centre which was scanned three times (listed as spectra 51,52 and 53), other bright particles which show high calcium content and others no content at all, and the bright silicon particle.

The simplest to identify was the central particle, which was on retrieval revealed to be a tiny splinter of wood. This explains the brightness, as fuzzy bright features usually correspond to poor conductance, as the electrons cannot travel away from their scanned spots and they in turn reflect electrons very well.
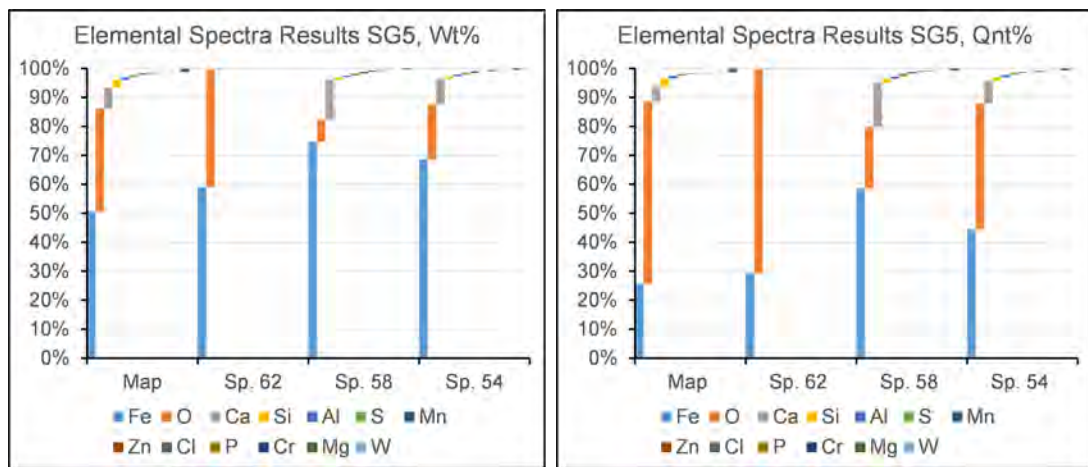
(a) Proportion of particle compositions by weight (b) Proportion of particle compositions by quantity

Figure 3.23: Elemental quantitative proportions in Size group 5

The targetted spectral counts in Figure 3.23 show some unexpected behaviour. The particle which corresponds to spectrum 58 shows a general high content of calcium and low iron content in Figure 3.24, and poor conductance. Yet the individual spectrum shows that it has very high iron content, higher than even spectrum 62, which corresponds to a particle which only has a response in the iron and oxygen spectra.

Spectrum 56 was of the particle with a high silicon response and no other response, and also showed a high oxygen content. Silicon dioxide exists in the form of glass but again, the oxygen spectrum did not show a response for this

(a) Iron Distribution

(b) Carbon Distribution

(c) Calcium Distribution

(d) Silicon Distribution
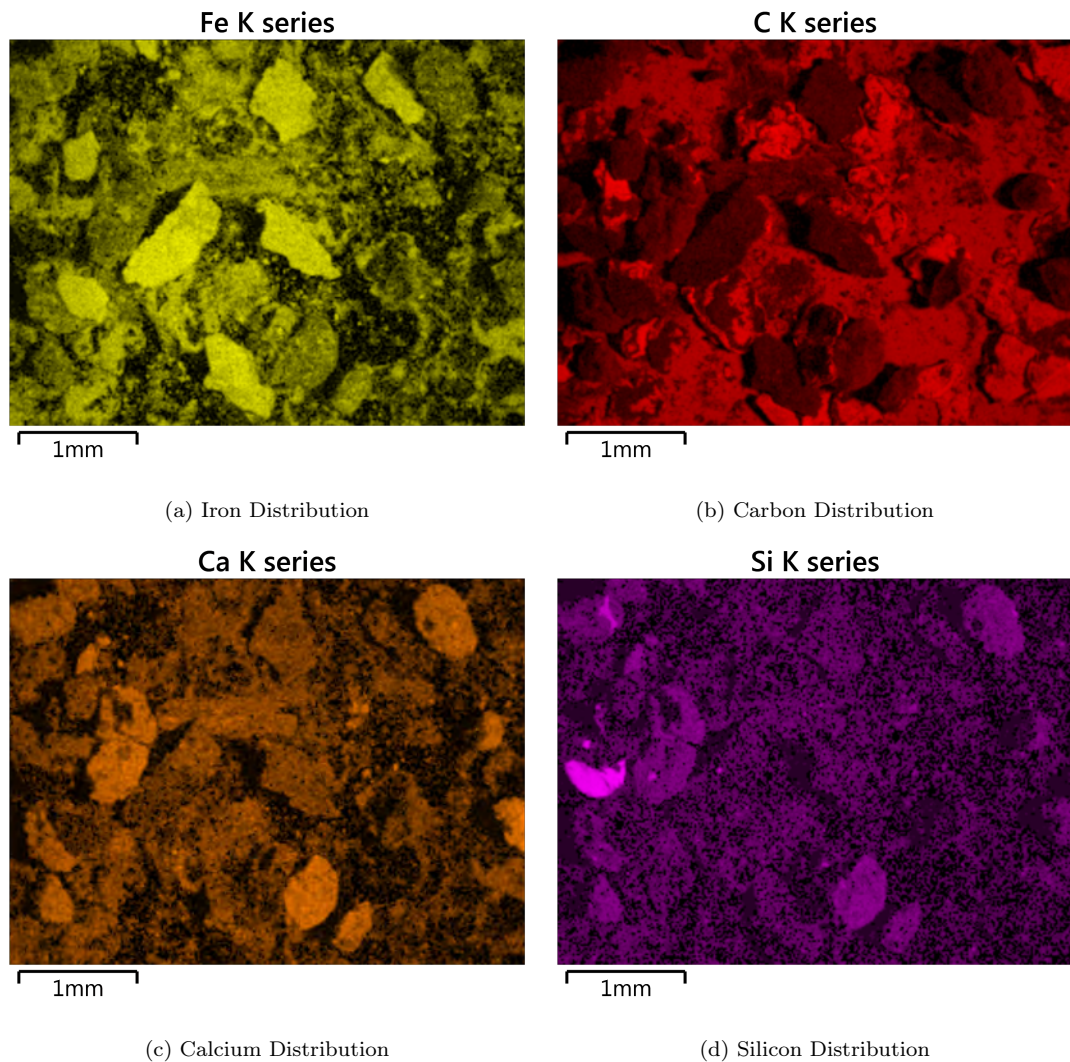
Figure 3.24: EDS elemental spectra for particle surfaces for some particles in Size group 5

particle.

The final particle of note is the almost transparent particle, below the label "Spectrum 60", which was not noticed until processing was being performed, and this shows a high brightness as well. This particle can be partially seen in the calcium spectrum, and in the not shown sulphur and oxygen spectra as well, suggesting possibly gypsum.

3.2.3.5 Size group 6: 250 µm to 200 µm
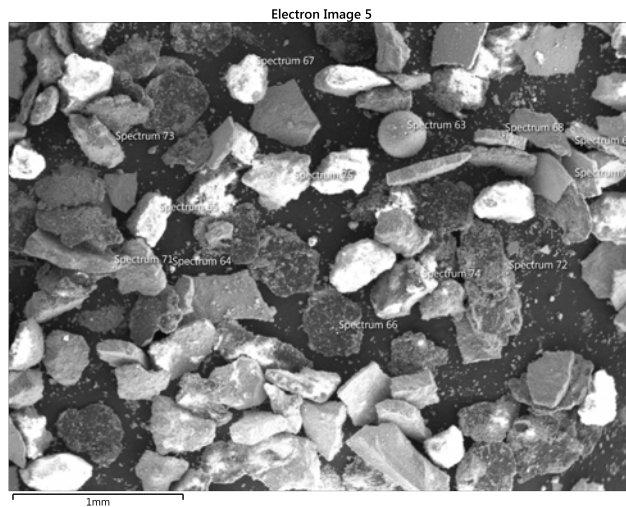
Figure 3.25: Electron microscope photograph of the particles between 250 µm to 200 µm

Figure 3.25 shows the particles in this size group, which show a wide range of particles and particle shapes. These range from perfect spheres, likely an anomalous solidified droplet of iron based on the iron content to the assorted flakes of iron ore, some of which are positioned ideally to get a scan of the inside layer.

The bulk spectra shows similar behaviour to others, but many individual particles were scanned, and their elemental compositions shown in Figure 7.13 show huge variation. Some particularly notable ones are spectrum 64, which shows nearly pure silicon oxide again, spectrum 71 which shows flourine and sodium, and 68, which shows the high iron content that is found in the centre of the flake.

The elemental scans in Figure 3.27 and Figure 3.28 and are useful in confirming the general patterns of morphology and composition, particularly for the carbon particles. A secondary feature of these particles is that they appear to almost clear out space around themselves, and are relatively spread out, while the other particles are more closely packed together.
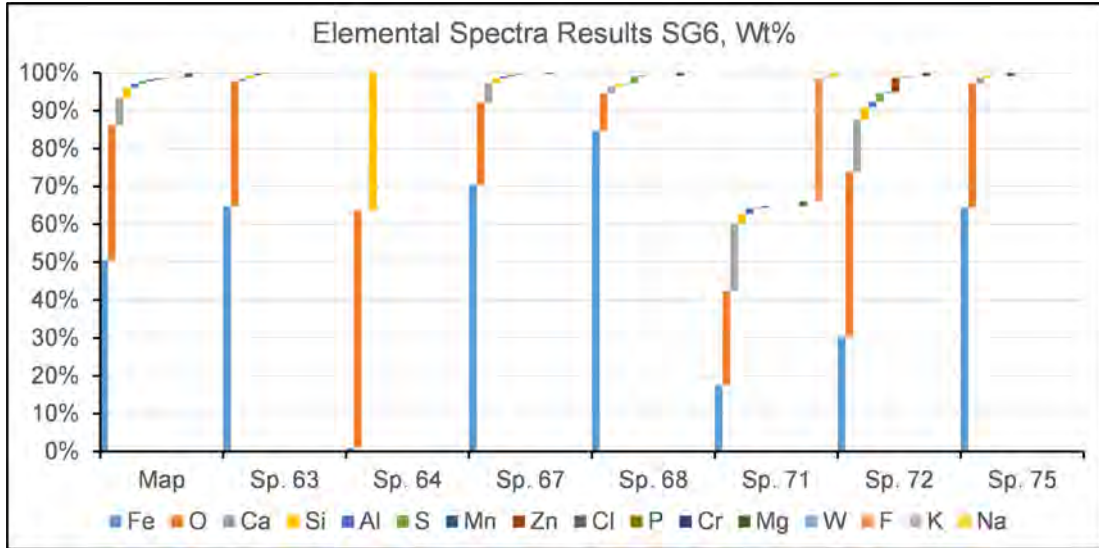
(a) Proportion of particle compositions by weight
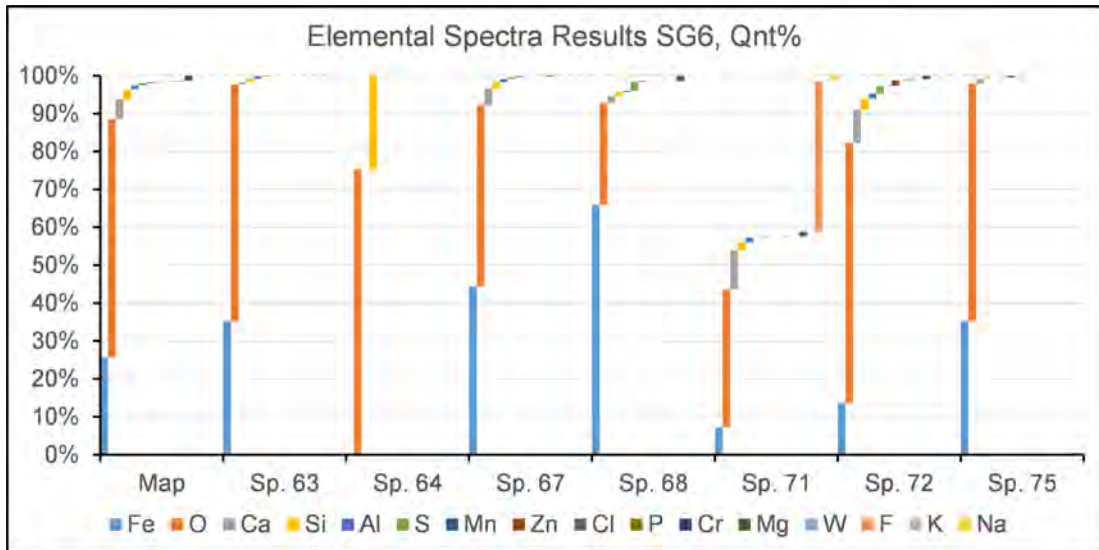
(b) Proportion of particle compositions by quantity

Figure 3.26: Elemental quantitative proportions in Size group 6

138

Fe K series

1mm

(a) Iron Distribution

C K series

1mm

(b) Carbon Distribution
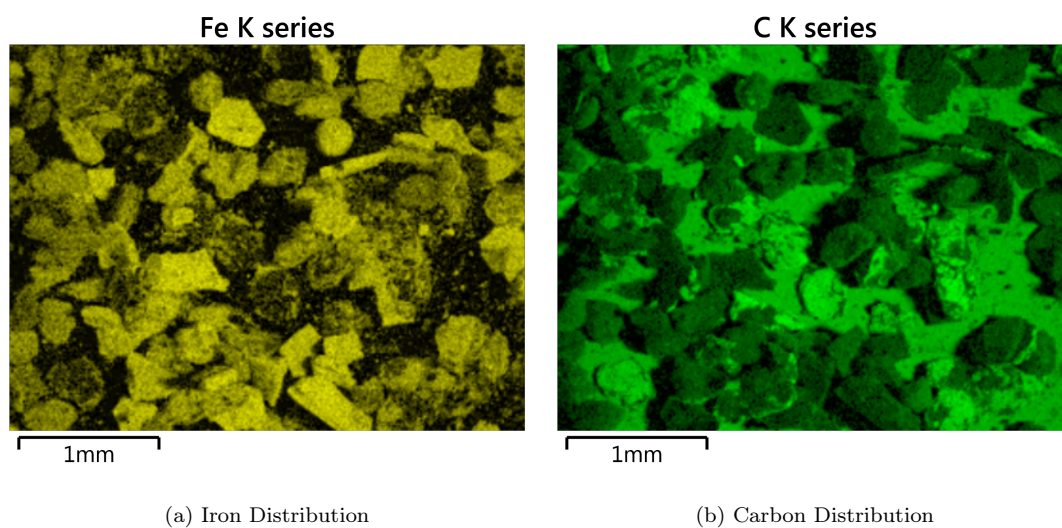
Figure 3.27: EDS elemental spectra for particle surfaces for some particles in Size group 6

O K series

1mm

(a) Oxygen Distribution

Ca K series

1mm

(b) Calcium Distribution
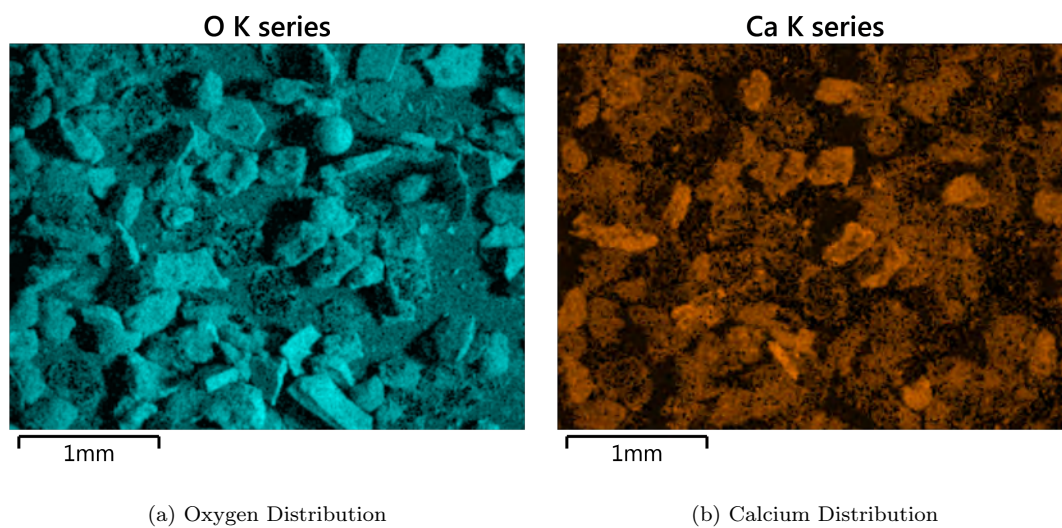
Figure 3.28: EDS elemental spectra for particle surfaces for some particles in Size group 6

3.2.3.6 Size group 7: 200 µm to 140 µm
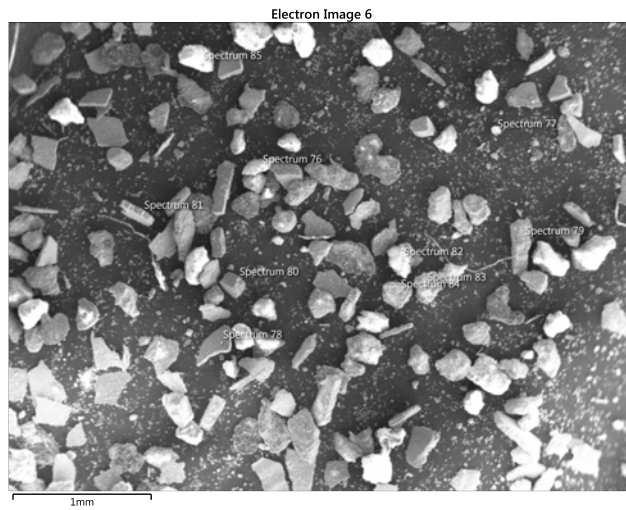
Figure 3.29: Electron microscope photograph of the particles between 200 µm to 140 µm

The particles in Figure 3.29 show similar morphologies as in other size bands, simply smaller. Figure 3.31 also shows that there are much fewer carbon flakes in this size range. Figure 3.30 show the presence of more unusual materials, such as aluminium-calcium oxides (spectrum 76) and the presence of more alloying metals, such as vanadium and nickel. The spectrum over the whole range also shows a slightly higher iron/oxygen proportion than in larger size groups.

(a) Proportion of particle compositions by weight
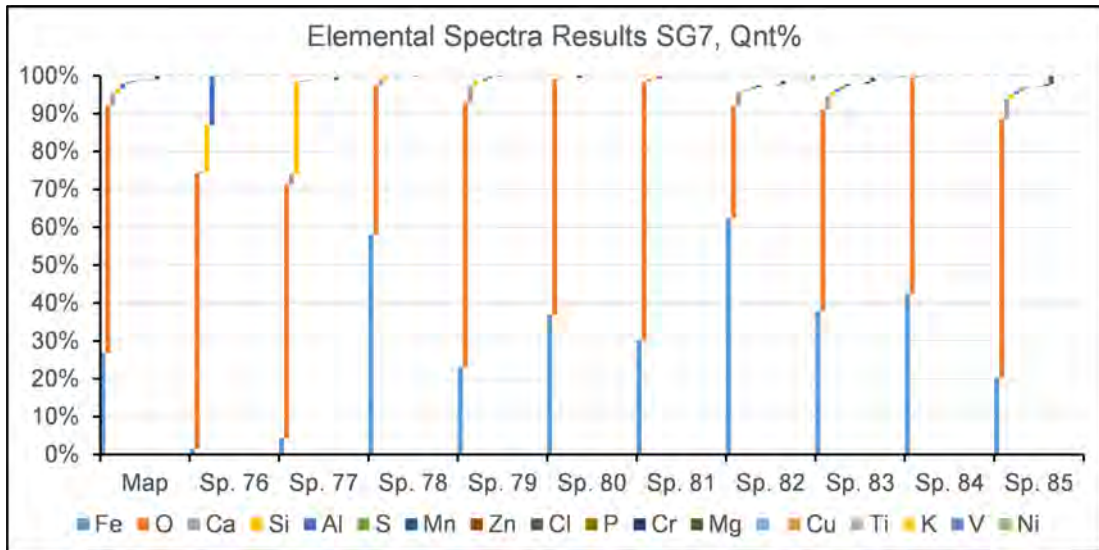
(b) Proportion of particle compositions by quantity

Figure 3.30: Elemental quantitative proportions in Size group 7

Fe K series

C K series

1mm

1mm

(a) Iron Distribution

(b) Carbon Distribution

Si K series

Ca K series

1mm

1mm

(c) Silicon Distribution

(d) Calcium Distribution
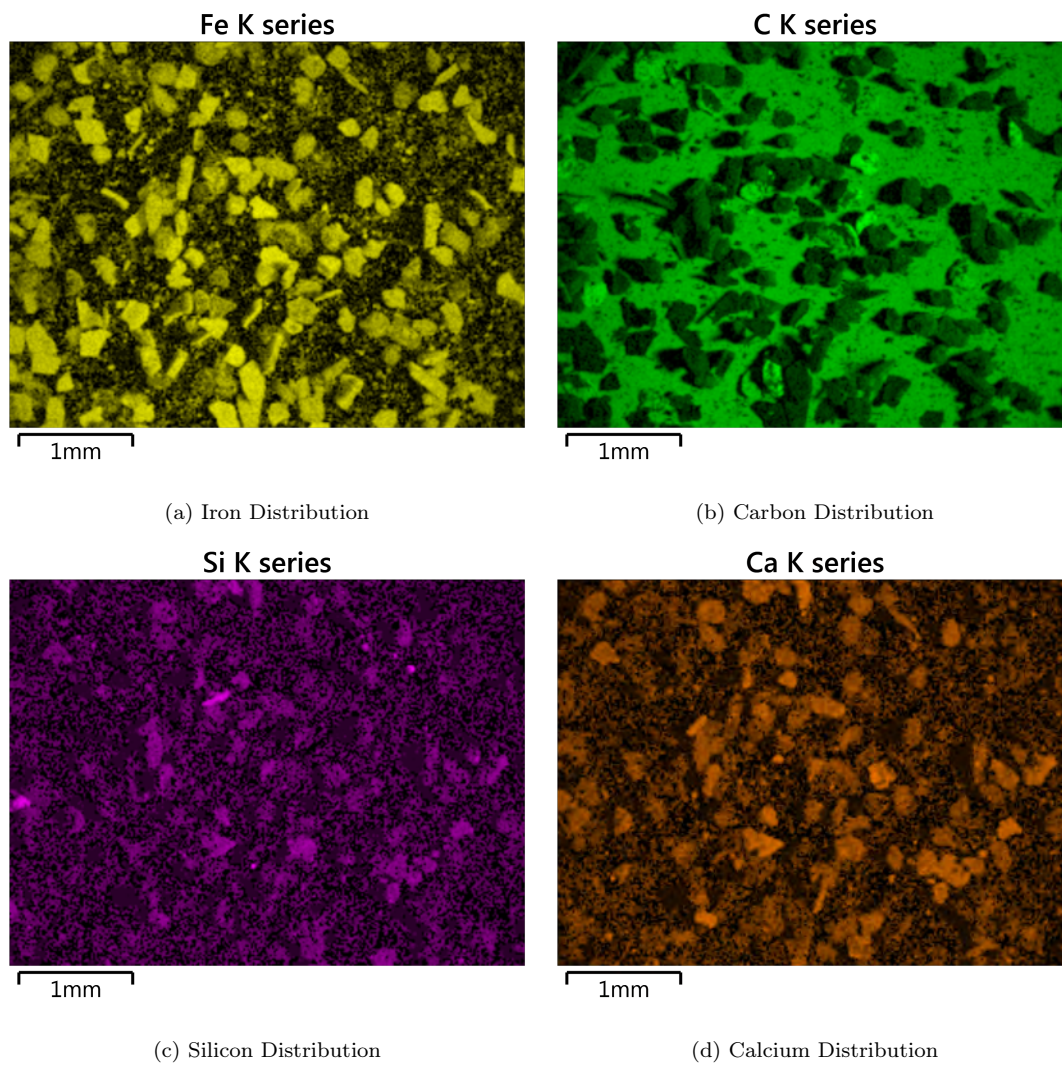
Figure 3.31: EDS elemental spectra for particle surfaces for some particles in Size group 7

3.2.3.7 Size group 8: 140 μm to 125 μm
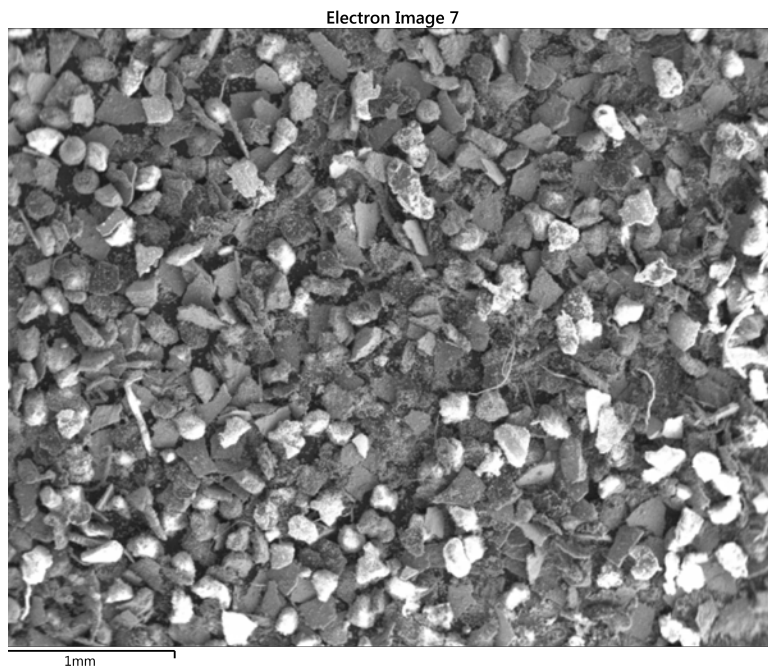
Figure 3.32: Electron microscope photograph of the particles between 140 μm to 125 μm
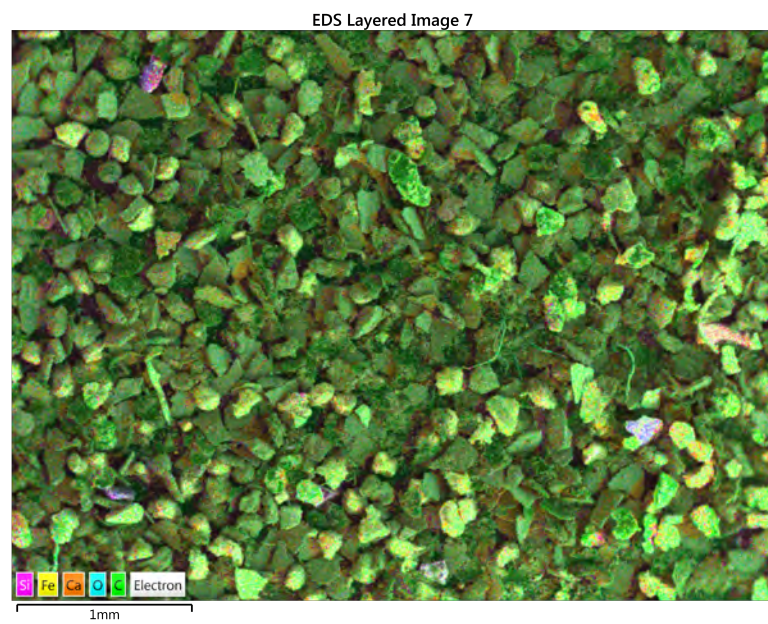
Figure 3.33: EDS composite scan of the particles between 140 μm to 125 μm

At this size range, given the previously observed huge amount of variability in the sizes, scans of interesting features were concluded. The morphology of the

particles in Figure 3.32 show that the particles in the smallest size ranges seem to have a lower aspect ratio, and are less flakey in appeerance. The iron and calcium K series in Figure 3.35 are in agreement with Figure 3.34, in that the calcium is relatively low compared to the very common iron, and the only areas with low iron are places where the carbon is on the surface. The iron content is also generally quite high, with a lower oxidation state. This could be from two reasons, which are discussed later.

The fibrous strands that can be seen very clearly in Figure 3.34 could not be identified, as they do not appear in any of the individual elemental scans, except oxygen, which does not narrow down the possibilities.
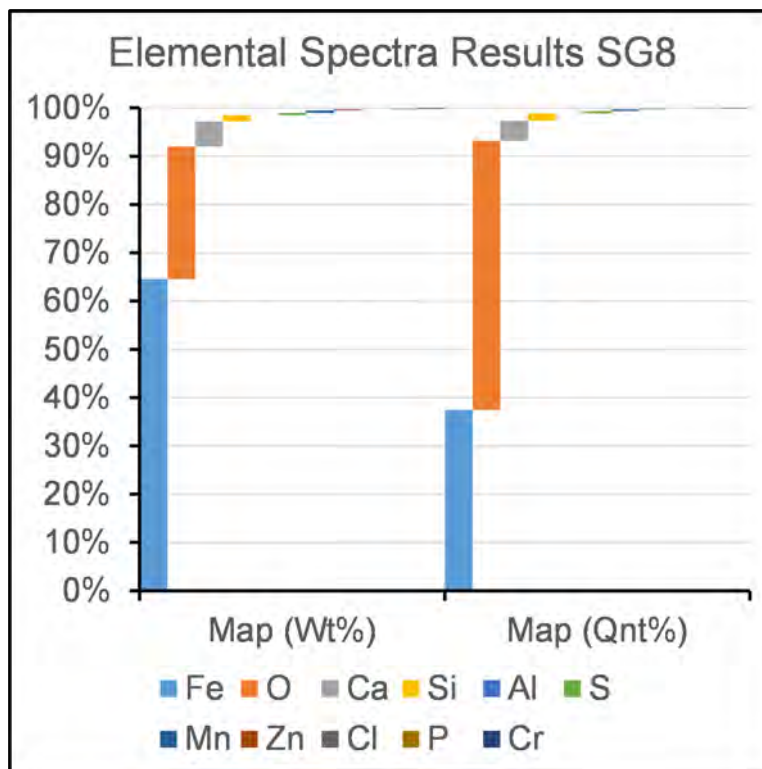
Figure 3.34: Proportion of particle compositions by weight and quantity

Fe K series

1mm

(a) Iron Distribution

C K series

1mm

(b) Carbon Distribution

Si K series

1mm

(c) Silicon Distribution

Ca K series

1mm

(d) Calcium Distribution
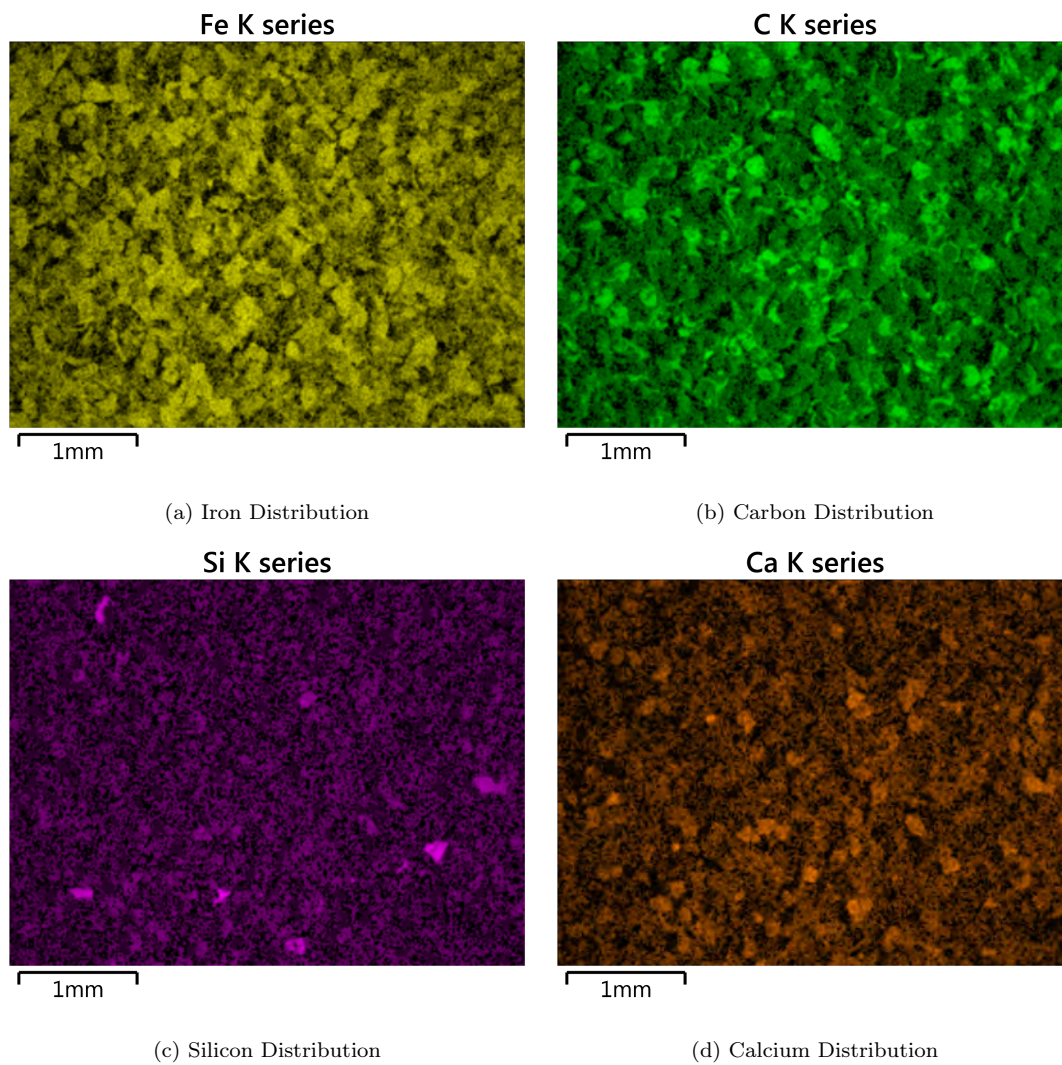
Figure 3.35: EDS elemental spectra for particle surfaces for some particles in Size group 8

3.2.3.8 Size group 9: 125 µm to 63 µm

Figure 3.36: Electron microscope photograph of the particles between 125 µm to 63 µm
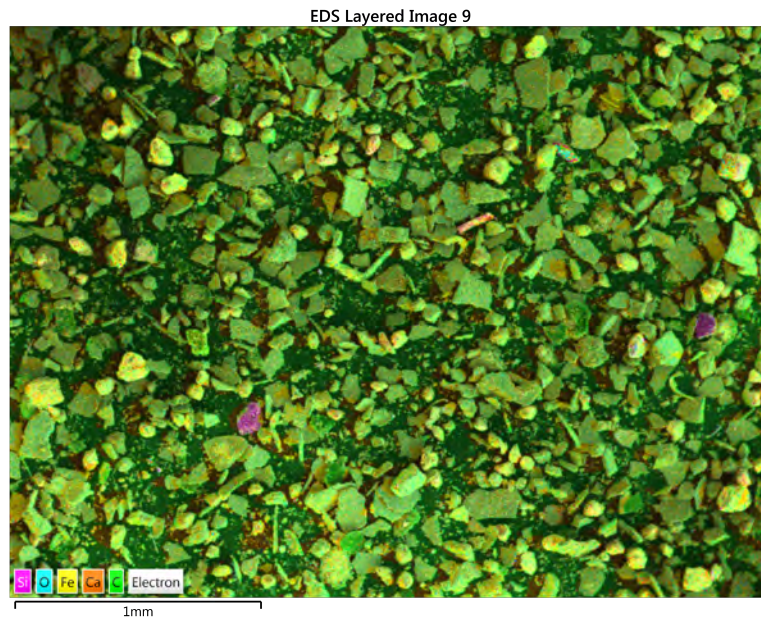
Figure 3.37: EDS composite scan of the particles between 125 µm to 63 µm

The particles in Figure 3.36 show a return to flake morphology, especially for
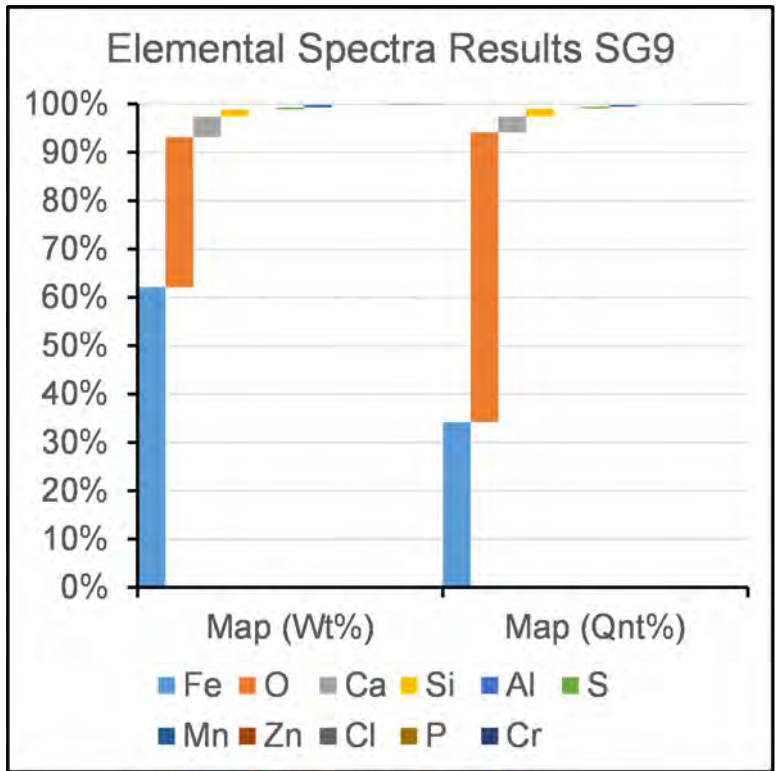
Figure 3.38: Proportion of particle compositions by weight and quantity

the larger particles. The smaller seem to have a more rounded general morphology, which is true regardless of morphology, Figure 3.39. The carbon flakes are also very rare, and there are some silica particles.

The lower oxygen/iron ratio trend seen in the previous size groups map spectrum is also observed in Figure 3.38, though not significantly lower.

Fe K series

1mm

(a) Iron Distribution

C K series

1mm

(b) Carbon Distribution

Si K series

1mm

(c) Silicon Distribution

Ca K series

1mm

(d) Calcium Distribution
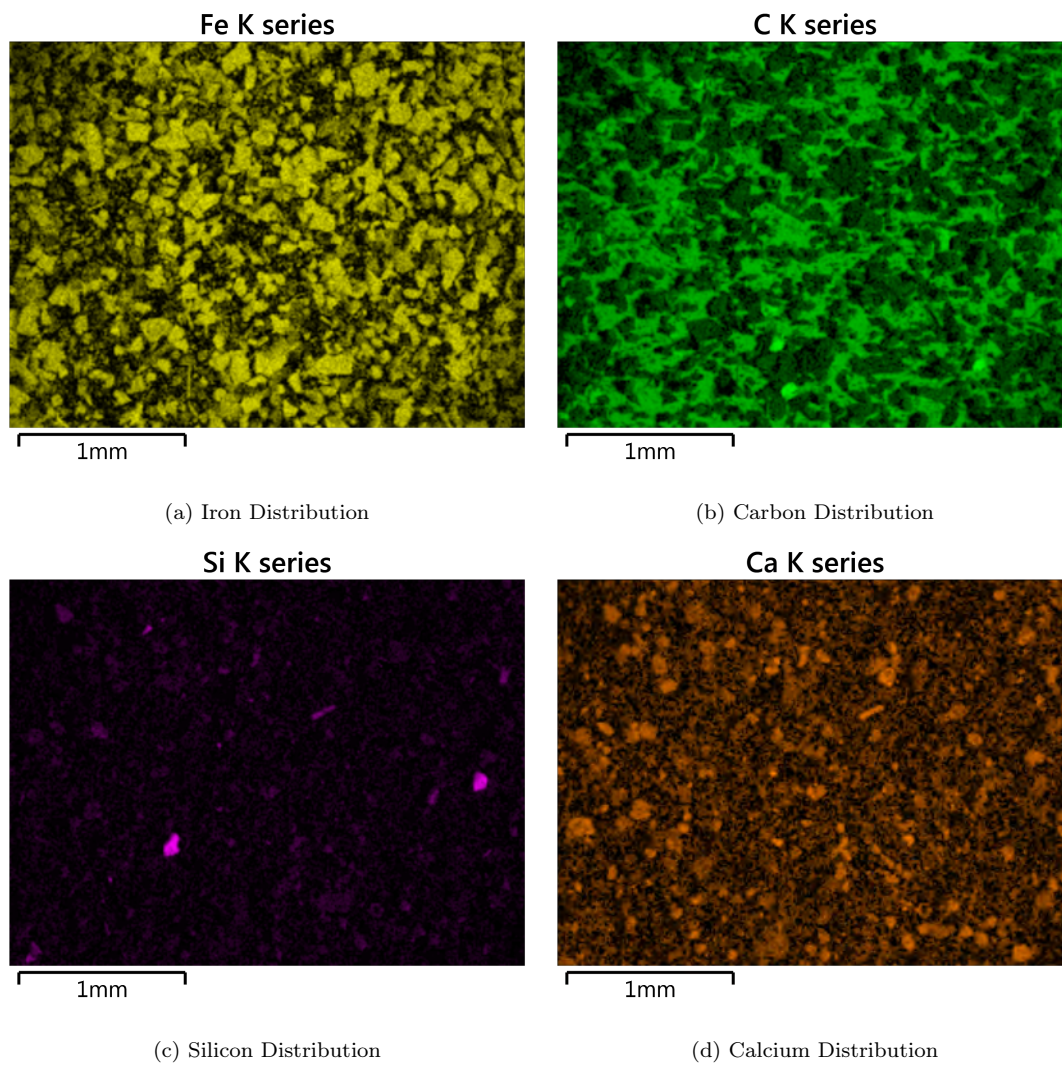
Figure 3.39: EDS elemental spectra for particle surfaces for some particles in Size group 9

3.2.3.9 Size group 10:<63 µm
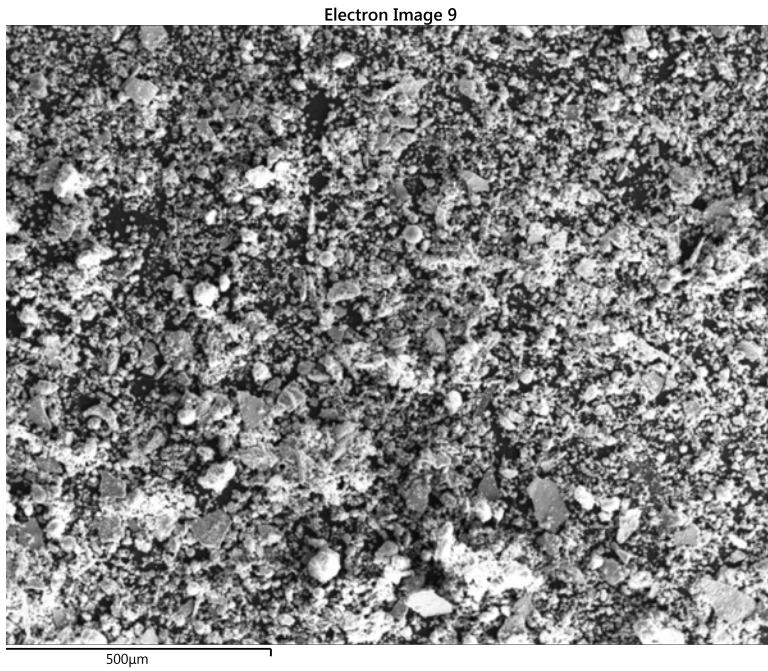
Figure 3.40: Electron microscope photograph of the particles <63 µm
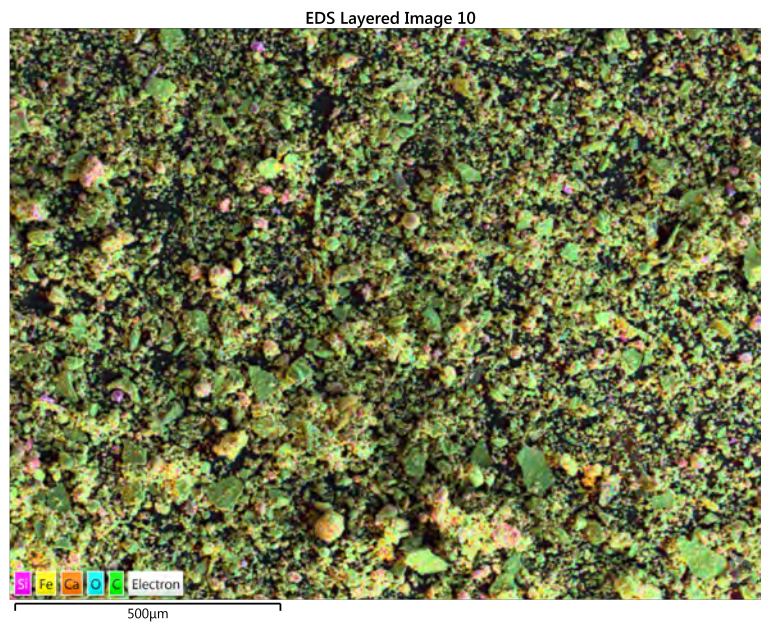
Figure 3.41: EDS composite scan of the particles between <63 µm

At this point the particles are simply dust. Even at a higher magnification,

most of the particles in 3.40 and Figure 3.41 the particles are simply an even distribution of fine dusts.
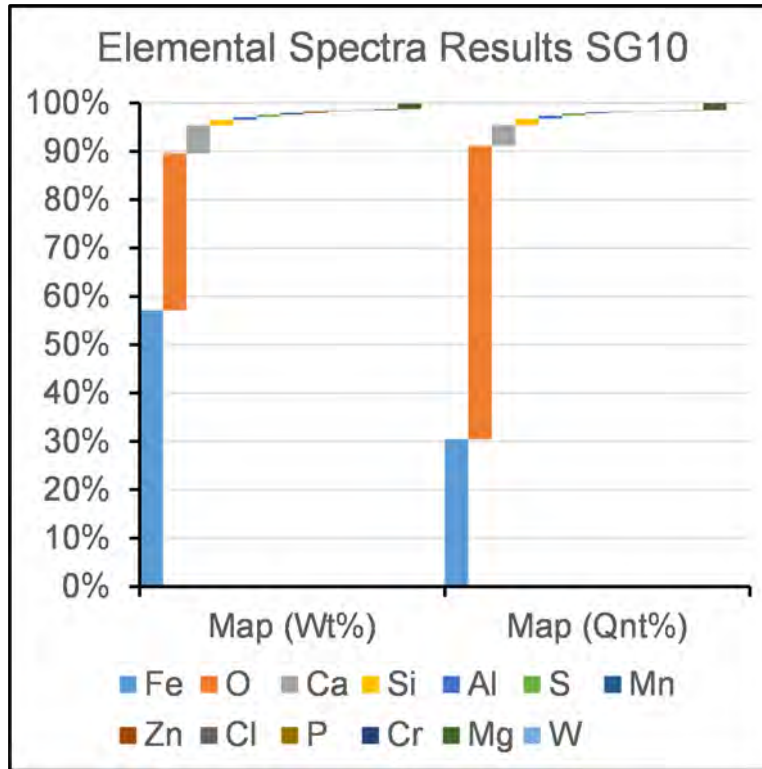
Figure 3.42: Proportion of particle compositions by weight and quantity

The oxygen content shown in 3.42 is lower than the largest size groups, but it is lower than the next size group larger.

the elemental scans in 3.43 show that the fines are primarily iron based, with the calcium and silicates being confined mostly though not entirely to the larger particles. The carbon also does not show any obvious signs of the crystalline carbon, perhaps one sliver in the bottom right quarters centre.

Fe K series

500μm

(a) Iron Distribution

C K series

500μm

(b) Carbon Distribution

Si K series

500μm

(c) Silicon Distribution

Ca K series

500μm

(d) Calcium Distribution
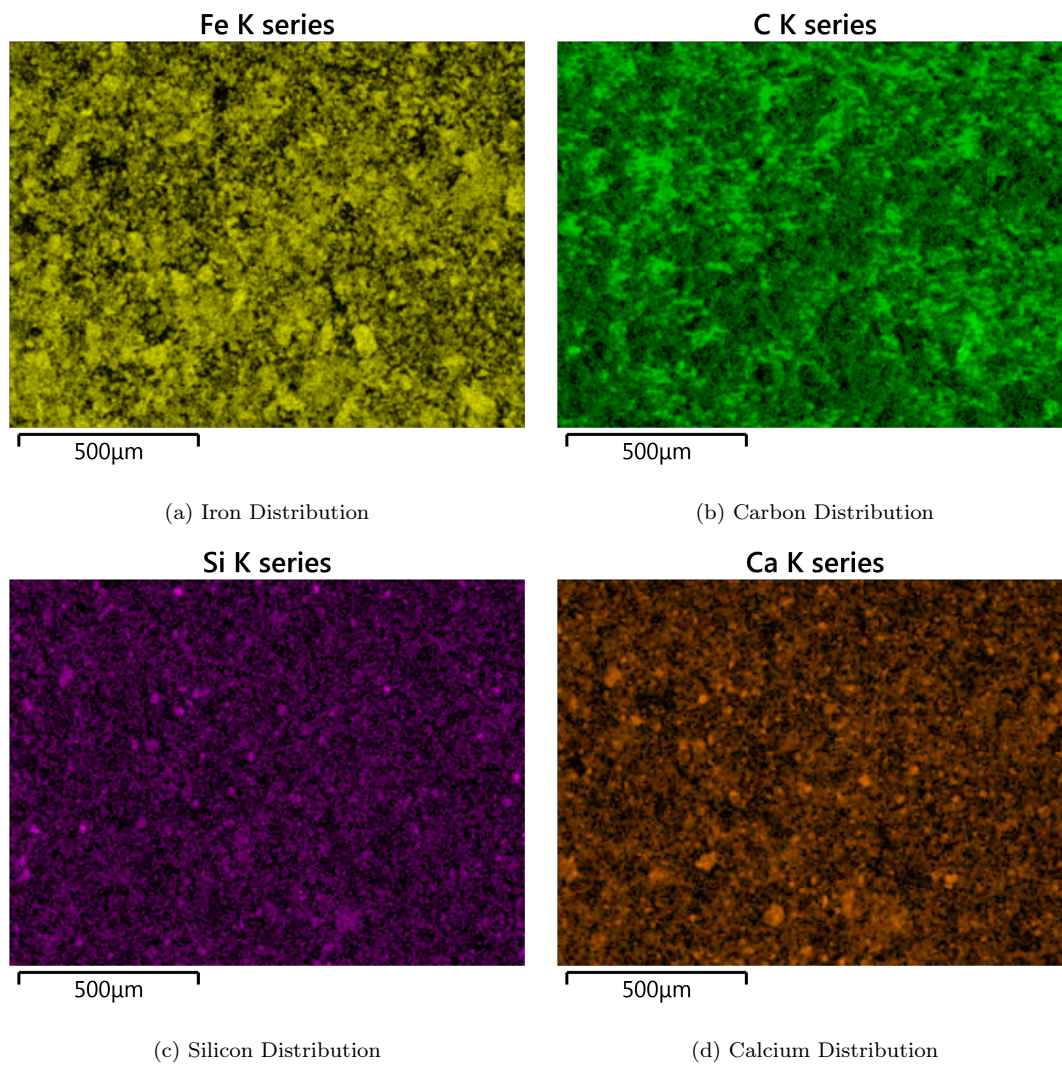
Figure 3.43: EDS elemental spectra for particle surfaces for some particles in Size group 10

Comments on Electron microscopy

The general trends as the size of the particles become smaller is that the larger particles have a higher oxygen to iron content than the smaller ones. Two possibilities are suggested for this, and they depend on when the fines are produced. Typically, one would expect smaller particles to oxidise more easily, and have a higher oxygen to iron content.

This leads into the first possibility: The particles were eroded away from the larger particles during the cleaning and sieving process. This would be in agreement with the scans which showed that the centre of the scales had a higher iron/oxygen ratio than the surfaces. If the fines were from the breakage of the smaller particles, this would account for this.

The other possibility does not require breakage and in turn presumes that the particle distributions previously determined are precisely what is present in the sludge. Though the iron is proportionally higher, this does not mean that it is very low oxidation, simply that there is a slight increase in the amount present. The variation simply comes from the increase in surface area consuming the oxygen more evenly.

Other possibilities may exist, and the composition may be a combination of the two. Perhaps the lower aspect ratio particles in Figure 3.33 come from breakage while the flakes which had high iron contents were protected by the oils. Further, as can be seen in Figure 3.22b dust was retained to some degree in the larger size groups.

In the end, the erosion theory seems most likely. The iron content for most of the size ranges is around 25% by number of atoms, which increases dramatically right when the particles are observed to become more rounded, as might be expected from a grinding action. Despite this, the ratio of iron to oxygen seems generally too high for simple iron oxides. Hematite, or Fe_2O_3 would give a number proportion of 40% iron and 60% Oxygen.

The presence of calcium, silicon and hydroxides therefore provide an explana-

tion. The calcium and silicon occur in 3:1 ratios fairly consistently throughout in the bulk scans. This ratio is reasonably close to the proportion found in Portland cement, though this differs between specific sources, and suggests that the calcium is from cement dusts and dispersal that would occur through the industrial processing, and is not from lime or slag which gets into the settling tanks through other means.

The calcium, silicon their hydroxides can, for some of the samples, account for enough oxygen that the iron could be composed of typical Fe_xO_y iron oxides. However, for some of the samples this cannot be enough. For example, spectrum 13 and spectrum 62 have no or very little calcium respectively. At (very) approximately 33% each, this accommodates FeO(OH) quite well, and this iron oxy-hydroxide forms in water, such as the settling pools.

There are a number of unexpected readings from other sources as well. Spectrum 58, taken of one of the high calcium particles, actually shows a higher than average iron content. The particle showed low conductivity and very little response in the Fe elemental scan. The reason for this is uncertain. It could be that the scan actually was conducted on a piece of dust which was on that exact point. This does unfortunately call into question the specificity of identifying the particles from scans, which was one of the reasons point scans were stopped after Size group 7. Scanning every point of unusual composition was also unlikely to bring any particularly major insights, as many of them were highly unrepresentative curiosities.

Some of these curiosities include the small silicate particles which seem to have an excess of oxygen such as spectrum 64 and 56 (not shown), the fluoride salt that formed part of spectrum 71, and the alumina particle for spectrum 76 and possible strangest being the almost transparent particle.

It had been established that there are many types of unexpected contaminants, but the large quantity of carbon particles was particularly unexpected. The crystalline nature and purity of these carbon particles suggest that they are

graphite. What they are doing in the scale is unknown. One possible source is Kish, graphite which forms in the steelmaking process as carbon condenses out of the steel solution. This is only speculation, but it is not coming from pencil lead, as this contains clay to control the hardness which would show up as silicon or calcium. A secondary feature of these particles is that they appear to almost clear out space around themselves, and are relatively spread out, while the other particles are more closely packed together.

An XRD scan could determine the precise composition, however this would not be able to compare the morphology to the composition, and would require further processing. The goal of determining if size affects the composition is intrinsically altered by the sieving process possibly breaking some of the particles, and an XRD would not be able to evaluate this any better. In the end, this would be unnecessary extra work, as the above finding that the scale forms hydroxides from an elemental scan as well as a colour view is satisfactory to modelling of the material as best as possible, and the aspect ratio of the material is extremely variable.

3.2.4 Liquids

The liquid components, decanted from the sludge, were sent off to gas chromatography labs at Tata Harborside. The results were provided as images, rather than as data points in a file, so subsequent manipulation is restricted by the loss of information as a result. Some results of the liquids are shown in subsection 3.1.1, which will be compared to here. The labelling is different in the chromatograph results due to a combination of a misleading initial naming scheme of samples if the source document was not available and a misreading of labels by technicians, which was used in the chromatography results images.

3.2.5 Liquid Content

The liquid content could be easily determined by comparing the pre and post cleaning weight of the samples. These results are shown in Figure 3.44.

The proportion of liquid mass in sample 2 and 3 are extremely high, and as mentioned in subsection 3.2.2, this is more than likely to be due rather to the original cleaning procedure leaving an excessive quantity of fines in the cleaning flasks.

Batch 2 and 3 were taken from the middle of the draining process, which explains why they have higher liquid content than batch 1 and 4. However, batch 2 was drawn from the last pile in the actual draining ponds, while batch 3 was drawn from the pile just removed from the pool. This could explain batch 2 having a higher proportion of >2mm particles proportionally, which allows for easier drainage during the sampling process.

Batch 5 is CMS, which was taken as a point of comparison, and its very low liquid content agrees with the visual observations of being quite clean and dry to begin with.

3.2.6 Chromatography Data

Not all the chromatography data was useful. A combination of the weathering process and initial unresolved oil composition, along with the poor resolution of the data, meant identification of the specific compounds was not feasible. Some useful data was able to be found.

Repeatability

Figure 3.45 shows the responses from sample 1 and 2. The liquids extracted from these samples were suitable, even if the size distributions were flawed. As both were drawn from the same batch, but extracted on different occasions, they were useful for comparing repeatability. These are useful for showing that the abundance of the distributions. these also show a similar shape to the 46 hydraulic
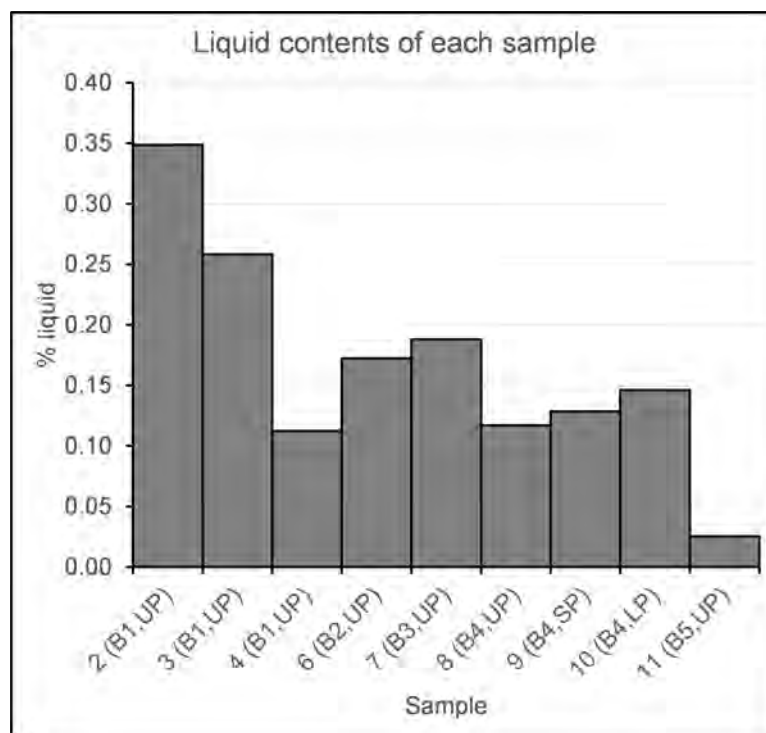
Figure 3.44: Proportion of liquid by mass of each sample, determined by comparing wet and dried mass after cleaning.

(a) Sample 1 Results

(b) Sample 2 results
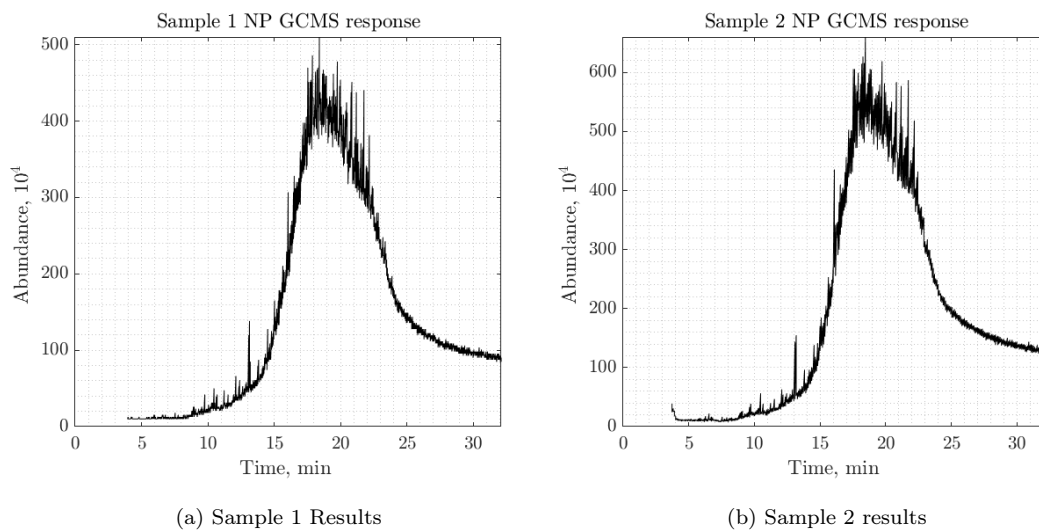
Figure 3.45: Gas Chromatograph responses for two samples from the same batch. They show that the overall curve is nearly identical, though the abundance differs a little, it is a matter of relative detection compared to a baseline. The overall shape of the response is the feature of interest.

oil in Figure 3.2, which is expected.

(a) Sample 6 Results (batch 2)

(b) Sample 7 Results (Batch 3)
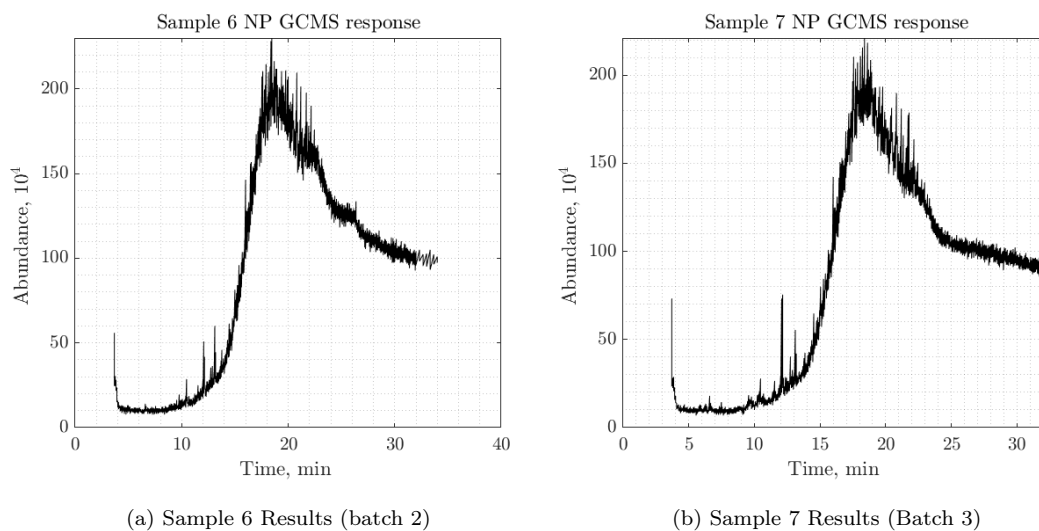
Figure 3.46: Gas Chromatograph responses for two samples from batches collected on the same day from different sources.the overall shape of the response is the feature of interest.

Figure 3.46 shows the responses of the samples taken of batches 2 and 3 which were collected on the same day, but at slightly different locations as mentioned. The exposure to the air was hypothesised to result in greater weathering occurring in batch 3 than 2, but the difference between the two is relatively minor. Whether the variation between the two is due to a difference in initial composition or weathering is hard to tell. The responses of samples 6 and 7 are similar to Figure 3.2 however they also have a much higher response in the longer time scale, which is closer to Figure 3.3 and Figure 3.4.

(a) Sample 9 Results (batch 4 Small pellets)   (b) Sample 10 Results (Batch 4 Large pellets)
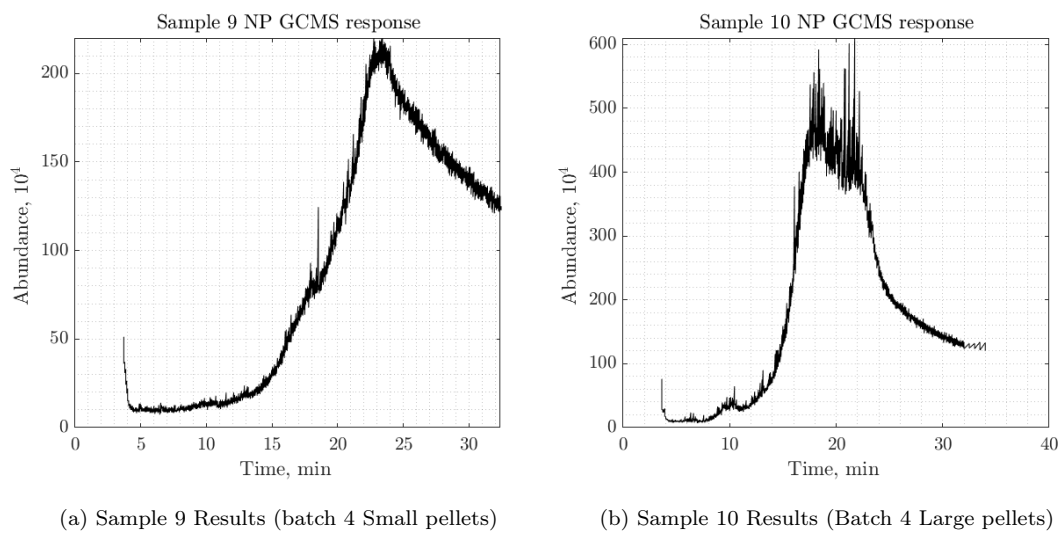
Figure 3.47: Gas Chromatograph responses for the large and small pellet sample oils.

Finally, the oil composition of the large and small pellets. Figure 3.47 was expected to show the larger pellet containing more viscous oil than the small pellets, however this does not seem to be the case. In fact, the smaller pellets had a lighter oil, which may suggest that the ability to consolidate is more important in the growth behaviour, as a viscous oil would slow this process down.

Proportionally, the small pellets appear to be comprised of the heavier oils rather than the large pellets. Overall Figure 3.47a looks quite similar to the heavy oils Figure 3.3 and Figure 3.4 while Figure 3.47b looks much more like the lighter oil Figure 3.2, with some added heavy oils.

158

The sample size was small, which may have affected the results. Additionally, the liquid content of the large pellets seems to be slightly greater than that of the small pellets in Figure 3.44.

The Polar sample responses were also tested, however these were contaminated with column bleed effects, and were not useful for any comparisons.

Discussion of Liquid Results

The liquid behaviour as noted by Tata steel and in the small amount of examination performed for this work is highly inconsistent. This inconsistency severely limits the benefits that could be gained from analysis in industrial practise, as the analysis would need to be applied to account for these variations consistently and be representative.

What can be observed is that there is heterogeneity both between batches and internally within the batches. The lighter oil being within the larger pellets suggests that an excessively viscous oil interferes with the ability of the smaller pellets to agglomerate further, which could be due to the consolidation behaviour. This is a potential direction of research in the self-selection of viscosity and pellet diameter in the production.

The fact that samples 6 and 7 showed similar results do suggest that there is some degree of continuity in the oil properties over time, though this may be due to small sample size.

The oils present in the pellets do seem to match the oils suggested by Tata as being the sources, but there is evidence of some alteration, and the quantity within each batch can vary significantly. This heterogeneity again means that such analysis is less useful from a practical standpoint unless a suitable method of response can be clearly established and a means of testing which is useful can be applied.

3.2.7 Unrecorded failed experimentation

To try and begin a process of evaluating the material effects on the pelletisation process, an experimental plan was designed which allowed pelletisation experiments to be performed carefully. The goal was to determine which variables affected the process in a repeatable fashion that would introduce variables one at a time. The scale and oil for example show high degrees of variability between batches, so determining a baseline which could be further developed would allow evaluation of what needs to be adjusted to each individual batch in a way that could be measured.

Ballotinis were prepared which were the same average diameter as the mass median determined above, and the oils were added to the dry particles to create a feed with 10% by mass oils, to which water would then be added in the pelletiser. The raw mixture behaved nothing like the iron sludge, and attempts at pelletising resulted in a greasy doughy mass. Follow ups, using finer ballotinis, conditioner and cement produced some pellets, but the product was still extremely different in characteristics compared to the iron sludge and no comparisons could be usefully made. In retrospect, the problem was caused by the simplifications that were the basis of the experimental design.

The use of ballotinis was a logical choice as they had been used in other studies of pellet behaviour [5, 100] and provided a consistent source of particles with minimal variations that could be subsequently altered in controlled ways. For reference, ballotinis are small glass spheres formed by the atomisation of molten glass which cools into spheres. After being produced, the size is then selected through sieving to produce consistent sizes.

This is supposed to be a blank state from which to work from. However, the smoothness, sphericity and low diameter variation actually have their own known influences on the properties of the product. For example, as established in section 2.3.2 and section 2.3.2, spherical particles result in a much lower packing state than particles of different aspect ratios. The choice of monodisperse parti-

cles will also result in the particles having significantly higher porosity values at minimum.

Secondly, the strength of the particles is dependent on the shape and interlocking of the particles, and spheres will have very little interlocking. The surfaces of ballotinis are also smoother than the scale particles, lowering the coefficient of internal friction, and both the internal friction and interlocking effects will be lowered by the use of the oils.

The oils too play their part in this inability to simplify the product. To perform the experiments consistently, clean 46,570 and 680 oils were used as they did not appear to have significantly different chromatography responses, and producing a consistently weathered oil product would not be simple, so these were used as a starting point. However, the weathering clearly resulted in some increase in cloudiness and browning not observed in the clean oils. The application of the oils in the feed first will have coated the ballotinis thus impeding the ability of the water to form any potential capillary bonds.

The application of the conditioner and cement did improve the ability of this feed to produce some pellets, but these were very oversized and generally not good comparisons and did not satisfy the goals of this experimental set. Some plans were considered to grind the CMS into smaller sizes and then produce an artificial sludge which was consistent, using a pelletiser with a spray that was included to carefully add moisture and rotate the drum at consistent revolutions etc. However COVID-19 lockdowns halted experimental work in this regard, and a much heavier focus was placed on the analytical side of the work, to such a point that after the lockdowns were lifted the theoretical work demonstrated much more useful results.

3.3 Discussion

That the ferrous components appear to have a large degree of hydroxides as part of their composition, based on both the colours and the iron:oxygen ratios [198] is beneficial to the pelletisation process, as hydroxides are more hydrophilic than the plain oxides [131]. Their presence is not unexpected, as they occur under alkaline conditions, and the raw sludge shows cement particles which would cause the settling ponds to become more alkaline [133]

The presence of the calcium, possibly being cement was not expected. On the other hand, the settling ponds are not exactly a highly secured location and so assorted dusts from the further processing or even the surrounding area could easily fall in. The total content of the calcium was relatively low, at around 5-10% of the measured elements. Other expected elements include the alloying elements such as tungsten, chromium and vanadium.

There were other tramp components that were much less expected. The fibres for example which could not be identified, and the particle of wood were possibly organic contamination. The high fluoride and sodium particle was also similarly unidentified, and generally indicate the fact that other particles do turn up, but these were specifically identified and are unusual.

The graphite may be a cause for concern. Where this appears from is unknown currently, though it is suspected to be kish, or precipitated graphite. There are other potential sources, as graphite is also used as a high temperature lubrication aid. Graphite is a highly hydrophobic material but is also quite oleophilic. Further work would be needed to determine this and the significance of it.

The morphology of the materials seemed to show generally that the scale was very flake shaped, as expected. The shape of the iron particles tended to be fairly similar across a range of particle sizes, with high angularity and relatively high aspect ratio. as the particles became smaller, the iron particles did start to have a lower aspect ratio, though still with a high degree of angularity. This might be

a consequence of the sieving process, the material is not handled gently when it is being prepared so breakage would still occur.

The other, non-iron particles show less angularity and have much lower aspect ratios in general, though they are present in a small enough quantity that this is unlikely to affect the overall behaviour.

The particle size distribution is surprisingly similar, on average to the Fuller curve, a commonly used starting point for efficient packing in concrete design for aggregate sizing [199]. This being the case, the packing may be expected to be more efficient than that for the ballotinis, which would be another reason for the failure of those experiments.

3.4   Conclusion

The black colouration of the sludge in Figure 3.1 appears to be derived from the combination of the mixture, as once cleaned the iron scale is a metallic grey while the oils are a brownish colour.

The material research above was mostly to get a basic understanding of the material and the context of pelletization to begin with. It gave a useful overview of the nature of the feed and its composition. Some of the main observations are the following:

- The particle distribution is highly variable, though within a given batch it seems to be relatively consistent.

- The liquid properties are highly variable between any given batch, and can even vary within a batch.

- There appears to be some degree of self-selection that occurs within the pelletisation process that contributes to pellet size variation.

- The scale distribution is roughly similar to that of the Fuller curve, which

is a high quality packing curve, reducing the cement needed and increasing the strength of a concrete mixture.

- The scale is significantly larger than typical pelletisation feed.

- The scale has high angularity, being flake-like at a variety of sizes.

- The surface of the iron has a high oxygen content and the colours of its oxides suggest that ferrous hydroxides are formed which is beneficial.

- The quality control is relatively low which is to be expected as it is ultimately a waste product. Even so the majority of the sludge is formed of iron which is fortunate.

- The composition of the liquid has relatively little correlation to the iron content.

With all this said, the impact of this is difficult to quantify, because the material is subsequently conditioned and cement is added. These alter the moisture and oil chemistry in ways that are difficult to quantify, since they also convert the liquid into a solid, altering the moisture content and generating smaller particles which would fill in the gaps. The conditioner manages the oil and water content, but as this is going to be dependent on the conditions of the surroundings where it is stored as well.

Given this, the inconsistency of the feed, and a generally poor understanding of what defines pellet size, simply testing different material additives would be a slow direction to go down and without any guarantee of producing meaningful results that could be used to enhance the production quality.

Once properties of the output have a reasonably well established theoretical backing, then would it be worth testing the effect of additives or alternative feed mixtures on the output. A suitable nondimensionalisation system would allow correlation between the additives to their effects on the process in a generalised

way, allowing evaluation of different feed types. Further, each batch could even be evaluated suitably and then corrected specifically with final additives with known effects on the production.

Chapter 4

DEM Kinetics Modelling

4.1 Context

One of the key factors in determining the growth rate was noted in the literature as being the value of St_{def} of the system. This nondimensional number is duplicated here:

$$St_{def} = \frac{\rho_g V_c^2}{\sigma_y} \tag{4.1}$$

This number describes the kinetic energy of collisions compared to the plastic deformation energy of those collisions. One estimate for the characteristic collision velocity is $V_c = 2R_{Dr}\omega$, based on the characteristic shear velocity of the pellet bed [4]. The yield strength is a matter of granular mechanics, which will be discussed in section 6.3, but the collision velocity is independent of this, and is well suited to being evaluated using a DEM model.

A DEM model is suitable for this problem because pelletisation is a discontinuous process. This makes it hard to model very well with a continuous solution, and a DEM is particularly well suited as it allows the tracking of every pellet in the system as desired by the solution. This has been performed in the past [43] as a solution to resolve the issues with scaling in pelletisation [34].

Population balance models have been applied in the past, however they require suitable calibration, without which a heavy reliance is made on assumed suitable interaction kernels. A kernel, for reference, is the function which takes in the relevant coordinates and alters the subsequent global distribution according to the interactions of each individual function. Non-physically based kernels exist and can provide suitable results for specific experiments, however these can be argued to be simply become a fitting exercise [200] and even when physical kernels are used fitting parameters are applied to provide results [81].

DEM can provide a method of modelling the interactions directly and test the behaviours with less assumptions about global properties or interaction rates or collision strengths than a population balance model. This in turn allows a more nuanced investigation of the emergent complexity of interacting parameters.

The conceptual framework of DEM, the mechanics of how this model will function and the surrounding software for this particular implementation will be covered in this chapter. This chapter will not contain results, as it simply lays the groundwork for subsequent chapters, with the initial kinetics results in the following chapter chapter 5. Further, because granular and agglomeration mechanics are quite complex and need significant discussion on their own, these will be examined in chapter 6 and chapter 7, and how they are implemented into the model will be discussed in chapter 8.

Given that particles are used to describe the component solids in agglomeration, to maintain a clear distinction in terms of definition, the spherical elements often referred to as "Particles" in DEM will be called "Spheres" only. Where necessary to distinguish between wall and spherical elements, wall elements will be referred to as such, noting that wall elements only apply force to the spherical elements, and are only moved according to pre-defined rotation parameters. Elements refers to all the elements both spherical and wall, or the general case beyond spherical elements.

4.1.1 Holmes DEM program

It must be recognised that this work builds on and uses previous work performed at Swansea university. The DEM model software being used is the one developed by Holmes [201], which is an extremely effective model and runs for a huge array of elements with great efficiency.

The program developed by Holmes [201] was designed to improve the previous DEM program used for TATA projects by Bridgeman [202]. The original model had a number of hard-coded functions, including moisture induced tension, and disregarded other functions, such as rotation behaviours and static friction. Though it was suitable for the purpose that it was designed for, that of slurry flow into a sinter house, it was ill-equipped for a broader specification, which lead to the re-development.

Holmes implemented a variety of systems which improved over the original, which are in summary:

- A generalised input system.

- Generalised mesh structure import system.

- Various Friction force components.

- More complex force application methods.

- An Octree system for collision detection efficiency.

- Parallelisation using OMP.

- Immediately readable VTU output system.

The program is extremely effective at managing the most difficult part to make efficient, the collision detection, with intricate inner workings, to the extent that most interactions with the codebase could significantly reduce the efficiency. Any contributions that were added always kept in mind the main strengths of the

code, though to be able to modify it at all required the code to be re-organised and many sections functionalised. There was some additions made, the most obvious being the eventual integration of the agglomeration subroutine, but these will be covered in the appropriate sections. Further, external codes were also developed which provided tools for both inputting and working with outputs.

4.2 Conceptual Framework

4.2.1 What is DEM

DEM describes a range of numerical methods that simulate the behaviour of discrete elements and their interactions. It is well suited to the modelling of granular flows, since every individual component can be treated separately, with their own properties. Here each granule of the granular material can be represented as a single sphere (defined by its coordinates and radius) with associated intrinsic and extrinsic variables (density, velocity, radius etc.). The physics are applied at specific time steps, with force giving acceleration, acceleration giving velocity, and so on. The sources of the physics can be external such as collisions or interactions with other elements, or body forces, which are defined solely by the internal parameters such as gravitational force.

The simulation can allow a better understanding of the behaviour at any stage, and behaviour that could not be determined without such a simulation can also be found, such as the collision strength. Other properties can be introduced such as saturation and stiffness based on the specifications of the model.

DEM Variants

As stated, DEM describes a range of models, since there are a few ways to model the interactions between discrete elements. Primarily, the distinction is whether the elements are permitted to intersect or not. Allowing them to intersect, and

169

from this intersection the subsequent behaviour develops is called a "Soft-sphere" model. A solution where the elements are not permitted to intersect, and instead the calculations are performed at the moment of interaction to determine the subsequent behaviour is called a "Hard-sphere" model.

The hard sphere model might seem to be the more realistic option, however in practise it is somewhat unstable when applied to packed beds and tends to only be suitable for sparse systems. Consider that the material does also have a very slight intersection, in that the strain of the granules pressing into one another applies a resistive force. A hard sphere model would require additional models, such as FEM to account for this strain based resistance.

There are other parts of the method that can vary between models. The interactions are defined by the developer of any given model, and these can differ depending on priorities or restrictions. In a soft sphere model, the degree of intersection and relative velocity is usually used to dictate the subsequent force response. This can be relatively simple, such as assuming a constant spring stiffness and thus a force response that is proportional to the intersection, to complex increasing slip and elastic-plastic interactions that are derived from hertzian mechanics.

For all such models, the challenge is balancing the computational cost versus the result benefit. A simpler model will be significantly faster, and in granular materials, the behaviour is intrinsically tied to the number of elements in the system. this is significant enough that a very physically realistic system for two individual elements interacting might be completely lost in the bulk behaviour that a very simple system can model perfectly well, and faster allowing more elements to be included.

4.3 Model Mechanics

The soft-sphere model is used in this work. The elements are permitted to overlap, and the contact forces are calculated in relation to this overlap. A linear Spring-Dashpot-Slider model is used to represent the degree of resistance, which will be covered in detail in subsection 4.3.1. This model provides a good approximation for granular flow behaviour for elastic-plastic granules, and the visco-elasticity that is approximated by the dashpot accounts for the coefficient of restitution. In the case of wet agglomerates, the strength and stiffness is explicitly strain rate dependent making this approximation even more suitable.

Other stiffness models which directly use the known stiffness values exist, but have practical limitations [203]. The variable spring stiffness causes problems for calculating the suitable time step, see subsection 4.3.3. It also requires knowing what the stiffness is, and as established in the literature the strength and stiffness calculations are simply not available for most wet agglomerates.

The model implements a material system, which allows the stiffness of each material and the friction and damping factor between materials to be introduced on a per-material basis, and then simply defining elements in terms of those materials.

The pellets are approximated using spheres, which is appropriate as they are very close to spherical to begin with. Were this not the case, then a few options would be available. Non-spherical elements in the form of both polyhedral as well as superellipsoidal elements have been implemented in the past [204]. They increase the complexity of the tracking and collision behaviours, and for granular flow behaviours adjusting the frictional parameters seem to be sufficient to account for the higher angularity and angular momentum [205].

The force calculations are almost completely unchanged from the original code developed by Holmes [201], with only the material variables changed appropriate to the material, and are reproduced below for clarity.
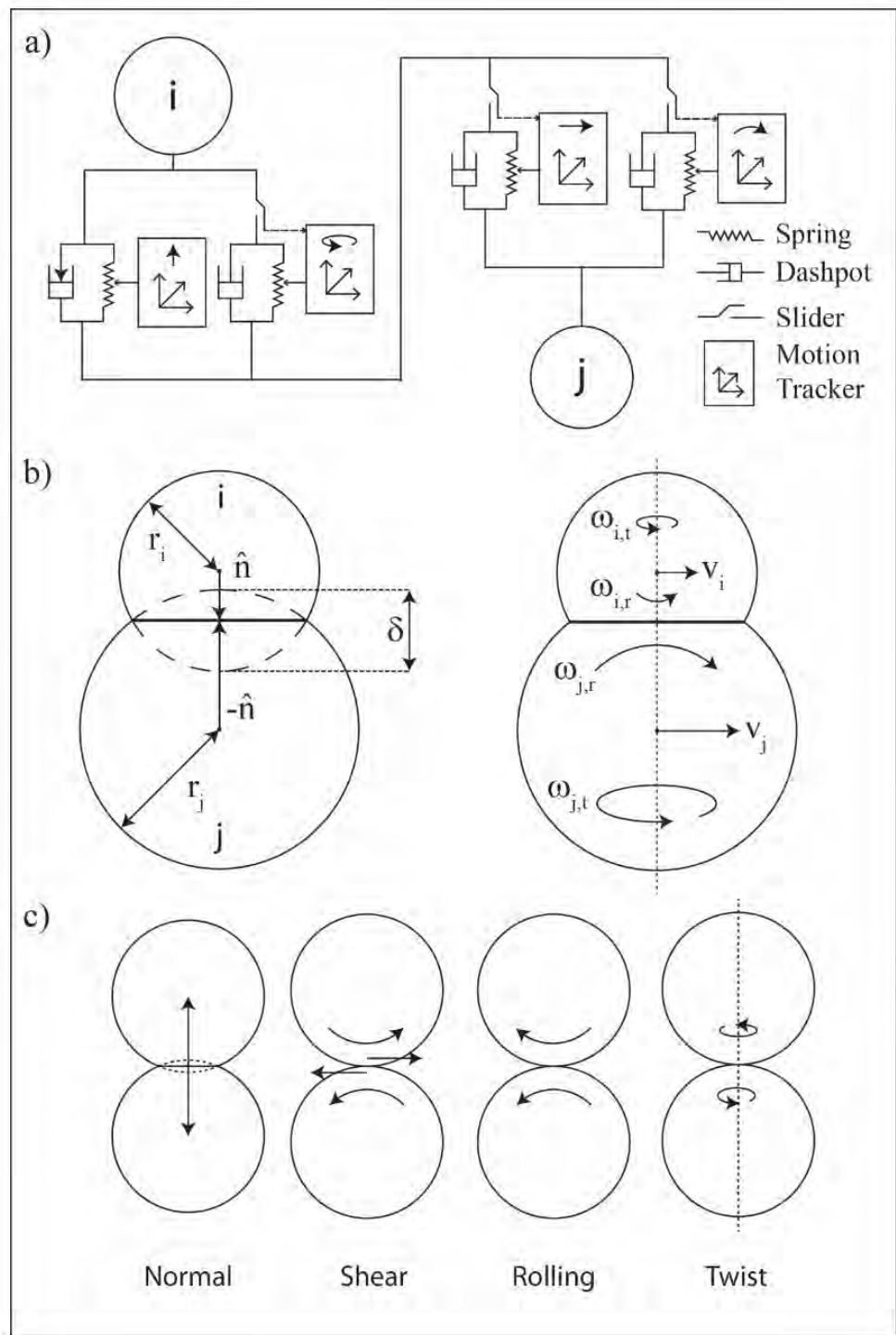
Figure 4.1: Model graphical overview. a) Shows the force model, b) provides the distance and velocity definitions and c) lists the degrees of freedom in the model. Figure 38 from [201]

172

4.3.1 Forces

A spring-dashpot system calculates the normal forces as the elements intersect and they apply a reaction force to one another (the spring), while losing kinetic energy to other effects such as plastic deformation or viscous damping (the dashpot). For tangential forces (such as shear, bending, and twist), a slider is included which limits the maximum strength of the spring-dashpot system, to represent slip between the elements which is greater the less overlap is occurring. A graphical overview of the model can be seen in Figure 4.2

The force being directly proportional to the extent of overlap, which allows a simple spring constant to suitably model the element interaction, is a very useful consequence of the nature of spherical interactions and how the depth of deformation and contact radius happen to cancel one another out. [114]

Overlap

The overlap δ is determined using Equation 4.2. This value is used by most of the following equations in some form or another.

$$\delta = |D| - (r_i + r_j) \tag{4.2}$$

Normal Forces

The normal translational forces in the spring-dashpot system are the simplest to describe. The spring forces simply directly use the overlap δ with a spring constant k , Equation 4.3.

$$F_{kn} = k\delta \tag{4.3}$$

The damping force meanwhile multiples the normal velocity V_n by a damping factor F_{dn} Equation 4.4.

$$F_{dn} = \zeta V_n \tag{4.4}$$

These two are added to give the total normal force Equation 4.5.

$$F_n = F_{dn} + F_{kn} \tag{4.5}$$

The force only needs to be calculated for one element, as the other element will experience the equal but opposite force.

A non-returning damper can be used, which simply sets $F_{dn} = 0$ while $V_n < 0$. This models the fact that the restitution resistance would not apply when the elements are moving away from one another.

Shear Forces

The tangential forces are more complex, as they need to account for the distance to the interaction surface, and also include sliders, as mentioned to account for slip. The shear friction, or the tangential translational force, is described via Equation 4.6

$$F_s = min\left(k_s\delta_s + \zeta_s\dot{s}, \mu|F_{kn}|\right)\hat{s} \tag{4.6}$$

$k_s\delta_s + \zeta_s\dot{s}$ gives the spring-dashpot calculation for the shear, while $\mu|F_{kn}|$ gives the slider, which uses only the normal spring force, not the entire normal force. This format will be seen for the remaining spring-dashpot-slider forces.

The Shear, being applied at the surface, also applies a torque. The shear torque can be calculated simply via Equation 4.7.

$$F_{kn} = k\delta \tag{4.7}$$

$r_{c,i}$ is the rotation vector, which is based on the centre of interaction of the elements colliding.

Rolling, Bending, and Twisting Forces

The remaining torque comes about as a result of rolling friction. This is decomposed into bending and twisting for model accuracy reasons.

The bending torque is most easily determined by first calculating the bending force at the centre:

$$F_{r,i} = -min\left(k_r\delta_r + \zeta_r\omega_{r,sum}, \frac{\omega_{r,sum}}{|\omega_{r,sum}|}\mu_r|F_{kn}|\right) \tag{4.8}$$

$\frac{\omega_{r,sum}}{|\omega_{r,sum}|}$ provides a vector for the force to apply in the correct direction. The reason to calculate the force is so that the torque can be applied appropriately to each element. The bending force is symmetric unlike most interactions which are anti-symmetric, which makes the calculation of the bending torque calculated as Equation 4.9

$$T_{r,i} = r_{c,i} \times F_{r,i}$$
$$T_{r,j} = r_{c,j} \times F_{r,i} \tag{4.9}$$

The twist friction is the final torque that needs to be accounted for. This is calculated using Equation 4.10

$$T_{t,i} = -min\left(k_t\delta_t + \zeta_t\omega_{t,sum}, r_{eff}\frac{\omega_{t,sum}}{|\omega_{t,sum}|}\mu_t|F_{kn}|\right) \tag{4.10}$$

The twist is anti-symmetric, unlike bending, which means that Equation 4.11 is used.

$$T_{t,j} = -T_{t,i} \tag{4.11}$$

Structure System

The representations of the granules are spherical elements, but the surrounding structures may ba much wider range of shapes. Given that a key part of the testing would be determining what effect the shape of the agglomeration drum

has on the dynamic and kinetic behaviour, being able to have complex geometries would be important.

The complex geometries were implemented using triangular meshes, which could be generated in any form desired. Each triangle is defined in terms of its three corners, which gave a plane, and the normal vector.

The plane of the triangle, along with the normal could be used to calculate the wall-pellet interactions using the same system as between pellets, including the depth of overlap calculated with respect to the plane. Additional adjustments need to be made to account for the fact that not all the interactions will be simple direct interactions, and could partially interact with multiple wall elements, as would be needed if any degree of convexity exists in the wall structure. To resolve this the intersection area is calculated.

For any given sphere-triangle intersection the sphere can be used to calculate a projected circle, see Figure 4.2. This circle can then be compared to the intersection of the triangle on the sphere. This allows the total force to be divided according to the amount of overlap. This method allows interactions of the sphere to occur between both convex and concave shapes at the same time by decomposition of the forces.
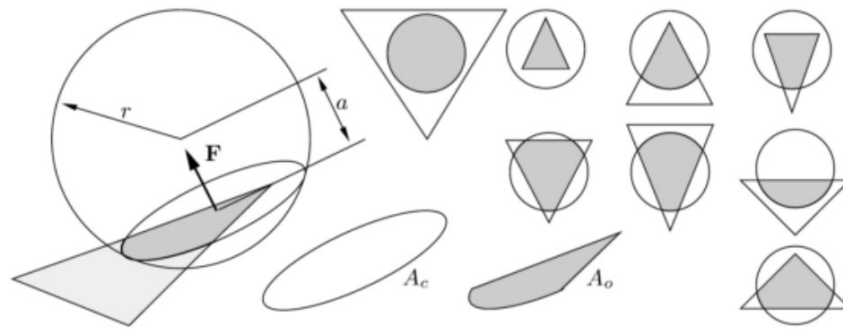
Figure 4.2: Possible sphere collisions with a triangular polygon. The A_0/A_c gives the proportion of the force applied according to each planar interaction. Figure 34 from [201]

176

Body forces

The body forces are applied last to the spheres, for efficiency reasons. The body forces are those which only consider the individual spheres own properties, ignoring other surrounding elements. In this case, this only applies to gravity.

One of the modifications to the model that was applied early on was a gravity vector $\hat{g}$. This results in a gravity force

$$F_g = mg\hat{g} \tag{4.12}$$

This solution allowed the rotation to be simply defined in terms of Euler angles over time, with the angle of the drum being altered using the gravity vector.

4.3.2   Integration

The forces are all separately calculated for each interaction, and then stored in an array, then summed up in a subsequent stage. Finally, the body forces are also added. Because the forces are all added at the end at the same time, the round off errors are reduced, improving the overall consistency and accuracy of the system. With all these forces calculated, the model finally integrates the resulting acceleration, velocity and displacement changes.

The integrator routine uses central difference Euler integration, which in turn utilises a Taylor expansion of the forces and velocities involved to improve the long term stability of the results.

4.3.3   Time Step

The time step is quite important for the simulation behaviour. Too large a time step causes instability and tunnelling of the spheres, while small timesteps take longer and longer. The critical timestep T_c where any longer than it results in instability varies between models, but the general formula is

$$\Delta t \leq C\sqrt{m/k} \tag{4.13}$$

With C being a constant [206], estimated between 0.2 and 0.2π system dependent, the equation being based on harmonic frequency of interactions. If this timestep is exceeded, energy conservation errors accumulate, resulting in unrealistic results.

An alternative time step limit noted by Holmes [201] is that because there is a spring in the rotation limit, an additional critical timestep occurs in the rotation direction, with the formula

$$\Delta t \leq C\sqrt{I_i/k_r} \tag{4.14}$$

This is the primary reason that the spring method is used. Because the value of k is constant, and m is a function of the diameter, the time step can be set to the lowest stable time step for the entire system. Other methods with a variable stiffness cause problems when applied in this regard.

4.3.4 Material system

The material system is part of the model which accounts for the variation in interaction parameters which exist between different materials. For some properties such as Poisson's ratio or stiffness, this is internal so only needs to be recorded once per material. For others, such as Friction or damping factor, this needs to adjust for both materials, leading to a lookup table for each material-material interaction being required. The effect of different spring stiffnesses for interacting elements can simply be calculated using the Poisson's ratio and the stiffness of both to adjust the force of the interaction.

This then allows the elements to simply have a material defined, which simplifies the subsequent defining procedure. The density of the materials is not

included in this material definition, rather this is defined during the element spawning section, and other properties can be defined here too.

This allows three levels of generality for the materials input, as needed for specificity:

1. Global: They can be defined using values that applies to all elements, such as the acceleration due to gravity,

2. Material: They can be defined using values that applies to only those elements with an assigned material, and link the property to the material, such as the spring stiffness or frictional response to other elements.

3. Spawn: They can be defined on a per spawner basis, such as the density or the material.

Wet agglomerates have a number of unique features which are not covered by these. The implementation of these require suitable mechanics, and so how the mechanics are introduced into the model are covered in chapter 8.

4.4 Software system

The model is part of a greater program, which has to perform many of the features abstracted away in the model equations. For example, the distance between the elements has to be actively determined in an efficient manner.

4.4.1 Codebase

The code was written in FORTRAN90. FORTRAN is a relatively low level language, and it struggles with I/O and has little object-oriented functionality. FORTRAN90 can work with structs, a data structure which can allow many data types to be associated together as a single unit and even type-bound procedures which can be restricted to them, but the language is not especially suited to

this. Overall, FORTRAN is well suited to numerically intensive algorithms that comprise the majority of the work that the program performs with only a small amount of I/O involved, and because it is low level the amount of overhead is minimised.

The supplied code, though efficient where it mattered, had a large degree of duplication and non-functionalisation. The top level code, which provided the start and end of the program, had over 4500 lines, which was able to be halved using functionalisation and removal of redundant sections and re-organisation of the assorted routines which allowed the code to be better manipulated and understood.

4.4.2 Collision Detection

When programming any sort of model, the computer cannot simply ask for "when" X occurs, do Y, as simply occurs in physical systems. Each interaction needs to be directly determined at each time step whether it is colliding or not. As such, this can lead to a very rapid increase in time spent checking whether collisions are occurring. If one used a naïve check on all possible interactions, the performance is $O(n^2)$. Further, determining distance requires performing a square root, which is a relatively complex and time-consuming operation.

The program significantly improves this using a variety of systems which minimises the total number of checks required before individual checks get performed. One of these which is easier to describe is the octree system. This divides up the simulation space into subdomains, and this can be done both recursively and efficiently. The first pass of searching can then be restricted only to those elements within specific boxes based on the current location, velocity and previous interactions. Further culls can then be applied, which results in a much more refined list of collision, stored as an array of structs that require testing. The elements require sorting, for which a specific parallel merge/binary sort was already present and not modified.

Only the collision structs were slightly adjusted. A Boolean variable was included which noted if the initial collision variables had been recorded.

4.4.3 Parallelisation

The program was written to run in parallel. This is a method which allows a program to run on multiple threads in a CPU, which theoretically allows it to run faster. The method is however limited by the communication requirements of the program, and the presence of parallel unique bugs.

The ideal problem to parallelise is one in which no communication is required, and the only input and output occurs once the program has concluded. These types of super scaling problems appear more like separate programs that all happen to be solving the same problem with slightly different setups, and work because they can find the answer once between them, and then let all the other threads know to stop.

A more typical parallel setup, such as one where the threads are all working on the same dataset, communication is required to divide the load as evenly as possible between the threads, ensuring that the threads are not overwriting any data that is by necessity shared, and re-collecting the data for re-distribution. The re-distribution is important since some threads might finish sooner than others, or the workflow might remove data from the work or add new data that will be in turn necessary to process. Managing the workflow thus is an important task, and an example is the use of a collision struct to ensure that each collision is tested once, while also allowing the collisions to be distributed between an arbitrary number of threads.

Other limits can be found in the intersection between the hardware and software, since the amount of data that each thread works with is intrinsically limited by the amount of data that can be supplied from the RAM at the rate of processing.

The parallelisation was implemented using Open MP, an open standard API

which facilitates thread communication. Though it has some flaws, it being an open standard means that implementation resources are reasonably available and the system is not overly complicated.

4.4.4 Compilation challenges

The code had certain specific requirements, which lead to unfortunate compilation bugs. More specifically, compilation pre-processor definition issues. Compilers are typically quite efficient at their task, and can have various settings chosen to define options, such as whether file size or speed should be optimised, which pre-processor definitions should be checked and compiled into the program, and so on.

This sometimes lead to a situation where the program was compiling successfully, but being unable to run a useful model. The first issue was that stack overflows were occurring in every model with any degree of complexity. Tracking this down identified a recursive function as the location where the memory would overflow. This suggested that the recursive function failed to ever trigger the exit parameter.

However, a sample pre-compiled program was provided with the original codebase, and this code was successfully running suitable model scales, only limited in that it would not output the required data and did not have a gravity vector, so was not suitable for direct implementation into this project. The makefiles for these, which provide compiler settings when compiling in a different way to visual studio, gave no hints.

After much testing, the found was that the compiler was failing to set the program to demand as much memory as it required. Setting the permissible memory to maximum resolved the stack overflow issues. However, the program was still not compiling in parallel, despite the apparent setting being selected in Fortran→general. This was because though the compiler was ready to compile in parallel, it was not set to read the OMP directives which automatically pro-

vide the instructions as to where compiling needs to occur, which were found in Fortran→language.

4.4.5 Modifications

Some modifications to the program and external procedure were developed as well. These do not include modifications for the purposes of testing granule mechanics or agglomeration, which as mentioned are discussed in chapter 8

Outputs

Another significant feature that was added directly into the program was the ability to output the collision behaviour, using OMP directives to track each collision only once, while remaining within the parallel region to maintain efficiency.

The collisions are recorded at the initial moment of collision. The method used is essentially the one used by Nakamura et al [43] where the collisional energy is recorded only on the first time step that the spheres are intersecting. A key difference is that in their system, the collision energy is tracked with the spheres, while here the collision properties themselves were recorded, such as the location of the spheres, their radii and their velocities in 3D space.

Other changes to how the results were stored was that the output spheres and structure .vtu files, and collision .bin files were placed into a subfolder which is noted with the date and time of the production of the file.

Additionally, as the original program output a lot of additional files that were unused in this solution, these outputs were removed from the system to reduce excess hard drive space used.

Gravity Vector

A minor, but relatively important feature that was added was the implementation of the gravity vector specification. This was useful in specifying the angle of the

drum quickly, but more importantly since the structure rotation code rotates around the global axes specifying a rotation of a rotating angle would require altering the global coordinates of the system, and the gravity vector is doing this with less computational overhead.

STL generator

The structures are composed of wall elements, and these wall elements are defined from input .STL files. STL files are 3D triangular surface mesh definitions, which include a normal for each triangle, allowing complete definition of the element.

Originally, the STL files for the structures required constructing them in solidworks, and then subsequently converting the object into an STL file using blender, which sometimes needed refining to ensure that all the surface normals functioned correctly.

The complex geometries were implemented using triangular meshes, which could be generated in any form desired. The file format in an STL file format. Each triangle was defined by the three corners and the normal, which allowed the plane of each triangle to be calculated.

Because STL files have a relatively simple data format, a shape could be defined, for which a mesh could be generated algorithmically. This mesh, including the direction of the normals could be decomposed into triangles, and then have those triangles along with a normal (which can be found automatically as well by figuring out which normal is closer to the central axis) be written out.

An external program using MATLAB was created which allowed the creation of axially symmetric shapes, such as drums, and plate sections which can be oriented in any direction for testing purposes. A method to allow the axially symmetric shape to be offset to introduce a helix was also included. This allowed rapid development of drum designs to fit the measurements of the drum being tested on site and theoretically test alternative designs.

VTU to .mat file converter

Another program was developed to analyse the results. Because the output is in VTU binary file format, it is possible to re-assemble the original data from the binary data directly using data casting, which was done in MATLAB.

This allowed the data to be extracted directly from the VTU files and from there any statistical data desired, while retaining the benefits of the original VTU Binaries relatively high efficiency data storage. Even so, because extracting the data takes a long time, one program was built that extracts the data and stores it as a .mat variable file, which is much faster to process for further statistical analyses.

Chapter 5

DEM Kinetics Results

With the concept of DEM, the model mechanics and the surrounding software covered, the results of the initial implementation will be covered in this chapter, with results.

The goal here is to determine first if granular flow behaviour can be modelled acceptably, and if so then determine if the behaviours thus observed can explain any of the variation in the size output, without agglomeration mechanics needing to be involved yet. Alternatively, are there any characteristics the granular flow that can be used to produce a more consistent output? This has been able to be done using active controls, but altering the drum shape could suggest ways of improving the consistency through passive means which would be much more reliable, since they would not require monitoring and simply use the granular mechanics itself to control the flow behaviour.

5.0.1   Models

Two sets of data are reported. One set is of the lab scale simulations, which were based on the measurements of the previously mentioned lab scale design which compared the effects of different setup variables, the other group compares the effect of varying the geometry of the drum. For both sets, a range of data is

evaluated, such as the segregation, the collision data and the velocity trends.

5.0.2 Diameter of elements

The distribution of the element sizes were either trimodal, or based on a Fuller curve distribution. Monodisperse elements were not tested as this would not be able to show the effect of segregation, and since polydispersity was going to be used a trimodel distribution was selected so as to represent the diameters of the undersize, the target size and the oversize. A power law curve was used for the continuous distribution as it is reproducible and consistent and describable using a simple formula, Equation 5.1 [207] and is used for maximum packing calculations, though it likely overestimated the quantity of the largest element sizes present in practise.

$$p = 100 \times \left(\frac{d_s}{D_s} \right)^m \tag{5.1}$$

where p is the percentage of material passing a sieve with an opening d_s , D_s is the maximum element diameter and m is a variable exponent. This predicts a maximum at around $m = 0.4 - 0.5$, assuming infinitesimally small particles. This is not feasible, due to time step limitations. Instead, the minimum and maximum radii were set to the same for both distributions, of 2.8mm radii minimum and 18mm radii maximum (5.6mm and 36mm diameter respectively), with m set to 0.5. the trimodal distributions meanwhile were set to an equal quantity by mass of each diameter.

5.0.3 Material Choices

The material choices were relatively simple. The pellet densities were calculated assuming the particles were 100% magnetite, with a porosity of 0.3, leading to a density of 70% of that of magnetite, rounded to 3640 kg/m³.

For the materials, the design is relatively simple. The walls and the pellets are formed of the same material, allowing the material to be assigned the same to both.

This is because the walls of the industrial drum are actually formed out of the feed material. When the walls of the drum are being crafted due to the previous wall being worn out, the old walls are removed and new walls are created by using the feed mixture. A batch is prepared and then a slight excess of moisture added, so that it forms a 'concrete'. This mixture is then poured into the drum, and the scrapers which prevent the pellets from sticking to the walls normally actually carve out the wall shape to perfectly match their shape. This is a cheap way to provide ablative reinforcement to the walls which also matches the scrapers perfectly, and can be fitted to any shape of interest. Further, the material of the pellets will leave traces on the walls, which will balance out the material surfaces even if the wall is dry and the pellets are not.

As such, the material setting, and hence frictional/damping values for the full scale models were identical to the material of the pellets. Even so, some simulations were run to examine the effect of varying the interaction variables between the pellets and the sidewall to determine what effect this might have.

The material stiffness was set to 4000N/m, which is relatively low for a DEM simulation [206] but not unreasonable, given the low stiffness values noted in the literature for wet agglomerates. Fortunately, for flow in a drum, the behaviour is relatively insensitive to the stiffness [208].

5.0.4   System Values

The non-material values consist of the geometry of the drum, and the rotation rate of the drum.

The geometries of the model drums are the lab scale drum, 1m in diameter, 20cm deep and 20cm high wall on the input side.

Meanwhile the geometry of the full scale drum is 2.2m in diameter, and 2.1

m long. The full length of the drum is longer at 8m, however modelling the full length was not needed to observe the steady state behaviour, so only modelling the input section was deemed acceptable. The ridged version had ridges 6cm tall, about 2cm thick and occurring roughly every 16cm (the ridges transition smoothly to the top of the ridge and down again leading to a slope). The helical ridge design is oriented such that the ridges smoothly transition in a continuous screw.

The rotation rates were intended to be scaled accurately between the two drum sizes. This was to be done using the froude number, $Fr = \frac{\omega^2 R_{Dr}}{g}/$, to maintain kinematic similarity between the two dimensions, such that the regimes would be the same comparing between the scales, see Figure 5.1 for the assorted regimes.
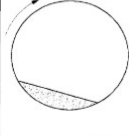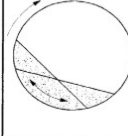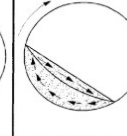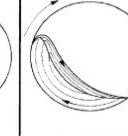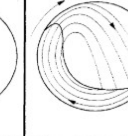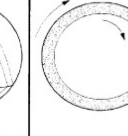
Basic form	Slipping motion		Cascading ("tumbling") motion			Cataracting motion	
Subtype	Sliding	Surging	Slumping	Rolling	Cascading	Cataracting	Centrifuging
Schematic							
Physical process	Slipping		Mixing			Crushing	Centrifuging
Froude number Fr [-]	$0 < Fr < 10^{-4}$		$10^{-5} < Fr < 10^{-3}$	$10^{-4} < Fr < 10^{-2}$	$10^{-3} < Fr < 10^{-1}$	$0.1 < Fr < 1$	$Fr \geq 1$
Filling degree f [-]	f < 0.1	f > 0.1	f < 0.1	f > 0.1		f > 0.2	
Wall friction coeff. μ_w [-]	$\mu_w < \mu_{W,c}$	$\mu_w \geq \mu_{W,c}$	$\mu_w > \mu_{W,c}$			$\mu_w > \mu_{W,c}$	
Application	no use		Rotary kilns and reactors; rotary dryers and coolers; mixing drums			Ball mills	no use

Figure 5.1: Forms of transverse motions of solids in rotating cylinders. Table 1 from [157]

This requires knowing the radius of the full scale drum as well as the rotation rate. This was reported to be 10rpm, and so the lab scale drum was scaled appropriately, to 14.2 rpm. This turned out to be an overestimation by the technicians, and explains why the results for the lab scale drums appear to be

189

cascading rather than rolling. When measured on site, the rotation rate of the full scale drum was determined to be 8 revolutions in 65s at full load, or 7.62 rpm. This would give an actual scaled rotation rate of 10.95 rpm. Because the simulations take a while to run, and some useful data was still found from the higher rotation rate values, these results are still reported. The tangential velocities of the drums from these rotation rates were 0.7766m/s for the small scale and 0.8506m/s for the full scale respectively.

The fill degree in the models is quite low for granular materials, especially compared to much of the literature on the topic in the field. However, in pelletisation the fill degree is low as well, with the actual drum filling on site typically being roughly less than 10% full.

5.0.5 Observations and hypotheses

Because the pellet distributions are known to have a large quantity of fines, as shown in Figure 3.6, this can be a useful method of testing the kinetic hypotheses suggested by some of the authors in the literature. Consistently, there is around 10% to 20% under 5mm regardless of moisture content, and the small pellets of 5-6.3mm diameter constitute another 20% to 40% . This is the ideal situation to test the scenario for the kinetic bounds for agglomeration.

For example, the Stokes criterion expects that as the collision energies increase, the total particle size will be smaller. Given that there is a range of pellet sizes observed, this means that if it is correct then the smallest spheres should be experiencing the strongest collisions, and the largest spheres experiencing the weakest collision. On the other hand, The Ouchiyama and Tanaka, or Bond Probability model meanwhile would predict such a distribution if there is regions of high collision strength to initiate the bonds for the larger granules as well as regions of high shear which would tear the formed bondsto limit indefinite growth.

The reason for the helical design being tested was because during conversation with technicians an idea for a passive growth control was considered. The effect

190

of segregation is that it forces larger objects to the top of a pile. therefore, if the granules could be all pulled back, using a helical screw design, then only the largest granules would tip over the ridges, eventually being output. This could be measured by seeing if there was a positive correlation between $\dot{z}$ and R meaning that the smaller particles are slower, meaning that the retention time is longer thus promoting growth.

The results shown primarily show the behaviour as values across an x-y domain averaged in the z direction. This is because the behaviour of the collisions will vary significantly in different positions around the radius of the drum, and this cannot be effectively captured using simply slices from the centre to the boundary. The behaviour is not rotationally symmetric, and the segregation is a feature of interest when considering the above interest in the kinetic behaviours that are expected by different models.

5.1 Results

The properties of the cases used are summed up in Table 5.1 and Table 5.2, which describes the universal values and the specific values of the properties applied respectively.

5.1.1 Table summaries of Model Data

Density	Stiffness	Poisson's Ratio	e_{rest}	
3640kg/m^3	4000N/m	0.1	0	

S-S μ	S-S μ_r	S-S ζ_r	S-S μ_t	S-S ζ_t
0.8	0.8	1.5	0.8	1.5

Table 5.1: Baseline values for the Spheres as they interact. S-S indicates Sphere Sphere contact.

191

The μ, μ_r, μ_t describe the sliding friction values of the spherical elements against one another for shear, bending and twisting interactions, and the ζ_r and ζ_t values describe the bending and twisting damping values referred to in sub-section 4.3.1. S-S indicates element-element interations, while W-E indicates wall-sphere interactions. The variations tested are the lab scale drum with a trimodal distribution, and three power curve distributions, one with baseline values, one with lowered rolling friction values across all spheres, and one with lowered interparticle friction values but baseline wall friction values.

Case	Lab Sim A	Lab Sim B	Lab Sim C	Lab Sim D
Distribution	Trimodal	Power Curve	Power Curve	Power Curve
S-S μ_r & μ_t	-	-	0.2	0.2
W-S μ_r & μ_t	-	-	0.2	-

Table 5.2: Model Details for Lab Scale tests. Values labelled - are same as in Table 5.1

The full scale models all use the frictional values listed in Table 5.1, but they differ significantly in the shapes of the respective drum designs. These will be shown in subsection 5.1.2. The results describe the three full scale models, Blank Trimodal Model (BTM), Ridged Trimodel Model (RTM), Helically ridged Trimodal Model (HTM)

The Trimodal distributions use an equal proportion of 5.6mm, 16mm, and 36mm diameter spherical elements by volume. The Power curve distributions meanwhile use Equation 5.1 to define the distribution, as a continuous function, from 5.6mm to 36mm and an m of 0.5.

Both the full scale and the lab scale drums were continuously filled, as the influx of new particles were expected to alter the behaviour of the particles within the drum in the full scale model.

5.1.2 Paraview Demonstration

The primary benefit of outputting the results in the VTU format is that the behaviour can be immediately evaluated using Paraview, an open source program used for visualisation. An image of the final frame for each of the simulations will be shown here to demonstrate the actual models, as well as the variation in the raw and smoother averaged data shown.
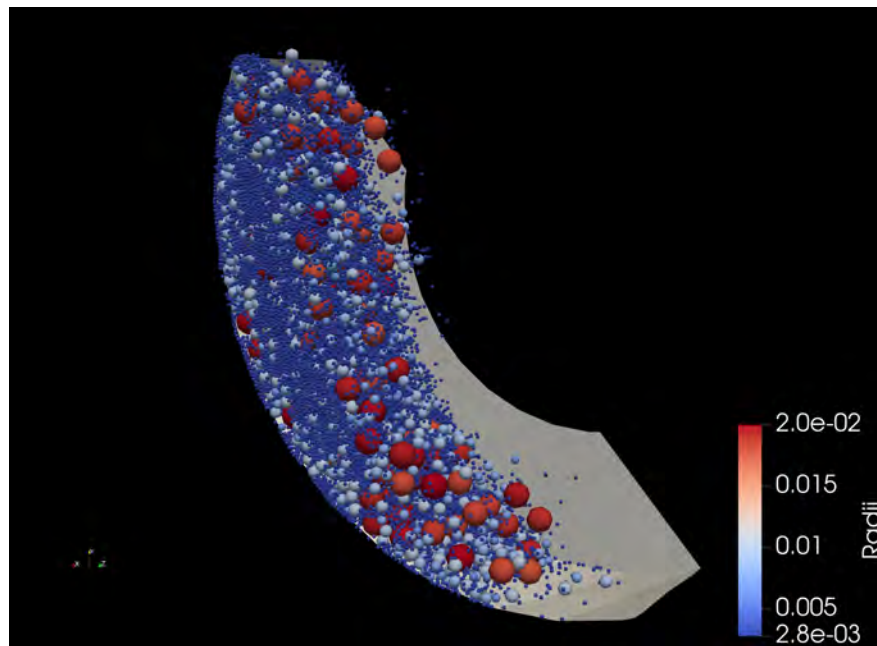
Figure 5.2: Paraview image of Lab Sim A - A DEM model of a Lab Scale drum simulation with a trimodal distribution of spheres. This image is the last frame of the simulation testing the kinetics of the drum.

Figure 5.2 and Figure 5.3 show that the shape of the pile, at least for this set of material parameters, is roughly independent of the distribution. Segregation can also be seen occurring, with the large spheres on the top of the pile, and the smallest in the middle.

The 3D perspective from this format allows a distinction not obtainable from a simple side view. Figure 5.8 shows how segregation can occur in multiple directions. This type of segregation is not seen in Figure 5.6 or Figure 5.7. To
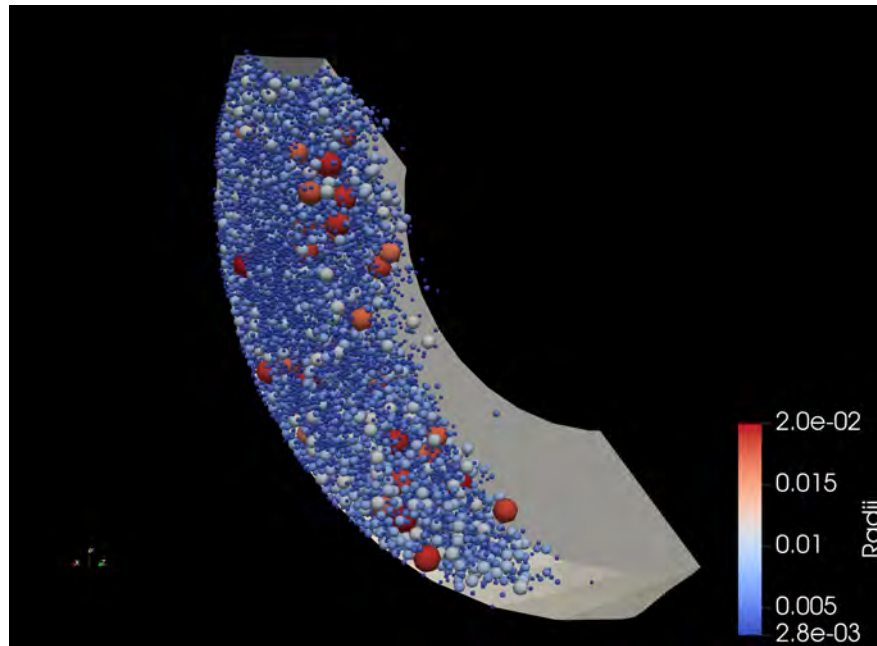
Figure 5.3: Paraview image of Lab Sim B - A DEM model of a Lab Scale drum with a power law curve distribution of spheres. This image is the last frame of the simulation testing the kinetics of the drum.

keep descriptions clear, cylindrical coordinate descriptors will be used. Therefore, Figure 5.8 shows axial segregation (the group of larger red sphere close to the end), radial (the red spheres emerging from the centre of the bed and pushing towards the centre) and azimuth segregation (the red spheres at the bottom of the pile and the deep blue small spheres at the top of the pile)
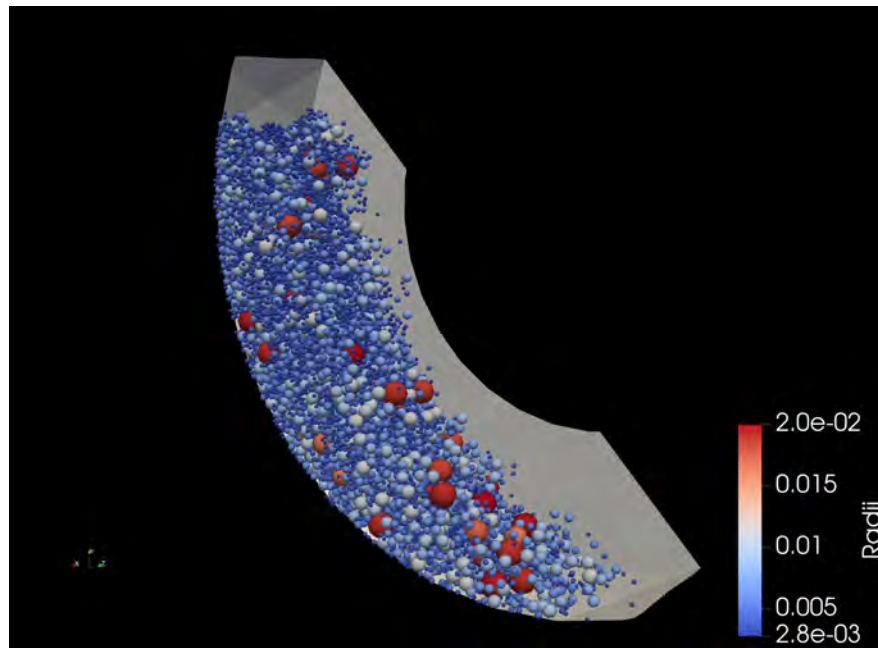
Figure 5.4: Paraview image Lab Sim C - A DEM model with a Power curve distribution spheres in a lab scale drum, with reduced rolling friction between spherical elements and against the wall elements . This image is the last frame of the simulation testing the kinetics of the drum.
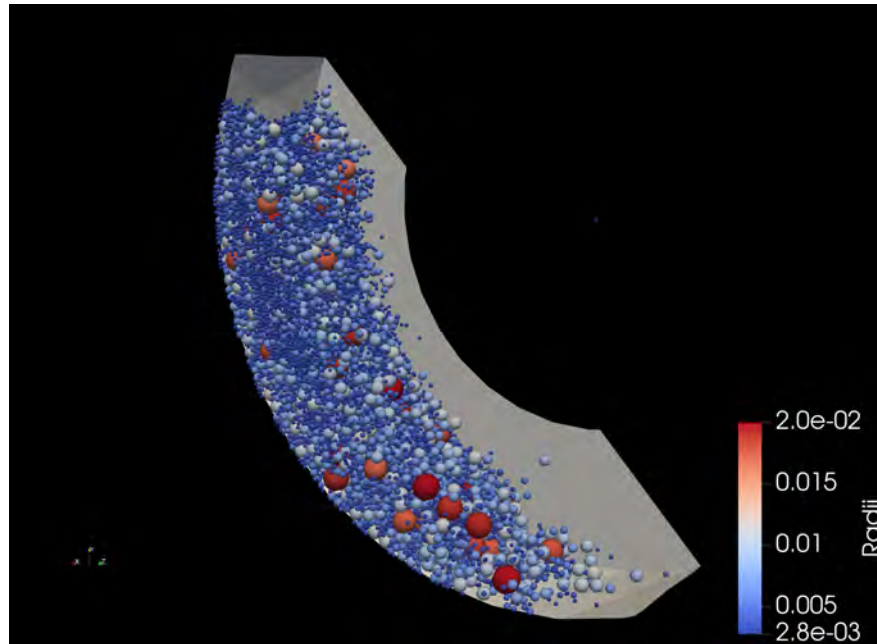
Figure 5.5: Paraview image Lab Sim D - A DEM model with a Power curve distribution spheres in a lab scale drum, with reduced rolling friction between spherical elements but not against the wall. This image is the last frame of the simulation testing the kinetics of the drum.
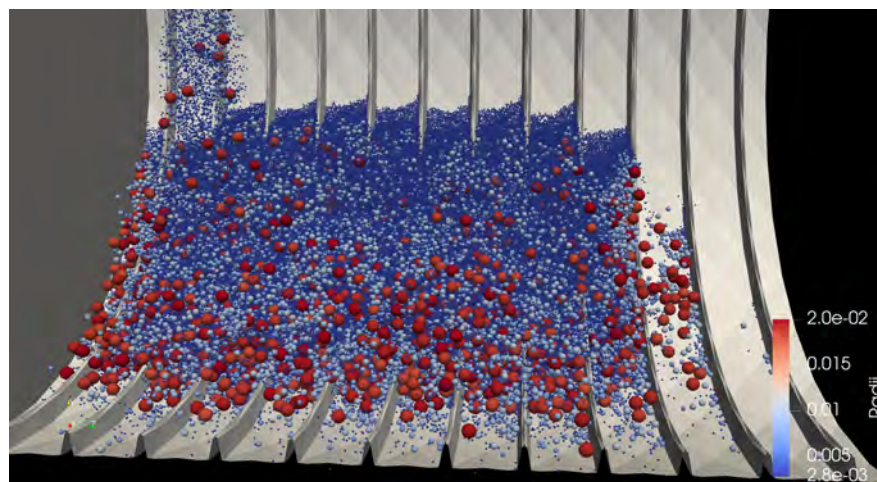
Figure 5.6: Paraview image of the Trimodal ridged model - A DEM model simulating the kinetic behaviour of a trimodal distribution of spheres in a drum of similar dimensions to the real world drum used on site.
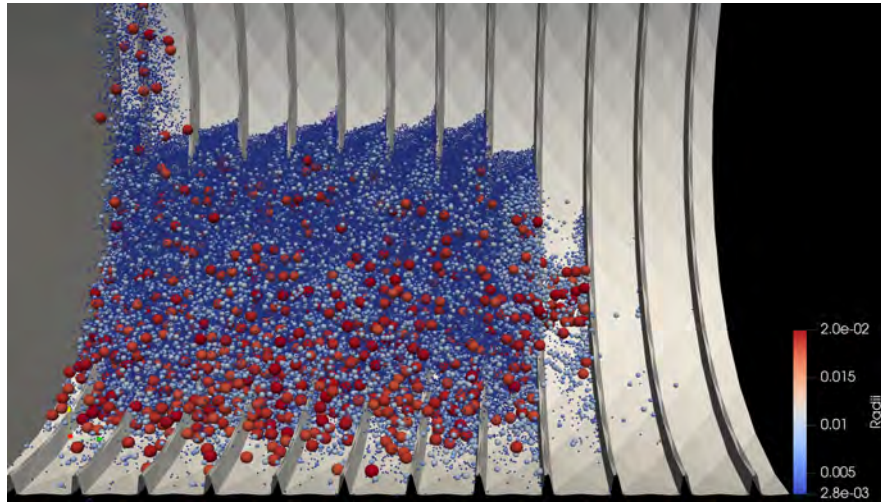
Figure 5.7: Paraview image of the Trimodal Helical Ridged model - A DEM model simulating the kinetic behaviour of a trimodal distribution of spheres in a drum of similar dimensions to the real world drum used on site.
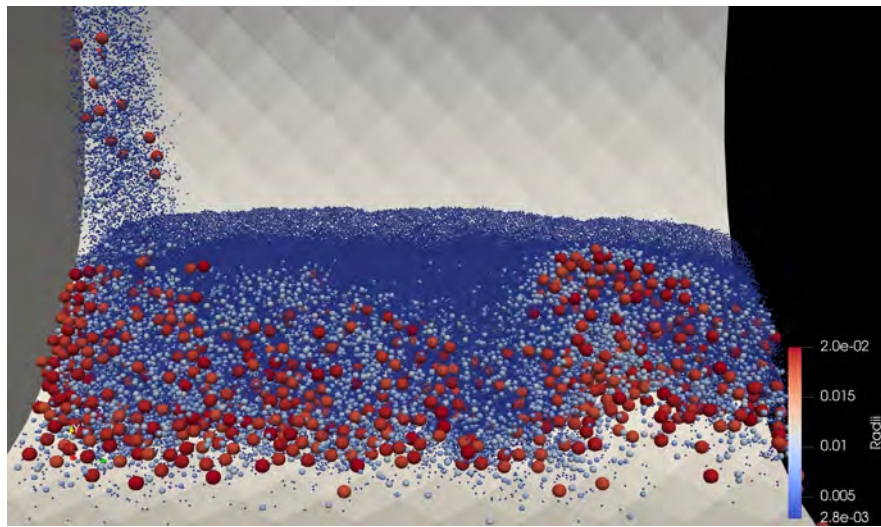
Figure 5.8: Paraview image of the Trimodal Blank Walled model - A DEM model simulating the kinetic behaviour of a trimodal distribution of spheres in a drum of similar dimensions to the real world drum used on site.

5.1.3 Coordinate Average Radius and Flow Patterns

The segregation can be defined in a few ways, such as the entropy of the pile or the amount of deviation in the granule size in any given sub-domain. Such definitions are more important for mixing simulation, however here the average radius per location is more useful as the segregation is so strongly related to the size, and some specific information is relevant for the pelletisation process.

The average sphere size across the full x-y domain is shown to examine where the smallest granules would collect in the drum, which should according to the stokes number theory be in the same locations where the largest collisions occur, which can then be compared against later.

The specific average radius measured is the $r_{4,3}$, to determine the volume mean radius. The measurements are taken across a set Z range. For the lab scale tests, this is the whole drum. Because the full scale drum has a continuous input and output, the bounds are cut to ensure that only the section demonstrating steady state is shown. Here the steady state is defined as the point when there are no transitional effects that can be seen as as a result of either the initial input, and the area of the rolling bed is consistent, having been filled up through the input spheres.

Further, the results are averaged over a range of timesteps after steady state is achieved to represent the data best. The axial segregation observed in the blank walled drum is not easily captured here, though the remainder of the distribution is captured well enough.

To ensure that the samples are reasonably representative, the subdomain sampled needs to have a minimum mass.

5.1.3.1 Lab scale drum models

Figure 5.9 shows various useful features of the effect of the sphere properties. First, by comparing Figure 5.9a and Figure 5.9b, the distribution has a very strong

(a) Trimodal Distribution Lab Scale

(b) Power Law Distribution Lab Scale, Base μ_r

(c) Power Law Distribution Lab Scale, μ_r Reduced

(d) LFDRough
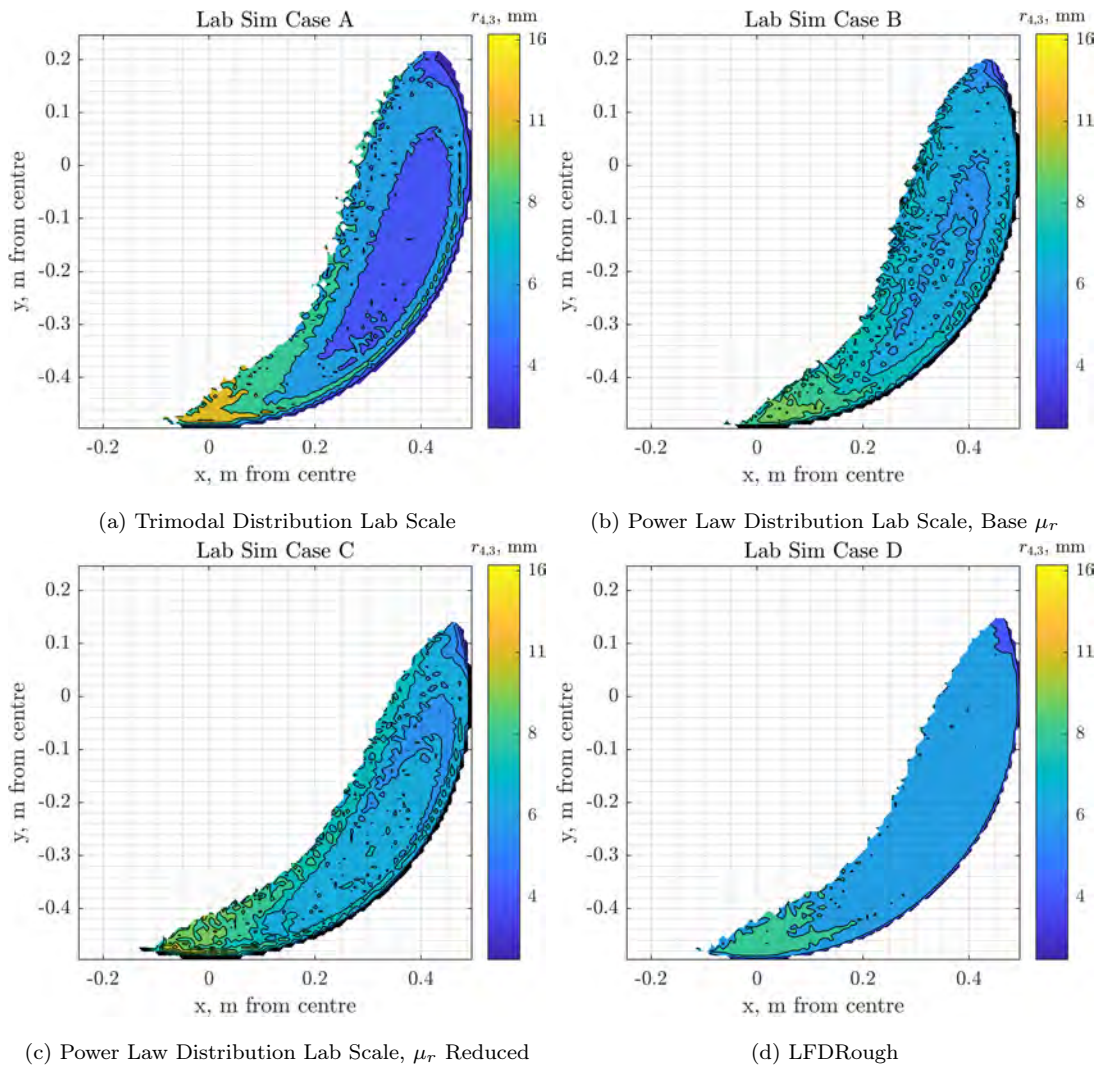
Figure 5.9: Lab scale models showing the correlation between the position and radii of spheres. The arrow starts at the centre of the rotation axis and points to the bottom of the drum.

influence on the segregation, as expected, and has relatively little influence on the overall shape of the flow, at least compared to the frictions. The wall friction meanwhile has less influence on the shape of the flow, and the inter-sphere rolling friction is more important.

5.1.3.2   Full scale drum models
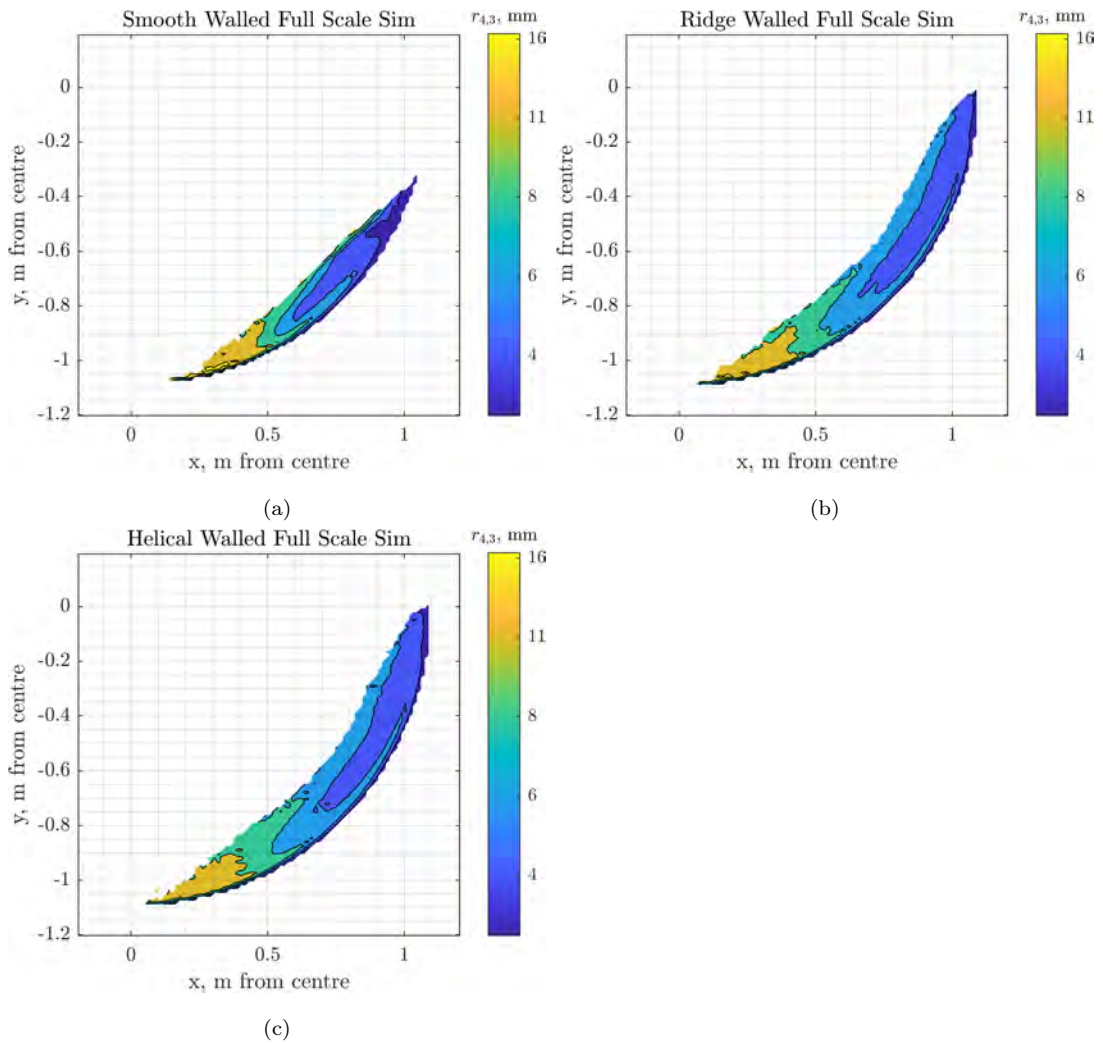
Figure 5.10: Full scale models showing the correlation between the position and radii of spheres. The arrow starts at the centre of the rotation axis and points to the bottom of the drum.

Figure 5.10 shows the radii distribution across the assorted full scale drums, and the segregation patterns are quite different between them. First of all, the effect of the ridges in holding up the flow is clearly observed, with a much larger area covered for the ridged and helical drums. Second, though the segregation

is still evident, with spheres in the upper wall region being more of the smallest, the largest are not on the surface, or at least not as concentrated on the surface.

The nature of the averaging of the results across the z-direction loses some of the information caused by the ridges in the ridged and helical drums. As such, the reduced segregation could indicate a generalised mixing effect, or it could simply be the nature of the larger spheres being pulled up the ridges. Such a quantification would be beyond the scope of this work, especially since reviewing the behaviour in Paraview suggests a combination of the two.

5.1.4 Z-R flow
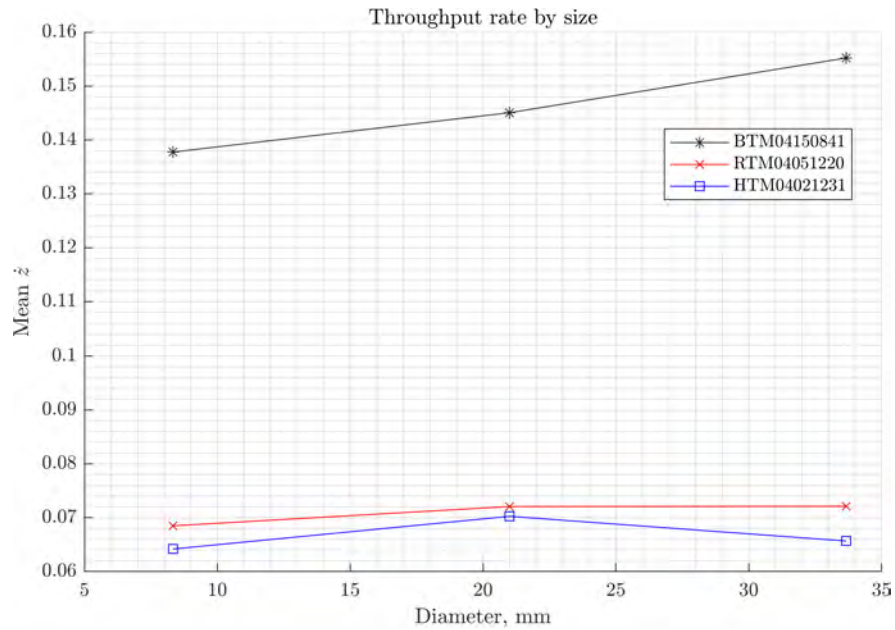
Figure 5.11: Throughput (z) flow through the full scale drums.

Figure 5.11 shows that ridges clearly slow down the overall throughput of the spheres, and the helical pattern slows the spheres further. However, the actual effect that the sphere diameters have on the throughput rate distribution is minimal, and actually appears to be strongest for the blank walled drum, with the helical design actually slowing the flow rate for the largest compared to the middle sphere diameter grouping.

5.1.5 Trajectory of flow

By capturing the position of the spheres at every recorded timestep, the trajectories of the sphere motion can be observed in a static image. By also recording the radii of the spheres, the variation in the distribution can also be observed in a different way to the simple mean shown in subsection 5.1.3. Specific spheres are taken from set size groups in order to ensure a consistent quantity and to more clearly observe the behaviour.

5.1.5.1 Size selected sphere trajectories, Lab scale

Figure 5.12 shows the segregation as before, and also shows that there is a relative lack of diffusion in the bed itself, with the greatest amount occurring at the bottom of the pile where the spheres get brought back in.

5.1.5.2 Size selected sphere trajectories, Full scale

The trajectories of the full scale drums are much less clear in Figure 5.13, because of the axial flow along with the radial and the azimuth motion of the spheres obscure the internal behaviour. The mixing is evident however, and large spheres are much more commonly reaching the top in the ridged variants Figure 5.13b and Figure 5.13b compared to the blank walled drum in Figure 5.13a.

Further, the increased axial flow can be seen in the blank walled drum compared to the other two, with the trajectories forming a more diagonal path.

(a) Trimodal Distribution Lab Scale

(b) Power Law Distribution Lab Scale, Base μ_r

(c) Power Law Distribution Lab Scale, μ_r Reduced

(d) Power Law Distribution Lab Scale, only S-S μ_r Reduced
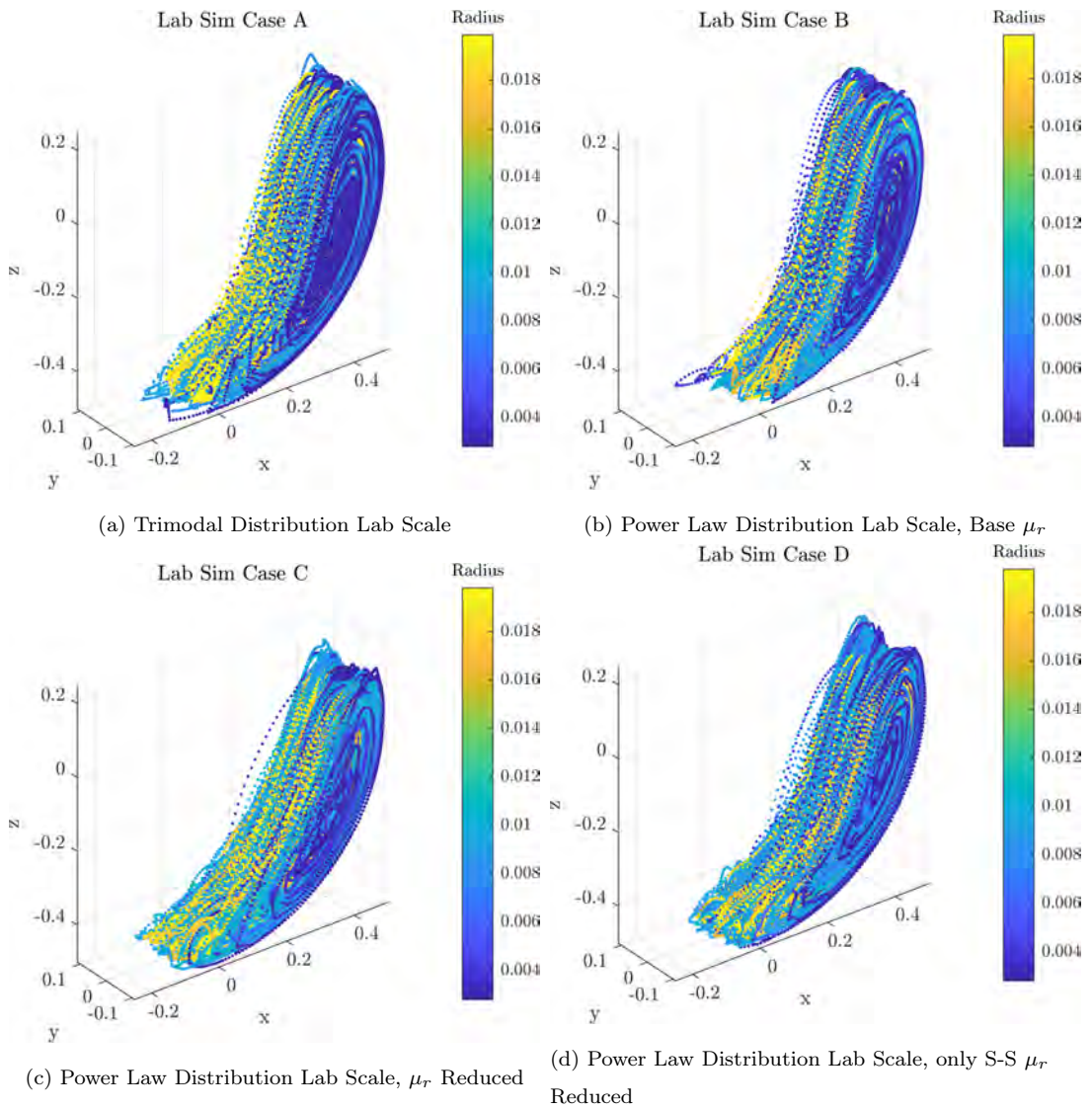
Figure 5.12: Trajectory plots displaying the coordinate of random spheres from assorted diameter subsets with colour corresponding to diameter, more yellow being larger and dark blue being smaller, after the steady state had developed.
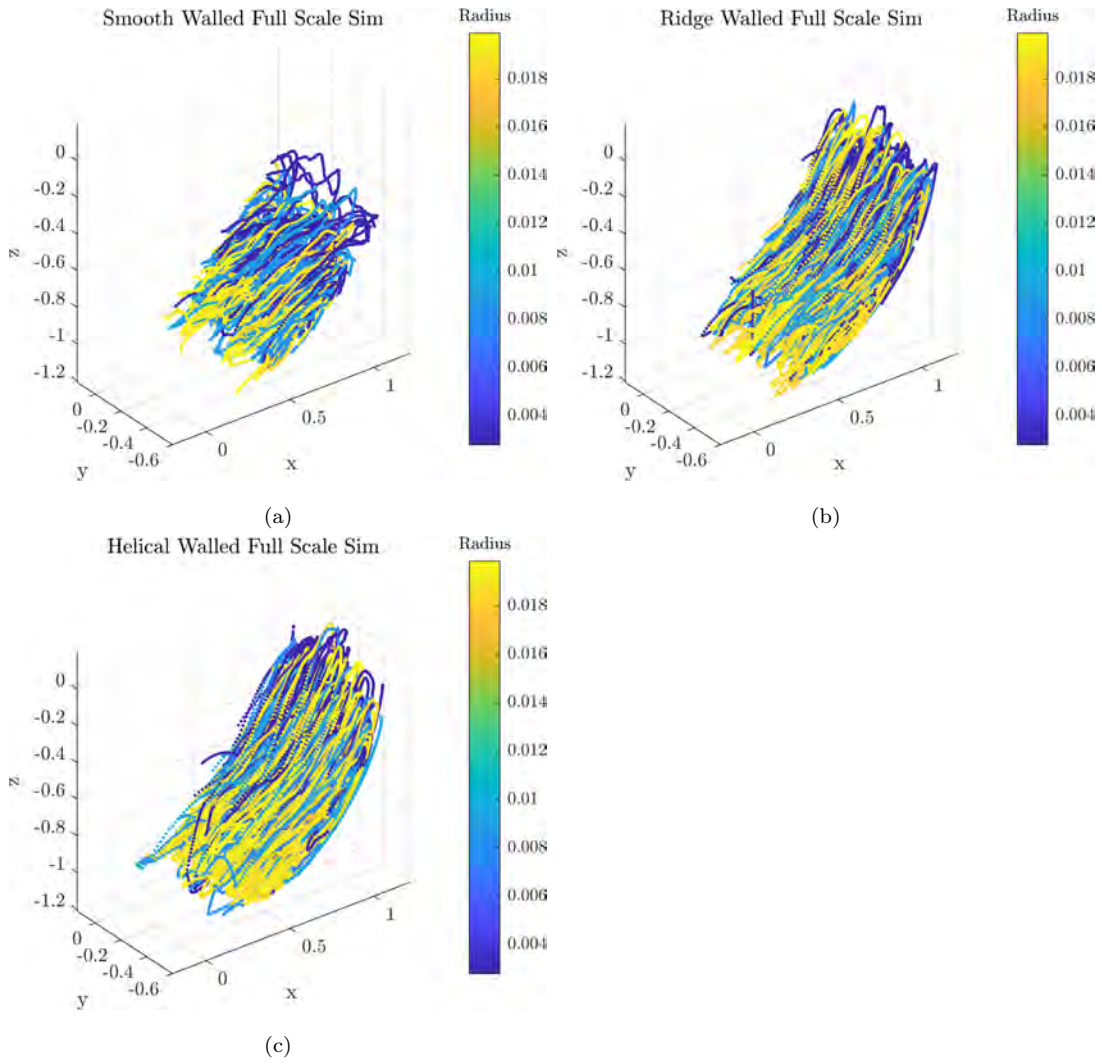
Figure 5.13: Trajectory plots displaying the coordinate of random spheres from assorted diameter subsets with colour corresponding to diameter, more yellow being larger and dark blue being smaller, after the steady state had developed.

5.1.6 Collision Frequency Heatmaps

The scales for all these plots were set to the same scale for all the cases, and between the small and larger scale values, so that comparisons could be made between them and how scale affects the behaviour. All the graphs are plotted on a log scale, because of the significant disparities in the proportion of collision events.

5.1.6.1 Collision Frequencies By Radii

Figure 5.16 shows that the greatest number of collisions occur between the smallest spheres. The asymmetric shape of the graphs is a consequence of the way that the collisions were recorded interacting with the spheres record system, and the data is in practise symmetric along the $r_i = r_j$ line.

Most importantly, the distribution of the spheres has an impact on the distribution of collisions, with a greater quantity of small-small collisions for the Power curve distribution, and a more smooth transition towards the large-large collision values from the mid-mid collision.

Meanwhile, since Figure 5.14b, Figure 5.14c and Figure 5.14d look nearly identical, the rolling friction seems to have little effect on the collision frequence.

Figure 5.15 shows similar behaviour to the small scale drums, primarily with Figure 5.14a which has the same sphere size distribution.

(a) Trimodal Distribution Lab Scale

(b) Power Law Distribution Lab Scale, Base μ_r

(c) Power Law Distribution Lab Scale, μ_r Reduced

(d) Power Law Distribution Lab Scale, only S-S μ_r Reduced
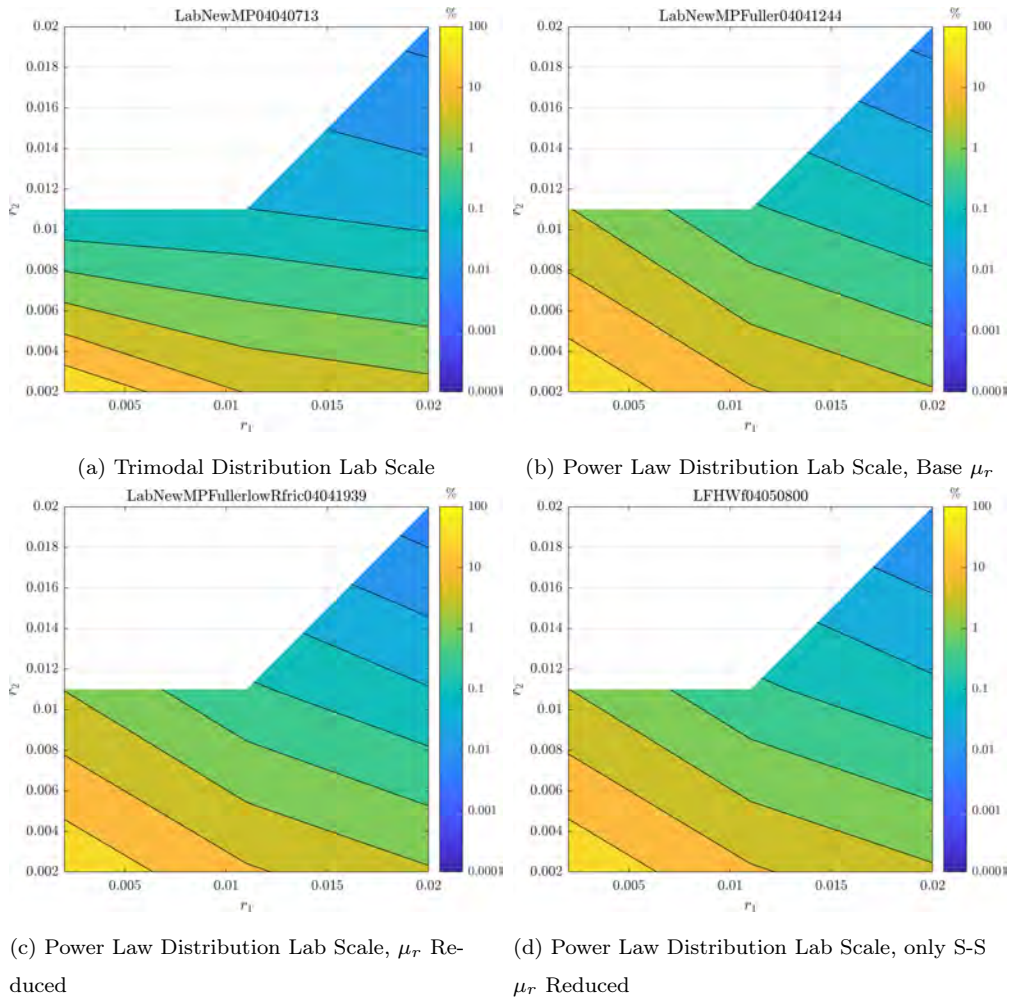
Figure 5.14: Heatmaps showing the frequency distribution of collisions by radii r1 and r2 of interacting spheres 1 and 2.
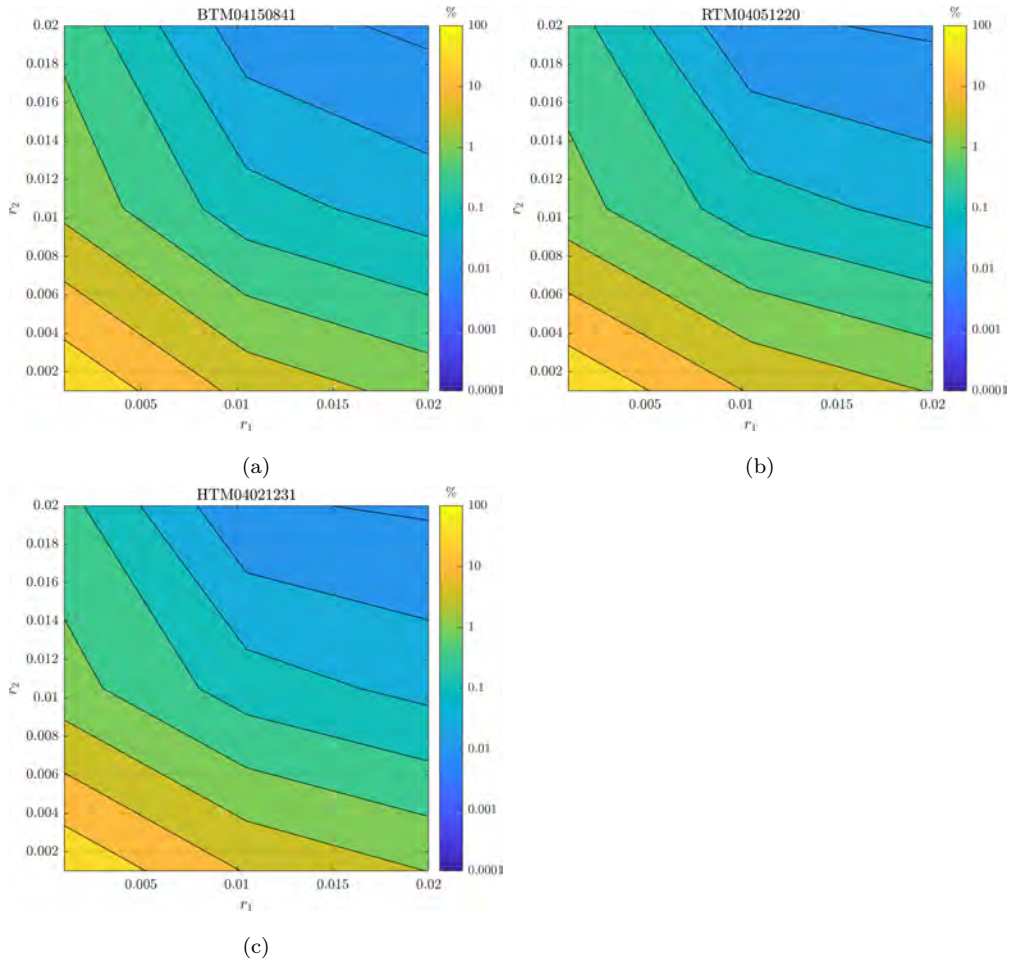
Figure 5.15: Heatmaps showing the frequency distribution of collisions by radii r_i and r_j of interacting spheres 1 and 2, for the full scale models.

5.1.6.2 Collision frequency for full scale models

(a) Trimodal Distribution Lab Scale

(b) Power Law Distribution Lab Scale, Base μ_r

(c) Power Law Distribution Lab Scale, μ_r Reduced

(d) Power Law Distribution Lab Scale, only S-S μ_r Reduced
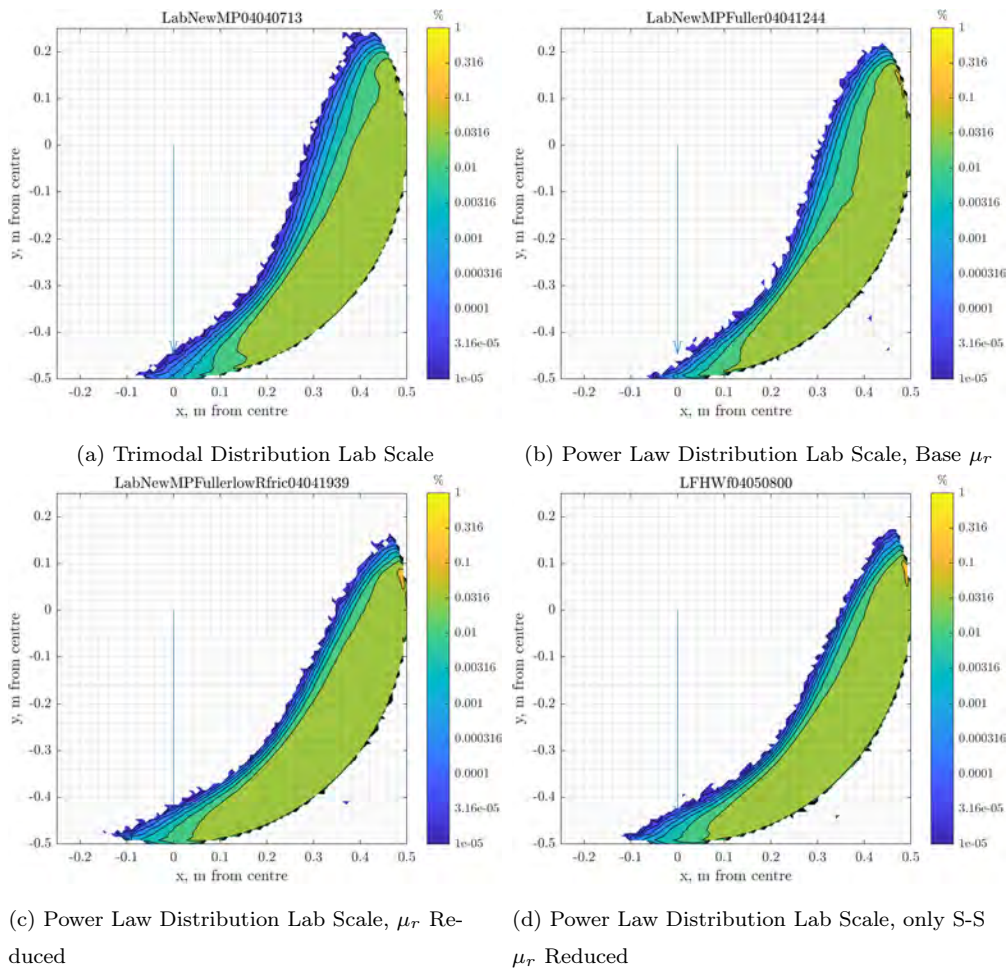
Figure 5.16: Heatmaps showing the frequency distribution of collisions by location of interacting spheres for lab scale models. The arrow starts at the centre of the rotation axis and points to the bottom of the drum.

Figure 5.16 shows no practical difference in the distributions of interactions. The collisions are of roughly equal probability in the bulk pellet bed. This might be due to a lack of sensitivity needed to record this, however this range was selected in order to compare against the larger scale drums. However it very clearly shows that there is no hotspots within the bulk. There is one small spot near the top, but the cause of this is unclear.
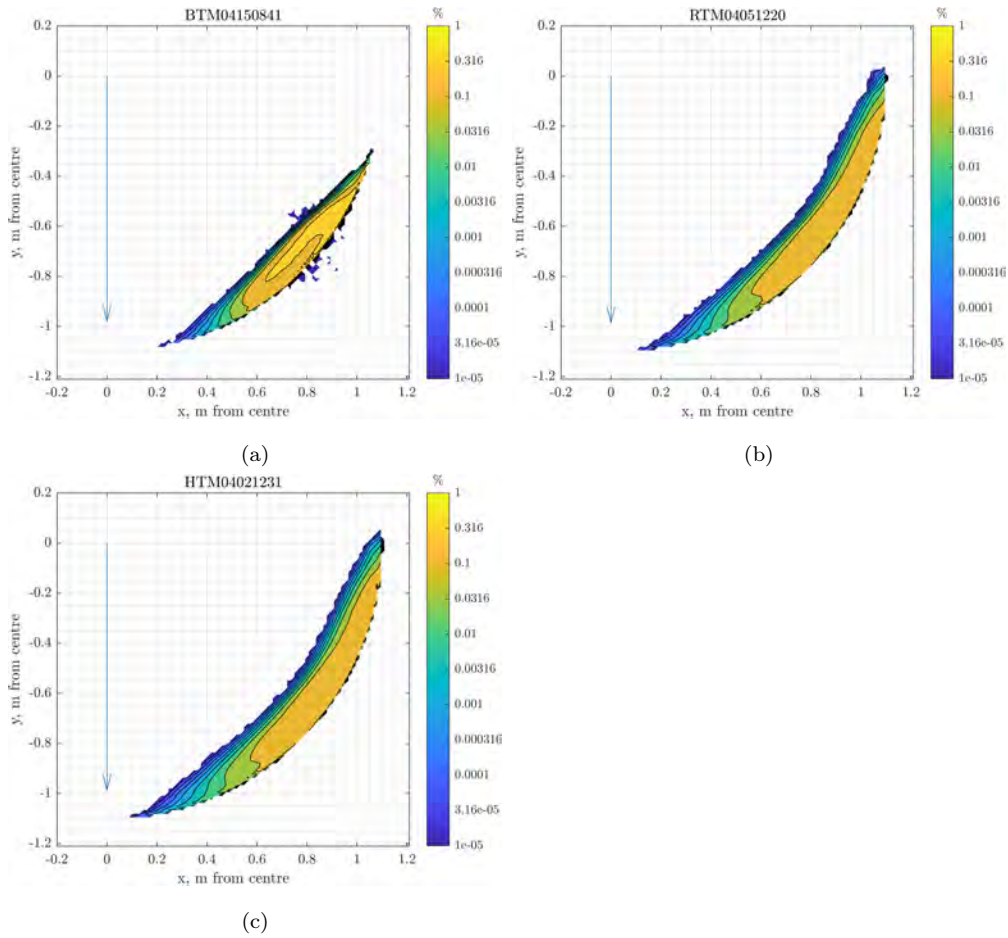
Figure 5.17: Heatmaps showing the frequency distribution of collisions by location of inter-acting spheres for the full scale models. The arrow starts at the centre of the rotation axis and points to the bottom of the drum.

Figure 5.17 shows that the full scale drums have a greater degree of het-erogeneity in the location of the collisions compared to the lab scale. In fact, Figure 5.17a has the highest degree, and this region lines up well with the region with the smallest spheres in Figure 5.10a. The other two full scale models do not demonstrate the same degree of focus, however they still show a higher degree of collision focus than Figure 5.16.

5.1.7 Collision Velocities

The collision velocities are some of the most important characteristics of the dynamics of the system. These will dictate the strength of the forces applied to the granules. The maximum collision velocity is higher in the location plots as the location has much higher variation in the average collision velocity. However, for the Stokes number model, the smaller radii would be predicted to have higher collisions velocities with one another, as otherwise they would agglomerate, which is why the radii-radii collision velocities are also shown, though the variation is not as significant as with the location

5.1.7.1 Collision Velocity by Radii

Figure 5.20 shows that the velocities appear to be correlated to the size of the colliding spheres. The two most interesting features are that of Figure 5.18a, which shows the strongest relation between the colliding spheres, while Figure 5.18c actually shows a maximum that is not at the large/large particle intersection, but rather at the large/mid intersection, and overall has the lowest mean collisions.

In a reversal from the frequency maps, Figure 5.19 shows that the ridged variants of the drums show a higher maximum value. The collision velocities are significantly higher for the ridged drum variants, but the overall collision velocities are similar to that as for Lab Sim A Figure 5.18a

(a) Trimodal Distribution Lab Scale

(b) Power Law Distribution Lab Scale, Base μ_r

(c) Power Law Distribution Lab Scale, μ_r Reduced

(d) Power Law Distribution Lab Scale, only S-S μ_r Reduced
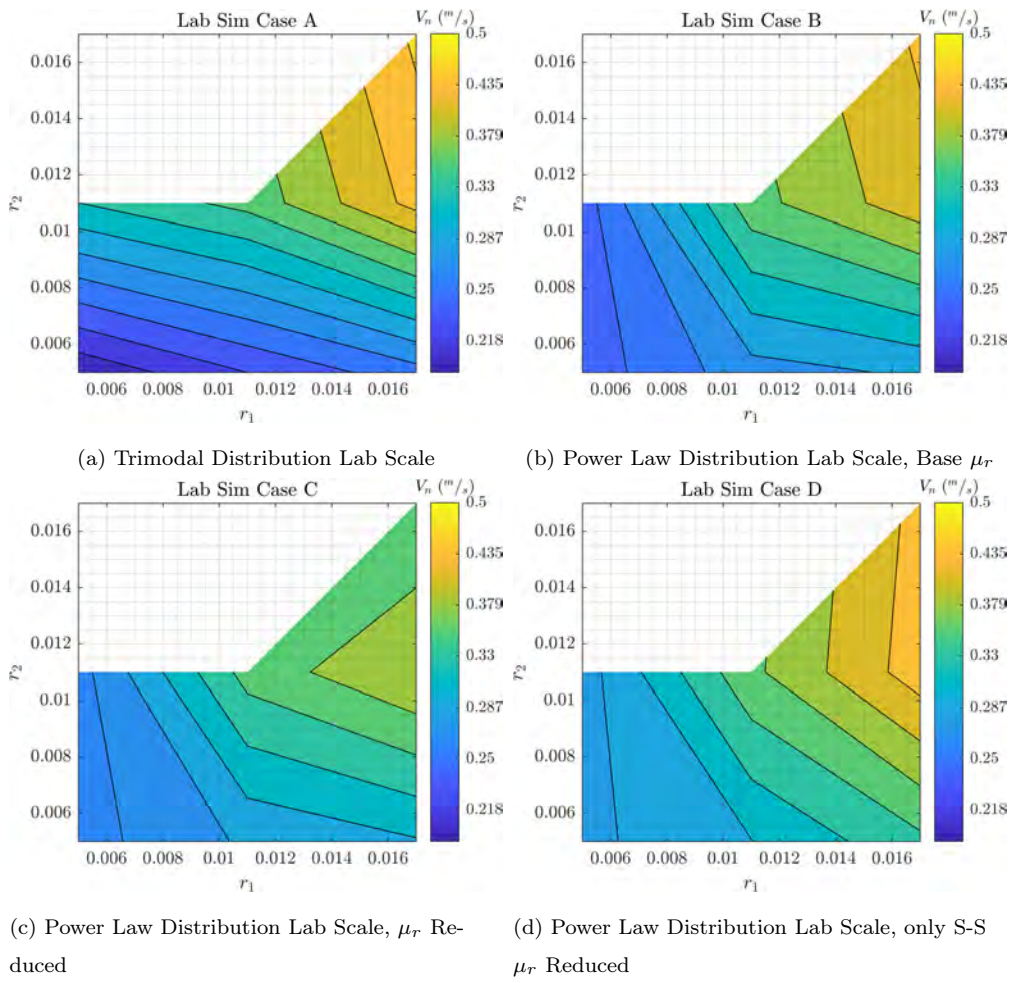
Figure 5.18: Heatmaps showing the mean V_n of collisions by radii of interacting spheres.

(a)

(b)

(c)
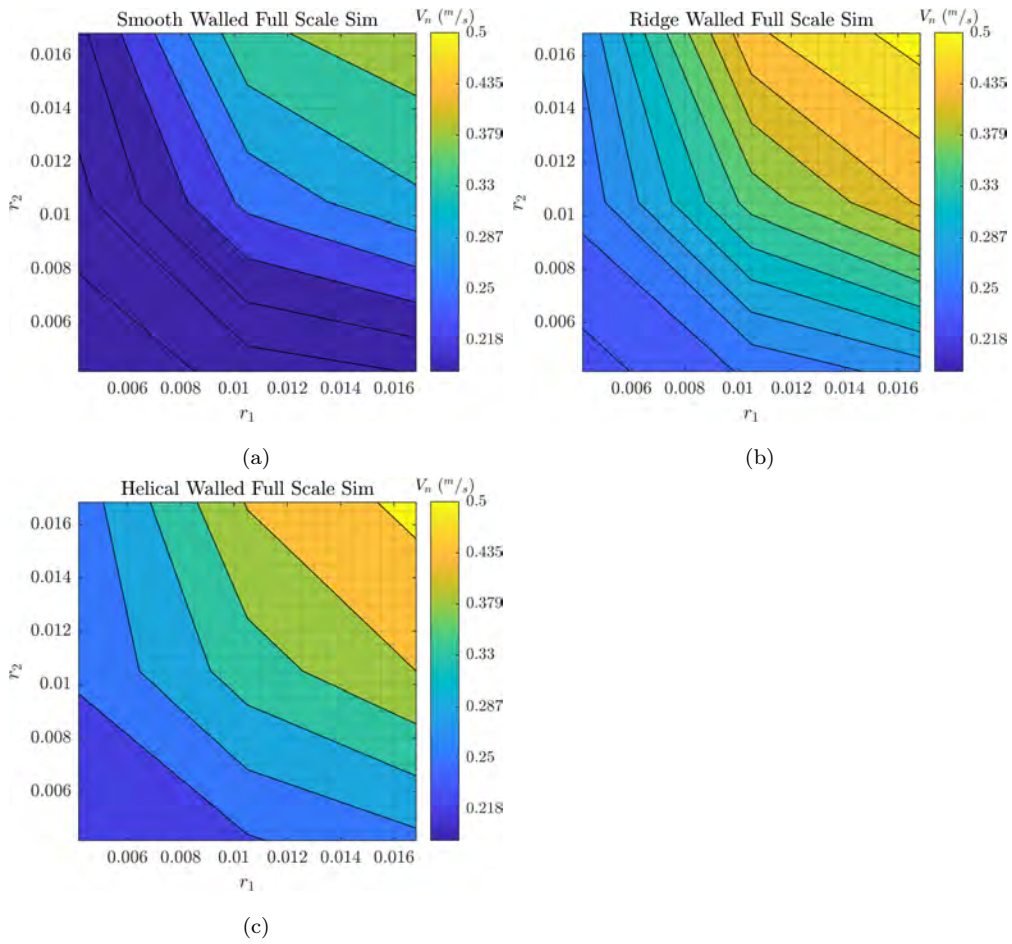
Figure 5.19: Heatmaps showing the mean V_n of collisions by radii of interacting spheres for the full scale drum models.

5.1.7.2 Collision Velocity by Location

(a) Trimodal Distribution Lab Scale

(b) Power Law Distribution Lab Scale, Base μ_r

(c) Power Law Distribution Lab Scale, μ_r Reduced

(d) Power Law Distribution Lab Scale, only S-S μ_r Reduced
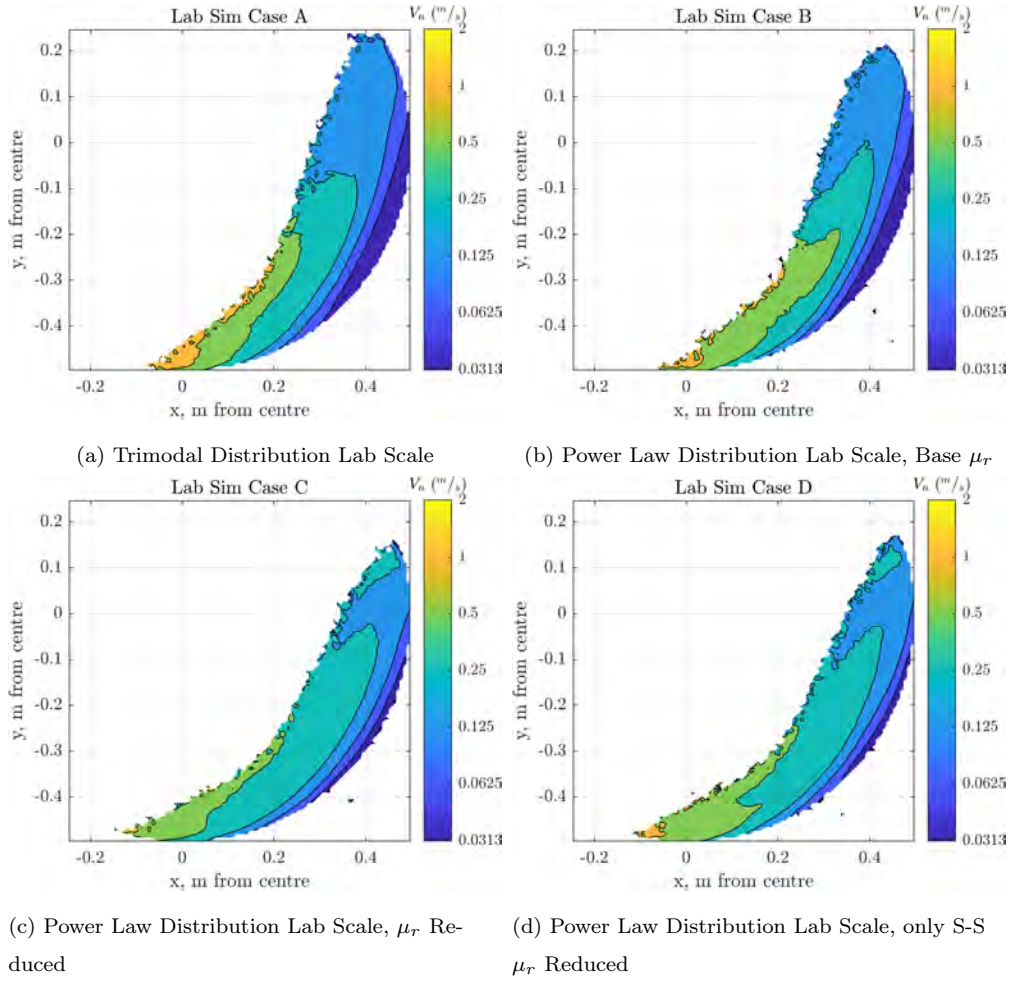
Figure 5.20: Heatmaps showing the mean V_n of collisions by X-Y location of interacting spheres.

Considering location on the other hand, Figure 5.20 shows that the colliding spheres clearly demonstrate variations. The bottom of the pile, where the spheres slow down after being drawn from the top and then get impacted by the spheres coming from above show the fastest collisions. The frictional parameters do also seem to affect the results, with the low friction cases showing lower collision velocity maximum and the collision strength is more evenly distributed.

The highest collision velocity regions do not solely depend on the cascade regions, at roughly $(0.2, -0.3)$, when comparing against the flow behaviour in the trajectory plots or the X-Y plots.

(a)

(b)

(c)
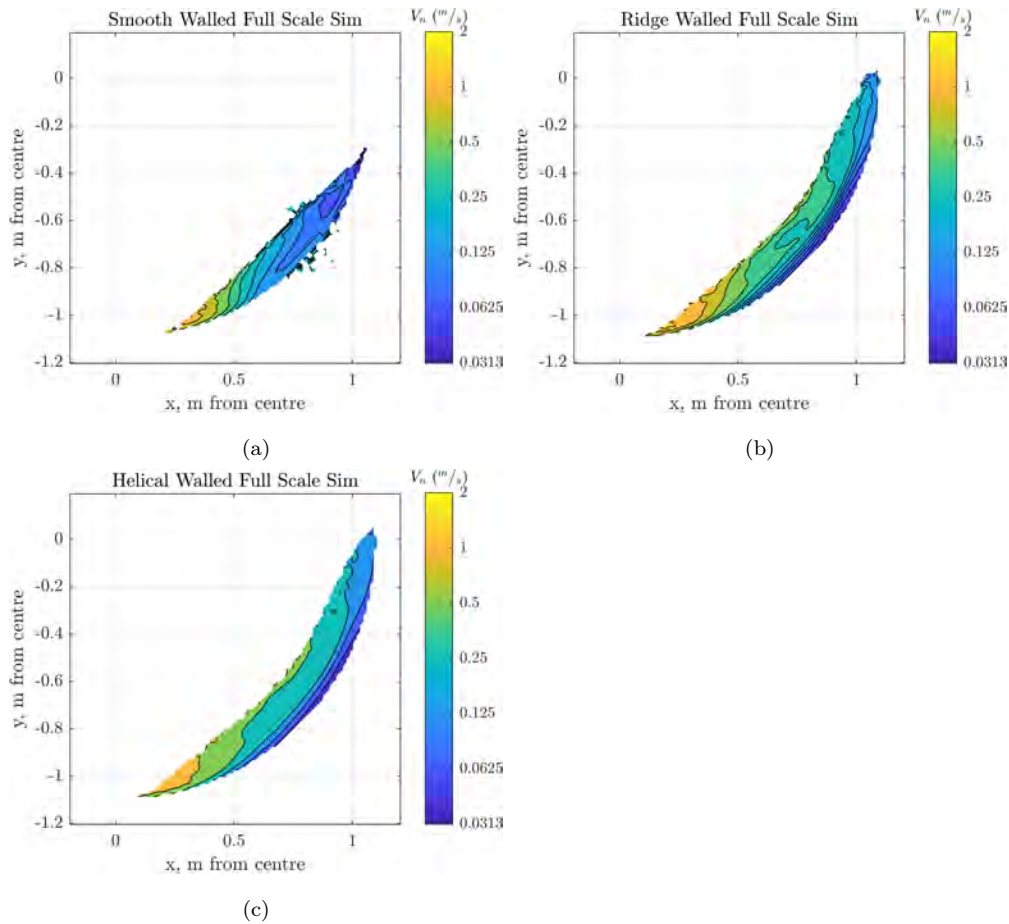
Figure 5.21: Heatmaps showing the mean E_k of collisions by X-Y position of interacting spheres for the full scale drum models.

Figure 5.21 shows similar behaviours in all cases, but significantly they all demonstrate high impact regions that are larger, relative to the total projected area. The ridged drum shows the greatest variation in the collisions, with some reaching $2m/s$. The variability in the mean collisions is much stronger by location than by the radii for both scales.

5.1.8 Collision Kinetic Energy

Finally, the strength of the kinetic energy of the collisions is tracked. This is directly correlated to the mass and therefore radii of the spheres as well as the velocity, so it should be predictable by those plots. Since there is a positive correlation with both of these, a positive correlation should be expected, but it is worth confirming.

5.1.8.1 Collision Kinetic Energy by Radii

(a) Trimodal Distribution Lab Scale

(b) Power Law Distribution Lab Scale, Base μ_r

(c) Power Law Distribution Lab Scale, μ_r Reduced

(d) Power Law Distribution Lab Scale, only S-S μ_r Reduced
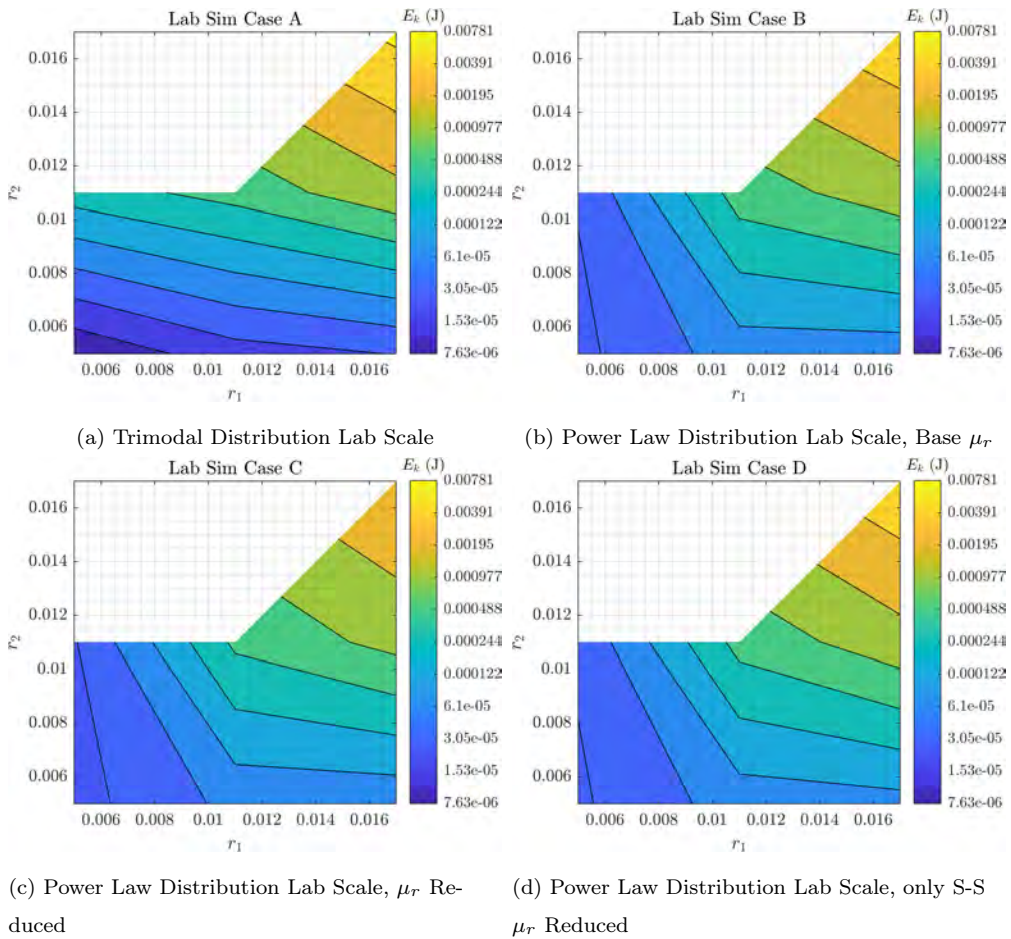
Figure 5.22: heatmaps showing the mean E_k of collisions by radii of interacting spheres.
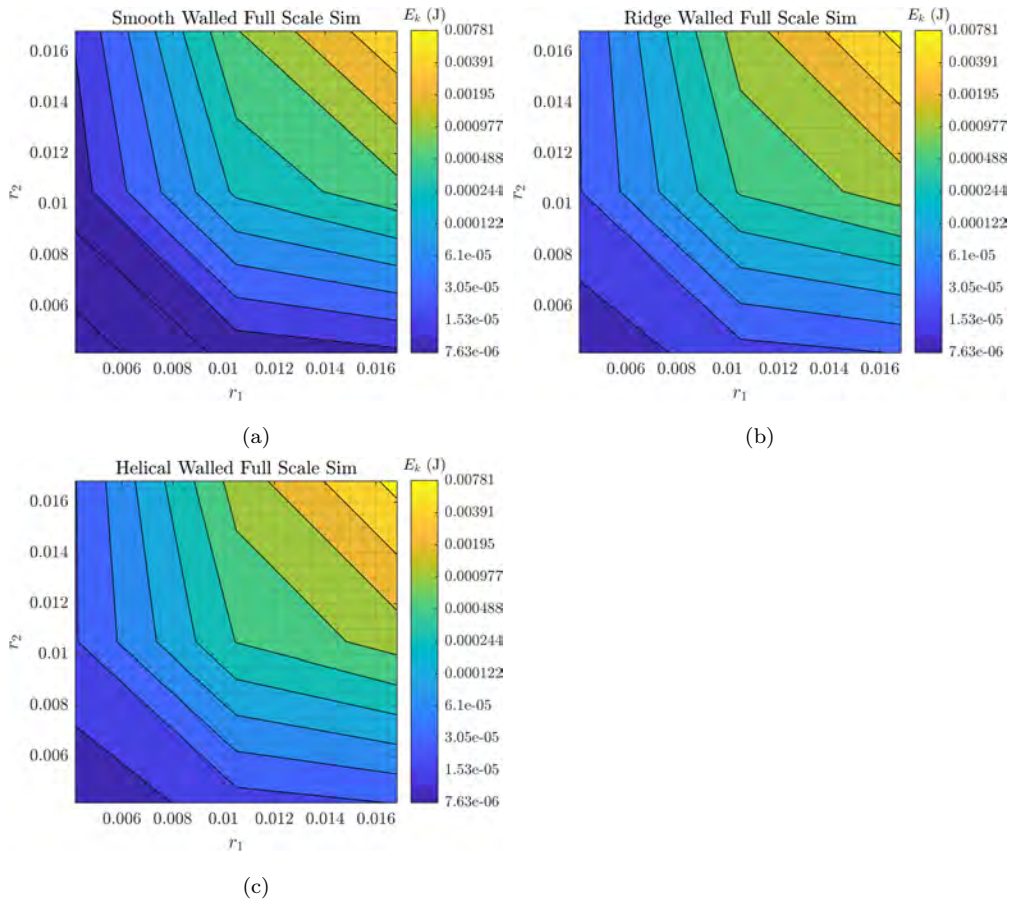
Figure 5.23: heatmaps showing the mean E_k of collisions by X-Y position of interacting spheres for the full scale drum models.

Based on the previous results observed, the behaviour shown in Figure 5.22 and Figure 5.23 are as expected. A strong positive correlation is found between the radii of the interacting spheres and the resulting kinetic energy of the collisions. Among all the cases, Figure 5.22a, Figure 5.23b, and Figure 5.23c are show the highest collision E_k values.

5.1.8.2 Collision kinetic energy by location

(a) Trimodal Distribution Lab Scale

(b) Power Law Distribution Lab Scale, Base μ_r

(c) Power Law Distribution Lab Scale, μ_r Reduced

(d) Power Law Distribution Lab Scale, only S-S μ_r Reduced
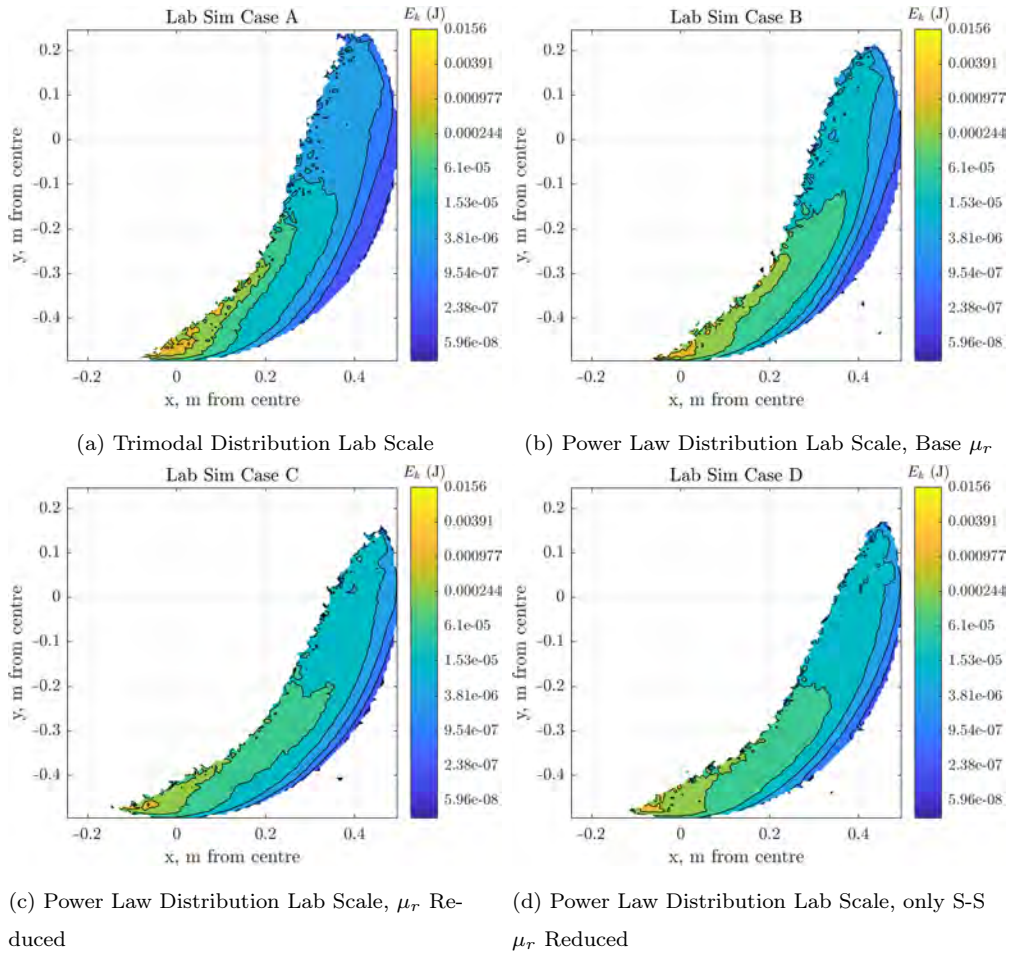
Figure 5.24: heatmaps showing the mean E_k of collisions by X-Y location of interacting spheres.

Here too, Figure 5.24 and Figure 5.25 show similar behaviours as would be expected, given the collision velocity behaviours observed as well as the segregation behaviours noted near the start of these results. Of these, the highest energy collisions occur in Figure 5.25b, though it is very similar to Figure 5.25c in overall appearance. Figure 5.25a does have some very small regions where the high energy collisions occur as well, though in general, the values are lower for most of the bed.
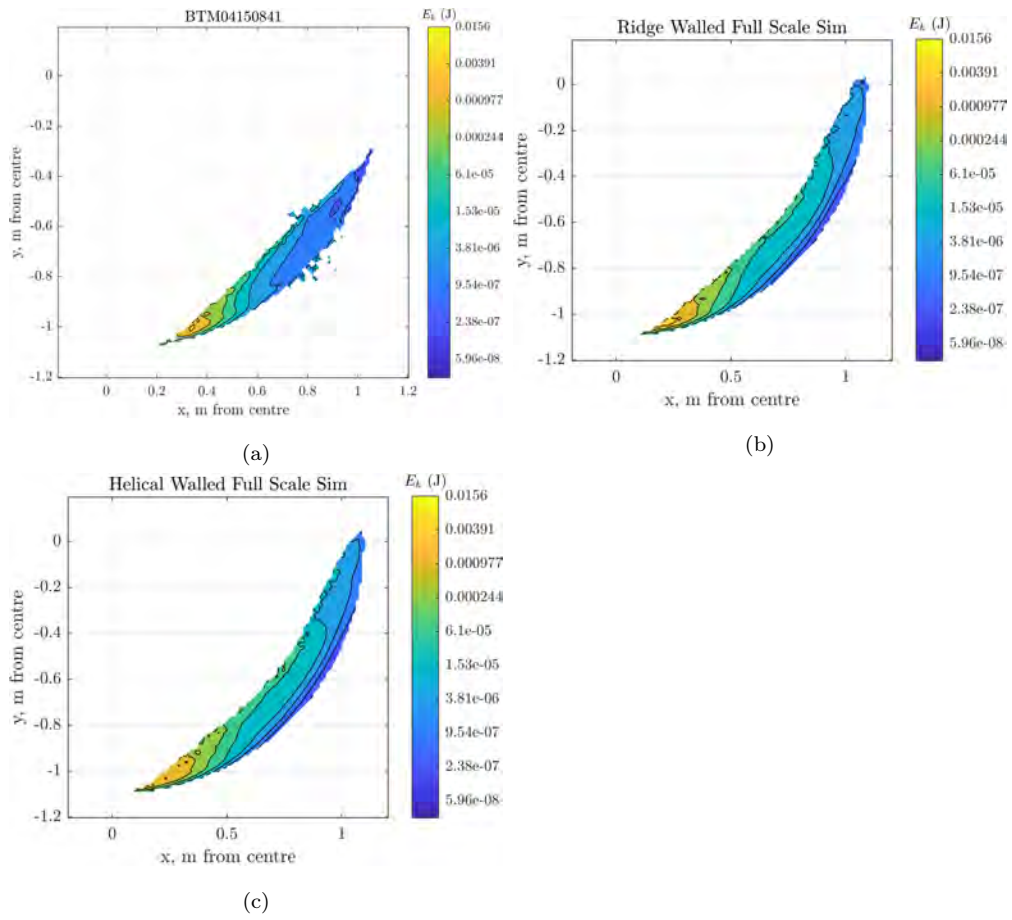
Figure 5.25: Heatmaps showing the mean E_k of collisions by X-Y position of interacting spheres for the full scale drum models.

5.2 Discussion

The stiffness values were set quite low, however, the models demonstrated both suitably accurate segregation and velocity profiles.The value of the stiffness is a relatively low priority value in producing realistic the flow behaviour [208], although if the stiffness is too low then the velocity profile looks strange. Specifically, the velocity of the elements in the active region becomes similar to that in the passive regions. Here in all cases, the active region has clearly higher velocities relative to the passive region.

Despite the error in the original rotational velocity of the small scale drums, much useful information can still be found from these results.

Starting with the segregation, the distribution of the sphere radii has a much stronger effect on the extent of the segregation than does the rolling frictional parameters, which was expected. All the trimodal distributions showed strong segregation, which was more or less consistent regardless of the actual shape or size of the drum.

Meanwhile, the power curve distributions of elements had a much weaker extent of segregation, though it was still present in all cases, with the largest at the bottom of the bed and smaller elements in the middle, though more distinctly as bands that followed the trajectories. Given that the range of the distribution is equal in all cases, the reason must be related to the distribution being smoother.

The fact that the lower inter-element friction combined with high wall friction resulted in the least segregation seems interesting, however this may be a result of the confined nature of the rolling. Wall segregation effects occur as predicted [188], and larger elements tend to collect to the wall in the absence of other factors, and the higher wall-element to element-element friction may have increased this effect.

While observing the behaviour of the elements and considering the wall segregation noted above, an explanation for the source of the wall segregation arose

that fits into the granular entropy behaviour previously noted. The entropy explanation suggests that the granules that these elements are modelling will sort themselves out into a configuration which has the fewest contacts with other granules. In a smooth distribution, this leads to a gradient between the smallest and largest, while in a bimodal case (or similar) this leads to distinct surfaces developing. In either case, if one considered the side walls not as walls but as significantly larger granules then the granules will inevitably arrange themselves such that the largest granules are in contact with the walls, so long as no other effects interfere with this.

The XY flow behaviour shows that the individual velocity fluctuations by diameter are extremely weak. The correspondence of this to segregation is weak, though this might be because the segregation happens quickly [155] upon initiation of flow, and is reinforced at specific locations such as the top and bottom of the flow where the direction changes the strongest where this effect is most observable.

The overall flow behaviour is not especially sensitive to the element size distribution , and instead it is more dependent on the rotation rate, geometry and friction parameters. This is reasonable, as the XY flow behaviour is simply a matter of the angle of repose of the elements, and the rate at which the elements at the bottom are transferred to the top of the drum.

The Froude number alone cannot define the flow regime, as the three full size drums have the same Froude number, yet the blank walled drum flow is more clearly in the rolling regime, while the ridged variants have more cascading effects. Given that in Figure 5.1 [157] the only effect that causes a shift in the regime from rolling to cascading noted is the froude number, this further demonstrates that the ridges are causing more kinetic effects than simply slowing down the axial flow.

This might be due to the flow over the ridges themselves, which would alter the collision frequencies by location as they pass over them. If the ridges simply

confine the elements and increase the effective frictional behaviour of the drums, the collision frequencies would not be altered similarly.

In fact, not only is the blank walled drum in the rolling regime, the upper half of the active region is slower than the lower half. This may be due to the presence of the smaller particles in this region having some effect, or it could be that this is what distinguishes the rolling regime from the cascade regime.

This suggests that scaling of a drum needs to account for the shape of the drum itself. This becomes important when the fact that the scale of the ridges are much closer to that of the pellets themselves, introducing another complicating factor in the scaling.

The throughput flow plot did not show much, though on reflection this would be expected. Because the mass is conserved, and no changes are occurring to the distribution, the overall flow must reach the same for all particles on average, with only some minor fluctuations as the flow builds. The input of the drum must after all be the same as the output, if there are no internal transformations. This throughput flow therefore is appropriate if agglomeration is actually implemented, but not as a measure on its own.

The flow trajectories are primarily useful in observing how the diffusion occurs, and more specifically how it differs between the two drum shapes. The small drums show very little diffusion, with the particle behaviour being in quite stable flow paths. the full scale drums however show more diffusion occurring. Why this is the case is not immediately identifiable, but it may simply be because the drums are in a lower Froude number regime, and so the centripetal force constrains the elements less. It could however also be because of the axial flow and the continuous introduction of new elements which are more equally mixed.

The collision frequency results for the radii show that the great majority of collisions occur between the smallest elements. However, these maps do not account for the proportion of elements of each type, and given that the distributions of elements were for similar quantity by mass rather than by number, this would

be expected to be seen even if every element collided with each other element just once.

The collision frequency results by location are more interesting though. The majority of the collisions are within the bulk of the bed. Again, this could be simple statistics because these regions host the largest quantities of elements, however this does not explain some of the finer details.

For example, in the top right corner of the lab scale models, there are small features which suggest that there is a higher proportion of collisions. And for the blank walled drum model, there is a clear pattern forming within the upper half of the central bed as the elements tumble down, just along the line between the active and passive regions. Comparing this to the results of the flow behaviour, the blank walled drum shows that this aligns relatively closely to the area in the bulk where the flow is slower. The segregation also may be playing some part; in the cases where the frequencies are greater in the upper bulk, the particles also tend to be on average smaller. With smaller particles, more can pack into the space and collide.

This would also explain why the frequencies tend to be lower in the regions where the average diameter is greater. The fact that this behaviour does not manifest in the lab scale drum with the trimodal distribution does not fit into this explanation.

To explain this, note that the flow in the Lab Sim A model is clearly in the cascade regime. The ridged distributions were noted as having a more cascade type flow behaviour compared to the blank walled drum. This could be a result of either the ridges actually causing a cascade flow specifically through mechanisms not specified in Figure 5.1, or simply pulling up the elements due to an amplification of the frictional effects.

Though the two effects are intertwined, the distribution of the collisions in the ridged models is more uniform compared to the distribution in the blank walled drum. This suggests that the cascade flow regime results in a more even collision

behaviour which is less strongly defined by the element size distribution.

Of the collision relative velocities, the velocities are clearly proportional to the radii, with larger radii experiencing larger collision velocities.

Once again the explanation could simply be due to segregation effects. Examining the location of the collisions, the highest velocity collisions occur at the bottom of the bed, as well as along the surface, especially at the landing section of the cascades. These regions also match the regions where the largest radii collect due to segregation and therefore the proportionality is due to this confounding variable.

With that said, directly comparing the results against one another suggests that somehow the wall friction has an effect on the distribution of collisions. Again, this could be a result of the flow behaviour. Of the lab scale models, the low rolling friction case had the least cascading flow behaviour. Of the full scale drums, the blank walled drum had by far the lowest collision velocities, and was also the most clearly in the rolling regime. This suggests that the increase is possibly due to the effect of the regime on the collisions.

This still does not explain all the details however. For example, the high wall friction case is very similar by all measures, and it had even less segregation. However, it had stronger collision behaviours, more similar to the case with high wall and rolling friction, which had dissimilar flow behaviour to the low friction case but similar segregation. Comparing velocity of collisions by location, the high friction power law distribution case shows patterns more similar to the trimodal distribution than to the low friction cases.

The trajectory results may provide some extra explanation. As the elements land during the cascade motion, they bounce off the surface. It is not the immediate point where they land which has a high collision velocity, as the elements they land on are also moving, but rather the subsequent bounce which retains some of the initial velocity as it moves to the bottom of the bed, where the elements have stopped and are being pulled back.

This still does not provide a very clear explanation for the disparity between the effect of the rough-walls and the smooth walls, when checking these results, as the trajectory behaviours between these seem again, quite similar.

As for the collision kinetic energies, the behaviour is very similar for all the small scale models though the trimodal distribution kinetic energy is more concentrated, suggesting that this is more strongly dependent on the size distribution than the wall friction or the other effects previously mentioned. For the full size models, the surfaces are in all cases the location where the greatest collision energies can be found, though the ridges do shift the internal pattern of collisions they do not seem to alter the area of the maximum energy collisions.

The size distribution causes a lot of confounding of the variables. The elements were added by mass, which here is equivalent to volume as the densities were identical. Because a doubling of the radii results in an eightfold increase in the volume, the quantity of the smallest elements (at radius of 2.8mm) would be 266 times the quantity of the largest (at 18mm radius). The projected area of the larger elements is greater, which may be why the collision frequency is not as low as might be expected based purely on the proportion of each element group.

On top of this, there is the segregation. This results in unexpected interactions such as the collision velocities being proportional to the radius, as mentioned. This presents a tricky task of separating the variables, for example what effect the drum wall shape has on the interparticle collision behaviours, if the wall shape affects both the flow shape and the segregation, which both contribute to the correlation between size and collision relative velocity.

The ridge walls do seem to affect the internal behaviour. This behaviour can be seen in the Paraview images, the trajectories, and comparing the frequency of collisions by location. The walls cause more of a stirring action, which while it does not completely remove the segregation, it does result in more agitation of the elements and more opportunities for the large elements to be drawn up the bed.

Another point to consider is the inherent nature of the limits of the simulation. The trajectory paths show the elements seeming to bounce off after the cascade falling. This was despite setting the coefficient of restitution to as close to 0 as possible at 10^-9, this is in practise 0 (setting it to 0 was not possible as during the conversion to a damping factor logarithms are used), based on the literature showing extremely small values of e_{rest} [5]. This is a limitation of DEM, as the elements will experience force pushing them apart from one another. The choice of a non-returning damping factor is reasonable, and more physically realistic for harder materials, however in the case of very soft materials, because the inter-penetration resulting in longer acceleration times due to the reaction forces, it results in an excessive return velocity.

The results though are still generally in line with the literature, so some implication will be noted, in particular the collision velocities and how they relate to the rotation rate. The full scale drums, with a lower rotation rate generally had larger collision velocities than the lab scale drums, and larger regions where the collision velocity was $1m/s$ or greater, and even some points where the average collision was $2m/s$.

The major difference between the small and large drums is naturally the scale. This is highlighted, since the length of the avalanche of the active region itself may be a contributing factor to the collision velocity. Further, note that the gradient of the lower portion of the avalanche of the full size drums tends to be larger than the smaller drums, even though they are rotating at a lower rate.

Connecting these, consider that for the blank walled drum, although it shows rolling motion, examining Figure 5.10 also shows that the actual region where the motion accelerates is at a similar point or even lower than for the other full scale drums. The maximal collision strength in all cases was at the bottom of the slopes, even in the cases where the drum was showing cascading motion. This is where the elements, or in the real case the elements avalanching will interact with those which have been stopped by the motion of the drum.

226

The velocity of the collisions then may be a matter of the length of the avalanche, as well as the angle of repose of the elements, which is a function of not just the rotation rate but also friction and wall interaction behaviour. The angle of repose is generally constant within a given rolling regime for a range of rotational speeds [157] , though the collision velocity also depends on the element which is being collided with, and this element will have its velocity changed by the wall rotation rate. The cascading motion appears to significantly alter the flow, but it does also reduce the length of this accelerating region, and so testing would be necessary to investigate, but it cannot apparently make up for the increase in scale associated with the larger drums.

Since some of the limiting granule diameters necessarily consider the velocity of collisions, a brief consideration of the approximations suggested are noted here. Most of these are kernel based for population balance models, which includes the behaviour of rate and strength effects as they relate to the size distributions involved. However, a common approximation is based on the shearing action of the granules as a whole. For drums, this is given by Equation 5.2 [4]

$$V_c = 2R_{Dr}\omega \tag{5.2}$$

With r_g being the radii of the granules, and ω being the rotation rate of the drum. This is off by a significant margin. It suggests that the Collision rate of the elements in the drums is a function of radius, which it is, but the values predicted are $V_c/R_{Dr} \approx 3m/s$ for the lab scale models, and $V_c/R_{Dr} \approx 1.6m/s$ for the full scale models. This is already incorrect, as the collisions of the full scale models were of an equal magnitude or greater than the smaller models. Taking the radii into account leaves the values significantly underestimating the true collision velocities, at $V_c \approx 0.05m/s$ and $V_c \approx 0.03m/s$ for the lab scale and the full scale models respectively for the largest radii collisions.

They also assume that the smaller drum has a larger collision velocity than the full scale drums, which is not the case. This suggests that either this approx-

imation is significantly undervaluing the collision strengths, or more likely, the premise of the collision strengths being derivable from the shearing action alone as done here is flawed.

Similarly, the high variation in the collisions behaviour also demonstrates consistent regions of low collision strength. This causes a contradiction when considering the Stokes number model, as these regions consistently also have high quantities of the smallest spheres. The Stokes number model suggests that growth is maximised at low velocities. Given that undersize pellets are found consistently in all cases in practise, this ultimately suggests that the model fails to account for the real behaviour of the collisions.

While the mechanisms are all interesting unfortunately the practical effects of this behaviour means that there are inconvenient consequences for industrial applications. The segregation means that the granules will sort themselves out in a way that is detrimental to ensuring an even distribution of moisture and hence growth. It also leads to significant variability in the collision behaviour, though what this means will require further investigation into the agglomeration behaviour, in chapter 7.

Segregation not only results in larger elements going to both the upper surface and the bottom of the bed makes the concept of a helical ridged design far less useful than initially hypothesised. The idea was that the larger granules, preferring the top of granular piles could be passively self selected to feed the largest granules forward, which were less inclined to coalesce with one another by most theories. More complex wall geometries could potentially make use of other segregation effects, such as a saw-tooth wall design which favours the passage of larger elements moving up the flat sections as seen in the lab scale drums..

There are more complicated geometries that would very possibly sort out the smaller and larger ones, however, there are real world limitations involved. The drum ideally should be axially symmetric, because the drum requires a scraper that runs along the top that cuts out the material that is stuck to the walls of the

drum. Without this, the drum clogs up as more and more of the feed sticks to the wall. The reason that the helical design was tested was because it was suggested by technicians to be practically possible, though the actual implementation of this would be more complicated.

5.3 Conclusion

The segregation acts a as confounding variable which correlates the element/granule size with the collision velocities, and complicates the analysis and overall behaviour of the flow. The segregation also may cause problems simply by preventing the smaller particles which need to grow more from getting as much binder, which promotes growth.

The general variability intrinsic to the feed will inevitably induce this segregation and further impede the ability to control the pellet properties. The inability to control the behaviour has been observed before [77], and the difficulties in affecting the final resulting distribution. The simulations examined here demonstrates how the kinetics alone can reinforce variability, as the self-selection due to segregation leads to the larger elements remaining on the surface where spray occurs and the smaller elements having weaker collisions, limiting opportunities to consolidation and compress together.

Also, assumptions concerning the collision velocities that are necessary for some of the models applied are challenged, and the significant variability in the collision behaviour from all relevant variables has been noted. An explanation for collision velocities being much greater than those predicted by the shear behaviour is provided as well, and also how the different regimes of the drum flow interfere with possible ways to scale the behaviour.

Though further tests to quantify these parameters, along with normalisation by quantity, displaying the standard deviation and distribution of all the contacts, and adjusting the contact model to produce an improved restitution behaviour,

could be performed and would quantify and clarify the relationships observed, these take a long time and other features of the behaviour need to be researched, such as granule mechanics. However, these results already provide a useful baseline for the behaviours as it stands.

Chapter 6

Non-Growth Wet Agglomerate Mechanisms

6.1 Introduction

Now that the key features of the kinetic behaviour of the granules, along with the system that will be used for the final model has been established, the granule mechanics need further understanding. This chapter will consider only the behaviour due to the granular assembly of a single pellet, and not the process by which multiple pellets will coalesce, which will be discussed in chapter 7.

Granule mechanics is the general field that considers how the interaction of particles in bulk that are distinct from the properties of the composition of the individual particles. The two primary features of note here are the strength, and the consolidation. Other related topics will be discussed as well. During the study of these properties, some of the assumptions applied in the field were brought into question, which in turn lead to the validity of an entire model of agglomeration being challenged.

Granules here are the bulk assembly of the particles bound by a liquid, pellets are the finished product, and particles are the individual solids.

6.2 Liquid bound granules

The liquid content is established as being connected to the strength, the growth and the final size of the pellets, however the specific details are not well established. To get a better understanding of how the liquid behaves, the fluidics were modelled and studied in detail. Partially this was to understand how the capillary strength responds to different conditions, and partially this was based on the requirement of the Stokes criterion to have a surface liquid content, which would by necessity be altered by the liquid bridge presence.

6.2.1 Capillary Cohesion

Capillary cohesion is the behaviour of liquids to draw themselves together, which in turn draws particles together as well which have been wetted. This therefore has been used to describe the strength of wet granular materials, [5,121], and the process of coalescence of granules [116,209,210]. The surface of a stable liquid will always satisfy Equation 6.1,the Laplace-Young equation mentioned previously, as this implies there are no pressure differences across the surface.

$$2H = \frac{\ddot{Y}}{(1+\dot{Y}^2)^{\frac{3}{2}}} - \frac{1}{Y(1+\dot{Y}^2)^{\frac{1}{2}}} = -2\frac{\Delta p}{2\gamma} \tag{6.1}$$

Capillary strength can provide significant strength for relatively little moisture [93,94] and provides static strength, so represents a reasonable starting point.

The capillary cohesion occurs through pendular bonds, shown in Figure 6.1. This pendular regime has been well studied [130, 212–214] since because the bridges are disconnected, the bulk behaviour can be decomposed into many single bridge interactions that are simpler to solve, which then result in the bulk behaviour. Allowing the bridge to be between three particles requires a method such as a "surface evolver" which adjusts the surface of the model liquid based on requirements of the Laplace-Young equation until a valid solution is found [101].
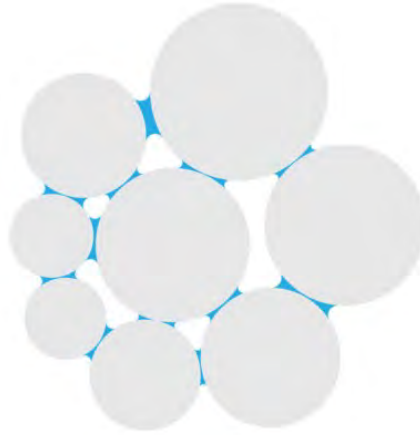
Figure 6.1: Pendular regime in wet granular materials, Figure 1 from [211]

Solving this case can determine a few useful parameters. For example, the strength of a powder with evenly distributed moisture can be predicted [121, 202] based on these, along with the moisture content of a system due to condensation due to the pressure differences [17].

The pressure difference is particularly notable. Part of this work was to investigate whether there is a hydrostatic pressure based limitation on the amount of moisture that would collect into the bridges. This is important, as the amount of surface liquid is very important in determining the coalescence behaviour in for the Stokes criterion agglomeration models [4, 6]. Determining an upper bound on the liquid per bridge would be necessary as soon as multiple bridges were assumed to be able to form.

The hydrostatic limited approach would assume that liquid could always reach the site of lowest pressure, but if this is not the case then a contact area limited approach would apply instead, and this has been tested with some success [212, 213]. This contact area limited case is not helpful if the bridges move around the particles, as would happen with shifting and rotating particles which would increase the contact area, whereas a hydrostatic upper bound will always be restricted, and will lose and gain moisture depending on the specific circumstances.

The reason for this that essentially fluids in any system is drawn to the lowest pressure region. Once all the fluid is arranged such that the hydrostatic pressure is equal everywhere then the bonds can be certain to be stable.

The breakage of the bridges would also be important for this, as if the coalescence does not succeed, then the amount of moisture in the bridge would redistribute between the interacting granules/particles and affect their subsequent interaction behaviours. This has a relatively easy calculation which can be applied in the model [212], if this is found to be a useful direction.

The solutions here are going to assume spheres, which will make a useful starting point, and the granules form decent approximations of spheres rapidly enough that this will be suitable for the scope of this work.

6.2.1.1 Calculation of the capillary force

The Capillary cohesion of the liquid is the result of a set of surface interactions between the liquid and the surrounding fluid (here air), and the solids (here the particles or granules). The interaction with the granules is described using the fill angle and the contact angle, which describe the degree to which the liquid favours interaction with the granules, while the interaction with the air is described using the curvature and the surface and the surface tension [102, 211, 215]. Of these, the filling angle and the curvature are extrinsic properties which depend on the volume of the bridge, and in turn are also affected by the contact angle and separation of the surfaces. Estimations have been made for the total capillary force based purely on the volume with some success [121], but these do not also describe the pressure which is part of the question being asked here.

Determination of the pressure of the bridge is relatively simple, if one knows the curvature. The pressure differential between the fluids is described by Equation 6.2

$$H = -\frac{\Delta p}{2\gamma} \tag{6.2}$$

234
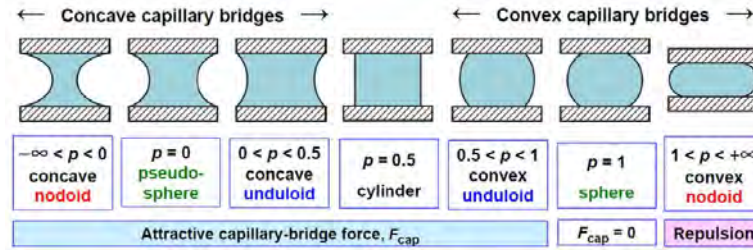
Figure 6.2: All the cylindrical cases for pendular bridges, Figure 6 from [216]

H is the curvature as calculated using the Laplace-Young equation Equation 6.1. As the curvature increases, so too does the pressure difference, resulting in greater suction. The curvature will be used alone here, as it is easier to nondimensionalise and highlight important values for.

The curvature varies depending on the volume, and so to find the pressure for a given volume requires numerical integration [102] or other numerical methods to determine the shape [211], followed in either case by disc integration of the shape formed to determine the curvature for a given volume, from which the pressure differential can be calculated.

The various bridge shapes develop as a response to the different volume, contact angles and surfaces, but always form (for cylindrically symmetrical contact surfaces) one of seven shapes, as shown in Figure 6.2 [216].

A classic approximate method is to assume that the bridges assume a shape determined by the inner space of a torus, with the spaces formed by the caps removed [82, 102, 217]. This corresponds to the pseudo-sphere case in Figure 6.2, though this is altered by the spherical nature of interactions. This toroidal approximiation has been used in DEM simulation of granules adhering to one another in motion [202]. As this method has a closed form solution, it is possible to directly calculate the volume from the fill angle, and from there the mean curvature. This is an approximation as it does not satisfy the Laplace-Young equation except in special cases, but as it is easy to calculate and the results are usually close enough to the actual results it is often used. Because the curvature is not
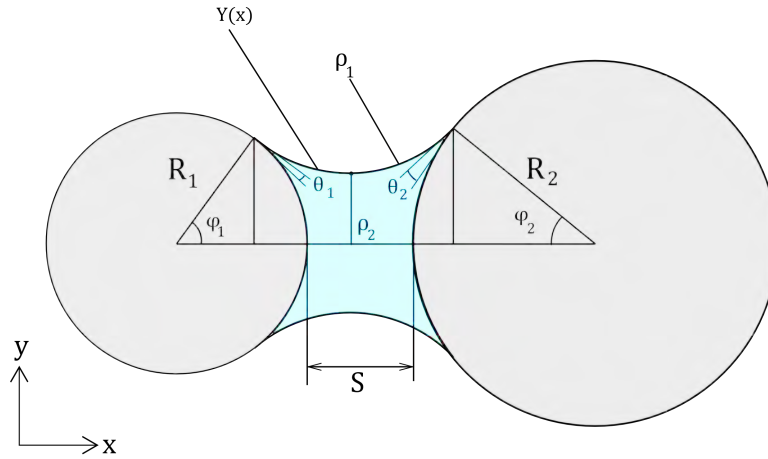
Figure 6.3: A liquid bridge between two spheres of differing size and parameters, with parameters labelled. Y(x) is the surface boundary of the bridge

equal everywhere, a choice must be made for where the curvature defined by the surface is taken. The gorge method which calculates the secondary curvature from the thinnest part of the torus, is the method used most in the literature, and appears to produce the most consistent results [218].

6.2.1.2 Dimensions for a pendular bridge

To define the liquid bridges, specifying the dimensions is necessary. Figure 6.3 lists these, which will be referred to further. R_1 and R_2 are the sphere radii, φ_1 and φ_2 are the half-filling angles, where the 3 point boundary occurs between the water, air, and particles. θ_1 and θ_2 are the contact angles. S_d is the separation distances of the surfaces of the two spheres. $Y(x)$ is the function of the shape of the surface of the bridge, which can be calculated numerically or approximated.

When applying the toroidal approximation, ρ_1 and ρ_2 are the two principal radii of curvature of the bridge. ρ_1 is the curvature of the tube, or meridian, that forms the torus and is defined by that, while ρ_2 is defined around the x-axis out into 3D space. These can be calculated using Equation 6.3 and Equation 6.4, which in turn can be used to calculate the curvature through Equation 6.5.

$$\frac{R_1(1 - cos\varphi_1) + R_2(1 - cos\varphi_2) + S_d}{cos\,(\varphi_1 + \theta_1) + cos\,(\varphi_2 + \theta_2)} \tag{6.3}$$

$$R_1 sin\varphi_1 \rho_1 \left[1 - sin\,(\varphi_1 + \theta_1)\right] \tag{6.4}$$

$$H = \left(\frac{1}{\rho_1} + \frac{1}{\rho_2}\right) \tag{6.5}$$

6.2.1.3 Dimensions for liquid on spherical surface

The curvature of the liquid on the surface of a sphere is trivial to calculate. From the reference diagram Figure 6.4, the curvature around the shell of the sphere can be calculated as Equation 6.6, where R_e is the external radius due to the liquid surface layer h_0 . From this, the curvature increases as the radius of the spherical shell decreases, which can be due to reduction in liquid or a reduction in particle size.

$$H = \left(\frac{1}{R_e}\right) \tag{6.6}$$
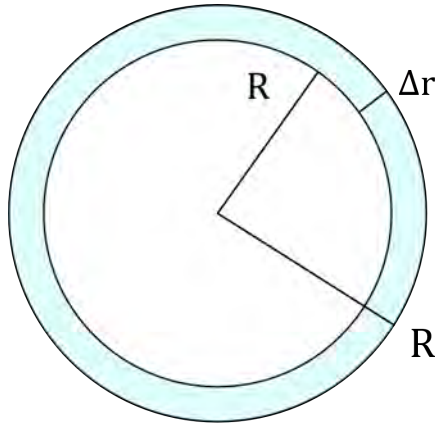
Figure 6.4: Diagram of the liquid around the surface of a sphere.

237

6.2.1.4 Nondimensionalisation and initial problems with hydrostatic limits of bridges

As the curvature is dependent on the dimensions of the spheres in question, the values need to be nondimensionalised for consistency at scale, Table 6.1.

Variable	Normalised Version	Meaning
H	$H^* = H \times R_1$	Surface Curvature
V	$V^* = V/(R_1{}^3)$	Liquid Volume in bridge
	$V_2{}^* = V/(R_2{}^3)$	Liquid Volume in bridge Scaled to R_2
R_2	$R_2{}^* = R_2/R_1$	Particle 2 Radius
S_d	$S_d{}^* = S_d/R_1$	Separation Distance

Table 6.1: Variables and Normalised or Dimensionless forms.

As H^* increases, this corresponds to an increasing degree of convexity, which in turn results in a decrease in the pressure differential. This may get confusing when discussing the relationships, but the implications will be explained where relevant. So long as $H^* < 1$, then the liquid prefers to be in the bridge rather than the surface of the spheres.

So far then, when considering the simple implications of Equation 6.5 and Equation 6.6, the curvature of the bridge will always be less than the curvature of the surface of the particle. Equation 6.6 shows that the nondimensional curvature of the particles surface will always be > 1, and because ρ_1 is negative for a convex bridge this means that the curvature of the bridge as a whole is always < 1 for any filling angle where the pendular state can be reasonably assumed ($\varphi_{1,2} < 90$).

In the context of the bridges that will be formed based on Figure 6.2 and assuming that the bridges have some degree of capillary strength ($F_c > 0$), this is evident in the nature that the pressure is always < 1 in the remaining cases, to the point where even convex bridges can have a pressure lower than that which

would be formed on the surface of the particles.

This already looks like a problem for any case of assuming hydrostatically limited bridges. In fact, the curvature of a bridge can result in not simply drawing the moisture from the surface of spheres, but even inducing condensation from the air, sufficient to cause problems [17]. This atmospheric condensation stops at the pseudosphere case in Figure 6.2, with a pressure differential of 0, but the surface of the sphere has a higher pressure than that of the surrounding air (this is in part why condensation seeds are needed for droplet formation to overcome this barrier).

There may be some other factors which could result in stability for the bridge volumes, when allowing the moisture to move freely. The contact area drawing in the moisture could impede the ability of the bridge to grow, but this does not account for the subsequent motion of the spheres around one another, which would allow the bridge to grow from moving around the surface, nor for other effects which would allow paths to form such as internal channels, such as in granules.

One other factor which could impact the bridge shape is gravity. This is normally tested using the Bond number, however for a pendular bridge this does not account for the support by the spheres. Instead a modified Bond number V^*Bo , can be used, which does account for this Equation 6.7 [219].

$$V^*Bo = \frac{\Delta\rho g V}{\gamma R} \qquad (6.7)$$

Where $\Delta\rho$ is the difference in densities between the liquid and the surrounding fluid. This is dependent on the nondimensional bridge volume V^* , using the same value from Table 6.1. So long as $V^*Bo < 0.01$, gravity can be ignored, and up to ≈ 0.15 the bond is in a transitional regime. In the transitional regime, the rupture distance decreases slightly, and after ≈ 0.15 the rupture distance decreases dramatically as the bond is weakened by the weight of the bridge itself. For $V^*Bo > 0.15$ the bridge invariably ruptures, as the liquid drains away until

the bridge is stable again.

$\Delta\rho$ is the density difference between the bonding liquid/surrounding fluid, which for water-air is ≈ 1000. Assuming water for the surface tension as well, Equation 6.7 gives:

$$0.15 > V^*Bo = \frac{\Delta\rho g V}{\gamma R} = 136250\frac{V}{R} = 136250VR^2 \tag{6.8}$$

From this, $VR^2 = 7.34 * 10^{-7}$. For small feed particles approximately $R = 1mm$, this permits the bridge V^* to be up to 0.7, which is well beyond the volume where the pendular regime is valid. For granules however, at $R = 6mm$ this decreases V^* significantly down to 0.02. This value will be important when considering the rupture distance later on.

6.2.2   Bridge Modelling

To test this, a number of bridges were numerically modelled to determine when the bridge would have a larger "convexity" than a sphere (i.e. H^* is larger than 1).

Toroidal methods were first implemented, however since numerical methods were required anyway to find volumetrically bounded bridges for some of the test scenarios, a more exact numerical method was implemented subsequently based on the exact form of the bridge [211]. Both bridges were still calculated for, simply to compare the results of the two models.

The nondimensional forms from Table 6.1 are used throughout. In all cases, the capillary bond will cease to draw in more moisture when $H^* = 1$, since the reduction in the surface volume of the spheres can only ever become as low as this.

Where otherwise not specified, the contact angle for both particles equals 0, and the separation distance is 0, and the particles are the same size ($R_2{}^* = 1$) the volume is always specified because the point is to measure the effect that drawing

in moisture will have on a pre-set bond.

6.2.2.1 Effect of Volume on Curvature

The most directly relevant variable is the volume of the bridge. As the bridge draws in moisture, this will affect the curvature as well as the fill angle, among other things. If there is a point where the increase in volume results in a curvature of the bridge greater than the particle surface, no more moisture will be drawn in.
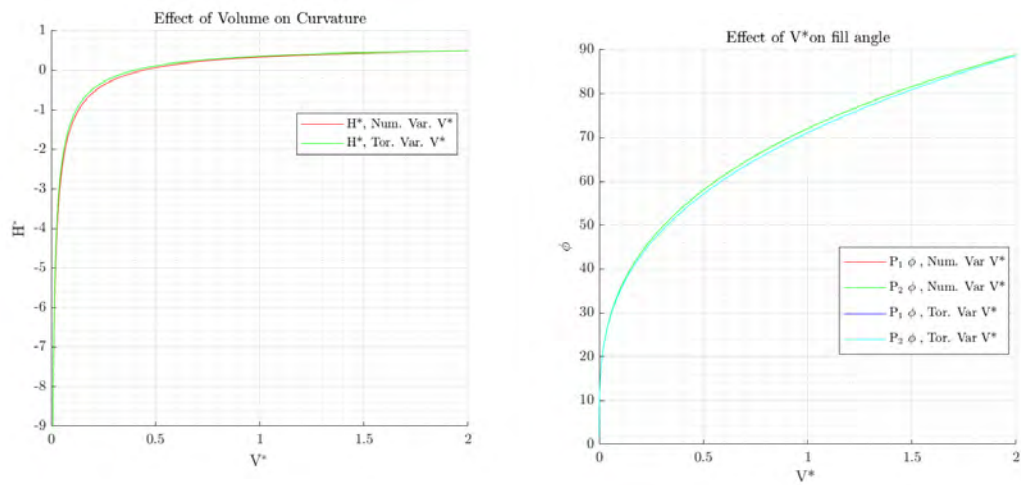
(a) Relation between Bridge Volume with Normalised Curvature.

(b) Relation between Volume and fill angles $\varphi_{1,2}$.

Figure 6.5: Relation between Bridge Volume on the curvature and the fill angles.

As can be seen in Figure 6.5, the Curvature rises extremely quickly from an asymptote at $V^* = 0$, but it does not reach $H^* = 1$ even when the fill angle $\varphi = 90°$. At this point, the liquid forms a cylindrical form between the two particles. For the toroidal case, $\rho_1 = \infty$, giving $H^* = 0.5$, which is what is shown in the plot. By this point in a real granular structure, such a large amount of fill would be well beyond a pendular bridge regime.

6.2.2.2 Sphere radius variation

The sphere radius will not vary during the process, however it may be a useful variable which can be used to map out the process behaviour and work in combination.

Testing every value of $R_2{}^*$ is impractical, so test cases are compared here and then an interesting correlation is identified which can be used to simplify the relationships. Not all $R_2{}^*$ & V^* combinations are stable, as sufficiently high volumes of liquid will engulf a smaller sphere completely.

The ratio range tested is from $R_2{}^* = 0.1$ to 1, with a fixed volume $V^* = 0.001$. This value of volume was chosen because it allowed a wide range of radii for testing before instability caused problems at the lower end of $R_2{}^*$, while still being usefully bounded on a graph.
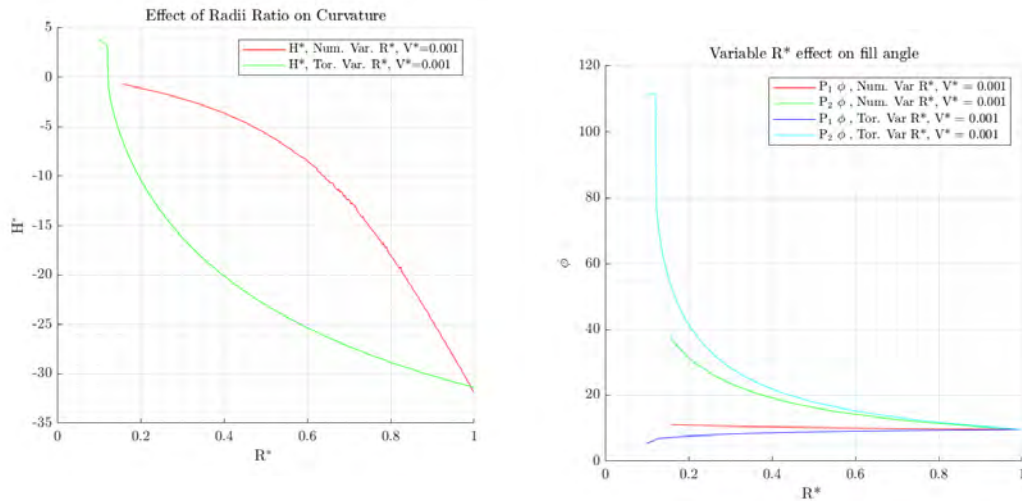
(a) Effect of varying $R_2{}^*$. As $R_2{}^*$ approaches 0.1, the functions break down, possibly due to degenerate cases.

(b) Variable $R_2{}^*$ effect on fill angle $\varphi_{1,2}$.

Figure 6.6: Relation between Bridge Volume on the curvature and the fill angles.

Figure 6.6 shows that the value of $R_2{}^*$ causes the greatest divergence between the toroidal approximation with dimensions specified in subsubsection 6.2.1.2 and the numerical method which calculates the shape exactly. In both cases, as the

variation increases, the curvature decreases. This always seems to be bounded below $H^* = 1$, which might be due to the shape that is formed.

The difference is likely due to the face that the numerical method can search for more unusual geometries, while the toroidal method is strictly limited to the inner volume of the torus, and when the diameters of the particles vary then the difference in the geometries becomes significant. In this case, the two are still demonstrating the same behaviour of interest for the majority of the range, as H^* is still negative for the majority of the range and so would draw moisture away from the surfaces of the particles.

Notice the curvature decreases as R_2^* decreased. This led to an idea that if the volume was nondimensionalised with respect to R_2^* in the form of $V_2^* = V/(R_2{}^3)$ then the solution would be easier to model, given that the radii variation tends to result in significant instability. With this scaling, Figure 6.7 shows that this gives a reasonably strong approximation. Only the numerical case is plotted, to prevent confusion between comparisons. The low V_2^* region shows the greatest variation, which is an asymptotic drop so the difference in practise is lessened.

Figure 6.7 is restricted to the values of V_2^* as beyond these is the point where the instability occurs and the line ends due to the bridge rupturing in Figure 6.6a. This plot more clearly shows that the bounds are limited to below 1, and instability is reached well before this occurs.

A final point to note is that the curvature of the smaller sphere becomes more convex as it gets smaller, so more of the moisture will be drawn from the second as the difference in pressure will be greater.

6.2.2.3   Contact angle

Testing the contact angle is more likely to result in a limiting bridge volume, as the contact angle can more directly alter the curvature towards the convex shape necessary. Here, multiple values of V^* can be tested without causing such severe instability issues, so three examples are plotted.
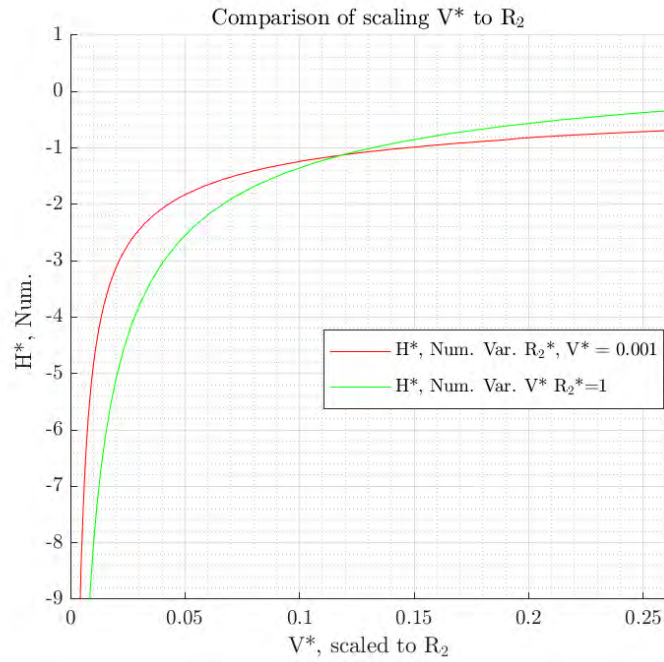
Figure 6.7: Comparison between H^* and varying V^* scaled to R_2 using two methods. V_2^*, where the torus is calculated as if the radii are the same but the volume changes by scaling to R_2^* instead of R_1, and by simply varying R_2, and calculating for a single volume.

Figure 6.8 shows that the value of H^* is positively correlated to θ, and even shows that the contact angle can push the value of H^* over 1. However the value does not have any simple transformation, such as a shear or rotation around a central point, and the threshold value of $H^* > 1$ does not correspond to $\theta_{1,2} + \varphi = 90°$ which was checked. This crossover point is more strongly dependent on the value of $\theta_{1,2}$ than V^*, but even for the generous case of $V^* = 0.8$, the crossover point is $\approx 60°$, at least for equal diameter particles. At this point, the material is beginning to become actively hydrophobic, making it much harder to granulate [220].
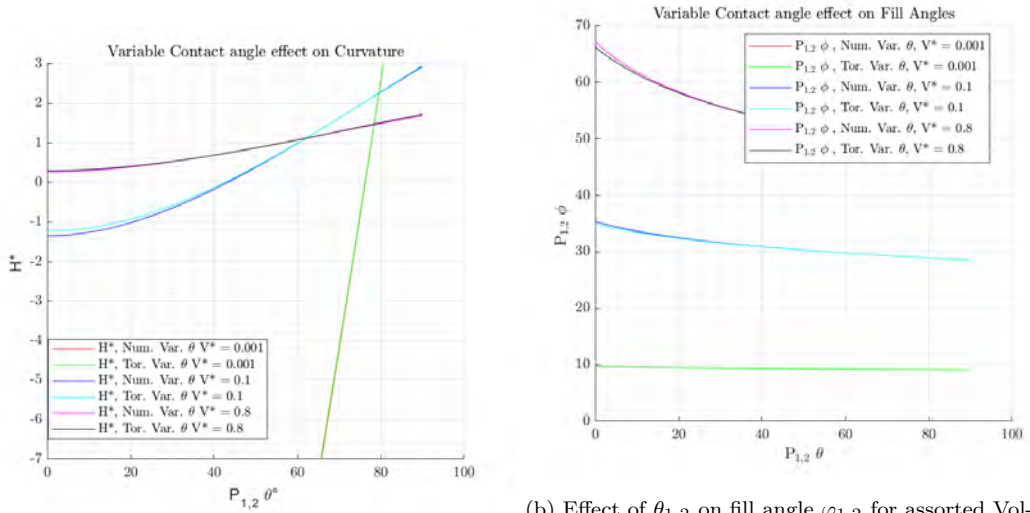
(a) effect of $\theta_{1,2}$ on H^* for assorted Volumes.

(b) Effect of $\theta_{1,2}$ on fill angle $\varphi_{1,2}$ for assorted Volumes. The fill angle for P_1 and P_2 is equal, as they are symmetric.

Figure 6.8: Relation between contact angle on the curvature and the fill angles.

6.2.2.4 Separation

The final geometric variable is the particle separation. The separation distance is known to be altered by the variation in size, the volume of the bridge and the contact angle. An empirical relationship has been found for the correlation between these values, Equation 6.9 [130].

$$S_{drup} = \left(1 + \frac{\theta}{4}\left(\frac{R_2}{R_1} + 1\right)\right)\left(V^{*\frac{1}{3}} + \left(\frac{R_2}{2R_1} - \frac{2}{5}\right)V^{*\frac{2}{3}}\right) \qquad (6.9)$$

The spheres will still be assumed to be equal sized, as before. The rupture distance S_{drup} for the volume limit for spheres R=6mm for a stable V^*Bo, $V^* = 0.02$, can be calculated using Equation 6.9. Doing so finds that the maximum separation distance gives (for $\theta = 0°$) $S_{drup} = 0.2788$mm. This is significantly smaller than the spheres in question, and would likely break immediately. However, the separation distance itself can alter the curvature.

To compare the effect of increasing the separation of the spheres, the nondimensional separation distance will be further reduced to $S_d^+ = S_d^*/S_{drup}$ which

245

provides a way to reduce the variation caused by the difference in volume and contact angle. Equation 6.9 is an empirical relation and not an exact analytical relation, and so though rupture would ideally be predicted at $S_d^+ = 1$, the actual bridge rupture distance, as indicated by the line ending as S_d^+ increases may not precisely match this as the line ends when there is no valid bridge shape that can be found.
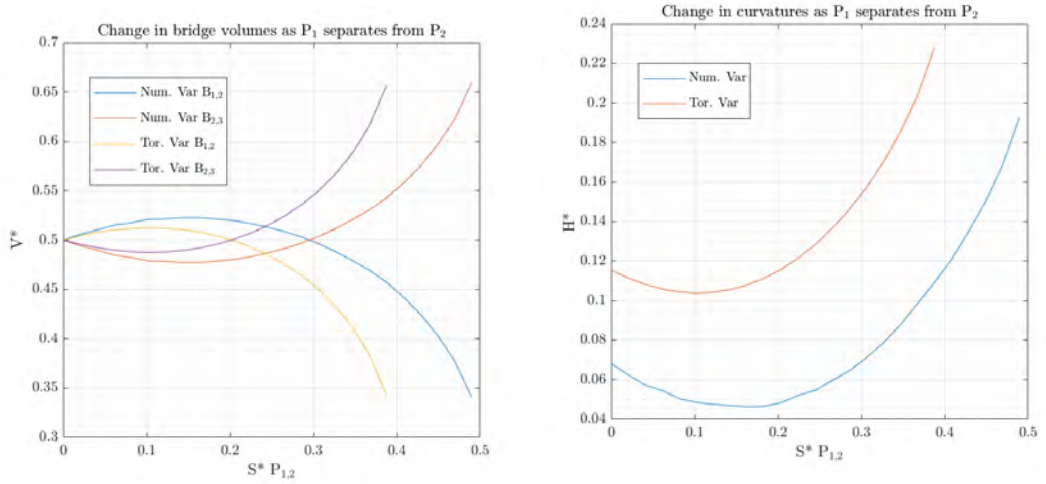
(a) Effect of varying S_d^+ on H^* for assorted Volumes.

(b) Effect of varying S_d^+ on fill angle $\varphi_{1,2}$ for assorted Volumes. The fill angle for P_1 and P_2 is equal, as they are symmetric.

Figure 6.9: Relation between Sep Distance on the curvature and the fill angles.

Figure 6.11 shows that initially, as the spheres move away from one another, H^* decreases slightly. This reaches a minima, at which point the curvature actually increases again above the starting value of H^* when the spheres were in contact. The contact angle does not appear to significantly alter the shape of H^*, however this was only checked for the large volume case.

Interestingly, the toroidal approximation is poor at predicting the effects due to the separation distance. The fill angles increase towards the end, especially for the $\theta = 0$ cases. These increases correspond to a shift in the geometry, however the toroidal approximation intrinsically assumes the geometry is constant throughout

of a circular arc.

Even so, at the very high volume and contact angle case of $V^* = 1$ and $\theta = 45°$ the bridge separated at the moment where $H^* \approx 1$.

6.2.2.5 3 sphere hydrostatics

The most interesting results came from the analysis of the simplest possible case where two bridges are connected. By assuming that the bridges are connected only hydrostatically, and that they do not significantly deform the pendular bonds, a case similar to a dimer is modelled, which is shown in Figure 6.10.
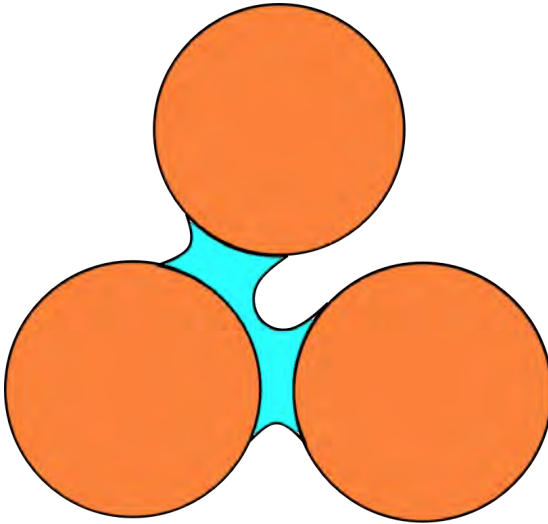
Figure 6.10: Diagram of distinct bridges hydrostatically linked. This is derived from [221], where it is an example of asymmetric draining of bridges as they separate.

Even though this case rarely appears in experiments, this does provide a useful method of examining the behaviour of a volume limited case. Essentially, the model examines the effect of two bridges that have equal H^* values. The effect of the separation of one of the bridges on the volume of the other will be considered. The same simplifications used previously are applied.

To see what effect the changing distance of one particle has on the bridges of both particles then, the total V^* for both bridges was kept constant as the distances changed. The change in each bridges volume then comes from the redistribution of volumes to keep H^* equal between the two. S_d^* is used rather

than the previous $S_d{}^+$ since V^* is used in calculating $S_d{}^+$, and the effect of the separation itself is being tested here on how it affects the volume

(a) The volumes of each bridge.

(b) The Curvature of the bridges.
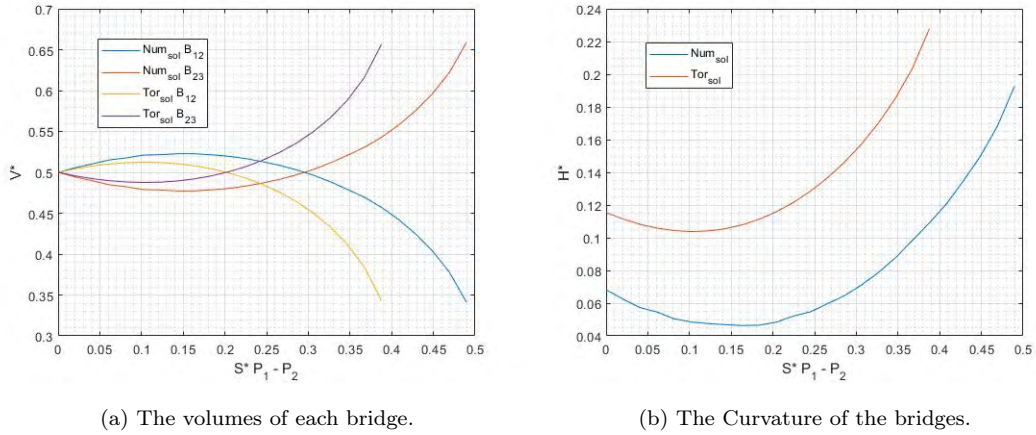
Figure 6.11: Relation between $S_d{}^*$ and V^* and H^*

as Figure 6.11 shows, the volume of the separating bridge actually increases before it decreases. This is a natural consequence of H^* decreasing as separation increases, which then requires the static bridge to reduce its volume by contributing some liquid to the separating bridge, which also increases H^* for that bridge. The bridges also rupture before they completely drain, though the two effects feed into one another. Note that the shapes of the H^* curves mirror those of the volumes.

The symmetry observed in Figure 6.11a is a result of there only being 2 bridges and re-distribution occurring between them. Additional bridges show the same behaviour, with more moving bridges reducing the rupture distance and more static bridges increasing the distance before rupture of the moving bridge.

6.2.2.6 Discussion

The effect of varying particle size showed an interesting scaling behaviour. This is probably because the smaller particle has the greatest effect on the curvature of the moisture. Figure 6.6b shows that the fill angle of the larger particle varies

very little. In some sense the size of the larger of the two spheres does not matter, as the bond approaches the case similar to that of a sphere and a plane, when the perspective is scaled to the smaller particle. For such a case, by decreasing the size of the smaller particle and holding the V^* stable, this results in V_2^* effectively increasing.

Overall though, all the above demonstrates that for nearly every practically relevant case, so long as the liquid can go into bridges, it will. Addition of extra surfaces to the network will immediately form new bonds which will further draw moisture to the low pressure states of the bridges, leaving no moisture on the surface.

This is reasonably intuitive, as liquids will bond between any vaguely hydrophilic surface. The only case where the bridge was not favoured was for the highest contact angles.

Simply considering Figure 6.2, the only case where the bridge begins to become disfavoured for liquid to move towards is also the point where the liquid acts as a repulsive force against the surfaces.

Given this, clearly there is no stable case for when the liquid prefers to be on the surface of a sphere. Although the hydrostatic assumption is idealised, the surfaces will move relative to one another as mentioned, which will draw moisture to the bridge in areas beyond the initial area of contact, meaning that the contact area limited case is also idealised though in a less immediately obvious way.

This interferes with the baseline assumption for the Stokes criterion, but this is a topic for chapter 7. It also makes it difficult to assume pendular behaviour for any situation where there is even the slightest amount of saturation. The volume will always fill bridges. Further, as established in the literature, this dimer case is very abnormal and the more stable case is usually the trimer bridge, when the pendular assumptions are no longer valid.

For the basic case using similar hydrophilic spheres described above, the fill angle before the bridges coalesce is 30° [17]. The value of V^* where this occurs

is only 0.1. Because of the nature of the nondimensionalisation not being directly related to the full sphere volume of both spheres, this corresponds to only $0.012 \times V_{P_1}$ (see section A.1 for the details), so the volume fraction $V_{l/s}$ only needs to be above 1.2% locally before the pendular regime starts to transition into the funicular regime. In the global case this is a significant underestimation due to the effect of many bridges per sphere [171]. This idea of locality will be returned to later when considering the effect of the spray.

The three particle bridge case was also useful in showing how the bridges will transfer moisture to one another to prevent pressure differences. This may give part of the explanation as to why the higher saturation cases tend to produce less brittle bonds, since the bridges can contribute additional liquid volume to extended bonds while they remain linked. This is relevant as the change in yield stress in saturated materials is not solely from a purely frictional effect which can be altered through lubricity changes [118].

The general findings of this section are that the bridges for any slightly hydrophilic material are extremely stable and favourable. The bridges will draw in all the moisture of any surrounding surfaces that are hydrostatically linked to them, converting the problem into an area limited one instead of a pressure limited one. On the other hand, since the granules are structurally formed of solids bound by liquids, they should be hydrostatically linked, at least at the scales and saturations expected in the problem. This raised other questions though, particularly regarding the logic of the Stokes criterion for granulation, which implicitly required an oversaturation of the granule surface [4, 37], which is a problem since oversaturated granules are well known to result in a slurry.

6.2.3 Funicular

The upper limit of S for iron ore pelletisation is significantly higher than the value for the pendular regime, with multiple sources reporting values of S from 0.8 to 1 [47, 116]. This is clearly significantly higher than that where the pendular

250

regime is relevant internally to the pellets, while also being too low for a surface layer to be developing.

6.2.3.1 Funicular Boundaries

The topic of the funicular state has been mentioned a couple of times now. It is worth examining in detail, since it comprises the boundary of states between the nearly fully saturated capillary state and the low saturation pendular state. The boundaries for these two states can be found for the ideal case of monodisperse spheres, with the value $S = 0.341$ for perfectly wetting spheres [171]. Other values can be calculated for, however this value is surprisingly close to the value found in Schubert and Rumpf's [94] experiments when the stress response changes. An upper limit is vaguely defined as being the point of $S = 1$, though this depends on how the pores are defined.

Definitions are not very clear in general for this topic. The funicular state is simply an arbitrary state which is between the pendular and capillary state, but unlike many transitional regimes which tend to be relatively narrow or avoidable, this is the primary regime which most wet granular materials exist under. It also depends on whether individual cases are being examined or bulk cases for the type of bond being considered.

This causes problems when attempting to define a suitable strength value for how the saturation affects the strength, since as established the coordination number is a better defining value for the pendular state, while the total saturation does appear to be relevant for the capillary state. This is further complicated by the apparent path dependence of the saturation on the strength [118].

This path dependence in particular highlights that the saturation alone cannot define the strength. This can be explained in terms of the previously considered curvature behaviour however, and therefore the appropriate descriptor defined.

Essentially, the forms of the liquid bonds are inhomogeneous. Some will be in larger networks of bonds, and some will be in individual pendular bonds,

251

and some contacts between particles may even have no liquid contact. This inhomogeneity has been observed in practise [112,169]. However, the implications of this behaviour has not been noted and collected with other research.

Ideally, matter seeks to be in the lowest energy configuration. In the case of the liquids, this corresponds to the lowest pressure configuration. This is why the liquid moves from high to low pressure regions, and would theoretically correspond to the case with a perfectly even distribution of liquid between all the bonds possible. In practise, this is not observed, because the liquids have to actually reach these other bond sites. If the liquid is being added from an external source, then the liquid can either connect new bonds, or add to a pre-existing network bond. Once in either of these states, unless further liquid is added or the system manipulated, it will be in a local minimum energy configuration.

This physical restraint causes the liquid to reach local minima. Once the liquid is in a local energy minima, it cannot move to other bonds even if they would be preferable. This leads to the situation where there can be dry interactions near large networks, even though the initial bridge contact forms an extremely low pressure state for the low volume that initially forms it, as seen in Figure 6.5. The hydrophilic, perfectly wetting assumption allows the liquid to move to any site where this is preferred, but if there is any contact angle then the liquid has to overcome an energy barrier to transfer from the network to the lower global energy bond, which is in excess of the local state.

The efficiency of network bonds comes from a reduction in the surface boundaries. Because of this, as additional particles are connected in a mutual single bridge the liquid is locked further away, until it cannot be contacted by further particles. The trimer and other more extensive capillary networks are more energetically efficient than pendular bonds *if* the pendular bridges make contact already [101, 168]. As the centre is now filled, a capillary bond requires more liquid to reach the point where the fill angle reaches 30°on the outer edge of the particles, where it can start connecting to other networks.

This being the case, because the networks enclose the liquid once trimers or further have been formed, though these are less globally efficient, they will be statistically favoured, as it is harder to separate into a trio of pendular bonds once the trimer is formed, rather the drainage tends to form dimers [221], which will contain more liquid than the original bonds and so will be easier to connect with other particles due to a higher fill angle.

A final piece of the puzzle comes from noting that pendular bonds are stiffer by volume as they only need a small amount of volume per bond, as the total number of bonds define their strength. Capillary bonds meanwhile have more volume and have a greater separation distance, which leads to greater resilience of the bonds, but as the volume is inefficiently placed this results in a lower overall strength, or even a loss of strength as there is no surface boundary which applies a tensile force to the connected particles.

By considering the energy efficiency, and network connections, this leads to an explanation as to why the suction behaviour is path dependent, as seen in Figure 2.40 and Figure 2.41. If the liquid is removed, then it is removed from the least energy efficient by volume regions first. This leads to a more even distribution of the liquid, which in turn results in more pendular bonds, in turn resulting in stiffer and greater yield stress assemblies, but less resilient overall bonds. Meanwhile, if the liquid is added, then there are more network bonds, which provide more resilient bonds but are less efficiently arranged for the strength and so produce a lower yield stress. Since the force transmission in granular materials is itself heterogeneous, with some paths experiencing greater or lesser stresses [194], this can make the variation in the capillary connections more relevant.

The funicular state then is therefore simply a poor descriptor of the heterogeneous nature of wet particulate assemblies. Rather than viewing it as a single state, a better way to view it is as a proportionality of the capillary bonds and the pendular bonds present in the assembly.

6.2.3.2 Funicular Definition

So, this having been established, this fits nicely into the examination of the resultant strength. The most effective methods Equation 6.10 which have previously worked [106, 107] are those which model the behaviour as a simple weighted combination of the strengths of the capillary and pendular states, weighted by the saturation boundaries of these states $S_{f,c}$ and $S_{p,f}$.

$$\sigma_{t,f} = \sigma_{t,p} \frac{S_{f,c} - S}{S_{f,c} - S_{p,f}} + \sigma_{t,c} \frac{S - S_{p,f}}{S_{f,c} - S_{p,f}} \tag{6.10}$$

In the above line of reasoning, Equation 6.10 works because the saturation is being continuously mixed in the cases where it is tested. This then acts to divide the moisture between the types of bonds accordingly, which fits into the idea that the funicular strength is determined by the proportionality of the two bond types.

That this weighted proportionality fits the evidence is promising. It suggests that the funicular strength is predictable.

Cases such as condensation of moisture from the air into the low pressure regions, and drainage from the bulk from higher pressure regions tend to favour pendular bonds. Meanwhile imbibition from a reservoir into a stationary granular mass will tend to result in more capillary networks being filled, and a more heterogeneous fill state where some regions have low strength due to a lack of surface tension and others have a low strength due to lack of any bridging.

Where the liquid and particles are agitated as in the shearing or presumably pelletisation, the networks form and break, resulting in a more homogenous distribution of bonds which can be approximated using Equation 6.10, at least for homogenous particle materials.

The breaking and re-connecting of bonds suggest that if the particles to be agglomerated have variable hydrophilicity, the bonds will preferentially form with the more hydrophilic particles.

Given the previous analysis that contact angle, which defines the hydrophilicity, is the only property which can make the bridge less preferred than the surface due to the curvature needed, will lead to separation of the moisture from the hydrophobic particles. If one is hydrophilic, and the other hydrophobic, the separation distance will result in preferential movement of the liquid from the hydrophilic to the hydrophobic.

This leads to a separation of the materials into agglomerates mostly formed of the hydrophilic particles and fines formed of un-bound hydrophobic particles, and this is found to be the case [66].

6.2.3.3 Simplest effective model for pendular to funicular state bonds

During the research for valid models of capillary bonds when this was still being considered as a method of modelling the process, an extremely effective solution was uncovered which also describes the transition to the funicular state well [123]. The authors show that a simple constant force applied to the particles, along with a viscosity, can satisfactorily model capillary bonds in a shearing granular material. This works because of the nature of pendular bonds being, as previously mentioned, more dependent on the coordination number rather than the volume, which simply increases the number of individual bonds in the bulk. This then allows the transition to the funicular state to be a matter of limiting the capillary component of bonds to the number of dimensions, to represent excess bonds lacking a surface boundary to form a pressure difference.

This is mentioned as the less localised nature of the bonds becomes relevant later for the yield strength.

6.3 Yield Strength

The yield strength of granular materials is evidently a complex affair, with various solutions to calculate the strength offered by various sources. Unfortunately,

many of these solutions do not provide much in the way of comparison between one another or keep track of assumptions. The assorted forms of yield strength will be examined here, so that the most appropriate can be applied to the simulation model.

First and foremost: the compressive yield strength and the tensile yield strength are two different values. As shown in Figure 2.39, the characteristic behaviours of the material depends on the direction of the force applied. Generally speaking, the compressive strength is greater than the tensile strength [36, 153], because ultimately the compressive strength also involves interparticle friction behaviours. The two are interrelated however, along with the hardness value of the material [222–224].

Given this, determining which is relevant is important. The answer to this is, both unsurprisingly and inconveniently, that are both important in different circumstances. The compressive yield strength is important for the granules resisting deformation, which is relevant for the Stokes Criterion of agglomeration for the plastic case [6], as well as the general situation of breakage in agglomeration [80]. The tensile strength is less generally relevant, however the Bond Probability Criterion [45] which provides one growth limit in Equation 7.3 is partially defined by σ_{bond} , the strength of the bond between pellets, which is dependent on the tensile strength [153].

The solutions considered must also be applicable to the circumstances at hand. For instance, as established in subsection 6.2.3, the saturation regime must be appropriate. Additionally, it is important whether or not the solution models the confined or unconfined yield strength. The unconfined yield strength allows the material to dilate and deform, weakening it, and is also more appropriate for the pelletisation process. Finally, it needs to suitably account for the dynamic behaviours, and the strain rate variance of the strength.

The solutions were mostly covered in subsection 2.2.3, but here they will be further synthesized and considered in more depth.

6.3.1 Dimensionless Yield Strength

The dimensionless yield strength is a practical method to evaluate the important variables that need to be accounted for in a theoretical model of the yield strength, and this fortunately applies for both the tensile and compressive strengths [100]. The dimensionless yield strength function described in [100] provides a reasonably comprehensive list of the important variables that need to be accounted for.

$$\sigma_y{}^* = \frac{\sigma_y d_p}{\gamma cos\theta} = f\left(\frac{\mu\dot{\varepsilon}d_p}{\gamma cos\theta}, \mu_f, S, \phi\right) \tag{6.11}$$

This is noted as not accounting for the shape of the particles, which is difficult to capture in a single variable, and the shape of the entire distribution as well. These two factors, while not directly included, are abstractly accounted for in μ_f and ϕ. Still, these will be returned to in time.

6.3.2 Capillary Cohesive Strength

A significant work from which many other solutions originate from is that developed by Rumpf and Schubert [93, 94]. The earliest solutions consider only the capillary forces for the pendular and capillary regimes. The friction and viscous forces are ignored, however Equation 2.19 proved to be effective at modelling the behaviour. The funicular is treated as the effect of the capillary and pendular solutions superimposed, similar to Equation 6.10.

The pendular case then is given previously in Equation 2.17, and the capillary case is Equation 2.19, and the superposition of these two does seem to work, as shown in Figure 2.38. The cases have constants and relationships to describe the coordination numbers and porosity functions to support them, and these are based on the monodisperse spherical cases.

One of their observations find that the yield strength drops to 0 when the agglomerate becomes oversaturated. This supports the case of capillary strength being the primary source of strength, since capillary strength relies on a surface

boundary, which ceased to exist if the internal space is completely filled.

Ultimately, only the capillary strength was tested, and in the steady-state case, and the liquid used was water, which has little viscosity. A variant, Equation 2.20 was developed which accounts for the fact that the viscous forces dominate at higher collision velocities [4, 100] a version which calculated the viscous forces as well was developed [95].

The viscous force alone cannot define the strength, as it would not be able to provide static strength. However, the capillary force alone does not provide a mechanism for the dynamic strength increase which has been observed. This is the reason that the viscous and the capillary forces were simply combined linearly in Equation 2.21, which is used for the yield strength modelling of breaking pellets [105], and to which the empirical findings from [111] are used to justify the inclusion of the aspect ratio, to account for the interparticle friction.

$$\sigma_y = \mathcal{R}^{-4.3} S \left[6 \frac{(1-\epsilon)}{\epsilon} \frac{\gamma cos\theta}{d_p} + \frac{9}{8} \left(\frac{(1-\epsilon)}{\epsilon} \right)^2 \frac{9\pi\mu v_p}{16 d_{3,2}} \right] \qquad (6.12)$$

Unfortunately, this is a case of simply re-using equations without considering their context or validity. For starters, the viscous model is simply incoherent. It depends on the relative velocity of the moving particles as a core basis for the definition of the strength. The choice of velocity used, however, is that of the tip speed of the impeller. This is inappropriate, since the particles in the bulk will not be moving at this rate towards or away from one another.

The fastest moving particles could be argued as those that were just impacted. But since these will be moving into the bulk of the granule, they cannot meaningfully be considered to be acting in tension, and the compressive strength would not apply at those particles but the surrounding particles being shifted. In the intervening pellet structure, the energy will be dissipated through re-arrangement of the particles, internal viscous dissipation, and frictional effects, all of which will reduce the velocities which are actually of interest.

Further, the application of the aspect ratio in this way, directly conflicts with

258

their choice of Equation 2.19 by using $C = 6$ in their case, since this is only verified for mono-sized spheres [93, 94], is dependent on the particle arrangement [107], specifically the relationship between the coordination number and the porosity [36], for which the monodisperse sphere case produces the lowest values, as visible in Figure 2.55 and Figure 2.59.

Inappropriate re-use could be why Equation 2.19 has been stated to consistently overpredict the strength of granules [36] as well as underpredict the strength for fine, widely sized particles (which would have greater coordination) [100].

Rumpf and Schubert's contact based model has been developed from a different angle, which applies the adhesion force F_{adh} of the particles directly, in Equation 6.13 [36].

$$\sigma_t = 17.5 \left(1 - \epsilon \right)^4 \frac{F_{adh}}{\sqrt{d_p a}} \tag{6.13}$$

The adhesive force F_{adh} , is assumed to be related to the pendular tensile strength, but the mechanism allows it to account for any form of adhesion. However, as it relies on a , the maximum flaw size, it is ultimately a fracture model, and so only suitable for brittle fractures. Where it has been applied in the brittle case, it has been found to work [225], which itself suggests it is unsuited to the higher saturation case necessary.

6.3.3 Dynamic Bulk Strength

The strain rate dependence of the strength is an important feature in the definition of the strength [108], and a series of works progressively account for this, as mentioned in the literature review. This research importantly accounts for the capillary number:

$$Ca = \frac{\mu \dot{\varepsilon} d_p}{\gamma cos\theta} \tag{6.14}$$

Which allows a dimensionless measure of the effect of the strain rate on the yield strength of the particles. The strength behaviour is shown to demonstrate

work softening behaviour, with a peak stress that falls to a constant flow stress [226]. Up to the peak stress the stress-strain curve does show a rough linearity, permitting a pseudo-elastic response.

Based on the above dimensionless form of the yield strength, the dynamic strength was measured at a range of capillary numbers [100] which were found to collapse to a single curve. In the first set of experiments the material used was limited to ballotinis, and the liquid was evenly mixed to a saturation of 0.7 and a porosity of 0.35. The results found were very consistent, with a final empirical relation Equation 6.15.

$$\sigma_y{}^* = k_1 + k_2 Ca^m \tag{6.15}$$

the values for k_1, k_2 and m for this initial case are $k_1 = 5.3 \pm 0.4$, $k_1 = 280 \pm 40$, and $m = 0.58 \pm 0.4$. k_1 is the constant dictating the strain rate independent strength and k_2 affects the strain rate dependent strength.

This work was technically followed up [110], though when other variables such as saturation and particle types were modified the behaviours experienced significant divergence and the data was only matched to Equation 6.15 for irregular copper at the same saturation as for the previous experiments. For these, $k_1 = 30$, $k_2 = 740$, and $m = 0.47$ provided the best line of fit for these particles. The experiments found that for some of the particle types, higher saturation resulted in greater compressive strength. These particles were generally highly irregular, so an increase in the saturation would have been expected to increase the lubrication distribution.

A significant amount of work was put forwards in Smith's thesis [111]. This work has been used to support published findings [105], for whom Smith is one of the authors. A major focus was to investigate the effects of different aspect ratios and particle size range spans on the behaviour, which provided a practical means of pre-determining some of the effects that were not included in the prior studies.

For large ballotini, a critical capillary number is identified where the deformation is plastic and semi-brittle occurs, which is also the point where the yield stress transitions from being strain rate independent to being strain rate dependent. However, this correlation is poorer for small ballotini and not applicable for lactose, meaning it is tied to the particle size and shape. Smaller particles tend to remain brittle for higher Ca values, and the non-spherical lactose particles also required higher Ca values, possibly due to increased interparticle friction and possibly a non-uniform porosity distribution. However, a wider size range of particles appeared to produce plastic deformation sooner in the lactose compared to the ballotini, possibly due to the fine particles lubricating contact between the larger ones.

Despite various particles being tested and at various saturations, only a small adjustment to Equation 6.15 is made to add the effect of aspect ratio, and m is left the same as found in the previous study, to give Equation 6.16.

$$\sigma_y^* = \left(7.0 + 221Ca^{0.58}\right)\cancel{R}^{-4.3} \tag{6.16}$$

For the strain rate dependent regime, where $Ca > 10^{-2}$, a more complex correlation was developed, in Equation 6.17. This region, which appears to correspond to the region where the multiplier from k_2 is relevant, was found using multi-variate regression analysis of the experimental results.

$$\sigma_y^* = 4346(Ca^{0.401}S^{1.577}\epsilon^{2.059}\cancel{R}^{-2.25}S_p^{0.799}) \tag{6.17}$$

With S being the pore saturation, ϵ being the pellet porosity, and S_p being the span of the particle distribution.

This however is another case of improper examination of assumptions. Equation 6.17 suggests that ϵ has a positive correlation with strength. This is counter to all other experiments and research in general. Even the premise is logically flawed, since it suggests that a real value of σ_y^* could be found with a porosity value of 1, when there would be no particles in the granule at all.

This is likely another case of confounding variables. The irregular powders used were found in related studies [110] to have a higher porosity than the spherical powders, and this irregularity would result in greater interparticle friction and interlocking.

This is pointed out to further highlight the necessity of analysing mechanisms behind a value and not taking pure statistical fitting at face value.

Another similar branch of research considers the effect of prior compression, in the form of the pre-compressive stress C_s on the strength of the granular material [126]. Equation 6.18 shows the strain rate dependency as well, but the form is still ultimately based on Equation 6.16, with slight adjustments to account for the inclusion of the pre-compression.

$$\sigma_y{}^* = \left(2.04 + 17.6Ca^{0.58} + 0.0019C_s\right)\mathcal{R}^{-4.3} \tag{6.18}$$

However, the fitting is fairly poor in some cases, with errors of up to 30%. Further, for some of the particles tested, the materials show a clear error that is directly proportional to Ca , suggesting an incorrect value of m. The evaluation is based on data fitting and selecting the fit with the greatest R^2 value while applying different fitting techniques to each to find the best value from each different fitting technique.

Further, the pre-compression would act to consolidate and reduce the porosity, which would lead to an increase in strength as well which is not considered in Equation 6.15.

Underlying mechanism

Despite these issues, all of these theories do agree in general with the deformation mechanism proposed by Iveson and Page in [109], where the transition between brittle and plastic behaviour in the strength is explained theoretically based on localised shearing.

In summary, when capillary (or other localised bonds it seems) forces dominate the strength behaviour, the material behaves like a dry powder. The strain as a result is applied in localised shear planes, which results in brittle fracture. When viscous forces dominate, the strain becomes distributed over a shear zone, which increases with the strain rate. This results in less strain in each individual layer, promoting plastic deformation.

Whether it must specifically be viscous forces, since they are strain rate dependent, or merely that the viscous forces are a de-localised bonding mechanism and the strain-rate dependence is simply due to the nature of viscous forces themselves being strain rate dependent is not discussed, but may be of interest to related fields.

Returning to the mechanism proposed, this proposes that the value of the peak stress has the relationship $\sigma_y{}^* \propto \overline{Ca}^m$, where $\overline{Ca}$ is the *average* capillary number across all the shear planes. When the capillary forces provide the strength and the mechanism is brittle (high Ca planes where the stresses are concentrated through) $m = 1$. Meanwhile, when the viscous forces dominate, the mechanism is plastic (the stresses are more evenly distributed through the network and there are many lower Ca planes all deforming), $m = 0.5$.

This bounding of $0.5 < m < 1$ is generally in agreement with all the above researchers works [100, 110, 111, 126]. Therefore this behaviour needs to be accounted for in any simulations which seek to model granule mechanical strength above the pendular regime [222], and though a fully coupled DEM-CFD simulation could be implemented, the previously mentioned high efficiency model for the funicular state by [123] could be better suited.

The proportionality between the capillary and viscous contribution to the strength in the bulk are considered with respect to the rate of shear in [109]. However, the premise suggests that this may still be applicable for other reasons that the stresses are localised or delocalised, such as higher or lower saturation regimes causing either pendular or capillary bonds to dominate.

This could explain earlier research where increasing the saturation increases the yield strength for viscous binders [5]. The same paper finds that for inviscid binders, the saturation has a very slight effect. The reason is suggested as being caused by the competing mechanism of reducing the interparticle friction, which outweighs the increased viscous strength.

6.3.4 Other Variables

Other properties which are not directly considered in yield strength theories but will be useful to note in the summary are noted here.

Friction

The internal friction coefficient relates the shear stress τ_f to the confinement pressure σ_n via the Mohr-Coulomb relation [112] as Equation 6.19

$$\tau_f = \mu_f \sigma_n \tag{6.19}$$

This internal friction coefficient can be measured using the angle of repose [118], with the simple relation $\mu_f = tan(\theta_c)$ where θ_c is the critical angle of repose.

Cohesion σ_c complicates this behaviour, extending Equation 6.19 to Equation 6.20 [118]

$$\tau_f = \mu_f \left(\sigma_n + \sigma_c \right) \tag{6.20}$$

This then results in the internal friction coefficient relation to the angle of repose of Equation 6.21

$$\mu_f = tan(\theta_c) \left(1 + \frac{\sigma_c}{\rho_s D_{pile} cos\left(\theta_c\right) g} \right)^{-1} \tag{6.21}$$

where D is the depth of the pile and not the diameter of the particles. Though this is still practical, further complicating matters is the fact that there are multiple values for the angle of repose, depending on the flow of the particles [162].

There is ultimately a limit where this method can be used, since by necessity the agglomeration of particles can lead to overhanging of agglomerates, where the cohesion completely overcomes gravity.

Instead a more direct relation for the effect of moisture on the internal coefficient of friction would be beneficial as is given in Equation 2.25 [112]. This is reproduced here, modified to use values more relevant to the wet agglomerate case to give Equation 6.22.

ϕ is specified as a function of (I, P^*), though here it is relevant to define it as $\phi = 1 - \epsilon$. Further, based on the relationship between the coordination and the porosity [36], the coordination number very approximately corresponds to $Z \approx (C/\epsilon)$, and this is the relationship also used by [93, 94]. Based on these relations, Equation 6.22 is developed.

$$\mu_{fw,theor}^*(I) = \mu_{f_d}^*(I) \left[\frac{\gamma}{\sigma_n} \frac{C}{d_p} \frac{(1-\epsilon)}{\epsilon} \right] \tag{6.22}$$

The experiments in [112] were restricted to the pendular regime and the lower end of the funicular regime, though ironically how this relates to the saturation is difficult to ascertain as the choice of liquid volume as being measured by the coordination number Z of the particles is unique. Once again, the porosity function arises, though now it is obvious that it is a result of expansion from $Z\phi$.

Unfortunately, this is where the applicability of this function ends. The I requires knowing the value of the $\dot{\gamma}$, and this is not trivial to determine for an impact, which will have changing shear rates.

Directly modelling these interactions in the simple pendular case [227], including friction suggests that generally speaking the frictional increases the strength for low friction values, but it levels off quickly. Within the setup modelled this is found to be at around $\mu_f \approx 0.2 \sim 0.4$. However, note that $\mu_{f_d}^*$ is a function of I. This relation is of a similar form to that of the capillary number to the strength [228].

In the end, tribology is a deep topic of its own. Even integrating the dry

friction value has yet to be implemented, instead focussing on the aspect ratio, to some success. It is suggested that as it quickly levels off it can be assumed to be a simple constant value independent of other values. However, the effect of lubrication in some cases may substantially reduce this, and the nature of collisions can even induce lubricating behaviour from liquefaction effects [37, 227].

The main takeaway that can be gathered from this is that even the Coulomb friction is rate dependent in a granular material, cohesion increases the effective internal frictional value, and that lubrication is unpredictable.

Span

A wider particle size range shows a consistent increase in the compressive strength in both the pendular [227] and the capillary regimes [111], and in actual tests with pellets [96].

However, as mentioned in the literature review, a wider particle size range increases the coordination number [184] as well as the packing ratio [96, 227], both of which also independently increase the strength.

As such, it may simply not be an independent variable beyond these effects.

Saturation

A brief return to saturation may be useful with respect to the tensile and particularly the compressive strength.

Discussed previously in this chapter with respect to the funicular state, the saturation increases the tensile strength consistently [93, 106, 107].

However, the effect it has on the compressive strength varies, depending it seems on the material in question [50, 111, 119]. It may be due to the specific binder used by [50, 119] that resulted in a consistent reduction in strength as saturation increased, as Kollidon® produces low viscosity polymer solutions which may have had a lubricating effect on the samples, though this cannot be known for certain.

The wide and thorough research by [111] testing a combination of particles and binder types finds that the effect of saturation increases the strength for all Ca values, though with differing behaviours. Further, the point where "high Ca" begins differs for different saturation contents, which fits with the suggestion that the de-localisation of the bonds is relevant.

At low Ca values, the strength was approximately proportional to the pore saturation, similar to that found by [93] for the tensile strength. At high Ca values however, the pellet strength is dominated by the viscous dissipation, and there is relatively little change in the strength for lower saturations, but a dramatic increase in strength when the liquid content increases above a critical saturation level.

Considering the behaviour observed in shear experiments such as [112] and tensile strength experiments by [93], this could be explained in terms of the pendular bonds being broken and re-forming [118]. For pendular bonds, the coordination number is the primary source of strength rather than the total saturation, being unable to spread the shearing behaviour sufficiently to gain the strength from distributed shearing [109].

Once sufficient saturation is applied however, the viscous forces can consistently distribute the shearing stresses applied in the compression, increasing the strength.

6.3.5 Conclusion

Based on all this, informed choices must be made for the value of σ_y for the model. The strain rate dependence is inconvenient, as this increases the complexity of any impact modelling, since the behaviour slows over time. The empirical results reported cannot simply be included, as they are highly dependent on the contexts of the materials used, such as spherical ballotinis or controlled viscosity of oils.

On the other hand, the compression and the tensile strengths seem to be much more closely related, with respect to the saturation regimes than previously

thought. The primary difference is, logically, only friction or more generally internal particle displacement related, which would explain why the ratio of tensile strength to compressive strength is between 0.5 to 0.8, though only one specific case could be found, that of limestone particles [153].

Additional to this point is the lack of consideration of the previous authors works to compare their research to previous results theoretically. This means that direct comparison of whether the same relations can be found between authors and so combine them, as in Equation 6.12 is on shaky ground.

Initial discussion with technicians regarding mechanical testing of the granules highlighted a reason why this may be the case. The very low stress values that need to be measured are difficult to capture on typical stress testing machinery, which are designed for testing strengths in the MPa range. One would also need to be able to test the strengths at different compression and tensile rates. Lacking these facilities impaired a direct experimental angle of research.

In the end, despite the previous criticisms for Equation 6.12, it was still used as the final choice of yield strength after testing the alternatives, for both the tensile and the compressive cases. This was ultimately a matter of pragmatism.

Of the solutions listed, it allows the most real observable values to be included. It accounts for the porosity function, which is now clarified to be based rather on the coordination number and the packing value, and the aspect ratio is included which accounts for the friction. The saturation has been clarified to be positively correlated in most cases, and it includes rate dependency in the strength, in the form of the viscosity.

As the power of v_p , assumed to be the normal velocity of the impact between granules, is left as 1, this corresponds to an $n = 1$ in the scenario described by [109]. Further the simplifications that imply monodisperse spheres, where the constant of the capillary term is left as 6 and the constant for the viscous term is 81/128 are also left as they are.

Finally, as the only power which is not a square is for the aspect ratio, which

is a constant, it is the simplest to calculate, as might be necessary many thousands of times in the model. A more complete model might account for the shear behaviour mentioned, and adjust the capillary number component for the compressive strength and not the tensile strength, or otherwise account for the different behaviours accordingly.

6.4   Soft Size limits

The breakage of granules is naturally limited by the size of granules produced, however the strength also significantly impacts the general deformation behaviours in ways which happen to also be related to the size. Some of the methods of measuring these have been using rapid and convenient empirical methods which only measure comparative values between setups without a strict mathematical backing, and so have been derided as "rituals" by some authors [38] as they do not provide quantitative explanation.

By defining and calculating these quick tests clearly, these empirical methods can be made into useful and comparable measurements between setups. These derivations make a number of assumptions, as they were a distraction from the main task at hand, however they may prove useful.

One of the assumptions is that σ_y is constant and not velocity dependent. The reason for this is that these derivations require integration, and since the general relationship is not clear, it would be overemphasising a particular theory to apply it. Another assumption is that the deformations are sufficiently small that the effect on the overall volume can be neglected.

Constraint Factor

Constraint K_φ is the relation between the hardness and the yield strength [36, 114, 223, 224]. As mentioned in the literature review, becuase the hardness is constrained by the surrounding material, it is greater than the yield strength. The

269

relation is typically linear, Equation 6.23, which makes implementation practical. For clarity, this value will be described as K_φ.

$$p_0 = K_\varphi \sigma_y \tag{6.23}$$

p_0 is the pressure applied to the sphere faces to deform them. K_φ ranges from 1 to 3 typically, though higher values occur for strain hardening materials, and lower for more ductile materials [114]. Given the response of granular materials as being similar to work softening, a lower estimate is more reasonable.

6.4.1 Drop Strength

The drop strength is a measurement of the number of drops that a pellet can survive. This has been shown to be proportional to the compressive strength [63], but without a specific correlation previously mentioned. The drop strength does not have an explicitly defined relation to the yielding behaviour.

Mechanically, it can be considered a measure of the total plastic deformation energy E_p that can be absorbed before breakage. This deformation energy comes from the conversion of Gravitational potential energy to Kinetic energy E_k , and so E_k can be pre-determined. Meanwhile, the integration of the deformation to the plastic energy of a sphere can be found in appendix section A.2. Dividing the two gives Equation 6.24.

$$\frac{E_k}{E_p} = \frac{\frac{1}{2}V_{cN}^2 m}{p_0 \pi R \delta^2} = \frac{4\pi}{3} \frac{\rho R^3 V_{cN}^2}{K_\varphi \sigma_y \pi R \delta^2} = \frac{4}{3} \frac{1}{K_\varphi} \frac{\rho V_{cN}^2}{\sigma_y} \frac{R^2}{\delta^2} \tag{6.24}$$

Since the mechanics are not restricted to granules, the the subscript for granule is not required. Here δ is the extent of deformation, R is the sphere radius, ρ is the density and V_{cN} is the normal collision velocity.

The equation is separated as it is to highlight the two significant terms in the last step. First, $\frac{\rho V_{cN}^2}{\sigma_y} = St_{def}$, and second, $\frac{R^2}{\delta^2} = \frac{1}{2^2 \varepsilon^2}$ since the strain ε is the deformation over the total length.

270

Because of this, Equation 6.24 allows a measure of the yield strength in the real case of deformation behaviour due to impact. By noting that when $e_{rest} = 0$, all the kinetic energy is converted into plastic energy, meaning that $\frac{E_k}{E_p} = 1$, Equation 6.24 can be rewritten to Equation 6.25

$$1 = \frac{4}{3} \frac{1}{K_\varphi} St_{def} \frac{1}{2^2 \varepsilon^2} = \frac{1}{3} \frac{1}{K_\varphi} \frac{\rho V_{cN}^2}{\sigma_y} \frac{1}{\varepsilon^2} \tag{6.25}$$

The velocity of a falling body can be calculated from its height via $V = \sqrt{2gh}$. Because this is knowable, in this case the form not using St_{def} is relevant here. Re-arranging Equation 6.25 to include the velocity from the gravitational drop, and placing the yield strength and the constraint on the left hand side of the equation gives Equation 6.26

$$K_\varphi \sigma_y = \frac{2}{3} \frac{\rho gh}{\varepsilon^2} \tag{6.26}$$

The constraint and the yield strength have to be put together as the relationship between them is not known a priori. However, given that the hardness is present with the yield strength in all the relevant compressive strength measurements, and the relationship is a known factor, this is not as much of a problem as it might appear.

Given that this is not simply at a single strain rate but decelerating in a fashion appropriate to that of the granule behaviour in collisions, this may be a practical method for determination of yield strength in other cases.

6.4.2 Stationary strength

In the particular case of cold bonded pellets, it may be relevant to know the degree of deformation that the pellets experience under their own weight. This deformation may cause subsequent bonding between already formed pellets after being output.

271

By considering the change in gravitational potential energy as a sphere deforms, the relation between the deformation and the energy of the pellet can be integrated through. The full form can be found in Appendix section A.3, with the relation between $\frac{E_g}{E_p}$ being described in Equation 6.27.

$$\frac{E_g}{E_p} = \frac{\frac{\rho g \pi}{3}\left(4R^4 - 4R^3\delta + R\delta^3 - \frac{\delta^4}{4}\right)}{p_0 \pi R \delta^2} \tag{6.27}$$

This ratio can be re-arranged to find the relation between the strain and the yield strength. However, in this case, the interest is on the amount of strain, as this is the relevant weakness being sought after, and would need correction with modification of the relevant values. As such, the relation Equation 6.28 is given, with the rearrangement listed in Appendix section A.3

$$\frac{3\sigma_y K_\varphi}{R\rho g} = \frac{4}{\varepsilon^2} - \frac{4}{\varepsilon} + \varepsilon - \frac{\varepsilon^2}{4} \tag{6.28}$$

The specific relation is not obvious, but plotting Equation 6.28, (holding σ_y ,K_φ, ρ , g constant) gives Figure 6.12. This function shows that the majority of the deformation occurs in the early sizes, and that the slope reduces as the granule size increases. This shows that, though the larger granules do experience more strain and thus proportionally more deformation, all granules will experience some deformation which would contribute to subsequent bonding behaviour simply from resting.

This does suggest that, since this gets proportionally less of an issue as the granule size increases that it is likely not another contributing factor that leads to growth after the fact, if this behaviour has a presence at all size scale and is not a self-accelerating process.
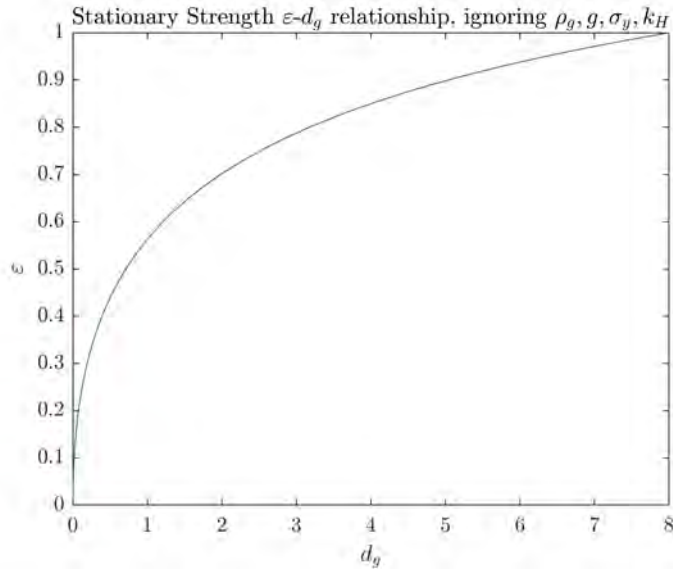
Figure 6.12: Relationship between granule diameter and strain, with σ_y , K_φ, ρ , g all set to 1 just to show the trend.

6.5 Consolidation

Granule consolidation describes the reduction in the void volume of the granules, reducing the porosity and increasing the saturation.

The consolidation of the granule is very important given how important the saturation is in the granular behaviour. The behaviour is generally known, though as will be shown, there are some uncertainties , and the research is spread between a number of disciplines sometimes making comparisons tricky.

The basic starting point is Equation 2.33 [229], given in the literature review. This consolidation model relates the initial to the minimum porosity through a power law relation, with rapid initial consolidation which slows over time.

This is accurate to a first approximation, and re-arranging the equation to give the porosity as a function of the other parameters gives Equation 6.29.

$$\epsilon\left(N\right) = \epsilon_{min} + \left(\epsilon_0 - \epsilon_{min}\right) e^{-kN} \tag{6.29}$$

In the case tested, $k \propto d_p/\mu^{0.25}$. Arranging the equation like this shows that the consolidation behaviour is equivalent to that found for confined packing of spheroids [190], as given in Equation 2.36, again, from the literature review.

Simply re-arranging the limits in the brackets, and noting that $\phi = 1 - \epsilon$, Equation 2.36 can be re-arranged to form

$$\epsilon(n) = \epsilon_{min} + [\epsilon_0 - \epsilon_{min}]\, e^{-(Cn)^{\beta}} \qquad (6.30)$$

C , in the case where Equation 6.30 is developed, was found to simply be dependent on ϵ_0 and ϵ_{min} , as it represents the Carr index, itself a measure of the flowability [190].

Shared by both cases is the value N and n , though in Equation 6.29 it represents the number of revolutions of a drum, while in Equation 6.30 it represents the number of individual compaction loadings. These are both relatively equivalent, given that the consolidation behaviour is likely induced by the collision behaviour which is an impact based loading process. The simple form of the consolidation equation is given in Equation 6.31

$$\epsilon(N) = \epsilon_{min} + [\epsilon_0 - \epsilon_{min}]\, e^{-k_\epsilon N} \qquad (6.31)$$

For which k_ϵ is proportional to the diameters, partially the viscosity, the flowability, and possibly some other unspecified variables, given that neither of the solutions consider the effect of stronger compaction on the consolidation behaviour [57, 129].

The value for the k_ϵ is here suggested to be based on St_{def} . This would account for the effect of the particle diameter and the partial relation to the viscosity [229], and the relation of C to the minimum and maximum values of the consolidation, as well as the strength of compaction on consolidation.

St_{def} is directly related to the deformation behaviour, and has the function

$$St_{def} = \frac{\rho_g V_c^2}{\sigma_y} \qquad (6.32)$$

Note that the collision velocity is divided by the yield strength. That it is divided fits the finding that the diameter and viscosity are proportional to the consolidation rate as has been measured. The yield strength is known to be itself proportional to the viscosity (but only depending on the rate of strain, which will vary with the collision strengths) as well as inversely proportional to the particle diameter. Greater flowability, as measured by k_ϵ , would result in more deformation and thus a lower σ_y . Meanwhile larger values of V_c would correspond to larger compaction impulses.

Initially, this would suggest that the consolidation relation should be of the form given in Equation 6.33.

$$\epsilon\left(N\right) = \epsilon_{min} + \left(\epsilon_0 - \epsilon_{min}\right) e^{-k_\epsilon St_{def} N} \tag{6.33}$$

However, when implemented and tested in later works, this was found not to be suitable. Instead, a slightly more complex version, Equation 6.34, which accounts for the relative importance of the strength of the collisions and the frequency separately as $k_{\epsilon A}$ and $k_{\epsilon B}$ respectively giving Equation 6.35, which was found to simply work exactly as expected.

$$k_\epsilon = k_{\epsilon A} e^{\frac{-1}{St_{def} k_{\epsilon B}}} \tag{6.34}$$

$$\epsilon\left(N\right) = \epsilon_{min} + \left(\epsilon_0 - \epsilon_{min}\right) e^{-\left(k_{\epsilon A} e^{\frac{-1}{St_{def} k_{\epsilon B}}}\right) N} \tag{6.35}$$

Because St_{def} itself depends in turn on the porosity this needs to be calculated numerically, although a final expected size can be found by setting ϵ_{min} to an assumed final porosity appropriate to the system.

There is some evidence to suggest that the consolidation behaviour is more complex [195], as a result of heterogeneity within the wetted granules. Individual granule heterogeneity is possible to model, but there must be a limit to the depth explored.

6.5.1 Arrhenius equation

Interestingly, Equation 6.34 has a similar form to the Arrhenius equation [230]

$$k = Ae^{\frac{-E_a}{RT}} \tag{6.36}$$

Where k is the rate constant, and will in turn affect the final proportion of a given chemical in a reacting mixture of chemicals, based on the activation energy E_a and the absolute temperature T. The comparisons are more readily apparent when considering that the temperature is simply a measure of the average kinetic energy , which is accounted for in k_ϵ with the ρV_c^2 term of St_{def} , and the activation energy corresponds to energy required for a reaction to take place, which corresponds to the need for the collision to overcome the strength of the granule to deform it. Expanding Equation 6.35 to account for this gives Equation 6.37 which particularly highlights the behaviour implicit to this form of the consolidation.

$$k_\epsilon = k_{\epsilon A}e^{\frac{-\sigma_y}{k_{\epsilon B}V_c^2\rho}} \tag{6.37}$$

Even the Gas constant and the pre-exponential factor were incidentally included as $k_{\epsilon B}$and $k_{\epsilon A}$respectively. The possibility of the collision strength being less relevant may come down to the pre-existing favourability of consolidation for a granules body, and that it is currently in a state which is only stable due to graunlar mechanics always needing external force to change porosity, however the favourability of this is dependent on the structure of the particles and liquid etc.

Given that Equation 6.34 was developed completely coincidentally, this is both reassuring and a bit strange at the same time. However, it does suggest that there is a promising direction in terms of connecting the fields of agglomeration to kinetic chemistry, especially when also including the granular thermodynamics previously mentioned.

Not to digress too much further, consider the relation of the granulation be-

haviour as a whole to polymerisation, as granulation is essentially just "polymerising" granules to larger granules. In the field of polymer chemistry, there is a concept referred to as T_c the ceiling temperature of polymerisation, where the same amount of dissociation as association is occurring. This would correspond to granules reaching a stable diameter as consolidation for larger granules is inhibited, as seems to be the case in some high shear systems [44].

6.5.2   Minimum and Maximum porosities

The maximum porosity is less important to obtain a rigorous theory for, since the initial consolidation behaviour tends to be much faster and less important than the minimum porosity, though if the maximum is very close then it might be.

The minimum porosity on the other hand is equivalent to the maximum packing, which has been researched by many authors. Most of this has been discussed in the packing section of the literature review, so only relevant topics mentioned will be discussed.

Given that the consolidation appears to be proportional to St_{def} , the effect that this has on ϵ_{min} is pertinent. The relation can vary heavily depending on the system. For some systems, a higher apparentSt_{def} can result in a lower porosity, such as [57]. In other systems, a higher St_{def} can result in an increased final porosity, such as in [51].

This may be due to competing compaction and dilation effects. Deformation of a granular material can result in distortion of the packing, overcoming the compaction [112]. This will prevent the stabilisation into the ideally packed state.

In the dry confined case, this has been measured by several authors. Different cases can be found where the minimum porosity monotonically increases and decreases as the agitation increases [231]. Additionally, cases exist where the porosity increases before decreasing again [232], or where the porosity decreases before increasing again [231].

In granular materials, the case where the porosity increases could be relevant in the "Crumb" growth case. Above $St_{def} = 0.02$, granules were found by one author to elongate and become unstable [233] and overly weak feed mixtures were also found to be unable to form granules, either a paste or crumbs [64]. This would result in mixtures which require large amounts of liquid to gain sufficient strength to form granules, but in so doing alter the consolidation behaviour where the consolidation overcomes dilation, which immediately results in oversaturation.

The great complexity of this issue may stem from the problem of the granular entropy. Granular entropy is more complicated than molecular entropy, as it can lead to a situation where a more well packed state and thus lower porosity granule has a lower granular entropy.

To understand this, note that entropy is a measure of the number of meaningfully equivalent states, with fewer equivalent states giving lower entropy. A more highly packed state restricts the ability of the particles to re-arrange to give equivalent average coordination numbers, and therefore reduces the entropy. As the particles become less tightly packed, this results in higher entropy as the particles can re-arrange more freely. This reaches a maximum, where the entropy begins to reduce again as the granules have to be more precisely arranged, which reduces the entropy again [234]. However, this subsequent case is rarely relevant as it is less kinetically stable than the more compressed case and so the granular assembly naturally compacts to the random loose packing state of the system, which roughly corresponds to the entropy maximum.

This results in a situation where the granular entropy is *lowered* (i.e the system is less "random") when the particles have more contacts. Thermodynamic stability trends towards a higher entropy. This means that the entropy of the system is at a minimum when the porosity is also at a minimum.

Thus, any addition of energy needs to actively work to lower the entropy. There may in turn be a point when the addition of liquid lubricates the particles or otherwise alters their interactions such that the decrease in entropy due to

improved packing itself is overcome, which is what is found in [161]. This in turn allows the increase in the packing density found between wet and dry packing.

In summary, becuase the physical minimum of the ideal packing state has a lower porosity than the "thermodynamically" lowest porosity which is dependent on the application of the forces and can vary, determining a true minimum of any individual granule is impossible. Since the porosity is tied to the saturation, this means that there is no true final saturation in a granulation system, even ignoring the effects of evaporation. Instead, only an average can be found. If the packing behaviour can be better analysed though, then this may allow for a better prediction of the development of the final porosity and the rate at which it occurs.

Chapter 7

Agglomeration Mechanics

7.1 Introduction

So, with everything laid out, from the material, to the known kinetics, to the general granular behaviour, a better evaluation of the agglomeration models can be made. In the literature review, three different size predictions could be made. However, they all relate the size to the granule properties differently, so this can be compared to the evidence.

Further, there are a few growth models described which are related to these size models. Iveson [235]classifies these growth models as "Class I" and "Class II" models. Class I models are distinguished by whether they determine if initial sticking occurs, and if that is determined to be successful, then the two are assumed to coalesce. Class II models meanwhile are those models which consider that every time particles come into contact, some sort of bond develops, and the bond that develops is then tested against separation events.

The fact that Class I models can determine whether an agglomeration event is successful based on the initial event makes it well suited to analysis generally, but specifically benefits DEM, as the properties can be tested at the moment of collision.

A Class II model would require either a prediction of the future strength of the collisions, or additional later checks so that the initial bonds can be tested later.

7.2   Stokes Number Criterion

The Stokes Number criterion Equation 7.2 is the criterion that was developed initially by Ennis, Tardos and Pfeffer [4]. This is a Class I model where the viscous dissipation of the liquid on the surface of the granules slows down the relative velocities of the granules until $\overline{V_R} = 0$, Equation 7.1. If this is satisfied, then coalescence occurs.

$$St_v \leq St_v{}^* \tag{7.1}$$

The full calculation is derived from previous work calculating the re-bound of spheres on a wetted flat surface [42], extended to spherical materials.

$$\frac{8\rho_g \widetilde{d_g} V_{cN}}{9\mu} \leq \left(1 + \frac{1}{e_{rest}}\right) ln\left(\frac{h_0}{h_a}\right) \tag{7.2}$$

This basic formulation has been expanded to account for plastic deformation [6] affecting the viscous damping as well as a changing geometry of the liquid [210,236] and the surface availability of the moisture [237]. The general/expanded forms have been applied in multiple population balance models [81, 200].

Based on this concept, and then considering the change of St_v of the system as a whole and how St_v varies over time, three regimes for granulation are derived.

1. The first is the non-inertial, or St_v^N granulation regime. This occurs when the system-wide distribution of the Stokes number St_v is well below $St_v{}^*$. In this case, all collisions result in coalescence.

2. The next regime, the inertial regime St_v^I begins when the largest St_v values begin to equal $St_v{}^*$ (i.e $St_{vmax} \approx St_v{}^*$), the viscosity and kinetic energy

of the collisions begin to matter, with greater viscosity and lesser kinetic energies growing more.

3. Finally, in the St_v^C regime, or the coating regime, $\overline{St_v} \approx St_v^*$ and on average coalescence growth does not occur, growth only occurring by coating, which can only happen with the addition of fresh feed.

Because the boundaries are defined, and based on the considerations made by the authors, the diameter where the limiting size occurs can be derived. For tumbling agglomeration, according to this theory, there is no St_v^I regime. Instead, a critical diameter occurs in the transition from the St_v^N directly to the St_v^C regime. the diameter is given as Equation 2.2.

One of the points mentioned in [4] is that regions of $St_v > St_v^*$ where growth would occur are balanced by the regions where $St_v > St_v^*$ where the granules dis-agglomerate or break apart, but provides no reasoning for this particular relation, given that Equation 7.2 only describes the slowing down due to viscous dissipation.

This solution, and the subsequently derived variants, have a number of properties favouring them. In the form of h_0 in St_v^*, the saturation is included, and the velocity is included in the St_v value. Both of these are noted as important variables in the growth behaviours. The other variables, such as asperity height h_a can also be applied using relations provided by the various authors in this work.

Because of this, this solution was explored and even implemented in the agglomeration DEM model. However, it was subsequently removed, for reasons explained in subsection 7.5.1.

7.3 Bond Probability Criterion

This model, initially developed by Ouchiyama and Tanaka [45], calculates the probability that a bond will survive the shearing action of the drum, which is why it has been given the name "bond probability Criterion".

This is a Class II model, since it assumes that every collision forms some sort of bond, however the strength of this initial bond has a probabilistic range based on the strength of the initial collision. This initial bond must then survive the subsequent shearing which is a function of the granule sizes and the system properties.

Based on the range of probabilities, Equation 7.3 gives the limiting size where the growth rate is impeded by the sizes of the granules themselves. This is reproduced here for accessibility.

$$\Delta_{lim} = \left(\frac{2^{\alpha - \frac{3\eta}{2}}}{B} Q_{max}^{\frac{3\zeta}{2}} K^{\frac{3}{2}} \sigma_{bond} \right)^{\frac{1}{4 - \frac{3\eta}{2}}} \tag{7.3}$$

The subsequent probability of growth is based on the averages of the granules available, as shown in Equation 7.4, and so this is a soft limit, since the granules can grow beyond this size.

$$\left(1 - \frac{P_n^{\frac{1}{n}}}{\lambda} \right)^{\frac{3\zeta}{2}} = \frac{(Dd)^{K_\gamma - \frac{3\eta}{2}}}{\left(\frac{D+d}{2} \right)^{2K_\gamma - 4 - \frac{3\eta}{2}}} \frac{1}{\Delta_{lim}^{4 - \frac{3\eta}{2}}} \tag{7.4}$$

This can be revised to a more accessible form, by noting the various relations between diameter means, to give Equation 7.5.

$$P_n = \left(1 - \left(\left(\left(\frac{\widehat{D}}{\overline{\overline{D}}} \right)^{2K_\gamma - 3\eta} \left(\frac{\overline{D}}{\Delta_{lim}} \right)^{4 - 3\frac{3\eta}{2}} \right)^{\frac{2}{3\zeta}} \right) \right)^n \tag{7.5}$$

$\widehat{D}$ is the geometric mean (GM) and $\overline{D}$ is the arithmetic mean (AM). This arrangement highlights two distinct ratios on the right-hand side, the first being

the layering component which changes the behaviour depending on the ratio of the two granules colliding, and secondly the "steady" component which is consistent. A second benefit to this arrangement is that, because of AM-GM inequality, the layering component is known to be always < 1 while $K_\gamma > 1.5$, and therefore growth can always occur if the difference in the granule size is large enough.

The value $\lambda = \frac{Q_{max}}{Q_{max}-Q_{min}}$, where Q_{min} is the minimum force that will be experienced in particle-particle collisions in the granulator which can always be assumed to be 0. Perhaps a more nuanced consideration of Q_{min} could be the minimum force which will result in coalescence sufficient to form the initial bond, which would explain the increase in probability of the bond surviving by limiting it to only the stronger collision events to begin with, but for now, leaving it as 0 allows a further simplification of the form Equation 7.6

$$
P_n = \left(1 - \left(\left(\left(\frac{\widehat{D}}{\overline{\overline{D}}} \right)^{2K_\gamma - 3\eta} \left(\frac{\overline{D}}{\Delta_{lim}} \right)^{4-3\frac{3\eta}{2}} \right)^{\frac{2}{3\zeta}} \right) \right)^n \tag{7.6}
$$

The limiting diameter does not, notably, depend on n, the number of collisions that need to be survived. Equation 7.6 assumes that the limiting diameter is the maximum diameter that is possible in the system, which is a function of the shearing behaviours, however n describes the total number of collisions that are required to be survived before the granule will no longer break from any collisions. Above a threshold size, the granules will not survive, and this threshold is based on the maximum initial collision strength, the separation strength, and the bond strength development.

However, even if the limiting size does not depend on n, the model is still impractical. The collision strength and separation strength values are not clearly defined, and the value K_γ is a system dependent constant to describe how the granule size affects the separation shearing behaviour as a whole. It also does not account for the saturation of the granules, which is known to be very important. Knowing n would also be important to modelling the growth behaviour over time.

This set of equations are system based, which makes it practical for the intended purpose of providing mechanistic explanations for the behaviours observed by previous authors regarding the growth behaviours [46], and generally observed in population balance models. The values of Equation 7.3 can be fitted based on the relations observed in the system, or simply set to a fixed value and then scaling applied.

This model was implemented into the simulation of agglomeration, using $n = 1$ as an arbitrary value, and the simulation was surprisingly good for the level of abstraction involved. However, because it lacked any direct mechanism for accounting for the saturation, it was severely lacking, though this would be overcome partially before another model was implemented. More details regarding how it was implemented and the choices made will be listed in chapter 9.

7.3.1 Number of collision Calculations

A method for determining a suitable value for n is to find the point where the bond strength exceeds the maximum potential separation force in the granulator. By assuming that the strength grows over time, in a similar manner as the consolidation behaviour Equation 7.7 , this can be somewhat pre-determined [235].

$$F_{bond}\left(t\right) = F_{bondmax} - \left(F_{bondmax} - F_{bond0}\right)e^{-k_{F_{bond}}t} \tag{7.7}$$

The value t is simply time, which makes the calculations clearer, with $n = It$, with I being the frequency of collisions. The bond strength development function then can be placed into Equation 7.8, which is based on survival analysis.

$$\ln\left(\frac{N_g\left(t\right)}{N_{g0}}\right) = -t\int_0^t P\left(F_{bond}\left(t\right)\right)dt \tag{7.8}$$

N_{g0} is the initial number of granules, while $N_g\left(t\right)$ is the number of granules remaining after time t . $P\left(F_{sep}\right)$ is the probability of a collision having an impact

force greater than F_{sep}. Equation 7.8 therefore calculates the proportion of granules remaining after t time has passed.

Since the bond strength also grows as a function of time, assuming that $F_{bondmax}$ is greater than $F_{sep_{max}}$, this will result in a time t^* where the bond strength is greater than the maximum force $F_{sep_{max}}$ of the collisions in the granulator. At this point, no further breakages will occur as a result of the breakage force.

Because of the nature of Equation 7.8, calculating this value is much less practical than might be desired. As observed in chapter 5, the collision strength varies by location and by colliding radii, and so will the distributions. Given that the radii distribution itself will change as a result, this means that inputting the initial distribution behaviours measured will also not work, so would need to be defined dynamically and locally for the various known factors based on the tracked behaviours.

$P\left(F_{sep}\right)$ places restrictions on attempting to develop an analytical value of $N_g\left(t\right)$. It is the cumulative probability distribution of $P\left(F_{sep}\right)$, which must have an upper and lower limit, and must also be able to be integrated. There is a family of probability distributions which satisfy these conditions, for which the integral from $P\left(F_{sep}\right)$ to $P\left(F_{sep_{max}}\right)$ are of the form Equation 7.9

$$\left(1 - \frac{F_{sep}}{F_{sep_{max}}}\right)^{p} \tag{7.9}$$

Where p can be any power value. This can in turn be integrated cleanly in Equation 7.8 as needed. There may be other distributions which can perform this function, though this particular distribution has the benefit of being able to adjust the power p as needed dynamically according to the local behaviours observed. The distribution of the particle collisions can then match p to give a general trend

This was tested briefly during this project in the later DEM agglomeration models, however it proved highly unstable. The large quantities of very light

286

collisions result in very large values of p , which in turn cause problems for further fitting work needed to match the observed collision distribution, resulting in overall unsatisfactory results, though it may be workable in other models.

7.3.2 Bond Strength

The initial bond strength requirement of Equation 7.3 and Equation 7.7 also impedes their implementation into a model. However, as mentioned, there is a model for this bond development [153].

This bond development is derived from cold welding caused by exposure of fresh metals to the surface of pressed together oxidised surfaces. For wet agglomerates, the behaviour is derived instead from the exposure of wet materials, which apply a moist surface through a drier surface. This is shown diagramatically in Figure 7.1.

(a) Surfaces prior to contact

(b) Contacting of the surfaces, inducing the capillary bonds and some particles to inter-mingle and generally initiating bonding.
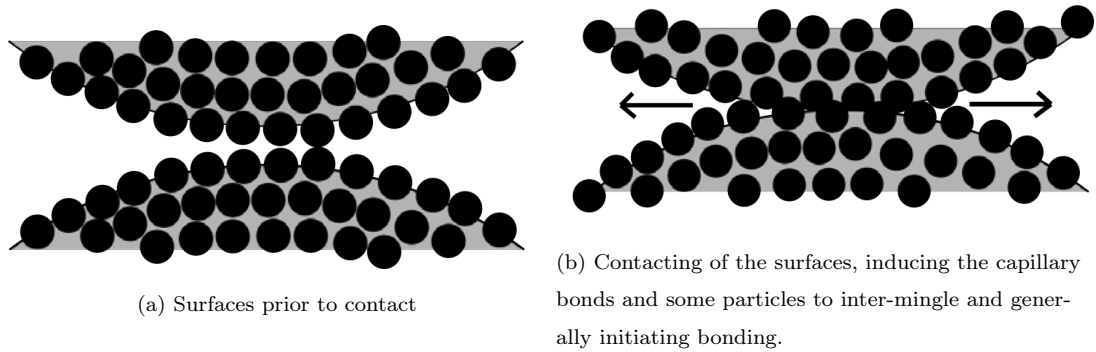
Figure 7.1: Diagram of the surface of highly saturated granules as they come into contact, as described in mechanism for [153]

The original bond strength formulation Equation 2.30 is given using atypical notation with the actual separation force required rather than separation stress required, so dividing through by the initial area of the cylinders in question gives Equation 7.10

$$\sigma_{bond\,r_0} = \ 0.65\sigma_y \left[\left(\varepsilon_r^2 + 2\varepsilon_r \right) + 1 - e^{(-K_s\varepsilon_r)} \right] \tag{7.10}$$

σ_{bond} is simply the initial strength, and will either break or increase in strength from further collisions, as mentioned in [235], possibly in a similar fashion as the consolidation. Importantly however, this period is when the bond is known to be weak.

Equation 7.10 can be re-arranged to find the bond strength of the final area of contact, which is necessary as spheres coming into contact will have an initial contact area of 0. In addition, the value 0.65 is based on the relationship between the compressive and tensile strengths, and is instead replaced with a constant $K_{\frac{t}{c}}$ to highlight the uncertainty of this value, which was originally based on limestone particulate agglomerates. This gives Equation 7.11

$$\sigma_{bond} = K_{\frac{t}{c}}\sigma_y \left(1 - \frac{e^{(-K_s \varepsilon_r)}}{(\varepsilon_r + \varepsilon_r)^2} \right) \tag{7.11}$$

Where K_s is a constant related to the immediate strength of the bond without prior compression and is expected to be inversely proportional to viscosity and generally related to saturation in some fashion, especially for saturation values greater than 1 when the surfaces will be wet. In [235], K_s is assumed to be 0, and the reported findings seem to tentatively agree with this assessment though the saturation is varied only slightly between 70% and 73%. The highly viscous silicone oils tested demonstrated that a lower load was required to form the bond as well as resulting in a higher strength of the bond which lasted longer.

Some further analysis can be applied to Equation 7.11, since the original was developed for cylindrical pellets rather than spherical pellets. It includes the original area of contact, so examining ε_r for spheres and how this affects the bond behaviour described as a whole is beneficial.

Radial Strain ε_r

Though Equation 7.11 was developed from cylinders, spheres are still radially symmetric structures, and the force is assumed to be applied along the axis of the symmetry in both cases, so the sphere is assumed to maintain a similar

relationship regarding the behaviour of ε_r and σ_{bond} . However, the value of ε_r at the surface does not appear to have a readily available solution for contacting spheres so this too will need to be solved for, or at least a reasoned approximation developed.

To determine the radial strain, the granule is assumed to be isotropic and follow the Poisson's ratio relationship:

$$\varepsilon_r = -\nu\varepsilon_z \tag{7.12}$$

From this, the radial strain from the compression can be found by noting that $\sigma_z = Q/A$ and for spheres $Q = p_0 A$ (Q being compression) [114]

$$\varepsilon_r = -\nu\varepsilon_z = -\frac{\nu\sigma_z}{E_z} = \frac{\nu Q}{E_z A} = \frac{\nu p_0}{E_z} \tag{7.13}$$

Finally, given that $p_0 = K_\varphi \sigma_y$, and considering that wet agglomerates can be assumed to be isotropic Equation 7.14 can be found:

$$\varepsilon_r = \frac{\nu K_\varphi \sigma_y}{E} \tag{7.14}$$

Equation 7.14 seems to suggest that the surface radial strain is constant. This might seem to suggest an error somewhere in the assumptions, however there are some results from previous researchers which can support this.

In plastic deformation experimental testing it was found that the deformed area of a sphere when pressed against a non-deformable surface was found to remain linear with respect to load, supporting the idea of a constant value for radial strain [238].

Another way to consider it comes from [100] which shows that for granular materials, the value E appears to be constant until the agglomerate fractures. This fracture point would then coincide with the appearance of the crumb state for excessive deformations.

Considering both at the same time in [89] there is almost no stress per unit strain from 0 strain to 0.4 units of strain, and only a slight raise from 0.4 to 0.5.

Future work to develop a model requiring less assumptions would be beneficial, however assuming it to be constant is sufficient, assuming that the initial deformation is small, which agrees with observations made in the subsection 6.4.2 where the majority of the strain is occurring in the immediate compression region.

7.3.3 σ_{bond} Summary

By combining Equation 7.11 and Equation 7.14, Equation 7.15 can be found:

$$\sigma_{bond} = K_{\frac{t}{c}}\sigma_y \left(1 - \frac{e^{-K_s \frac{\nu K_\varphi \sigma_y}{E}}}{\left(\frac{\nu K_\varphi \sigma_y}{E} + 1 \right)^2} \right) \tag{7.15}$$

This seems to have overcomplicated matters, however given that $\frac{\nu K_\varphi \sigma_y}{E}$ is assumed to be a constant, and that K_s is also a constant, the third term as a whole is reduced by defining $\alpha_{wet}\left(\varepsilon_r\right)$ in Equation 7.16.

$$\alpha_{wet} = \left(1 - \frac{e^{-K_s \frac{\nu K_\varphi \sigma_y}{E}}}{\left(\frac{\nu K_\varphi \sigma_y}{E} + 1 \right)^2} \right) \tag{7.16}$$

$\alpha_{wet}\left(\varepsilon_r\right)$ is the nondimensional constant of proportionality which describes the adhesion developed as a result of the exposure of fresh, wet material. This term is similar to that used in Equation 2.4 from the literature, where α_0 describes an intrinsic interaction term, which also relates the amount of saturation to the degree of binding within a granule. The values are derived differently, as the boundary between granules is slightly different than for a single full granule, but provide a useful comparison to previous applications of a similar function. Equation 7.16 is likely in practise also related to the saturation, due to the K_s and σ_y term, though this will be resolved shortly in section 7.4

Returning to σ_{bond} , putting $\alpha_{wet}\left(\varepsilon_r\right)$ into Equation 7.15 gives Equation 7.17.

$$\sigma_{bond} = K_{\frac{t}{c}}\sigma_y \alpha_{wet}\left(\varepsilon_r\right) \tag{7.17}$$

One final point regarding this value is that adhesion was not assumed when considering the deformation behaviour of the granules, despite the investigation being directly into the bond strength. Adhesion models such as that developed by Johnson, Kendall and Roberts [239], also referred to as the JKR model [240] are designed to balance elastic and adhesive forces against one another within elastic spheres during the deformation, but here the granules are assumed to be perfectly plastic.

7.4   Saturation Criterion

An equation describing the relation between saturation and granule size is given by Butensky and Hyman in [41]. This has been termed the "Saturation Criterion" for consistency. This model does not describe the manner of growth, and so does not fit into the class system previously mentioned.

The original equation is given in Equation 7.3, however, this can be rearranged into a much more useful form,Equation 7.18. The re-arrangement is given in Appendix section A.5.

$$\overline{d_g} = \Delta_{limCoh} = \frac{K_g d_p}{1 - \left(\frac{S}{K_{Smax}}\right)^{\frac{1}{3}}} \tag{7.18}$$

This form relates the liquid content in the form of Saturation which has been shown to be a much more reliable predictor of diameter than mass or volume ratios. Equation 7.18 provides the volume of liquid necessary to fill the inside of the granule, leaving a surface boundary which is defined by $K_g d_p$. The relationship between S and d_g , nondimensionalised, is shown in Figure 7.2

This hyperbolic trend matches the correlations found by the majority of the literature where saturation is tracked [37, 40, 48–50, 119, 200].

The value of K_{Smax} is theoretically 1, however this can vary between formulations as it is simply the maximum saturation before indefinite growth occurs, and
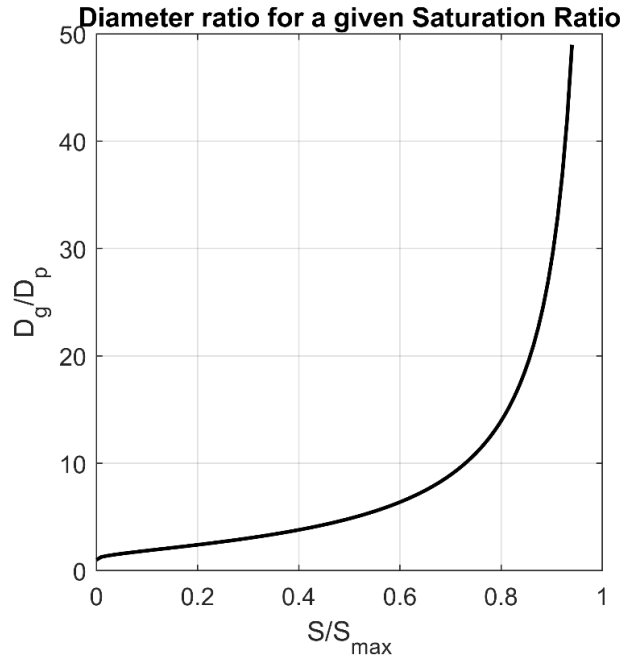
Figure 7.2: Shape of relation between the granule diameter and the saturation as described by Equation 7.18, Granule diameter normalised with respect to particle diameter.

this can be affected by factors as simple as entrapped air. It can also apparently vary if the minimum porosity estimation is flawed, and as established this value is not clearly defined. A lower minimum porosity in the granulation process than the estimate would result in a lower value of $K_{S_{max}}$, while a lower predicted porosity than that actually developed can result in values of $K_{S_{max}}$ in excess of 1.

K_g meanwhile is a function which describes how deep the moisture is from the surface of the granule relative to the diameter of the particles, and is likely a function of the liquid-solid contact properties [41] and the particle shapes [237], as well as the current actual saturation relative to the expected saturation. K_g is bounded between 0 and 2 as a physical requisite to ensure that all particles within the granule are wetted, and can be assumed to be around 1. Figure 7.3 shows the physical parameter that this value describes.
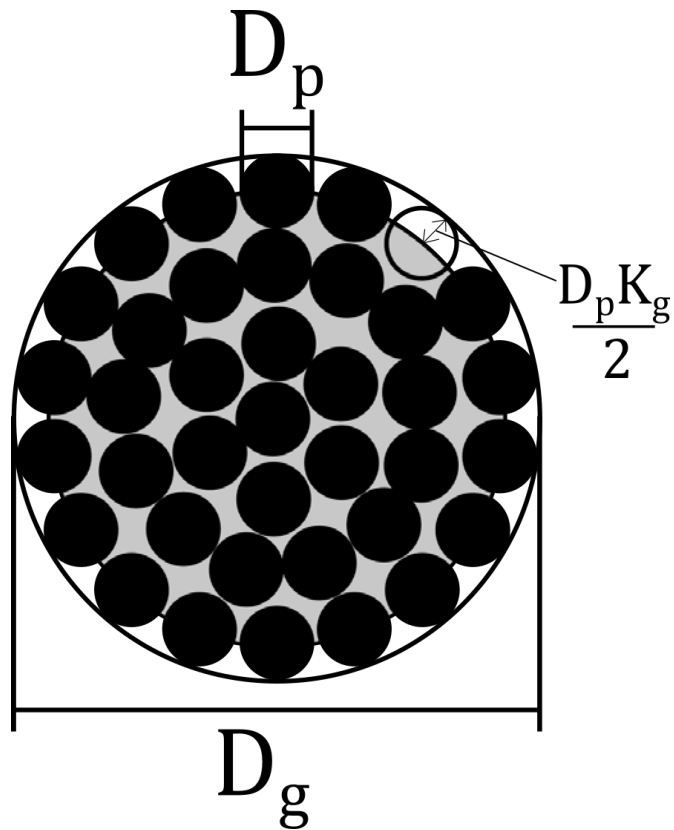
Figure 7.3: Physical meaning of K_g from Equation 7.18. The internal saturated space may not be completely filled, due to air bubbles which are trapped by surface tension, allowing a value of K_{Smax} lower than 1.

This behaviour is reported as only being tested for the "nuclei period", however, this is for an older version of "nucleation" where the granules are growing relatively rapidly until reaching the "balling" stage where the agglomerates are more clearly pellets and the growth has slowed [67]. This is in contrast to purely being based on the nuclei being developed from a spray addition to the moisture [72]. This may have lead to confusion by some authors [37], considering the wide range of granule sizes produced and literature that it matches.

Though this gives a useful expected value to relate the saturation and the diameter, it does not actually provide a coalescence or growth predictive behaviour, and does not account for the dynamic behaviour at all. Nonetheless, it can still

be applied to a model, requiring the final coalesced granule to satisfy the implicit condition specified in Equation 7.18, with the diameter being less than this. It can also be used to compare the growth of other models which incorporate saturation.

Relation to σ_{bond}

Since Equation 7.18 is based on the assumption of particles just on the surface, with moisture just below them, this matches precisely the circumstances that the original σ_{bond} strength was developed for.

Therefore, Equation 7.17 can be assumed to function when coupled to Equation 7.18 in some fashion. This would be consistent with findings showing that critical strain changes with saturation [50].

Further, some findings suggest that the bulk strength behaviour of the granule is relatively similar across a wide range of liquid contents, softening only once the liquid solid ratio goes over 100% [89]. This suggests that that on an individual level the granules can be assumed to have similar internal saturations.

This would correspond to the internal saturations of the granules being at the maximum, as predicted by Equation 7.18, where the difference in saturation between granules comes from the surface boundary lacking moisture. A consistent internal saturation, from which the bulk strength derives, allows the granule strength to actually be assumed to be relatively independent of the saturation once the strength from the internal, filled volume exceeds the effect due to boundary, consisting of unfilled volume.

7.5   Intrinsic problems with the class system

The Class I and Class II divisions proposed by Iveson in [235] are not actually very useful, or at least the premise of any Class I makes it not very useful in application of granulation modelling, and without a Class I there is no need to distinguish a Class II model. In fact, as pointed out by Iveson et al [37], most

systems are in practise some combination of the two behaviours.

Class I models are those models which assume that coalescence occurs if the initial collision is successful. This allows a very broad approach for what constitutes a Class I model. In describing different models, any solution which models two particle interactions where the coefficient of restitution can be determined to be 0 (i.e. relative motion at the end is 0) can and is considered "Class I" [37].

This, despite the fact that the behaviours that are actually being described by the specific models suggested are not be necessarily related to agglomeration or coalescence as a whole, and so require and involve different assumptions.

An example is that [241] and [6] are given nearly identical comments in the summary of different models and their classification in [37], the comments only differentiating them by noting that the former uses adhesion and the latter uses a viscous fluid layer.

However, examination of [241] and [6] show that the actual papers consider vastly different problems and contexts, and the former in fact has no particular relation to agglomeration.

A deeper problem lies at the central premise of Class I models, i.e. the determining factor for coalescence is whether or not there is relative motion afterwards. As a consequence, all lighter collisions will also be more likely to coalesce by Class I model bases. As shown in chapter 5, for drums, in the lifting, passive section of the granule bed, the particles will have essentially no relative motion between one another. Similar light interactions occur within other granulation systems as well [33, 43].

To get around this problem, those Class I models which do apply the behaviour to agglomeration have other requirements, an example being Equation 7.2 requiring the presence of some surface liquid layer. Alternatively, during the development, some models specify that they *only* model the coalescence behaviour, and that additional solutions are required for the breakage behaviours.

This however simply shifts the burden of complexity of these granulation

models to the external factors, extraneous requirements. If these are abstracted and permitted, then the size cannot actually be controlled by the Class I model. If coalescence is present, but not overwhelming, instead being managed using breakage behaviour, then the Class I model as implemented serves no purpose.

A final point to be made is that even if a Class I model is modelled, and a breakage behaviour is also separately modelled, then it cannot account for the effect that variations in the initial bond strength would have on the breakage model. This would implicitly require a separate tracking behaviour to be implemented to the Class I model for this behaviour, at which point it would essentially be a Class II model spread out over multiple different functions.

Meanwhile, a suitably prepared Class II model would be able to integrate this into the coalescence criterion itself, with breakage being based specifically on the breakage properties of complete granules, rather than having to consider the weakness due to the fresh bonds formed.

Class II models also deal with a secondary issue which is how to manage a behaviour that tends to be ignored, i.e. collisions will rarely be head on.

If the granules are colliding, and the normal vector of their relative motion is halted, which is what is actually modelled in most of the solutions, that does not mean that the particles have no relative velocity. Collisions should however occur in all possible directions, and some directions may result in more coalescence or breakage and so the effect needs to be accounted for in the coalescence considerations. As far as could be determined, none of the class I models specifically designed for wet agglomeration [4,6,81,200,210,236] accounts for this effect, they assume all collisions would be head on.

7.5.1 Specific issues with Stokes criterion

The Stokes Criterion has other issues which have not previously been mentioned in the literature. These behaviours were fully recognised after it had been implemented into the DEM model, and it was not working at all as expected.

A full 3 case system for wet-elastic, wet-plastic and dry-plastic was implemented. This was implemented both in a test environment as well as a lab drum environment.

These issues came to attention when the models were tested for the lab scale drum, with a mix of surface wet and surface dry elements, (i.e. $S < 1$ and $S > 1$). It was noticed that only when dry-plastic collisions were occurring would merging occur, and that when either of the elements were wet, no coalescence would occur. This could be seen in the Paraview images as the presence of only a few merged elements which had a total $S < 1$. This required active tracking of the properties of the elements using debugging to identify.

This lead to further detailed analysis of what would induce the growth, and identification that the root cause was due to the underlying mathematics, rather than the implementation, though that was checked first.

To aid in demonstrating the problem, the three cases are reproduced here.

The first case,Equation 7.19 is that which dictates the behaviour for elastic particles with a surface wet layer [4].

$$\frac{8\rho_g \widetilde{d_g} V_{cN}}{9\mu} \leq \left(1 + \frac{1}{e_{rest}}\right) ln\left(\frac{h_0}{h_a}\right) \tag{7.19}$$

The second case, Equation 7.20 is the extension of Equation 7.19 to plastic particles. The extension comes about because of the plastic deformation altering the viscous response, as the particles deform and return [6].

$$\left(\frac{\sigma_y}{E}\right)^{\frac{1}{2}} (St_{def})^{-\frac{9}{8}} < \frac{0.172}{St_v} \left(\frac{\widetilde{d_g}}{h_0}\right)^2 \left[1 - \frac{1}{St_v} ln\left(\frac{h_0}{h_a}\right)\right]^{\frac{5}{4}} \times$$
$$\left[\left(\frac{h_0^2}{h_a^2} - 1\right) + \frac{2h_0}{\delta''}\left(\frac{h_0}{h_a} - 1\right) + \frac{2h_0^2}{\delta''^2} ln\left(\frac{h_0}{h_a}\right)\right] \times$$
$$\left[1 - 7.36\left(\frac{\sigma_y}{E}\right)(St_{def})^{-\frac{1}{4}}\left(1 - \frac{1}{St_v} ln\left(\frac{h_0}{h_a}\right)\right)^{-\frac{1}{2}}\right]^2 \tag{7.20}$$

Finally, this is extended to the plastic, surface dry case in Equation 7.21 when the liquid is assumed to be beneath the surface but the viscous damping behaviour still takes place as the particle deforms.

$$\left(\frac{\sigma_y}{E}\right)^{\frac{1}{2}} (St_{def})^{-\frac{9}{8}} < \frac{0.172}{St_v} \left(\frac{\widetilde{d_g}}{h_0}\right)^2 \left[1 - 7.36 \left(\frac{\sigma_y}{E}\right) (St_{def})^{-\frac{1}{4}}\right]^2 \qquad (7.21)$$

The formula for determining the liquid surface layer h_0, which is crucial for determining the extent of viscous dissipation, is based on the volume of a spherical shell is [6]:

$$h_0 \begin{cases} (d_g \epsilon \, (S - K_{Smax})) \, /6 & \text{if } S > K_{Smax} \\ 0 & \text{if } S \leq K_{Smax} \end{cases} \qquad (7.22)$$

More complicated is the value of δ''. This is the deformation of the granule surface including any elastic reformation effects, and it differs depending on whether the granule is surface wet or surface dry. This is especially important in the surface dry case, as the liquid surface layer is intrinsic to the solutions provided, and the deformation in the surface dry case is assumed to provide this liquid surface layer. The deformation in the surface wet case is calculated through Equation 7.23 and in the surface dry case, the deformation is found via Equation 7.24 [6]. The surface dry case liquid layer, in Equation 7.21 can use this deformation calculated as a proxy, assuming that the indentation releases some liquid, with either a fixed thickness if deformation occurs or the thickness being proportional to this deformation. Of the two, a fixed thickness is less realistic.

$$\delta''_{wet} = \left(\frac{8}{3\pi}\right)^{\frac{1}{2}} (St_{def})^{\frac{1}{2}} \widetilde{d_g} \left[1 - \frac{1}{St_v} ln\left(\frac{h_0}{h_a}\right)\right]$$
$$\left[1 - 7.36 \left(\frac{\sigma_y}{E}\right) (St_{def})^{-\frac{1}{4}} \left(1 - \frac{1}{St_v} ln\left(\frac{h_0}{h_a}\right)\right)^{-\frac{1}{2}}\right] \qquad (7.23)$$

$$\delta''_{dry} = \left(\frac{8}{3\pi}\right)^{\frac{1}{2}} (St_{def})^{\frac{1}{2}} \widetilde{d_g} \left[1 - 7.36 \left(\frac{\sigma_y}{E}\right) (St_{def})^{-\frac{1}{4}} \left(1 - \frac{1}{St_v} ln \left(\frac{h_0}{h_a}\right)\right)^{-\frac{1}{2}}\right]$$

$$(7.24)$$

The nature of these functions make them extremely difficult to evaluate as to what each of the individual variables do to the behaviour as a whole. This has likely been the reason that these equations have not been challenged, as they do involve St_{def} and S (in the form of h_0).

Whether or not they have a maximum size they can granulate to, or how the established St_{def} or S values affect the behaviours predicted have not been numerically defined, only showing Figure 2.24 which does not provide any values. The fact that δ'' , St_v and h_0 also have their own complex equations which depend on the size, and σ_y , St_{def} , St_v and δ'' are all altered by the velocity, and the saturation relates to the coalescence parameter through h_0 , making comparing the results to the basic growth regime map Figure 2.23 and the observed drum granulation behaviours Figure 2.28 extremely difficult. Not impossible though.

Stokes Criterion Regime map

Through simply brute forcing the solution at every saturation value and St_{def} in a useful range , (St_{def} from 10^{-4} to 0.3, S from 0 to 2) at every dimensionless Harmonic diameter($\widetilde{d_g}^* = \widetilde{d_g}/d_p$), the diameters where coalescence occurs and stops could be identified. These could then be expanded to the case present in the simulation if neccesary.

The above cases were programmed into MATLAB, and a sufficient range of velocities were tested to provide the useful range of values of St_{def} needed to cover the map were applied. The expectation was that there was some slight problem with the boundary between the dry and wet cases, simply as a consequence of the recognised assumptions involved in the use of δ'' as h_0 in Equation 7.21, however the function $f(St_v)$ referred to in Figure 2.24 would be identifiable. Overall, the

behaviour sought was the maximum value, by noting whether or not a given $\widetilde{d_g}^*$ collision at each point could result in growth, and if not, that was the limiting diameter.

What was actually found is shown in Figure 7.4, and they demonstrate that the Stokes criterion has some serious problems.
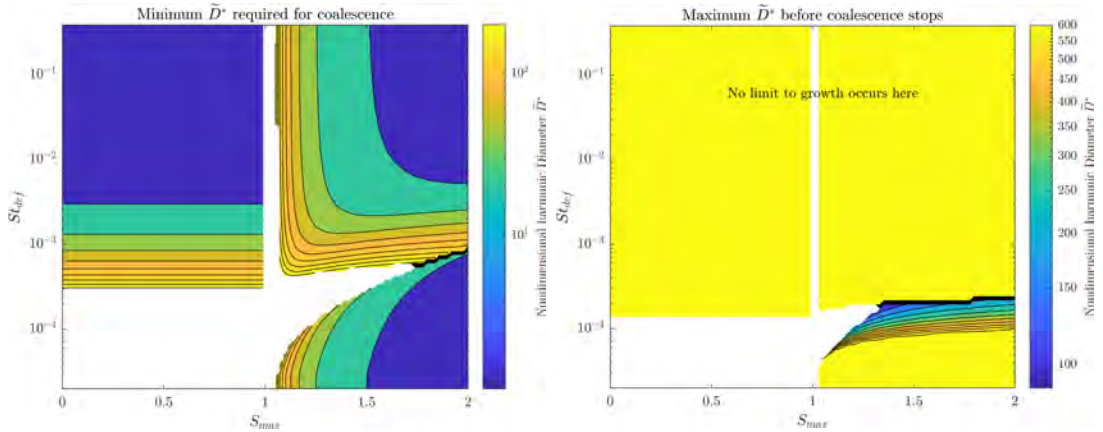
(a) Graph showing the minimum $\widetilde{d_g}^*$ required before coalescence can occur

(b) Graph showing the Maximum $\widetilde{d_g}^*$ before coalescence stops

Figure 7.4: contour plots describing the minimum and maximum size predicted by the Stokes Criterion, for a range of St_{def} values and S_∞ values. The nondimensionalised Harmonic diameter of collision is defined by $\widetilde{d_g}^* = \widetilde{d_g}/d_p$.

The values determined in Figure 7.4 do not account for every single possible combination of variables, however the problems that will be discussed occur for various other variables tested, and they demonstrate an intrinsic issue at the core of the criterion.

The three distinct regions that define the surface wet-elastic Equation 7.19, surface wet-plastic Equation 7.20 and surface dry-plastic Equation 7.21 cases can all be identified here in the bottom right, top right and top left corners respectively.

The first major problem that can be seen is that of the three cases, only the surface wet elastic case has a maximum diameter before coalescence stops.

Related to this, and even more of a problem, all of them have a *minimum* diameter before coalescence can start.

Stokes criterion Criticism

However there is a much more serious issue that is fundamental to the nature of the criterion as a whole, that can be immediately identified by the presence of the discontinuity which cannot be there if the solution assumptions are valid. In the original work where the plastic cases are developed from the elastic case [6], the authors write:

> "Please note that because of the simplification that $p = 3.0$ Y_d used to derive δ^*, for small amounts of deformation (low u_1 it is possible for Eq.18 [this equation derives the amount of deformation] to predict a negative value of δ'' (which is a physical impossibility).when this occurs, assume that $\delta'' = 0$ and $e = 1$"

This becomes important when considering the subsequent quote which describes the interaction between the degree of deformation and the viscous dissipation of energy:

> "For negligible deformation, ($\delta'' \approx 0$) this reduces to
>
> $$F_{vis} = \frac{3\pi\mu R^2}{2h}\left(\frac{dh}{dt}\right)$$
>
> Which is the equation for squeeze flow between two spheres used in the original model of Ennis et al (1991) in this case, the model will give the same critical viscous stokes number (St_v^*) for coalescence:
>
> $$St_v^* = \left(1 + \frac{1}{e}\right)\ln\left(\frac{h_0}{h_a}\right)"$$

The plastic case is clearly specified to be a continuous extension of the elastic case. This is reasonable, and logically appropriate. Therefore, the boundaries should provide the same results, and yet they clearly do not, as seen in Figure 7.4b and Figure 7.4a.

The fundamental problem with the maths of the Stokes criterion might be limited to simply taking the plastic case as a whole as flawed, and not simply using inappropriate assumptions as the surface dry plastic case recognises, but this itself means that the surface dry case cannot be considered useful.

Such an argument is supported by the consideration of the fact that the asperity height h_a is used in the plastic case, despite the fact that the resistance to deformation will simply vary the deeper the impressing granule is, and the surface asperities will simply be part of this variation of depth that is intrinsically simplified due to the already applied spherical assumption.

However, the problems with the asperity height application lay deeper, but first, a consideration of the value h_0 , the liquid surface layer.

h_0 requires, intrinsically, the granules to be severely oversaturated to the point of forming a paste before the granules can coalesce without the need of external nucleation, and yet coalescence is observed in many cases without this. Non-spherical particles exacerbate this, increasing the saturations required before surface liquid has a significant presence [237].

When actually calculating the actual saturations used in the validation of this model, more issues arise. In the original paper [6], the parameters used to validate the model would result in a liquid surface layer of thickness 2mm for the largest granules. This would be immediately visible and obviously demonstrable, and in any real world application would be inducing a slurry, with oversaturation being very easy to observe rendering it impractical to handle.

So, returning to h_a , the real reason for inclusion is simply that it acts to hide an infinite value that otherwise occurs when integrating the viscous force equation necessary in even the original elastic-wet case Equation 7.19. If the

302

asperity height was not included as an arbitrary limit, then the coalescence could occur between any colliding granules. It is for this same reason that the original source uses a value of e_{rest} , even though this is completely unreasonable. It would predict significantly higher values than otherwise predicted, and would also be far less useful as a method of describing the relation between saturation and coalescence. So the issue was simply ignored.

In fact, the assumption of elasticity is itself rather doubtful in the context of granules, since due to a lack of long range order and weak inter-particle bonds, granules deform plastically [36].

The lack of a maximum size for the plastic case means that the solution will predict indefinite growth. While this is, in fact, the expected result of other predictions, not all pelletisation experiments result in indefinite growth. Further, if it was found, then because of the requirement of oversaturation for growth to occur, and the conclusion that they lead to indefinite growth would not itself demonstrate that these equations were correct even if they were both shown to be true, as the condition of oversaturation resulting in indefinite growth is also demonstrated by Equation 7.18.

The wet elastic case does predict a maximum size, however this is highly dependent on the coefficient of restitution, which as mentioned is extremely low for granular materials [5], and with lower coefficient of restitutions the easier it is to grow based on these equations. In fact, when the saturation is too high, resulting in a surface layer, granules become too "sloppy" to handle [5].

Further of note for the wet elastic case, as chapter 5 shows, the collision velocity approximations that were used to validate the model significantly underestimate the values. This in turn would require even higher saturations, though again, it is slightly irrelevant given the high dependence of the coefficient of restitution. The validation also did not account for the serious variability.

Some attempts have been made to resolve the issues in the wet-elastic case, by accounting for the capillary hysteresis and the liquid bridge volume along with

some other corrections [236]. However, in so doing, comparisons are made by the newer models to the original source of the solutions [42] and the relationship between the $St_v{}^*$ and $ln\left(\frac{h_0}{h_a}\right)$ is found to nonetheless be the most accurate, and none of the solutions proposed explain the divergences observed.

The point made regarding the discontinuity between the wet and dry cases is recognised in the original source, however the behaviour of the granules as a whole is considered extremely unnaturally. A serious disconnect between the real behaviour of the liquid and the solid phases of the granule is ignored. The liquid that forms on the surfaces of the granules that subsequently slows down incoming granules is assumed to apparently just stay perfectly still, ignoring the hydrodynamics that would, if it is not absorbed into the body of the granule, immediately form liquid bridges, which are always preferable than remaining loose on the surface. In fact, this would occur regardless on a micro scale, as the liquid on the surface absorbs into the bulk of the granule as this is preferential to the curvature formed on the surface.

The stokes number criterion, as stated, only works because it is written into a larger model where the bulk of the solution is carried by other tasks.

The problem of the minimum size requirement before growth is resolved by assuming that nucleation has occurred previously, using the new definition of nucleation based on droplets being applied to the surface of the particles which coalesce new nuclei. This can then be modelled using droplet size prediction and flow of the powder bed beneath it.

The problem of rate of growth is resolved by assuming that consolidation effects are occurring in the background, which will increases the saturation over time until the liquid begins appearing on the surface, and then as soon as this does the agglomeration occurs right away.

And the problem of a maximum size is resolved by including breakage phenomena as an assumed part of any population balance type model, which then acts to balance the sizes of the granules present to a maximum size, as the coalescence

would occur indefinitely otherwise.

In conclusion, the entire Stokes criterion is flawed. It is flawed from every angle. It only works when heavy abstractions are applied regarding the existence of the granule, it ignores fundamental behaviours of wet agglomerates, and it requires other processes to perform the actual work of modelling the granulation distribution.

7.6 New Model

Realising how broken the Stokes criterion model was, and having tested the effects of crudely using Equation 7.18 as the limiting diameter in DEM simulations where Equation 7.6 was the simulator for growth, a new model was developed. The goal was to develop a model which could, in fact, predict a maximum granule size.

The seeds of the new model came the realisation that Equation 7.18 was effective, the premise of Equation 7.10 matched the basis of it, and that the simple modification of Equation 7.6 was surprisingly effective for something that was lacking so many expected components. Once all the parts were in place, other features intrinsic to granulation could be introduced explicitly, such as consolidation, not simply as assumptions in the background.

The simplest method to perform this is to have two distinct limits which are intrinsically linked together by some physical phenomena. This model will be referred to as the "Cohesion-Adhesion Criterion" to keep the naming system applied, and to highlight the two component nature of the solution and their general functionalities.

Most of the contents of section 7.7 has been submitted, and accepted in Powder Technology as of 11 May 2022, under the paper title "Towards a theory of wet agglomeration" [242].

However, some features which were not included in the paper (due to space restraints) are also discussed within.

7.6.1 Core elements

The basis for this solution relies, as mentioned, on connecting the Bond Probability Criterion to the Saturation criteria in a physically meaningful way.

Both Criterion provide solutions which determine the granule size, but each is limited in some respects:

1. Both lack one half of the solution. The Saturation Criterion lacks the dynamic size limit, and the bond probability criterion lacks a dependency on saturation.

2. The Bond Probability Criterion intrinsically is defined a part of a probabilistic solution, which inhibits its application to systems where the probability distribution of the relevant variables change

3. Neither criterion describes the growth rate, which though not necessary for describing the limiting size, is useful for defining the behaviour of a system

4. There does not appear to be a natural method of integrating the two solutions because of their distinct premises.

The proposed solution sets out to combine the two solutions using a key bridging framework that is physically meaningful, and resolves all the above issues.

All nondimensional constants which are related to the system without having a specific property they are tied to will be labelled as K_{value} to highlight the need to better understand them. e.g. the value relating the hardness to the yield strength will be labelled K_φ.

7.6.2 Cohesion limit

The saturation limit in Equation 7.18 is assumed to be sufficient to maintain the structural integrity of the granules. The reason being that, if the granules satisfy that condition, then they have experienced enough of the consolidation procedured and the overall collisions. To maintain the consistency of

labelling, Equation 7.18 has been adjusted in this document, and is reproduced here asEquation 7.25.

$$\Delta_{limCoh} = \frac{K_g d_p}{1 - \left(\frac{S}{K_{Smax}}\right)^{\frac{1}{3}}} \tag{7.25}$$

7.6.3   Dynamic limit

The dynamic limit of the granules is essentially defined by the inequality Equation 7.26

$$\sigma_{bond} > \sigma_{sep} \tag{7.26}$$

7.6.4   Bond Strength

The bond strength development extension and equation Equation 7.17 described in subsection 7.3.2 was developed as part of this problem originally. This is the bridging element that resolves issue item 4. All the points in favour of it and assumptions applied in subsection 7.3.2 are also applied here.

7.6.5   Separation Strength

The expression for σ_{sep} is developed from the original solution by Ouchiyama and Tanaka in [45]. This defines the separation forces in terms of the maximum moment that will be applied during the process, which comes from the bulk shear motion of the granules. For the stress induced by moments around the centre of the bond, the basic equation is

$$\sigma_{sep} = \frac{3M}{4\pi^{\frac{3}{2}} A^{\frac{3}{2}}} \tag{7.27}$$

To calculate σ_{sep} thus requires the moment M and the area of contact A .

Area of contact A

The area of contact can be calculated by considering the normal kinetic energy of the collision of two particles as it dissipates while being plastically absorbed.

$$\int_0^{\delta^*} Q d\delta = E_p = E_{kN} = \frac{1}{2} V_{cN}^2 \widetilde{m} \tag{7.28}$$

From [114]:

$$Q = p_0 \pi a^2 = p_0 \pi \widetilde{R} \delta \tag{7.29}$$

from which the area can be shown to be proportional to the kinetic energy of the collision, See Appendix section A.6 for the full derivation.

$$A = \pi a^2 = \pi \sqrt{\frac{4}{3}} \sqrt{\frac{\rho_g}{K_\varphi \sigma_y}} V_{cN} \sqrt{\widetilde{R} \widetilde{R^3}} \tag{7.30}$$

Separating moment M

To determine M , Equation 7.31 is also applied in the original calculation [45].

$$M = A_M \frac{g_M (D, d)}{2^\alpha} \tag{7.31}$$

$\frac{g_M(D,d)}{2^\alpha}$ is a function of granule diameters related to different cases where volumes can be related to separating forces. A_M is a dimensioned constant of proportionality which relates these forces. A_M is unrelated to the granule sizes, as this is managed through $g_M (D, d)$.

$g_M (D, d)$ is a function which switches between five different cases to describe how the shearing is occurring, however they can be well approximated using a single function, Equation 7.32, using a sliding parameter K_γ to distinguish between the solutions [45].

$$M = A_M \frac{g_M (D, d)}{2^\alpha} \tag{7.32}$$

This in turn can be re-arranged to the following form:

$$g_M(D, d) = \left(\frac{\widehat{D}}{\overline{\overline{D}}}\right)^{2K_\gamma} \overline{D}^4 \tag{7.33}$$

The next step is managing A_M. This is an unspecified dimensioned constant in [45], which relates the forces applied to the granules to the volumes of the granules. As the effect of the volume in the separating moment is accounted for by $g_M(D, d)$, A_M itself is explicitly unrelated to the granule sizes. As it has dimensions and a specific role in the solution, it is well suited to dimensional analysis. As A_M is specified as being unrelated to the granule size, deriving the variables which it is constituted from is made easier.

To begin with, first, decompose the constant into the known relation, and then into the given dimensions.

$$A_M = \frac{F}{V} = \frac{M}{T^2 L^2} \tag{7.34}$$

Since A_M is relating the size of the particles to a force, then it is reasonable to assume that it is a function of granule density. In addition, assuming A_M is related to the velocity of the particles (or some other characteristic velocity such as that of an impactor) which is also reasonable, squaring A_M allows it to correspond to the change in kinetic energy due to such impacts. This leaves another variable, L^{-1}. This can be expressed as

$$A_M \propto \frac{M}{L^3} * \left(\frac{L}{T}\right)^2 * \frac{1}{L} \tag{7.35}$$

Adding a nondimensional scaling constant then gives:

$$A_M\left(\rho_g, V_{ch}^2, L_{ch}\right) = \frac{K_A \rho_g V_{ch}^2}{L_{ch}} \tag{7.36}$$

Where L_{ch} is a characteristic length scale. It cannot be the granule diameter, and it must be some variable that results in lesser intensity of separation forces as it grows. A suitable analogy then is the "mean free path", λ, as applied

in kinetic theory of gasses. This is more complex in granular materials, due to the inelastic nature of the collisions, and some work on this regard is covered in [243]. This mean free length would also be the length between *significant* collisions, since minor collisions are beneficial to developing the bond strength through consolidation [235], and not all collision directions result in a separating moment.

Combining Equation 7.36 and Equation 7.33 an inserting them into Equation 7.31 gives

$$M = \frac{A_M \left(\rho_g, V_{ch}^2, L_{ch}\right)}{2^\alpha} \left(\frac{\widehat{D}}{\overline{\overline{D}}}\right)^{2K_\gamma} \overline{D}^4 \tag{7.37}$$

Since α is just a constant tied to the collision behaviour, 2^α is incorporated into K_A to form K_α , the agitation constant.

$$M = \frac{K_\alpha \rho_g V_{ch}^2}{\lambda_{ch}} \left(\frac{\widehat{D}}{\overline{\overline{D}}}\right)^{2K_\gamma} \overline{D}^4 \tag{7.38}$$

σ_{sep} Collection

Collecting Equation 7.38 and Equation 7.30 and substituting them into Equation 7.27

$$\sigma_{sep} = \frac{3M}{4\pi^{\frac{3}{2}} A^{\frac{3}{2}}} = \frac{3\frac{K_\alpha \rho_g V_{ch}^2}{\lambda_{ch}} \left(\frac{\widehat{D}}{\overline{\overline{D}}}\right)^{2K_\gamma} \overline{D}^4}{4\pi^{\frac{3}{2}} \left(\pi\sqrt{\frac{4}{3}}\sqrt{\frac{\rho_g}{K_\varphi \sigma_y}} V_{cN} \sqrt{\widetilde{R}\widetilde{R^3}}\right)^{\frac{3}{2}}} \tag{7.39}$$

7.6.6 Dynamic Limit Defined

Substituting Equation 7.17 and Equation 7.39 into Equation 7.26 gives:

$$K_{\frac{t}{c}} \sigma_y \alpha_{wet} \left(\varepsilon_r\right) > \frac{3\frac{K_\alpha \rho_g V_{ch}^2}{\lambda_{ch}} \left(\frac{\widehat{D}}{\overline{\overline{D}}}\right)^{2K_\gamma} \overline{D}^4}{4\pi^{\frac{3}{2}} \left(\pi\sqrt{\frac{4}{3}}\sqrt{\frac{\rho_g}{K_\varphi \sigma_y}} V_{cN} \sqrt{\widetilde{R}\widetilde{R^3}}\right)^{\frac{3}{2}}} \tag{7.40}$$

This can be rearranged (See Appendix section A.7) to form

$$\left(\frac{\widehat{D}}{\overline{\overline{D}}}\right)^{2K_\gamma - 4} \frac{\left(\overline{DD^3}\right)^{\frac{3}{4}}}{\widehat{D}^2} < C_m \frac{K_{\frac{t}{c}}}{K_\alpha K_\varphi^{\frac{3}{4}}} \alpha_{wet} \frac{\sigma_y^{\frac{1}{4}}}{\rho_g^{\frac{1}{4}}} \frac{V_{cN}^{\frac{3}{2}}}{V_{ch}^2} \lambda_{ch} \qquad (7.41)$$

Which, in turn, by defining $d = r_d D$ and noting that the merged granule diameter between two granules D and $r_d D$ is $D\sqrt[3]{1 + r_d}$, can be re-arranged (See Appendix section A.8) to give Equation 7.42.Further, C_m can be simply assumed to be included within K_α , as it can scale to any arbitrary extent.

$$\Delta_{limAdh} < \frac{K_{\frac{t}{c}}}{K_\alpha K_\varphi^{\frac{3}{4}}} \alpha_{wet} \frac{\sigma_y^{\frac{1}{4}}}{\rho_g^{\frac{1}{4}}} \frac{V_{cN}^{\frac{3}{2}}}{V_{ch}^2} \lambda_{ch} \frac{(1 + r_d)^{2K_\gamma - 2\frac{11}{12}}}{r_d^{K_\gamma - 3} (1 + r_d^3)^{\frac{3}{4}}} \qquad (7.42)$$

Δ_{limAdh} is now the limiting size that the merged granule can reach. The presence of $1/\left(r_d^{K_\gamma - 3}\right)$ means that while $K_\gamma > 3$, $\lim\limits_{r_d \to 0} \Delta_{limAdh}(r_d) \to \infty$ and so the bond does not limit the ability for such mergers to occur. This is relevant, not just for layering systems but also for heterogeneous systems, since some of the granules would grow faster than the bulk by consolidating with smaller feed granules, even if this means they grow larger than the system Δ_{limAdh} .

7.6.7 Consideration of the Components

The nature of the collision behaviour, being $\Delta_{limAdh} \propto \frac{V_{cN}^{\frac{3}{2}}}{V_{ch}^2}$ is very valuable, as it resolves some issues with the collisions statistics and oblique contacts. Because $V_{ch} \geq V_{cN}$ by necessity, this means that the maximum value that $\frac{V_{cN}^{\frac{3}{2}}}{V_{ch}^2}$ can form is when $V_{ch} = V_{cN}$, which occurs at a head on collision. This then gives an answer to why the collisions should be assumed to be head on, which is simply that the collisions will occur in all directions, however the maximum diameter which is being investigated will occur only from head on collisions, at which point $V_{cN} \propto V_{ch}$. The value V_{ch} describes the surrounding collision events but will be related to the bonding collisions, and the constant of proportionality can be included in K_α . Doing so allows Equation 7.42 to be written in the form

$$\Delta_{lim\,Adh} < \frac{\lambda_{ch} K_\varphi^{\frac{3}{4}}}{K_\alpha St_{def}^{\frac{1}{4}}} K_{\frac{t}{c}} \alpha_{wet} \frac{(1 + r_d)^{2K_\gamma - 2\frac{11}{12}}}{r_d^{K_\gamma - 3} (1 + r_d^3)^{\frac{3}{4}}} \tag{7.43}$$

There are three major terms in this equation, the agitation term,

$$\frac{\lambda_{ch} K_\varphi^{\frac{3}{4}}}{K_\alpha St_{def}^{\frac{1}{4}}} \tag{7.44}$$

the adhesion term

$$K_{\frac{t}{c}} \alpha_{wet} \tag{7.45}$$

and the size fraction term

$$\frac{(1 + r_d)^{2K_\gamma - 2\frac{11}{12}}}{r_d^{K_\gamma - 3} (1 + r_d^3)^{\frac{3}{4}}} \tag{7.46}$$

The presence of $St_{def}^{-\frac{1}{4}}$ in Equation 7.43 is promising, as it retains the relationship reported by Watano et al [44], where the average granule size was related to $(V_I^2)^{-\frac{1}{4}}$, and St_{def} is directly proportional to V_c^2, meaning that $(V_I^2)^{-\frac{1}{4}} \propto St_{def}^{-\frac{1}{4}}$.

The granule size ratio term Equation 7.46also has the interesting property that, for values of $K_\gamma > 4$, below r_d value of around 0.2 it favours dissimilar granules and above around 0.2 it favours the merging of larger granules. This may explain the somewhat contradictory results observed in [84] where the overall behaviour of the granule growth is best described with an equipartition of kinetic energy kernel which favours large-small coalescence, but the tracer distribution appeared to be better described by a shear kernel which favoured large-large coalescence.

Though there are many constants which suggest that any result could be fixed to the model, most are bounded and have explanations as to their sources which will allow for correlation in future work.

The structural constants consist of $K_{\frac{t}{c}}$ and K_φ. $K_{\frac{t}{c}}$ is the constant relating the tensile strength to the compressive strength, which is more complex for granular materials than continuum materials as the inter-particle friction will have

a greater impact at this stage, but in general it must be below 1, and a value of 0.65 has been found in previous research. K_φ is the constraint, which relates the hardness to the yield strength, and much work has been done on this for continuum materials but in general it is bounded between 1 to 3, and 2.8 has been used here as it has been used in related literature.

The liquid constants meanwhile consist of K_g and K_{Smax}. K_g describes the degree of liquid penetration from the core to the surface, and must be between 0 to 2 because of the physical requirement for the liquid to contact all particles in the granule, and is expected to be roughly 1. Similarly, K_{Smax} is restricted to less than 1 as beyond this by definition results in slurry formation in bulk, though may be a small amount less due to voidage inclusion.

Finally K_γ and K_α are constants related to the system in general. K_α is, based on the way that it alters the size ratio term Equation 7.46 between 3 to 4.5 to satisfy the kernels observed with other researchers findings. The only value which is unbounded is K_α, which is a value from the dimensional analysis performed on the separation force. Evaluating how this fits into the greater system would be important as part of future work on this model, and correlating coefficients are not unheard of, see for example coefficient of lift or drag in fluid flow analyses.

In the end, these are simply the best values, and most can be tested using alternative methods than simply application of granulation which is a valuable point in their favour.

7.6.8   Results of Adhesion-Cohesion Criterion

The model above is termed the "Adhesion-Cohesion Criterion" as the dynamic limit specified tests whether the **adhesion** of the two granules together is sufficient to hold the granules together depending on the agitation behaviour of the system at the moment of the collision, and the value of K_{Smax} and K_g in Equation 7.18 describe the **Cohesion** of the granule against major breakage.

7.7 Application of new model

With the criterion defined, an analytical exploration of the results predicted can be performed. Some simplifications are necessary as part of this, such as only equal size granules merging $r_d = 1$, and perfectly even distribution of forces in the consolidation process.

For these results:

$$\Delta_{lim} = min(\Delta_{limAdh}, \Delta_{limCoh}) \qquad (7.47)$$

From Equation 7.43 and Equation 7.18. The consolidation behaviour will be the primary method of defining growth.

Whether or not the granules turn into a slurry is simply determined by whether the granule saturation is larger than K_{Smax} . It may be possible for granules in certain systems to not form into a slurry with an excess of saturation, such as in very high viscosity systems, but in such cases a different form of the yield strength equation may be necessary as well and so cannot be assumed to be within the scope of this solution.

Variable	$K_{\frac{t}{c}}$	K_α	K_φ	K_g	K_{Smax}	K_γ
Value	0.65	253	2.8	1	1	4.5

Table 7.1: The K constants used in the results when not specified otherwise.

Variable	γ	θ	μ	d_p	$Æ\!R$
Value	0.072N/m	30°	1 mPas	50µm	1

Table 7.2: The liquid and particle properties used.

The baseline variables used are spread into three tables, Table 7.1, Table 7.2, Table 7.3. Some of the variables were chosen based on realistic values, for example the liquid properties were based on water, and others such as K_γ were based on

Variable	λ_{ch}	$\alpha_{wet}\,(\varepsilon_r)$	ϵ_{min}
Value	1mm	1	0.3

Table 7.3: Other system parameters defined and used.

previous researchers work [45] that lined up with other behaviours observed [84]. This is considered in greater depth in subsection 7.6.7

However, some of the parameters were simply chosen to highlight different features of the model, especially since values such as K_α are explicitly intended to be scaling parameters. Many features can affect this, as even simply changing the type of impeller can result in different shearing behaviours [244]. The yield strength used is Equation 6.12, to allow the collision strength to be relevant, hence the inclusion of the aspect ratio.

7.7.1 Final diameter prediction
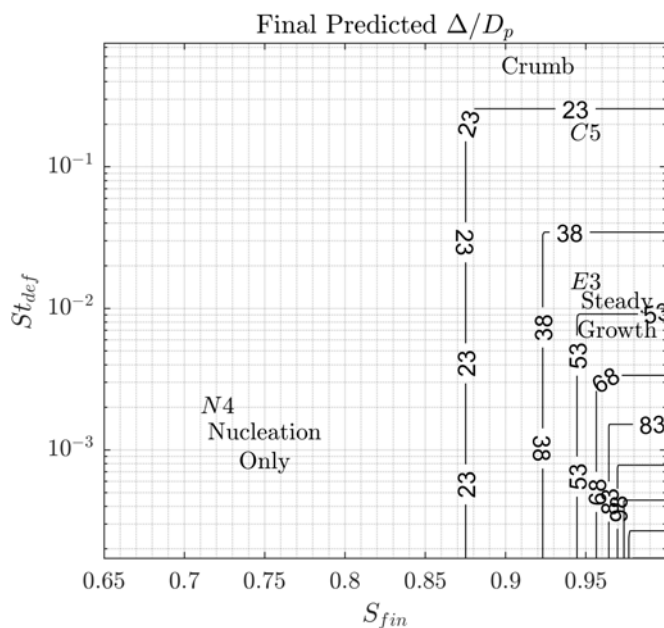
Figure 7.5: Limiting size predicted for different conditions.

The Combination of the two limits as specified by Equation 7.47 can be used to demonstrate the same distribution of dominant mechanisms in the classical mechanism map format. The value of Δ_{lim} will be nondimensionalised to the diameter of the component particles. Figure 7.5 shows the final predicted diameter, based on the saturation and Bond limits calculated.

S_∞ is used in these results to describe the final saturation reached, to differentiate between the final saturation and the maximum saturation the system can have before turning into a slurry.

Already Crumb and Nucleation regions can be observed, and the region where growth does occur, whether by steady growth or induction can also be seen in Figure 7.5.

7.7.2 Growth behaviour predictions

The consolidation equation previously described, Equation 6.35, is used to calculate the change in porosity over time. For each $V_{l/s}$, a unique saturation value can be found at each ϵ_0, and this will change as a result of varying St_{def} values. The determined Δ_{lim} values will be plotted according to their S_∞ values to maintain consistency with the literature. This allows a growth behaviour to be predicted. The values for the consolidation equation are given in Table 7.4

Variable	ϵ_0	ϵ_{min}	$k_{\epsilon A}$	$k_{\epsilon B}$
Value	0.5	0.3	1e-3 1/s	1e3

Table 7.4: Consolidation variables used when otherwise unspecified.

The term τ_A is used to refer to the dimensionless time as defined by $\tau_A = t \times k_{\epsilon A}$

Figure 7.6, Figure 7.7 and Figure 7.8 show the growth behaviour at sequential points in time, representative of early, middle and late stages of growth.

In Figure 7.6, note the presence of the rapid growth, the steady growth and the nucleation regions, and that the growth rate diminishes as the granule defor-
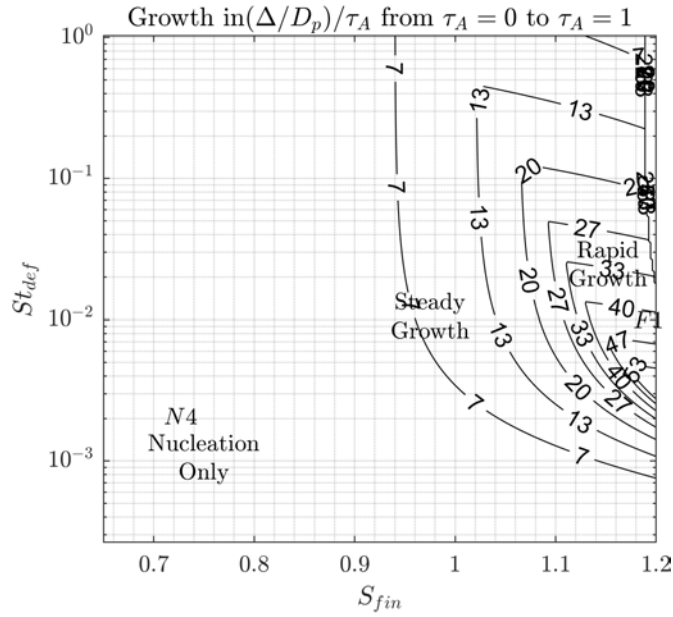
Figure 7.6: the growth rate between $\tau_A = 0$ and $\tau_A = 1$.

mation approaches the crumb region but is still faster than the low deformation region where consolidation is not sufficient to develop the levels of saturation required to grow beyond nuclei.

In Figure 7.7 much of the region previously described as rapid growth has turned into slurry, or some has ceased growing, being in the crumb regime, while the steady growth region continues to grow. Also note the progress of the growth moving downwards to the low deformation number region.

And finally, in Figure 7.8 the steady growth region has slowed down in growth rate, as it approaches equilibrium. The region around $St_{def} = 10^{-3}$ has started growing at significant rates, though due to the changing rate nature of induction, it is easier to observe on individual plots at points in the region over time.

The induction region in particular is impressive because it lines up very well with the [90] findings of the viscous force dominating in the $St_{def} = 10^{-3}$ region, which agrees with the findings elsewhere regarding the link between viscous binders and induction.
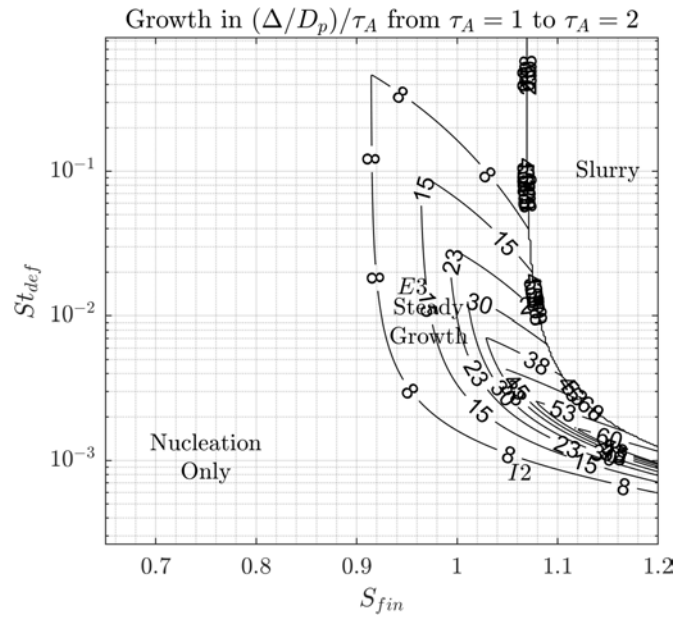
Figure 7.7: the growth rate between $\tau_A = 1$ and $\tau_A = 2$
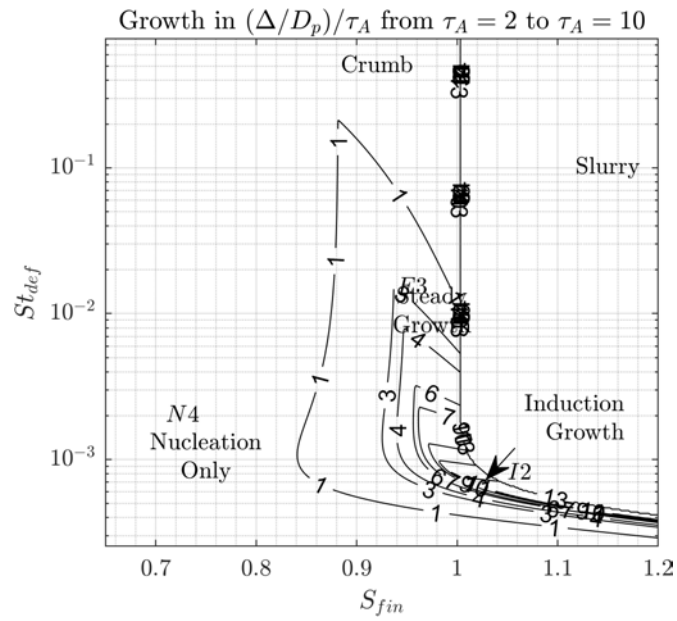
Figure 7.8: – the growth rate between $\tau_A = 2$ and $\tau_A = 10$.

The growth predictions for specific points on the map are shown in the following graphs. In each case, the value of

$$\Omega_{def} = \frac{K_\alpha St_{def}^{\frac{1}{4}}}{\lambda_{ch}} \tag{7.48}$$

which corresponds to the agitation term above is listed. This describes the intensity and frequency of the collisions the granules experience, to highlight how different feedstocks might react differently even within the same granulator which can nonetheless be described using the equations above.

The choice of positions to plot out is based on descriptions of the various accepted granule growth behaviours in [38], as well as the various growth behaviours previously described in the introduction.

Figure 7.9b,Figure 7.9d and Figure 7.9a show growth phenomena, Figure 7.9c and Figure 7.10 show the limiting cases of the crumb and nucleation, and finally Figure 7.11 tests the equations growth prediction for granules of different sizes.

In Figure 7.9b, Fast growth without limit is shown, observed in systems such as drum granulation of coarse particles with low viscosity binders in drums, or medium viscosity binders in mixers [29, 64, 89, 189]. d_p in this case was set to 500µm to represent the coarser particles.

Figure 7.9d shows induction behaviour. Once induction is initiated, the growth rate is rapid enough to cause indefinite growth, though the granulation is usually stopped once the growth hits this state [39, 89]

Figure 7.9a shows the equilibrium growth, which is found when the saturation is below the amount required for a slurry. In the case shown, the size is at a boundary where changes in both the saturation and the deformation number can result in changes in the granule size. This is the ideal growth regime as it is controllable, and found in [4, 47, 50, 64, 67, 78, 82, 89]

Nucleation, shown in Figure 7.9c is the result of insufficient binder to grow the granules. Because the distribution is not perfectly even in granulation processes, the droplets that are initiated result in localised higher saturation, which result in the observed nuclei and the size dependence on the droplets, in accordance to nuclei size growth observed by [72, 245]. The generally observed nuclei limited

(a) Equilibrium growth – E3 in Figure 7.7

(b) Fast growth without limit - F1 in Figure 7.6

(c) N4 – Nucleation – N4 in Figure 7.5

(d) Induction growth– I2 in Figure 7.7
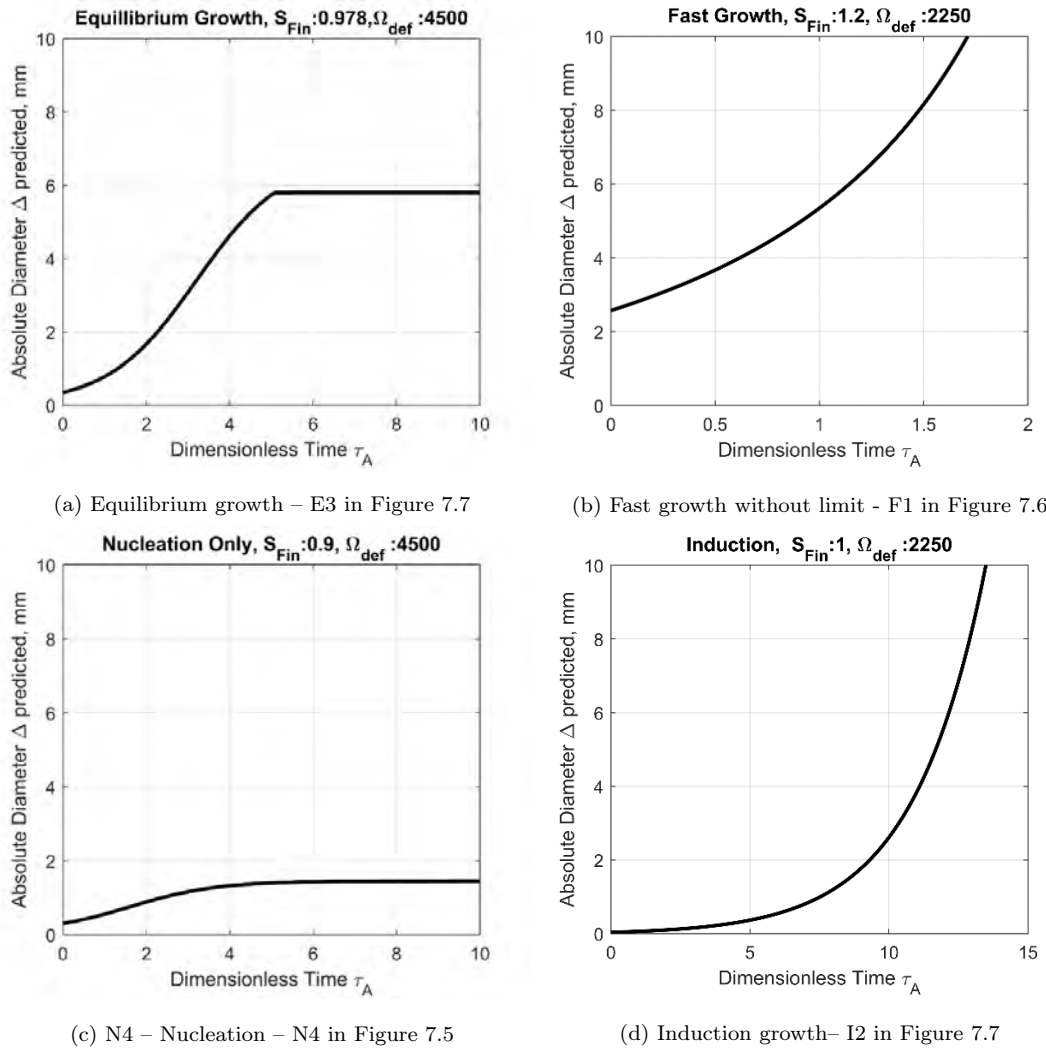
Figure 7.9: Comparison of results

growth is found in [39,40,50,246] for low saturation and no observed growth, and the same can be said for saturation cases previously mentioned in section 7.4.

Figure 7.10 shows the Crumb region. This regime is in fact not a clearly defined region, other than granule diminution due to excessive agitation.

This is further muddied by the fact that for some granulation conditions, the "crumb" state is temporary [195], before the mixture actually forms into a slurry. [247] test the breakage of nucleated, rather than pressed, pellets, which
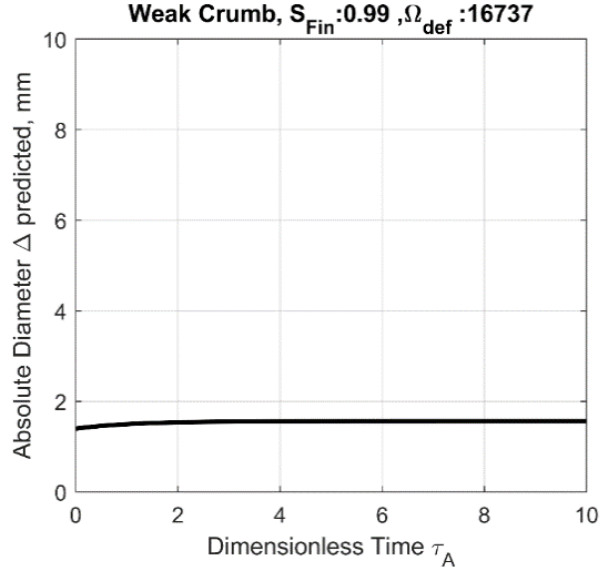
Figure 7.10: Crumb region

would be more realistic comparison as this ensures that the saturation distribution is accurate, though [105] does show that the number of survivors, and hence, Δ_{limAdh} stabilises quickly into the more stable smaller size.

Crumbling can also be the result of insufficient saturation but if the granules are introduced at a larger size due to being manufactured in that shape the binder will re-distribute into the lower size. Other experiments finding the stability of low size of crumbs are [64, 233].

As discussed in section 6.5, the interaction between St_{def} and ϵ_{min} is complex. If ϵ_{min} is allowed to increase for high deformation numbers, then the granules could weaken even further as a result of increasing porosity, but this may also lead to the saturation of an oversaturated mix converting into granules. This phenomenon has been observed by [248] so this is not completely implausible.

Figure 7.11 shows how Layering is predicted using Equation 7.43 as a kernel, and it matches the general trends found in [71, 248]. The prediction comes from the r_d terms, and the growth rate depends on the rate of interaction, which would be linked to λ_{ch} . It would also be limited by the saturation, though
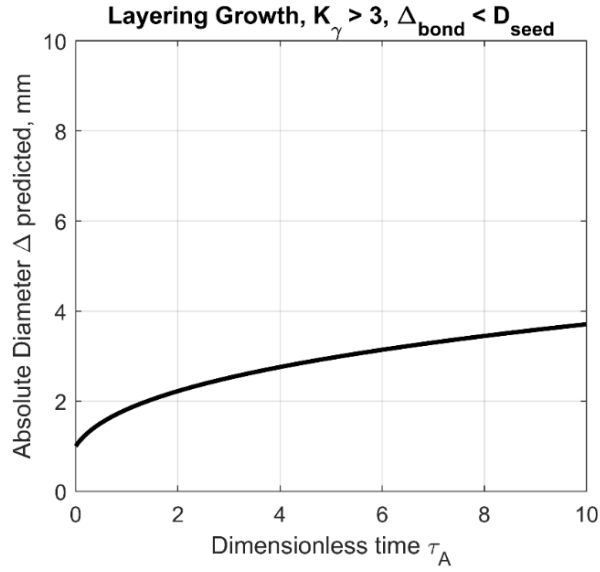
Figure 7.11: Layering growth prediction

layering systems often include binder with the feed particles. [78] interestingly demonstrates the effect of providing enough saturation to nucleate the granules evenly. In such a case the layering decreases, as there are fewer free feed granules that are not nucleated, and the r_d term is relatively linear above $r_d = 0.2$, which would also suggest a limit on the size of layering growth if a finite feed is provided, which is observed in [248].

In the end, the solution gives the intuitive result that one would desire as high a collision speed as possible to ensure that the initial contact connects and bonds plastically, but then as little subsequent speed if you want agglomeration.

7.8 Additional Commentary

7.8.1 Cohesion Criterion

The reason for re-defining the saturation criterion as the cohesion is because, as noted in the literature review, increasing the amount of bentonite binder signifi-

cantly increases the average diameter, while also increasing the drop number all for similar % moisture contents [63].

It may also be that the adhesion criterion is being altered, however the nature of the bonds of bentonite being fibrous may suggest that less moisture is required to bond the granule satisfactorily, allowing a lower value of K_{Smax} to reach an equivalent size.

On the other hand, this behaviour is also observed in the use of Peridur, which is an organic binder which is water soluble, which might argue against it, so would benefit from more research.

7.8.2 Size Fraction term

The Size Fraction term of the bond strength solution is interesting because it can be used to generate a kernel for population balance models, if one assumes that, being a system solution, this is the only limiting factor for coalescence. This is a matter of simplifying it to a form similar to the other kernels:

$$\beta_{Adh}\left(t, r_d, K_\gamma\right) = \beta_0 \frac{\left(1 + r_d\right)^{2K_\gamma - 2\frac{11}{12}}}{r_d^{K_\gamma - 3}\left(1 + r_d^3\right)^{\frac{3}{4}}} \tag{7.49}$$

This was done to generate Figure 7.10. Considering only the r_d term gives a kernel along the lines of the Equipartition of kinetic energy (EkE) kernel or the Orthokinetic (OK) kernel as compared in [84], where they find that different behaviours were observed for the base particles and the tracer granules that were added halfway through granulation, having been pre-formed. Currently no name is given for this kernel, so it will be labelled the adhesion kernel for now, though there is a suspicion of it being related to the entropy of granules due to the nature of how it favours packing behaviours.

Comparing all three of the kernels, Figure 7.12 shows the degree to which the kernel favours different interactions. For a $K_\gamma \approx 4.5$, the coalescence does match the growth behaviour between the small and large particles, which is in line with
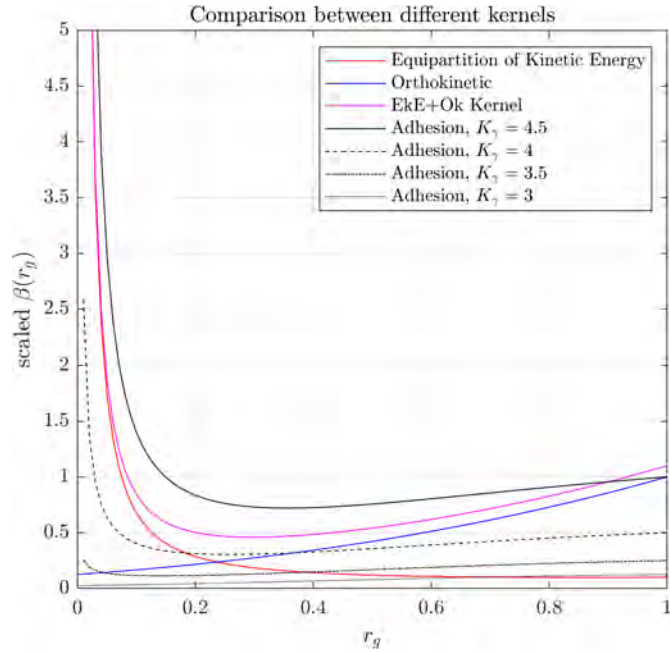
Figure 7.12: Comparison between the relative magnitudes of coalescence predicted by β_{eke} , β_{OK} , $(\beta_{OK} + \beta_{eke})$ and β_{Adh} for $K_\gamma = 4.5, 4, 3.5$ & 3 as a function of r_d .

expectations, especially as since in [45], $K_\gamma = 4.5$ represented the case where the force applied was proportional to the granule volumes, which is essentially an inertial force.

7.8.3 Breakage

The descriptor does not include minor behaviours, such as abrasion or direct shattering. This is because it assumes that any such breakage happens to prevent growth in the first place, as it would prevent the initial adhesion to occur. If the adhesion-cohesion criterion is to be modelled using a system which does have an increase in the speed over time, then it would be important to include in future work.

However, one benefit of the above model is that V_{cN} and V_{ch} are separate and the implementation of each is clarified, which is useful for modelling. For

example, in an impeller granulator with a chopper, the V_{ch} could be the chopper speed, while the impeller speed could be associated with the V_{cN}. Such an implementation would explain the results observed in [62], shown in Figure 7.13a. The findings in that paper were in direct contrast to other findings, [57], but this could be explained by the fact that the former has a chopper which is constant for all tip speeds, and this chopper speed would dictate the characteristic velocity that the granules, once merged, need to survive.
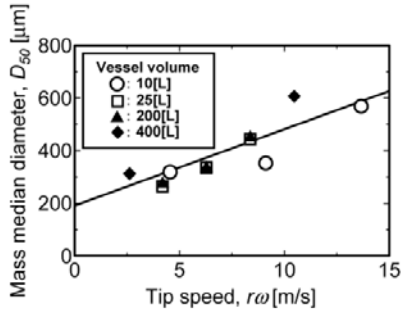
Fig. 10. Effect of Tip Speed on Granule Mass Median Diameter

(a) The effect of increasing tip speed on granule mass median diameter. Figure 10 from [62]
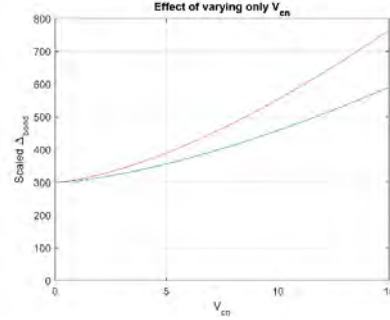
(b) The effect of altering only V_{cN} on the scaled granule limiting diameter, for Equation 7.42. The lines correspond to different values of λ_{ch}

Figure 7.13: Comparison of results

If V_{cN} only is adjusted, as shown in Figure 7.13a then the results found in [62] fit into the bond strength solution. To account for the increase in vessel size, multiple values of λ_{ch} were tested, which does show a similar increase with larger λ_{ch} also resulting in larger diameter granules as larger vessels do.

Other features may be causing the increase in diameter as the velocity increases. In [62] the strength increases linearly as the velocity increases, which may be a result of increased compaction. Increased strength results in a slight increase in the diameter, since Equation 7.42 $\Delta_{limAdh} \propto \sigma_y^{\frac{1}{4}}$. If the porosity is reduced, then this would also suggest there is greater saturation, which would interact with both the cohesion component, as well as the value of $\alpha_{wet}(\varepsilon_r)$ in the adhesion term.

Chapter 8

DEM Granule and Agglomeration Modelling

8.1 Introduction

This chapter is separated to maintain clarity, as this collects the findings from the previous chapters regarding granule mechanics such as the liquid content, the consolidation and yield strength, along with agglomeration behaviours, and describes their implementation in DEM.

One of the primary features of the DEM model used was the exceptional speed when managing large quantities of particles, at the cost of increased complexity. The former was to be maintained as much as possible, so how the complexity was managed in this context are covered.

The two features that interfered with these two effects were the large quantities of small particles that would be needed given the importance of granule size variation in the behaviour, and how to efficiently perform agglomeration in the model without breaking the complex system.

8.2 Granule Properties

The pellets have a fundamentally different structure to the typical solid materials which are modelled using DEM, examples from the original modelled system being coal and iron ore chunks.

8.2.1 V_s, V_l, V_v considerations

The first difference is that they are composed of solid, liquid and gas components, which combine to alter the mass and ultimately the radius of the spheres. The density of the material is a function of the proportions of the three, preventing the density from being applied in the normal manner.

This was a slight problem since the spawning system expects a density for the spheres ahead of time, to calculate the number of spheres to add when a set mass is specified. Fortunately, this is actually only an estimate, and the spawning system tracks the actual mass added, so underestimating the density allows the program to halt early when it detects that the correct amount of mass has been added.

The system also requires the radius of the spheres to be specified. Therefore the effect of the porosity and the saturation on the mass of the granule still requires the total mass to be determined, since the volume of the sphere as a whole will be known as will the densities of the parts, which will be divided accordingly.

The saturation is assumed to begin appearing on the surface when $S = K_{Smax}$. This causes complications for calculations of the volume when $S > K_{Smax}$

In the case for $S \leq K_{Smax}$ the relations are fairly simple, since the porosity and saturation divide this total volume V_T into the pore volume V_ϵ and from the pore volume the liquid volume V_l , and then from here the mass can be calculated.

However, when $S > K_{Smax}$, things become complicated. The liquid volume needs to be separated into the internal liquid and the external liquid. The internal

liquid is then assumed to fill the pores completely, and then the total pore volume is divided by $S - K_{Smax}$ to find the volume fraction outside the pellet. The volume fraction then needs to be specified in describing the volume fractions of the solids in the final sphere mass as defined by the specific radius.

After the initial spawning however, calculating the radii from the volumes is slightly easier. The porosity is specified, and the pore volume can be calculated via V_s by noting that $V_\epsilon = V_s \frac{\epsilon}{1-\epsilon}$, and if $S > K_{Smax}$ then $V_l = V_\epsilon K_{Smax}$ and the remainder of the liquid appears on the surface, which can then be calculated as a spherical shell.

All of the variables were tracked for each sphere, even though they can all be derived from just the basic volume variables V_s, V_l, V_v. This was so that they did not have to be continuously re-calculated as many were needed regularly, such as the saturation when being tested.

8.2.2   Additional Compositions

Once the solid, the liquid and the void contents could be clearly defined, the compositions could be further divided. This was explored, since the binder is a combination of water and cement and the conditioner may not have completely removed the oil. All of these were noted in the literature review as having interactions with each other and with particle mixtures.

This was tested briefly with cement, as cement explicitly sets, and the change in viscosity and setting would be based on those found in the early stages of the wetting [249, 250]. However, during the implementation, it became quickly apparent that the time dependent nature of the cementitious viscosity would cause serious problems when the agglomeration of two separately wetted spheres were considered. The degree of setting would have to be tracked for two separate parts, or alternatively the average applied, but this would be an unsatisfying method.

With a bit more exploration, the problem of mixing was realised to be a major

impediment. The relationships between liquid mixtures and their properties are generally very unclear at the time of writing, and can vary depending on many factors, this was not deemed to be a valuable use of time in general, given how minor a part the viscosity would have overall.

Similar reasoning was made for the particle properties. Allowing the average particle diameter to vary per sphere would have been slightly more feasible than the mixing of different liquids, but still not simple.

However, considering that the feed is thoroughly mixed beforehand, and as the kinetic behaviour is demonstrated to induce segregation during the process, the feed composition can be assumed to be homogenous enough. Based on this, the liquid and solid properties are defined as singular global values.

8.2.3 Material Properties

The material properties will be specified in chapter 9, however the Poisson's ratio is noted here as 0.5 due to the fundamental nature of pellets.

Partly it comes from soft materials tending to have higher Poisson's ratios. More fundamentally, given that the granules do not reform after experiencing deformation, if the Poisson's ratio was any lower then it would suggest that compression is occurring, which is covered in consolidation.

8.3 Granule mechanics

The granule mechanics as specified in chapter 6 were applied as practically as could be.

8.3.1 Stiffness

The stiffness of the materials was an important feature. As mentioned in chapter 4, the stiffness is directly related to the critical timestep of the simulation.

However, an excessively low stiffness can result in unrealistic behaviour. For flow behaviour in a drum the behaviour is very insensitive, though there is still a lower bound [208].

A model which implemented granule yield strength as part of the stiffness, by noting that the strain at peak stress was consistently at $\varepsilon_{peak} = 0.05$, and is strain rate dependent similar to σ_y [100]. Based on this, an approximate stiffness was derived from $E = \sigma_{y_{peak}}/\varepsilon_{peak}$.

However, this implementation has two major problems. First, E is related to the spring stiffness k through A, the radius of the contacting spheres [203], which allows k to vary depending on the depth of interaction. Second, it would require re-calculation at each time step since the stiffness is rate dependent, and the effect of acceleration or deceleration on the yielding behaviour is not specified. This leads into a related problem which is that once the spheres have slowed down relative to one another, the stiffness may reduce significantly. If re-calculation is not performed, the initial, often very high E value would be used.

When implemented, this combined to form a strange behaviour where the spheres would bounce off each other initially, but then slide through each other when the collision velocity was slowed, acting like Silly Putty. Increasing the stiffness to the point where this does not occur results in excessively high initial values of k, which would require a reduction in timestep, which was not desirable.

Because this strain rate dependency of the stiffness interacted poorly with the time stepped nature of the simulation, and the regime in which these were tested were for constant strain rate rather than impacted, in the end this solution was removed as being unsuitable and not further pursued. The spring-dashpot model already does account for the rate dependent behaviours and overall provides efficient and consistent simulations. Granular behaviour is highly dependent on the quantity of spheres, so using more spheres was a priority.

By setting a range of materials which were identical except for the stiffness, as the spheres agglomerated and grew in size, the mass could be tested and if

above a certain value the material could be changed, which allowed a stepwise increase to larger stiffness values. Granular behaviour is highly dependent on the distribution, and flow relatively insensitive to the stiffness. This was a precaution if the larger granule sizes were more affected by lower stiffness values than the smallest, though the flow behaviour overall appeared to be as expected.

8.3.2   Cohesion

A pendular bonding model was also tested, based on previous workers implementations of agglomeration using capillary bonding. The work from subsection 6.2.1 was also applied here. It was superficially satisfying for small interactions. This was prior to large scale interaction capabilities being developed, and the more effective funicular solution also being discovered which shows how to model it entirely using linear bonds, so it was abandoned. Due to the reasons previously stated as this would not be suitable for full granule modelling.

Some sort of cohesion would have been useful however. The low stiffnesses had an unfortunate side effect of causing more bouncing than would be preferable. During the granular strength modification tested previously, the effect of the returning dampener was found to be beneficial for resolving this. This was not implemented in the final system though as it is defined during compile time and in the process of resolving a bug where force was not applied to one of spheres, the option was set to non-returning dampener without realising, which was only realised during this write-up.

The results should be mostly unaffected by this, since technically the non-returning dampener is the more realistic option, however, it does cause a false cohesion between the spheres. In the case of the wet agglomerates though, this cohesion is probably.

8.3.3 Consolidation

Consolidation was fairly easy to implement, using the consolidation equation found in section section 6.5, using a value of $n = 1$. The yield strength is calculated using the old porosity and this is modified, and then the new value of the void volume was calculated from this, eventually leading to a recalculation of the total volume and saturation.

The consolidation is only calculated from interactions between granule spheres, rather than wall spheres. This does not appear to have had much effect, as the spheres in contact with the wall will be in the passive state. This was because the consolidation was calculated as an impact based system, including the walls would be much more complicated for little benefit due to their significantly different calculations required.

Further, only impacts are calculated, not continuous pressure effects. Continuous pressure does not lead to as high a consolidation, which makes this reasonable, though the real reason this is not applied is that the program would have to record the history of the pressure applied which would be memory intensive and complicated. The velocity for St_{def} was the initial impact velocity, and checks were made such that the simulation would only check each collision only once, even over multiple time steps.

One weakness of Equation 6.35 that was determined through the use of the DEM model is that it does not account for variability of the relative masses of the colliding granules. For monodisperse particles this is fine, however the masses should have some effect, since currently it allows a single fast moving particle colliding with a large granule to consolidate the same amount as two granules of equal size. One possible way to account for this would be to calculate the quantity of strain experienced by each granule as a function of their relative sizes, and then calculate the extent of the consolidation based on that. In a monodisperse case this is being described by St_{def} , which would be why it seems to work.

332

8.3.4 Altering the Liquid content

The only source of changes in the liquid content are the material inputs, either as a initial moisture or as droplets sprayed in. Water could in theory evaporate, convert to hydrates, or increase through dehydration reactions, however these are ignored for the sake of simplicity. The short time span limits the time in which all of these could occur.

8.3.5 Recalculation of Radii

Technically, the radii would change after every consolidation event. However, as this requires determining a cube root which is computationally expensive, and more importantly could affect subsequent collisions in the program flow, this is not performed. Instead, the radii are re-calculated either at agglomeration events, or after every output time step. The changes in radii from consolidation are small enough that this should be frequent enough.

8.4 Agglomeration Simulation

The agglomeration simulations tested the spheres based on various different agglomeration models. For those models using the saturation criterion such as adhesion-cohesion criterion, the saturation required was based on the theoretical merged sphere's properties. The yield strength previously mentioned is used here.

8.4.1 Sphere Merge Routine

The collision routines were able to only test each collision once, which is used in the record keeping for the collisions, as well as for the consolidation. This was thought to be sufficient for the agglomeration. This turned out not to be the case, and because of the parallel nature of the solution, along with edge cases, an interesting resolution was implemented.

Testing whether an agglomeration event occurred was as simple as testing against the agglomeration criterion in use, which varied over time. If it was successful though, the two could not simply be merged, as there are other collisions occurring, potentially in other parallel threads. As such, the identities of the two spheres were noted in a list, for agglomeration later. This list could be updated in a similar fashion as the collision routines, using directives to ensure that the position in the list was always updated.

This worked most of the time. The properties of the merged sphere would either be summed (for the volumes) or an average found, weighted appropriately (weighted by mass for velocity and acceleration, by volume for position, by inertia for rotation rate, etc.).

However, this could very occasionally lead to aberrant effects, such as the duplication of mass, or the disappearances of spheres without being tracked. The reason was because occasionally one sphere would appear in the collision multiple times, which, if it had been noted, then the properties would be duplicated or deleted without coalescence and contribution of mass to another sphere, depending on the specific state of the sphere at the time of being checked.

This being the case, the entire merge list had to be checked, with every merging pair being copied to a new array, checked if either appeared again in the collision list, and if it did, then the additional sphere added to the new array and then every sphere in the merge list checked again, and so on.

This was extremely inefficient, especially since a triple merge is a reasonably rare event as it requires the right combination of saturation and collision velocities. Significant slowdown was observed when this system was in place, though it may also have been because a less efficient directive was being used to prevent overwriting than the one used in the final form. Nonetheless, a much more efficient method was implemented which overcame these problems regardless.

8.4.2   Merge Tree

This is called a merge tree as it essentially creates a branching tree data structure which linked all potential merging spheres.

Once the agglomeration test function had been applied, the merging spheres were recorded, as before, in a simple two column array, simply the "merge_list", in the form shown in Table 8.1

Sphere 1	Sphere 2
1	2
3	4
2	7
7	8

Table 8.1: Structure of merge_list. The numbers indicate the spheres' indices, which is used to locate their properties.

At the end of the time step, in the serial region, when all the forces have been applied, the program runs through the merge_list array, and then begins to sort them into the "merge_frame" array, with structure shown in Table 8.2.

As the values are copied over, some other variables are checked and modified. Each sphere has an associated "Last merge_list appearance" variable, which tracks the most recent row that the variable appeared in, and is set to 0 if the sphere has not appeared previously. For both spheres, this value is copied to their respective "Previous Row E" columns, resulting in Table 8.3 necessarily for the first row of Table 8.2.

Then, the current row is copied into the "Last merge_list appearance" variable for each of the spheres in question. Finally, both spheres have their "List_Appearances" accumulators increased by one, for validation at the end.

This sequence is repeated for each row, which for Table 8.1 results in an array like so:

Sphere 1	Sphere 2	Previous Row S 1	Previous Row S 2	Merged
1	2	-	-	0
-	-	-	-	0
-	-	-	-	0
-	-	-	-	0

Table 8.2: Structure of merge_frame. The numbers in the first two rows indicate sphere indices, the third and fourth row numbers indicate the previous appearence of the spheres with indices specified in column 1 and 2, and the fifth row is a checking value for subsequent work to not perform multiple merges. A - indicates that this value has not been filled yet by the subroutine.

Sphere 1	Sphere 2	Previous Row S 1	Previous Row S 2	Merged
1	2	0	0	0
-	-	-	-	0
-	-	-	-	0
-	-	-	-	0

Table 8.3: Structure of merge_frame after checking Sphere 1 and Sphere 2 previous rows. The numbers in the first two rows indicate sphere indices, the third and fourth row numbers indicate the previous appearence of the spheres with indices specified in column 1 and 2, and the fifth row is a checking value for subsequent work to not perform multiple merges. A - indicates that this value has not been filled yet by the subroutine.

Because this is performed in serial, no race conditions will cause one later row to miss another. Then, during the actual merging routine, the merge_frame array is read from the bottom up.

First, the "List_Appearances" are updated, decrementing each by one. Then, the previous row E1 and Previous row E2 columns are checked. If both have a 0, then the merge proceeds as a basic two sphere merger, and noting in the fifth column "merged" a 1. If not, then multi-particle merging is occurring, and

Sphere 1	Sphere 2	Previous Row S 1	Previous Row S 2	Merged
1	2	0	0	0
3	4	0	0	0
2	7	1	0	0
7	8	3	0	0

Table 8.4: Structure of merge_frame after checking testing all rows.The numbers in the first two rows indicate sphere indices, the third and fourth row numbers indicate the previous appearence of the spheres with indices specified in column 1 and 2, and the fifth row is a checking value for subsequent work to not perform multiple merges. A - indicates that this value has not been filled yet by the subroutine.

the two sphere indices are stored. The previous row appearances are then used to recursively check for the rows with the previous appearance of the sphere, noting only the new sphere index, and only if the "merged" column is a 0, as otherwise it indicates that this row has been reached by another path. Each time decrementing the "List_Appearances" of the two appearing spheres, and noting the column "merged" as 1.

When a row is reached when both "previous row E" columns are 0, this is the final appearance in this branch. The recursive search is set as a sequence of non exclusive if statements so that any branching is fully searched for. At the end of this procedure, the "List_Appearances" of each sphere should equal 0, which is easily checked.

If this is not the case, for example if , the first sphere row consisted of 3 and 2, which could cause row 2 to be missed, then first, the "Last merge_list appearence" can be checked for each sphere which has a "List_Appearence" greater than 1. This will always find the lowest appearance of the sphere present, which should always allow the final list appearances not noted to be subsequently filled.

A triple loop, for example if , the first sphere row consisted of 1 and 8 is

accounted for through the merged column being checked for any new sphere notations.

If, somehow, this does not satisfy the requirements that all spheres in the merger should have a "List_Appearances" of 0, then a brute force search can still be applied for each of the spheres noted as merging, as before, though this has not occurred during testing.

This method efficiently checks the connectivity of the spheres, only testing those rows which are relevant. This system limits the memory involved to simply 5 times the quantity of successful mergers, which may be very high, though this would be hard to verify, when hundreds of thousands of spheres are involved, limiting the overhead is necessary.

Once all the spheres have been noted, the merging can proceed as normal, with the summation of volumes and weighted averaging of properties as relevant, recalculating the porosity etc from the volumes. Each sphere that is merged has a variable "Is_merged" set to true, for later cleanup.

Once every merger has occurred, with all new spheres placed, the octree placer is called. This places the newly created spheres into the octree all at once, and the routine which removes out of bounds spheres has been modified to also remove spheres which have "Is_merged" set to true.

This leaves a net result of a single sphere with the property of the merged spheres, which is for all intents and purposes merging them. Moving one of the spheres as a master sphere and contributing to it the volumes and momentum of the other spheres was no more reliable, and harder to debug.

After the merging routines are completed, the associated arrays and lists are cleared, to ensure that the next time step runs smoothly and cleanly.

8.4.3 Choice of V_{ch}

The Adhesion-Cohesion Criterion lists two values for velocity, the collision velocity normal and the characteristic velocity. The collision velocity normal can

338

be easily calculated, but the characteristic velocity would necessarily depend on the system. This characteristic value could be argued as the average value of the collision velocities in the region, or the tangential collisions experienced by a dumbbell of two spheres in that region. In the end, a simple 5 case system was devised.

V_{ch} could be defined as any of the following:

1. the normal velocity of the interaction

2. the full magnitude of the relative velocity of the interaction

3. flat, predefined value representing collision forces

4. the maximum of either the normal collision velocity or the predefined value

5. the maximum of either the full magnitude of the relative velocity of the collision or the predefined value

Cases 4 and 5 account for the fact that the predefined value is representative of the general collision behaviour, while also noting that the maximum value of the two indicates that the initial collision itself is a high shear force which could tear others or itself apart, and that if it is particularly high then the granule will probably be in a higher collision strength region. Case 5 also accounts for the difference in collision velocity in greater shear regions. As such, Case 5 is used for all the models that will be shown, though others were experimented with in some trial simulations.

8.4.4 Water

The material system was also altered to make application of a spray easier. Materials with a value 1 are hard coded to represent water (though technically any liquid can be represented as the liquid properties are set in the input files separately). This allows special effects to be applied, such as being able to ignore one

another during motion thus ignoring water-water collisions, and that they always successfully merge with spheres. They are also deleted whenever in contact with the drum walls. This lacks elegance, as the drum wall moisture could be considered important, and the sphere sizes are often far larger than reality when added as spheres.

Implementation of ray-casting would model the behaviour of high velocity and arbitrary size liquid droplets and has potential for future work, though this would require integration with the octree to account for the collision detection which would involve additional separate computational cost as well. In the end, the simple water model is considered sufficient for the purposes of the project.

8.4.5 Other Mechanisms for Agglomeration

Other agglomeration mechanisms were considered, before the Cohesion-adhesion criterion was developed. At the time, the focus was either on a sphere record system, which would allow the spheres to break, or a dumbbell system, which would allow spheres to bond, and then break if oblique contacts separated them.

The only remnants of these earlier explorations are the "layer" property used to note the amount of mergers, and the considerations regarding the oblique contacts in the previous criterion considerations.

The focus was on systems where coalescence could be tested on a single contact, which is why the Stokes criterion was so appealing, since it could be tested immediately at the moment of collision and then forgotten.

A dumbbell model would have been interesting. This would require spheres to generate bonds between one another, and lock the spheres into a dumbbell like shape. Consolidation could push the two spheres together, increasing the volume of each to account for the lens overlap between the two, until one enclosed the other and it could be deleted. This would also allow for the particles to be separated due to oblique collisions that nonetheless do not result in coalescence.

This would require significant alteration to the code, and in particular, loca-

tion and the rotation behaviour of the spheres would be intrinsically linked and very complex.

8.5 Computer limitations

A big question though was DEM spherical sphere size. The size of the spheres in the granulator would matter significantly, because of the reasons mentioned before concerning time steps and management of real energy values.

The smaller the sphere size, the greater the impact on the run-time of the simulation. This might impact the ability of the system to truly demonstrate growth behaviours. If a distribution of sphere sizes does not include the very smallest sizes, which appropriately merge when layering considerations take place then it might artificially favour similar size merging events when layering would be occurring instead.

Resolving this would require modelling using the smallest spheres as possible, but to maintain a manageable time step the spring constant would be unreasonably small, and the collision detection would also increase the time taken to calculate each time step.

The simulation, because of the need to use many small spheres will always be quite slow. It can take up to a day per second once it has reached steady state, which is impractical.

A system whereby "feed" spheres can attrit and lose volume associated with the solids could perform this role, though the issue of the mass/spring remains as they distribute their solid volumes. Pragmatically, to get the model running, the decision to simply use the smallest spheres, with very low stiffnesses was used.

8.5.1 Memory issues

The virtual memory issues arose in these simulations again, despite the appropriate compilation settings applied.

The extremely large number of spheres can cause virtual memory crashes to develop, despite forcing the computer to make all the virtual memory to be available from startup. The reason for this is unclear, as the program rarely uses the whole amount of memory available to the computer.

The reason is suspected to be related to the distribution of the spheres in the octree, and the uneven distribution of spheres, and especially when there was significant variation in sphere size, which explains why some of the simulations crashed and others did not.

8.6   Summary of changes due to Pellet nature

In the end, the simple spring-dashpot-slider model was used in this solution in order to model the behaviour. Assorted additional contact mechanics and cohesive models were tested however, they did not behave either realistically or were unrealistic in their assumptions.

In the end, the response model component was left as developed by Holmes because it successfully modelled many patterns very well, from the granules falling down a chute in a measured pattern to slump testing and drum granule testing.

More complicated methods would need to be justified in more realistic behaviours, but where tested they did not prove their value. The DEM models were ultimately meant to provide an environment to test agglomeration conditions, so the response model was deemed suitable.

The only notable development was to make use of the materials system specified to include varied stiffnesses so that more small spheres could be included without paying a timestep penalty.

Chapter 9

Agglomeration Model Results

This chapter covers the actual results of integrating the granule and agglomeration mechanics into the DEM to allow the kinetics to derive behaviours naturally. The naming conventions for the simulations primarily focussed on the drum and the model, and the Bond probability criterion did not have a particular name, so was referred to by the first authors name during the work.

Again, "spheres" will be used to refer to the spherical discrete spheres in the simulation, while granules and pellets refer to the real world implications, and particles the real world solid materials.

9.1   System and material choices

The material choices in the system were based on the simplified assumption that the solids were magnetite with a surface coating of ferrous hydroxide, to improve the interfacial tension. Other model features were varied on a case by case basis, with a general aim to find what properties altered the distributions to match the known distributions.

Some properties were constant throughout the testing, as they could be kept constant without significantly altering the procedure.

Π is used as a shorthand for plasticity, which describes both ζ and η through $\zeta = \Pi/3 + 2/3$ and $\eta = (2/3)(1 - \Pi)$ and is bound to either 0 or 1

9.1.1 Settings for the Bond Probability models

Variable	γ	θ	μ	d_p	$\mathcal{R}$
Value	0.072N/m	30°	1 mPas	50µm	1

Table 9.1: Universal Parameters

As multiple different models were tested, not all models use the same variables. If a model does not use a variable, it is indicated with a - . As these were run after the full scale models were tested, the drum rotation rate of the small scale models have been reduced, the results of which can be observed as now demonstrating similarity of regime as the large scale models.

9.1.2 Material parameters for the Bond probability Simulations

For the Bond probability criterion tests using Δ_{limCoh} , the maximum saturation was set to 0.9 for all as this was found to be reasonable in [41], this is revised to 1.0 since this is more clear.

Case	Δ_{lim}	K_γ	Π	λ	r_{g_0}, mm	Drum Model
BP Full Scale A	12	4.5	0	1	1.5-3	Full Scale
BP Full Scale B	12	4.5	0	1	1.5-3	Full Scale
BP Full Scale C	12	4.5	0	1	1.5-3	Full Scale
BP Lab Scale D	10	0	0	1	1.5-3	Lab Scale
BP Lab Scale E	5	4.5	0	1	1.5-3	Lab Scale
BP Lab Scale G	10	0	0	1	1.5-3	Full Scale
BP Lab Scale F	5	4.5	0	2	1.5-3	Lab Scale
BP Lab Scale H	5	4.5	1	2	1.5-3	Lab Scale

Table 9.2: Parameters for Bond Probability Tests.

Case Name	S	$\pm S$	$K_{S_{max}}$	$d_p, \mu m$	K_γ	Π	λ	r_{g_0}	Drum
BP &Δ_{limCoh} A	0.805	0.105	0.9	100	4.5	1	2	1.5-3	Lab Scale
BP &Δ_{limCoh} B	0.805	0.105	0.9	100	4.5	1	2	1-1.5	Lab Scale
BP &Δ_{limCoh} C	0.805	0.105	0.9	100	4.5	1	2	2-3	Lab Scale
BP &Δ_{limCoh} D	0.805	0.105	0.9	100	4.5	1	2	2-3	Lab Scale
BP &Δ_{limCoh} E	0.8	0.5	0.9	100	4.5	0	1	1-2	Lab Scale
BP &Δ_{limCoh} F	0.8	0.5	0.9	100	4.5	0	1	1-2	Lab Scale
BP &Δ_{limCoh} G	0.8	0.5	0.9	100	4.5	1	1	1-2	Lab Scale
BP &Δ_{limCoh} H	0.8	0.5	0.9	100	4.5	0	1	1-2	Lab Scale
BP &Δ_{limCoh} I	0.8	0.5	0.9	100	4.5	0	1	2.5-4	Lab Scale
BP &Δ_{limCoh} J	0.8	0.5	0.9	100	4.5	1	1	1-2	Lab Scale
BP &Δ_{limCoh} K	0.8	0.5	0.9	100	4.5	0	1	1-4	Lab Scale
BP &Δ_{limCoh} L	0.8	0.9	0.9	100	4.5	0	1	1-4	Lab Scale
BP &Δ_{limCoh} M	0.8	0.9	0.9	100	4.5	0	1	1-4	Lab Scale
BP &Δ_{limCoh} N	0.8	0.8	0.9	100	1	0	1	1-4	Lab Scale
BP &Δ_{limCoh} O	0.8	0.8	0.9	100	4.5	0	1	1-4	Lab Scale

Table 9.3: Parameters for Bond Probability criterion simulations using Δ_{limCoh} .

Case Name	S	$\pm S$	$K_{S_{max}}$	$d_p, \mu m$	K_γ	Π	λ	r_{g_0}	Drum
BP &Δ_{limCoh} , Spray	0.1	0.1	0.9	100	4.5	0	1	2-4	Lab Scale

Table 9.4: Parameters for Bond Probability criterion simulation using Δ_{limCoh} and liquid applied as a spray.

9.1.3 Settings for the Adhesion-Cohesion models

For the Adhesion-Cohesion models, there are many material variables that could be listed for them such as the contact angle, the viscosity, the aspect ratio of the particles. Not all of these will be listed for three reasons. One, most of the results found below do not particularly depend on them, as the behaviour is highly dependent on the geometry and the kinetics of the system and the input spheres. Two, many are only relevant by virtue of how they relate to approximations which are used for practicality (such as σ_y and $\alpha_{wet}(\varepsilon_r)$). And three, there are a few critical control variables, listed in Table 9.5 which can be adjusted to account for much of the properties otherwise considered by these values, and some similarly important extrinsic variables that interact with scaling in complex ways Table 9.6. These have potential for nondimensionalisation and scaling, if the issues of the geometry can be managed.

Control Variable	effect
K_α	Adhesion limit scaling
$k_{\epsilon B}$	Consolidation strength scaling
$k_{\epsilon A}$	Consolidation rate scaling
K_g	Saturation limit scaling
K_{Smax}	Saturation limit scaling

Table 9.5: Controlling intrinsic Variables.

The only variables changed between tests are those listed in Table 9.5 and Table 9.6, with all the other variables kept the same as either in section 7.7 or Table 9.1, with those used in section 7.7 taking priority such as for K_{Smax} .

The other variables do matter in various ways of course, however their significance is a matter for determining for individual setups (such as K_{Smax} or K_g for bentonite alteration of binder), and are assumed to be 1 for both here, as they are relatively predictable in their effects. Finally, the value of V_{cN} is directly a

consequence of the kinetics, which naturally varies.

Control Variable	effect
d_p	Saturation limit and σ_y
V_{ch}	Adhesion limit, agitation component scaling.
r_{g_0}	initial input sphere radius
Granulator Geometry	Kinetics

Table 9.6: Controlling extrinsic variables.

What is of primary concern here is the interaction between the kinetics, the saturation and the consolidation, and all global behaviours this can be described using Table 9.5 and Table 9.6. These are listed in Table 9.4. Note that V_{chmin} is the minimum value that V_{ch} can take, based on the system previously specified, and that the maximum is the total collision velocity.

Case Name	K_α	$k_{\epsilon A}$	$k_{\epsilon B}$	r_{g_0} , mm	d_p , μm	V_{chmin}	Drum
Adh-Coh Model A	1000	0.002	1000	2.8-4	100	0.1	Full Scale
Adh-Coh Model B	100	0.002	1000	2.8-4	100	1	Full Scale
Adh-Coh Model C	100	0.002	1000	1.9-2.95	400	1	Full Scale
Adh-Coh Model D	100	0.002	1000	1.9-2.95	400	1	Full Scale
Consolidation A	1	0.001	1000	3-4	100	0.1	Full Scale
Consolidation B	1	0.02	1000	3-4	100	0.1	Full Scale
Consolidation C	1	0.0002	1000	3-4	100	0.1	Full Scale
Consolidation D	1	0.0002	1000	6-8	100	0.1	Full Scale
Consolidation E	1	0.0002	1000	3-8	100	0.1	Full Scale

Table 9.7: Parameters for Adhesion-Cohesion Model Tests.

9.2 Previous results

The produced pellet distributions were shown before as a function of the moisture contents. To compare against the results here, the cumulative distributions of the data are also shown in Figure 9.1.
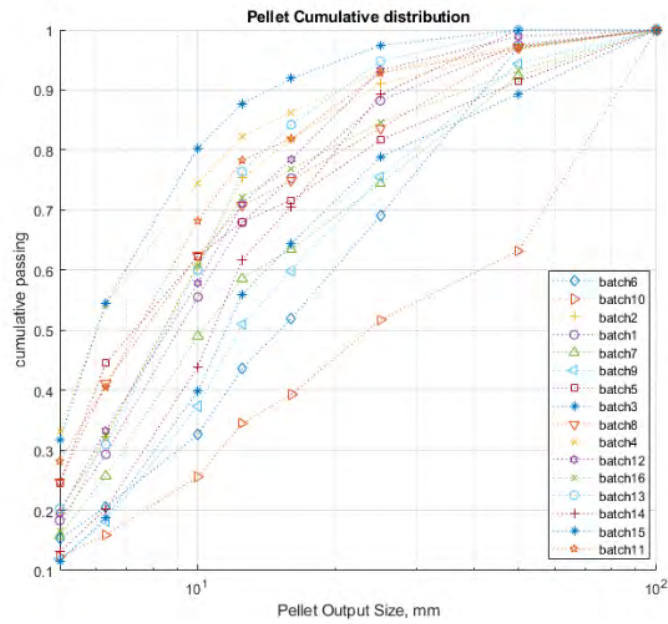
Figure 9.1: The cumulative Pellet output diameter of the real batches produced, data received from Darlow Lloyd and Sons.

The mean of the probability distribution rather than the cumulative distribution is plotted in Figure 9.2, as this allows easier identification of additional modes and general features to identify. As there is significant variation, this is not definitive though serves as a starting point.

The general trends from Figure 9.1 and Figure 9.2 provide three key details that a realistic distribution should have:

1. A significant amount of fines, (pellets <5mm diameter) between 10-30%

2. A rapid rise up to about 16-20mm diameter pellets
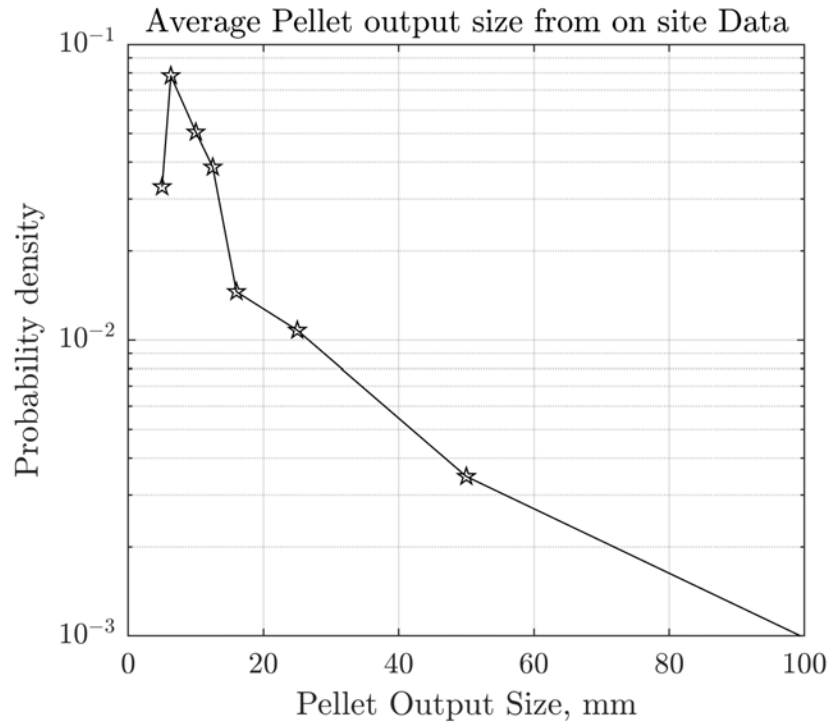
Figure 9.2: Average pellet PDF of the average pellet data

3. A long tail for oversize pellets (up to and beyond 50mm diameter), and that
   the quantity of fines does not have a very strong relation to the quantity of
   oversize pellets

These details can be seen in the non-cumulative function, shown in Figure 9.2.
Additionally, an important feature which was very useful in analysing results is
the presence of the change in gradient at 16mm diameter. This suggests that
there were two modes occurring in the distribution, and a bimodal distribution
tends to suggest that there are two underlying distributions being combined into
one [251].

9.3 Distribution Results

The goal of these experiments was primarily to determine a distribution which most resembled Figure 9.2, which could then subsequently be altered if necessary to match the individual distributions in the Figure 9.1. This is the reason why the variables were changed as they were, which may seem otherwise arbitrary.

Some cases that were tested and the results of which are displayed later demonstrate behaviours of the pelletisation process unrelated to distribution results, for example simulations in section 9.5 demonstrate the location of consolidation rather than growth behaviours directly.

9.3.1 Bond Probability Criterion, Arbitrary Δ_{limCoh}

The first really successful agglomeration criterion was the Bond Probability criterion, which, although the limiting size was set to an arbitrary value based on a target size of 12mm.

Figure 9.3 shows the successful runs of this model. Other, less successful runs are shown later which demonstrate some weaknesses of the model in this application.

The limiting diameter was set to 12mm in both cases, yet almost all the spheres were larger than this. The reason is that because of the way that Equation 9.1 works, coalescence probability is simply reduced as the diameters approach Δ_{limCoh} , not eliminated.

$$P_n = \left(1 - \left(\left(\left(\frac{\widehat{D}}{\overline{\overline{D}}} \right)^{2K_\gamma - 3\eta} \left(\frac{\overline{D}}{\Delta_{lim}} \right)^{4 - 3\frac{3\eta}{2}} \right)^{\frac{2}{3\zeta}} \right) \right)^n \tag{9.1}$$

It only reaches 0 probability for equal diameters after both have reached the limiting diameter, so two spheres with 11mm have a small probability of merging. When the layering component is considered on top of this, the distribution will
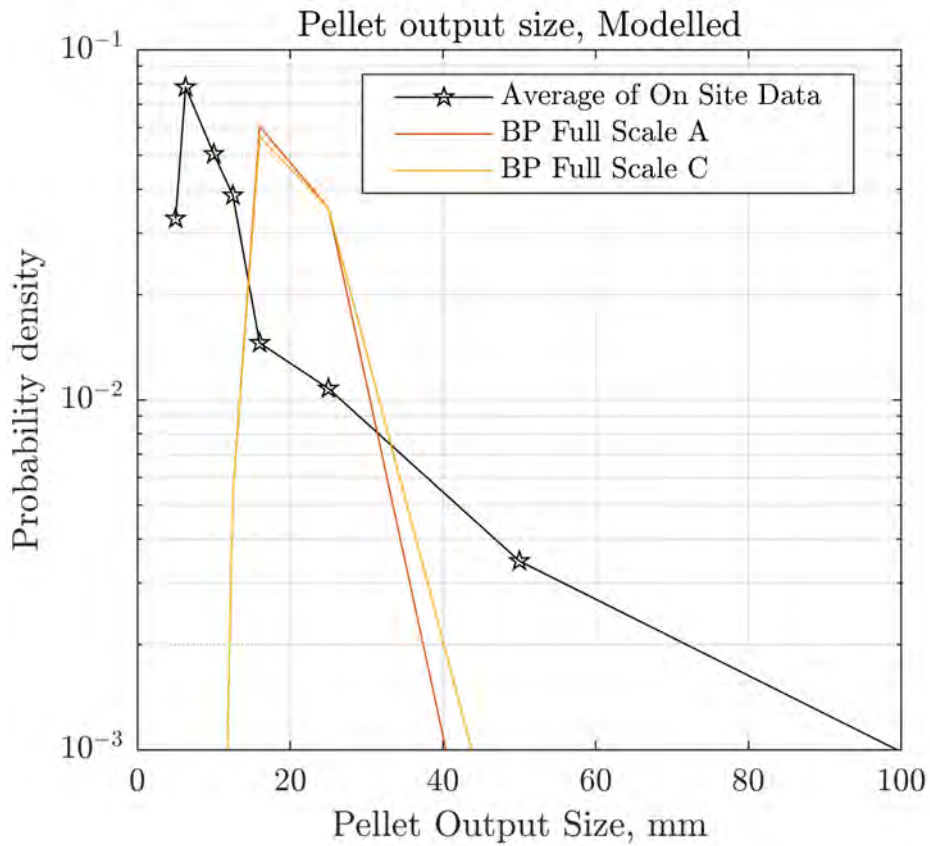
Figure 9.3: Comparison between the average size distribution of pellets as from DLS, and the size distribution of the spheres formed by the Bond Probability criterion models

always have spheres larger than the limiting diameter, though it is still places a restriction on the average size of the distribution.

However, since there is no intrinsic requirements for coalescence other than merely coming into contact, this model is unable to produce a very wide distribution. If, for the sake of argument, an even distribution of spheres was placed in the drum and it was run with coalescence deactivated, allowing segregation to occur as normal, then this would lead to an outer boundary of larger spheres and an inner core of smaller spheres. When coalescence is turned back on, all the spheres in the centre will be able to merge with one another to reach the limiting size, returning the distribution to a single tight mode.

9.3.2 Bond Probability criterion, Saturation Criterion as Δ_{limCoh}

The Saturation Criterion specified a value of Δ_{limCoh} , but not a growth mechanism. Meanwhile the Bond probability criterion had a difficult to measure and somewhat impractical limiting size calculation, and no accounting for the saturation. As such, the Δ_{limCoh} from the Saturation criterion was put directly into the value of Δ_{lim} for the bond probability criterion.

This was implemented prior to the development of the Adhesion-Cohesion model. At this point though, awareness of the requirement for the collisions to be above some minimal value was found to be neccesary. An assumption was made that, since most collisions are of low strength and that these occur throughout the pelletiser, if understrength collisions resulted in growth then it would occur without the need for any granulation device at all. This neccesarily implies that the strength of the collisions must be over some critical value.

As such, an additional requirement was set for merging that the collision velocity normal had to be greater than the average collision velocity. This value is easy enough to track through the simulation, and it allows for some consideration of dynamics to be applied in the coalescence behaviour.

Though the physical justification for this solution is weak, it was found to be quite effective and helped lead directly to the Adhesion-Cohesion Criterion.

A definite widening of the distribution can be observed in Figure 9.4. This is to be expected, since by including the saturation, the limiting size of the spheres is now set on an individual basis and can vary between spheres.

Two distinct groups can be identified in the distributions, and some additional distributions between the two, based on the various initial inputs selected. The on-site data was being targeted through these modifications, hence the steady increase in the tail section of the distribution.

However, as is evident in the plot, the distributions are limited to either form-
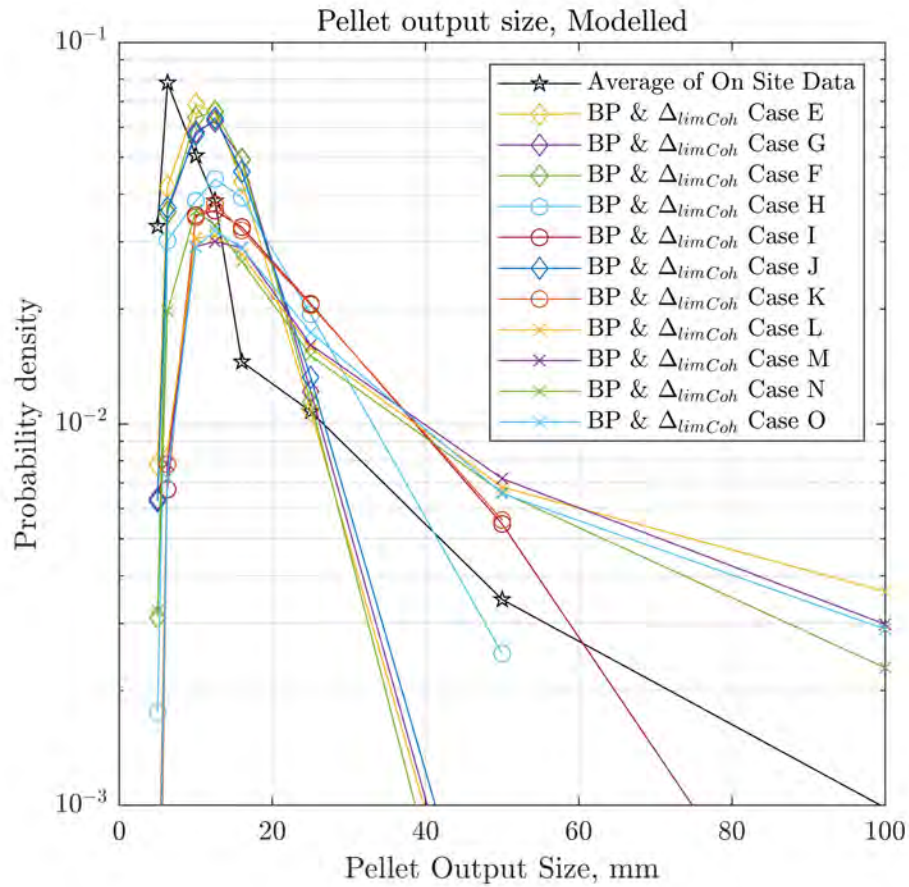
Figure 9.4: Comparison between the average size distribution of pellets as from DLS, and the size distribution of the spheres formed by the Modified Bond Probability criterion using Δ_{limCoh} models, Liquid added as a random distribution among the spheres

ing more fines, or forming the long tail, reducing the quantity of fines significantly.

This trade-off is likely due, in part, to the evenly spread initial saturation, even if it is randomly distribution by amount. Though this is easy to implement, it is less realistic than the more homogeneous initial distribution and a stronger heterogeneity introduced by the external spray.

9.3.3 Δ_{limCoh} Modified Bond Probability criterion, Spray effects
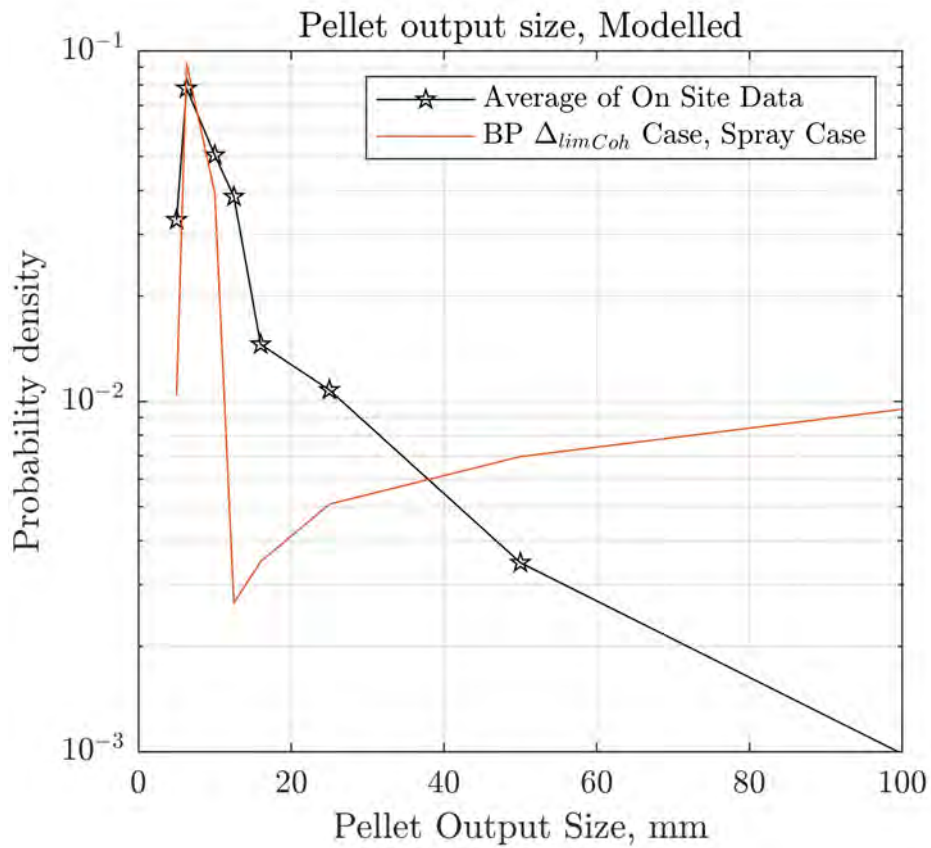
Figure 9.5: Comparison between the average size distribution of pellets as from DLS, and the size distribution of the spheres formed by the Modified Bond Probability criterion using Δ_{limCoh} models, Liquid added as a spray.

The distribution of the spheres in Figure 9.5 shows how the spray clearly affects the distribution of the output spheres. The most important feature is that there is still a large quantity of fines, while also having large spheres.

The excessive quantity of the largest spheres suggests that these may be excessively favoured, but this may also be a consequence of the geometry of the test model being the lab scale with a single circulating loop, and how it was sprayed,

leading to the largest spheres continuously getting more spray.

This was the last model tested before the Adhesion-Cohesion Criterion was developed.

9.3.4 Adhesion-Cohesion Criterion

Figure 9.6 gives the results of the distribution formed by the adhesion-cohesion model, for the full scale model. The varition comes from the kinetic behaviour as well as the properties listed previously.
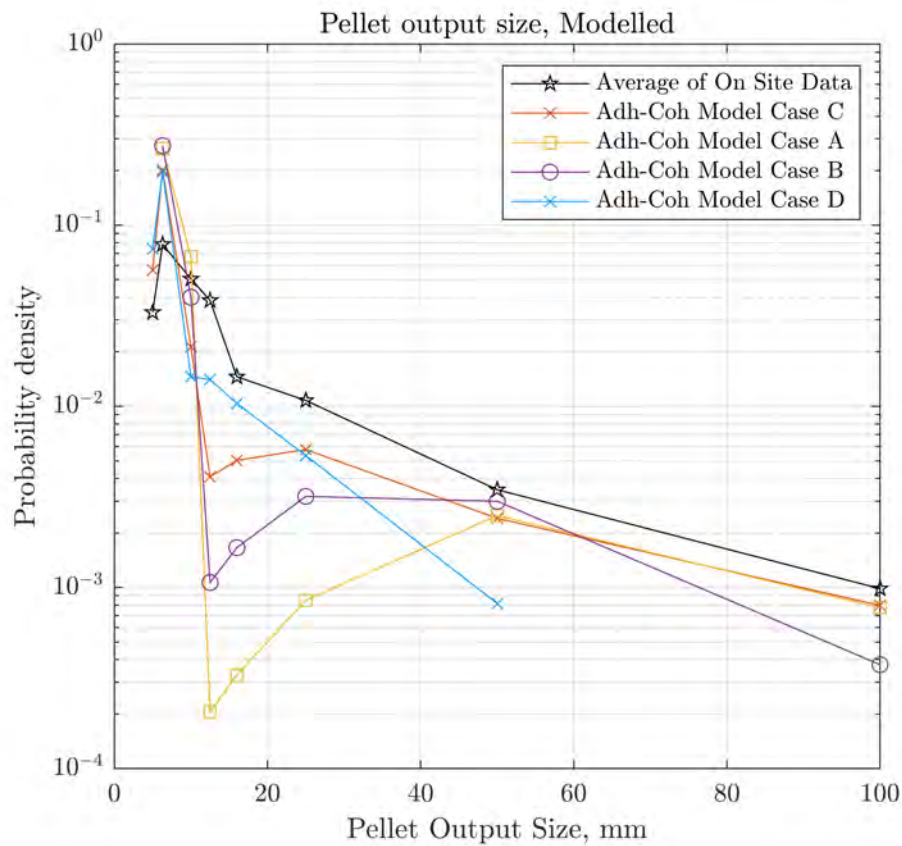
Figure 9.6: Comparison between the average size distribution of pellets as from DLS, and the size distribution of the spheres formed by the Adhesion-Cohesion models, Liquid added as a spray.

Due to memory issues encountered due to the large quantity of spheres required to account for fines and variability of sphere sizes reducing the capability of the the octree in refining the quantity of collisions required to test, the models could not be run to the end of the drum. What is demonstrated throughout the different cases is the clear boundary caused by the saturation being added as a spray, and the adhesion criterion promotes growth between the larger, wetter spheres and smaller dry spheres, explaining how some consistency of diameter can develop at all.

9.4   Model Images

The distributions above are useful for comparison against the real data, however for the case of agglomeration, the images of the simulation are very useful in highlighting features such as segregation and the overall flow behaviours as well as features such as where the consolidation occurs. Some models are shown for demonstrating behaviours unrelated to the final diameter, instead the location of growth or consolidation, or simply bugs encountered along the way.

The "Layer" value describes the quantity of component spheres which combined to form the final sphere. This is primarily useful in identifying the onset of growth, however it is also useful in determining if lots of small spheres or a few larger spheres were more common in the largest sizes, since the initial input size may vary a small amount.

9.4.1   Bond Probability Criterion, Arbitrary Δ_{lim}

9.4.1.1   BP Full Scale Cases, Table 9.2

These were the first to be tested when the agglomeration mechanism was implemented, since the full scale drum was already modelled. However, issues arose that demonstrated tht some smaller scale modelling would be required.

Figure 9.7: An image showing the DEM Model of the BP Full Scale C Case. This is an agglomeration simulation showing the behaviour in a full industry scale drum with spheres coloured according to Radii., 80% of the way through the simulation

Figure 9.8: An image showing the DEM Model of the BP Full Scale C Case. This is an agglomeration simulation showing the behaviour in a full industry scale drum with spheres coloured according to Layer., 80% of the way through the simulation

Figure 9.7 and Figure 9.8 show the behaviour of the agglomeration later in the process, showing a generally consistent distribution, with an even spread of the larger spheres, with little observable segregation, except perhaps at the top of the troughs.

There seems to be slightly greater degree of merging at the beginning of these drums, as indicated by Figure 9.8 trending towards more blue towards the output end. Whether this is a result of axial segregation as the smaller spheres move along the drum quicker, or because the small feed spheres have the chance to merge with the incoming spheres is uncertain. This slightly larger extent of growth is likely due to the feed being introduced at this end, which can agglomerate through the layering component of the growth equation.

Figure 9.9: An image showing the DEM Model of the BP Full Scale C Case. This is an agglomeration simulation showing the behavour in a full industry scale drum with spheres coloured according to Radii., shortly before the simulation was manually aborted.

The end results of this can be seen in Figure 9.9, which shows the weakness in using just the bond probability criterion. An excessively oversized sphere can be observed as having formed at the input site, and this is a consequence of the layering term discussed in section 7.3

359

There is a point when the $\left(\frac{\widehat{D}}{\overline{D}}\right)$ term dominates the agglomeration equation over the $\frac{\overline{D}}{\Delta_{lim}}$ term. Given that this large sphere exists at the input, and the feed spheres are the smallest available in the system, once the tipping point is reached then there is a large supply of the smallest spheres to contribute to the layering term.
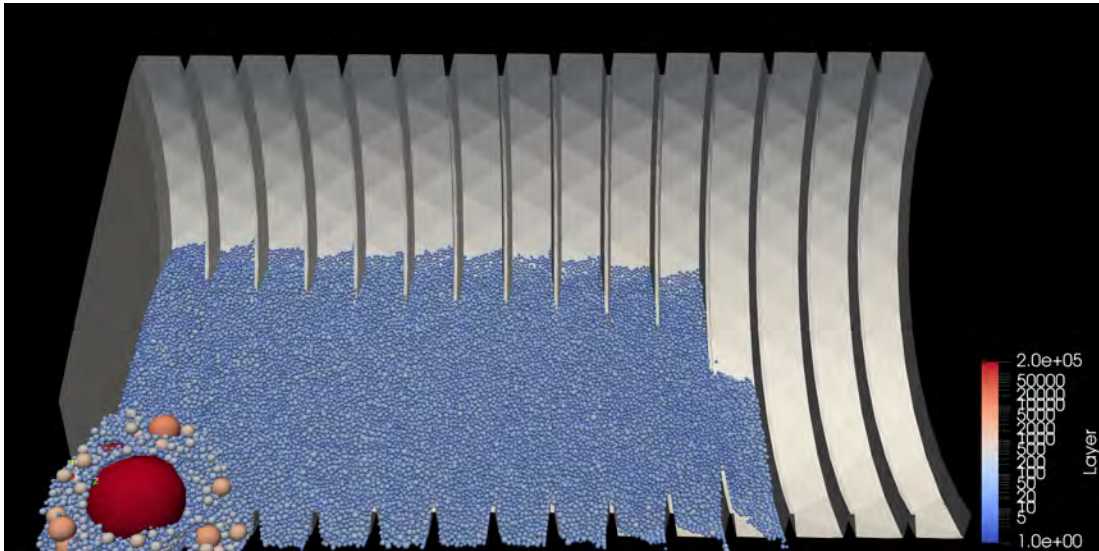
Figure 9.10: An image showing the DEM Model of the BP Full Scale C Case. This is an agglomeration simulation showing the behavour in a full industry scale drum with spheres coloured according to Radii., final frame of the simulation after it had been aborted.

Figure 9.10 shows the final frame of the BP Full Scale C simulation. The model was allowed to run for a longer time, to determine if the issue would resolve itself. As can be seen, it did not. The presence of smaller spheres on the surface, which should merge, is likely due to the fact that once contact is initiated, the merging is assumed not to take place.

This assumption is reasonable for the merging routine, since under normal circumstances the pellets in the real drums will be continuously colliding, and static compression is not expected to be a major factor.

9.4.1.2 BP Lab Scale D , Table 9.2

Figure 9.11: An image showing the DEM Model of the BP Lab Scale D Case. This is an agglomeration simulation showing the behavour in a small lab scale drum with spheres coloured according to Radii.. This simulation tested what effect $K_\gamma = 0$ had on the spread of the distribution.

Though the full scale drums did run acceptably fast for the Bond Probability criterion cases, the Lab scale drums were still used as they required fewer spheres, and so could be run more quickly. The BP Lab Scale D tested what effect K_γ had on the spread of the distribution, and there appears to be some effect, based on the range indicated in Figure 9.11 being 10-14mm, compared to 5-15mm from Figure 9.7.

This could also be a result of a smaller bulk volume and thus easier mixing, so

this possibility is also tested in subsequent simulations. The previously mentioned segregation can also be observed here a bit more clearly. Smaller spheres in the centre of the bed and larger on the outside.

9.4.1.3 BP Lab Scale E , Table 9.2

Figure 9.12: An image showing the DEM Model of the BP Lab Scale E Case. This is an agglomeration simulation showing the behavour in a small lab scale drum with spheres coloured according to Radii.. This simulation tested the effect of varying the maximum size alone had on the final distribution

BP Lab Scale E was also set up to test the effect of varying the maximum size had on the final distribution. As Figure 9.12 shows, this primarily came in the form of reducing the general sphere size. However, there are a few significantly larger spheres, more than twice the radii of most. This is likely a consequence of the layering previously mentioned, and may be how the oversize spheres shown before begin to grow.

9.4.1.4 BP Lab Scale G , Table 9.2

(a) An image showing the DEM Model of the BP Lab Scale G Case. This is an agglomeration simulation showing the behavour in a full industry scale drum with spheres coloured according to Radii.

(b) An image showing the DEM Model of the BP Lab Scale G Case. This is an agglomeration simulation showing the behavour in a full industry scale drum with spheres coloured according to Layer.

Figure 9.13: Behaviour of the BP Lab Scale G simulation case. This simulation tested the effect of setting BP Lab Scale G to 0 in a full scale drum.

As mentioned, the effect of K_γ needed to be tested on the large scale. To perform this, the BP Lab Scale G simulation was run. The range seen here, of 9-18mm suggests that the reduction in sphere radii range was more than likely just a result of the smaller scale drum, which increased the likelihood of the smaller spheres coalescing with one another before they could contribute to lay-

ering growth.

Additionally, this test was also the first to implement a spray system. This is the reason that the starting trough in Figure 9.13b has a higher layer count than the following troughs, since the sprayed spheres coalesce easily, being small spheres interacting with large spheres.

This was valuable in highlighting a few things that would need resolving before a liquid spray could be fully implemented in future, and ultimately lead to the implementation of the hardcoded water material. For example, the sprayed "water" spheres would bounce, and being very small and numerous occupied a lot of the collision time for little benefit, which lead to pre-checks allowing two water spheres to not have their collisions calculated for, though they are still tracked which is needed to avoid octree bugs.
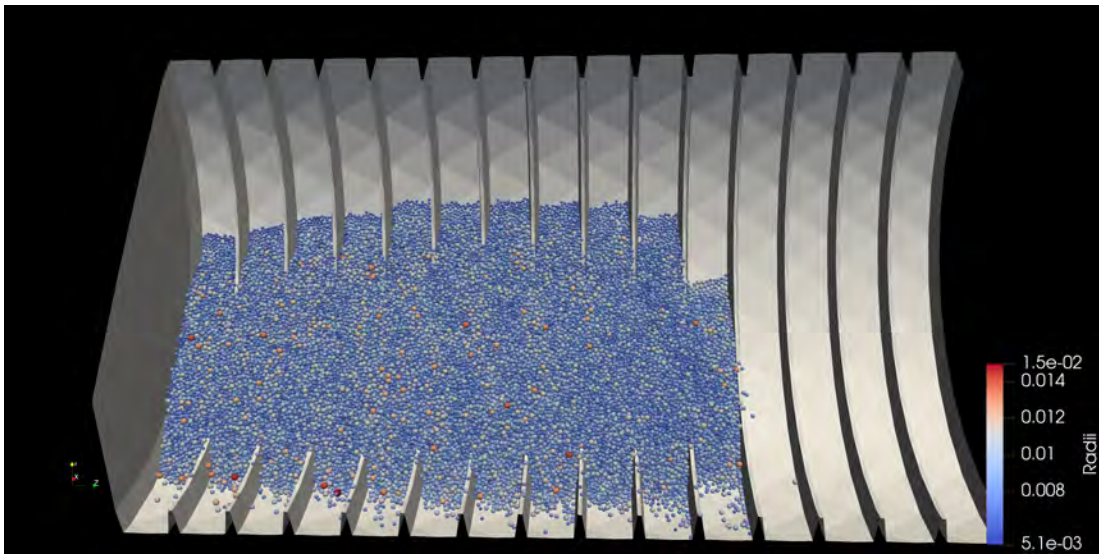
9.4.1.5 BP Lab Scale F , Table 9.2

Figure 9.14: An image showing the DEM Model of the BP Lab Scale F Case. This is an agglomeration simulation showing the behavour in a small lab scale drum with spheres coloured according to Radii.. This test considered considered the effects of increasing λ to 2.

Figure 9.14 was a test to consider the effects of modifying λ , and is otherwise identical to BP Lab Scale E . Generally, λ is assumed to be 1 since it expresses the range of compressive strengths that are considered in separation events, for which 1 considers all values. Modifying λ may be relevant if only the stronger compressive events are considered, however it does not affect the limiting size, which is a function of the maximum strength of the collisions. Rather, it affects the probability of any given collision resulting in merging, in a similar fashion as the quantity of collisions to be tested n . As such, this was not expected to

alter the results of the size distribution, and this hypothesis does appear to be the case.

9.4.1.6 BP Lab Scale H , Table 9.2
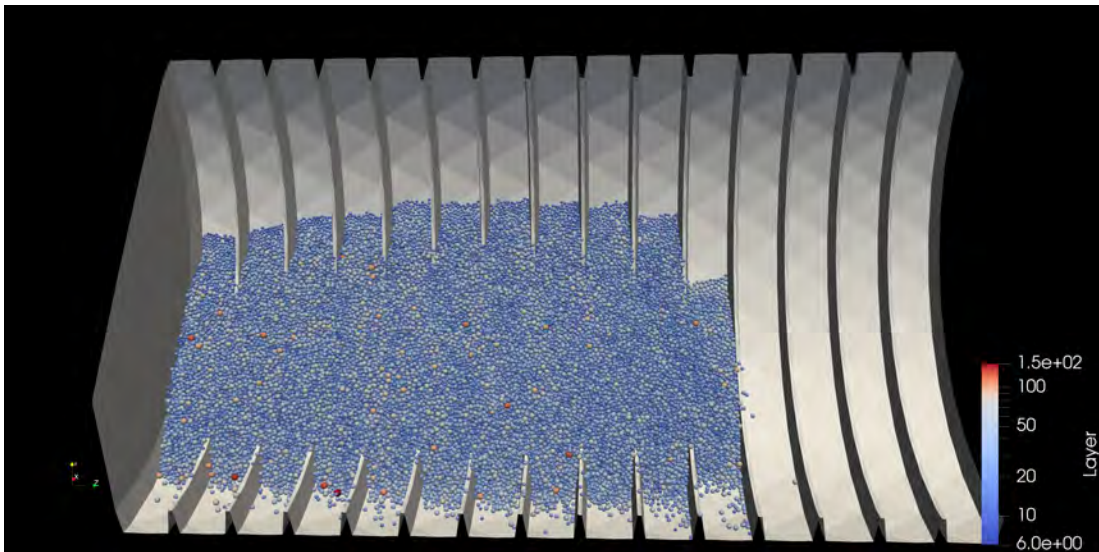

(a) An image showing the DEM Model of the BP Lab Scale H Case. This is an agglomeration simulation showing the behavour in a small lab scale drum with spheres coloured according to Radii.

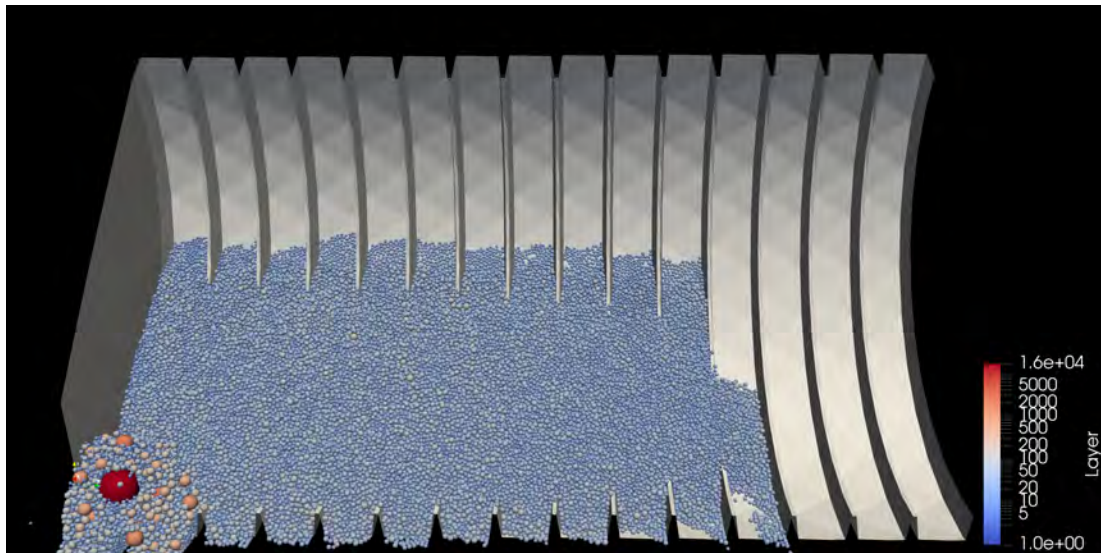(b) An image showing the DEM Model of the BP Lab Scale H Case. This is an agglomeration simulation showing the behavour in a small lab scale drum with spheres coloured according to Radii.

Figure 9.15: Behaviour of the BP Lab Scale H simulation case. This sim considered the effect of increasing lambda as well as assuming plastic behaviour.

BP Lab Scale H was run to test the effect of altering the plasticity, compared to case BP Lab Scale F . Though the spheres are assumed to deform plastically, this was not as well established at this point during the project, especially since [4] suggested that elastic behaviours are suitable for drum granulation, though that was simply necessary for the authors' assumptions.

The plasticity is expected to alter the effect of the size distribution, since unlike λ it varies the powers of the two diameter ratio terms, and it alters them differently to one another, similar to K_γ .

The effect is clearly evident. The range of the sphere radii has been widened, from 2.5-18mm to 2.5-23mm. The plasticity likely caused this by altering the layering component. The largest spheres have a significantly greater layer value,

possibly from coalescing preferentially with smaller spheres.

The size variation is sufficiently large that the largest spheres are able to coalesce with the smallest, even though the average diameter is larger than the limiting diameter, which would induce runaway coalescence as seen in Figure 9.9. The only thing preventing this is likely the segregation itself, ironically leading to a situation where the segregation actually reduces the variation. This segregation is most visible in Figure 9.15b

9.4.1.7 Summary of Bond Probability model using Arbitrary Δ_{lim} Cases

With neither true saturation nor granule dynamics effects, and given the effects of layering able to cause very unrealistic behaviour, these tests provide limited detail about the true nature of the behaviour.

The most important information that these results show is that size segregation behaviours are retained through the agglomeration process, and that the size segregation behaviours do alter the kinetic behaviours. Segregation effects group the spheres in simulations, or granules in real drums, which is relevant given the size ratio component of the agglomeration behaviour.

9.4.2 Bond Probability Criterion, Saturation based Δ_{lim}

9.4.2.1 BP &Δ_{limCoh} F , Table 9.3

This is the first simulation which ran to completion as planned, and it shows that the saturation in Figure 9.16b corresponds to the radii in Figure 9.16a.

9.4.2.2 BP &Δ_{limCoh} G , Table 9.3

The BP &Δ_{limCoh} G simulation, tested the effect of plasticity in this version of the model, to compare against the elastic case in BP &Δ_{limCoh} F . The plasticity
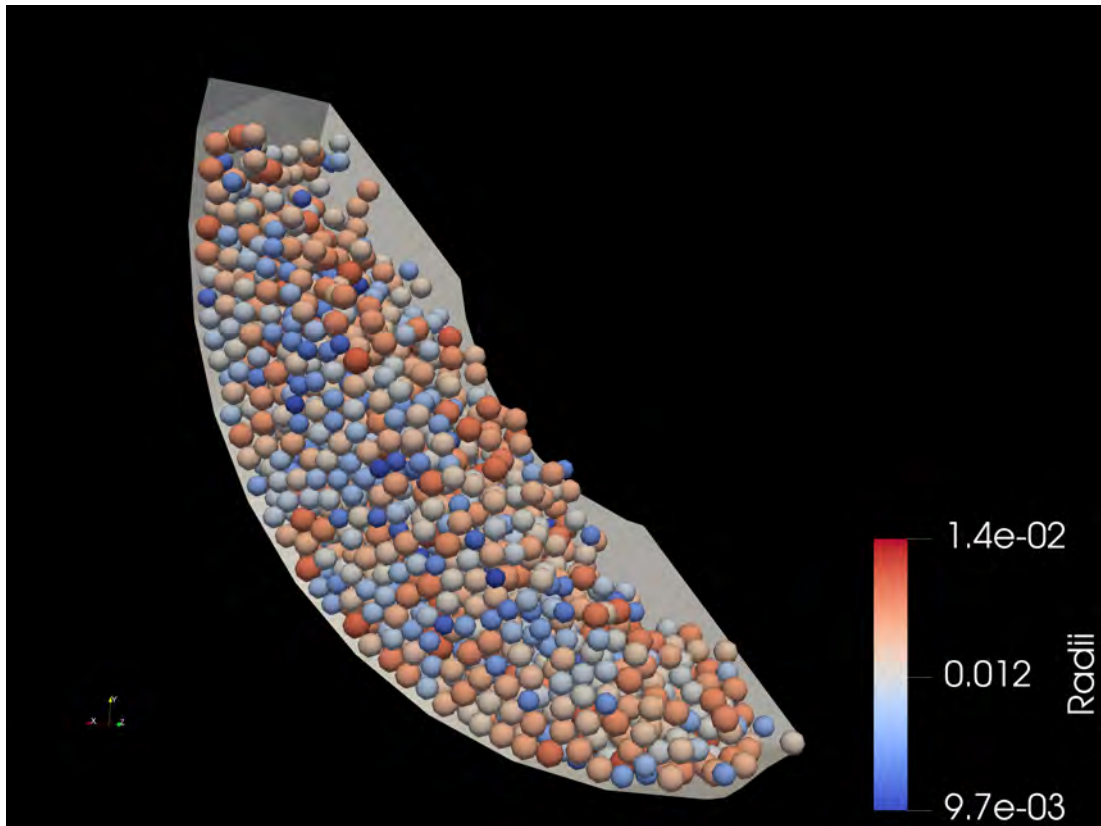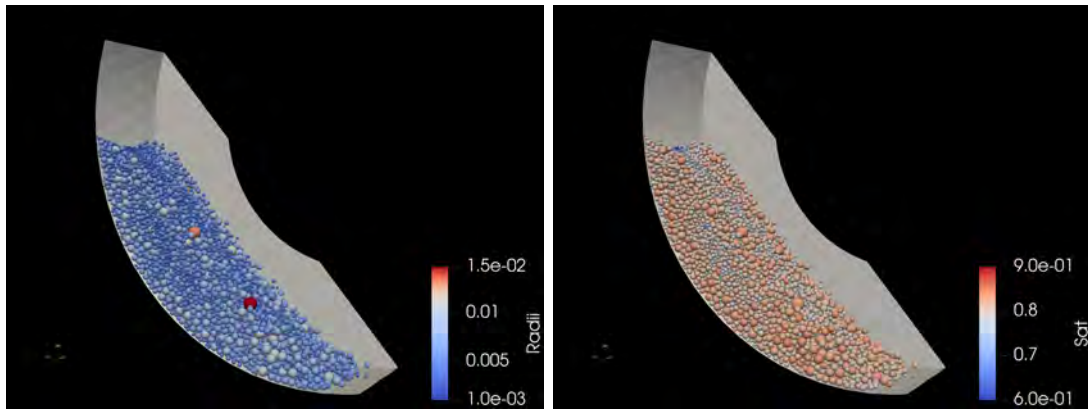
(a) An image showing the DEM Model of the BP $\&\Delta_{limCoh}$ F Case. This is an agglomeration simulation showing the behavour in a small lab scale drum with spheres coloured according to Radii.

(b) An image showing the DEM Model of the BP $\&\Delta_{limCoh}$ F Case. This is an agglomeration simulation showing the behavour in a small lab scale drum with spheres coloured according to Saturation.

Figure 9.16: Behaviour of the BP $\&\Delta_{limCoh}$ F simulation case
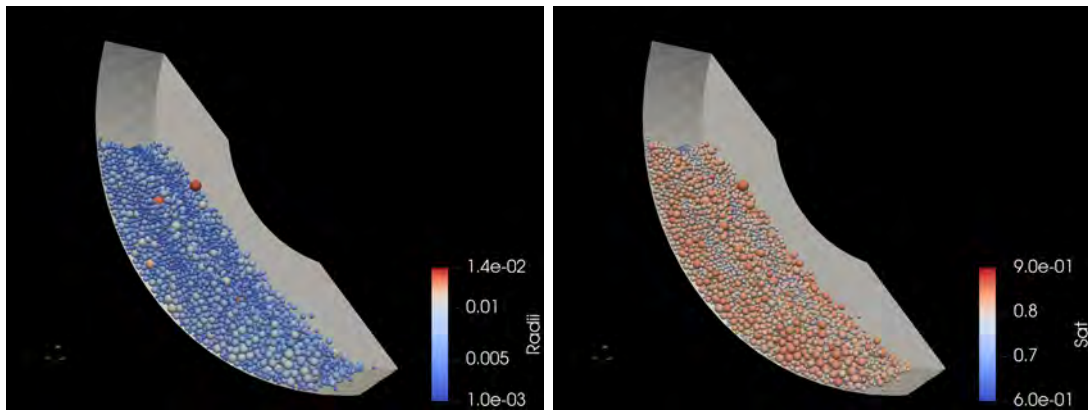
(a) An image showing the DEM Model of the BP $\&\Delta_{limCoh}$ G Case. This is an agglomeration simulation showing the behavour in a small lab scale drum with spheres coloured according to Radii.

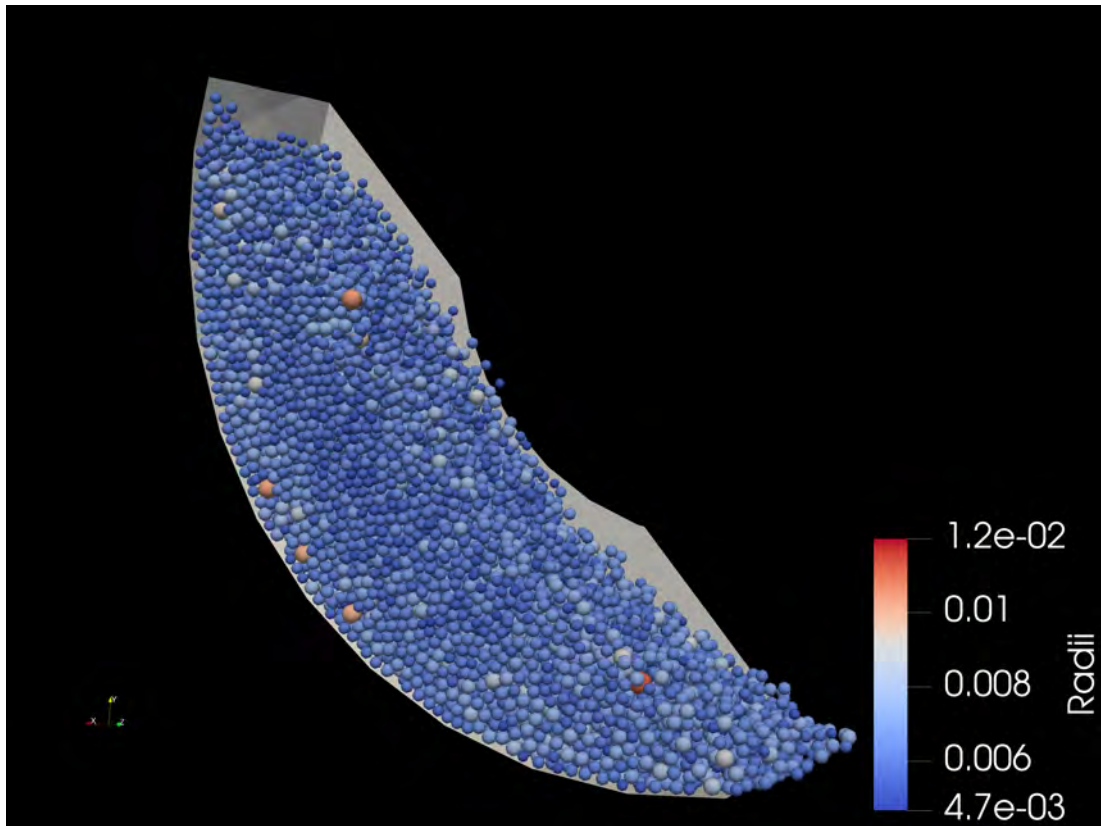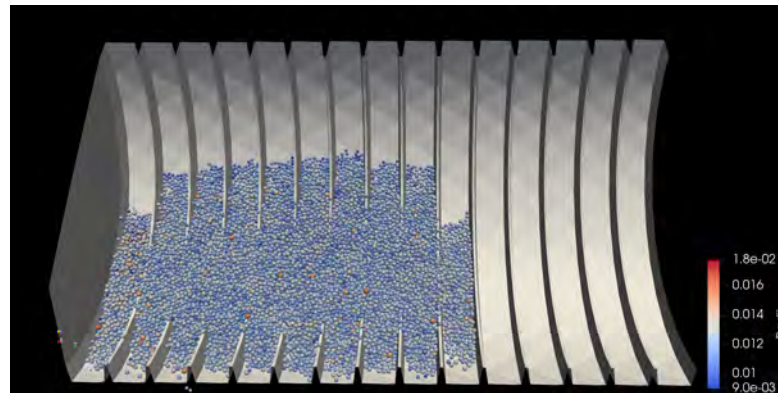(b) An image showing the DEM Model of the BP $\&\Delta_{limCoh}$ G Case. This is an agglomeration simulation showing the behavour in a small lab scale drum with spheres coloured according to Saturation.

Figure 9.17: Behaviour of the BP $\&\Delta_{limCoh}$ G simulation case. This case tested the effect of assuming plasticity in the agglomeration model

has a much weaker effect now that the saturation is in control of the size, and the two are quite similar. Again, the segregation can be seen in Figure 9.17a.
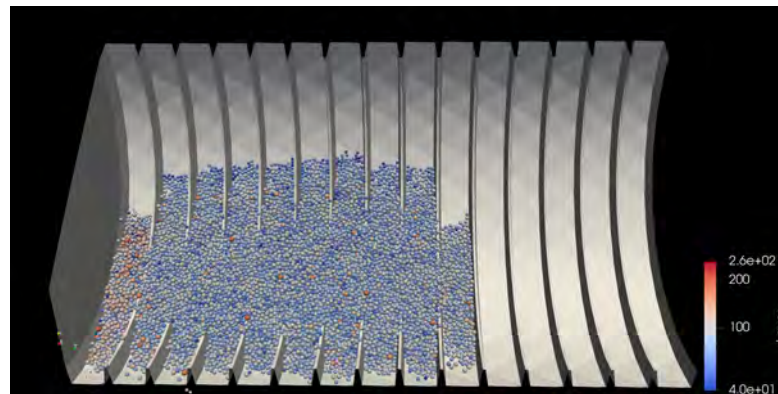
9.4.2.3 BP &Δ_{limCoh} I , Table 9.3

(a) An image showing the DEM Model of the BP &Δ_{limCoh} I Case. This is an agglomeration simulation showing the behaviour in a small lab scale drum with spheres coloured according to Radii.

(b) An image showing the DEM Model of the BP &Δ_{limCoh} I Case. This is an agglomeration simulation showing the behaviour in a small lab scale drum with spheres coloured according to Saturation.

Figure 9.18: Behaviour of the simulation case. This tested the effect that larger initial sphere sizes has on the behaviour, returning to elastic behaviour.

Returning to elastic spheres and a larger initial sphere size, Figure 9.18 shows a greater extent of growth than previous tests. However, examining the saturation and the radii of the spheres in Figure 9.18b and Figure 9.18a shows a weakness of this system. Though the saturation seems to permit growth, above a certain size the growth appears to be unrelated to the saturation.

In part this is justified, since the radii-saturation curve becomes steeper as saturation approaches K_{Smax} but the three simulations shown thus far using this model have had identical saturation distributions. Instead, the initial sphere radii of this simulation has contributed to the presence of larger spheres. The implications of this will be considered in the model summary.

9.4.2.4 BP &Δ_{limCoh} K , Table 9.3

Since the BP &Δ_{limCoh} K test had a larger upper and lower limit to the initial sphere distribution, and showed larger spheres at the end, the lower limit was
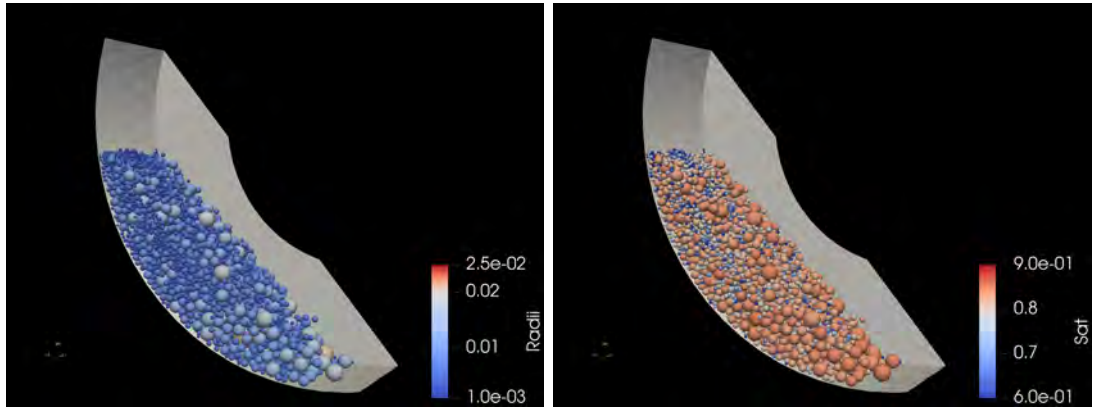
(a) An image showing the DEM Model of the BP $\&\Delta_{limCoh}$ K Case. This is an agglomeration simulation showing the behaviour in a small lab scale drum with spheres coloured according to Radii.
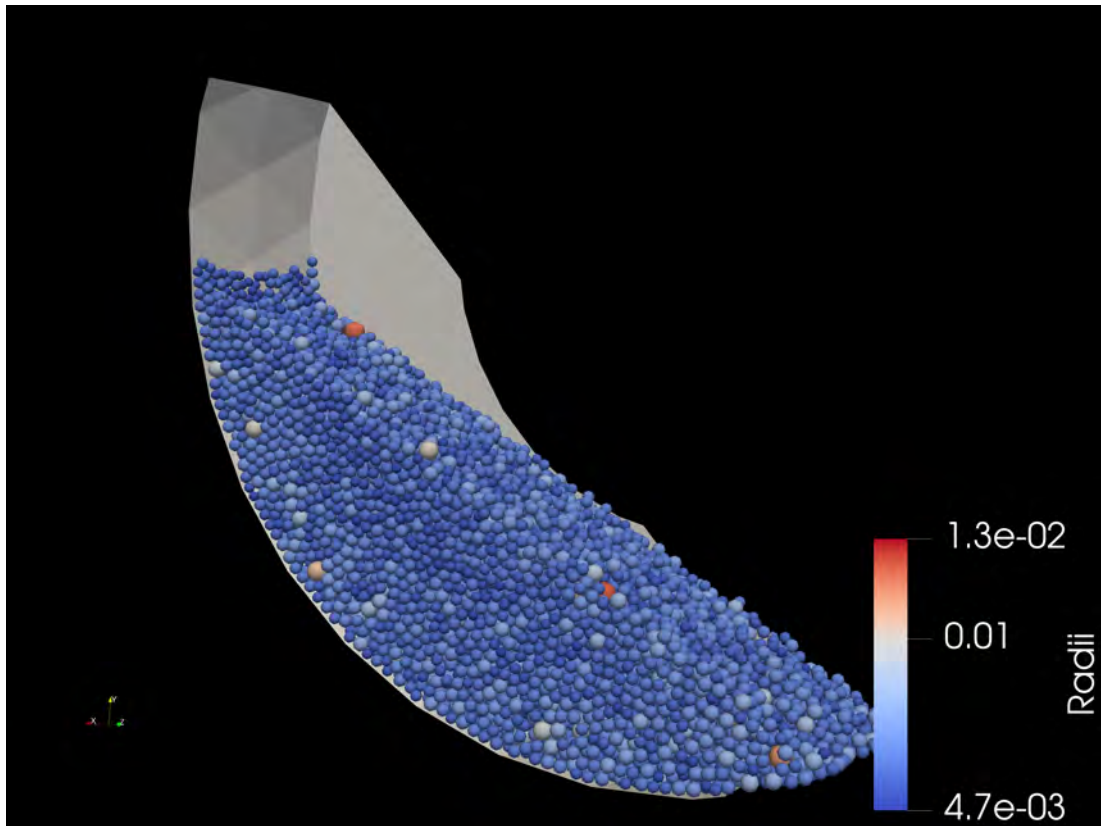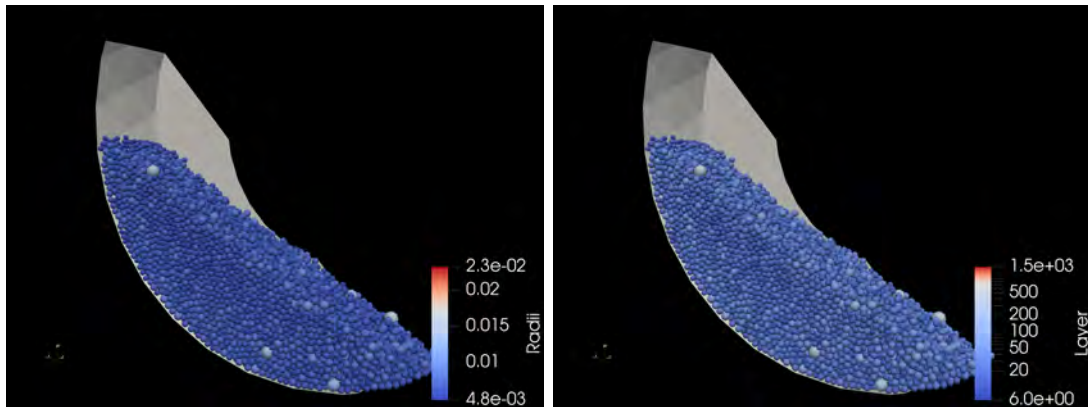
(b) An image showing the DEM Model of the BP $\&\Delta_{limCoh}$ K Case. This is an agglomeration simulation showing the behaviour in a small lab scale drum with spheres coloured according to Saturation.

Figure 9.19: Behaviour of the BP $\&\Delta_{limCoh}$ K simulation case. This case tested what effect the initial sphere size distribution has on the coalescence behaviour.

reduced to match the previous simulation lower values. The final distribution in Figure 9.19a seems to be similar to the previous test despite this.

As such, it is suspected that the saturation probably has the dominant effect at the start of the agglomeration process here. The spheres can always coalesce if the merged sphere has a saturation larger than K_{Smax} , as this implies a $K_{Smax} = \infty$. These can only exist at the start of the process, as they will quickly approach the average over time through layering with the drier spheres.

9.4.2.5 BP $\&\Delta_{limCoh}$ L , Table 9.3

The initial saturation for this was set to 0.8 ± 0.9, due to an oversight when editing the input files. Obviously saturation cannot be negative, as this requires a negative liquid volume. Mathematically it worked fine, and could be seen as the case where the water combines chemically with part of the feed, as might happen with cement for example, therefore it was included.

Again, no variability in the saturation as seen in Figure 9.20b is observed at
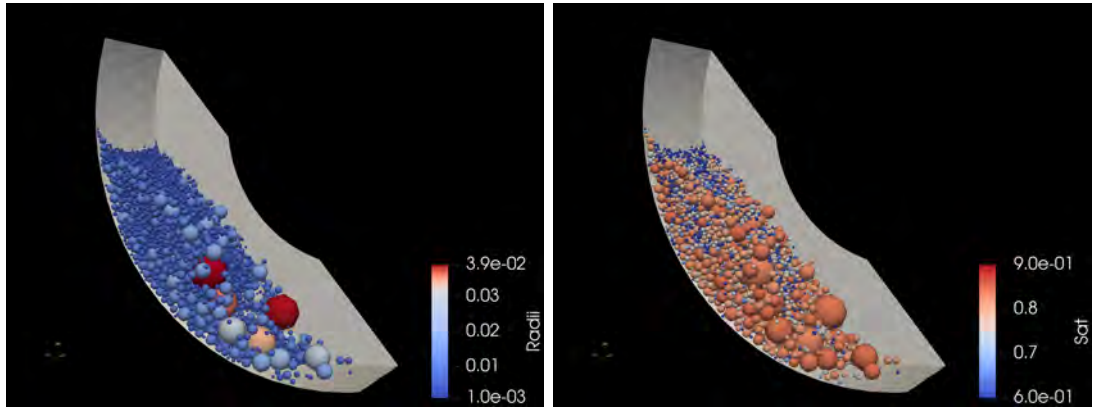
(a) An image showing the DEM Model of the BP $\&\Delta_{limCoh}$ L Case. This is an agglomeration simulation showing the behavour in a small lab scale drum with spheres coloured according to Radii.

(b) An image showing the DEM Model of the BP $\&\Delta_{limCoh}$ L Case. This is an agglomeration simulation showing the behavour in a small lab scale drum with spheres coloured according to Saturation.

Figure 9.20: Behaviour of the BP $\&\Delta_{limCoh}$ L simulation case

the larger sizes, and Figure 9.20a shows that there is very significant variation in the sphere sizes.

Further supporting the explanation that the early stage agglomeration dominates the subsequent size distribution, there are many smaller spheres which have yet to merge which all show low saturations as might be expected, but not all of the spheres at this size are similarly low saturation.

9.4.2.6 BP $\&\Delta_{limCoh}$ N , Table 9.3

The BP $\&\Delta_{limCoh}$ N test case had a reduced value for K_γ , which only affects the layering component, but more importantly the saturation had been corrected. However, the end results are not significantly different from the previous BP $\&\Delta_{limCoh}$ L case. The effect of reducing the strength of the layering can be seen clearly, i.e. by checking Figure 9.4, the total number of the smallest spheres is highest in this case.

There are still nonetheless very large spheres in the simulation, as seen in Figure 9.21a, and these always correspond to the least saturated spheres in Fig-
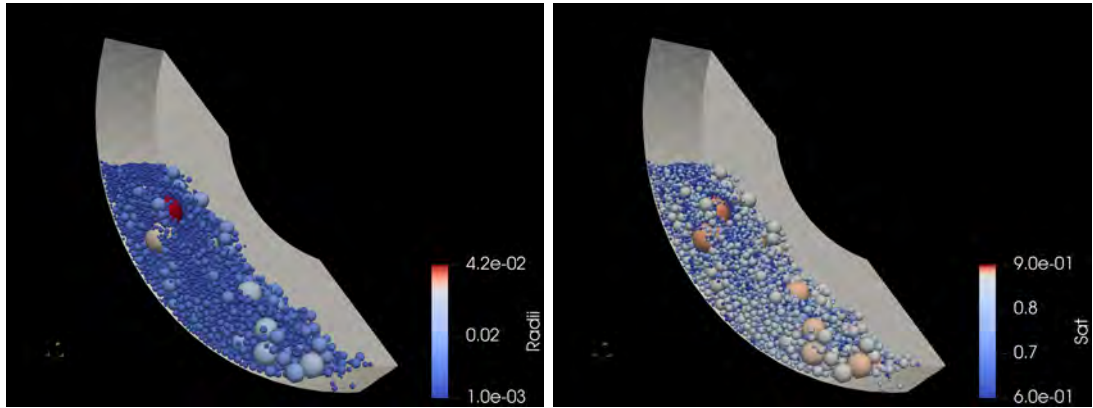
(a) An image showing the DEM Model of the BP $\&\Delta_{limCoh}$ N Case. This is an agglomeration simulation showing the behavour in a small lab scale drum with spheres coloured according to Radii.

(b) An image showing the DEM Model of the BP $\&\Delta_{limCoh}$ N Case. This is an agglomeration simulation showing the behavour in a small lab scale drum with spheres coloured according to Saturation.

Figure 9.21: Behaviour of the BP $\&\Delta_{limCoh}$ N simulation case. Here a wide span, a low value of K_γ , and a larger saturation variation is applied compared to the baseline.

ure 9.21b.

9.4.2.7 BP $\&\Delta_{limCoh}$ O , Table 9.3

To test whether the adjusted K_γ was actually the reason, or possibly simply the saturation bounds, BP $\&\Delta_{limCoh}$ O was run.

Though the sphere radii appear to be much more consistent in Figure 9.22a, this is simply the result of the largest spheres being more hidden, as there is a large sphere in the centre of the bed. Again, Figure 9.22b shows that the saturation is generally consistent.

9.4.2.8 Combination model Summary

The combination model is clearly better at demonstrating a distribution of sphere sizes compared to the bond probability model alone. The layering still allowed a lot more coalescence of smaller spheres which reduced the smaller sphere count, leading to a general balance of choice between larger spheres or smaller spheres.
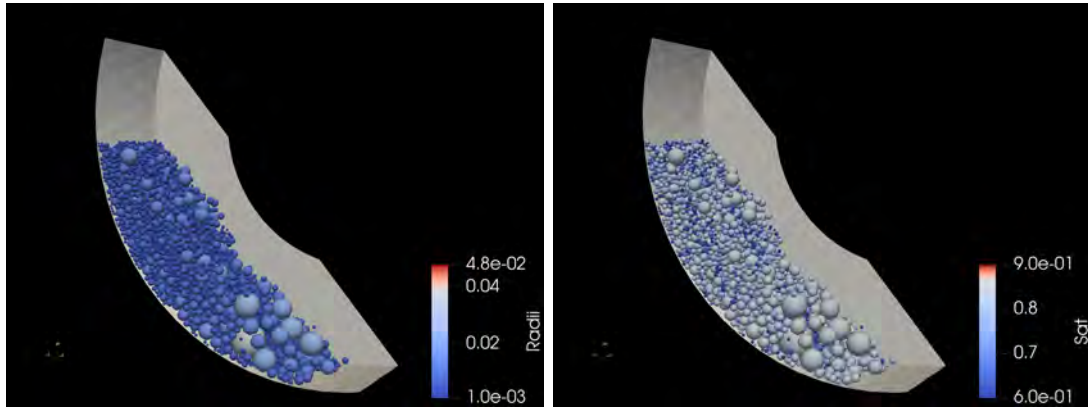
(a) An image showing the DEM Model of the BP $\&\Delta_{limCoh}$ O Case. This is an agglomeration simulation showing the behaviour in a small lab scale drum with spheres coloured according to Radii.
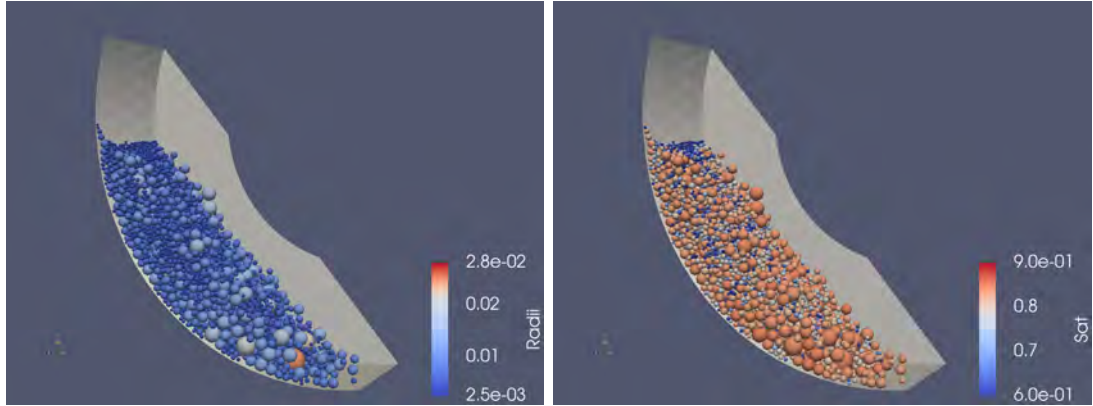
(b) An image showing the DEM Model of the BP $\&\Delta_{limCoh}$ O Case. This is an agglomeration simulation showing the behaviour in a small lab scale drum with spheres coloured according to Saturation.

Figure 9.22: Behaviour of the BP $\&\Delta_{limCoh}$ O simulation case. Here only a wide span and wider saturation bound is applied compared to the baseline.

Obviously, the saturation distribution was seen to have some impact, as many, though not all, of the small spheres had lower saturations. Being able to observe the saturation and radius was a real benefit to checking the results. The initial sphere size distribution also had some impact, broadening the distributions. This is unfortunate, since it meant that the behaviour could not be easily scaled by reducing the sphere count and using increased sphere sizes.

However, in the real case, there is an overlapping presence of both large and smaller spheres. This suggests a heterogeneous distribution of effects, and there is a natural cause of this, the spray.

9.4.3 Bond Probability Criterion with Saturation limited size, Moisture Sprayed in

The spray had been partially implemented, however with a number of adjustments it was significantly improved. This allowed determining the effect of the spray.

9.4.3.1 BP $\&\Delta_{limCoh}$, Spray, Table 9.4

In all three of the results for BP $\&\Delta_{limCoh}$, Spray, Figure 9.23a, Figure 9.23b and Figure 9.24a, the spray is shown as a cyan colour to distinguish it from the other spheres.
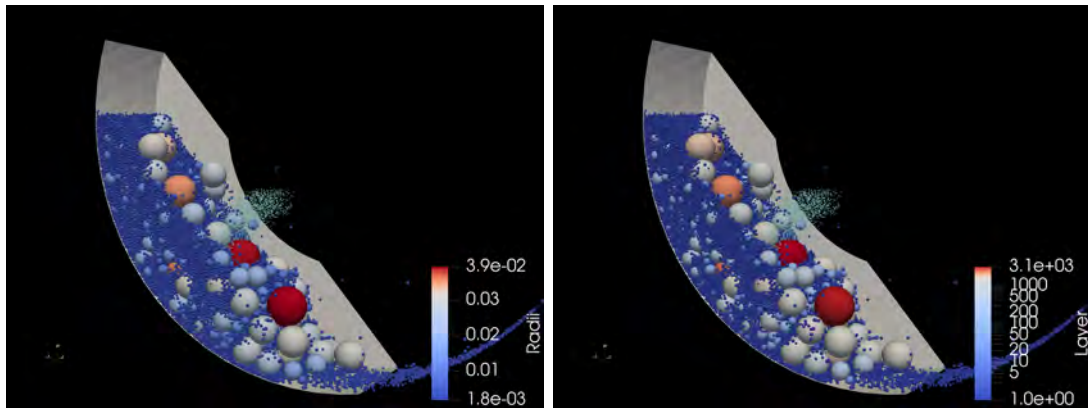
(a) An image showing the DEM Model of the BP $\&\Delta_{limCoh}$, SprayCase. This is an agglomeration simulation showing the behavour in a small lab scale drum with spheres coloured according to Radii.

(b) An image showing the DEM Model of the BP $\&\Delta_{limCoh}$, SprayCase. This is an agglomeration simulation showing the behavour in a small lab scale drum with spheres coloured according to Layer.

Figure 9.23: Behaviour of the Calvark06261444 simulation case. This simulation started with a very low initial saturation, and instead the liquid is added as a "spray" of small water spheres.

In some of the previous cases, spheres had been added for a short while during the process, as this was thought to better represent the turnover motion in the full scale drum. They were not added in the pile but rather at the other end, so that it would be drawn in with the rest of the fines at the bottom. This can be seen in Figure 9.23b, as the grey spheres with only 1 layer, signifying they have not coalesced.

In this case, this was very useful in demonstrating a critical feature of the heterogeneity. To show this, the various volumes of liquid and pore space must be accounted for.

The total Pore volume that is not filled with liquid (Void Volume V_v) added
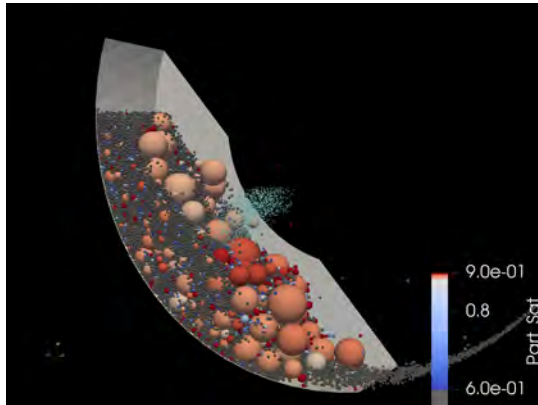
(a) An image showing the DEM Model of the BP $\&\Delta_{limCoh}$, SprayCase. This is an agglomeration simulation showing the behavour in a small lab scale drum with spheres coloured according to Saturation.
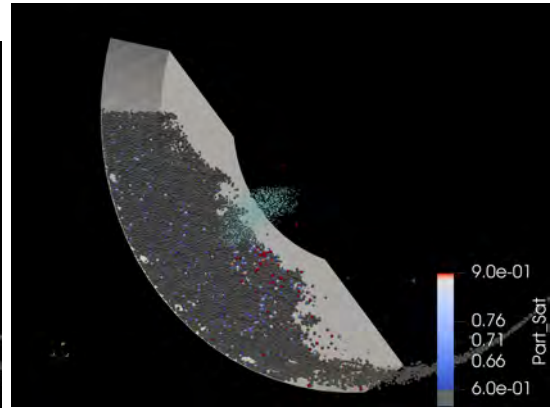
(b) An image showing the DEM Model of the BP $\&\Delta_{limCoh}$, SprayCase. This is an agglomeration simulation showing the behavour in a small lab scale drum with spheres coloured according to Saturation.. Here the spheres are only shown if they are unmerged (Layer=1).

per second is 63 ml/s, after consolidation has completed. Meanwhile, the total liquid added per second in the form of spray is 50 ml/s. The initial saturation of the spheres also adds an additional 19.3 ml/s of liquid.

This gives a final theoretical global saturation S of the spheres of 0.839, which is below the value of K_{Smax} which is sufficient for some growth but not total merging.

Figure 9.24b only shows unmerged spheres, those with a Layer value of 1 (the amount of spray spheres which merge do not alter this value as water spheres are hardcoded not to increase the layer count when it merges). This clearly corresponds to almost completely being dominated by unsprayed spheres, as those which are sprayed get sufficient moisture to change from brown to blue in the figure.

What can be clearly seen then is the significant disparity between the dry, unsprayed feed and the moistened feed. This is the result of a combination of the spray location (which leads to the surface being more moistened), moist spheres being more inclined to merge, (which grows them) segregation (which ensures

that the large spheres stay on the outside) and low diffusion (which, even when coalescence has not become dominant, results in the moistened spheres staying closer to the outside).

The larger the sphere, the lower the increase in saturation from each individual droplet. Meanwhile, the increase in projected area, combined with the hyperbolic nature of the relation between saturation and final size, reduces the increase in saturation needed for additional growth.

Since K_{Smax} is based on the merged sphere saturation, this means that a moistened sphere is more likely to merge with another moist sphere, as they are more likely to satisfy the merged spheres requirement. This requirement was applied as it was the only way to make sense of a single sphere requirement being applied to a merging criterion, however it is reasonable since it is a measure of the cohesion of the spheres, and a failure to satisfy would suggest an overall internal weakness due to lack of binder.

Clearly, the heterogeneity shown here directly affects the distribution. Other possibilities will be considered further on.

9.4.4   Adhesion-Cohesion Criterion

This model applies two hard limits, rather than using the hard limit of growth of K_{Smax} as the limiting diameter for the bond probability equation, which determines a soft limit based on the proportional sizes involved.

These models were run for as long as possible, and they were applied in the full scale, along with the spray right away, as all the components were in principle working. However, the issue of memory would cause the simulation to fail sooner than hoped.
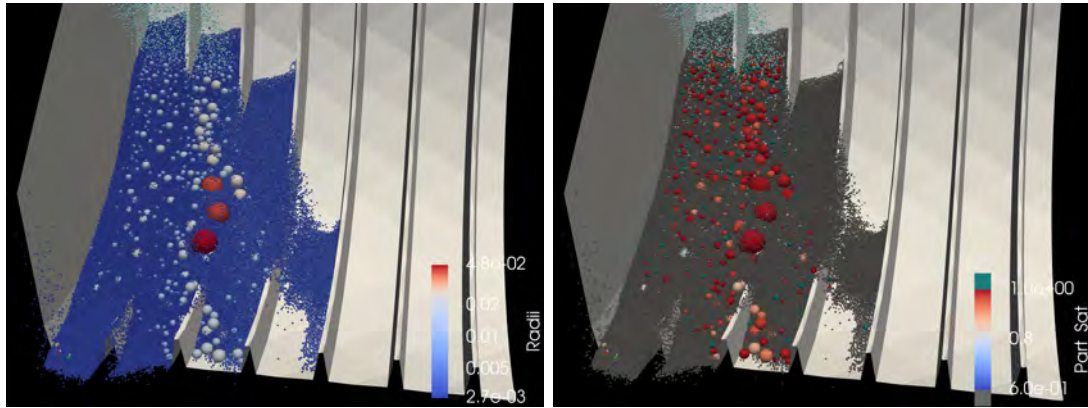
(a) An image showing the DEM Model of the Adh-Coh Model A Case. This is an agglomeration simulation showing the behavour in a full industry scale drum with spheres coloured according to Radii.

(b) An image showing the DEM Model of the Adh-Coh Model A Case. This is an agglomeration simulation showing the behavour in a full industry scale drum with spheres coloured according to Saturation.

Figure 9.25: Behaviour of the Adh-Coh Model A simulation case. This uses the Adhesion-Cohesion model, and assumed a very low value of V_{chmin} compared to subsequent tests.

9.4.4.1 Adh-Coh Model A , Table 9.7

The growth clearly occurs very rapidly in this case as seen in Figure 9.25a, with coalescence occurring immediately as soon as a merge which provides a suitable saturation for the diameter is achieved. This case had a low value for K_α , and so the collision velocity required was very low. This explains why in Figure 9.25b there are no oversaturated spheres.

For these models, showing only the merged spheres, as in Figure 9.25 provides a comparison of where and how quickly the growth is occurring. Note that simply getting moistened does not increase the layer count.

The radii in Figure 9.26a are coloured logarithmically, and when comparing against Figure 9.26b the saturation has a much stronger relation with the size, with the largest spheres clearly having higher saturation.

Some of the spheres have a relatively low saturation for their size and this may be due to the parallelisation of the merging routine. If a collision can occur between multiple sphere within a single time step that, for each individual col-

378

lision that is determined to be valid for the combined sphere, then when all the particles are merged the saturation of the total merged sphere may be lower than that expected for the Cohesion Criterion.

This was found to be one possible explanation based on the simple test environment also used to evaluate the merging model as working as intended. This could be something to resolve in future, however given that real pellets have some variability in their saturations this is not a significant concern.

The spray location in this test is very close to the top of the pile. this was chosen since segregation was expected to allow only the smallest spheres to reach there. However, this did not take into account the dimensionless spray flux. as the spheres are relatively slowly moving there, and the adhesion criterion is not a major factor in this test, the slowly moving spheres are much more able to coalesce with one another, and are more likely to encounter one another.

This simulation crashed after this time step, with the likely reason being a merging event occurring between two of the three very large spheres in the centre.
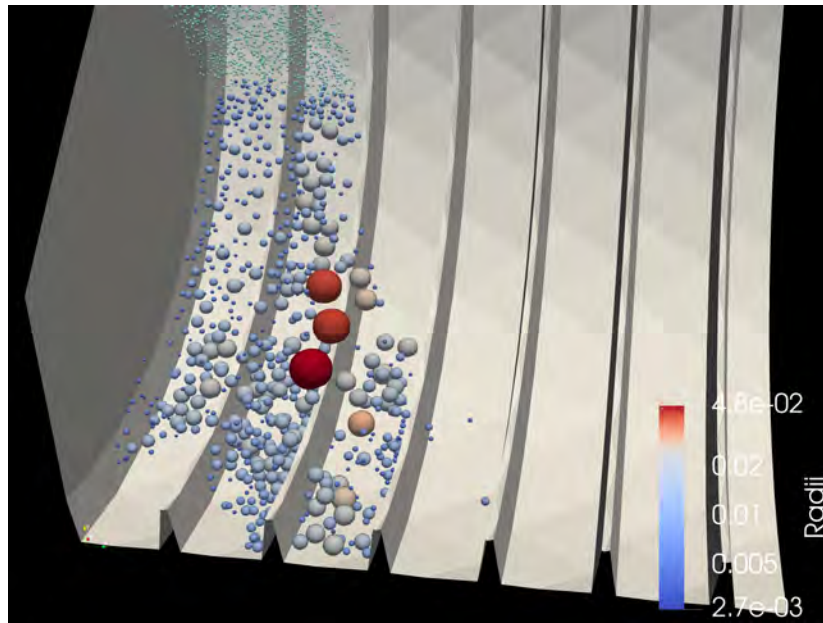
(a) An image showing the DEM Model of the Adh-Coh Model A Case. This is an agglomeration simulation showing the behavour in a full industry scale drum with spheres coloured according to Radii.
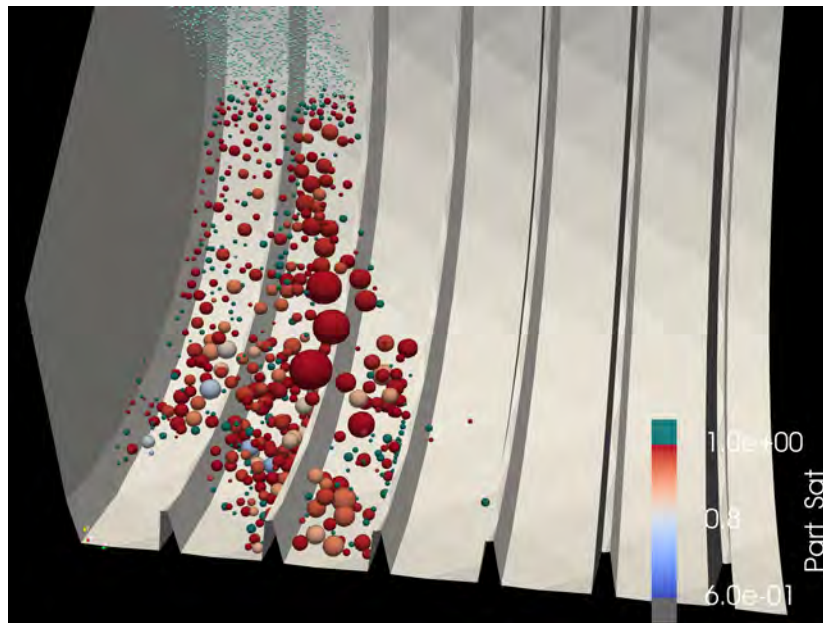
(b) An image showing the DEM Model of the Adh-Coh Model A Case. This is an agglomeration simulation showing the behavour in a full industry scale drum with spheres coloured according to Saturation.

Figure 9.26: Behaviour of only the spheres which have merged in the Adh-Coh Model A Simulation

9.4.4.2 Adh-Coh Model B , Table 9.7

The Adh-Coh Model B simulation used a similar setup to Adh-Coh Model A , but the value of V_{chmin} was increased, while reducing K_α to allow some growth to occur. This meant that the growth would occur where the granules would be hitting each other with collision energies higher than incidental touching.

(a) An image showing the DEM Model of the Adh-Coh Model B Case. This is an agglomeration simulation showing the behaviour in a full industry scale drum with spheres coloured according to Radii.

(b) An image showing the DEM Model of the Adh-Coh Model B Case. This is an agglomeration simulation showing the behaviour in a full industry scale drum with spheres coloured according to Saturation.

Figure 9.27: Behaviour of the Adh-Coh Model B simulation case. This case tested a larger value of V_{chmin} , which would require better collision dynamics for the coalescing granules, and it also reduced K_α to compensate to account for this.

As can be seen in Figure 9.27b, the effect of reducing K_α while increasing V_{chmin} results in a larger quantity of oversaturated spheres which do not merge immediately. Though this might question the validity of the model, these spheres would also be collecting the dry spheres immediately below them in the real case, which would provide some surface dryness, though this would consolidate quickly enough. However, the model is admittedly limited by the nature of the requirements of DEM.

This then provides a mechanism by which Figure 9.27a does not have the same extent of oversized spheres, though a flaw can be spotted where the spheres

are merging in the second trough, and then are brought back up for a second round of spray.

Figure 9.28 shows only the merged spheres in order to see where the spheres grow again. The growth is more consistent this time, and the previously mentioned issue of saturation requirement not being as strongly adhered to is not the case here. This is likely because of the overall reduction in merging, which in turn reduces the likelihood of the aforementioned triple merging.

Additionally, the merging appears to be occurring at the bottom of the slopes where the larger spheres appear. This is expected behaviour, as this region will have the largest collision velocities. Figure 9.28a shows much larger spheres also appear as the spheres are tumbling to the less filled fourth trough. This appears to be some sort of transient state, as the very large particles seem to be more prevalent the further along the path of motion of the particles.
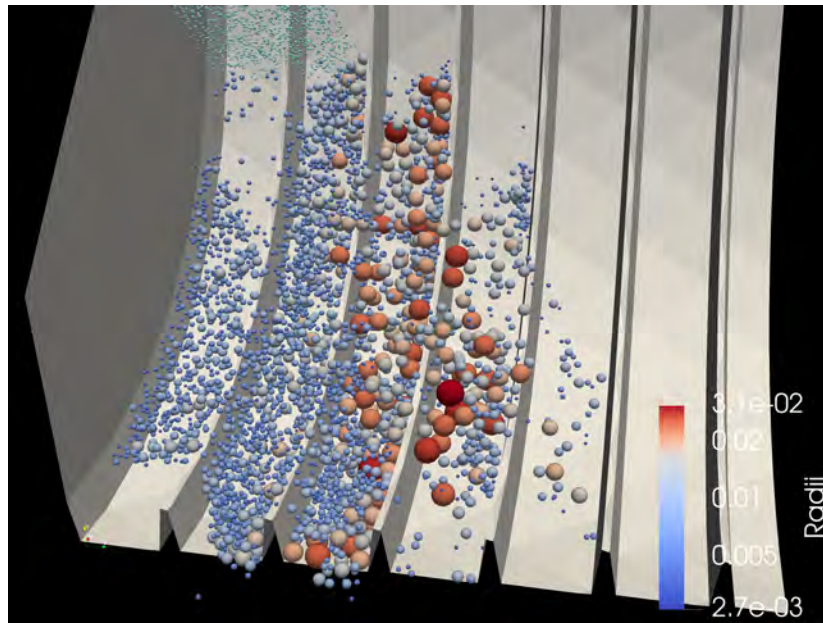
(a) An image showing the DEM Model of the Adh-Coh Model B Case. This is an agglomeration simulation showing the behavour in a full industry scale drum with spheres coloured according to Radii.
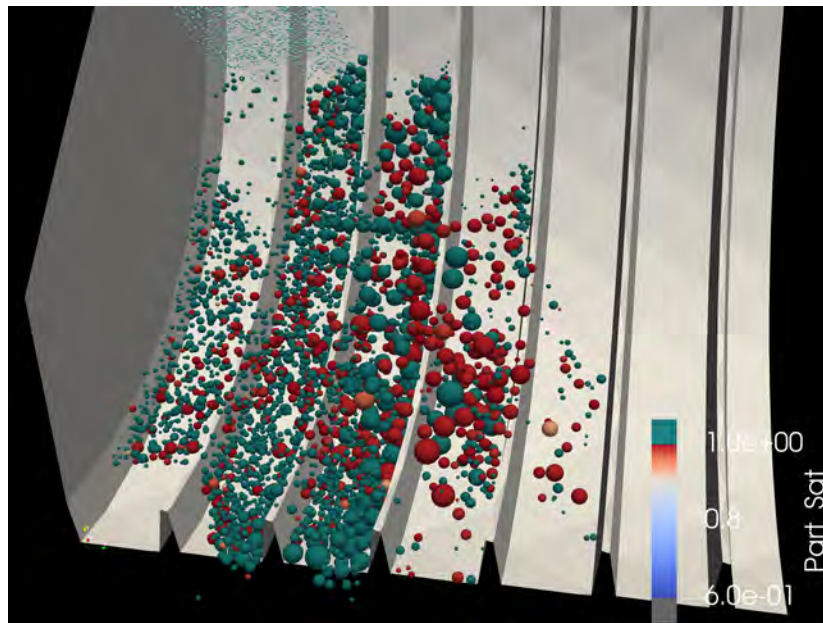
(b) An image showing the DEM Model of the Adh-Coh Model B Case. This is an agglomeration simulation showing the behavour in a full industry scale drum with spheres coloured according to Saturation.

Figure 9.28: Behaviour of the Adh-Coh Model B simulation case, where only the spheres which have merged (layer> 1) are shown

9.4.4.3 Adh-Coh Model C, Table 9.7

This uses smaller spheres so as to reduce the size difference between d_p and d_g , in turn to improve the layering component of the growth. Additionally, to move past the transient state sooner, a large quantity of spheres were added initially. This was still slightly limited due to memory constraints, though as seen above, this produced a similar distribution to that found in the real case.
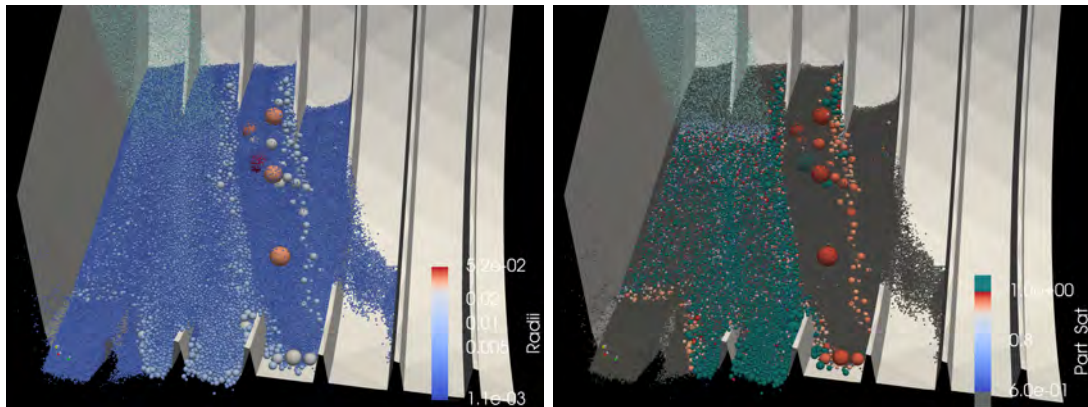
(a) An image showing the DEM Model of the Adh-Coh Model CCase. This is an agglomeration simulation showing the behaviour in a full industry scale drum with spheres coloured according to Radii.

(b) An image showing the DEM Model of the Adh-Coh Model CCase. This is an agglomeration simulation showing the behaviour in a full industry scale drum with spheres coloured according to Saturation.

Figure 9.29: Behaviour of the Adh-Coh Model Csimulation case. The spheres in this case are spawned in even smaller than in the previous cases, and d_p is also increased, to manipulate the cohesion criterion to allow more dry spheres to merge.

The effect of the transience can be seen again in Figure 9.29, with a large clump of oversize spheres at the top, caused by the initial falling over into the third trough.

Showing only the merged spheres in Figure 9.32, the turnover behaviour of the spheres can be observed. The first spheres to reach the region will be the the fines that were unwetted prior to the spray activation. Then the sprayed spheres from the second trough will collide with them first. Then those spheres sprayed the first time round wil be larger as they have been sprayed twice, increasing

384

their total saturation and opportunities to merge with similarly wetted spheres.

Figure 9.30a shows larger spheres in the oversize group, this likely arises from the transient effects combined with the layering which was easier to apply due to the smaller initial sphere sizes.

Finally, Figure 9.29a shows inter-trough segregation effects. The larger spheres tend to favour touching the walls of the ridges, which tends to draw them further up the pile. Notice the top of the troughs which shows the effect of the variation in the initial dry sizes as well.

The increase in d_p should make it easier to control the maximum size due to a lower sensitivity, as the gradient is less steep at lower S values, however the results obtained do not necessarily find this, as the most developed granules seem to be larger than in the Adh-Coh Model B simulation. However, this may simply be the result of the initial transient state, which will be tested in the next simulation.
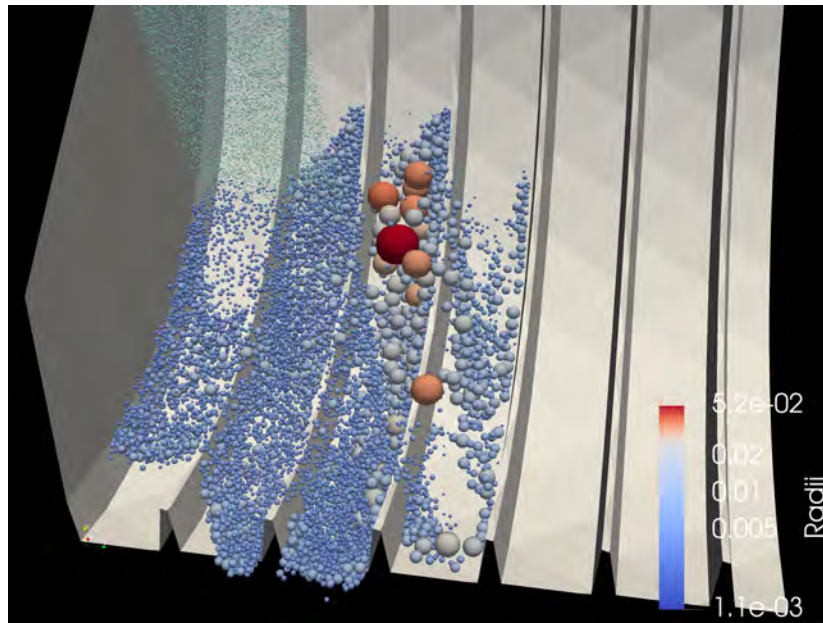
(a) An image showing the DEM Model of the Adh-Coh Model CCase. This is an agglomeration simulation showing the behavour in a full industry scale drum with spheres coloured according to Radii.
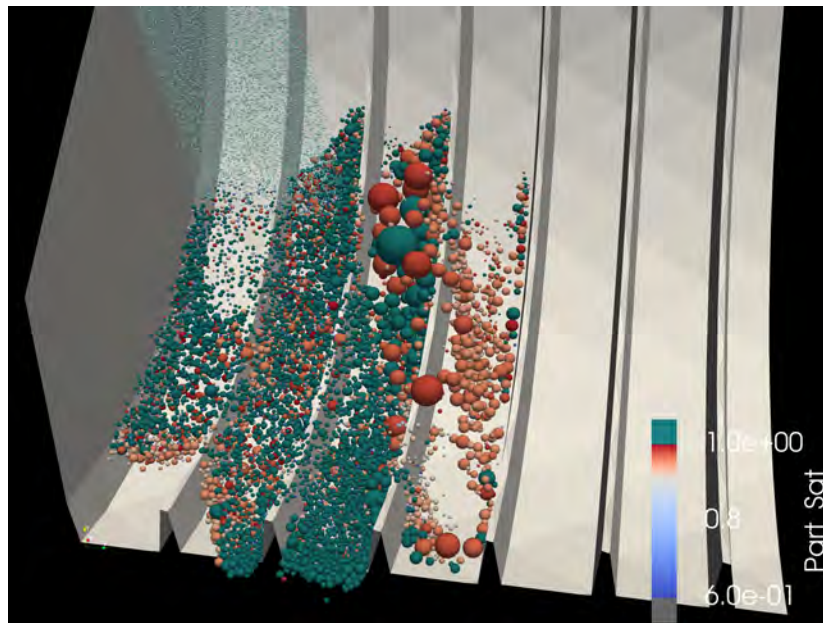
(b) An image showing the DEM Model of the Adh-Coh Model CCase. This is an agglomeration simulation showing the behavour in a full industry scale drum with spheres coloured according to Saturation.

Figure 9.30: Behaviour of the Adh-Coh Model Csimulation case, where only the spheres which have merged (layer> 1) are shown

9.4.4.4 Adh-Coh Model D, Table 9.7

This simulation is designed to skip the transient state, by spawning in a large set of feed spheres to begin with, and also improve the memory issues by limiting the range of the simulation, given that the octree collision system struggles to manage high concentrations of spheres in some areas relative to others in the region managed.
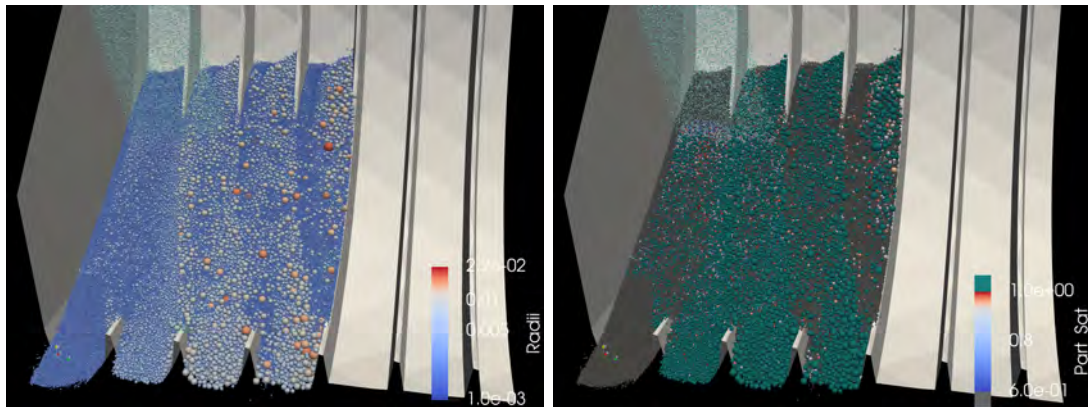
(a) An image showing the DEM Model of the Adh-Coh Model DCase. This is an agglomeration simulation showing the behavour in a full industry scale drum with spheres coloured according to Radii.
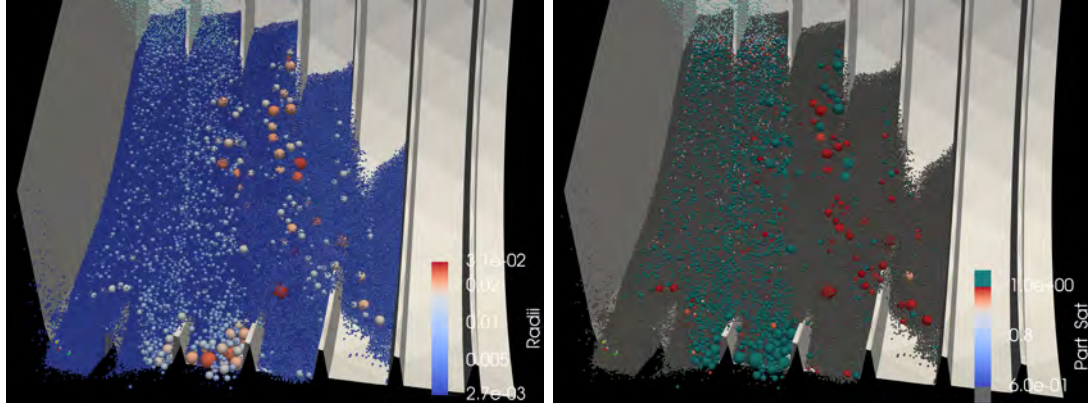
(b) An image showing the DEM Model of the Adh-Coh Model DCase. This is an agglomeration simulation showing the behavour in a full industry scale drum with spheres coloured according to Saturation.

Figure 9.31: Behaviour of the Adh-Coh Model Dsimulation case. The spheres in this case are spawned in even smaller than in the previous cases, and d_p is also increased, to manipulate the cohesion criterion to allow more dry spheres to merge. Further, the bounds are much more restricted than in the previous cases, to help manage memory issues in the DEM program.

By skipping the transient state, the behaviour in Figure 9.31 shows a much more consistent distribution of spheres and sphere diameters. This could be a false distribution, as they are also generally highly saturated, and they are simply limited in their mergers due to the effects of V_{chmin} . Even so, the fourth trough shows an increase in the quantity of spheres which have $S < K_{Smax}$.

The division of the inputs and the outputs in this way could also be a way

to subdivide the process similar to previous attempts, but with a clear physical component.

Figure 9.32a shows that the spheres do indeed have a much more consistent diameter distribution, and Figure 9.32b shows that the saturation is reducing, with more spheres showing up as orange and red rather than the dark green used for oversaturated spheres. This is because as the spheres travel along, they grow and pick up more of the dry spheres. This effect is likely to continue the further down the drum that is travelled, but the boundary of this simulation makes this unable to be observed, though future simulations will need to test this.

(a) An image showing the DEM Model of the Adh-Coh Model DCase. This is an agglomeration simulation showing the behavour in a full industry scale drum with spheres coloured according to Radii.
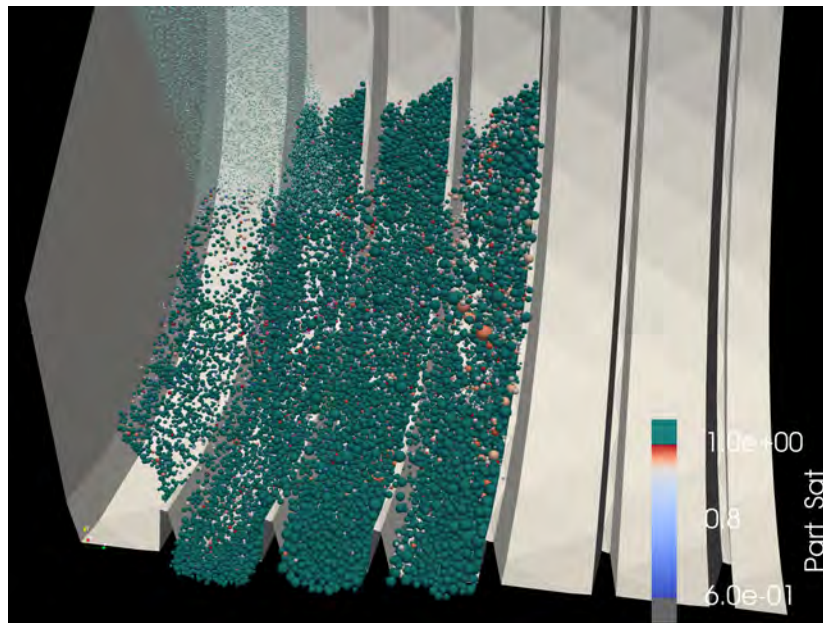
(b) An image showing the DEM Model of the Adh-Coh Model DCase. This is an agglomeration simulation showing the behavour in a full industry scale drum with spheres coloured according to Saturation.

Figure 9.32: Behaviour of the Adh-Coh Model Dsimulation case, where only the spheres which have merged (layer> 1) are shown

9.5 Consolidation behaviours

The consolidation behaviours have a number of interesting features, which all depend on the relative importance of $k_{\epsilon A}$ and $k_{\epsilon B}$, which respectively scale the effect of collision frequency and collision strength on the consolidation. The primary feature to note is the variation in consolidation as well as the extent based on location.

9.5.1 Lab Scale consolidation

9.5.1.1 AllSameSatEv

The saturation distribution was monodisperse here, and the spheres were all added in one single event to ensure that any variability was entirely due to consolidation effects.

9.5.1.2 Consolidation A , Table 9.7

This first test applied low values of $k_{\epsilon A}$ and $k_{\epsilon B}$. These are relative, since the simulations also needed to be run in a reasonable time, so while the longest of these ran for less than half a minute, real residence times are usually a few minutes, though once steady state is achieved this is a matter of scaling by $k_{\epsilon A}$.

Figure 9.33 shows the properties of the spheres at the final time step, in particular, the radii and the porosity. The radii are shown to highlight the relatively low importance of segregation in the subsequent results. Though consolidation does have an appreciable effect on the final volume in these cases, which will be demonstrated later, the size of the starting spheres does not noticably correspond to the extent of the consolidation.

The distributions in Figure 9.34 demonstrate the various locations of greatest consolidation over time, by applying a decreasing threshold with increasing time. This shows that the consolidation is initially relatively evenly distributed, though
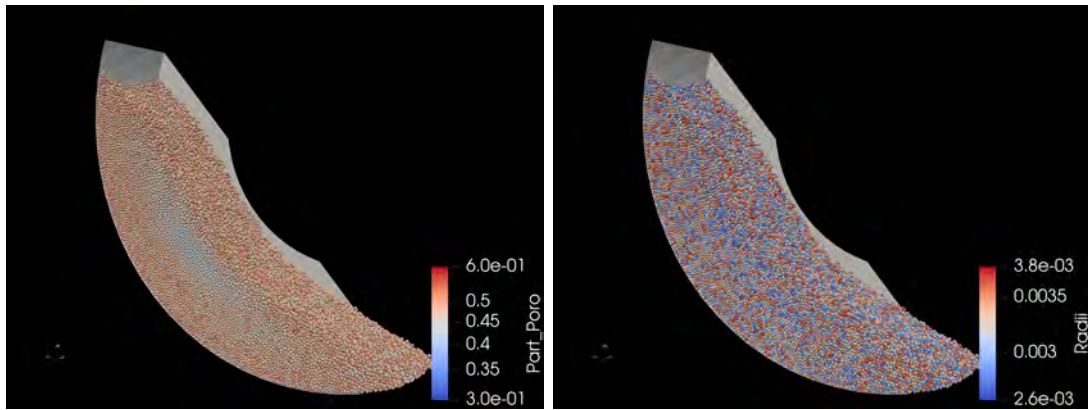
(a) An image showing the DEM Model of the Consolidation A Case. This is a consolidation simulation showing the behaviour in a small lab scale drum with spheres coloured according to Porosity.

(b) An image showing the DEM Model of the Consolidation A Case. This is a consolidation simulation showing the behaviour in a small lab scale drum with spheres coloured according to Radii.

Figure 9.33: Consolidation A final timestep. This simulation shows the effect of consolidation, and the nature that the centre has the largest extent of this.

there is an obvious clump in the centre. This may simply arise from the initial placement of the spheres, where they are simply dropped in. However, this would not account for the subsequent timesteps, where the centre clearly demonstrates consistently the greatest consolidation over time. This may contribute to the perception of induction, which will be considered in the discussion.

(a) Porosity distribution, ϵ max 0.55, $t = 4$s

(b) Porosity distribution, ϵ max 0.5, $t = 8$s

(c) Porosity distribution, ϵ max 0.45, $t = 12$s

(d) Porosity distribution, ϵ max 0.4, $t = 17$s
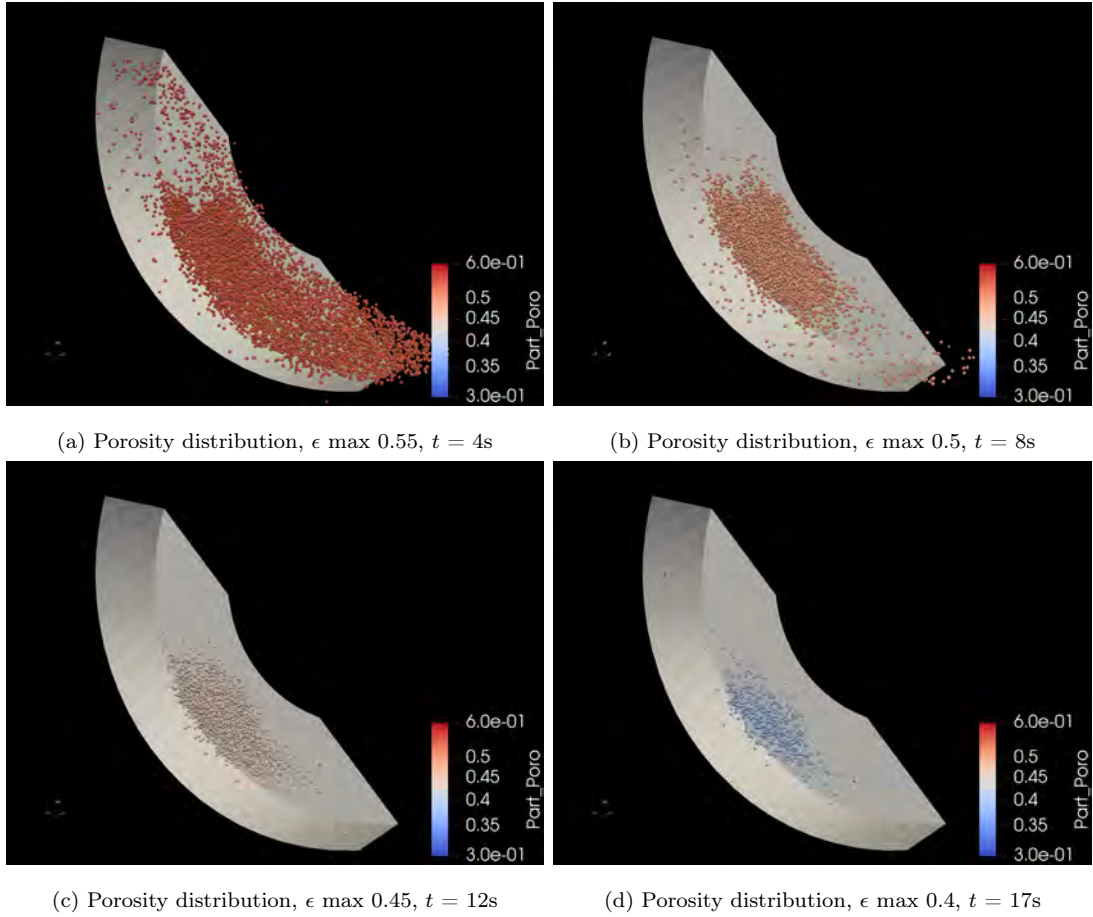
Figure 9.34: Consolidation A Porosity distributions over time with different thresholds of porosity being displayed.

9.5.1.3   Consolidation B , Table 9.7

A variety of calibration efforts went into determining a useful consolidation rate which was fast enough to demonstrate results, but not so fast that the spheres immediately consolidated on contact with the drum walls and agglomerated. Most are not shown, except for the Consolidation B , which was able to capture the appeerence of rapid growth if consolidation is very rapid.
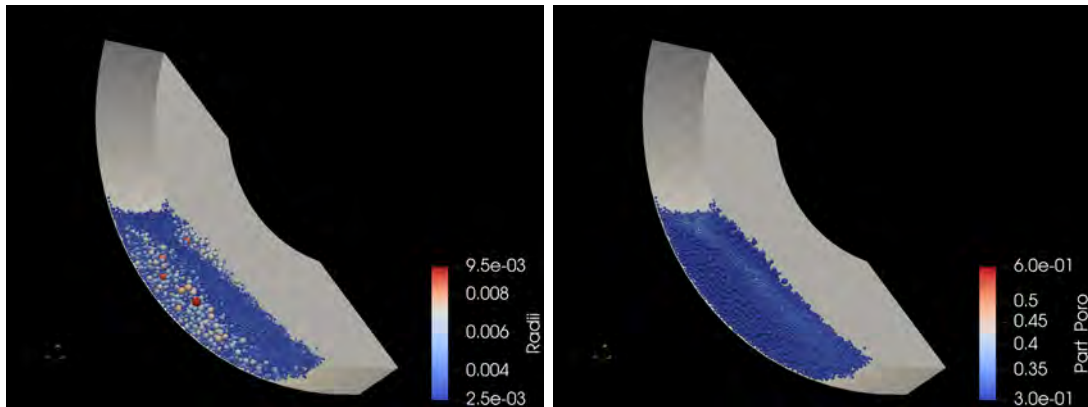
(a) An image showing the DEM Model of the Consolidation B Case. This is a consolidation simulation showing the behaviour in a small lab scale drum with spheres coloured according to Radii.

(b) An image showing the DEM Model of the Consolidation B Case. This is a consolidation simulation showing the behaviour in a small lab scale drum with spheres coloured according to Porosity.

Figure 9.35: Behaviour of the Consolidation B simulation case. $k_{\epsilon A}$ was increased 20-fold, and the consolidation is significantly increased commensurably.

Figure 9.35 shows the rapid consolidation behaviour which occurs initially along the walls. This can partially be seen in Figure 9.34a, though the effect is particularly noticable here since the saturation grows rapidly enough to permit growth. Figure 9.35b also shows how little the difference in porosity needs to be for the saturation to be significant enough to grow, with porosity variation less than 5% across all the spheres.

Figure 9.36 shows the saturation and the layers to elaborate on this further. The minor porosity difference has a much larger effect on the saturation, with the least consolidated spheres having saturations around 0.8, though most appear to
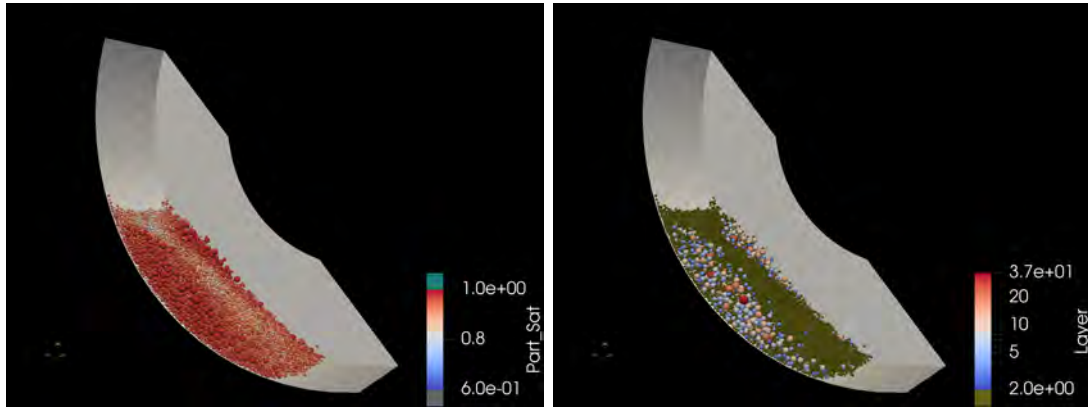
(a) An image showing the DEM Model of the Consolidation B Case. This is a consolidation simulation showing the behaviour in a small lab scale drum with spheres coloured according to Saturation.

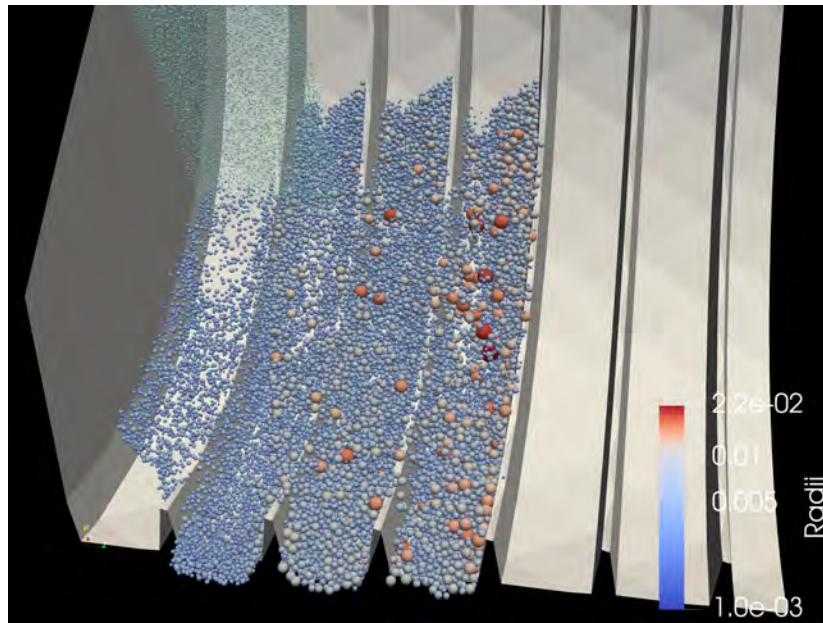(b) An image showing the DEM Model of the Consolidation B Case. This is a consolidation simulation showing the behaviour in a small lab scale drum with spheres coloured according to Layer.

Figure 9.36: Behaviour of the Consolidation B simulation case

be around 0.9. Figure 9.36b shows which spheres have or have not grown, and this does match the previously noted observations about the sphere sizes, and demonstrates that the centre explicitly has more coalescence occurring.

The consolidation appears to be primarily occurring at the boundaries with the walls. This is not due to segregation, as the saturation, seen in Figure 9.36a can also be seen to be maximal at the walls, and this is very visible when observing the behaviour at each time step, though this cannot be shown here.

Because for this case $k_{\epsilon A}$ was set relatively high, the effect of each collision was magnified. This resulted in the greatest consolidation occurring at the walls where most of the collisions were occurring, since the spheres would be slowed down more due to the shearing action of the drum wall. The strength of the individual collisions on the consolidation behaviour is less important than the total quantity. That the behaviour demonstrated is unrealistic is appropriate, as the consolidation behaviour should be more sensitive to the collision strength than the collision rate.

Even so, this is another mechanism by which the wall design may alter the

394

mixing and collision behaviour of granules when comparing between test and full scale versions when performing experiments.

9.5.1.4   Consolidation C, Table 9.7

Some full scale tests were also performed on the consolidation, since the axial flow behaviour likely affects the behaviour. Due to the large quantity of spheres in these tests, the length of time they ran for was limited.
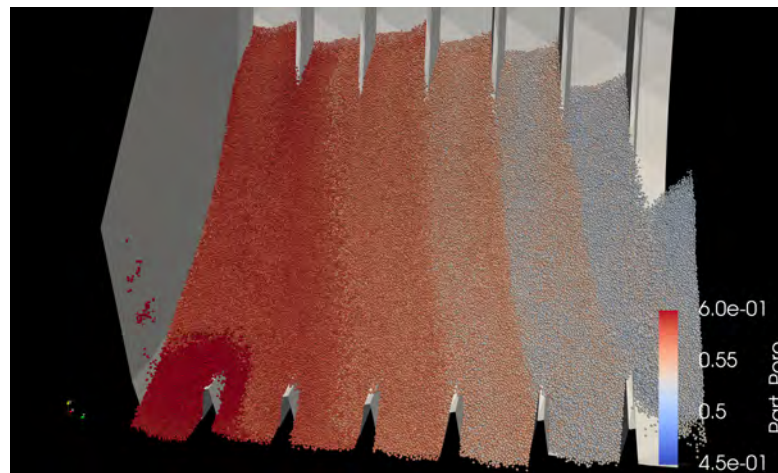
Figure 9.37: Porosity distribution of Consolidation Csimulation at the final time step simulated. The consolidation behaviour here shows the behaviour of consolidation in the full scale drum, with a reduced value of $k_{\epsilon A}$compared to the previous tests to allow for a longer simulation examining just the consolidation.

Figure 9.37 shows how the porosity decreases over time, and the periodic nature of the flow is very clear. Less clear is the time taken to establish, with the sphere flow passing to the next trough needing to fill it, and in filling it leads to the first spheres to arrive in a given trough forming the core. Due to low diffusion rates as well, these spheres will also tend to stay in this core, since only the outer spheres in the bed move through the drum.

The porosity unsurprisingly reduces as the spheres travel. This is not simply an effect of the length of time in which they have been active, as the time since the spheres contacted the walls is tracked. Figure 9.38 compares the values by showing only those spheres which have been active for a given length of time next to the spheres below a given porosity value, this is clear
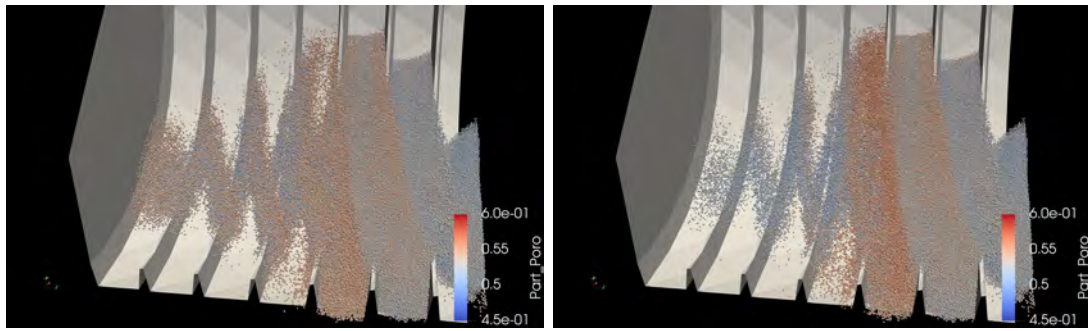
396

(a) Porosity coloured distribution, showing only those spheres below a porosity of 0.55.

(b) Porosity coloured distribution, showing only spheres which have been active for more than 12s

Figure 9.38: Consolidation Cdistribution of porosity and time partially capped, to demonstrate the location, time and consolidation relation in a complex shaped drum.

Both of the figures in Figure 9.38 show the distributions at the final time step. the main area of interest is closer to the start of the drum. Figure 9.38a shows that there are many spheres which have a porosity below 0.55 near the start which have not been active for 12s, and similarly there are some spheres which have been active for more than 12s and have porosity greater than 0.55. The centre of the drum is again shown to be a primary location of consolidation. This effect is even more clearly distinguished in Figure 9.39, where the internal path of the spheres with a porosity less than 0.5 is clearly different than those spheres with a time active longer than 17.4 seconds, which corresponds to the very first few spheres to come into contact with the wall.

9.5.1.5   Consolidation D , Table 9.7

To determine whether the diameter could be scaled and therefore model the location and rate of consolidation usefully, the spheres were doubled in diameter while all other variables kept the same. This simulation ran for longer than the previous test, however it did also crash.

The consolidation of the spheres in Consolidation D is shown in Figure 9.40 was found to be significantly slower than that in the Consolidation Ccase. A

(a) Porosity coloured distribution, showing only those spheres below a porosity of 0.5.

(b) Porosity coloured distribution, showing only spheres which have been active for more than 17.4 s
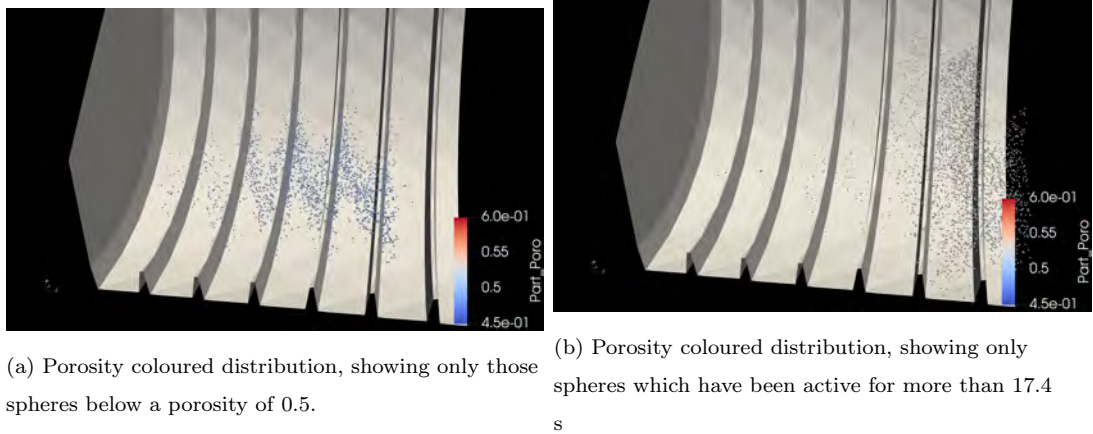
Figure 9.39: Consolidation Cdistribution of porosity and time partially capped, to demonstrate the location, time and consolidation relation in a complex shaped drum.
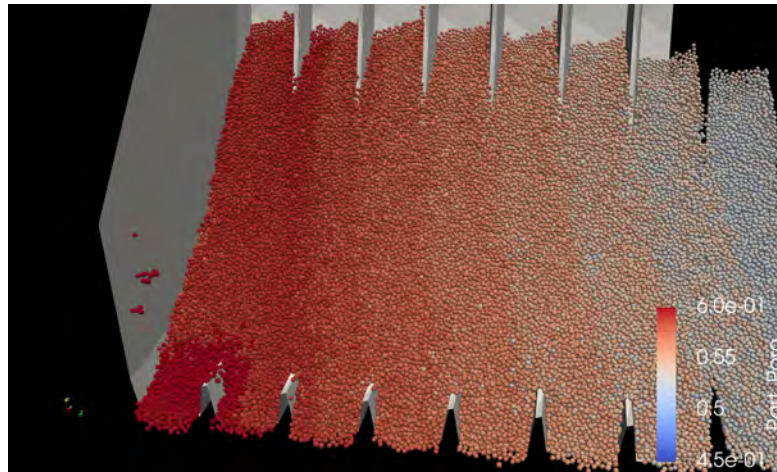
Figure 9.40: Porosity distribution of Consolidation D at the final time step simulated. This is similar to Consolidation C, however the initial sphere sizes are doubled, to evaluate scaling potential.

comparison will be made between all three of the full scale consolidation behaviours at the same timesteps to show the effects of the spheres on the porosity distributions.

For now though, the same behaviour where the length of time of consolidation does not strictly correspond to the extent of consolidation is observable in this

case and is shown in Figure 9.41.
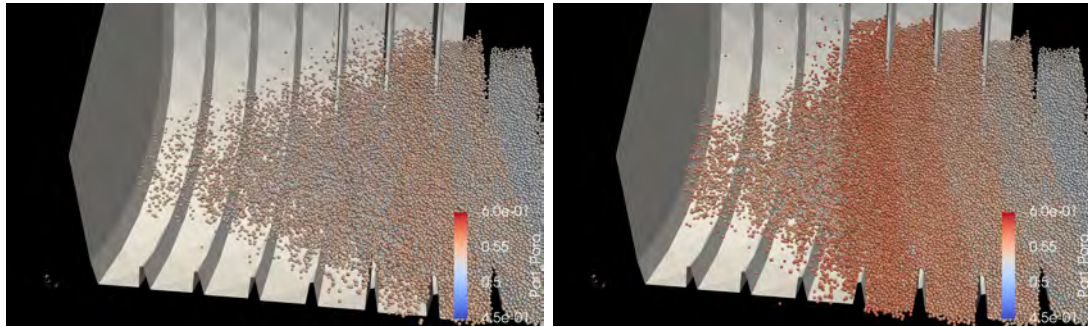
(a) Porosity coloured distribution, showing only those spheres below a porosity of 0.55.

(b) Porosity coloured distribution, showing only spheres which have been active for more than 12s

Figure 9.41: Consolidation D distribution of porosity and time partially capped, to demonstrate the location, time and consolidation relation in a complex shaped drum.

9.5.1.6   Consolidation E, Table 9.7

The diameter clearly has an effect on the rate of the process, which would be to some extent expected. However, as with all things in granular materials, the distribution of the components are also expected to have some result. The Consolidation Ecase was simulated with a mixture of half initial spheres the size found in Consolidation Cand the other half of the spheres those the size used in Consolidation D . This was hypothesised to be perhaps an average of the two. This simulation crashed even sooner than the previous two, however this was long enough to demonstrate some interesting results that highlight a current weakness of the consolidation solution as currently applied.

Figure 9.42 shows the porosity distribution of Consolidation D at $t = 15.4$s, and yet though it ran for a shorter time than even Consolidation Cit has a similar extent of consolidation, suggesting that the consolidation is faster when a mixture of sphere sizes are involved.

Figure 9.43 compares the time and porosity again, and significantly, the majority of the more consolidated spheres are from the larger sized half of the initial
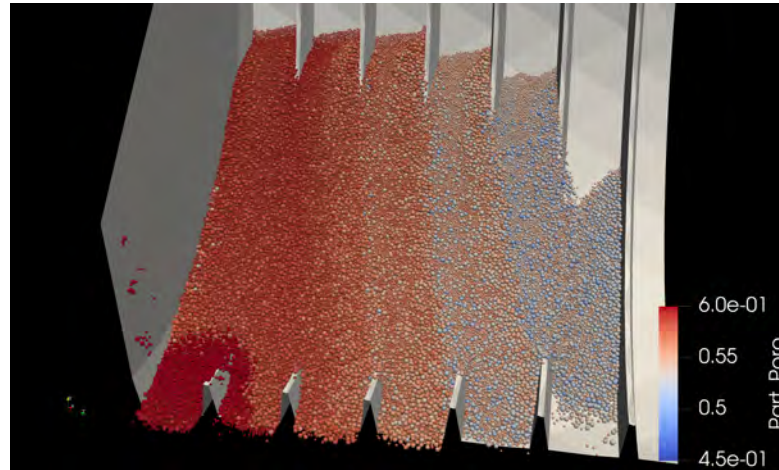
Figure 9.42: Porosity distribution Consolidation Eat the final time step simulated. This is similar to Consolidation Cand Consolidation D , the difference being that the sphere distribution added is a mixture of the two.
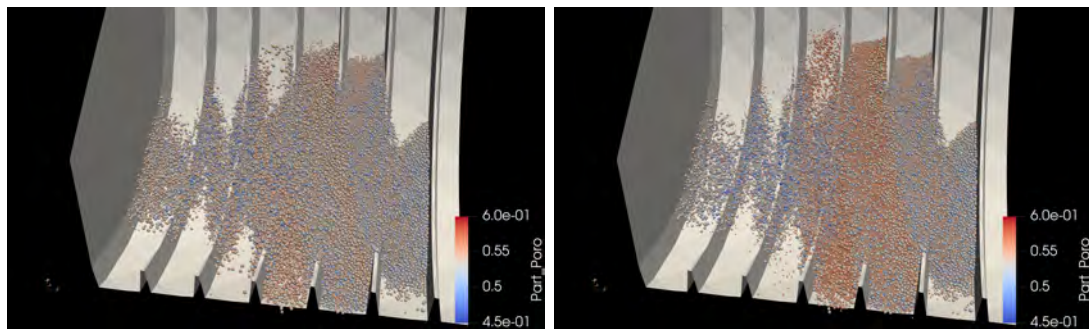
(a) Porosity coloured distribution, showing only those spheres below a porosity of 0.55.

(b) Porosity coloured distribution, showing only spheres which have been active for more than 12s

Figure 9.43: Consolidation D distribution of porosity and time partially capped, to demonstrate the location, time and consolidation relation in a complex shaped drum.

distribution. This may simply be a result of segregation pushing the largest spheres to the surface which obscures the smallest spheres, but showing only those spheres with $\epsilon < 0.5$, Figure 9.44 shows that the most consolidated spheres exclusively consist of the larger spheres.

To better understand this behaviour, some direct comparisons between the three models will be made.
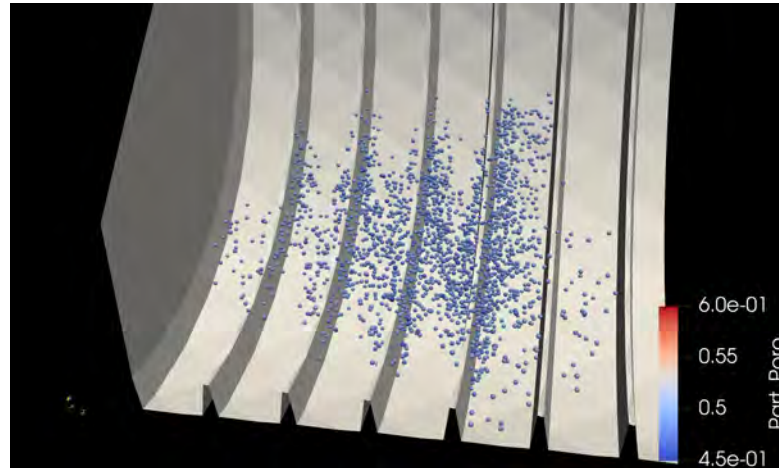
Figure 9.44: Porosity distribution at the final time step, with an upper limit of $\epsilon < 0.5$

9.5.1.7 Comparing the three ridgeCons simulations

All three models are shown together in Figure 9.45, all at the same time step. Figure 9.45 shows that the Consolidation Ecase most resembles the behaviour of Consolidation C. The minimum porosity is actually lower than that found in Consolidation C, however it actually only occurs in the largest spheres, as previously noted. The flow behaviour can also be seen to be altered by the size of the spheres. The larger spheres pass down the drum at a slower rate. All the simulations have the same volume of spheres added per second, so it is entirely the result of the size of the spheres.

However, this gives a potential method of scaling, at least for equal size spheres. If the flow rate is slower, as is the consolidation rate, then perhaps time can be used as the scale factor. This however does not seem to be applicable, or at least it is not so simple as a direct translation.

Comparing the final timestep of each, with a minimum cut-off point of the porosity of $\epsilon < 0.5$, the overall flow behaviour is significantly different, as is the locations of where the lowest porosity spheres occur. This is despite $t_{large} = 1.56t_{small}$, and so the larger spheres have had much longer to consolidate. Similar observations can be made when comparing the motion, with the porosity of the

401
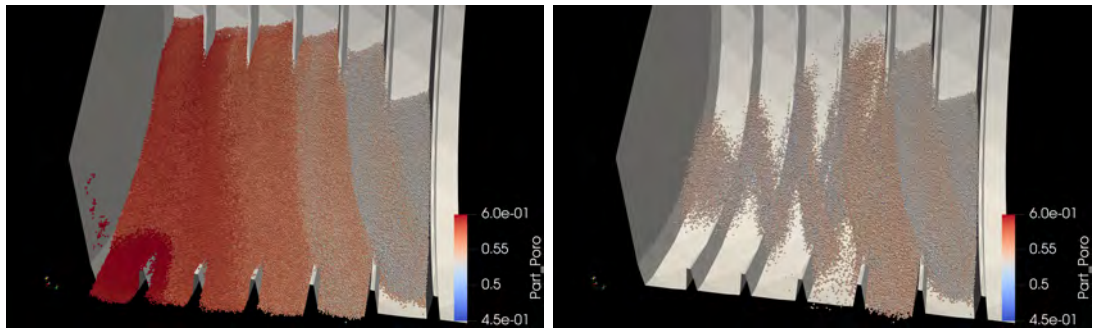
(a) Porosity coloured distribution for Consolidation C, at $t = 15.4$s

(b) Porosity coloured distribution for Consolidation C, at $t = 15.4$s, showing only spheres with $\epsilon < 0.55$
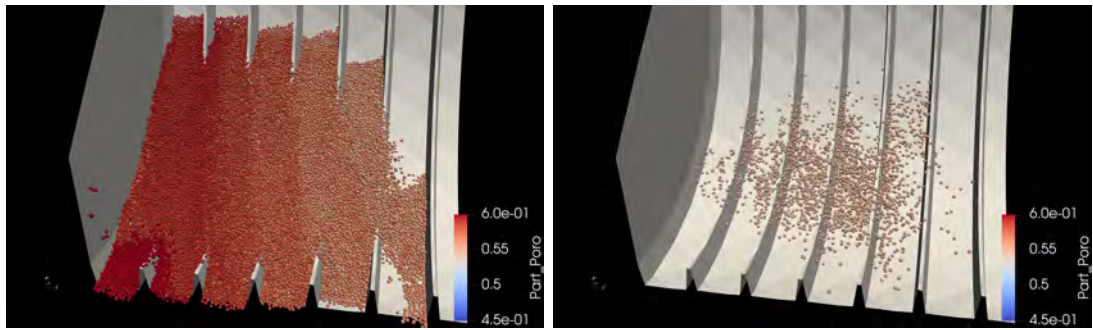
(c) Porosity coloured distribution for Consolidation D , at $t = 15.4$s

(d) Porosity coloured distribution for Consolidation D , at $t = 15.4$s, showing only spheres with $\epsilon < 0.55$
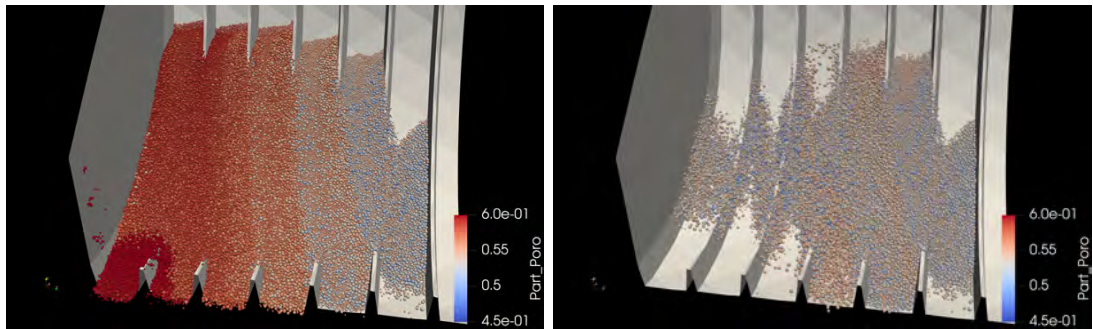
(e) Porosity coloured distribution for Consolidation E, at $t = 15.4$s

(f) Porosity coloured distribution for Consolidation E, at $t = 15.4$s, showing only spheres with $\epsilon < 0.55$

Figure 9.45: All RidgeCons cases at $t = 15.4$s, showing the full porosity distribution next to the distributions of spheres below $\epsilon < 0.55$

larger spheres being consistently lower than the smaller spheres even when the overall flow positions are similar.

The reasons for this effect is possibly the relative scale of the spheres them-
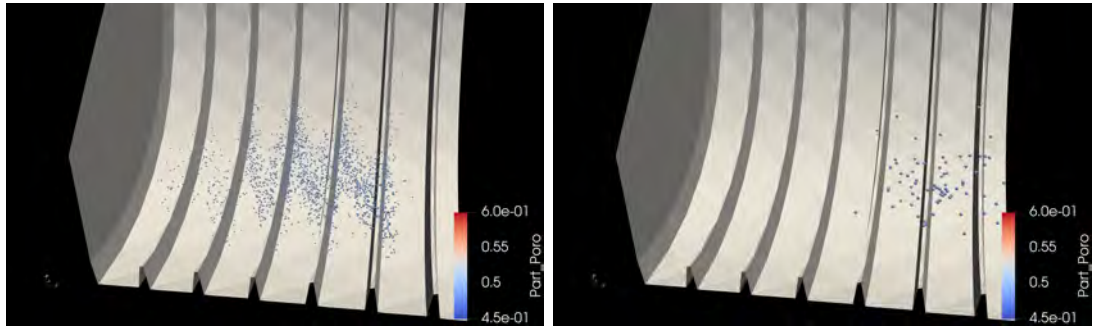
(a) Porosity coloured distribution for Consolidation C, at $t = 17.8$s showing only spheres with $\epsilon < 0.5$

(b) Porosity coloured distribution for Consolidation D , at $t = 27.9$s, showing only spheres with $\epsilon < 0.5$

Figure 9.46: Comparison of the location of minimum porosity spheres between Consolidation Cand Consolidation D

selves to the overall bed. The quantity of the collisions is likely related to the quantity of spheres encountered along the trajectory of the path. The number of collisions therefore is only slightly related to the total flow behaviour.

9.6 Discussion

The extent of the model as shown above showed many important features. A full scale model would be useful, however, ironically the problem of scaling in pelletisation has arisen again. The granular behaviour clearly depends on the size of the granules, and the quantity of the granules scales very quickly as the radius reduces for a given mass of granules. DEM has difficulties when modelling large quantities of small spheres, resulting in very long run-times and memory crashing. The three RidgeCons models took about 6 weeks to complete or rather crash. This would have to be a key feature in future programming work for this software.

The development of the agglomeration model did not all occur at the end of the project, rather it is all placed here so that all the appropriate context is available when comparing the quality of the different models. The obligation to

model the actual forces and interaction behaviours of the spheres at an individual level forced the models to reveal any weaknesses, which led to the identification of the flaws in the Stokes criterion, for example. Even the alternative solutions to model the agglomeration process in DEM that were not followed, such as the dumbbell of two bonded spheres, fed into the development of the new process. The requirement of the relative velocity being greater than average was in particular very useful in the reasoning that lead to the Adhesion-Cohesion Criterion.

The feed distribution could not be upscaled without intrinsically altering the distribution, which demonstrates another way in which the various scales interact as noted by [34]. This is observed in the various simulations where the only alteration was with the initial feed size, though this can also be shown directly from the Cohesion criterion, Equation 9.2.

$$\Delta_{limCoh} = \frac{K_g d_p}{1 - \left(\frac{S}{K_{Smax}}\right)^{\frac{1}{3}}} \tag{9.2}$$

This describes the limiting size in terms of the current saturation, however by rearranging it to determine the saturation ratio required for a given granule size, Equation 9.3 ths behaviour is easy to explain.

$$\frac{S}{K_{Smax}} < \left(1 - \frac{K_g d_p}{d_g}\right)^3 \tag{9.3}$$

In short, Equation 9.3 demonstrates a similar hyperbolic relationship of saturation requirement for the ratio of $d_p/d_{g_{comb}}$, where $d_{g_{comb}}$ is the merged granule diameter. If $d_{g_{comb}}$ can be any size, then the growth behaviour will smoothly correspond to the value of S_{comb}/K_{Smax}. However, since the initial values of the merging granules are by necessity larger than the real feed which will range from the size of the particles up to the fines of the previous batches, themselves limited to diameters of 6mm or so, then this increases the value of $d_{g_{comb}}$, and in turn raises the requirement of S_{comb}/K_{Smax}. This issue can be ignored, however, if $S_{comb} > K_{Smax}$, since at this point the granule is able to grow indefinitely. These

two factors combine in an interesting way that highlights the issue of the current inability to apply enough small spheres into the simulation.

Many spheres are undersaturated (in that when they are generated they do not satisfy Equation 9.3), and their growth is impeded until they collide with spheres which have enough of an oversaturation that it overcomes their undersaturation. During this time those spheres which are saturated at the value determined by Equation 9.3 with those which are slightly oversaturated and then reach the saturation limit, or merge with those which are oversaturated, which will result in a larger sphere which is still oversaturated. This repeats itself until all oversaturated spheres have coalesced with sufficient undersaturated spheres that they are no longer able to grow indefinitely. The larger the initial starting sizes, the higher the saturation demands are for the oversaturated spheres to make up for the undersaturated spheres to overcome.

This requirement by itself also demonstrates the fairly high saturations required for pelletisation and thus the difficulty in controlling it. Taking the median diameter of the scale particles tested previously of $d_p \approx 400$ µm, the saturation bounds of the ideal pellet sizes, (10mm to 12.5mm) are 0.907 and 0.885, which is a difference of only around 2% saturation. It is therefore not a surprise that pellet production industrially can vary significantly, even for well refined inputs.

There are some other mechanical features to understand though. The Adhesion criterion provides some stabilisation of the production output. Small-large coalescence is easier than large-mid coalescence and generally speaking easier than large-large merging, as can be seen in Figure 7.12, and even if the spheres are sprayed on the surface, they will roll down the length of the bed and along the way there will be some smaller spheres which are preferred to be picked up by the adhesion criterion.

In so doing they will also reduce their saturation, and ultimately this may allow a greater stability of output distribution. To this end, the central core of the small spheres acts as a reservoir of dryness.

405

This behaviour can be observed in the Adhesion-Cohesion tests. The spheres that go down to the bottom tend to be oversaturated, however as they get drawn back up, they encounter lots of smaller spheres, which reduce their stability. Those spheres which did not get drawn up to the bulk of the bed and instead merged with one another to form excessively large spheres, merged before the second trough had filled and started spilling over again. This transient behaviour is observed in practise, and the start of the pellet batch tends to be quite variable, before stabilising, which is promising from a modelling perspective.

The consolidation simulations gave some interesting results. For example, even for low values of $k_{\epsilon A}$, the position where the greatest extent of consolidation occurs is in the centre rather than at the bottom where the collisions are strongest. This highlights the nature of the low diffusion combined with the effect of many slightly weaker collisions that are consistently applied to the same spheres. The high collision frequency positions, in the centre of the bed where there is a large degree of shearing occurring internally, further exaggerates the sensitivity at high saturations of induction growth.

For the slower consolidation tests, the fact that the centre in the lab scale and the full scale tests showed the greatest extent of consolidation suggest a method of scaling induction behaviours, with further experimentation. Induction growth has already been shown to be scalable, and more significantly, induction based growth was scaled successfully based on the kinetic energy of the collisions [43].

This increased consolidation in the centre does not necessarily mean immediate growth however, as the collisions in the centre of the bed also tend to have weaker individual collision strengths. A small amount of variation can allow them to escape from the centre and be well suited to coalescing quickly with any surrounding spheres.

This in turn means that any sampling system where the granules are taken during the flow must account for this. The location where the largest granules can grow by dynamic means and the location where the largest granules can

grow by consolidation are in different regions of the drum. Thus induction type growth can be the result of the surface experiencing less consolidation than the centre. The inducted particles then rapidly grow once they overcome a threshold of saturation, and appear on the surface, where they are also not limited by the low collision velocities relative to the separation velocities, i.e the dynamic limits are raised. The surface particles then move to the centre of this new shape, though they have been consolidating already, and consolidate faster and have more ability to coalesce with the rapidly growing surface large granules.

The comparison between the three distributions showed that the consolidation equation needs to account for the relative size or possibly masses of the spheres being tested. Equation 6.35 only directly accounts for the velocity and density. When all the spheres are of equal size, this may not matter, however given that consolidation does itself result in a volume change as the pores are reduced, and agglomeration is also occurring, it may be pertinent to account for this in the equation.

Since the masses of the spheres colliding did not matter in the current method, given that the larger spheres were found to be consolidating significantly more, this was likely due to colliding with many of the small spheres. This is to be expected when the spheres are considered in terms of the surface areas and volume swept. Equation 6.35 likely serves well for a general statistical measure. However for individual collisions the effect of deformation of a collision may be necessary to calculate instead to appropriately scale the extent of consolidation applied to each sphere.

Despite some of the weaknesses, the DEM simulations that are produced are still very useful. They clearly demonstrate that a significant source of the size distribution is the spray system. Therefore, if the correct spray location can be found which maximises the amount of turnover of the freshly wetted spheres into the drier fines in the centre of the bed, this might produce a more consistent end product, as it can take advantage of the layering effects.

The location of the spray in combination with the drum shape may also be exploitable. Since the spheres only ever pass over the ridges, if the length of the ridge is sprayed rather than across it, this might provide a more even distribution of moisture.

9.7   Conclusion

A wide variety of models were tested, and were immensely helpful in identifying how realistic different solutions appeared, and also their flaws.

Overall the agglomeration models were hampered by the poor scaling capability of the process. Despite this they demonstrated many real effects, bimodal distribution. This distribution is shown to be primarily a consequence of the spray being applied on the surface of the spheres, and that the saturation boundary of ideal size is very tight.

The Adhesion-Cohesion model demonstrated its ability to account for many effects quite well, while also remaining physically plausible. The Adhesion criterion gives some explanation as to how there is some degree of consistency within the pellet output distributions, by requiring large pellets to collide with more force to coalesce together, despite their saturations. Instead, the large supply of drier but smaller spheres in the central fines reservoir are much more easy to merge, which also allows the larger pellets to reduce their saturation, in turn limiting further excess growth through coalescence of similar size pellets.

The smallest granules effectively hidden by size segregation leads to the next limit of the saturation not being able to penetrate inside and grow the feed granules. The smaller granules require more saturation per radius than the larger granules, which is another factor which contributes to the lack of growth of the smaller granules. The reservoir of small granules in the centre of the bed is valuable to the consistency, since without it then the larger granules would not be able to reduce their saturation easily, resulting in more excess growth.

The consolidation behaviour is modelled and provides a number of interesting results regarding the location of peak consolidation. It explains both the measured and apparent differences between the growth behaviours of induction and steady growth as partly being governed by the location of greatest consolidation.

Chapter 10

Discussion

Because the direction of the project shifted, and the early expectations of simply applying a well established agglomeration model into DEM did not come to pass for various reasons, the work has not been presented in strict chronological order. The order of the work has been re-arranged to allow a clear and consistent understanding of the process and final explanations neccesary.

The wide variety of variables (many of the most important being hard to measure), combined with the significant interaction between the behaviours explains why it has been difficult to produce consistent answers. That the field is primarily an industrial processing mechanism with a relatively low value addition relative to this complexity, that in many cases is relatively easy to simply internally recycle, also likely contributes to the low extent of research in the field.

However, on examining the literature there was also a significant amount of questionable quality work applied and conclusions drawn which are less than valid. In particular, the Stokes Criterion was the model which much of the early work of the project was built on, came apart slowly. Meanwhile other aspects of the field had been ignored for unclear reasons. For example, the drop strength has been demonstrated as being a useful tool for the examination of σ_y in a simple and relevant context of impacts.

Most of the subsequent results speak for themselves, or where they intersect, this has been clarified during the chapter discussions. The underlying mechanisms are probably the most important parts of this work. The simulation models are useful in providing some validation, but giving the underlaying mechanisms a thorough examination and drawing out the key features that need to be accounted for in any subsequent work was vital in producing a satisfactory model. The many disparate components of the mechanisms only arose because of the intense scrutiny paid to alternative models, and ultimately how natural they appeared. The Bond probability criterion was always kept in mind as it included both a growth mechanism and a limiting size, but the arrangement was extremely impractical. It was through the observation that one of the variables was not dimensionless that it could be disassembled as it was. The new form was still thought to require a collision number variable, but on checking the dimensions of the result the number of collisions would automatically have to be included in the new form, and this is why λ is so relevant, as it accounts for the probabilistic behaviour previously applied.

The new form was then combined with the surface bond strength development model to form the Adhesion criterion. This criterion still requires work, but importantly all the variables are clearly laid out, and so future development on it will be practical. Many of the variables will vary within the drum, (especially V_{ch}), however various simplifications can be justified in the short term due to the nature of the equation. For example, as applied in the DEM simulation $V_{ch} = max(V_{chmin}, V_c)$.

The Saturation criterion meanwhile was hidden away very deep in the literature, and the form in which it is originally presented is extremely impractical to work with. Because it provides a prediction of a limiting size though, it was similarly heavily investigated, with the variables re-arranged to first focus on the size of the pellet thus produced, and subsequently since it referred to mass ratios, determine what these would be in terms of volume ratios. The re-arrangement

411

into the saturation form came fairly quickly when some of the unnecessary variables were removed, variables included in the original research for experimental reasons.

The bond strength function was implemented into the Adhesion Criterion before the connection to the Saturation Criterion was realised, however this connection essentially confirmed the physicality of the Adhesion-Cohesion Criterion and locked it as the prime focus of the model. The two parts of the model are currently separate and apply separate bounds to any coalescence, but this is simply the current approximation for what is actually going on. The Cohesion criterion specifies the ideal diameter for the pellet, within some degree of statistical variation. If the pellet saturation deviates from this diameter by being in excess, then this in turn alters K_s, which then permits further growth. On the other hand, if it deviates by being deficient, then this results in a lower overall σ_y which increases the chance of breakage.

This allows the model to function quite well despite the somewhat approximate nature of the parts, as shown by the contour diagrams and growth diagrams in chapter 7. The kinetic behaviour is then subsequently shown to be significant in the analysis of the distribution problems, due to the segregation behaviour and the innate nature of the spray being applied to the surface of the drum. The fines which collect in the centre provide a buffer to prevent growth of oversaturated pellets as they are preferable to coalesce based on the Adhesion criterion, which prevents the Cohesion model from continuously agglomerating larger and larger elements, and allows some degree of consistency in the throughput.

The consolidation results are also interesting in how they demonstrate the relative importance of the collision quantity and the collision strength, as well as the importance of consideration of distribution of the pellets consolidating. The consolidation behaviour itself is conceptually fairly simple. However, the fact that the granular entropy can be used to analyse the behaviour of how particles pack together, and that the entropy actually lowers when the elements become compact

412

is messy. Further research in to the granular entropy and consolidation would be interesting, and potentially expanding this to investigating what relations can be made between this research and chemistry kinetics.

The scope of the project ended up being extremely broad, though this is likely more due to the need to re-evaluate much of the field before any useful modelling could be performed rather than the intended design of the project.

10.1   Reccomendations for Future research

There are many avenues of further research that can be built from this.

The most basic is that the yield strength of granules in a relevant context can be performed using the previously mentioned drop testing. This should be fairly simple and consistent, allowing a quantifiable comparison between different yield strength models, as well as between different binders and particle combinations.

More directly on the topic of why this work was started is the work which was partially performed but not fully investigated, which is the effect of novel drum designs on the pelletisation process, and how the altering the application of spray can be used to better control the output.

In general, the further development of the DEM simulation side. Through improved management of the memory and the underlying data systems in use, the simulations can be run for longer, and potentially with more elements or for a longer drum length, to determine what importance the full scale drums length has, or if it simply keeps the pellets moving and prevents setting of the cement.

Other systems could also be implemented into the DEM simulation. For example a ray-casting system would allow a finer mist to be modelled, with droplets of any size. More complex collision behaviours could also be implemented, with abrasion of the surfaces of elements transferring some liquid and solids. An extension of this would then be to implement fines as a larger element which continuously abrades on contact, and automatically coalesces with other fines el-

ements to maintain a lower bound for mass to maintain DEM flow characteristic stability.

Dumbbell cohesion and separation based on the same principles as the Adhesion criterion could also be another option. This could also allow some mechanism of testing K_γ , which relates the particle diameter ratios to the separating shear.

Other nondimensional constants could also be tested experimentally. These are important to the behaviour of the model, and getting stronger baselines for them would allow comparison between different pelletisation schemes, and scaling between different sizes. The same can be said for dimensioned parameters, such as λ_{ch} V_{chmin} or K_g .

Applying the Adhesion-Cohesion Criterion to other granulation models would be useful. Analytically it works, however confirming this is another matter. Potentially, it may even be able to be applied to Population balance models which account for the different properties appropriately.

Examining the inter-relation between the various phenomena in the agglomeration process and values and kinetic chemistry and granular thermodynamics as described.

Chapter 11

Conclusion

11.1   Aims evaluations

The aims of this work are re-iterated here, along with the conclusions regarding them based on this works findings.

1. Understand the composition of the Mill Sludge
   Samples of the OMS have been examined, and show that the solids are primarily comprised of scale and the oils are a mixture of the expected three oils used, which have undergone weathering processes. The solids do contain some additional tramp elements, and portland cement particles get into the settling ponds, but overall these are not major constituents. The most important feature is the size distribution of the solids, which seems well suited to low porosities due to the power curve they represent, and the surface of the scale, which appears to have a large amount of hydroxides present, which is beneficial to the pelletisation process.

2. Model the granular flow process using discrete element methods
   Models for granular flow were successfully implemented using DEM. Various Drum models are shown to be implemented, including the real sized drum.

3. Understand the kinematics of pelletisation

   The Kinematics of pelletisation were evaluated, and the importance of the segregation on both the kinetic and dynamic behaviours have been identified. Further, the effects of the geometry and system parameters are shown to be complex and inter-connected.

4. Simulate granule agglomeration

   Granule agglomeration has been simulated, with early implementations demonstrating that the solution worked, and later implementations using the subsequent models.

5. Evaluate the existing models of agglomeration
   and their effectiveness in the context of DEM

   Existing models of agglomeration were evaluated. Many which were designed for PBMs were not applicable to this work, so left out of the consideration. Others were left due to impracticalities in implementation or did not cover all the required parameters. The best agglomeration model, taken at face value, was the Stokes number model, however on detailed investigation this was found to have severe flaws in both the logic and the mechanical basis. To resolve this, several other partial solutions were found to be appropriate for describing different parts of the same behaviour, and so a new model was developed. This model is very appropriate for DEM, and has excellent room for expansion, as it accounts for the saturation, the collision, and the behaviour of the granules after the initial coalescence to some extent which is a valuable resource as it does not require a record of the history of each granules formation. This model is called the "Adhesion-Cohesion" model here.

6. Determine how to improve the granule size distribution
   using passive methods

   Determining how to improve the granule size distribution using passive

methods proved to be significantly more complex than expected. Manipulating the materials appears to be unlikely to be able to achieve this, as it is the bulk properties of the pellets such as particle diameter rather than behaviours which can be altered through additives. The kinetic behaviour also inhibits the growth of fines due to segregation, and the nature of the Cohesion criterion means that large pellets are more sensitive to increases in saturation than small pellets. The geometry of the drum, along with the spray placement, along with the general findings from this work should allow future work to be performed that will allow this to be achieved.

11.2   General summary

The general overview of these results from a purely mechanical perspective is that controlling the size of pelletisation is much more complicated than simply attempting to find the right mixture of additives, since no additives will alter the kinetic behaviour of the pelletisation process. There are many interacting parameters, and in particular the particle diameter d_p which interacts with both σ_y and Δ_{limCoh} . Different mechanisms also interact in convoluted ways. The consolidation is affected by the kinetic behaviour and the strength, which alters the saturation, and the saturation affects the size, which affects the segregation, which affects the kinetic behaviour.

The Adhesion-Cohesion Criterion, as modelled, shows great promise. It is fully physically explained, and can be modelled appropriately in DEM. The primary limitation is that pelletisation is highly dependent on the size distribution internally, which affects many of the behaviours. Attempting to model the size distribution is impractical as it is extremely taxing computationally. This aligns with pelletisation historically having difficulties regarding scaling, though it also does provide a few nondimensional variables which may be able to be applied to improve this feature in practical cases. The model has some currently open

questions, but the assumptions and sourcing for all the problems are clearly laid out and can be researched much better than previous models. Many other granular behaviours were examined and applied in the search for acceptable model for simulations, many of which do not appear to have been previously covered, at least, not in the topic of agglomeration.

The answer as to how to control the size seems to lay primarily in the kinetic behaviour, rather than the material properties. Using segregation as a mechanism for control of motion of the pellets by size, and application of moisture to the locations where the fines will grow the most using similar knowledge will allow the behaviour to be best controlled. Combine this with dynamic behaviour, to improve the preferential growth of the smaller pellets to one another rather than layering should allow the pellet size to be controlled.

Many aspect of pelletisation are very complex and the intertwining of different scales makes finding any solution very difficult. There are no simple solutions, but by recognising ones assumptions and comparing them to the real scenario that is being described then answers can be drawn out, if slowly, through theoretical understanding.

References

[1] M. Geerdes, R. Chaigneau, I. Kurunov, O. Lingiardi, and J. Ricketts, "Modern blast furnace ironmaking an Introduction," *Modern Blast Furnace Ironmaking. An Introduction*, pp. 1–218, 2009.

[2] J. Litster, "Scaleup of wet granulation processes: science not art," *Powder Technology*, vol. 130, pp. 35–40, feb 2003.

[3] S. Pohl and P. Kleinebudde, "A review of regime maps for granulation," *International Journal of Pharmaceutics*, vol. 587, no. July, p. 119660, 2020.

[4] B. J. Ennis, G. Tardos, and R. Pfeffer, "A microlevel-based characterization of granulation phenomena," *Powder Technology*, vol. 65, no. 1-3, pp. 257–272, 1991.

[5] S. M. Iveson and J. D. Litster, "Liquid-bound granule impact deformation and coefficient of restitution," *Powder Technology*, vol. 99, no. 3, pp. 234–242, 1998.

[6] L. X. Liu, J. D. Litster, S. M. Iveson, and B. J. Ennis, "Coalescence of deformable granules in wet granulation processes," *AIChE Journal*, vol. 46, no. 3, pp. 529–539, 2000.

[7] V. Smil, "Energy Costs and Environmental Impacts of Iron and Steel Production," *Still the Iron Age*, pp. 139–161, 2016.

[8] Y. dong Pei, S. li Wu, S. guo Chen, Z. xing Zhao, G. An, Z. ming Cheng, and Y. sheng Luo, "Sintering of solid waste generated in iron and steel manufacturing process in Shougang Jingtang," *Journal of Iron and Steel Research International*, vol. 24, no. 7, pp. 697–704, 2017.

[9] N. M. Gaballah, A. A. Zikry, N. A. El-Hussiny, M. G. D. Khalifa, A. E. F. Farag, and M. E. M. Shalabi, "Reducibility mill scale industrial waste via coke breeze at 850-950°C," *Science of Sintering*, vol. 47, no. 1, pp. 95–105, 2015.

[10] V. I. Shatokha, O. O. Gogenko, and S. M. Kripak, "Utilising of the oiled rolling mills scale in iron ore sintering process," *Resources, Conservation and Recycling*, vol. 55, no. 4, pp. 435–440, 2011.

[11] T. Umadevi, M. G. Sampath Kumar, P. C. Mahapatra, T. Mohan Babu, and M. Ranjan, "Recycling of steel plant mill scale via iron ore pelletisation process," *Ironmaking & Steelmaking*, vol. 36, no. 6, pp. 409–415, 2009.

[12] H. T. Makkonen, J. Heino, L. Laitila, A. Hiltunen, E. Pöyliö, and J. Härkki, "Optimisation of steel plant recycling in Finland: Dusts, scales and sludge," *Resources, Conservation and Recycling*, vol. 35, no. 1-2, pp. 77–84, 2002.

[13] Y. P. Dalal, D. Khambholja, D. Vashi, and E. Jha, "Recycling and re-utilization of steel plant waste using design of experiment : A IE28 Recycling and reutilization of steel plant waste using design of experiment : A Review," no. July, 2017.

[14] B. Liu, S. G. Zhang, J. J. Tian, D. A. Pan, Y. Liu, and A. A. Volinsky, "Recycle of valuable products from oily cold rolling mill sludge," *International Journal of Minerals, Metallurgy and Materials*, vol. 20, no. 10, pp. 941–946, 2013.

[15] B. K. Biswal, S. N. Tiwari, and S. Mukherji, "Biodegradation of oil in oily sludges from steel mills," *Bioresource Technology*, vol. 100, no. 4, pp. 1700–1703, 2009.

[16] K. Jirasripongpun, "The characterization of oil-degrading microorganisms from lubricating oil contaminated (scale) soil," *Letters in Applied Microbiology*, vol. 35, no. 4, pp. 296–300, 2002.

[17] Z. Afrassiabian, M. Leturia, M. Benali, M. Guessasma, and K. Saleh, "An overview of the role of capillary condensation in wet caking of powders," *Chemical Engineering Research and Design*, vol. 110, pp. 245–254, 2016.

[18] A. Andersson, *Recycling of Blast Furnace Sludge within the Integrated Steel Plant: Potential for Complete Recycling and Influence on Operation*. PhD thesis, 2019.

[19] L. Hooey, J. Riesbeck, J.-O. Wikström, and B. Björkman, "Role of Ferrous Raw Materials in the Energy Efficiency of Integrated Steelmaking," *ISIJ International*, vol. 54, no. 3, pp. 596–604, 2014.

[20] F. Przemysław and J. Mróz, "Ability for Self-Pelletization of Iron Ores and Magnetite Concentrates," *Journal of Iron and Steel Research International*, vol. 18, no. 6, pp. 1–7, 2011.

[21] J. Halt and S. Kawatra, "Review of organic binders for iron ore agglomeration," *Minerals and Metallurgical Processing*, vol. 31, no. 2, pp. 73–94, 2013.

[22] F. Su, H. O. Lampinen, and R. Robinson, "Recycling of sludge and dust to the BOF converter by cold bonded palletizing," *ISIJ International*, vol. 44, no. 4, pp. 770–776, 2004.

[23] S. Prakash, "Reduction and sintering of fluxed iron ore pellets-a comprehensive review," *The J. of the South African Ins. of Mining & Metallurgy*, pp. 3–16, 1996.

[24] F.-p. Tang, S.-j. Yu, P. Fei, H.-y. Hou, F. Qian, and X.-f. Wang, "Novel concept of recycling sludge and dust to BOF converter through dispersed in-situ phase induced by composite ball explosive reaction," *International Journal of Minerals, Metallurgy, and Materials*, vol. 24, no. 8, pp. 863–868, 2017.

[25] J. W. Park, J. C. Ahn, H. Song, K. Park, H. Shin, and J. S. Ahn, "Reduction characteristics of oily hot rolling mill sludge by direct reduced iron method," *Resources, Conservation and Recycling*, vol. 34, no. 2, pp. 129–140, 2002.

[26] B. Liu, S. G. Zhang, J. J. Tian, D. A. Pan, L. Meng, and Y. Liu, "New technology for recyclingmaterials from oily cold rollingmill sludge," *International Journal of Minerals, Metallurgy and Materials*, vol. 20, no. 12, pp. 1141–1147, 2013.

[27] B. Liu, S.-g. Zhang, D.-a. Pan, and C.-c. Chang, "Synthesis and Characterization of Micaceous Iron Oxide Pigment from Oily Cold Rolling Mill Sludge," *Procedia Environmental Sciences*, vol. 31, pp. 653–661, 2016.

[28] M. F. Bleeker, S. R. Kersten, and H. J. Veringa, "Pure hydrogen from pyrolysis oil using the steam-iron process," *Catalysis Today*, vol. 127, no. 1-4, pp. 278–290, 2007.

[29] D. M. Newitt and J. M. Conway-Jones, "A contribution to the theory and practice of granulation," 1958.

[30] S. K. Kawatra and V. Claremboux, "Iron Ore Pelletization: Part I. Fundamentals," *Mineral Processing and Extractive Metallurgy Review*, vol. 00, no. 00, pp. 1–16, 2021.

[31] D. Oulahna, F. Cordier, L. Galet, J. A. Dodds, D. Oulahna, F. Cordier, L. Galet, J. A. Dodds, D. Oulahna, F. Cordier, L. Galet, and J. A. Dodds, "Wet granulation : the effect of shear on granule properties To cite this version : HAL Id : hal-01593344 Wet granulation : the effect of shear on granule properties," 2018.

[32] E. L. Chan, K. Washino, H. Ahmadian, A. Bayly, Z. Alam, M. J. Hounslow, and A. D. Salman, "Dem investigation of horizontal high shear mixer flow behaviour and implications for scale-up," *Powder Technology*, vol. 270, no. PB, pp. 561–568, 2015.

[33] L. Fries, S. Antonyuk, S. Heinrich, D. Dopfer, and S. Palzer, "Collision dynamics in fluidised bed granulators: A DEM-CFD study," *Chemical Engineering Science*, vol. 86, pp. 108–123, 2013.

[34] P. R. Mort, "Scale-up of binder agglomeration processes," *Powder Technology*, vol. 150, no. 2 SPEC. ISS., pp. 86–103, 2005.

[35] S. Hogekamp, H. Schubert, and S. Wolf, "Steam jet agglomeration of water soluble material," *Powder Technology*, vol. 86, no. 1, pp. 49–57, 1996.

[36] D. G. Bika, M. Gentzler, and J. N. Michaels, "Mechanical properties of agglomerates," *Powder Technology*, vol. 117, no. 1-2, pp. 98–112, 2001.

[37] S. M. Iveson, J. D. Litster, K. Hapgood, and B. J. Ennis, "Nucleation, growth and breakage phenomena in agitated wet granulation processes: A review," *Powder Technology*, vol. 117, no. 1-2, pp. 3–39, 2001.

[38] J. D. Litster and B. J. Ennis, *The science and engineering of granulation process, Particle Technology Series, vol.15*, vol. 15. 2004.

[39] S. M. Iveson and J. D. Litster, "Growth regime map for liquid-bound granules," *AIChE Journal*, vol. 44, pp. 1510–1518, jul 1998.

[40] J. B. Wade, G. P. Martin, and D. F. Long, "Feasibility assessment for a novel reverse-phase wet granulation process: The effect of liquid saturation and binder liquid viscosity," *International Journal of Pharmaceutics*, vol. 475, no. 1, pp. 450–461, 2014.

[41] M. Butensky and D. Hyman, "Rotary Drum Granulation. An Experimental Study of the Factors Affecting Granule Size," *Industrial and Engineering Chemistry Fundamentals*, vol. 10, no. 2, pp. 212–219, 1971.

[42] G. Barnocky and R. H. Davis, "Elastohydrodynamic collision and rebound of spheres: Experimental verification," *Physics of Fluids*, vol. 31, no. 6, p. 1324, 1988.

[43] H. Nakamura, H. Fujii, and S. Watano, "Scale-up of high shear mixer-granulator based on discrete element analysis," *Powder Technology*, vol. 236, pp. 149–156, 2013.

[44] S. WATANO, Y. SATO, and K. MIYANAMI, "Scale-Up of Agitation Fluidized Bed Granulation. IV. Scale-Up Theory Based on the Kinetic Energy Similarity.," *Chemical and Pharmaceutical Bulletin*, vol. 43, no. 7, pp. 1227–1230, 1995.

[45] N. Ouchiyama and T. Tanaka, "The Probability of Coalescence in Granulation Kinetics," *Industrial and Engineering Chemistry Process Design and Development*, vol. 14, no. 3, pp. 286–289, 1975.

[46] P. Kapur, "Kinetics of granulation by non-random coalescence mechanism," *Chemical Engineering Science*, vol. 27, no. 10, pp. 1863–1869, 1972.

[47] P. A. Wauters, R. Van de Water, J. D. Litster, G. M. Meesters, and B. Scarlett, "Growth and compaction behaviour of copper concentrate granules in a rotating drum," *Powder Technology*, vol. 124, no. 3, pp. 230–237, 2002.

[48] M. Ritala, P. Holm, T. Schaefer, and H. G. Kristensen, "Influence of Liquid Bonding Strength on Power Consumption During Granulation in a High Shear Mixer," *Drug Development and Industrial Pharmacy*, vol. 14, pp. 1041–1060, jan 1988.

[49] T. Schaefer, P. Holm, and H. G. Kristensen, "Melt granulation in a laboratory scale high shear mixer," *Drug Development and Industrial Pharmacy*, vol. 16, no. 8, pp. 1249–1277, 1990.

[50] H. G. Kristensen, P. Holm, and T. Schaefer, "Mechanical properties of moist agglomerates in relation to granulation mechanisms part II. Effects of particle size distribution," *Powder Technology*, vol. 44, no. 3, pp. 239–247, 1985.

[51] J. B. Wade, G. P. Martin, and D. F. Long, "The development of a growth regime map for a novel reverse-phase wet granulation process," *International Journal of Pharmaceutics*, vol. 512, no. 1, pp. 224–233, 2016.

[52] K. Pitt, R. Peña, J. D. Tew, K. Pal, R. Smith, Z. K. Nagy, and J. D. Litster, "Particle design via spherical agglomeration: A critical review of controlling parameters, rate processes and modelling," *Powder Technology*, vol. 326, pp. 327–343, 2018.

[53] P. K. Le, P. Avontuur, M. J. Hounslow, and A. D. Salman, "The kinetics of the granulation process: Right from the early stages," *Powder Technology*, vol. 189, no. 2, pp. 149–157, 2009.

[54] J. S. Thella and R. Venugopal, "Modeling of iron ore pelletization using 3 ** (k-p) factorial design of experiments and polynomial surface regression methodology," *Powder Technology*, vol. 211, no. 1, pp. 54–59, 2011.

[55] S. WATANO, Y. SATO, K. MIYANAMI, T. MURAKAMI, Y. ITO, T. KAMATA, and N. ODA, "Scale-Up of Agitation Fluidized Bed Granulation.

425

I. Preliminary Experimental Approach for Optimization of Process Variables.," *Chemical and Pharmaceutical Bulletin*, vol. 43, no. 7, pp. 1212–1216, 1995.

[56] S. WATANO, Y. SATO, K. MIYANAMI, Y. ITO, T. KAMATA, and N. ODA, "Scale-Up of Agitation Fluidized Bed Granulation. III. Effects of Powder Feed Weight and Blade Angle on Granule Size, Density and Shape.," *Chemical and Pharmaceutical Bulletin*, vol. 43, no. 7, pp. 1224–1226, 1995.

[57] S. WATANO, Y. SATO, K. MIYANAMI, T. MURAKAMI, N. NAGAMI, Y. ITO, T. KAMATA, and N. ODA, "Scale-Up of Agitation Fluidized Bed Granulation. II. Effects of Scale, Air Flow Velocity and Agitator Rotational Speed on Granule Size, Size Distribution, Density and Shape.," *Chemical and Pharmaceutical Bulletin*, vol. 43, no. 7, pp. 1217–1220, 1995.

[58] S. WATANO, H. TAKASHIMA, and K. MIYANAMI, "Scale-Up of Agitation Fluidized Bed Granulation. V. Effect of Moisture Content on Scale-Up Characteristics.," *Chemical and Pharmaceutical Bulletin*, vol. 45, no. 4, pp. 710–714, 1997.

[59] G. I. Tardos, M. I. Khan, and P. R. Mort, "Critical parameters and limiting conditions in binder granulation of fine powders," *Powder Technology*, vol. 94, no. 3, pp. 245–258, 1997.

[60] J. S. Ramaker, M. A. Jelgersma, P. Vonk, and N. W. Kossen, "Scale-down of a high-shear pelletisation process: Flow profile and growth kinetics," *International Journal of Pharmaceutics*, vol. 166, no. 1, pp. 89–97, 1998.

[61] T. Schaefer, P. Holm, and H. G. Kristensen, "Wet granulation in a laboratory scale high shear mixer," *Pharmazeutische Industrie*, vol. 52, no. 9, p. 1147 1153, 1990.

[62] S. Watano, T. Okamoto, Y. Sato, and Y. Osako, "Scale-Up of High Shear Granulation Based on the Internal Stress Measurement," *Chemical and Pharmaceutical Bulletin*, vol. 53, no. 4, pp. 351–354, 2005.

[63] T. C. Eisele and S. K. Kawatra, "A review of binders in iron ore pelletization," *Mineral Processing and Extractive Metallurgy Review*, vol. 24, no. 1, pp. 1–90, 2003.

[64] S. T. Keningley, P. C. Knight, and A. D. Marson, "An investigation into the effects of binder viscosity on agglomeration behaviour," *Powder Technology*, vol. 91, no. 2, pp. 95–103, 1997.

[65] M. Błaszczyk, A. Heim, and T. P. Olejnik, "The Effect of Wetting on The Course of The Drum Granulation," *Chemical and Process Engineering*, vol. 38, no. 2, pp. 331–342, 2017.

[66] T. Nguyen, "Percolation concentration threshold: Connecting the murky region between hydrophilic and hydrophobic wet granulation," 01 2010.

[67] P. C. Kapur and D. W. Fuerstenau, "Coalescence Model for Granulation," *Industrial & Engineering Chemistry Process Design and Development*, vol. 8, pp. 56–62, jan 1969.

[68] P. A. Wauters, R. B. Jakobsen, J. D. Litster, G. M. Meesters, and B. Scarlett, "Liquid distribution as a means to describing the granule growth mechanism," *Powder Technology*, vol. 123, no. 2-3, pp. 166–177, 2002.

[69] R. Ramachandran, J. M. Poon, C. F. Sanders, T. Glaser, C. D. Immanuel, F. J. Doyle, J. D. Litster, F. Stepanek, F. Y. Wang, and I. T. Cameron, "Experimental studies on distributions of granule size, binder content and porosity in batch drum granulation: Inferences on process modelling requirements and process sensitivities," *Powder Technology*, vol. 188, no. 2, pp. 89–101, 2008.

[70] K. P. Hapgood, J. D. Litster, S. R. Biggs, and T. Howes, "Drop penetration into porous powder beds," *Journal of Colloid and Interface Science*, vol. 253, no. 2, pp. 353–366, 2002.

[71] M. J. Hounslow, M. Oullion, and G. K. Reynolds, "Kinetic models for granule nucleation by the immersion mechanism," *Powder Technology*, vol. 189, no. 2, pp. 177–189, 2009.

[72] K. P. Hapgood, J. D. Litster, and R. Smith, "Nucleation regime map for liquid bound granules," *AIChE Journal*, vol. 49, no. 2, pp. 350–361, 2003.

[73] R. Plank, B. Diehl, H. Grinstead, and J. Zega, "Quantifying liquid coverage and powder flux in high-shear granulators," *Powder Technology*, vol. 134, no. 3, pp. 223–234, 2003.

[74] H. R. Charles-Williams, R. Wengeler, K. Flore, H. Feise, M. J. Hounslow, and A. D. Salman, "Granule nucleation and growth: Competing drop spreading and infiltration processes," *Powder Technology*, vol. 206, no. 1-2, pp. 63–71, 2011.

[75] T. Glaser, C. F. Sanders, F. Y. Wang, I. T. Cameron, J. D. Litster, J. M. Poon, R. Ramachandran, C. D. Immanuel, and F. J. Doyle, "Model predictive control of continuous drum granulation," *Journal of Process Control*, vol. 19, no. 4, pp. 615–622, 2009.

[76] R. Ramachandran and A. Chaudhury, "Model-based design and control of a continuous drum granulation process," *Chemical Engineering Research and Design*, vol. 90, no. 8, pp. 1063–1073, 2012.

[77] D. Barrasso and R. Ramachandran, "Multi-scale modeling of granulation processes: Bi-directional coupling of PBM with DEM via collision frequencies," *Chemical Engineering Research and Design*, vol. 93, pp. 304–317, 2015.

[78] K. V. Sastry, P. Dontula, and C. Hosten, "Investigation of the layering mechanism of agglomerate growth during drum pelletization," *Powder Technology*, vol. 130, no. 1-3, pp. 231–237, 2003.

[79] P. C. Kapur and V. Runkana, "Balling and granulation kinetics revisited," *International Journal of Mineral Processing*, vol. 72, no. 1-4, pp. 417–427, 2003.

[80] G. K. Reynolds, J. S. Fu, Y. S. Cheong, M. J. Hounslow, and A. D. Salman, "Breakage in granulation: A review," *Chemical Engineering Science*, vol. 60, no. 14, pp. 3969–3992, 2005.

[81] D. A. Pohlman and J. D. Litster, "Coalescence model for induction growth behavior in high shear granulation," *Powder Technology*, vol. 270, no. PB, pp. 435–444, 2015.

[82] S. M. Iveson, P. A. Wauters, S. Forrest, J. D. Litster, G. M. Meesters, and B. Scarlett, "Growth regime map for liquid-bound granules: Further development and experimental validation," *Powder Technology*, vol. 117, no. 1-2, pp. 83–97, 2001.

[83] M. J. Hounslow, R. L. Ryall, and V. R. Marshall, "A discretized population balance for nucleation, growth, and aggregation," *AIChE Journal*, vol. 34, no. 11, pp. 1821–1832, 1988.

[84] M. J. Hounslow, J. M. Pearson, and T. Instone, "Tracer studies of high-shear granulation: II. Population balance modeling," *AIChE Journal*, vol. 47, no. 9, pp. 1984–1999, 2001.

[85] P. Tandon and D. E. Rosner, "Monte Carlo simulation of particle aggregation and simultaneous restructuring," *Journal of Colloid and Interface Science*, vol. 213, no. 2, pp. 273–286, 1999.

[86] J. Bouffard, F. Bertrand, and J. Chaouki, "A multiscale model for the simulation of granulation in rotor-based equipment," *Chemical Engineering Science*, vol. 81, pp. 106–117, 2012.

[87] B. J. Ennis, "Agglomeration and size enlargement session summary paper," *Powder Technology*, vol. 88, no. 3, pp. 203–225, 1996. First International Particle Technology Forum.

[88] F. Hoornaert, P. A. Wauters, G. M. Meesters, S. E. Pratsinis, and B. Scarlett, "Agglomeration behaviour of powders in a Lodige mixer granulator," *Powder Technology*, vol. 96, no. 2, pp. 116–128, 1998.

[89] M. Adepu, S. Hate, A. Bétard, S. Oka, M. Schongut, M. Sen, Y. Sood, D. Wolf, S. Wieland, F. Stepanek, F. Muzzio, B. Glasser, and R. Ramachandran, "Quantitative validation and analysis of the regime map approach for the wet granulation of industrially relevant zirconium hydroxide powders," *Powder Technology*, vol. 294, no. December 2017, pp. 177–184, 2016.

[90] A. C. Santomaso, R. Baggio, F. Zorzi, G. Salviulo, N. Realdon, and E. Franceschinis, "Sugars with different thickening power in high shear granulation," *Powder Technology*, vol. 317, pp. 391–399, 2017.

[91] P. K. Le, P. Avontuur, M. J. Hounslow, and A. D. Salman, "A microscopic study of granulation mechanisms and their effect on granule properties," *Powder Technology*, vol. 206, no. 1-2, pp. 18–24, 2011.

[92] R. Alizadeh, J. J. Beaudoin, and L. Raki, "Mechanical properties of calcium silicate hydrates," *Materials and Structures/Materiaux et Constructions*, vol. 44, no. 1, pp. 13–28, 2011.

[93] H. Rumpf and H. Schubert, "The behavior of agglomerates under tensile strain," *Journal of Chemical Engineering of Japan*, vol. 7, no. 4, pp. 294–298, 1974.

[94] H. Schubert, W. Herrmann, and H. Rumpf, "Deformation behaviour of agglomerates under tensile stress," *Powder Technology*, vol. 11, no. 2, pp. 121–131, 1975.

[95] K. Van Den Dries and H. Vromans, "Relationship between inhomogeneity phenomena and granule growth mechanisms in a high-shear mixer," *International Journal of Pharmaceutics*, vol. 247, no. 1-2, pp. 167–177, 2002.

[96] F. Chen, Y. feng Guo, T. Jiang, F. qiang Zheng, S. Wang, and L. zhi Yang, "Effects of high pressure roller grinding on size distribution of vanadium-titanium magnetite concentrate particles and improvement of green pellet strength," *Journal of Iron and Steel Research International*, vol. 24, no. 3, pp. 266–272, 2017.

[97] P. C. Knight, "Structuring agglomerated products for improved performance," *Powder Technology*, vol. 119, no. 1, pp. 14–25, 2001.

[98] K. Johanson, Y. Rabinovich, B. Moudgil, K. Breece, and H. Taylor, "Relationship between particle scale capillary forces and bulk unconfined yield strength," *Powder Technology*, vol. 138, no. 1, pp. 13–17, 2003.

[99] T. Wollborn, M. F. Schwed, and U. Fritsching, "Direct tensile tests on particulate agglomerates for the determination of tensile strength and interparticle bond forces," *Advanced Powder Technology*, vol. 28, no. 9, pp. 2177–2185, 2017.

[100] S. M. Iveson, J. A. Beathe, and N. W. Page, "The dynamic strength of partially saturated powder compacts: The effect of liquid properties," *Powder Technology*, vol. 127, no. 2, pp. 149–161, 2002.

[101] J. P. Wang, E. Gallo, B. François, F. Gabrieli, and P. Lambert, "Capillary force and rupture of funicular liquid bridges between three spherical bodies," *Powder Technology*, vol. 305, no. January, pp. 89–98, 2017.

[102] G. Lian, C. Thornton, and M. J. Adams, "A Theoretical Study of the Liquid Bridge Forces between Two Rigid Spherical Bodies," *Journal of Colloid and Interface Science*, vol. 161, pp. 138–147, nov 1993.

[103] H. N. G. Nguyen, O. Millet, and G. Gagneux, "Liquid bridges between a sphere and a plane - Classification of meniscus profiles for unknown capillary pressure," *Mathematics and Mechanics of Solids*, vol. 24, no. 10, pp. 3042–3060, 2019.

[104] F. Radjai and V. Richefeu, "Bond anisotropy and cohesion of wet granular materials," *Philosophical Transactions of the Royal Society A: Mathematical, Physical and Engineering Sciences*, vol. 367, no. 1909, pp. 5123–5138, 2009.

[105] L. X. Liu, R. Smith, and J. D. Litster, "Wet granule breakage in a breakage only high-hear mixer: Effect of formulation properties on breakage behaviour," *Powder Technology*, vol. 189, no. 2, pp. 158–164, 2009.

[106] P. Pierrat and H. S. Caram, "Tensile strength of wet granular materials," *Powder Technology*, vol. 91, no. 2, pp. 83–93, 1997.

[107] H. Louati, D. Oulahna, A. de Ryck, and A. D. Ryck, "Effect of the particle size and the liquid content on the shear behaviour of wet granular material," *Powder Technology*, vol. 315, pp. 398–409, 2017.

[108] S. M. Iveson, N. W. Page, and J. D. Litster, "The importance of wet-powder dynamic mechanical properties in understanding granulation," *Powder Technology*, vol. 130, no. 1-3, pp. 97–101, 2003.

[109] S. M. Iveson and N. W. Page, "Brittle to Plastic Transition in the Dynamic Mechanical Behavior of Partially Saturated Granular Materials," *Journal of Applied Mechanics, Transactions ASME*, vol. 71, no. 4, pp. 470–475, 2004.

[110] S. M. Iveson and N. W. Page, "Dynamic strength of liquid-bound granular materials: The effect of particle size and shape," *Powder Technology*, vol. 152, no. 1-3, pp. 79–89, 2005.

[111] R. M. Smith, *Wet Granule Breakage in High Shear Mixer Granulators*. PhD thesis, The University of Queensland, 2005.

[112] M. Badetti, A. Fall, F. Chevoir, P. Aimedieu, S. Rodts, and J. N. Roux, "Rheology and microstructure of unsaturated granular materials: Experiments and simulations," *arXiv*, vol. 1175, 2018.

[113] R. Kandasami and T. Murthy, "Effect of particle shape on the mechanical response of a granular ensemble," *Geomechanics from Micro to Macro*, no. August, pp. 1093–1098, 2014.

[114] M. R. Brake, "An analytical elastic-perfectly plastic contact model," *International Journal of Solids and Structures*, vol. 49, no. 22, pp. 3129–3141, 2012.

[115] M. Dinkgreve, J. Paredes, M. M. Denn, and D. Bonn, "On different ways of measuring "the" yield stress," *Journal of Non-Newtonian Fluid Mechanics*, vol. 238, pp. 233–241, 2016.

[116] S. P. Forsmo, A. J. Apelqvist, B. M. Björkman, and P. O. Samskog, "Binding mechanisms in wet iron ore green pellets with a bentonite binder," *Powder Technology*, vol. 169, no. 3, pp. 147–158, 2006.

[117] M. Scheel, R. Seemann, M. Brinkmann, M. Di Michiel, A. Sheppard, B. Breidenbach, and S. Herminghaus, "Morphological clues to wet granular pilestability," *Nature Materials*, vol. 7, no. 3, pp. 189–193, 2008.

[118] N. Mitarai and F. Nori, "Wet granular materials," *Advances in Physics*, vol. 55, no. 1-2, pp. 1–45, 2006.

[119] P. Holm, T. Schaefer, and H. G. Kristensen, "Granulation in high-speed mixers Part V. Power consumption and temperature changes during granulation," *Powder Technology*, vol. 43, no. 3, pp. 213–223, 1985.

[120] N. Berger, E. Azéma, J. F. Douce, and F. Radjai, "Scaling behaviour of cohesive granular flows," *Epl*, vol. 112, no. 6, 2015.

[121] V. Richefeu, M. S. El Youssoufi, E. Azéma, and F. Radjaï, "Force transmission in dry and wet granular media," *Powder Technology*, vol. 190, no. 1-2, pp. 258–263, 2009.

[122] J. Lin and W. Wu, "A comparative study between DEM and micropolar hypoplasticity," *Powder Technology*, vol. 293, pp. 121–129, 2016.

[123] N. Mitarai and H. Nakanishi, "Simple model for wet granular materials with liquid clusters," *Epl*, vol. 88, no. 6, 2009.

[124] J. Y. Delenne, F. Soulié, M. S. El Youssoufi, and F. Radjai, "Compressive strength of an unsaturated granular material during cementation," *Powder Technology*, vol. 208, no. 2, pp. 308–311, 2011.

[125] G. V. Franks, M. L. Sesso, M. Lam, Y. Lu, and L. Xu, "Elastic plastic fracture mechanics investigation of toughness of wet colloidal particulate materials: Influence of saturation," *Journal of Colloid and Interface Science*, vol. 581, pp. 627–634, 2021.

[126] M. De Stefani, *Mechanistic analysis of the dynamic strength of wet granular materials*. PhD thesis, 2019.

[127] I. Mehdipour and K. H. Khayat, "Understanding the role of particle packing characteristics in rheo-physical properties of cementitious suspensions: A literature review," *Construction and Building Materials*, vol. 161, pp. 340–353, 2018.

[128] S. I. Farag Badawy and M. A. Hussain, "Effect of starting material particle size on its agglomeration behavior in high shear wet granulation," *AAPS PharmSciTech*, vol. 5, no. 3, pp. 1–7, 2004.

[129] J. Tsubaki and G. Jimbo, "Theoretical analysis of the tensile strength of a powder bed," *Powder Technology*, vol. 37, no. 1, pp. 219–227, 1984.

[130] C. D. Willett, M. J. Adams, S. A. Johnson, and J. P. Seville, "Capillary bridges between two spherical bodies," *Langmuir*, vol. 16, no. 24, pp. 9396–9405, 2000.

[131] S. M. Iveson, S. Holt, and S. Biggs, "Contact angle measurements of iron ore powders," *Colloids and Surfaces A: Physicochemical and Engineering Aspects*, vol. 166, pp. 203–214, jun 2000.

[132] X. B. Huang, X. W. Lv, J. J. Song, C. G. Bai, R. D. Zhang, and M. J. Zhou, "Contact angle of water on iron ore fines: Measurement and analysis," *Journal of Mining and Metallurgy, Section B: Metallurgy*, vol. 51, no. 1, pp. 33–40, 2015.

[133] C. Retnhardf, "1 The Iron Oxides," pp. 5–18, 2001.

[134] N. M. Gaballah, A. A. Zikry, N. A. El-Hussiny, M. G. D. Khalifa, A. E. F. Farag, and M. E. M. Shalabi, "Reducibility mill scale industrial waste via coke breeze at 850-950°C," *Science of Sintering*, vol. 47, no. 1, pp. 95–105, 2015.

[135] E. Koos, "Capillary suspensions: Particle networks formed through the capillary force," *Current Opinion in Colloid & Interface Science*, vol. 19, pp. 575–584, dec 2014.

[136] M. Fingas, *Oil Spill Science and Technology*. Saint Louis, UNITED STATES: Elsevier Science & Technology, 2010.

[137] A. Deblais, R. Harich, D. Bonn, A. Colin, and H. Kellay, "Spreading of an Oil-in-Water Emulsion on a Glass Plate: Phase Inversion and Pattern Formation," *Langmuir*, vol. 31, no. 22, pp. 5971–5981, 2015.

[138] C. G. De Mendonça, C. G. Raetano, and C. G. De Mendonça, "Surface tension of mineral oils and vegetable oils," *Engenharia Agricola*, vol. 27, no. SPEC. ISS., pp. 16–23, 2007.

[139] M. Fingas, "Behaviour of Oil in the Environment," in *The Basics of Oil Spill Cleanup, Second Edition*, CRC Press, sep 2000.

[140] B. Hollebone, "Oil Physical Properties: Measurement and Correlation," in *Oil Spill Science and Technology: Second Edition*, pp. 185–207, Elsevier, 2017.

[141] K. Obla, H. Kim, and C. Lobo, "Effect of Continuous (Well-Graded) Combined Aggregate Grading on Concrete Performance, Phase A: Aggregate Voids Content (Packing Density)," *NRMCA Research Laboratory*, p. 29, 2007.

[142] K. Obla, H. Kim, and C. Lobo, "Effect of Continuous (Well-Graded) Combined Aggregate Grading on Concrete Performance, Phase B: Concrete Performance," *NRMCA Research Laboratory*, p. 29, 2007.

[143] M. Kang and L. Weibin, "Effect of the Aggregate Size on Strength Properties of Recycled Aggregate Concrete," *Advances in Materials Science and Engineering*, vol. 2018, pp. 1–8, 2018.

[144] V. K. Singh and U. K. Mandal, "Effect of lime on the properties of portland cement," *Transactions of the Indian Ceramic Society*, vol. 39, no. 5, pp. 161–164, 1980.

[145] N. Shafiq, C. S. Choo, and M. H. Isa, "Effects of used engine oil on slump, compressive strength and oxygen permeability of normal and blended ce-

ment concrete," *Construction and Building Materials*, vol. 187, pp. 178–184, 2018.

[146] R. Cepuritis, S. Jacobsen, S. Smeplass, E. Mørtsell, B. J. Wigum, and S. Ng, "Influence of crushed aggregate fines with micro-proportioned particle size distributions on rheology of cement paste," *Cement and Concrete Composites*, vol. 80, pp. 64–79, 2017.

[147] L. Struble and G. K. Sun, "Viscosity of Portland cement paste as a function of concentration," *Advanced Cement Based Materials*, vol. 2, no. 2, pp. 62–69, 1995.

[148] R. Ylmén, U. Jäglid, B. M. Steenari, and I. Panas, "Early hydration and setting of Portland cement monitored by IR, SEM and Vicat techniques," *Cement and Concrete Research*, vol. 39, no. 5, pp. 433–439, 2009.

[149] K. L. Scrivener, *THE DEVELOPMENT OF MICROSTRUCTURE DURING THE HYDRATION OF PORTLAND CEMENT*. PhD thesis, 1984.

[150] L. M. Amaratunga, "Cold-bond agglomeration of reactive pyrrhotite tailings for backfill using low cost binders: Gypsum β-hemihydrate and cement," *Minerals Engineering*, vol. 8, no. 12, pp. 1455–1465, 1995.

[151] I. U. Bhuiyan, J. Mouzon, B. Schröppel, A. Kaech, I. Dobryden, S. P. Forsmo, and J. Hedlund, "Microstructure of bentonite in iron ore green pellets," *Microscopy and Microanalysis*, vol. 20, no. 1, pp. 33–41, 2014.

[152] J. R. Field and A. P. Allen, Apr 1994.

[153] S. Iveson and N. Page, "Tensile bond strength development between liquid-bound pellets during compression," *Powder Technology*, vol. 117, pp. 113–122, jun 2001.

[154] R. Hogg, "Mixing and segregation in powders: Evaluation, mechanisms and processes," *KONA Powder and Particle Journal*, vol. 27, no. 27, pp. 3–17, 2009.

[155] J. M. N. T. Gray, "Particle Segregation in Dense Granular Flows," *Annual Review of Fluid Mechanics*, vol. 50, pp. 407–433, 2018.

[156] M. J. Metzger, B. Remy, and B. J. Glasser, "All the Brazil nuts are not on top: Vibration induced granular size segregation of binary, ternary and multi-sized mixtures," *Powder Technology*, vol. 205, no. 1-3, pp. 42–51, 2011.

[157] J. Mellmann, "The transverse motion of solids in rotating cylinders-forms of motion and transition behavior," *Powder Technology*, vol. 118, no. 3, pp. 251–270, 2001.

[158] X. Li, Y. Feng, and G. Mustoe, "Understanding Size Segregation in Tumbling mills," *Springer Proceedings in Physics*, vol. 188, no. December 2017, pp. v–vi, 2017.

[159] J. W. Vallance and S. B. Savage, "Particle Segregation in Granular Flows Down Chutes," pp. 31–51, 2000.

[160] C. Wightman and F. J. Muzzio, "Mixing of granular material in a drum mixer undergoing rotational and rocking motions II. Segregating particles," *Powder Technology*, vol. 98, pp. 125–134, aug 1998.

[161] D. Geromichalos, M. M. Kohonen, F. Mugele, and S. Herminghaus, "Mixing and Condensation in a Wet Granular Medium," *Physical Review Letters*, vol. 90, no. 16, p. 4, 2003.

[162] N. S. Cheng and K. Zhao, "Difference between static and dynamic angle of repose of uniform sediment grains," *International Journal of Sediment Research*, vol. 32, no. 2, pp. 149–154, 2017.

[163] A. A. Adetayo, J. D. Litster, and M. Desai, "The effect of process parameters on drum granulation of fertilizers with broad size distributors," *Chemical Engineering Science*, vol. 48, no. 23, pp. 3951–3961, 1993.

[164] M. H. Wang, R. Y. Yang, and A. B. Yu, "DEM investigation of energy distribution and particle breakage in tumbling ball mills," *Powder Technology*, vol. 223, pp. 83–91, 2012.

[165] I. Govender, M. C. Richter, A. N. Mainza, and D. N. D. Klerk, "A Positron Emission Particle Tracking Investigation of the Scaling Law Governing Free Surface Flows in Tumbling Mills," vol. 63, no. 3, pp. 903–913, 2017.

[166] R. L. Jackson, I. Green, and D. B. Marghitu, "Predicting the coefficient of restitution of impacting elastic-perfectly plastic spheres," *Nonlinear Dynamics*, vol. 60, no. 3, pp. 217–229, 2010.

[167] T. Schwager, V. Becker, and T. Pöschel, "Coefficient of tangential restitution for viscoelastic spheres," *European Physical Journal E*, vol. 27, no. 1, pp. 107–114, 2008.

[168] M. E. D. Urso, C. J. Lawrence, and M. J. Adams, "Pendular, funicular, and capillary bridges: Results for two dimensions," *Journal of Colloid and Interface Science*, vol. 220, no. 1, pp. 42–56, 1999.

[169] M. Scheel, R. Seemann, M. Brinkmann, M. Di Michiel, A. Sheppard, B. Breidenbach, and S. Herminghaus, "Morphological clues to wet granular pilestability," *Nature Materials*, vol. 7, no. 3, pp. 189–193, 2008.

[170] X. Lv, C. Bai, G. Qiu, S. Zhang, and M. Hu, "Moisture capacity: Definition, measurement and application in determining the optimal water content in granulating," *ISIJ International*, vol. 50, no. 5, pp. 695–701, 2010.

[171] C. L. Flemmer, "On the regime boundaries of moisture in granular materials," *Powder Technology*, vol. 66, no. 2, pp. 191–194, 1991.

[172] A. K. Kwan and W. W. Fung, "Packing density measurement and modelling of fine aggregate and mortar," *Cement and Concrete Composites*, vol. 31, no. 6, pp. 349–357, 2009.

[173] A. K. Kwan, V. Wong, and W. W. Fung, "A 3-parameter packing density model for angular rock aggregate particles," *Powder Technology*, vol. 274, pp. 154–162, 2015.

[174] G. Roquier, "The 4-parameter Compressible Packing Model (CPM) for crushed aggregate particles," *Powder Technology*, vol. 320, pp. 133–142, 2017.

[175] H. J. Brouwers, "Particle-size distribution and packing fraction of geometric random packings," *Physical Review E - Statistical, Nonlinear, and Soft Matter Physics*, vol. 74, no. 3, pp. 1–15, 2006.

[176] K. Sobolev and A. Amirjanov, "Application of genetic algorithm for modeling of dense packing of concrete aggregates," *Construction and Building Materials*, vol. 24, no. 8, pp. 1449–1455, 2010.

[177] M. Wackenhut, S. McNamara, and H. J. Herrmann, "A hierarchical model for simulating very polydisperse granular media," *Powders and Grains 2005 - Proceedings of the 5th International Conference on Micromechanics of Granular Media*, vol. 2, pp. 1311–1315, 2005.

[178] M. Kolonko, S. Raschdorf, and D. Wäsch, "A hierarchical approach to simulate the packing density of particle mixtures on a computer," *Granular Matter*, vol. 12, no. 6, pp. 629–643, 2010.

[179] M. Djurić, R. Marinković-Nedučin, J. Ranogajec, and M. Radeka, "Particle size range as a factor influencing compressibility of ceramic powder," *Ceramics International*, vol. 21, no. 4, pp. 227–230, 1995.

[180] P. M. Chaikin, A. Donev, W. Man, F. H. Stillinger, and S. Torquato, "Some observations on the random packing of hard ellipsoids," *Industrial and Engineering Chemistry Research*, vol. 45, no. 21, pp. 6960–6965, 2006.

[181] B. C. Aschenbrenner, "A new method of expressing particle sphericity," *Journal of Sedimentary Research*, vol. 26, pp. 15–31, 03 1956.

[182] M. Reisi and D. M. Nejad, "A Numerical Method to Predict Packing Density of Aggregates in Concrete," *Advanced Materials Research*, vol. 337, pp. 313–316, 2011.

[183] R. P. Behringer, "Jamming in granular materials," *Comptes Rendus Physique*, vol. 16, no. 1, pp. 10–25, 2015.

[184] U. K. Deiters, ""Coordination numbers for rigid spheres of different sizes-estimating the number of next-neighbour interactions in a mixture" by G.H. Eduljee," *Fluid Phase Equilibria*, vol. 12, no. 1-2, pp. 193–197, 1983.

[185] S. F. Edwards and R. B. Oakeshott, "Theory of powders," *Physica A: Statistical Mechanics and its Applications*, vol. 157, no. 3, pp. 1080–1090, 1989.

[186] S. McNamara, P. Richard, S. K. De Richter, G. Le Caër, and R. Delannay, "Measurement of granular entropy," *Physical Review E - Statistical, Nonlinear, and Soft Matter Physics*, vol. 80, no. 3, pp. 1–14, 2009.

[187] J. L. Finney and L. V. Woodcock, "Renaissance of Bernal's random close packing and hypercritical line in the theory of liquids," *Journal of Physics Condensed Matter*, vol. 26, no. 46, 2014.

[188] M. Schröter and K. E. Daniels, "Granular segregation in dense systems: the role of statistical mechanics and entropy," pp. 1–16, 2012.

[189] S. M. Iveson and J. D. Litster, "Fundamental studies of granule consolidation. Part 2: Quantifying the effects of particle and binder properties," *Powder Technology*, vol. 99, no. 3, pp. 243–250, 1998.

441

[190] P. Parafiniuk, M. Bańda, M. Stasiak, J. Horabik, J. Wiącek, and M. Molenda, "Effect of aspect ratio on the mechanical behavior of packings of spheroids," *Physica A: Statistical Mechanics and its Applications*, vol. 501, pp. 1–11, 2018.

[191] I. Muthancheri, A. Chaturbedi, A. Bétard, and R. Ramachandran, "A compartment based population balance model for the prediction of steady and induction granule growth behavior in high shear wet granulation," *Advanced Powder Technology*, vol. 32, no. 6, pp. 2085–2096, 2021.

[192] O. R. Arndt, R. Baggio, A. K. Adam, J. Harting, E. Franceschinis, and P. Kleinebudde, "Impact of Different Dry and Wet Granulation Techniques on Granule and Tablet Properties: A Comparative Study," *Journal of Pharmaceutical Sciences*, vol. 107, no. 12, pp. 3143–3152, 2018.

[193] S. P. Forsmo and J. P. Vuori, "The determination of porosity in iron ore green pellets by packing in silica sand," *Powder Technology*, vol. 159, no. 2, pp. 71–77, 2005.

[194] T. Keller, M. Lamandé, S. Peth, M. Berli, J. Y. Delenne, W. Baumgarten, W. Rabbel, F. Radjaï, J. Rajchenbach, A. P. Selvadurai, and D. Or, "An interdisciplinary approach towards improved understanding of soil deformation during compaction," *Soil and Tillage Research*, vol. 128, pp. 61–80, 2013.

[195] S. L. Rough, D. I. Wilson, and D. W. York, "Effect of solids formulation on the manufacture of high shear mixer agglomerates," *Advanced Powder Technology*, vol. 16, no. 2, pp. 145–169, 2005.

[196] S. D. Emsbo-Mattingly and E. Litman, "5 - Polycyclic aromatic hydrocarbon homolog and isomer fingerprinting," in *Standard Handbook Oil Spill Environmental Forensics (Second Edition)* (S. A. Stout and Z. Wang, eds.), pp. 255–312, Boston: Academic Press, second edition ed., 2016.

[197] "Iron ores and direct reduced iron. Determination of size distribution by sieving," standard, International Organization for Standardization, Geneva, CH.

[198] C. Retnhardf, "3 Methods of Characterization 3.1," pp. 27–54, 2001.

[199] F. de Larrard, *Concrete mixture proportioning: A scientific approach*, vol. 9. 1999.

[200] L. X. Liu and J. D. Litster, "Population balance modelling of granulation with a physically based coalescence kernel," *Chemical Engineering Science*, vol. 57, pp. 2183–2191, 2002.

[201] M. Holmes, *A NUMERICAL SIMULATION OF PARTICULATE DISTRIBUTION OF THE BLAST FURNACE RAW MATERIAL BURDEN THROUGH THE PAUL WORTH BELL-LESS TOP APPARATUS Marc Andrew Julien Holmes requirements for the Degree of Doctor of Engineering Swansea University*. PhD thesis, Swansea University, 2015.

[202] L. Bridgeman, "Simulation of Industrial Granular Flow Using Discrete Element Method and its Effects On the Steel Making Operation," *Materials Research*, 2010.

[203] C. Thornton, *Granular Dynamics, Contact Mechanics and Particle System Simulations: A DEM study*, vol. 24. 2015.

[204] A. Carr, *The Application of Non-Spherical Discrete Element Methods to the Blast Furnace*. PhD thesis, Swansea University, 2021.

[205] Y. Yu and H. Saxén, "Flow of pellet and coke particles in and from a fixed chute," *Industrial and Engineering Chemistry Research*, vol. 51, no. 21, pp. 7383–7397, 2012.

[206] K. F. Malone and B. H. Xu, "Determination of contact parameters for discrete element method simulations of granular systems," *Particuology*, vol. 6, no. 6, pp. 521–528, 2008.

[207] J. J. Myers, "Particle Size Optimization for Reduced Cement High Strength," no. October 2005, 2015.

[208] H. Chen, Y. G. Xiao, Y. L. Liu, and Y. S. Shi, "Effect of Young's modulus on DEM results regarding transverse mixing of particles within a rotating drum," *Powder Technology*, vol. 318, pp. 507–517, 2017.

[209] T. Trung Vo, S. Nezamabadi, P. Mutabaruka, J. Y. Delenne, E. Izard, R. Pellenq, and F. Radjai, "Agglomeration of wet particles in dense granular flows," *European Physical Journal E*, vol. 42, no. 9, 2019.

[210] P. Darabi, K. Pougatch, M. Salcudean, and D. Grecov, "A novel coalescence model for binary collision of identical wet particles," *Chemical Engineering Science*, vol. 64, no. 8, pp. 1868–1876, 2009.

[211] H. N. G. Nguyen, O. Millet, and G. Gagneux, "Exact calculation of axisymmetric capillary bridge properties between two unequal-sized spherical particles," *Mathematics and Mechanics of Solids*, vol. 24, no. 9, pp. 2767–2784, 2018.

[212] D. Shi and J. J. McCarthy, "Numerical simulation of liquid transfer between particles," *Powder Technology*, vol. 184, no. 1, pp. 64–75, 2008.

[213] K. Washino, K. Miyazaki, T. Tsuji, and T. Tanaka, "A new contact liquid dispersion model for discrete particle simulation," *Chemical Engineering Research and Design*, vol. 110, pp. 123–130, 2016.

[214] A. F. Payam and M. Fathipour, "A capillary force model for interactions between two spheres," *Particuology*, vol. 9, no. 4, pp. 381–386, 2011.

[215] G. Lian and J. Seville, "The capillary bridge between two spheres: New closed-form equations in a two century old problem," *Advances in Colloid and Interface Science*, vol. 227, pp. 53–62, 2016.

[216] K. D. Danov, M. T. Georgiev, P. A. Kralchevsky, G. M. Radulova, T. D. Gurkov, S. D. Stoyanov, and E. G. Pelan, "Hardening of particle/oil/water suspensions due to capillary bridges: Experimental yield stress and theoretical interpretation," *Advances in Colloid and Interface Science*, vol. 251, pp. 80–96, jan 2018.

[217] Y. G. Tselishchev and V. A. Val'tsifer, "Influence of the type of contact between particles joined by a liquid bridge on the capillary cohesive forces," *Colloid Journal of the Russian Academy of Sciences: Kolloidnyi Zhurnal*, vol. 65, no. 3, pp. 385–389, 2003.

[218] Y. Chen, Y. Zhao, H. Gao, and J. Zheng, "Liquid bridge force between two unequal-sized spheres or a sphere and a plane," *Particuology*, vol. 9, no. 4, pp. 374–380, 2011.

[219] M. J. Adams, S. A. Johnson, J. P. Seville, and C. D. Willett, "Mapping the influence of gravity on pendular liquid bridges between rigid spheres," *Langmuir*, vol. 18, no. 16, pp. 6180–6184, 2002.

[220] K. P. Hapgood and B. Khanmohammadi, "Granulation of hydrophobic powders," *Powder Technology*, vol. 189, no. 2, pp. 253–262, 2009.

[221] D. Lievano, S. Velankar, and J. J. McCarthy, "The rupture force of liquid bridges in two and three particle systems," *Powder Technology*, vol. 313, pp. 18–26, 2017.

[222] T. T. Vo, P. Mutabaruka, S. Nezamabadi, J. Y. Delenne, E. Izard, R. Pellenq, and F. Radjai, "Mechanical strength of wet particle agglomerates," *Mechanics Research Communications*, vol. 92, pp. 1–7, 2018.

445

[223] E. J. Pavlina and C. J. Van Tyne, "Correlation of Yield strength and Tensile strength with hardness for steels," *Journal of Materials Engineering and Performance*, vol. 17, no. 6, pp. 888–893, 2008.

[224] P. Zhang, S. X. Li, and Z. F. Zhang, "General relationship between strength and hardness," *Materials Science and Engineering A*, vol. 529, no. 1, pp. 62–73, 2011.

[225] V. Vivacqua and M. Ghadiri, "Modelling of auto-agglomeration of cohesive powders," *Chemical Engineering Research and Design*, vol. 133, pp. 137–141, 2018.

[226] A. H. Cottrell, "A theory of work softening," *Philosophical Magazine Letters*, vol. 81, no. 1, pp. 23–28, 2001.

[227] T. T. Vo, P. Mutabaruka, J. Y. Delenne, S. Nezamabadi, and F. Radjai, "Strength of wet agglomerates of spherical particles: Effects of friction and size distribution," *EPJ Web of Conferences*, vol. 140, 2017.

[228] S. Khamseh, J. N. Roux, and F. Chevoir, "Flow of wet granular materials: A numerical study," *Physical Review E - Statistical, Nonlinear, and Soft Matter Physics*, vol. 92, no. 2, pp. 1–19, 2015.

[229] S. M. Iveson, J. D. Litster, and B. J. Ennis, "Fundamental studies of granule consolidation part 1: Effects of binder content and binder viscosity," *Powder Technology*, vol. 88, no. 1, pp. 15–20, 1996.

[230] "A glossary of terms used in chemical kinetics, including reaction dynamics (iupac recommendations 1996)," *Pure and Applied Chemistry*, vol. 68, no. 1, pp. 149–192, 1996.

[231] M. Nicodemi, "Dynamical response functions in models of vibrated granular media," *Physical Review Letters*, vol. 82, no. 19, pp. 3734–3737, 1999.

[232] L. A. Pugnaloni, I. Sánchez, P. A. Gago, J. Damas, I. Zuriguel, and D. Maza, "Towards a relevant set of state variables to describe static granular packings," *Physical Review E - Statistical, Nonlinear, and Soft Matter Physics*, vol. 82, no. 5, pp. 1–4, 2010.

[233] M. I. Khan and G. I. Tardos, "Stability of wet agglomerates in granular shear flows," *Journal of Fluid Mechanics*, vol. 347, pp. 347–368, 1997.

[234] C. Song, P. Wang, and H. A. Makse, "A phase diagram for jammed matter," *Nature*, vol. 453, no. 7195, pp. 629–632, 2008.

[235] S. M. Iveson, "Granule coalescence modelling: Including the effects of bond strengthening and distributed impact separation forces," *Chemical Engineering Science*, vol. 56, no. 6, pp. 2215–2220, 2001.

[236] J. Shabanian, M. A. Duchesne, A. Runstedtler, M. Syamlal, and R. W. Hughes, "Improved analytical energy balance model for evaluating agglomeration from a binary collision of identical wet particles," *Chemical Engineering Science*, vol. 223, p. 115738, 2020.

[237] F. Štěpánek, P. Rajniak, C. Mancinelli, R. T. Chern, and R. Ramachandran, "Distribution and accessibility of binder in wet granules," *Powder Technology*, vol. 189, no. 2, pp. 376–384, 2009.

[238] J. Jamari and D. J. Schipper, "Experimental investigation of fully plastic contact of a sphere against a hard flat," *Journal of Tribology*, vol. 128, no. 2, pp. 230–235, 2006.

[239] K. L. Johnson, K. Kendall, and A. D. Roberts, "Surface energy and the contact of elastic solids," *Proceedings of the Royal Society of London. A. Mathematical and Physical Sciences*, vol. 324, no. 1558, pp. 301–313, 1971.

[240] E. Barthel, "Adhesive elastic contacts – JKR and more," *Journal of Physics D: Applied Physics*, vol. 41, p. 163001, 2008. http://stacks.iop.org/0022-3727/41/163001.

[241] C. Thornton and Z. Ning, "A theoretical model for the stick/bounce behaviour of adhesive, elastic- plastic spheres," *Powder Technology*, vol. 99, no. 2, pp. 154–162, 1998.

[242] W. K. Walls, J. Thompson, and S. Brown, "Towards a unified theory of wet agglomeration," *Powder Technology*, p. 117519, 2022.

[243] I. Goldhirsch, "Introduction to granular temperature," *Powder Technology*, vol. 182, no. 2, pp. 130–136, 2008.

[244] M. Börner, M. Michaelis, E. Siegmann, C. Radeke, and U. Schmidt, "Impact of impeller design on high-shear wet granulation," *Powder Technology*, vol. 295, pp. 261–271, 2016.

[245] S. Bellinghausen, E. Gavi, L. Jerke, P. K. Ghosh, A. D. Salman, and J. D. Litster, "Nuclei size distribution modelling in wet granulation," *Chemical Engineering Science: X*, vol. 4, p. 100038, 2019.

[246] B. Waldie, "Growth mechanism and the dependence of granule size on drop size in fluidized-bed granulation," *Chemical Engineering Science*, vol. 46, no. 11, pp. 2781–2785, 1991.

[247] R. M. Smith, L. X. Liu, and J. D. Litster, "Breakage of drop nucleated granules in a breakage only high shear mixer," *Chemical Engineering Science*, vol. 65, no. 21, pp. 5651–5657, 2010.

[248] S. A. L. de Koster, "Experimental investigation and modelling of consolidation and layering mechanisms in high-shear granulation," no. April, 2018.

[249] D. Feys, R. Cepuritis, S. Jacobsen, K. Lesage, E. Secrieru, and A. Yahia, "Measuring Rheological Properties of Cement Pastes: Most common Techniques, Procedures and Challenges," *RILEM Technical Letters*, vol. 2, pp. 129–135, 2017.

[250] G. Girskas and D. Nagrockienė, "the Effect of Synthetic Zeolite on the Viscosity of Cement Paste / Sintetinio Ceolito Priedo Itaka Cemento Tešlos Klampumui," *Engineering Structures and Technologies*, vol. 4, no. 4, pp. 119–124, 2013.

[251] T. R. Knapp, "Bimodality revisited," *Journal of Modern Applied Statistical Methods*, vol. 6, no. 1, pp. 8–20, 2007.

Appendices

Appendix A

Maths Appendix

A.1 Maximum Pendular case

Volume of the bridge:

$$V^* = 0.1 = \frac{V_l}{R_1{}^3} \tag{A.1}$$

Volume of the spheres, assuming $R_1 = R_2 = R$:

$$V_s = 2 \times \frac{4}{3}\pi R^3 \tag{A.2}$$

Finding $V_{l/s}$

$$\frac{V_s \times 3}{2 \times 4 \times \pi} = R^3 \tag{A.3}$$

$$R^3 = \frac{V_l}{0.1} \tag{A.4}$$

$$\frac{3 \times 0.1}{8\pi} = \frac{V_l}{V_s} = V_{l/s} = \frac{0.3}{8\pi} \approx 0.012 \tag{A.5}$$

A.2 Plastic deformation integration

$$E_p = \int_0^{\delta^*} Q d\delta = \frac{p_0 \pi \widetilde{R} \delta^{*2}}{2} \tag{A.6}$$

A.3 Gravity potential energy integration

This finds the change in GPE as a sphere deforms under its own weight into a spherical cap. The volume is assumed to be approximately the same, as otherwise the radius would then be a function of δ as well.

$$E_g = mgh = \rho g V h = \rho g \int_\delta^{2R} V dh = \rho g \int_\delta^{2R} \frac{\pi}{3}(4R^3 - 3Rh^2 + h^3)dh \quad \text{(A.7)}$$

$$\rho g \frac{\pi}{3} \int_\delta^{2R} (4R^3 - 3Rh^2 + h^3)dh = \frac{\rho g \pi}{3} {\left[4R^3 h - Rh^3 + \frac{h^4}{4} \right]}_h^{2R} \quad \text{(A.8)}$$

$$\frac{\rho g \pi}{3} {\left[4R^3 h - Rh^3 + \frac{h^4}{4} \right]}_h^{2R} =$$
$$\frac{\rho g \pi}{3} \left(\left(8R^4 - R8\delta^3 + \frac{16\delta^4}{4} \right) - \left(4R^3\delta - R\delta^3 + \frac{\delta^4}{4} \right) \right) =$$
$$\frac{\rho g \pi}{3} \left(4Rh^4 - 4Rh^3\delta + R\delta^3 - \frac{\delta^4}{4} \right) = E_g \quad \text{(A.9)}$$

A.4 GPE/PDE re-arrangement

$$\frac{E_g}{E_p} = \frac{\frac{\rho g \pi}{3} \left(4R^4 - 4R^3\delta + R\delta^3 - \frac{\delta^4}{4} \right)}{p_0 \pi R \delta^2} \quad \text{(A.10)}$$

The when $E_g = E_p$,

$$\frac{\rho g \pi}{3} \left(4R^4 - 4R^3\delta + R\delta^3 - \frac{\delta^4}{4} \right) = p_0 \pi R \delta^2 \quad \text{(A.11)}$$

noting that

$$\varepsilon = \frac{\delta}{R} \quad \text{(A.12)}$$

gives

$$\frac{4R^4 - 4R^3\delta + R\delta^3 - \frac{\delta^4}{4}}{r\delta^2} = \frac{4R^4}{R\delta^2} - \frac{4R^3\delta}{R\delta^2} + \frac{R\delta^3}{R\delta^2} - \frac{\frac{\delta^4}{4}}{R\delta^2} = \frac{3p_0}{\rho g} \qquad (A.13)$$

$$\frac{4r^3}{\delta^2} - \frac{4R^2}{\delta} + \frac{\delta}{1} - \frac{1}{4}\frac{\delta^2}{r} = \frac{3p_0}{\rho g} \qquad (A.14)$$

Divide both sides through by R, noting that $R = D$ and that $p_0 = K_\varphi \sigma_y$,

$$\frac{6\sigma_y K_\varphi}{\rho g D} = \frac{4}{\varepsilon^2} - \frac{4}{\varepsilon} + \varepsilon - \frac{\varepsilon^2}{4} \qquad (A.15)$$

$$. \qquad (A.16)$$

A.5 Butensky Simplification

beginning with the original equation in [41]

$$\frac{1}{\overline{d_{g/p}}} = \frac{1}{K_g} - \frac{1}{K_g f^{\frac{1}{3}}} \frac{m_{l/s}^{\frac{1}{3}}}{\left(m_{l/s_\infty}^{\frac{1}{3}}\right)} \qquad (A.17)$$

$$\frac{1}{\overline{d_{g/p}}} = \frac{1}{K_g}\left(1 - \frac{1}{f^{\frac{1}{3}}}\left(\frac{\frac{m_{l/s}}{m_{l/s_\infty}}}{f}\right)^{\frac{1}{3}}\right) \qquad (A.18)$$

$$\overline{d_{g/p}} = \frac{K_g}{\left(1 - \left(\frac{m_{l/s}}{m_{l/s_\infty}}\right)^{\frac{1}{3}}\right)} \qquad (A.19)$$

f describes the amount of internal volume which is occupied by voidage within a given granule, and its meaning is captured within the subsequent K_{Smax}. K_{Smax} is the maximum saturation that the granule can contain before the liquid begins to emerge to the surface, which corresponds to the oversaturated state. This does not neccesarily equal 1, due to internal air pockets etc.

$$m_{l/s} = \frac{\rho_l V_l}{\rho_s V_s}, \; m_{l/s_\infty} = \frac{\rho_l V_{lmax}}{\rho_s V_s} = \frac{\rho_l V_{lmax}}{\rho_s V_s} \qquad (A.20)$$

453

noting that $\overline{d_{g/p}}$ is final granule size to particle size ratio

$$\overline{d_{g/p}} = \frac{\Delta_{limCoh}}{d_p} \tag{A.21}$$

$$S = \frac{V_l}{V_\epsilon}, V_l = V_\epsilon S \tag{A.22}$$

$$\frac{\Delta_{limCoh}}{d_p} = \frac{K_g}{\left(1 - \left(\frac{\frac{\rho_l V_l}{\rho_s V_s}}{\frac{\rho_l V_{lmax}}{\rho_s V_s}}\right)^{\frac{1}{3}}\right)} \tag{A.23}$$

S is the liquid saturation of the pores, which can be defined as

$$\frac{\Delta_{limCoh}}{d_p} = \frac{K_g}{\left(1 - \left(\frac{\rho_L}{\rho_s}\right)^{\frac{1}{3}} \left(\frac{\frac{V_\epsilon S}{V_s}}{\frac{V_\epsilon K_{Smax}}{V_s}}\right)^{\frac{1}{3}}\right)} \tag{A.24}$$

$$\frac{\Delta_{limCoh}}{d_p} = \frac{K_g}{\left(1 - \left(\frac{V_\epsilon S}{V_\epsilon K_{Smax}}\right)^{\frac{1}{3}}\right)} \tag{A.25}$$

$$\Delta_{limCoh} = \frac{K_g d_p}{\left(1 - \left(\frac{S}{K_{Smax}}\right)^{\frac{1}{3}}\right)} \tag{A.26}$$

A.6 Kinetic energy area of contact

Since

$$Q = p_0 \pi \widetilde{R} \delta \tag{A.27}$$

With $\widetilde{R}$ being the harmonic mean of the radii The following can be found (δ^* being the final deformation)

$$\int_0^{\delta^*} Q d\delta = \frac{p_0 \pi \widetilde{R} \delta^{*2}}{2} = E_p \tag{A.28}$$

This then allows the area to be found through the relation

$$Q = p_0 \pi a^2 \tag{A.29}$$

Where a is the radius of the area of contact. Since the force at depth δ^* is

$$Q^* = \pi p_0 \widetilde{R} \delta^* \tag{A.30}$$

Therefore

$$\delta^* = \frac{Q^*}{p_0 \pi \widetilde{R}} \tag{A.31}$$

To find the final force, and hence, the final area of contact:

$$\frac{1}{2} V_{cN}^2 \widetilde{m} = \frac{p_0 \pi \widetilde{R} \left(\frac{Q^*}{p_0 \pi \widetilde{R}} \right)^2}{2} = \frac{Q^{*2}}{2 p_0 \pi \widetilde{R}} \tag{A.32}$$

$$Q^* = V_{cN} \left(\widetilde{m} p_0 \pi \widetilde{R} \right)^{\frac{1}{2}} = V_{cN} \sqrt{\widetilde{R} \widetilde{R^3}} \sqrt{\frac{4\pi}{3} \rho p_0 \pi} \tag{A.33}$$

The harmonic mean of the masses of the particles is separated to get the harmonic mean of the radii cubed, which will be necessary later when determining the limiting diameter. Allowing $p_0 = K_\varphi \sigma_y$, and re-arranging, gives

$$\pi a^{*2} = \pi \sqrt{\frac{4}{3}} \sqrt{\frac{\rho}{K_\varphi \sigma_y}} V_{cN} \sqrt{\widetilde{R} \widetilde{R^3}} = A \tag{A.34}$$

A.7 Rearrangement of Bond Limit Equation

Substituted form of the bond limit equation:

$$K_{\frac{t}{c}} \sigma_y \alpha_{wet} \left(\varepsilon_r \right) > \frac{3 \frac{K_\alpha \rho_g V_{ch}^2}{\lambda_{ch}} \left(\frac{\widehat{D}}{\overline{\overline{D}}} \right)^{2K_\gamma} \overline{D}^4}{4\pi^{\frac{3}{2}} \left(\pi \sqrt{\frac{4}{3}} \sqrt{\frac{\rho_g}{K_\varphi \sigma_y}} V_{cN} \sqrt{\widetilde{R} \widetilde{R^3}} \right)^{\frac{3}{2}}} \tag{A.35}$$

Expanding this gives:

$$K_{\frac{t}{c}} \sigma_y \alpha_{wet} \left(\varepsilon_r \right) > \frac{3}{4\pi^{\frac{3}{2}} \left(\sqrt{\frac{4}{3}} \pi \right)^{\frac{3}{2}}} \frac{K_\alpha \rho_g}{\left(\sqrt{\frac{\rho_g}{K_\varphi \sigma_y}} \right)^{\frac{3}{2}}} \frac{\frac{V_{ch}^2}{\lambda_{ch}}}{V_{cN}^{\frac{3}{2}}} \left(\frac{\widehat{D}}{\overline{\overline{D}}} \right)^{2K_\gamma} \frac{\overline{D}^4}{\sqrt{\widetilde{R} \widetilde{R^3}}^{\frac{3}{2}}} \tag{A.36}$$

Note that

$$\widetilde{R} = \frac{\widetilde{D}}{2}, \ \ \widetilde{R^3} = \frac{\widetilde{D^3}}{2^3} \tag{A.37}$$

$$K_{\frac{t}{c}}\sigma_y\alpha_{wet}\left(\varepsilon_r\right) > \frac{3\times^3}{4\pi^{\frac{3}{2}}\left(\sqrt{\frac{4}{3}}\pi\right)^{\frac{3}{2}}} \frac{K_\alpha\rho_g}{\left(\sqrt{\frac{\rho_g}{K_\varphi\sigma_y}}\right)^{\frac{3}{2}}} \frac{\frac{V_{ch}^2}{\lambda_{ch}}}{V_{cN}^{\frac{3}{2}}} \left(\frac{\widehat{D}}{\overline{\overline{D}}}\right)^{2K_\gamma} \frac{\overline{D}^4}{\left(\widetilde{D}\widetilde{D^3}\right)^{\frac{3}{4}}} \tag{A.38}$$

Arranging with diameters as focus, and noting that

$$\left(\widetilde{D}\widetilde{D^3}\right)^{\frac{3}{4}} = \left(\frac{2dD}{\left(d+D\right)}\frac{2d^3D^3}{\left(D^3+d^3\right)}\right)^{\frac{3}{4}} =$$
$$\left(\frac{2\widehat{D}^2}{2\overline{D}}\frac{2(\widehat{D})^{2^3}}{2\overline{D^3}}\right)^{\frac{3}{4}} = \left(\frac{\widehat{D}^2}{\overline{D}}\frac{\widehat{D}^6}{\overline{D^3}}\right)^{\frac{3}{4}} = \frac{\widehat{D}^6}{\left(\overline{D}\overline{D^3}\right)^{\frac{3}{4}}} \tag{A.39}$$

$$\left(\frac{\widehat{D}}{\overline{\overline{D}}}\right)^{2K_\gamma} \frac{\overline{D}^4}{\frac{\widehat{D}^6}{\left(\overline{D}\overline{D^3}\right)^{\frac{3}{4}}}} < K_{\frac{t}{c}}\sigma_y\alpha_{wet}\left(\varepsilon_r\right) \frac{4\pi^{\frac{3}{2}}\left(\sqrt{\frac{4}{3}}\pi\right)^{\frac{3}{2}}\left(\sqrt{\frac{\rho_g}{K_\varphi\sigma_y}}\right)^{\frac{3}{2}}}{3\times 2^3} \frac{\lambda_{ch}V_{cN}^{\frac{3}{2}}}{K_\alpha\rho_g} \frac{V_{cN}^{\frac{3}{2}}}{V_{ch}^2} \tag{A.40}$$

Another re-arrangement to get like variables together, and to group the mathematical constants into a single value C_m gives

$$\left(\frac{\widehat{D}}{\overline{\overline{D}}}\right)^{2K_\gamma} \frac{\overline{D}^4\left(\overline{D}\overline{D^3}\right)^{\frac{3}{4}}}{\widehat{D}^6} < C_m\frac{K_{\frac{t}{c}}}{K_\alpha K_\varphi^{\frac{3}{4}}}\alpha_{wet}\left(\varepsilon_r\right)\frac{\sigma_y}{\sigma_y^{\frac{3}{4}}}\frac{\rho_g^{\frac{3}{4}}}{\rho_g}\frac{V_{cN}^{\frac{3}{2}}}{V_{ch}^2}\lambda_{ch} \tag{A.41}$$

Dividing through gives:

$$\left(\frac{\widehat{D}}{\overline{\overline{D}}}\right)^{2K_\gamma-4} \frac{\left(\overline{D}\overline{D^3}\right)^{\frac{3}{4}}}{\widehat{D}^2} < C_m\frac{K_{\frac{t}{c}}}{K_\alpha K_\varphi^{\frac{3}{4}}}\alpha_{wet}\frac{\sigma_y^{\frac{1}{4}}}{\rho_g^{\frac{1}{4}}}\frac{V_{cN}^{\frac{3}{2}}}{V_{ch}^2}\lambda_{ch} \tag{A.42}$$

A.8 Finding the bond limit

Base form of the bond limit equation:

$$\left(\frac{\widehat{D}}{\overline{\overline{D}}}\right)^{2K_\gamma-4} \frac{\left(\overline{D}\overline{D^3}\right)^{\frac{3}{4}}}{\widehat{D}^2} < C_m\frac{K_{\frac{t}{c}}}{K_\alpha K_\varphi^{\frac{3}{4}}}\alpha_{wet}\frac{\sigma_y^{\frac{1}{4}}}{\rho_g^{\frac{1}{4}}}\frac{V_{cN}^{\frac{3}{2}}}{V_{ch}^2}\lambda_{ch} \tag{A.43}$$

With $d = r_d D$, the various means are:

$$\overline{D} = \frac{D + r_d D}{2} = \frac{D}{2}(1 + r_d), \ \ \widehat{D} = (Dr_d D)^{\frac{1}{2}} = Dr_d^{\frac{1}{2}} \quad \text{(A.44)}$$

This allows the re-arrangement of the left hand side of Eq. A.43 through the following steps:

$$\left(\frac{\widehat{D}}{\overline{\overline{D}}}\right)^{2K_\gamma - 4} \frac{\left(\overline{D}D^3\right)^{\frac{3}{4}}}{\widehat{D}^2} =$$

$$\left(\frac{Dr_d^{\frac{1}{2}}}{\frac{D}{2}(1 + r_d)}\right)^{2K_\gamma - 4} \frac{\left(\frac{D}{2}(1 + r_d)\frac{D^3}{2}(1 + r_d^3)\right)^{\frac{3}{4}}}{\left(Dr_d^{\frac{1}{2}}\right)^2} =$$

$$\left(\frac{r_d^{\frac{1}{2}}}{\frac{(1+r_d)}{2}}\right)^{2K_\gamma - 4} \frac{\frac{D^3}{2}\left((1 + r_d)(1 + r_d^3)\right)^{\frac{3}{4}}}{D^2 r_d} =$$

$$\frac{(1 + r_d^3)^{\frac{3}{4}}}{(1 + r_d)^{2K_\gamma - 3\frac{1}{4}}} r_d{}^{K_\gamma - 3} D =$$

$$\left(\frac{(1 + r_d^3)}{(1 + r_d)}\right)^{\frac{3}{4}} \frac{r_d{}^{K_\gamma - 3}}{(1 + r_d)^{2K_\gamma - 4}} D \quad \text{(A.45)}$$

D is by definition the size of the larger of the two granules being merged. This means that the total diameter of granule that is formed by the merger of the two granules being merged is

$$D(1 + r_d)^{\frac{1}{3}} = \Delta_{lim\,Adh} \quad \text{(A.46)}$$

so

$$\frac{\Delta_{lim\,Adh}}{(1 + r_d)^{\frac{1}{3}}} = D \quad \text{(A.47)}$$

Applying the steps in A.45 to Eq. A.43 and substituting A.47 gives

$$\left(\frac{(1 + r_d^3)}{(1 + r_d)}\right)^{\frac{3}{4}} \frac{r_d{}^{K_\gamma - 3}}{(1 + r_d)^{2K_\gamma - 4}} \frac{\Delta_{lim\,Adh}}{(1 + r_d)^{\frac{1}{3}}} < C_m \frac{K_{\frac{t}{c}}}{K_\alpha K_\varphi^{\frac{3}{4}}} \alpha_{wet} \frac{\sigma_y^{\frac{1}{4}}}{\rho_g^{\frac{1}{4}}} \frac{V_{cN}^{\frac{3}{2}}}{V_{ch}^2} \lambda_{ch} \quad \text{(A.48)}$$

457

$$r_d{}^{K_\gamma - 3} \left(1 + r_d{}^3\right)^{\frac{3}{4}} \frac{(1 + r_d)^{2\frac{11}{12}}}{(1 + r_d)^{2K_\gamma}} \Delta_{lim\,Adh} < C_m \frac{K_{\frac{t}{c}}}{K_\alpha K_\varphi^{\frac{3}{4}}} \alpha_{wet} \frac{\sigma_y^{\frac{1}{4}}}{\rho_g^{\frac{1}{4}}} \frac{V_{cN}^{\frac{3}{2}}}{V_{ch}^2} \lambda_{ch} \qquad (A.49)$$

$$\Delta_{lim\,Adh} < C_m \frac{K_{\frac{t}{c}}}{K_\alpha K_\varphi^{\frac{3}{4}}} \alpha_{wet} \frac{\sigma_y^{\frac{1}{4}}}{\rho_g^{\frac{1}{4}}} \frac{V_{cN}^{\frac{3}{2}}}{V_{ch}^2} \lambda_{ch} \frac{(1 + r_d)^{2K_\gamma - 2\frac{11}{12}}}{r_d{}^{K_\gamma - 3} \left(1 + r_d{}^3\right)^{\frac{3}{4}}} \qquad (A.50)$$

Appendix B

Future researcher help

Guidance for future researchers of this topic. Has guidance on what to keep an eye out during your research.

B.1   research families

The 7 primary families of research that I could determine during the project and through the literature, and their focusses.

B.1.1   Iveson family

Iveson, Hapgood, Ennis, Litster, R. Smith, Liu Stokes Criterion, focus on stepwise processes. Discrete processes of nucleation, growth, breakage important.

B.1.2   Schaefer family

Schaefer, Ritala, Holm, Kristensen Pharmaceutical research, methodical, excellent work overall

B.1.3 Tardos family

Mort, Tardos, Khan Have some links to Iveson family, but not much. (Tardos and Hapgood have co-authored a paper) Critical parameters, holistic view of the process

B.1.4 Hounslow family

P. K. Le, Avontuur, Hounslow, Reynolds Lot more diverse, much heavier focus on the kinetic features and analytically defining things. Also a lot of work on population balance models.

B.1.5 Tanaka Family

Tanaka, Ouchiyama in 70's, newer co-authors include Washino, E. L. Chan, Miyazaki, Tsuji.

Ouchiyama put significant emphasis on the disaggregation of partial bonded bridges. But other physical considerations for the general physical model.

B.1.6 Watano family

Watano, Takashima, Miyanami, Sato, Hiroyuki, Nakamura, Fujii. Generally most notable work is scale up series. Other work generally on scaling processes.

B.1.7 Ramachandran family

Ramachandran, Chaudhury, Štěpánek, Oka, Fu-Yang Wang, Cameron, Bétard, Cameron, Sanders, Glaser, Immanuel, Doyle III, Poon, Muzzio

Some collaboration with Litster.

Very large collaborative works, modelling lots of properties at once to control the output products, favour population balance modelling but include DEM work as well, and compare to produced outputs.

B.2 Important Reviews

The important reviews on the topic, and what to watch out for, what they do and don't contain.

B.2.1 Mechanical properties of agglomerates

[36] - Practical granular mechanical behaviour review, whcih also includes much of the theoretical work for the time, doesn't include ivesons work on the topic that comes shortly after.

B.2.2 Nucleation, growth and breakage phenomena in agitated wet granulation processes: A review

[37] - Nucleation agglomeration and breakage review - Nucleation, growth and breakage phenomena in agitated wet granulation processes: A review - Be very aware that this review is not neutral despite being well written to appear as if it is simply presenting the best solution available. The researchers are invested in the Stokes Criterion model, which is why it specifically separates the processes as it does. As such it glosses over some research which is contradictory or does not examine them in great detail. It is still useful as a general rule but should be used with caution. Has had a huge impact on the literature, likely because of the separation of the phases, which can then be studied atomically, and the ease of access of the review.

B.2.3 Breakage in granulation:A review

[80] - discusses different features to [36]. Breakage reviewed as a phenomena in the agglomeration process, and applies the behaviour as a feature in population balance models, which has the most math heavy part of the review.

B.2.4 Scale-up of binder agglomeration processes

[34] - Mort discusses the range of scales that granulation occurs over, and this is very important to not lose sight of. Very useful, but low on math.

B.2.5 A review of regime maps for granulation

[3] - almost a meta-review, as regime maps tend to be implicitly collections of data. Useful review, as it analyses the work and the consequences of the work.

B.2.6 Wet granular materials

[118] - another useful overview on granular materials and strength, especially the more unclear aspects of it. However, it is an examination of granular materials, not agglomeration or granules.

B.2.7 Review of organic binders for iron ore concentrate agglomeration

[21] - Similar. Does not translate the results to maths other than general trends to expect, though organic binders have more complexity as they will burn off so knowing the ignition temperature is neccesarily useful.

B.3 Lessons regarding computational work

Be very aware of compilation options. Especially when doing high performance work, the compiler options really do alter the behaviour you can expect. Stack overflow can appear not only due to infinite recursion but also simply that the stack doesn't get enough memory allocated, which is very rare without significant recursion but relevant for high performance work and moving large arrays. When using input files to produce consistent outputs, code the output files to be placed

in a new directory, along with a copy of the input file, as it can be very easy to lose.